Investigating the Climatic Impacts of Stratospheric Aerosol Injection

Anthony Crawford Jones

Supervised by
Prof. James M. Haywood
Dr. Andy Jones

Submitted by Anthony Crawford Jones
To the University of Exeter as a thesis
For the degree of Doctor of Philosophy (Mathematics)
In March, 2017

University of Exeter
United Kingdom

I certify that all material in this thesis which is not my own work has been identified and that no material has previously been submitted and approved for the award of a degree by this or any other University.

Signature: ……..

Abstract

In this thesis, we assess various climatic impacts of stratospheric aerosol injection (SAI) – a geoengineering proposal that aims to cool Earth by enhancing the sunlight-reflecting aerosol layer in the lower stratosphere. To this end, we employ simple radiative transfer models, a detailed radiative transfer code (SOCRATES), and two Hadley Centre general circulation models (HadGEM2-CCS and HadGEM2-ES). We find that the use of a light-absorbing aerosol (black carbon) for SAI would result in significant stratospheric warming and an unprecedented weakening of the hydrological cycle. Conversely, we find that SAI with sulphate or titania aerosol could counteract many of the extreme climate changes exhibited by a business-as-usual scenario (RCP8.5) by the end of this century. In a separate investigation, we show that volcanic aerosol dispersion following low-altitude volcanic eruptions can exhibit high sensitivity to the ambient weather state. Volcanic aerosol may get 'trapped' in a single hemisphere or transported to the opposite hemisphere depending simply on the meteorological conditions on the day of the eruption. In a final study, we investigate the impacts of SAI on North Atlantic tropical storm frequency. We find that SAI exclusively promoted in the southern hemisphere would increase North Atlantic storm frequency, and vice versa for northern hemisphere SAI. The results of this thesis should promote further research into SAI, which could conceivably be deployed to maintain global-mean temperature below the COP21 target of +1.5 K above pre-industrial levels, whilst society transitions onto a sustainable energy pathway. Conversely, the possibility of SAI being weaponised, for instance, to specifically increase North Atlantic tropical storm frequency, should motivate policymakers to implement effective regulation and governance to deter unilateral SAI deployments.

Acknowledgements

I thank my supervisors James Haywood and Andy Jones for their assistance throughout the duration of this work, and for their helpful suggestions when reviewing this thesis. I also thank Peter Cox, Steven Rumbold, Florent Malavelle, Steven Hardiman, Angus Ferraro, Valentina Aquila, James Manners, Matthew Hawcroft, Kevin Hodges, Simone Tilmes and Nick Dunstone for their vital assistance at various stages of this work. Lastly, I thank my wife Aimee for her unwavering support and helping me to bring this thesis to fruition.

This work was supported by a Met Office/NERC CASE (ref. 580009183) PhD studentship

Cite as:

Jones, A. C. (2017), Investigating the climatic impacts of stratospheric aerosol injection, PhD dissertation, University of Exeter, Exeter

For the journal-published chapters (4 and 5), it is customary to cite the journal articles

Contents

List of figures and tables

Chapter 1

Chapter 2

Chapter 3

Chapter 4

Chapter 5

Chapter 6

Chapter 7

Abbreviations

AEW	African easterly wave
Al_2O_3	Aluminum oxide (aerosol)
AOD	Aerosol optical depth
AR5	The IPCC's fifth assessment report (2013)
ARF	Adjusted radiative forcing
AVHRR	Advanced Very High Resolution Radiometer (instrument)
BC	Black carbon (aerosol)
BDC	Brewer-Dobson circulation
BECCS	Bioenergy and carbon capture and storage (geoengineering)
CCN	Cloud condensation nuclei
CCS	Carbon capture and storage
CCT	Cirrus cloud thinning (geoengineering)
CDR	Carbon dioxide removal (geoengineeering)
CERES	Clouds and the Earth's Radiant Energy System (satellite)
CFC	Chlorofluorocarbon (gas)
CH	Cerro Hudson (1991 volcanic eruption)
CH_4	Methane (gas)
CLASSIC	Coupled Large-scale Aerosol Simulator for Studies in Climate (model)
CLFR	Cloud fraction
CMIP3 / CMIP5	Coupled model intercomparison projects stage 3 / 5
CO_2	Carbon dioxide (gas)
COP21	2015 United Nations Climate Change Conference in Paris
CRE	Cloud radiative effect
CS_2	Carbon disulphide (gas)
DACS	Direct air capture [of CO_2] and storage (geoengineering)
DJF	December-February season
DMS	Dimethyl sulphide (gas)
ERA-I	ERA-interim reanalyses [Dee *et al*., 2011]
FDH	Fixed Dynamical Heating (model)
G1 / G2 / G3 / G4	GeoMIP geoengineering scenarios [Kravitz *et al.*, 2011]
G4NH/SH	Single-hemisphere geoengineering scenarios [Haywood *et al.*, 2013]
GCM	General circulation model or global climate model
GeoMIP	Geoengineering model intercomparison project
geoSulf /BC/TiO_2	Geoengineering scenarios in Chapter 4
GHG	Greenhouse gas
GMSL	Global-mean sea level
GMST	Global-mean surface temperature
GPE	Global Permafrost Extent

H_2S	Hydrogen sulphide (gas)
H_2SO_4	Sulphuric acid (gas / aerosol)
HadGEM2 / HG2	Hadley Centre Global Environment Model version 2 [Martin *et al*., 2011]
HALOE	HALogen Occultation Experiment (instrument)
HCFC	Hydrofluorocarbon (gas)
HIST	Historical reference periods used in Chapter 4 (1980-2005) and Chapter 6 (1950-2005). Simulations conducted using HadGEM2-CCS and HadGEM2-ES respectively
HURDAT2	Tropical storm "Best track" dataset from the Hurricane Research Division of NOAA (USA)
IN	Ice nuclei
IPCC	Intergovernmental Panel on Climate Change
IRF	Instantaneous radiative forcing
ITCZ	Intertropical convergence zone
IWC	Cloud ice water content
JJA	June-August season
JJASON	June-November season (Chapter 6)
LW	Longwave (radiation spectrum)
LWC	Cloud liquid water content
MCB	Marine cloud brightening (geoengineering)
MDR	(Hurricane) Main Development Region
MetUM	Met Office Unified Model
MIP	Model Intercomparison Project
MMR	Mass mixing ratio (relative to dry air)
MSLR	Mean Sea Level Rise
N_2O	Nitrous oxide (gas)
NAS	US National Academy of Sciences
NH	Northern Hemisphere
NH_3	Methane (gas)
$(NH_4)_2SO_4$	Ammonium sulphate (aerosol)
NIOSH	National Institute for Occupational Safety and Health (USA)
NO_3	Nitrate (aerosol)
NPP	Net Primary Productivity
O_3	Ozone (gas)
OA / POA / SOA	Organic aerosol (primary / secondary)
OC	Organic carbon
OCS	Carbonyl sulphide (gas)
ODS	Ozone-depleting substance
OH	Hydroxyl (free radical)
OIF	Ocean iron fertilisation (geoengineering)
PBAPS	Primary biogenic aerosol particles
PCF	Permafrost-carbon feedback
piControl	Pre-industrial control (~1860) (simulation)

PSC	Polar Stratospheric Cloud
QBO	Quasi-Biennial Oscillation
RCP2.6/4.5/6.0/8.5	Representative Concentration Pathways (no. refers to RF in 2100)
RE	Renewable energy
RF	Radiative forcing
RTE	Radiative transfer equation
SAGE II/_4λ	Stratospheric Aerosol and Gas Experiment v.2 (instrument)
SAI	Stratospheric aerosol injection (geoengineering)
SG	Solar geoengineering (i.e. SRM)
SH	Southern Hemisphere
SiO_2	Silicon dioxide (aerosol)
SO_2	Sulphur dioxide (gas)
SO_4	Sulphate (aerosol)
SOCRATES	Suite Of Community RAdiative Transfer Codes based on Edwards and Slingo (model)
SRM	Solar radiation management (geoengineering)
SS	Sea-salt (aerosol)
SST	Sea-surface temperature
SURF	Earth's surface
SW	Shortwave (radiation spectrum)
TC	Tropical cyclone
TiO_2	Titanium dioxide / titania (aerosol)
TOA	Top of the atmosphere
TOA-Imb	Top of the atmosphere annual and global-mean energy imbalance
TRACK	Kevin Hodges' feature tracking model [Hodges, 1995]
TROP	Tropopause
UKCA	United Kingdom Chemistry and Aerosol (model and group)
UKESM1	United Kingdom Earth System Model vn.1
UNFCCC	United Nation's Framework Convention on Climate Change
UV	Ultraviolet (radiation spectrum)
UV_{ERY}	Ultraviolet radiation weighted by erythemal action spectrum
VSL	Very Short Lived [Halogens] (gas)
WGII/III	IPCC Working Group (III – mitigation, II – adaptation)
WRST	Wilcoxon rank sum test

Introduction

The Intergovernmental Panel on Climate Change's (IPCC) 5th assessment report (AR5) provides compelling evidence of the extent of recent global warming and related climate changes. Global warming is primarily the result of the accumulation in the atmosphere of greenhouse gases (GHG) released as by-products of anthropogenic processes [IPCC, 2013]. Recent international efforts to mitigate GHG emissions have been vociferous but largely ineffective, which is exemplified by a 54% increase of global carbon dioxide (CO_2) emissions between 1990 and 2011 [IPCC, 2013]. This insufficient mitigation, coupled with projections of severe climate changes in the future, has led to the development of alternative strategies for dealing with climate change. One such strategy is adaptation, which aims to reduce the impacts of climate change, while another strategy is geoengineering, defined as the intentional large-scale manipulation of the environment with the aim of reducing global warming [Keith, 2000]. Geoengineering can be broadly split into two categories: methods that aim to sequester atmospheric CO_2 in an inert form - carbon dioxide removal (CDR) methods, and methods that aim to reflect more sunlight back to space - solar radiation management (SRM) or alternatively solar geoengineering (SG) methods [Shepherd, 2009]. A widely researched SRM proposal is stratospheric aerosol injection (SAI), which aims to cool the Earth by enhancing the reflective aerosol layer in the stratosphere.

In this thesis, the climatic impacts of SAI will be explored for scenarios in which sulphate (SO_4), black carbon (BC), and titania (TiO_2) aerosols are injected into the stratosphere. Additionally, the related phenomena of volcanic eruptions will be investigated. In Chapter 1, we present an overview of global warming and climate change, followed by an assessment of mitigation, adaptation, and geoengineering. In Chapter 2, simple energy balance models are employed to investigate the radiative effects of various stratospheric aerosol layers. In Chapter 3, a detailed radiation code is employed to assess the radiative effects of various stratospheric aerosol layers in further detail. In Chapter 4, we present the results of general circulation model (GCM) simulations of SAI with SO_4, BC, and TiO_2 injection against a high GHG-concentrations scenario. In Chapter 5, we present the results of GCM simulations of large-scale volcanic eruptions. In Chapter 6, we investigate the impacts of SAI on

North Atlantic tropical cyclone (TC) frequency. In Chapter 7, we summarise the results of this thesis and discuss future research for understanding the climatic impacts of SAI.

Chapter 1 An overview of global warming, climate change, and geoengineering

1.1. Global warming

1.1.1. Earth's energy balance

In order to discuss global warming, it is first necessary to describe Earth's energy balance and the factors controlling the climate. The term 'climate' refers to the complete distribution of weather events in a region over some time period, which includes the average weather state and the extreme weather events. Often climate is represented by a selection of variables such as temperature, pressure and precipitation [Seinfeld and Pandis, 1998]. 'Climate change' refers to a divergent trend in a climatic variable over some timescale greater than an averaging timescale; the classical averaging period is 30 years [Seinfeld and Pandis, 1998]. Climate change can refer to changes to the average weather state or to changes to variability, including the frequency of extreme events. An imposed climate change is unlikely to be exclusive to one climatic variable due to the relationships that exist between different components of the climate system [Trenberth, 2011].

Climate is the product of the absorption of solar energy by components of the Earth system, and the subsequent redistribution of the energy as radiation or as latent and dynamical heat transfer within the atmosphere, land and oceans [Gill, 1982]. Climate change is caused by changes to Earth's energy budget, either through the redistribution of energy within the climate system or by changes to Top-Of-the-Atmosphere (TOA) radiative fluxes. In an equilibrium state, the solar radiative flux into the atmosphere is balanced by the sum of the outgoing thermal radiative flux and the reflected solar radiative flux [Gill, 1982]. Radiation emitted by the sun is predominantly shortwave (SW) radiation and radiation emitted by terrestrial sources is predominantly longwave (LW) radiation. When the TOA energy fluxes are out of balance and Earth is absorbing more energy than it is emitting, Earth's atmosphere and surface warm which increases the outgoing thermal radiative flux. This negative feedback loop continues (with Earth continuously warming) until the TOA energy balance is restored. Conversely, Earth's temperature will decrease if the planet emits

more energy than is absorbed, in order to restore the TOA energy balance. Not all of the incident solar radiation is absorbed by Earth; a fraction is reflected by Earth-system constituents such as clouds, gases, aerosols, and the surface. The fraction of the incident solar radiation reflected by Earth is denoted the planetary albedo (α). Assuming that Earth radiates with a single temperature T_e, a simple zero-dimensional model incorporating the Stefan-Boltzmann law can be used to describe Earth's energy balance, neglecting the presence of the atmosphere [Seinfeld and Pandis, 1998]:-

$$\sigma T_e^4 = \frac{S_0}{4}(1-\alpha) \tag{1.1}$$

The term σT_e^4 in Eq. 1.1 is the blackbody emission, where σ is the Stefan-Boltzmann constant (σ = 5.67$\times$10^{-8} Wm^{-2} K^{-4}). The solar radiative flux (S_0) at Earth's distance from the sun is approximately 1370 Wm^{-2} [Seinfeld and Pandis, 1998]. As the projected area of Earth is a quarter of its total surface area, the average solar radiative flux at the TOA is 343 Wm^{-2}. The planetary albedo is approximately 0.3 [Kiehl and Trenberth, 1997]. Hence, of the 343 Wm^{-2} of solar irradiance incident at the TOA, approximately 103 Wm^{-2} is reflected to space and 240 Wm^{-2} is absorbed by components of the atmosphere, land and ocean. In a state of equilibrium, energy fluxes at the TOA are balanced and therefore the outgoing thermal radiation emitted by the atmosphere must equal 240 Wm^{-2}. Therefore the simple model gives the equilibrium temperature of Earth as $T_e \approx 255$ K. This is not Earth's actual temperature; rather it is the temperature of a blackbody (a perfect emitter and absorber of radiation) that emits the same amount of radiation as Earth in radiative balance.

The simple model can be extended to include an isotropic atmosphere with temperature T_A and a surface with temperature T_S [Gill, 1982]. The parameter ε can be used to represent both the fraction of the upwelling LW radiation from the surface that is absorbed by the atmosphere and the emissivity of the atmosphere. Assuming that energy fluxes at the surface and at the TOA are in equilibrium, one can derive equations for the temperatures T_A and T_S.

$$T_S = \left(\left[\frac{2}{2-\varepsilon}\right]\frac{S_0(1-\alpha)}{4\,\sigma}\right)^{1/4} \tag{1.2}$$

$$T_A = \left(\left[\frac{1}{2-\varepsilon}\right]\frac{S_0(1-\alpha)}{4\,\sigma}\right)^{1/4} \tag{1.3}$$

Earth's global-mean surface temperature (GMST, T_S) is approximately 288 K [Seinfeld and Pandis, 1998], which can be used in the Eq. 1.2 to attain a value for the atmospheric emissivity of ε = 0.77, and a value for the atmospheric temperature of T_A = 242 K. This value for T_A is approximately equal to the atmospheric temperature at the scale height of the atmosphere (≈ 7 km) [Jacob, 1999]. Certain atmospheric constituents absorb LW radiation and therefore affect the atmosphere's absorption efficiency (ε). These constituents include water (H_2O - as vapour, cloud droplets, hydrometeors or ice crystals) and LW-absorbing gases such as CO_2, methane (CH_4), nitrous oxide (N_2O) and halogen-based compounds such as chlorofluorocarbons (CFC) and hydrochlorofluorocarbons (HCFC) [Seinfeld and Pandis, 1998]. Atmospheric gases that absorb thermal radiation are collectively referred to as greenhouse gases. If the atmospheric emissivity (which often equals the atmospheric absorptivity) were to increase by 2.5 % to ε = 0.79, the model predicts that equilibrium temperatures would increase to T_S = 289 K and T_A = 243 K. Therefore a rise in the LW-absorptivity of the atmosphere would increase the surface and atmospheric temperatures; a phenomenon known as the enhanced greenhouse effect [Forster *et al*., 2007].

1.1.2. The enhanced greenhouse effect

The atmospheric greenhouse effect was first theorized in the early 19th Century, when scientists such as Joseph Fourier recognized the importance of the atmosphere in regulating Earth's surface temperature. By developing a simple energy budget model, Fourier deduced that without the atmospheric absorption and re-emission of terrestrial heat radiation, Earth's surface would be considerably cooler than observed [Fourier, 1824]. Although the analogy of a greenhouse has been historically applied to this phenomenon, the mechanisms of heat entrapment by the atmosphere and by greenhouses are different. In the atmosphere, GHGs absorb outgoing terrestrial LW radiation and then re-emit some of the radiation back to the surface, whilst in an actual greenhouse the glass exterior suppresses convection which limits the dynamical transfer of heat. In 1859, John Tyndall showed that certain atmospheric trace gases such as CO_2 and water vapour are opaque to LW radiation whilst the ambient air is comparatively transparent [Tyndall, 1861]. The first attempt to quantify the enhanced greenhouse effect was made by Svante Arrhenius in 1896. Arrhenius combined a simple energy balance model with estimates of the

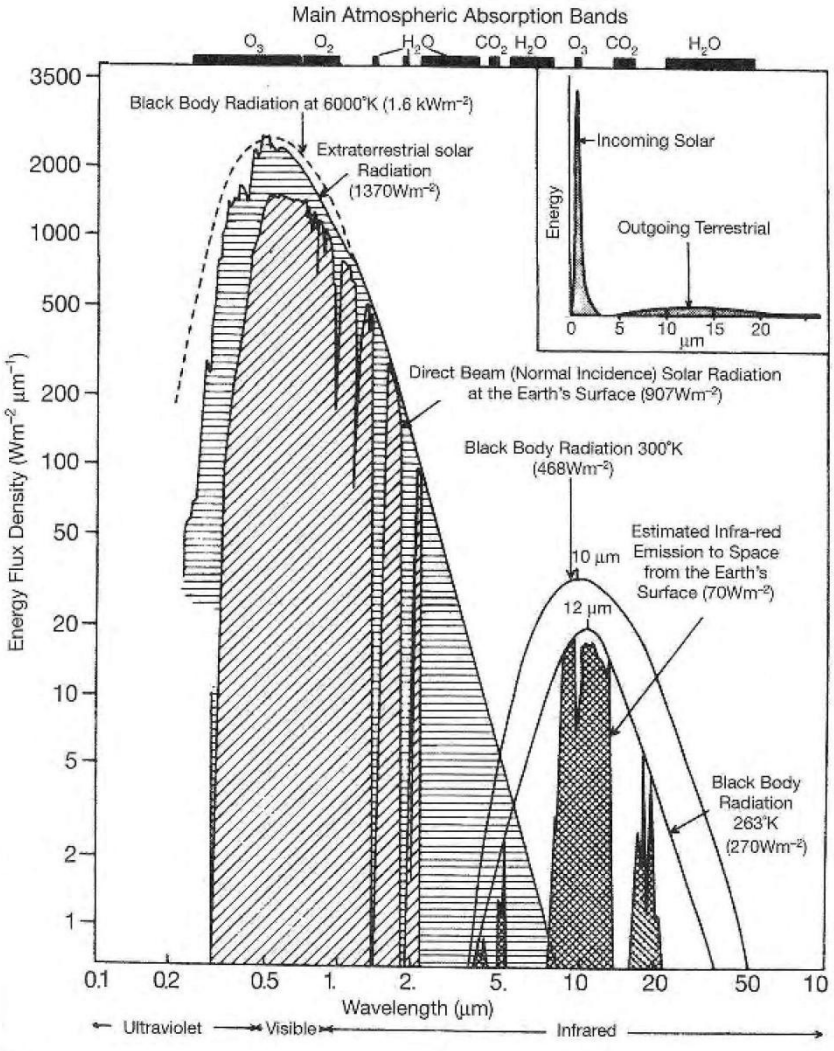

Figure 1.1. Observed solar and terrestrial spectral irradiances and the equivalent blackbody emission for 6000 K and 300/263 K respectively. Fig 4.1 from Barry and Chorley (2003)

---

global climatology to calculate the change in surface temperature for various levels of atmospheric CO_2 and water vapour. Arrhenius found that a doubling of the CO_2 concentration would produce a global temperature increase of approximately +5 K [Arrhenius, 1896].

In order to accurately describe the enhanced greenhouse effect, it is necessary to neglect the presuppositions that the atmosphere is isotropic and that radiation is monochromatic, as used in Section 1.1.1. Instead, the atmosphere should be considered as consisting of layers, with the layer temperatures decreasing with altitude. Rather than being monochromatic, solar and terrestrial radiations span a wide spectrum of wavelengths. Assuming that Earth's surface acts as a blackbody, the radiation emitted by the surface (F_B) at a certain wavelength (λ) is related to the surface temperature (T) according to Planck's law (Eq. 1.4) [Planck, 1900].

$$F_B = \frac{2\pi c^2 h\lambda^{-5}}{e^{ch/k\lambda T} - 1} \quad (1.4)$$

In Eq. 1.4, h is Planck's constant, c is the speed of light in a vacuum, and k is the Boltzmann constant. As the temperature increases, the emissive power of a body increases at all wavelengths and the maximum value of $F_B(\lambda)$ moves to shorter wavelengths according to Wien's displacement law [Wien, 1893]. The sun emits radiation at an effective temperature of ~6000 K which has a peak emission power at λ = 0.48 μm (Fig. 1.1), while Earth's surface emits at an effective temperature of ~300 K with a peak emission at 10 μm. As the sun's temperature is much greater than Earth's, the sun emits ~2×10^5 more energy per unit square metre. Approximately 40% of the solar radiation is between 0.4-0.7 μm (the visible SW spectrum), while most of the terrestrial radiation is in the LW spectrum (>4 μm) [Seinfeld and Pandis, 1998].

As noted, solar and terrestrial radiation do not traverse the atmosphere unimpeded. Instead a fraction of the radiation is attenuated by interactions with gases, aerosols and clouds. Some atmospheric gas molecules (dimers) scatter radiation via Rayleigh scattering, and some gas molecules absorb radiation at wavelengths which are specific to the molecule's composition. These wavelengths (or absorption lines) coincide with the energy levels of electrons in the molecule. Certain atmospheric conditions result in a broadening of absorption lines which instead appear as narrow absorption bands [Drake, 2000]. The spectral irradiances for solar and terrestrial radiation are shown in Fig. 1.1. The spectral regions where solar and terrestrial radiation pass through the atmosphere relatively unimpeded such as between 0.3-0.8 μm and 7-13 μm are called atmospheric windows. Approximately 80% of the terrestrial radiation emitted between 7-13 μm escapes to space [Seinfeld and Pandis, 1998]. However, this spectral region coincides with strong absorption bands of GHGs such as ozone (O_3), CH_4, N_2O and CFCs. CO_2 has strong absorption bands at 2 μm and 15 μm, with the latter approximately corresponding to the wavelength of peak thermal emission from Earth's surface [Barry and Chorley, 2003]. Absorption bands for different GHGs may coincide, such as at 2 μm for H_2O and CO_2 [Seinfeld and Pandis, 1998]. O_3 absorbs efficiently in the ultraviolet (UV) spectrum (<0.35 μm); an effect which forms the main source of stratospheric heating

[Lacis and Hansen, 1974]. By absorbing most of the solar radiation with wavelengths below 0.29 μm, O_3 modulates the UV radiation that reaches Earth's surface. UV radiation is potentially harmful to humans, animals and plants [Solomon *et al.*, 1999].

The atmospheric greenhouse effect is enhanced by elevated GHG concentrations. In equilibrium, LW radiation emitted by Earth's surface is absorbed by GHGs in the atmosphere and then re-emitted at a lower ambient temperature. The LW radiation is consecutively absorbed and re-emitted at increasingly lower temperatures by ascending layers in the atmosphere until the air is thin enough for the radiation to escape to space. Enhancing the GHG concentrations in these high and thin atmospheric layers increases the layer's absorption efficiency and prevents LW radiation from being transmitted. Therefore, the altitude of effective emission of LW radiation to space is shifted to a higher and cooler layer that is unable to radiate heat as efficiently as before. The atmosphere is now in a state of radiative imbalance (with a surplus of radiation being absorbed by the system) and so the lower atmospheric layers collectively warm to restore the radiative balance [Seinfeld and Pandis, 1998; Turco, 1997]. If the atmospheric concentration of a GHG is negligible then increasing its concentration will proportionately increase the radiative absorption in its absorption bands [Seinfeld and Pandis, 1998]. Eventually though, an absorption wavelength will become saturated which reduces the radiative impact of further GHG concentration increases. This saturation effect has a caveat: increases to GHG concentrations at an altitude different to the altitude of saturation will still have a radiative impact.

Atmospheric GHG concentrations have increased since the start of industrialisation (ca. 1800) due to the accumulation of GHGs emitted as by-products of anthropogenic activity. For instance, the IPCC estimates that from 1750 to 2011, 555 PgC[1] of CO_2 was released to the atmosphere from fossil fuel combustion and land use activity, of which 240 PgC remained in the atmosphere while the rest was absorbed by the oceans and land [IPCC, 2013]. The average atmospheric CO_2 concentration increased from 280 ppm (parts per million by volume) in 1750 to 391 ppm in 2011, and at the time of writing exceeds 400 ppm on an annual average basis. Additionally, atmospheric CH_4 concentrations have increased from 772 ppb

[1] 1 PgC = 1 x 10^{12} kgC ≈ 3.7 x 10^{12} kg[CO_2]

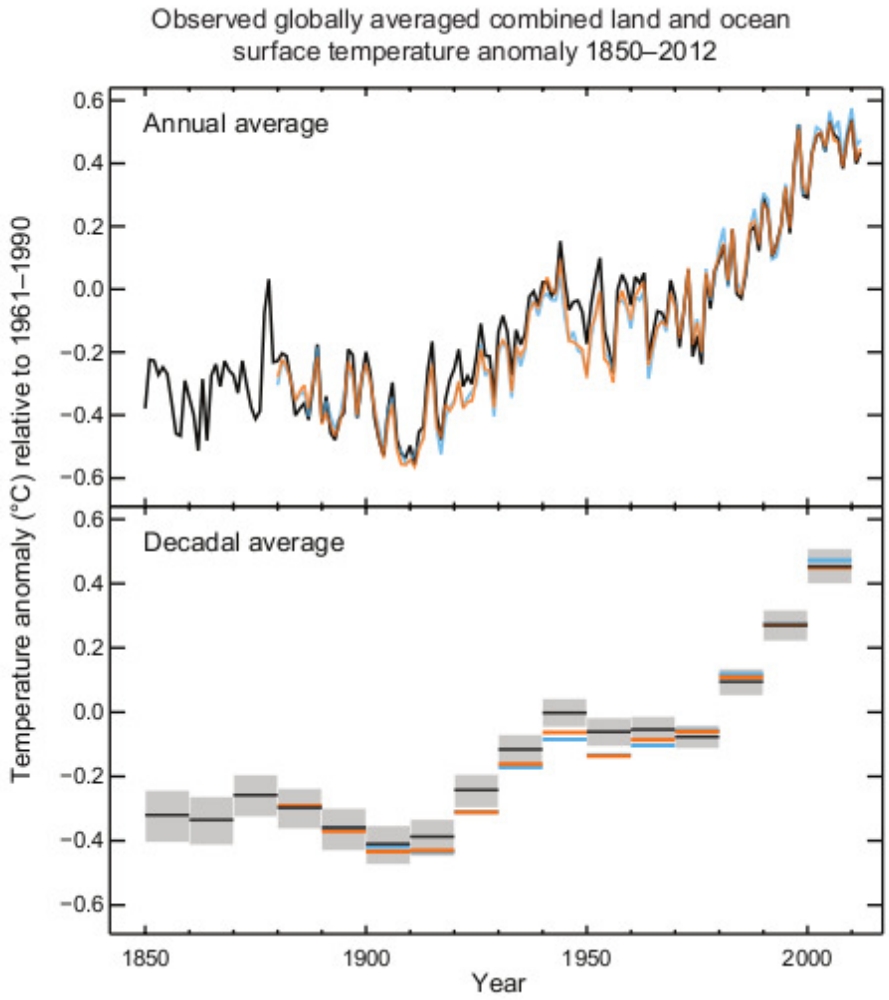

Figure 1.2. Observed GMST anomalies for 1850-2012 relative to the mean of 1961-1990. Figure and caption SPM.1 from IPCC (2013)

(parts per billion by volume) in 1750 to 1803 ppb in 2011, primarily as the result of CH_4 emissions from agricultural activity. As well as contributing to the greenhouse effect, these gases have changed the chemistry of the atmosphere and oceans, for instance, global near-surface oceanic pH has decreased by 0.0018 yr^{-1} since 1991 owing to the dissolution of CO_2 [Lauvset *et al.*, 2015].

As a result of rising atmospheric GHG concentrations and the enhanced greenhouse effect, Earth's atmosphere and surface have warmed since 1850 (Fig. 1.2). Observations indicate that the GMST increased by +0.85 K from 1900 to 2011 with most of Earth's surface experiencing a warming trend [IPCC, 2013]. The oceans have absorbed over 90% of the energy that has accumulated in the climate system since 1971. This is because the density of water is a factor of 800 greater than the average density of air (which varies with temperature, pressure, and humidity), and consequently the specific heat capacity of water is four times that of air [Gill, 1982].

Global warming is therefore not restricted to the atmosphere, but also affects the oceans resulting in thermal expansion which is an important long-term component of projected sea-level rise.

1.1.3. Recent climate changes

As noted in Section 1.1.1, climate change is unlikely to be exclusive to one climatic variable. Therefore, global warming has impacts that extend to the hydrosphere, the cryosphere, the biosphere and the geosphere due to interactions and feedbacks between these systems [Baede *et al.*, 2001]. The study of physical climate change can broadly be grouped into two fields: identifying historical and recent climate changes through observational and system-modelling research; and predicting future climate changes through scenario-dependent system-modelling. These two fields of research are inextricably entwined, for example, the development of GCMs that are capable of accurately simulating past and current climate is an essential aspect of both fields. Climate change has implications for all Earth's inhabitants but, due to the complexity of the Earth system and energy transfer between the various components, the magnitude and manifestation of climate change varies with region [IPCC, 2013]. Consequently, climate change research has garnered significant social and political traction invoking the need for regular, widely-publicised, scientific summary reports provided by the IPCC. The latest report (AR5), which was released in 2013, offers a comprehensive study of the state of understanding of recent anthropogenic climate change and makes scenario-based predictions of future climate changes. It is therefore instructive to summarise the AR5's findings.

In Section 1.1.2 we discussed how atmospheric GHGs affect the global energy budget. Other natural and anthropogenic mechanisms also alter Earth's energy budget and therefore induce climate change. The metric 'radiative forcing' (RF) is widely used to quantify the global energy budget perturbation for a given forcing agent [Myhre *et al.*, 2013]. Although there are many definitions for RF, we often use the 'adjusted' RF (ARF) in this thesis. The ARF is the annual and global-mean radiative flux change at the tropopause after stratospheric temperature adjustment following the introduction of a forcing agent [Forster and Shine, 1997] and is normally defined as the difference between pre-industrial and present day conditions. The tropopause demarcates the overlying stratosphere from the underlying troposphere

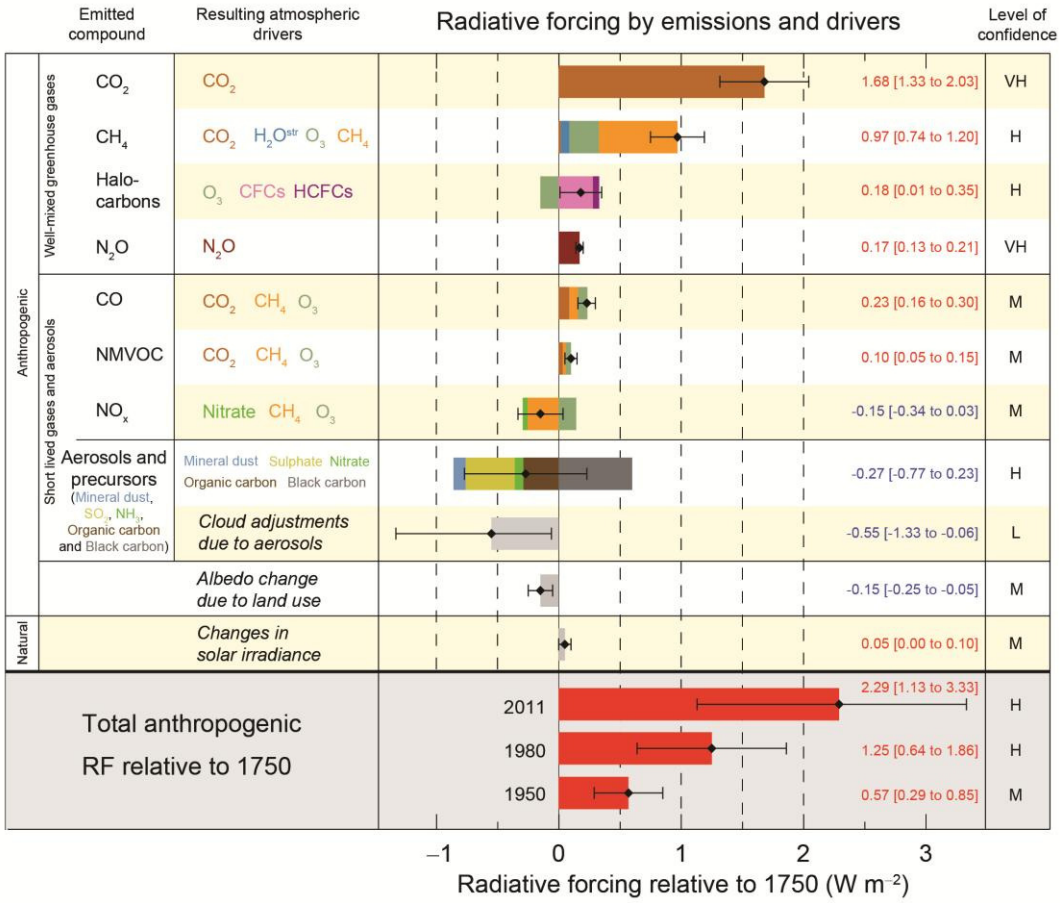

Figure 1.3. Radiative forcing estimates in 2011 relative to 1750 and aggregated uncertainties for the main drivers of climate change. Figure and caption SPM.5 from IPCC (2013)

(the atmospheric layer closest to the surface), and is commonly defined as the minimum in the vertical profile of temperature [Trenberth *et al.*, 2007]. A positive RF leads to surface warming; a negative RF leads to surface cooling. The total RF from increasing GHGs for 2011 relative to 1750 was around +3 Wm^{-2}, comprising +1.68, +0.97, +0.17, and +0.18 Wm^{-2} for changes in atmospheric CO_2, CH_4, N_2O, and halocarbon concentrations respectively (Fig. 1.3). Aerosols (solid or liquid particles suspended in air) contribute to Earth's energy budget directly by scattering or absorbing radiation and indirectly by modifying cloud properties, altering atmospheric chemistry or by changing the surface albedo. Just as the concentrations of CO_2 have been enhanced by anthropogenic activities, the concentration of aerosols such as SO_4, BC, organic carbon (OC) and nitrate (NO_3) aerosols have also increased owing to industrial and agricultural practices. Although BC contributes a positive RF of +0.64 Wm^{-2}, the total aerosol effect is -0.9 Wm^{-2} (-0.27 Wm^{-2} for the direct effect, -0.55 Wm^{-2} for the indirect effect – Fig. 1.3), due primarily to the backscatter of solar radiation by most atmospheric aerosols [Haywood and Boucher, 2000]. The aerosol

RF (in particular indirect effects due to aerosol-cloud interactions, which are described in more detail in Section 2.2) contributes the largest uncertainty to the total anthropogenic RF estimate of +2.29 Wm^{-2} (Fig. 1.3).

A myriad of observations indicate that global and regional climate changes have occurred as a direct consequence of anthropogenic activity. The most well-known realisation of climate change is global warming (Fig. 1.2). Observations suggest that global warming over the 20th century was intermittent, with certain 'hiatus' periods occurring such as within the last 15 years in which the GMST only exhibited marginal increase (+0.05 K $decade^{-1}$). This hiatus has been variously attributed to enhanced ocean heat uptake [Meehl *et al.*, 2011], reduced stratospheric water concentrations [Solomon *et al.*, 2010], and increased atmospheric aerosol concentrations [Kaufmann *et al.*, 2011; Haywood *et al.*, 2014]. Regardless of the source of the hiatus, global warming continues to be pervasive. For instance, observations indicate that the surface layer of the ocean (<75 m depth) has warmed by +0.11 K per decade since 1971 on a global-mean basis, with warming observed to a depth of 7000 m. Since 1971, 60 % of the net increase of energy in the climate system appears to have accumulated in the upper ocean (< 700 m depth) and 30 % has been stored in the deep ocean (>700 m depth) [IPCC, 2013]. In addition to global warming, observations indicate that since 1950 the frequency of heat waves over Northern Europe and the frequency and intensity of heavy precipitation events over North America have increased [Schär *et al.*, 2004; DeGaetano, 2009]. This indicates that both the mean temperature state and the distribution of temperature extremes (such as the incidence of heat waves) have changed.

In the cryosphere, global warming has contributed to glacier melt, snow cover retreat in the northern hemisphere (NH), and sea-ice loss. Glacial ice loss between 1971 and 2009 amounted to 226 Gt yr^{-1}. From 2002 to 2011, the average rates of ice loss from the Greenland and Antarctic ice sheets were 251 and 147 Gt yr^{-1} respectively. The rate of ice loss from the West Antarctic ice sheet has increased by ~70 % in the last decade [Paolo *et al.*, 2015], which has concomitantly led to the possible destabilisation of buttressed glaciers [Jacobs *et al.*, 2011]. Additionally, NH snow cover has decreased since the mid 20th century and permafrost temperatures have increased by +3 K in Northern Alaska (1980s-2000s) and up to +2 K in parts of Russia (1971-2011) [Romanovsky *et al.*, 2010a,b]. Permafrost thawing is of

particular concern due to the high concentrations of organic carbon stored in the permafrost which, if released into the atmosphere in the form of CH_4, could aggravate global warming. This phenomenon is known as the permafrost carbon feedback (PCF) [Schaefer *et al.*, 2014]. The melting of land and sea ice has contributed to observed changes in sea level. From 1993 to 2010, the observed global-mean sea level (GMSL) rose by +2.8 mm yr^{-1} with contributions of +1.1 mm yr^{-1} from ocean thermal expansion, +0.76 mm $yr^{-1}$from glacial changes, +0.33 and +0.27 mm yr^{-1} from changes to the Greenland and Antarctic ice sheets respectively, and +0.38 mm yr^{-1} from changes to land water storage [Church *et al.*, 2013]. The GMSL rise since the mid 19th century is unprecedented in the past two millennia [IPCC, 2013].

1.1.4. Future climate changes

Predicting future climate changes is complicated by uncertainties regarding future GHG emissions, land-use changes, and other scenario-dependent unknowns. Additional complexity arises from inter-model variability, internal meteorological variability, and due to the inability of current GCMs to accurately model aerosol-cloud interactions due to their coarse parameterisations of sub-grid-scale processes. To overcome these uncertainties, the IPCC routinely uses results from Model Intercomparison Projects (MIP) in which various GCMs simulate a suite of predefined future scenarios. For example, the IPCC's 4th Assessment report used Coupled Model Intercomparison Project 3 (CMIP3) data [Meehl *et al.*, 2007] which utilised scenarios from the IPCC-commissioned report 'Special Report on Emissions Scenarios' (SRES) [Nakicenovic *et al.*, 2000]. The transient SRES scenarios ranged from the societally-optimistic B1 scenario (+1.9 K global-mean surface warming in 2100 relative to 1750) to the "high growth" A1FI scenario (+4 K global-mean surface warming in 2100 relative to 1750) [IPCC, 2007]. The IPCC's 5th assessment report used CMIP5 data [Tayor *et al.*, 2012], which utilised Representative Concentration Pathway (RCP) scenarios. RCP replaced the SRES scenarios by using a policy-driven platform to provide more relevant realisations of future emissions scenarios [Moss *et al.*, 2010]. The RCP deck specified GHG concentrations, contrasting with SRES's specification of GHG emissions, in order to avoid inter-model carbon-cycle uncertainties. The RCP scenarios ranged from the mitigation-intensive RCP2.6 scenario [van Vuuren *et al.*, 2011] to the carbon-intensive RCP8.5 scenario [Riahi *et*

al., 2011]. The suffixes '2.6' and '8.5' refer to the approximate GHG-induced RF in 2100 with respect to 1850. By 2100, CO_2 emissions in RCP2.6 and RCP8.5 are zero and ~25 PgC yr^{-1} , while the GMST rise by 2100 (relative to the pre-industrial period) is 1.6 K in RCP2.6 and 4.3 K in RCP8.5, with *likely*[2] ranges of [0.9, 2.3] and [3.2, 5.4] K respectively [Stocker *et al*., 2013]. For the summary of projected climate changes given here, we discuss the key findings of the RCP projections.

Over the next half century, climate models predict that GMST will continue to rise at a rate that is approximately independent of the mitigation (i.e. RCP) scenario (Fig. 1.4 – left), but subsequent GMST changes are significantly affected by the choice of scenario (Fig. 1.4 – right). For example, RCP2.6 exhibits a GMST rise of +1 K by 2100 with respect to 1986-2005, while RCP8.5 exhibits an equivalent rise of +3.7 K [Figure SPM.7 in IPCC, 2013]. The Arctic region will warm comparatively more than the global mean due to the positive temperature feedback [e.g. Pithan and Mauritsen, 2014] and surface-albedo feedback [e.g. Kharin *et al.*, 2013]. This temperature feedback primarily arises from the lack of convective coupling between vertical atmospheric layers in the Arctic; therefore a greater surface temperature change is required to enhance outgoing LW radiation than at lower latitudes. The surface-albedo feedback arises from sea-ice melt and snow-cover retreat, which results in increased solar absorption at the surface. Over land regions, the frequency and duration of heat waves is projected to increase over the century regardless of mitigation scenario. In certain parts of Asia, for example, temperature extremes in the RCP8.5 scenario by 2100 are predicted to exceed the threshold for human adaptability [Pal and Etahir, 2015].

Changes to the hydrological cycle in the near term will be dominated by the internal variability of the climate system. However, by 2100 in the RCP8.5 scenario, the high-latitudes and equatorial Pacific Ocean will likely experience an increase in annual-mean precipitation, while many mid-latitude and subtropical land regions will *likely* experience a reduction in precipitation [Stocker *et al.*, 2013]. Projections of subtropical drying in regions such as southern Africa, south-western United States of

[2] The IPCC use a specific terminology to quantify uncertainty in observations and projections. From highest to lowest likelihood (with likelihood ranges in brackets), these include: *virtually certain* (99-100%), *very likely* (90-100%), *likely* (66-100%), *about as likely as not* (33-66%), *unlikely* (0-33%), *very unlikely* (0-10%), and *exceptionally unlikely* (0-1%) [IPCC, 2013]

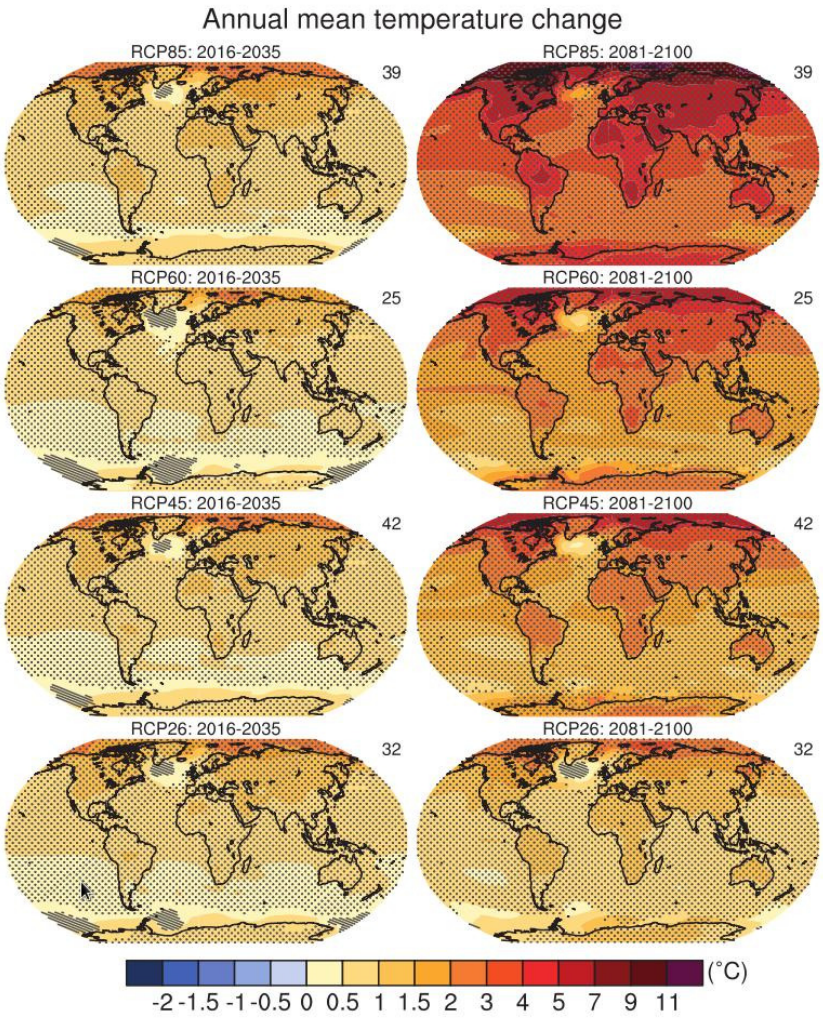

Figure 1.4. CMIP5 ensemble and annual-mean near-surface air temperature anomaly for (left) 2016-2035 and (right) 2081-2100 relative to 1986-2005 for the four RCP scenarios. Adapted from Fig. TS.15 in Stocker et al. (2013)

America (USA), and the Mediterranean are related to the predicted poleward expansion and weakening of the Hadley Cell [Lu *et al.*, 2007]. Consequently, the risk of agricultural droughts in semi-arid areas within these regions increases by the end of this century in the RCP8.5 scenario [Collins *et al.*, 2013]. Annual and global-mean precipitation will increase with GMST by 1-3 % K^{-1}, which results from the enhanced moisture capacity of warmer air. Extreme precipitation events are *very likely* to increase in intensity in the tropics and mid latitudes in the 21st century. Over parts of Central America, Africa, and Australia, the intensity of extreme precipitation events is also projected to increase despite a reduction in annual-mean precipitation [Kharin *et al.*, 2013; Sillmann *et al.*, 2013].

Arctic sea-ice extent is highly sensitive to atmospheric temperature changes [Mahlstein and Knutti, 2012] and is predicted to continue to diminish under global

warming. Over the next century, the September Arctic sea-ice extent (the annual minimum) is predicted to decrease by between 43% (RCP2.6) and 94% (RCP8.5) [Collins *et al.*, 2013]. Some CMIP5 models predict a sea-ice free Arctic in September by the end of the century in the RCP8.5 scenario [Hezel *et al.*, 2014]. The snow-covered area in the NH during boreal spring is predicted to retract by between 7 % (RCP2.6) and 25 % (RCP8.5) over the next century [Brutel-Vuilmet *et al.*, 2013]. Snow-cover retreat exposes underlying frozen ground (permafrost) to the warm atmosphere. NH permafrost extent is therefore predicted to decline over the next century, with 37 % and 81 % total area reductions predicted for RCP2.6 and RCP8.5 respectively, which could incur a strong PCF and concomitantly enhanced global warming [Collins *et al.*, 2013].

The uptake of atmospheric CO_2 by land is limited by a deficiency of nutrients required for photosynthesis, such as nitrogen and phosphorous [Goll *et al.*, 2012]. The representation of the nitrogen and phosphorous cycles in GCMs differs significantly and hence there is significant inter-model uncertainty surrounding how much additional CO_2 will be stored in the land in the future, although most CMIP5 models predict that the land remains a net sink for CO_2 over the 21st century [Friedlingstein *et al.*, 2014a]. The net CO_2 flux from the atmosphere to the ocean is predicted to decrease with global warming (particularly over the Southern Ocean). The oceans will continue to warm in the near and long-term future, with the top 100 m layer experiencing a global-mean warming of approximately +0.6 and +2 K in RCP2.6 and RCP8.5 respectively over the next century. GMSL is affected by changes to oceanic heat and salinity content, and by net water flux changes. The GMSL rise in 2081-2100 relative to 1986-2005 is *likely* to be in the following 5-95% ranges: 0.26-0.55 m for RCP2.6 and 0.45-0.82 m for RCP8.5 [Stocker *et al.*, 2013].

In summary, the climate changes predicted for the next century are mostly scenario dependent. A mitigation-intensive scenario (e.g. RCP2.6) would avoid much of the climate change and associated risks to societies and ecosystems encountered by a business-as-usual scenario (e.g. RCP8.5). For instance, a recent study found that by 2050 there would be 529,000 mortalities worldwide due to food production changes in the RCP8.5 scenario, with 71% less mortalities in the RCP2.6 scenario [Springmann *et al.*, 2016]. The magnitude of future climate changes will be proportional to humanity's aggregated CO_2 emissions.

1.2. Mitigation, adaptation, and geoengineering

1.2.1. Mitigation

Reducing GHG emissions (i.e. mitigation) is the safest solution to averting global warming and deleterious climate change [Shepherd, 2009]. Nevertheless, total anthropogenic GHG emissions have continued to rise in recent years; for instance, increasing from 39 to 49 GtCO2eq/yr[3] between 2000 and 2010. The fundamental drivers of increasing GHG emissions are population growth and economic growth. Although population growth has increased steadily since 1970, economic growth has increased more rapidly [Canadell *et al.*, 2007].

Mitigation refers to strategies that aim to reduce GHG emissions or enhance GHG sinks. Internationally, there is consensus that the installation of effective mitigation technology is imperative in order to avoid dangerous climate change [UNFCCC, 2015]. Mitigation comprises strategies to decarbonise the energy supply, alter societal behaviour, and to increase the energy efficiency of existing infrastructure and industrial practices. Effective mitigation is only achievable with all-inclusive international cooperation as many anthropogenic GHGs (e.g. CO_2 and CFCs) have long atmospheric lifetimes and become well-mixed regardless of their source. However, certain international and domestic issues have limited the effectiveness of mitigation strategies (see Box 1). Despite the emergence of widely-agreed international pledges to reduce GHG emissions such as the Kyoto protocol, current pledges for future emissions are consistent with scenarios that exhibit global warming of greater than +3 K relative to pre-industrial levels [e.g. Boyd *et al.*, 2015]. In contrast, the United Nations Framework Convention on Climate Change (UNFCCC) have declared +2 K warming to be the upper tolerance level in order to avert 'dangerous' climate change. Remarkably, the recent Paris agreement agreed an even more optimistic target of +1.5 K warming, the achievement of which would require the "immediate up-scaling of mitigation action and the development of a low-energy demand trajectory" [IPCC, 2014a]. The IPCC (2013) have proposed an interpretation of anthropogenic global warming which relates the cumulative anthropogenic CO_2 emissions to the global-mean warming since pre-industrial times

[3] The metric $GtCO_2eq/yr$ represents the sum of the anthropogenic emissions of each GHG weighted by their global warming potential (GWP) relative to the GWP of CO_2 [Forster *et al.*, 2007].

Box 1. A brief summary of why existing mitigation policies have failed

(1) ***Disconnection between science and policy*** **-** Possible reasons for this disconnection are that policy and science have different rules, values, goals, and languages, and that policymakers adopt the elements of the science that best support their own interests or ideas, or are consistent with the policies of the organisations that they represent [Gupta, 2010].

(2) ***Weakening domestic support*** - Domestic support for climate change policy has diminished over time as alternative international or domestic events have become more important [Lorenzoni *et al.*, 2007]. A possible reason for the diminishing public support could be the perceived personal sacrifices in the short term necessary to achieve long-term (and therefore less palatable) benefits [Bernauer and McGrath, 2016]. Additionally, the prevalence of climate scepticism in the media has possibly weakened public acceptance of climate change's validity.

(3) ***Climate change is complex*** - Climate change is more complex than originally perceived, for instance, there is a general uncertainty over what constitutes dangerous climate change and what emissions caps are required to stabilise climate. There is also the question of whether industrialised nations should take responsibility for past GHG emissions. Additionally some countries might benefit from climate change, e.g. easier extraction of natural resources, and therefore are less incentivised to mitigate GHG emissions. There are also serious free-rider incentives, i.e. countries reaping the benefits in terms of economic advantage of other countries' emissions reductions. Additionally climate change policy has to be integrated in the context of other international agenda such as sustainable development, trade negotiations, migration and human rights concerns [Helm, 2009].

(4) ***Ineffective policy*** – The Kyoto protocol did not specify binding emissions caps for the USA or Russia, or any emissions targets for India or China. Under the Kyoto protocol, industrialised countries could 'export' emissions to developing countries. For instance, although the United Kingdom's (UK)

Continued overleaf

primary-production GHG emissions decreased by 12.5 % between 1990 and 2008; if GHG emissions from imported goods are accounted for, effective emissions actually increased by 19 % during this period [Helm, 2009]. Additionally, the Kyoto protocol did not account for GHG emissions from aviation or shipping, and provided no emissions targets beyond 2012. There were no incentives for compliance, and no enforceable penalties for missing targets. Barrett (2009) argues that effective emissions reductions can only be achieved by fundamental policy changes.

(Fig. 1.5). Using this metric, the +1.5 K warming threshold will likely be exceeded with cumulative CO_2 emissions of ~600 GtC. As current cumulative CO_2 emissions stand at ~550 GtC and the global CO_2 emission rate is ~10 GtC/yr [Friedlingstein *et al.*, 2014b], the +1.5 K budget will likely be reached within 5 years without significant mitigation.

Working Group III's (WGIII) contribution to AR5 was a comprehensive analysis of potential mitigation strategies. WGIII found that scenarios in which atmospheric GHG concentrations are stabilised at ~450 ppm CO_2eq would likely obtain a peak global warming below +2 K [IPCC, 2014a]. These scenarios unanimously show that substantial GHG emissions cuts would be required by mid 21st century to successfully offset +2 K warming. These cuts would amount to total GHG emissions in 2050 which are 40-70 % lower than in 2010, with further reductions toward net zero or negative emissions by 2100. Negative emissions refer to the CDR proposals which remove CO_2 from the atmosphere (see Section 1.2.3). Existing CDR schemes are currently too expensive and ineffective to be employed on a large scale.

One method of reducing GHG emissions is to reduce the global energy demand by transitioning to low-energy societies. This could be induced by incentivising environmentally friendly transport schemes such as cycling and walking, by switching to low-carbon fuels such as hydrogen fuels, or by influencing lifestyle and behavioural choices [IPCC, 2014a]. However climate policy also has to be accommodating of other societal goals such as sustainable development. Goal 7 of the United Nations' sustainable development program is to "ensure access to

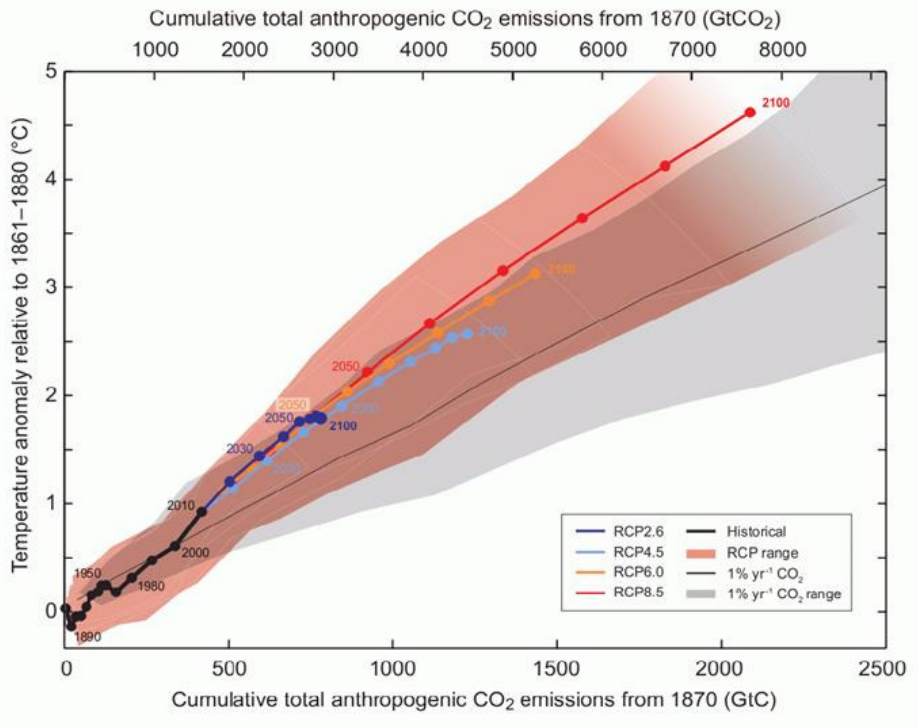

Figure 1.5. GMST anomaly plotted against cumulative anthropogenic CO_2 emissions for the RCP scenarios. Fig SPM.10 from IPCC (2013)

affordable, reliable, sustainable and modern energy for all"[4]. Therefore, policies that discourage the development of certain energy sources in developing countries might also contravene societal development targets. Decarbonisation of the energy supply sector is an alternative strategy to reducing energy demand [Bruckner, 2016]. Specifically, decarbonisation refers to methods of reducing GHG emissions within the energy supply sector by, for instance, switching to Renewable Energy (RE) sources, increasing nuclear energy production or by installing Carbon Capture and Storage (CCS) at existing fossil fuel plants [IPCC, 2014a]. RE comprises technologies that harvest energy from earth system processes. Existing RE technologies include bioenergy, solar energy, geothermal energy, hydropower, ocean energy and wind energy. The deployment of RE has proliferated rapidly in recent years due to policy changes, declining costs of technology, changes to the price of fossil fuels, and a general increase in global energy demand [IPCC, 2011]. The cost of replacing an existing carbon-intensive energy source with RE varies with technology and location. In many regions of the world, RE is not economically competitive with fossil fuels after accounting for the costs of infrastructure replacement, and therefore policies for the subsidisation of RE, combined with carbon taxation, are often required to encourage investment [IPCC, 2011].

[4] http://www.un.org/sustainabledevelopment/energy/

Nuclear power is already utilised by 30 countries and contributed 11 % of the global electricity generation in 2011 [Bruckner *et al.*, 2014]. However, this contribution decreased from 17 % in 1993 with the decline attributed to operational and mining risks, financial and regulatory risks, waste management concerns, nuclear weapon concerns, and negative public conceptions [IPCC, 2014a]. CCS technologies are already used by the fossil fuel extraction industry but, up until recently, had not been integrated into a large-scale fossil fuel plant [Boot-Handford *et al.*, 2014]. The large-scale deployment of CCS will initially require incentives to encourage investment and additional regulations to monitor the storage of CO_2 [Herzog, 2009]. Additional decarbonisation of the energy sector could be provided in the short term by switching from coal-based power plants to natural gas combined-cycle power plants or combined heat and power plants, or by improving the efficiency of fossil fuel extraction and redistribution. Most of the IPCC future scenarios that achieved peak global warming of less than +2 K implicitly used natural gas as a 'bridge' technology in the near future [Bruckner *et al.*, 2014].

Any effective mitigation strategy will also need an overhaul of other sectors that contribute GHG emissions. For instance, the global transport sector could cut their CO_2 emissions by 15-40 % by 2050 by switching to fuel efficient vehicles, utilising biofuels, and incentivising rail and public transport [IPCC, 2014a]. These changes would also contribute to improved regional air quality and therefore human health. The buildings sector could adopt very low energy building codes for new buildings and apply retrofits for old buildings to reduce the energy usage for heating and cooling. Additionally, the encouragement of societal lifestyle and behavioural changes could reduce energy demand in the buildings sector by ~50 % by mid 21st century. The industrial sector could reduce their GHG emissions by increasing the efficiency of electrical equipment, adopting efficient material-use and recycling procedures, and by promoting product innovations. The agriculture and forestry industries could reduce their GHG emissions by better land-management practices to enhance soil carbon storage, improved use of fertilisers to limit N_2O emissions, and by utilising better forest-conservation practices [IPCC, 2014a]. The installation of sector-specific policies is an effective means of achieving the necessary reductions to GHG emissions. In summary, to achieve effective mitigation would require all-inclusive international participation, a general decarbonisation of each sector (with

emphasis on energy supply), effectual governance and regulation, and for these processes to be instigated promptly.

1.2.2. Adaptation

Certain climate changes are now unavoidable due to the accumulation of historical GHG emissions. As discussed in Section 1.1.3, climate change is already detectable in regional and global observations. Consequently, ecosystems and societies are already impacted by the various manifestations of climate change. Adaptation consists of coping strategies that aim to reduce the impacts of climate change that are already happening and to increase resilience to future impacts [Adger *et al.*, 2005]. Poorer nations have the highest demand for adaptation due to their inability to finance adaptation projects and their increased susceptibility to the risks of climate change [Adger *et al.*, 2003]. Often climate impacts, adaptation and vulnerability are researched in tandem, such as by the IPCC's Working Group II (WGII) in their contribution to AR5. This is because climate impacts are often contextual; varying from location to location, and the vulnerability and status of the local society has to be accounted for when designing a suitable adaptive response [IPCC, 2014b]. Science and policy must therefore be integrated in a local context, i.e. within a deliberative engagement framework with all stakeholders [Richardson *et al.*, 2011]. Learning lessons from previous strategies is also important for adaptation. The IPCC has highlighted eight specific climate risks where adaptation will be important: 1) impacts on low-lying coastal areas from storms, flooding, and sea-level rise; 2) impacts on large urban populations from inland flooding; 3) impacts on critical services (e.g. energy supply) from extreme weather events; 4) impacts on vulnerable urban populations from heat waves; 5) impacts on food security from warming, droughts, and flooding; 6) impacts on water availability and irrigation in semi-arid regions; 7) impacts on marine ecosystems, biodiversity, and dependent communities; 8) impacts on terrestrial ecosystems, biodiversity and dependent communities (Fig. 1.6) [IPCC, 2014b].

Adaptation schemes are transitioning from a phase of development to the implementation of specific strategies [Mimura *et al.*, 2014]. For instance, the Arctic is experiencing climate changes such as sea-ice retreat, snow-cover loss and permafrost thawing. In response, targeted adaptation strategies have been

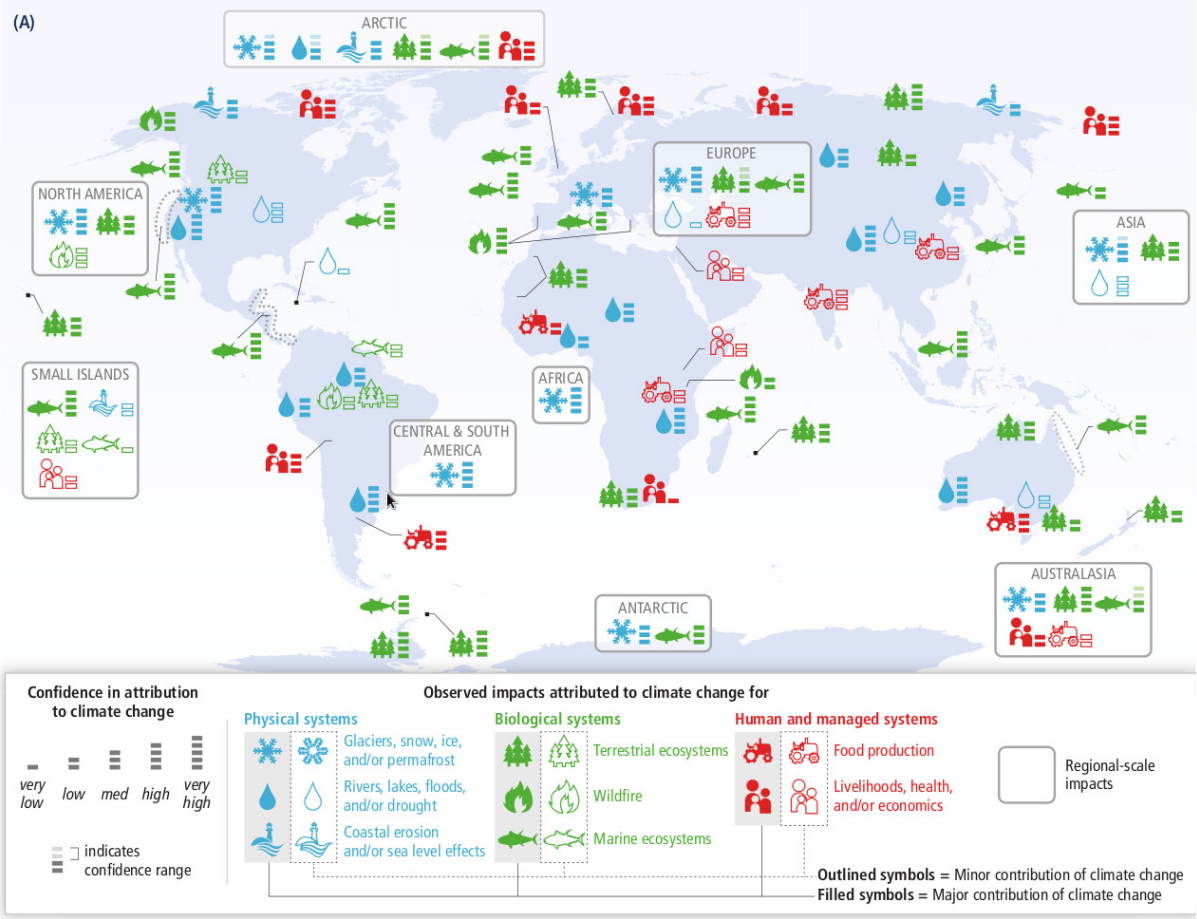

Figure 1.6. Global patterns of recent impacts attributed to climate change. Symbols indicate categories of impacts, the relative contribution of climate change (major or minor) to the observed impact, and confidence in attribution to climate change. Copy of Figure SPM.2 from IPCC (2014b)

introduced such as the International Maritime Organization's international 'Polar Code' for controlling Arctic shipping to reduce sea-ice degradation, and the installation of heat exchangers in roadways to slow permafrost thawing [Ford *et al.*, 2016]. Climate change is also impacting the prevalence of infectious diseases such as malaria and dengue fever in the tropics [Altizer *et al.*, 2013]. Effective adaptation strategies for limiting disease prevalence have been introduced, including mosquito control, the development of early-warning systems for predicting epidemics, the provision of safe water supplies and sanitation systems, and effective flood control in affected areas [Richardson *et al.*, 2011]. The number of adaptation policies and strategies implemented by Annex I (i.e. industrialised) nations increased by 87 % between 2010 and 2015 [Lesnikowski *et al.*, 2015]. In Europe, these strategies include coastal and water management, environmental protection, and disaster risk management policies [IPCC, 2014b]. In semi-arid regions such as Saharan Africa, climate change is impacting water resources and dependent ecosystems, resulting in

increased risk of crop failure and additional weed, pest, and disease pressure on crops and livestock [Niang *et al.*, 2014]. Effective adaptation schemes such as crop management and conservation of agriculture and forestry are being implemented in these regions, but are limited by the low adaptive capacities of these countries. In response, the Adaptation Fund has been created by the United Nations (with finance provided by the clean development mechanism project) to finance adaptation projects in developing countries[5]. While adaptation projects are currently unregulated by the UNFCCC, adaptation is increasingly growing in importance in international climate change policy [Ford *et al.*, 2015].

1.2.3. Geoengineering

Most of the social and political discourse on tackling climate change has focused on mitigation and adaptation. However, there is a limit to the adaptive capacity of certain societal and natural systems [Smit and Wandel, 2006], and international mitigation efforts have thus far proven unsuccessful at reducing GHG emissions. Additionally, there is uncertainty over the actual climate sensitivity to enhanced GHGs and the existence and location of tipping points in the climate system [Lenton and Vaughan, 2009]. Therefore, climate changes might occur more rapidly and irreversibly than current predictions indicate [Roe and Baker, 2007]. Significant interest has arisen in alternative strategies for tackling climate change, in particular strategies that aim to alleviate global warming (i.e. geoengineering) [Crutzen, 2006]. Geoengineering comprises strategies to remove CO_2 from the atmosphere (CDR), and strategies to reduce solar absorption by the Earth system (SRM). CDR is inherently less risky than SRM as it aims to return the climate system closer to its natural state by targeting the source of the problem (i.e. elevated GHG concentrations) and also directly counteracts side effects such as ocean acidification [Caldeira *et al.*, 2013]. However, no existing CDR proposal has been demonstrated to be effective at an affordable cost and CDR suffers from other limitations such as a slow global temperature response (order of decades) and logistical uncertainties over the transport and storage of sequestered CO_2. In Section 1.1.2, we showed that global warming is induced by the trapping of LW radiation by atmospheric GHGs. Therefore, by removing CO_2 from the atmosphere, CDR aims to cool Earth by

[5] http://unfccc.int/cooperation_and_support/financial_mechanism/adaptation_fund/items/3659.php

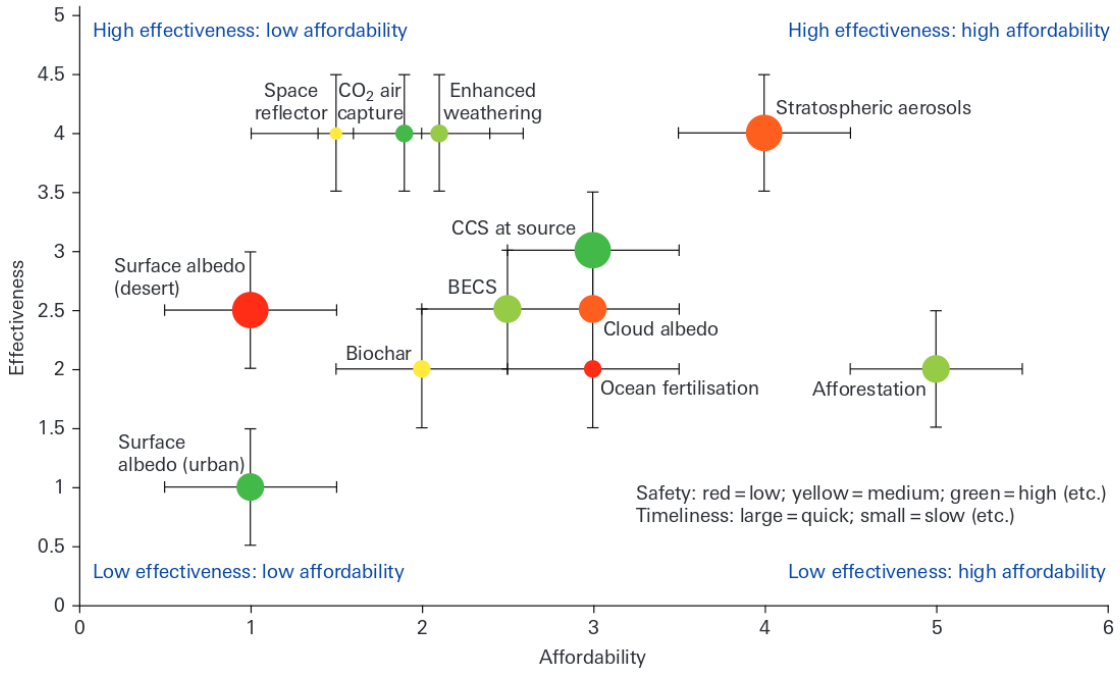

Figure 1.7. The Royal Society's graphical comparison of the relative effectiveness, safety, affordability, and timeliness of various geoengineering proposals [Shepherd, 2009]

intervening in the LW budget. Alternatively, SRM aims to cool Earth by reflecting more SW radiation to space or by reducing the SW irradiance at the TOA. SRM therefore intends to resolve a LW problem by intervening in the SW budget, which inherently poses greater climate risks than CDR due to the different spatiotemporal distributions of LW and SW radiation within the Earth system [Seinfeld and Pandis, 1998]. However, SRM could reduce global-mean temperature within 1 to 2 years and could be implemented at a substantially lower cost than current CDR proposals [Shepherd, 2009].

After conducting an extensive comparison of geoengineering proposals in 2009, the Royal Society concluded that no existing SRM or CDR proposal offers an immediate alternative to mitigation, however further research should be conducted for both strategies [Shepherd, 2009]. The impetus for further research is clear – SRM provides the only known means of rapidly cooling Earth in the event of a climate emergency, and CDR could provide a useful accessory to mitigation in reducing the net flux of CO_2 to the atmosphere and therefore offsetting climate change. It is important to note that any geoengineering strategy would have to be subjected to strict regulation and governance, and would also endure uncertain societal and political implications (these topics are outside the scope of this thesis) [Vaughan and Lenton, 2011]. Figure 1.7 schematically compares the effectiveness, affordability,

safety and timeliness of the various geoengineering proposals assessed by the Royal Society [Shepherd, 2009]. An ideal geoengineering strategy would occupy the top right quadrant of Fig 1.7, and be green (safe, i.e. low risk) and sizeable (i.e. quick to produce global cooling). No existing proposal fulfils all of these criteria (Fig. 1.7). In the next section we will discuss the main facets of existing geoengineering proposals and make reference to Fig. 1.7 where necessary.

1.2.3.1. Carbon dioxide removal

CO_2 emissions from anthropogenic sources currently amount to ~10 GtC yr^{-1}, of which ~50 % remains in the atmosphere [Caldeira *et al.*, 2013]. The rest of the CO_2 is sequestered in the land and ocean via a wide spectrum of interlinked physical, chemical, and biological processes. CDR strategies aim to store atmospheric CO_2 in an inert form within the land and ocean reservoirs by enhancing natural processes or by installing artificial processes [Vaughan and Lenton, 2011]. Alternatively, GHGs other than CO_2 could be removed from the atmosphere, for instance Boucher and Folberth (2010) discuss CH_4 extraction methods. However, GHG-removal proposals other than CDR have received little attention thus far; therefore we concentrate on CDR here.

Land-use management, reforestation, afforestation, and 'avoided deforestation' strategies are variously referred to as CDR and mitigation approaches. Terrestrial ecosystems remove ~30 % of the total CO_2 that is currently emitted to the atmosphere by fossil fuel combustion. Of the total carbon stored in the land, ~75 % is stored in soil and ~25 % is stored in vegetation [Vaughan and Lenton, 2011]. Land-use management by growing cover crops or applying manure or compost to soil in agricultural land could enhance land carbon uptake by 1.4 GtC yr^{-1} by 2030 [NRC, 2015]. Changes to land use by, e.g., deforestation, contribute 20 % of current anthropogenic CO_2 emissions; therefore avoiding deforestation could effectively augment mitigation [Shepherd, 2009]. The conversion of land from unforested areas to woodland by afforestation (establishment of new forests) or reforestation (restoration of previous forests) may conflict with sustainable development goals such as equitable food production and conservation of biodiversity [Vaughan and Lenton, 2011]. Additionally, there is uncertainty over the effectiveness of these approaches at sequestering CO_2; for instance, the CO_2

emissions from soil disturbance might outweigh the CO_2 sequestered within the newly formed vegetation [Caldeira *et al.*, 2013]. However, these approaches are generally safe, affordable and could be implemented immediately (bottom right quadrant of Fig. 1.7).

There are multiple approaches to using biomass for CDR. The first is to burn biomass in a zero-oxygen environment (pyrolysis) to form charcoal (**biochar**), which is a relatively stable form of organic carbon that can then be stored in soils or the deep ocean [Shepherd, 2009]. However, this process would require significant energy consumption for transport, production and burying of the biochar, and the residence time of biochar within these natural reservoirs is uncertain [NRC, 2015]. Also, pyrolysis only stores 50 % of the available carbon as charcoal; the rest is emitted as CO_2 which would need to be sequestered [Vaughan and Lenton, 2011]. Alternatively, biomass or biofuels could be burnt in place of conventional fossil fuels for electricity and heat generation, with the resulting CO_2 emissions sequestered using CCS (**BECCS**). The sequestered CO_2 would then be pumped underground for long-term storage [Caldeira *et al.*, 2013]. A large-scale BECCS scheme could potentially offset the radiative forcing from a carbon-intensive mitigation scenario, although this would require substantial land-use requirements for biomass growth which could conflict with land requirements for food production and biodiversity [Vaughan and Lenton, 2011]. Many mitigation scenarios utilised in the literature (such as RCP2.6) implicitly assume extensive reliance on BECCS by the end of the century [Smith *et al.*, 2015].

Enhanced weathering techniques aim to accelerate the removal of atmospheric CO_2 by promoting reactions with carbonate and silicate rocks at Earth's surface [Shepherd, 2009]. Eventually, the bicarbonate products of these reactions are transported to the deep oceans. Natural weathering processes remove ~0.1 GtC of CO_2 per year from the atmosphere, which amounts to ~1 % of current emissions [Caldeira *et al.*, 2013]. Therefore, the complete removal of anthropogenic CO_2 from the atmosphere by natural weathering would take thousands of years [NRC, 2015]. Land and ocean-based enhanced weathering methods have been suggested such as: the dispersal of silicate-bearing olivine in soils, the dispersal of silicate/carbonate minerals in the ocean, or the addition of lime to the oceans [Shepherd, 2009]. Lime is a strong base therefore adding lime would also counteract ocean acidification.

Enhanced weathering proposals are inhibited by their necessary scale, cost, and potential environmental risks (Fig. 1.7 – affordability = 2). For instance, the manufacture of lime from carbonate salts would be energy demanding and also produce hydrochloric acid which would need to be safely disposed of [Shepherd, 2009]. The scale of industry required for the mining and transport of minerals would be significant, approximately 100 billion tons yr^{-1} of minerals would be needed to offset current CO_2 emissions [NRC, 2015]. Additionally, the environmental impacts of artificially increasing silicate or carbonate concentrations in soils and in the ocean are unknown [Shepherd, 2009].

CO_2 could be captured from ambient air by a catalytic reaction with a sorbent, with the resultant pure CO_2 stream compressed and stored in geological reservoirs (i.e. using CCS) [Keith *et al.*, 2006]. This strategy is referred to as **Direct Air Capture and Storage (DACS)**. The CO_2 concentration in ambient air is 100-300 times less than in the flue gas from a power plant, therefore much more energy would be required to extract the equivalent amount of pure CO_2 using DACS than BECCS or conventional CCS [Caldeira *et al.*, 2013]. Energy would be required for regeneration of the sorbents and the compression and transport of the CO_2 gas, and the provision of sorbents such as sodium hydroxide would also be necessary [Vaughan and Lenton, 2011]. However, DACS power plants would not suffer the same positional restrictions as CCS or BECCS, and could be placed near to the storage reservoir [Shepherd, 2009]. Additionally, DACS would require less land than BECCS, and would therefore conflict less with global agricultural needs [Vaughan and Lenton, 2011].

Ocean Iron fertilisation (OIF) strategies aim to enhance the biological carbon pump that transfers CO_2 from the atmosphere to the deep oceans [Buesseler *et al.*, 2008]. The deep oceans contain ~35,000 GtC of combined CO_2 and organic carbon, compared to ~750 GtC in the atmosphere [Shepherd, 2009]. The transfer of CO_2 to the deep ocean from the surface is very slow (i.e. thousands of years) therefore ocean fertilisation aims to expedite this process. In certain areas of the ocean, CO_2 that has been absorbed into the surface layer is 'fixed' via photosynthesis by microorganisms such as algae. A fraction of the fixed carbon sinks to the deep ocean as faecal or organic material from the remains of the algal bloom. In the deep oceans, bacteria and other microorganisms use the organic carbon for respiration,

concomitantly releasing CO_2 into the ambient water [NRC, 2015]. This biological CO_2 pump is limited by the deficiency of nutrients in certain areas for algal growth. OIF seeks to promote algal growth by providing the necessary nutrients to these areas. Specifically, the Redfield ratio describes the algal composition in terms of relative masses of constituent elements. The relative values for carbon, nitrogen, phosphorous and iron are 106: 16: 1: 0.001 respectively. Therefore, one iron atom could theoretically sequester ~106,000 organic carbon atoms [Shepherd, 2009]. Although OIF appears promising on paper, field experiments indicate that only a fraction of the CO_2 fixed at the surface would eventually be transported into the deep ocean [Caldeira *et al.*, 2013]. Additionally, the promoted algal bloom might reduce the algal production downstream due to nutrient robbing, and the effects of the additional nutrients on local ecosystems are uncertain [Buesseler *et al.*, 2008].

1.2.3.2. Solar radiation management

In Section 1.1, a simple energy balance model was used to demonstrate that increasing the absorptivity of the atmosphere would result in atmospheric and surface warming (Eq. 1.1-1.3). In contrast, increasing the planetary albedo (α) or reducing the solar constant (S_0) in the same model results in atmospheric and surface cooling. These effects form the basis of the majority of SRM strategies, which aim to offset the positive RF from rising GHGs by increasing the planetary albedo or by reducing the solar irradiance at the TOA and thereby reducing the absorption of SW radiation at Earth's surface [Shepherd, 2009]. SRM methods could be implemented at the surface, in the atmosphere or in space; either uniformly over the globe or in specific regions (Fig. 1.8). Although SRM could offset the positive RF from enhanced GHG concentrations on a global-mean basis, the RF cancellation would not be exact regionally [Shepherd, 2009]. Therefore, there would likely be disparities in regional climate changes under SRM such as differing rainfall perturbations [Kravitz *et al.*, 2014a]. SW forcing perturbs the hydrological cycle comparatively more than LW forcing, therefore SRM would not be able to restore global-mean temperature and precipitation simultaneously [Bala *et al.*, 2008]. The climate achieved by SRM would only approximate the equivalent 'stabilised GHGs' climate [Ricke *et al.*, 2010]. Additionally, SRM would not directly counteract side effects of the greenhouse effect such as ocean acidification and would likely incur other side effects such as O_3 depletion [Vaughan and Lenton, 2011].

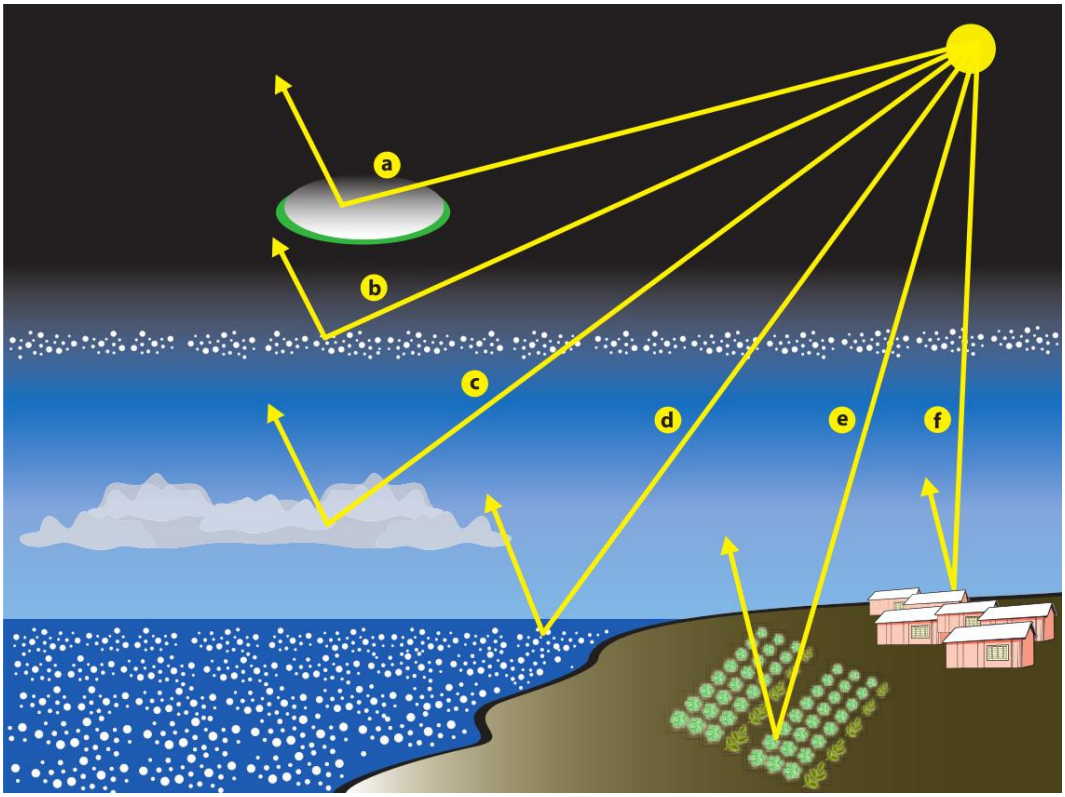

Figure 1.8. Illustration of various SRM proposals: a) space-based reflectors, b) stratospheric aerosol injection, c) marine-cloud brightening, d) ocean albedo enhancement, e) crop-albedo enhancement, f) brightening of human settlements. Fig. 2 from Caldeira et al. (2013)

Various surface albedo modification strategies have been suggested, such as the brightening of human settlements, selective growing of reflective crop varieties, or the brightening of the deserts or the ocean surface. Although the **brightening of human settlements** would reduce urban heat island effects, this method is prohibitively expensive for SRM and would have a negligible radiative effect on a global scale (bottom left quadrant of Fig 1.7) [Vaughan and Lenton, 2011]. **Crop albedo modification** (CAM) would involve exchanging current vegetation for crops with a higher albedo [Shepherd, 2009]. Crop albedo varies with plant properties such as colour, morphology and canopy structure [Irvine *et al.*, 2011]. CAM could be applied to cropland, pastures or wild grassland, and could potentially increase surface albedo in these areas by 0.02-0.08 [Ridgwell *et al.*, 2009]. However, on a global scale, CAM would be unable to induce significant cooling, although regional cooling would be more pronounced and could significantly alter atmospheric circulation patterns [e.g. Doughty *et al.*, 2011]. **Desert albedo modification** would involve covering desert areas with a highly reflective surface such as polyethylene-aluminium, which would increase the local surface albedo from ~0.35 to ~0.8

[Gaskill, 2004]. Desert region covers 2-3.5 % of Earth's surface area [Crook *et al.*, 2015]. The primary limitations of this approach are the risk of local climate changes and widespread ecological impacts, potential changes to atmospheric circulation patterns, the costs of installing and maintaining the reflective surfaces, and potential conflicts with competing land-use requirements (Fig 1.7 – red circle) [Shepherd, 2009; Vaughan and Lenton, 2011; Irvine *et al.*, 2011; Crook *et al.*, 2015].

Atmospheric albedo modification proposals comprise stratospheric aerosol injection, marine cloud brightening, and cirrus cloud thinning. SAI will be discussed in detail in Section 1.4. **Marine cloud brightening** (MCB) would involve brightening clouds over parts of the ocean by modifying their physical properties. Two MCB methods have been suggested: the injection of sea-salt aerosol into the boundary layer and the stimulation of biological emissions of cloud condensation nuclei (CCN) precursor gases [Vaughan and Lenton, 2011]. The specific goal of MCB is to enhance the CCN concentration in low-level marine clouds (which cover ~17.5 % of Earth's surface) and therefore increase the cloud reflectivity (the 'Twomey effect') and possibly the cloud lifetime [Schäfer *et al.*, 2015]. MCB would be most effective in unpolluted environments where clouds have naturally lower CCN concentrations, such as over the Southern Ocean or the west coasts of North and South America and the west coast of Africa [Jones and Haywood, 2012; Caldeira *et al.*, 2013]. As the aerosol residence time in the troposphere is ~1-2 days, the injected aerosols would need regular replenishment [Schäfer *et al.*, 2015]. An effective MCB scheme would need to generate a consistent supply of aerosols of a sufficient diameter to serve as CCN, and utilise an effective means of dispersing the aerosol [Shepherd, 2009]. Suggested methods of injecting aerosols include dispersing hydrophilic powder from aircraft or generating and spraying sea-salt from wind-driven, unmanned, remotely-controlled seacraft [Salter *et al.*, 2008]. If the latter method were used, only a few percent of the aerosol released at the surface would actually reach the cloud base [Shepherd, 2009]. Wang *et al.* (2011) investigated the impacts of various sea-salt injection strategies on cloud albedo and found that the effectiveness would be highly sensitive to the ambient meteorology, the proximity of spray-generators, and the baseline cloud properties. Brightening a region might unintentionally reduce the albedo of adjacent regions (Fig. 1.9). An advantage of MCB relative to other SRM methods is that, should unforeseen problems arise, MCB could be turned off

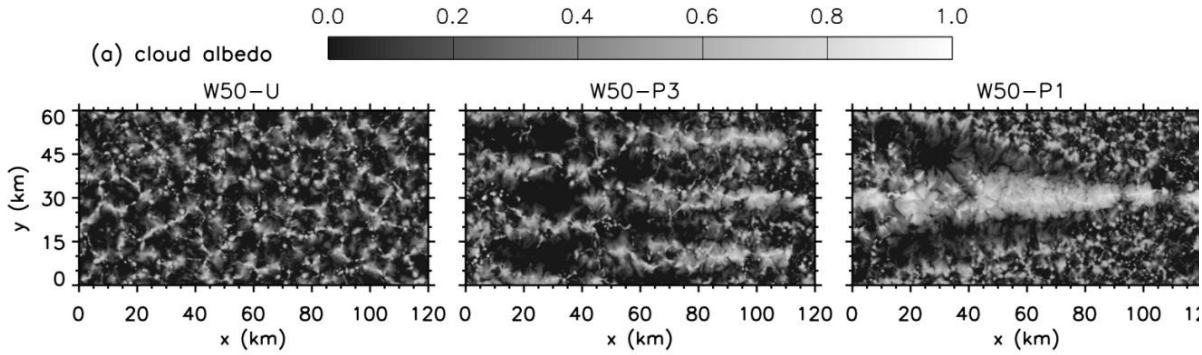

Figure 1.9. Snapshot of simulated cloud albedo for three MCB approaches: (left) uniform spraying, (centre) 3 spray generators, (right) 1 spray generator, when sprayers are at x = 24 km on their second journey. Figure 1a and caption from Wang et al. (2011)

immediately and the sea-salt would rain out within ~10 days [Shepherd, 2009]. Additionally, there is more flexibility over the location of the applied forcing than for SAI. However, the effectiveness of MCB is a complex function of the local meteorology and baseline cloud properties; spraying into polluted or heavily precipitous clouds would have negligible effect and injection of large particles might act to increase cloud drizzle and be counterproductive [Wang *et al.*, 2011]. The localised forcing applied by MCB would have to be much greater than the global-mean forcing (due to the limited area of application) to have a global effect; hence MCB is likely to significantly modify regional weather patterns [Niemeier *et al.*, 2013].

Cirrus cloud thinning (CCT) is not a conventional SRM method as it aims to enhance the outgoing LW radiation by stripping high-altitude cirrus clouds that contribute to the greenhouse effect [Mitchell and Finnegan, 2009]. CCT would involve the seeding of cirrus-forming regions with a sufficient concentration of ice nuclei (IN) such as bismuth tri-iodide, in order to force a transition from homogeneous to heterogeneous freezing, which would lead to larger ice particles with greater sedimentation velocities [Kristjánsson *et al.*, 2015]. IN could be injected from commercial aircraft, with a mid to high-latitude emission preferable due to the enhanced cirrus greenhouse effect at higher latitudes [Storelvmo *et al.*, 2014]. An advantage of CCT over conventional SRM is that it specifically targets LW radiation, and therefore directly counteracts the enhanced greenhouse effect [Kristjánsson *et al.*, 2015]. Concomitantly, CCT would alleviate the polar amplification of global warming and would also act to increase global-mean precipitation by instigating radiative cooling of the atmosphere [Muri *et al.*, 2014; Crook *et al.*, 2015]. However,

overseeding could promote cirrus lifetime and lead to smaller ice particles which would counterproductively induce global warming (an IN injection of 0.02 cm^{-3} has been found to be optimal for CCT) [Storelvmo and Herger, 2014]. Additionally, the microphysical processes of cirrus formation are poorly constrained in climate models due to a lack of observations, and it is unclear as to what extent CCT could be effective [Storelvmo *et al.*, 2014; Penner *et al.*, 2015].

Space-based reflectors could be deployed in solar orbit or in Earth's orbit, and could potentially be advantageous over other SRM approaches by providing a spatially uniform RF [Vaughan and Lenton, 2011]. In contrast to the albedo modification proposals (e.g. MCB, CAM), space-based reflectors intercept SW radiation outside of the Earth system, and concomitantly reduce the solar irradiance at the TOA (S_0 in Eq. 1.1-1.3) rather than altering the planetary albedo (α in Eq. 1.1-1.3). Govindasamy and Caldeira (2000) found that a ~2 % reduction to the solar constant could counterbalance the positive forcing from a doubling of atmospheric CO_2 concentrations. Angel (2006) suggest that a sunshade of ~3 million km^2 (which amounts to ~10 trillion refracting disks) placed at the L1 Lagrangian point would offset the current greenhouse forcing. However, the necessary technological scale of space-based methods is currently prohibitive; it would be several decades before any scheme could be implemented [Schäfer *et al.*, 2015]. Additionally the costs of development, implementation and maintenance would be an order of magnitude greater than other SRM approaches (Fig 1.7 – affordability = 1), and therefore space-based SRM methods have received limited attention [Shepherd, 2009].

1.3. Stratospheric aerosol injection

1.3.1. Background

The emphasis in this thesis will be on a specific SRM method: SAI, which the Royal Society determined was the most promising of all exisiting SRM proposals (top quadrant - Fig. 1.7) [Shepherd, 2009]. SAI involves the injection of light-scattering aerosol into the stratosphere in order to reduce solar irradiance at the surface. The aerosol residence time in the stratosphere is longer than in the troposphere (~1 year compared to ~1 week), therefore less aerosol would need to be injected into the stratosphere than the troposphere to achieve a desired surface cooling [Rasch *et al.*, 2008a]. The natural analogue of SAI is a major volcanic eruption such as Mt.

Pinatubo in 1991, which injected ~20 Tg of sulphur dioxide (SO_2) into the tropical stratosphere [McCormick *et al.*, 1995]. SO_2 oxidises in the lower stratosphere to form sulphuric acid (H_2SO_4) vapour, which condenses in high concentrations and in the presence of water vapour, organic compounds and ammonia to form SO_4 aerosol [Yu *et al.*, 2007]. The newly nucleated SO_4 aerosol is highly efficient at reflecting SW radiation. After Pinatubo, a global-mean lower tropospheric cooling of ~0.3 K was observed for the subsequent 2 years [Soden *et al.*, 2002]. Over time, aerosols are removed from the stratosphere in mid-latitude tropopause folds and in the diabatic descent of air at high latitudes [Tegtmeier *et al.*, 2008].

SAI was conceptualised by Budyko (1977), who suggested that injection of SO_2 into the tropical stratosphere (an 'artificial volcano') could be used to counteract global warming. Budyko suggested that the large-scale Brewer-Dobson circulation (BDC) in the stratosphere would disperse the SO_4 evenly over the globe therefore making the location of injection peripheral. Following its conception, SAI received little attention for 15 years [Keith, 2000]. The emergence of SAI as an active research topic in the early 1990s resulted from the significant rise in publicity garnered by global warming. In an expansive report on geoengineering, the USA National Academy of Sciences [NAS, 1992] compared the cost-effectiveness of various SAI strategies such as using aircraft, balloons and artillery shells to disperse aerosol. However, Schneider (1996) notes that many scientists in the 1990s were still concerned that SAI research would detract from mitigation efforts (the 'moral hazard' problem) and would conflict with efforts to reduce atmospheric pollution. Additionally, there was concern over the environmental risks posed by SAI, and therefore research remained fragmented until the turn of the century. In 2000, Govindasamy and Caldeira used a GCM to assess the climate response to an idealised SRM scenario in which the solar constant (S_0) is uniformly reduced by 1.8 %. This approach more closely resembles a 'space-based reflectors' scenario than SAI, but is seen as a useful proxy for understanding the climate response to SAI [Kravitz *et al.*, 2011]. Rather conclusively, the results showed that SRM could induce a sufficient global-mean surface cooling to counterbalance the warming from a doubling of CO_2, whilst approximately offsetting regional climate changes. The results of this investigation led Keith (2000) to state that "the assumption that albedo geoengineering could not do an effective job of countering CO_2-induced climate change must be re-examined". Further modelling

experiments were conducted by Govindasamy *et al.* (2002, 2003) to evaluate the impacts of the idealised SRM scheme on the terrestrial biosphere. In 2006, the Nobel prize laureate Paul Crutzen felt compelled by the "grossly disappointing" international mitigation efforts and worrying signs of potentially dangerous climate changes to write an editorial in *Climatic Change* in which he advocated SAI research [Crutzen, 2006]. This endorsement, combined with a similar appraisal from Tom Wigley [Wigley, 2006], instigated a period of sustained research into the viability of SAI. Since 2006, modelling studies of SAI have increased in complexity from the use of simple energy balance models [e.g. Wigley, 2006] to intricate GCMs with explicit aerosol representation [e.g. Heckendorn *et al.,* 2009] and coupled atmosphere-ocean models [e.g. Schmidt *et al.*, 2012]. In the summary presented here, we discuss the technical viability and potential climate impacts of SAI.

1.3.2. Injection strategy

Budyko (1977) suggested the use of existing commercial aircraft to disperse SO_2 over the globe, by using either enhanced sulphur fuel or an external SO_2-injecting mechanism. However, Laakso *et al.* (2012) found that simply modifying current commercial aircraft's fuel content would not induce an appreciable radiative effect. NAS (1992) compared the relative benefits of aircraft with other possible delivery mechanisms such as firing SO_2-bearing artillery shells into the stratosphere, or releasing balloons filled with SO_2 from the surface. NAS (1992) found that the use of aircraft would likely be the most cost-effective delivery system of those proposed. Turco (1996) proposed releasing carbonyl sulphide (OCS) at the surface rather than SO_2 in situ, which would remove the costs associated with transport of aerosol. However, Crutzen (2006) estimates that ~95% of the emitted OCS would be sequestered by the land or removed by chemical reactions in the troposphere, with only ~5 % reaching the lower stratosphere. OCS is also very long-lived in the troposphere and should an OCS injection scheme produce unintended negative climate effects it would be difficult to extract the OCS from the atmosphere [Rasch *et al.*, 2008b]. Rasch *et al.* (2008b) discussed the use of high-altitude aircraft as a SO_4 delivery mechanism in some detail. A problem they identified is that the increased coagulation and sedimentation rates immediately after injection would lead to large and optically-inefficient particles. Smaller SO_4 particles efficiently scatter SW radiation, while larger particles also absorb LW radiation and are more rapidly

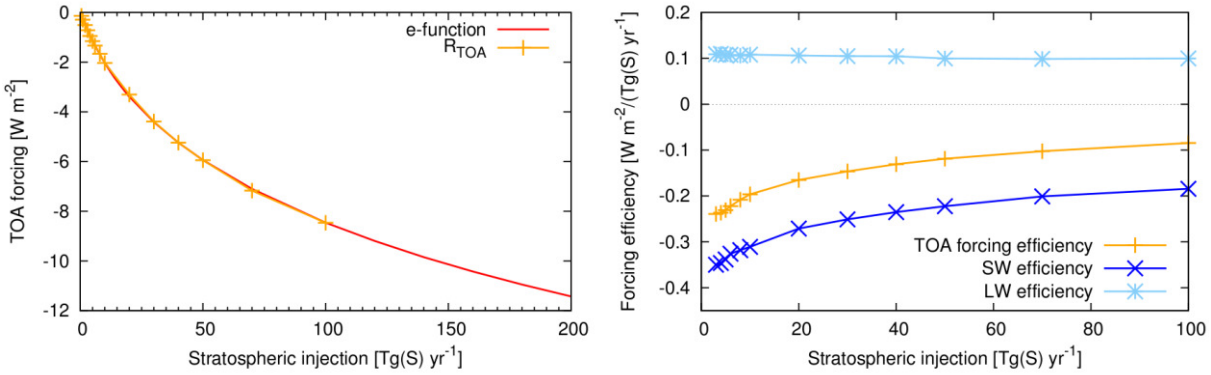

Figure 1.10. (left) Top of the atmosphere net radiative flux perturbation for SAI with different injection rates, plotted with an exponential fit (red line). (right) radiative forcing per injection for different injection rates. Fig. 1 from Niemeier and Timmreck (2015)

removed from the stratosphere via sedimentation [Stenchikov *et al.*, 1998]. Smaller particles (with radius < 1 μm) are therefore optimal for SAI. However, the immediate coagulation of newly-nucleated aerosol or condensation onto background aerosol would limit the effectiveness of any SAI scheme, necessitating further injections [Heckendorn *et al.*, 2009]. Niemeier and Timmreck (2015) found that the effectiveness of SAI would decrease exponentially with SO_2 injection rate (Fig. 1.10). Pierce *et al.* (2010) suggested that injecting H_2SO_4 vapour instead of SO_2 would produce comparatively smaller particles, although English *et al.* (2012) found no discernible difference in the resultant SO_4 sizes or mass burdens between these approaches. Niemeier *et al.* (2011) found that aerosol injection at 30 hPa instead of 50 hPa altitude would increase aerosol burdens by ~50 %. However, the burdens and aerosol sizes that would result from SAI still remain uncertain due to current model limitations and scenario unknowns.

Various analyses have been conducted to assess the affordability and technological feasibility of SAI [e.g. Robock *et al.*, 2009]. In terms of field experiments, a small-scale experiment was performed in Russia in 2009 which investigated aerosol generated from a helicopter [Izrael *et al.*, 2009] and various other experiments have been suggested [Keith *et al.*, 2014]. Despite this, the technology required to perform SAI on a large scale does not currently exist [Robock, 2014]. The cost of SAI would depend on the means of delivery and the amount of aerosol injected. Robock *et al.* (2009) estimate that employing a fleet of existing military aircraft to inject 1 Tg[S] yr^{-1} at 20 km altitude could cost $4 billion yr^{-1}. Davidson *et al.* (2012) estimate that a 10 Tg yr^{-1} injection rate would cost $10 billion yr^{-1} using aircraft; whereas tethered

balloons could provide the same injection for $400 million yr^{-1}. McClellan *et al.* (2012) found that specially designed aircraft would be the most cost-effective deployment strategy, with running costs of $2.6 billion yr^{-1} to transport 1 Tg of aerosol to 30 km altitude. All three studies suggested that deployment strategies other than aircraft could be prohibitively expensive, although Davidson *et al.* (2012) was the only study to find balloons the most cost-effective strategy. The costs of SAI are unlikely to be prohibitive compared with environmental concerns and social and political barriers [Robock, 2014].

1.3.3. Choice of aerosol

SO_4 injection strategies benefit from the extensive research of volcanic eruptions and of the natural sulphur cycle [Carslaw and Kärcher, 2006]. The stratosphere already contains a background SO_4 layer formed from the upward transport of sulphur precursor gases from the troposphere, which exerts a negative radiative forcing of approximately -0.1 Wm^{-2} [Solomon *et al.,* 2011]. Volcanic eruptions can significantly alter the stratospheric SO_4 concentration. Stratospheric SO_4 aerosols provide surfaces for heterogeneous reactions between free radicals and O_3 which can result in O_3 depletion [Tilmes *et al.,* 2008]. Stratospheric O_3 efficiently absorbs solar UV radiation, which would otherwise be harmful to humans and ecosystems. An O_3 hole develops over Antarctica in the austral winter every year as the result of O_3 destruction within polar stratospheric clouds (PSC). After the Pinatubo eruption, the Antarctic O_3 hole extended well beyond the area of PSC formation due to heterogeneous chemistry on the Pinatubo aerosol [Solomon, 1999]. O_3 depletion (and concomitant UV changes at the surface) in a SO_4 injection scenario would be more pronounced at high latitudes than in the tropics [Tilmes *et al.*, 2012; Pitari *et al.*, 2014].

SAI research has predominantly focussed on SO_4 due to the volcanic analogue. However, a variety of other aerosols have also been proposed, including minerals [Pope *et al.*, 2012], dust [NAS, 1992], and BC [Ferraro *et al.*, 2011]. Teller *et al.* (1997) suggested that dielectric material, electrical conductors or resonant molecules could be utilised due to their high SW scattering efficiency, therefore less mass would be required than for SO_4 to produce a desired radiative cooling. Alternatively, certain nanoparticles could be lofted to the upper stratosphere by photophoretic

levitation [Keith, 2010]. A BC injection scenario is analogous to a conceptual nuclear winter. BC efficiently absorbs SW radiation; therefore a stratospheric BC layer would reduce the solar irradiance at Earth's surface and cool the troposphere. By absorbing SW radiation, BC would also warm the stratosphere and impact O_3 chemistry [Kravitz *et al.*, 2012]. An ideal candidate particle for SAI would only interact with SW radiation, would have a long atmospheric residence time, would not affect atmospheric chemistry, and would not be toxic [Robock, 2014]. Minerals such as TiO_2 and diamond scatter SW radiation more efficiently per mass than SO_4 and have therefore been suggested for SAI [Pope *et al.*, 2012]. Injection of solid particles could potentially reduce the risks of O_3 depletion associated with SAI, although the rate coefficients of O_3 reactions on solid aerosol surfaces are poorly constrained [Tang *et al.*, 2014; Weisenstein *et al.*, 2015].

SAI with alternative aerosols has received limited attention despite offering the possibility of avoiding certain negative impacts of SO_4 injection. Pope *et al.* (2012) identify TiO_2 as having the greatest refractive index at the peak wavelength of solar emission of the various minerals assessed in that study, therefore TiO_2 can be thought of as an optimal sunlight-scatterer. Conversely BC is an effective sunlight-absorber [Kravitz *et al.*, 2012] and hence provides an interesting contrast to SO_4 and TiO_2. In Chapters 2-4 we will investigate the radiative and climatic implications of injecting these aerosols into the stratosphere.

1.3.4. Potential climate impacts

GCMs are useful tools for assessing the potential climatic impacts of SAI. Early GCM-based research used a uniform solar reduction to represent SAI [e.g. Govindasamy and Caldeira, 2000], but this simple representation ignores the nuances of SAI, such as stratospheric O_3 changes that result from heterogeneous chemistry on the aerosol surfaces [Pitari *et al.*, 2014], stratospheric warming and related circulation changes [Aquila *et al.*, 2014], changes to diffuse and direct solar radiation at the surface [Kalidindi *et al.*, 2015], and the effects of upper tropospheric warming on the hydrological cycle [Ferraro *et al.*, 2014]. Note, however, that aerosol injected into the tropical stratosphere is transported poleward by the BDC; therefore a tropical aerosol injection would produce a global aerosol layer that approximates a uniform solar reduction [Robock *et al.*, 2008; Niemeier *et al.*, 2013]. For this brief

Experiment	Description
G1	Instantaneously quadruple the CO_2 concentration (as measured from pre-industrial levels) while simultaneously reducing the solar constant to counteract this forcing
G2	In combination with a 1% increase in CO_2 concentration per year, gradually reduce the solar constant to balance the changing radiative forcing
G3	In combination with RCP4.5 forcing, starting in 2020, gradual ramp-up the amount of SO_2 or sulphate aerosol injected, with the purpose of keeping global average temperature nearly constant. Injection will be done at one point on the Equator or uniformly globally
G4	In combination with RCP4.5 forcing, starting in 2020, daily injections of a constant amount of SO_2 at a rate of 5 Tg SO_2 per year at one point on the Equator through the lower stratosphere (~16– 25 km in altitude) or the particular model's equivalent. These injections would continue at the same rate through the lifetime of the simulation

Table 1.1. A summary of the GeoMIP experiments [*Kravitz et al.,* 2011]

discussion, we will refer to both approaches (the simple solar reduction method and the explicit aerosol injection method) as SAI, although important differences will be noted.

The Geoengineering Model Intercomparison Project (GeoMIP) was formed to compare the results of different GCMs simulating the same suite of idealised solar geoengineering scenarios (Table 1.1, [Kravitz *et al.*, 2011]). In this section, we discuss the robust results of GeoMIP. Fig. 1.11 shows the near surface air temperature changes in the G1 scenario relative to a scenario in which atmospheric CO_2 concentrations are instantaneously quadrupled. The overcooling in the tropics and residual warming at high latitudes in G1 (Fig. 1.11 – *right*) occurs because there is more sunlight in the tropics on an annual-mean basis and therefore SRM is more effective at lower latitudes, and because the greenhouse effect is approximately globally uniform as GHGs are well-mixed. Therefore, the net TOA radiative effect under SAI is positive at high latitudes and negative at low latitudes [e.g. Fig. 3 in Kravitz *et al.*, 2013]. Yu *et al.* (2015) found that the pattern of temperature changes is qualitatively the same for solar reduction (G1, G2) and SAI (G3, G4) scenarios.

A robust feature of SAI is the tendency for climate to rapidly rebound toward a base-state climate following SAI's cessation. As an example, Fig. 1.12 shows the global-mean temperature evolution for the GeoMIP G2 experiment (Table 1.1) [Jones *et al.*,

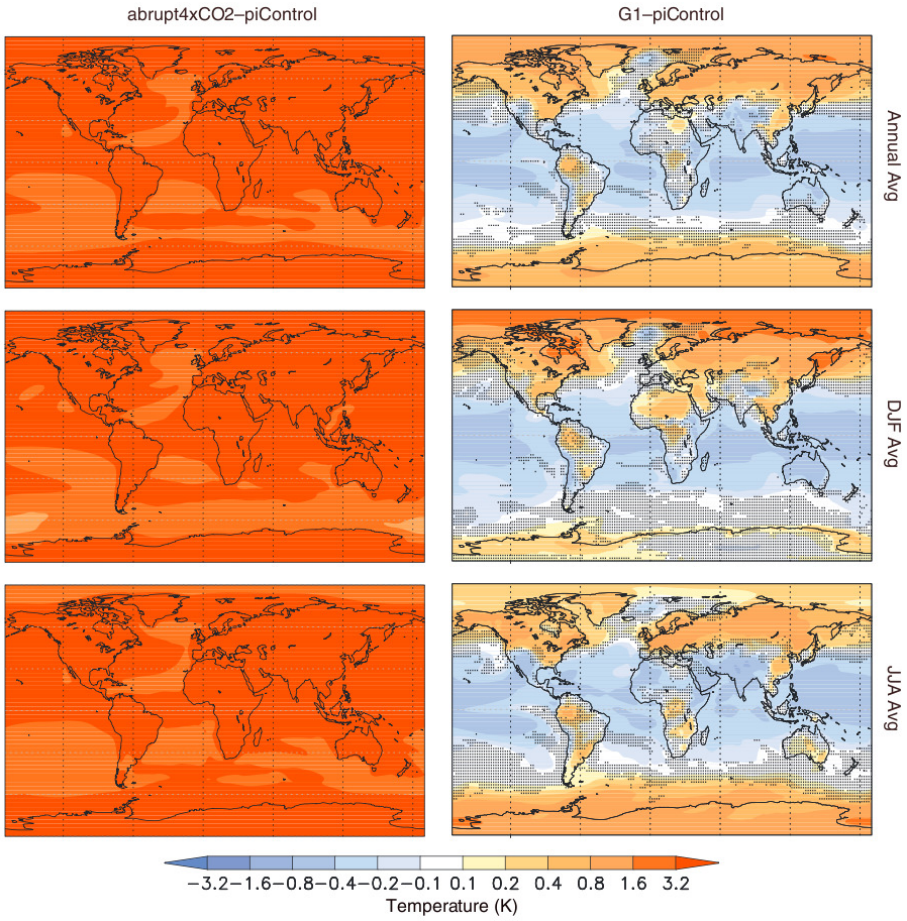

Figure 1.11. GeoMIP multi-model ensemble surface temperature anomaly with respect to pre-industrial conditions for: (left) abrupt quadrupling of CO_2, (right) uniform solar reduction, (top) annual-mean, (middle) December-January-February, (bottom) June-July-August. Stippling indicates where fewer than 75% of the models agree on the sign of the difference. Fig. 2 from Kravitz et al. (2013)

2013]. In the 50th model year of G2 (indicated by vertical dashed lines in Fig 1.12a), SAI was instantaneously terminated and the experiment continued for an additional 20 years. Immediately after the cessation of SAI, the climate undergoes a rapid rebound toward the state it would have attained in the absence of SAI (Fig. 1.12a). Such rapid climate changes could exceed the threshold of adaptability for certain ecosystems and economies [Alley *et al.*, 2003]. Rapid climate change would be observed in many climatological fields such as precipitation, sea ice and ocean dynamics [e.g. Jones *et al.*, 2013]. This 'termination effect' was highlighted by Robock (2008) as a key impediment of SAI.

Another robust feature of SAI is a deceleration of the hydrological cycle arising from the increased moist static stability of the troposphere [Bala *et al.*, 2008], and from surface changes due to elevated CO_2 concentrations [Fyfe *et al.*, 2013]. SW forcing

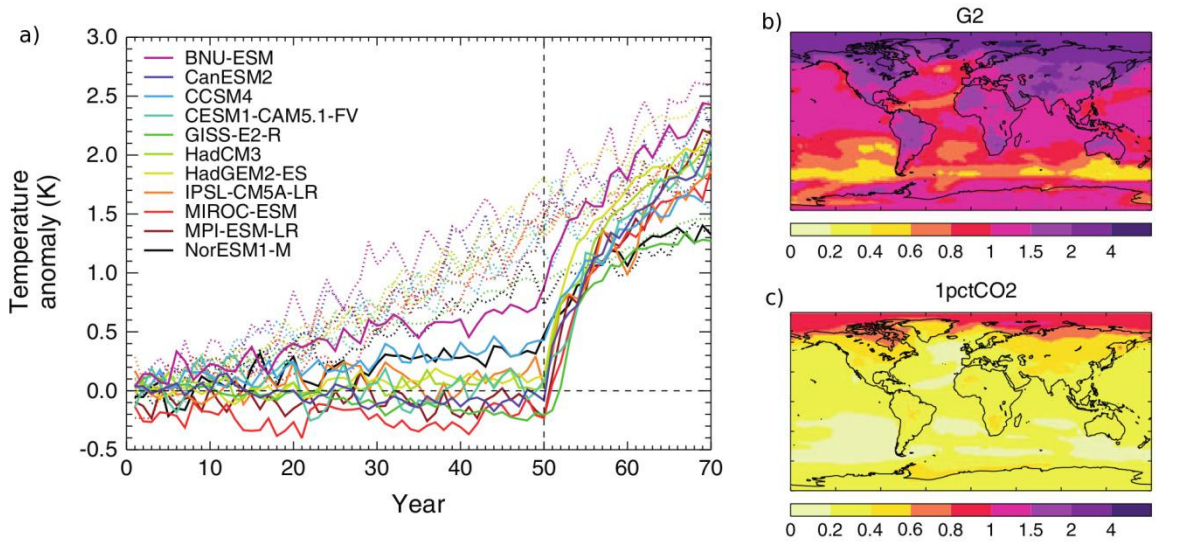

Figure 1.12. a) Global-mean surface temperature anomaly for the GeoMIP 1pctCO2 experiments (dotted lines) and the SRM 'G2' experiment (solid lines). The vertical dashed line indicates termination of SRM. b) Rate of increase of surface temperature (K/decade) immediately after termination in G2. c) Rate of increase of temperature in the 1pctCO2 experiment. Adapted from Fig. 1 and Fig. 5 in Jones et al. (2013)

preferentially cools the surface while elevated GHG concentrations warm the atmosphere. The net effect is a loss of energy by the atmospheric column which is compensated by reduced latent heat fluxes at the surface and therefore a slowing down of the hydrological cycle [Schmidt *et al.*, 2012; Bala *et al.*, 2008]. A stratospheric SO_4 layer would further weaken the hydrological cycle by absorbing and re-emitting terrestrial LW radiation and concomitantly warming the upper troposphere [Fyfe *et al.,* 2013; Niemeier *et al.*, 2013; Ferraro *et al.*, 2014]. As an example of this effect, a deceleration of the hydrological cycle was observed in precipitation and streamflow records in the year following the Pinatubo eruption [Trenberth and Dai, 2007]. Additionally, in a high CO_2 environment, plants are able to absorb CO_2 faster and therefore close their stomata for longer which limits evapotranspiration and weakens the hydrological cycle [Fyfe *et al.*, 2013; Tilmes *et al.,* 2013]. This phenomenon is denoted the CO_2 fertilisation effect [Kravitz *et al.*, 2013]. Changes to the hydrological cycle from the CO_2 fertilisation effect and the enhanced moist static stability are denoted 'fast responses' to elevated CO_2 [Tilmes *et al.*, 2013]. The long-term response to elevated CO_2 concentrations is atmospheric warming, which increases the moisture-holding capacity of the atmosphere and concomitantly strengthens the hydrological cycle. This 'slow feedback' eventually dominates the 'fast response', for instance, in the GeoMIP abrupt4xCO_2 scenario global-mean precipitation increases by +7 % relative to pre-industrial conditions

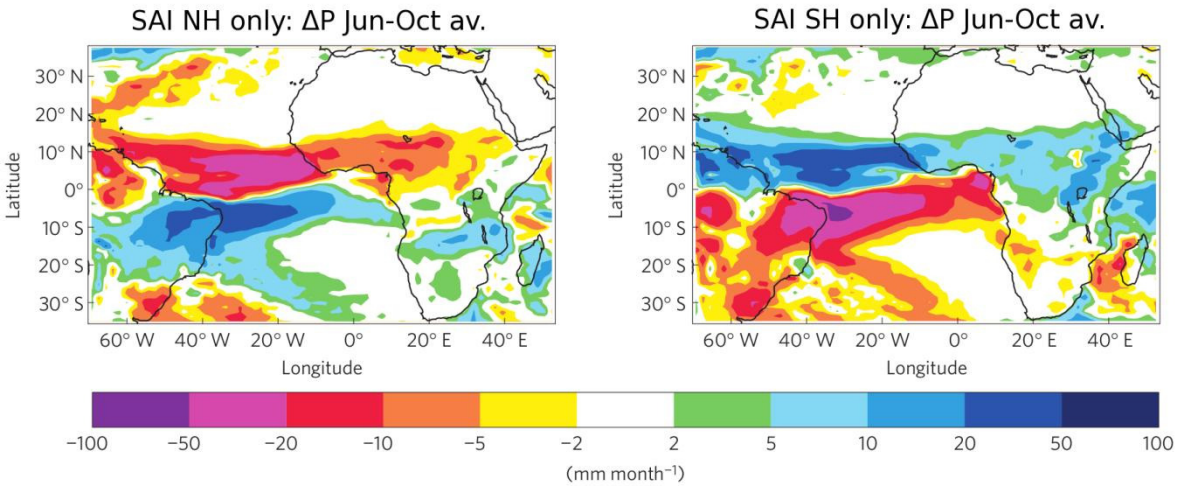

Figure 1.13. June-October precipitation anomaly when SAI is applied in the NH only (left) and the southern hemisphere (SH) only (right) from 2020-2070 relative to RCP4.5. Fig. 4 from Haywood et al. (2013)

[Tilmes *et al.*, 2013]. Conversely, in scenario G1 global-mean precipitation decreases by 4.5 %, with the largest reductions occurring in tropical monsoon regions and NH mid latitudes [Tilmes *et al.,* 2013; Crook *et al.*, 2015]. This is because SAI suppresses the 'slow feedback' whilst augmenting the 'fast response'. The hydrological cycle also responds to changes in temperature gradient. For instance, a hemispherically asymmetric SAI application would displace the Inter-Tropical Convergence Zone (ITCZ) towards the warmer hemisphere (Fig. 1.13), which could have ramifications for Sahelian rainfall and Atlantic storm tracks [Haywood *et al*., 2013; 2016].

An area of research that remains comparatively undeveloped is the impacts of SAI on tropical and extratropical storms. Moore *et al.* (2015) assessed the impact of the GeoMIP SO_2 injection scenarios (G3 and G4) on Atlantic hurricane activity and found that the preferential cooling of the tropics in G3 effectively maintained the number of Hurricane Katrina-sized storms in 2050-2070 at present day levels; offsetting the increase in hurricane activity exhibited by RCP4.5. North Atlantic tropical cyclone frequency is intrinsically related to the position of the ITCZ and interhemispheric aerosol gradients [Dunstone *et al.*, 2013; Haywood *et al.*, 2016]. This provides the motivation for work presented in Chapter 6, in which we assess whether single-hemisphere SAI could effectively modulate North Atlantic tropical storm frequency.

Various studies have investigated whether SAI could be used to maintain Arctic and Antarctic seasonal sea-ice extent. Berdahl *et al.* (2014) assessed changes to sea-ice extent in the GeoMIP G3 and G4 scenarios, and found that neither SAI scenario was

able to completely mitigate global or Arctic warming trends over the period 2020-2070 due to committed warming from historical GHG emissions. Concomitantly, March and September sea-ice extents progressively declined during the SAI era in G3 and G4, albeit at a slower rate than in RCP4.5. McCusker *et al.* (2015) assessed the ability of SAI to maintain the West Antarctic ice sheet, by applying SAI at a sufficient rate to counterbalance the radiative forcing from the RCP8.5 scenario. McCusker *et al.* (2015) found that, although SAI could return GMST and GMSL to 1990s levels, SAI would not completely mitigate the poleward displacement of the Antarctic vortex or the concomitant upwelling of warmer water below the ice sheets. Applegate and Keller (2015) suggest that the effectiveness of SAI at restoring sea ice and preserving ice sheets would be sensitive to the baseline GHG concentrations, the year of SAI initiation, and the magnitude of SAI applied.

Land and ocean carbon storage will be impacted by climate changes and atmospheric CO_2 changes in the future. Over vegetation, elevated CO_2 concentrations act to enhance stomatal resistance which reduces evapotranspiration and plant respiration and increases CO_2 retention [Fyfe *et al.*, 2013]. At low latitudes, water and heat stress are at present the primary impediments for crop growth, while at high latitudes the cold climate limits the duration of crop growing seasons [Glienke *et al.*, 2015]. SAI would ameliorate the tropical heat stress from global warming and, combined with the CO_2 fertilisation effect, increase net primary productivity (NPP) at low latitudes [Pongratz *et al.*, 2012]. However, SAI would offset some of the warming at high latitudes (Fig. 1.11) and therefore partially restrict the enhancement of plant growth in these regions [Glienke *et al.*, 2015]. SO_4 aerosols scatter solar radiation, which increases the diffuse to total (diffuse + direct) SW radiation ratio at the surface. Diffuse radiation is able to penetrate deeper into plant canopies than direct radiation and therefore illuminate a greater fraction of the vegetation, which enhances photosynthesis [Kalidindi *et al.*, 2015]. This effect is suppressed for high atmospheric aerosol burdens where the direct to total radiation ratio at the surface exceeds a critical threshold of ~0.4 [Xia *et al.*, 2016]. Kalidindi *et al.* (2015) found that the enhancement of photosynthesis by the diffuse fertilisation effect under SAI would be overcompensated by the reduced direct radiation at the surface. In contrast, Xia *et al.* (2016) found that the diffuse fertilisation effect in an SAI scenario could enhance the land CO_2 sink. Therefore, the importance of the diffuse fertilisation effect on land

CO_2 storage under SAI remains uncertain. Many climate models do not incorporate a nitrogen cycle and instead specify an unlimited nitrogen supply for photosynthesis. As nitrogen is often a limiting nutrient in soil, the CO_2 fertilisation effect is often overestimated in predictions of future NPP changes [Glienke *et al.*, 2015]. Tjiputra *et al.* (2016) found that nitrogen limitation would inhibit the CO_2 fertilisation effect and therefore reduce the positive impact of SAI on NPP in low latitudes. The inconsistencies amongst the findings presented here suggest that the true response of the land to climate and CO_2 changes under SAI remains uncertain. Tjiputra *et al.* (2016) additionally found that intensive SAI could stabilise the Atlantic meridional overturning circulation (AMOC) in the NH oceans which would increase the oceanic CO_2 sequestration relative to a no-SAI scenario. However, this would come at the cost of intensified ocean acidification, which could deleteriously impact oceanic ecosystems.

Tropical lower-stratospheric warming under SAI would enhance the local upwelling velocity and transport O_3-poor air in the lower stratosphere to higher altitudes where O_3 is more easily destroyed [Schoeberl *et al.*, 1993a; Tilmes *et al.*, 2009]. Additionally, stratospheric warming acts to modify wind fields through the thermal wind relationship, which could result in a prolonged easterly phase of the Quasi-Biennial Oscillation (QBO) under SAI [Aquila *et al.*, 2014]. Stratospheric aerosols provide sites for catalytic heterogeneous reactions which destroy O_3, for instance, record low O_3 concentrations were observed in Antarctica for the successive two winters after Pinatubo [McCormick *et al.*, 1995]. Although O_3 depletion results in more UV radiation at the surface, stratospheric SO_4 could potentially counteract this effect by backscattering UV radiation. Tilmes *et al.* (2012) and Pitari *et al.* (2014) found that surface UV increases due to O_3 depletion under SAI would be entirely mitigated by aerosol scattering at low to mid latitudes (Fig. 1.14), but that this compensation would be less successful at high latitudes. O_3 depletion in an SAI scenario would diminish over time as anthropogenic CFCs are removed from the stratosphere [Pitari *et al.,* 2014].

1.1. Summary

SAI has received much attention recently as it is the only known mechanism for rapidly cooling Earth in the event of a climate emergency. The technological

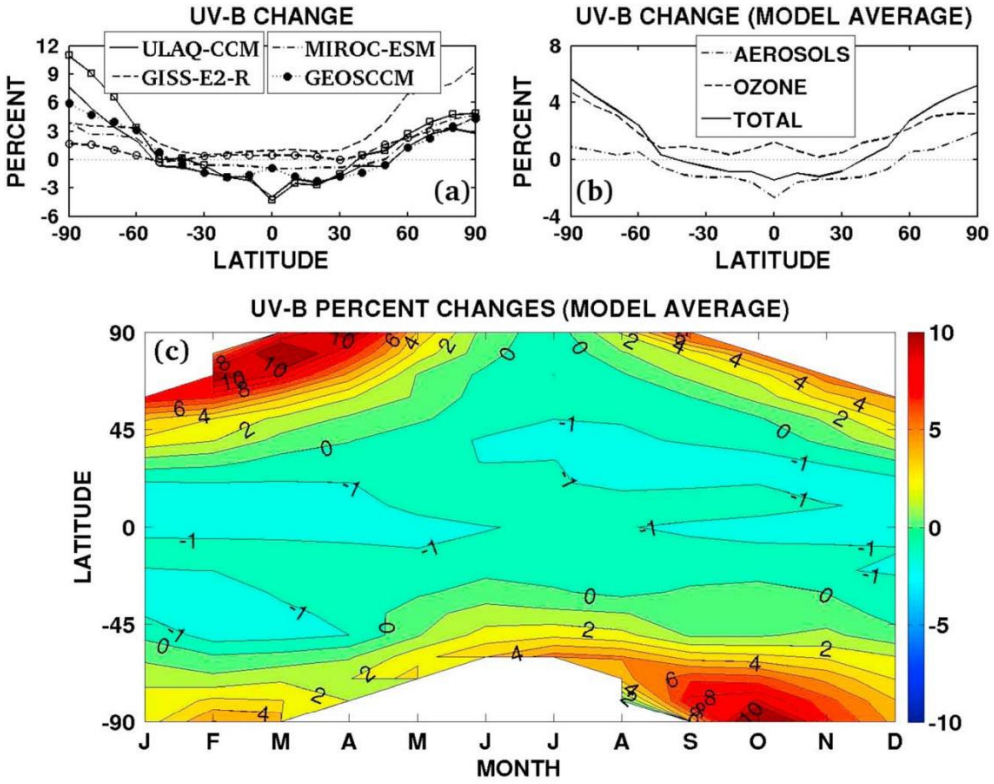

Figure 1.14. Surface UV-B changes for G3 and G4 with respect to RCP4.5 (2040-2049) for (a) all models, (b) model averages split into contribution from aerosol and O_3 changes, (c) zonally-averaged 'total' changes as a function of months. Fig. 15 from Pitari et al. (2014)

feasibility of SAI remains uncertain, in particular the logistics of transporting sufficient aerosol to the stratosphere and producing and maintaining an optically efficient aerosol layer are unresolved [Robock, 2014]. Additionally, the political and social barriers to SAI deployment are poorly understood, for instance, public acceptance of SAI would be pivotal for deployment yet SAI remains a peripheral topic in the climate change agenda [Corner *et al.*, 2013]. However, scientific research into the climatic impacts of SAI has proliferated due in part to the continued development of GCMs. A wide variety of research has been conducted, assessing various components of the climate system, for instance, the impacts of SAI on temperature, rainfall, sea ice, and atmospheric dynamics are relatively well established [Kravitz *et al.*, 2013].

A notable area of SAI research that remains undeveloped is the potential utility of alternative aerosols to SO_4. Ferraro *et al.* (2011) assessed the atmospheric temperature changes for various aerosols using a fixed dynamical heating code, and found that BC would produce a significantly greater stratospheric warming than SO_4 per injected mass. However, research on the climate impacts of SAI with alternative aerosols has generally received little attention. Alternative aerosols to SO_4 might

prove advantageous by avoiding the known side effects of SO_4 injection such as O_3 depletion and stratospheric warming [Pope *et al.*, 2012]. Additionally, aerosols such as TiO_2 scatter more sunlight per unit pass than SO_4 and therefore less aerosol would need to be injected for an equivalent radiative effect.

The general aim of this thesis is to explore the viability of counteracting anthropogenic climate change by injecting various aerosols into the stratosphere. In the literature review (Section 1.3) we identified SO_4 as the preeminent SAI candidate, TiO_2 as an efficient sunlight scattering aerosol, and BC as an efficient sunlight absorber. An interesting investigation (and the overarching aim of this thesis) is to compare the associated climate changes for SAI with these three aerosols. Thus, the main questions this thesis aims to answer are:

Goal 1. What are the associated climate changes (aerosol-induced and residual) for an equal amount of geoengineering for SO_4, TiO_2 and BC injection?

Goal 2. What are the relative quantities of each aerosol needed to produce an equal amount of geoengineering?

Goal 3. How effective is SAI at counteracting global warming and climate change and what are the robust residual climate changes that would arise?

In Chapters 2-4, we will assess the climatic impacts of injecting alternative aerosols to SO_4 using simple radiative transfer models (Chapter 2), an offline radiation code (Chapter 3), and a coupled atmosphere-ocean GCM (Chapter 4). As a means of testing the GCM's aerosol scheme, the 1991 Pinatubo eruption was simulated, with the results of the simulations presented in Chapter 5.

Another area of research that we identified in the literature review (Section 1.3) as being undeveloped is the impacts of SAI on tropical storm frequency. In Chapter 6, we will assess whether single-hemisphere SAI could be used to effectively modulate North Atlantic tropical storm frequency, in a complementary investigation to Haywood *et al.* (2013) who instead looked at single-hemisphere SAI and Sahelian precipitation.

Chapter 2 An introduction to atmospheric aerosols and simple models of their radiative effect

2.1. Introduction

The aim of this chapter is to introduce atmospheric aerosols and to investigate how atmospheric aerosol layers influence the solar radiation budget. We begin by discussing important aerosols, their sources and sinks, and their functions in the climate system. We then focus on SO_4, and discuss its precursor gases, chemistry, and relevant atmospheric processes. We then discuss how spherical aerosol particles interact with radiation (i.e. Mie theory) and we investigate specific aerosol optical properties. We conclude this chapter with a description of simple radiative transfer models for an atmospheric aerosol layer and explore applications to idealised aerosol layers that are chosen to represent SAI.

2.2. Atmospheric aerosols

2.2.1. Background

Aerosols refer to solid or liquid particles suspended in a gas, although cloud droplets and hydrometeors (e.g. rain droplets) are not included in this definition despite fulfilling this criterion [Boucher *et al.*, 2013]. Although the common definition of aerosol covers both the particle and the surrounding gas, we define aerosol as simply the particle in this thesis. Important atmospheric aerosols include SO_4, mineral dust, BC, OC, NO_3, and sea-salt (SS). Aerosols are either directly emitted to the atmosphere (primary aerosols) or form from the gas phase via chemical reactions (secondary aerosols). Anthropogenic processes have significantly altered the atmospheric aerosol composition, for instance, the majority of BC, SO_4 and NO_3 is of anthropogenic origin [Boucher *et al.*, 2013].

Aerosols are removed from the troposphere within seconds to weeks by wet and dry deposition processes; therefore, the global distribution of tropospheric aerosol exhibits significant spatiotemporal heterogeneity [Haywood and Boucher, 2000]. In contrast, stratospheric aerosol has an average atmospheric residence time of 1-2 years due to the lack of wet deposition in the stratosphere [Carslaw and Kärcher,

2006]. Aerosols directly influence Earth's radiation budget by absorbing and scattering radiation and, by acting as CCN, aerosols modify cloud microphysical properties and indirectly influence Earth's radiation budget.

2.2.2. Aerosol size distributions

Aerosol particles are predominantly microscopic in size, ranging from a few nanometres to tens of micrometers in diameter. A particle's microphysical properties are modified during its atmospheric lifetime by processes such as coagulation, chemical reactions, state changes, condensation and re-evaporation of water vapour and volatile chemical species on the aerosol surface, and the activation of cloud droplets [Seinfeld and Pandis, 1998]. Solid aerosols, such as BC, often exist as long particle chains (agglomerates), and may be coated with liquids such SO_4 or water. Liquid aerosols such as SO_4 or NO_3 are spherical, with sizes dependent on the age of the particle. Nucleation mode particles (i.e. newly nucleated particles) contain very few molecules and are therefore only a few nanometres in radius. Over time, nucleation particles grow by coagulation, condensation and evaporation to obtain sub-micrometre sizes (denoted Aitken mode 0.1-0.3 μm and accumulation mode 0.3-1 μm aerosols). Large aerosols, such as coarse mode (radius > 1 μm) mineral dust, experience greater gravitational settling velocities than smaller aerosols and are therefore deposited closer to their sources [Prospero, 1999].

The atmosphere contains aerosol number concentrations that may exceed 10^7-10^8 particles per cm^3. It is therefore impractical to monitor the precise size distribution of atmospheric aerosol. Instead, statistical relationships are often used to model the number concentrations of aerosol particles. The lognormal distribution provides a good fit to observations and is often used to model aerosol size distributions in GCMs [Seinfeld and Pandis, 1998]. Using the lognormal distribution, the number concentration (m^{-3}) of particles with radii between r and $r + dr$ ($N(r)$) is given by Eq. 2.1.

$$N(r) = \int_r^{r+dr} n(r)\,dr = \int_r^{r+dr} \frac{N_0}{r\ \ln\sigma\sqrt{2\pi}} e^{-\frac{(\ln r - \ln r_m)^2}{2\ \ln^2\sigma}} dr \qquad (2.1)$$

N_0 is the total aerosol number concentration, r_m is the median radius and σ is the geometric standard deviation (or spread) of the lognormal distribution. It is also

useful to model the aerosol volume concentration ($V(r)$), in order to determine the aerosol mass distribution. Assuming that the particles are spherical, the volume concentration ($m^3\ m^{-3}$) of particles with radii between r and $r + dr$ is given by Eq. 2.2.

$$V(r) = \int_{r}^{r+dr} \frac{4\pi r^3}{3} n(r)\, dr \tag{2.2}$$

$V(r)$ peaks at a larger radius than the $N(r)$, which means that most of the mass is contained in particles with larger radii and most of the number concentration is in particles with smaller radii. Often, atmospheric aerosol distributions will comprise multiple modes (e.g. nucleation, Aitken and coarse), each of which can be represented by a separate size distribution.

2.2.3. Important atmospheric aerosols

Mineral dust contributes over half of the total atmospheric aerosol mass burden, with surface emissions of ~2000 Tg yr^{-1} from semi-arid regions such as the Saharan desert and South West Asia [Huneeus *et al.*, 2011]. The transport of mineral dust to urbanised areas can result in reduced air quality and associated negative human health effects [Knippertz and Todd, 2012]. However, mineral dust contains high iron content and, when deposited into the ocean, can influence oceanic biogeochemistry by providing an important nutrient for phytoplankton [Choobari *et al.*, 2013]. Approximately 25 % of current mineral dust emissions are from land that has been disturbed by anthropogenic factors such as land-use changes and climate change [Ginoux *et al.*, 2012]. Although primary mineral dust is hydrophobic, coagulation with soluble particles in the atmosphere allows aged dust particles to act as CCN and nucleate cloud droplets (see Box 2) [e.g. Carslaw *et al.*, 2010].

SS is emitted to the atmosphere from bubble bursting from wind-generated waves at the ocean surface [Boucher *et al.*, 2013]. Bubble bursting occurs during wave breaking and from friction between the overlying wind and the ocean surface, consequently, oceanic SS emissions are sensitive to the speed of near-surface winds [Athanasopoulou *et al.*, 2008]. Global SS emissions are poorly constrained by observations and climate models, which is due to the model specific representations of both SS and the sea spray source function [de Leeuw *et al.*, 2011]. Boucher *et al.* (2013) estimate natural SS emissions of 1400 to 6800 Tg yr^{-1}. SS is primarily

Box 2. Aerosol-cloud interactions

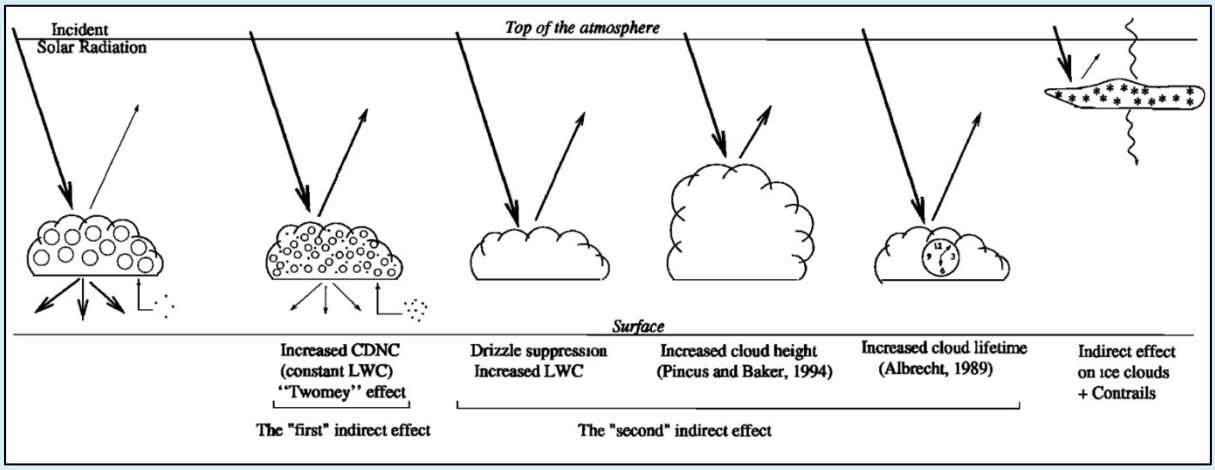

Figure 2.1 Schematic of the aerosol-cloud interactions (Fig. 1 from Haywood and Boucher (2000))

When the ambient atmosphere is supersaturated with water vapour, aerosol particles act as CCN and nucleate cloud particles. Cloud droplet activation depends on a complex interplay between a particle's surface curvature (the Kelvin effect) which tends to oppose activation, and its solute concentration (the Raoult effect) which reduces the ambient vapour pressure required to instigate activation [Lohmann *et al.*, 2016]. Very small aerosol particles are therefore unlikely activate due to their high surface curvature. The homogeneous nucleation of liquid cloud droplets requires water vapour supersaturations of ~400 % whereas heterogeneous nucleation on aerosol surfaces may occur at supersaturations of <1 % [Seinfeld and Pandis, 1998].

Clouds contribute to the planetary albedo by reflecting solar radiation and contribute to the greenhouse effect by absorbing terrestrial LW radiation and then re-emitting at a lower temperature [Lohmann *et al.*, 2016]. On a global and annual-mean basis, the cloud albedo effect dominates with a cloud radiative effect of -47 Wm^{-2} compared to +26 Wm^{-2} for the cloud greenhouse effect [Boucher *et al.*, 2013]. Cloud microphysical properties are sensitive to the ambient aerosol distribution. For instance, an increase in CCN concentration can enhance the cloud particle concentration for a constant liquid water content. As smaller particles have greater surface area than larger particles, and the optical thickness

Continued overleaf

of the cloud is proportional to the total particle surface area, this results in an enhanced cloud albedo [Twomey, 1977]. This process, which is denoted the 'first indirect effect', is schematically shown in Fig. 2.1. Other aerosol-cloud interactions may act to suppress precipitation and modify cloud lifetime [Albrecht *et al.*, 1989] and are denoted 'second indirect effects'. The first indirect effect has been studied with respect to volcanoes [e.g. Gassó, 2008; Yuan *et al.*, 2011; McCoy and Hartmann, 2015] and in ship tracks [e.g. Chen *et al.*, 2012]. Aerosol-cloud-radiation interactions remain the most uncertain of all known climate forcing agents [Rosenfeld *et al.*, 2014].

composed of inorganic sodium chloride (NaCl), organic aerosol (OA), and water as an internal mixture, with particles ranging from 0.05 to 10 μm in diameter [Andreae and Rosenfeld, 2008]. SS is hygroscopic and therefore fine mode SS particles efficiently act as CCN, which is an important factor for cloud distributions over unpolluted ocean regions where concentrations of other hygroscopic aerosols are negligible. SS also scatters SW radiation, which results in an annual-mean direct radiative effect over the Southern Ocean of -2 W m^{-2} [Ayash *et al.*, 2008].

BC is a primary aerosol formed from the incomplete combustion of biomass, biofuels, and fossil fuels. Total global BC emissions amount to ~8 Tg yr^{-1}, while OC is co-emitted from these sources at a total rate of ~34 Tg yr^{-1} [Bond *et al.*, 2004]. BC remains in the atmosphere for approximately a week and is therefore concentrated near to regions of high fossil fuel and biomass burning activity such as over NH continents [Chung and Seinfeld, 2005]. Although pure BC aerosol is hydrophobic, atmospheric ageing via coagulation with hygroscopic material can enhance a BC particle's hygroscopicity and concomitantly increase the efficacy of moisture uptake [Liu *et al.,* 2013]. Aged BC particles are therefore able to act as CCN and IN, and are more likely to be removed through wet deposition than fresh BC particles. BC efficiently absorbs SW radiation and therefore anthropogenic BC emissions from fossil fuel burning have contributed a radiative forcing of +0.4 Wm^{-2} [IPCC, 2013]. BC deposition on snow and sea ice decreases the albedo of the surface, which enhances ice melt and asserts a positive feedback on climate [Flanner *et al*., 2007].

Other atmospheric aerosols include NO_3, primary organic aerosol (POA), secondary organic aerosol (SOA) and primary biogenic aerosol particles (PBAPs). NO_3 forms

from the reaction of nitric acid (HNO_3) with ammonia (NH_3), and from the reaction of HNO_3 with mineral dust or SS [Andreae and Rosenfeld, 2008]. The first reaction requires a high ambient concentration of HNO_3 and NH_3 and low concentration of H_2SO_4, and results in the formation of submicron ammonium nitrate (NH_4NO3) particles [Bauer *et al.*, 2007]. The second reaction produces coarse-mode nitrate salts [Xu and Penner, 2012]. POA is emitted to the atmosphere from fossil fuel combustion, biomass burning and bubble bursting at the ocean surface [Jimenez *et al.*, 2009; Gantt *et al.*, 2011]. SOA is formed from the oxidation products of volatile organic compounds of biogenic origin (e.g. monoterpene, isoprene) and anthropogenic origin (e.g. petroleum) [Andreae and Rosenfeld, 2008; Ehn *et al.*, 2014]. OA (POA + SOA) comprises ~50 % of the atmospheric sub-micron aerosol mass and influences climate by acting as CCN [Spracklen *et al.*, 2011]. PBAPs are solid particles emitted from biological sources. PBAPs include microorganisms such as bacteria and viruses, and other organic matter such as fungal spores, pollen and plant debris [Després *et al.*, 2012]. Global PBAP emissions are noteworthy at 50-1000 Tg yr^{-1} [Boucher *et al*., 2013] and local emissions over vegetation may be enhanced during precipitation events [Huffman *et al.*, 2013]. Additionally, PBAPs are important vectors for the spread of airborne viruses, and may play an important climatic role as IN [Huffman *et al.*, 2013].

2.2.4. The sulphur cycle

SO_4 plays an important role in the climate system by scattering solar radiation and acting as CCN. Atmospheric SO_4 is the final oxidation product of reduced sulphur gases emitted from the surface. The atmospheric sulphur cycle is dominated by anthropogenic SO_2 emissions and natural dimethyl sulphide (DMS) and OCS emissions. Additionally, large volcanic eruptions can significantly perturb the tropospheric or stratospheric sulphur budget [Gettelman *et al.*, 2015; Schlesinger and Bernhardt, 2013]. Reduced sulphur plays an important biological role in providing structure to protein chains [Charlson *et al.*, 1992], while acidic sulphur compounds deposited at the surface contribute to the natural weathering of rocks [Calmels *et al.*, 2007]. In this section, we explore the key components of the sulphur cycle in order to establish the primary functions and origins of SO_4 in the climate system.

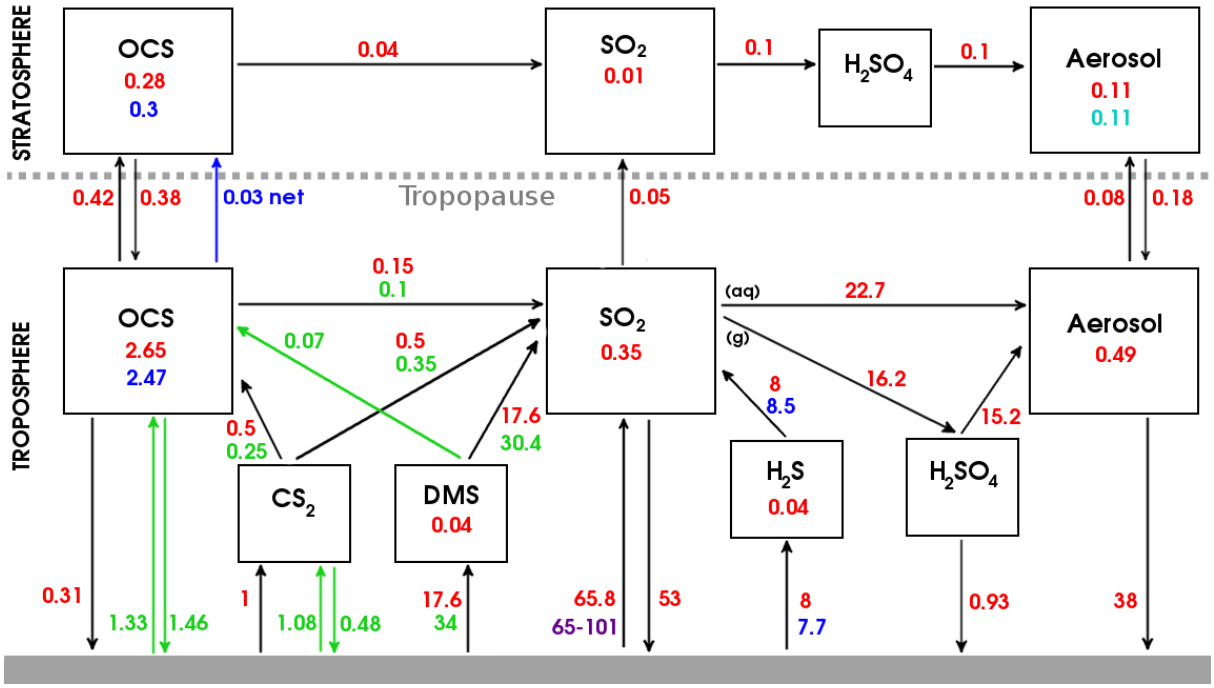

Figure 2.2. The atmospheric sulphur cycle, adapted from Fig. 3 of Sheng et al. (2015a). Arrows point in the direction of fluxes, with adjoining numbers denoting the magnitude of the flux (Tg[S] yr^{-1}). Numbers in the boxes indicate the atmospheric burden (Tg[S]). Red numbers are results from the SOCOL-AER chemistry-transport model [Sheng et al., 2015a]. Green numbers are estimates from Lee and Brimblecombe (2016). Blue numbers are estimates from Watts (2000). Purple numbers are from Notholt and Bingemer (2006). The stratospheric aerosol burden (cyan) is from SAGE_4λ observations [Arfeuille et al., 2013]

2.2.4.1. Precursor gases

Dimethyl sulphide (DMS)

The main natural source of atmospheric SO_4 is from the oxidation of DMS [Haywood and Boucher, 2000]. DMS forms from the decomposition of dimethylsulphonium proprionate, which is produced by marine organisms such as phytoplankton and algae [Carslaw *et al.*, 2010]. The ocean-to-atmosphere transmission of DMS is sensitive to the atmospheric wind-speed, the temperature difference between the atmosphere and the ocean surface, and the DMS concentration in the seawater [Andreae and Crutzen, 1997]. The annual-mean DMS flux from the ocean to the atmosphere is approximately 28 Tg[S] yr^{-1} [Lana *et al.*, 2011]. DMS is oxidised in the atmosphere within days by reaction with the hydroxyl (OH) radical or the NO_3 radical. The OH oxidation pathway is predominant in the marine atmosphere, and only occurs during the daytime due to the prerequisite photolysis of OH, which requires sunlight [Seinfeld and Pandis, 1998]. The primary oxidation product of DMS is SO_2

with lesser amounts of methane sulphonic acid, OCS, and other gases produced. SO_2 is oxidised in the troposphere with a lifetime of a week to form SO_4 [Carslaw *et al.*, 2010]. GCM simulations indicate that DMS emissions account for ~30 % of the global atmospheric SO_4 burden [Kloster *et al.*, 2006].

Carbonyl sulphide (OCS)

OCS is the most abundant sulphur gas in the atmosphere, due to its low reactivity and concomitantly long tropospheric residence time [Seinfeld and Pandis, 1998]. The primary sources of atmospheric OCS include the oxidation of DMS and carbon disulphide (CS_2) gases, and the direct emission of OCS from the ocean [Notholt and Bingemer, 2006]. Minor sources include emissions from wetlands, fossil fuel burning, biomass burning, and photochemical processing in raindrops [Schmidt *et al.*, 2013a]. Total global OCS emissions amount to ~1.65 Tg[S] yr^{-1}, of which oceanic fluxes comprise 55 %, oxidation processes 20 %, and anthropogenic activities 25 % [Lee and Brimblecombe, 2016]. The primary OCS sinks include uptake by land vegetation and soils, and oxidation by the OH radical in the troposphere [Watts, 2000]. As the tropospheric residence time for OCS is long (~2-6 years), a fraction of the OCS is transported to the stratosphere. In the stratosphere, OCS is converted to SO_2 via photodissociation or oxidation pathways, which is then further oxidised to form SO_4 aerosol [Barkley *et al.*, 2008]. The lower stratosphere contains a background SO_4 layer known as the Junge layer, which is maintained in volcanically quiescent periods by contributions from OCS [Brühl *et al.*, 2012], SO_2 from moderate volcanic eruptions [Vernier *et al.*, 2011], and anthropogenic SO_2 emissions [Myhre *et al.*, 2004]. The relative contributions of these sources to the Junge layer remain a subject of contention [e.g. Solomon *et al.*, 2011].

Carbonyl disulphide (CS_2) and hydrogen sulphide (H_2S)

CS_2 is emitted from anthropogenic sources such as rayon, cellophane, and pigment production, and natural sources such as the ocean, anoxic soils and wetlands [Chin and Davis, 1993]. Total global emissions are estimated to be ~1.1 Tg[S] yr^{-1}, although this is highly uncertain due to lack of observations [Lee and Brimblecombe, 2016]. In the troposphere, CS_2 is oxidised within days to form OCS and SO_2.

H_2S is emitted from natural sources such as vegetation, salt marshes, wetlands, coastal waters, and the oceans, and from anthropogenic sources such as automobiles, natural gas extraction and paper refineries [Möller, 1984; Kourtidis *et al.*, 2004]. H_2S observations are sparse; therefore, emissions estimates are subject to large uncertainty. In particular, volcanic H_2S emissions estimates range from 1-35 Tg[S] yr^{-1} [Carn *et al.*, 2016]. Part of the difficulty in measuring H_2S arises from its weak infrared absorption lines, which overlap with H_2O and CO_2 [Clarisse *et al.*, 2011]. Watts (2000) estimates global H_2S emissions to be ~7.25 Tg[S] yr^{-1} with a 43 % anthropogenic contribution. In the troposphere, H_2S has a lifetime of days and is readily oxidised to form SO_2 [Seinfeld and Pandis, 1998].

Sulphur dioxide (SO_2)

Atmospheric SO_2 occurs naturally as an intermediate oxidation product between reduced sulphur gases such as DMS, OCS, CS_2 and H_2S, and fully oxidised SO_4 (Fig. 2.2). However, current anthropogenic SO_2 emissions from fossil fuel combustion, sulphide ore smelting, and biomass burning amount to ~52 Tg[S] yr^{-1}, which exceeds natural sources such as continuous volcanic degassing (~10 Tg[S] yr^{-1}) and the oxidation of reduced sulphur gases (~35 Tg[S] yr^{-1}) [Notholt and Bingemer, 2006; Klimont *et al.*, 2013]. SO_2 is oxidised in the troposphere to form SO_4 aerosol through an aqueous pathway involving dissolution of SO_2 in water droplets, and via direct oxidation in the presence of the OH radical [Charlson *et al.*, 1992]. SO_2 is directly absorbed by Earth's surface (dry deposition) and is subject to wet deposition due to its high solubility in water [Seinfeld and Pandis, 1998].

Anthropogenic SO_2 emissions increased from 10 Tg[S] yr^{-1} in 1900 to 65 Tg[S] yr^{-1} in 1980, due to global economic expansion and the associated proliferation of coal combustion [Smith *et al.*, 2011]. Of particular noteworthiness, the post-war period (1950-1970) experienced an unprecedented SO_2 emissions growth of ~17 Tg[S] per decade. This resulted in enhanced tropospheric SO_4 concentrations which contributed to two major environmental problems - air pollution (e.g. smog) and acid rain [Stern, 2006]. Major smog events in London (1952) and Los Angeles (1966) caused ~3500 and 169 deaths respectively, and galvanised the UK and US governments to introduce 'clean air' regulation acts [Stern, 1982; Brimblecombe, 2006]. From 1990 to 2000, global SO_2 emissions decreased due to a policy-driven

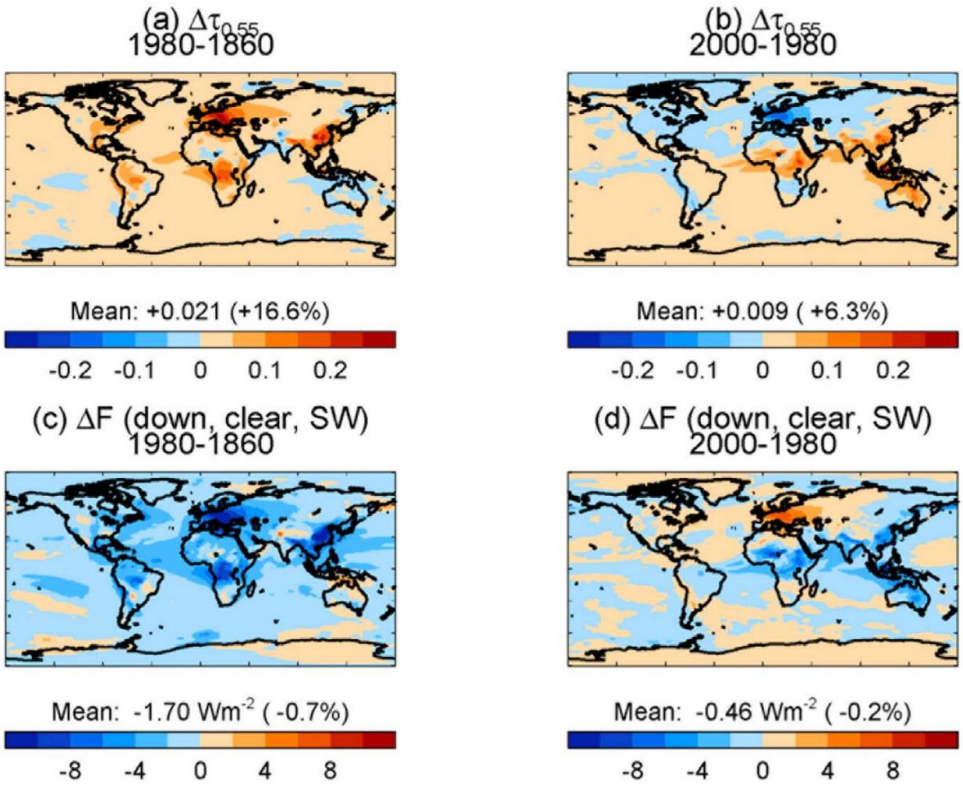

Figure 2.3. Aerosol 550nm optical depth anomaly during periods of (a) high SO_2 emissions and (b) low SO_2 emissions and clear-sky radiative effect (c,d) for the respective periods. Data are from HadGEM2-ES historical simulations. Fig. 1 from Haywood et al. (2011)

shift from coal to natural gas energy resources and from the development of flue-gas desulphurization (FGD) techniques [Smith *et al.*, 2011]. Although SO_2 emissions in Asia continued to increase from 2000-2005 due to intensive industrialisation, the recent proliferation of FGD in China has resulted in a national SO_2 emissions reduction since 2006 [Klimont *et al.*, 2013]. SO_2 emissions reductions improve regional air quality and affect climate by altering the planetary albedo. For instance, concerted SO_2 emissions reductions in Europe since the 1980s have inadvertently enhanced the polar amplification of global warming [Navarro *et al.*, 2016].

The SO_2 emission trends outlined above were implicated in myriad climatic changes observed over the 20th century, for instance, a weakening of the South Asian monsoon [Bollasina *et al.*, 2011], a southward shift of the tropical rainbelt [Hwang *et al.*, 2013], and North Atlantic storm changes [Dunstone *et al.*, 2013]. Additionally, observed atmospheric SO_4 burdens were closely correlated to observed surface solar radiation changes from 1950-2000 [Wild, 2012]. Therefore, Wild (2012) suggests that the observed solar 'dimming' episode from 1950 to 1980 was the result of increasing anthropogenic SO_2 emissions, and the observed solar 'brightening'

episode from 1980 to 2000 resulted from emissions reductions. Figure 2.3 shows the 550nm aerosol optical depth anomaly and surface clear-sky solar radiation anomaly between: (a,c) 1860 and 1980, and (b,d) 1980 and 2000, from HadGEM2-ES simulations performed by Haywood *et al*. (2011). It is clear that the solar dimming (negative ΔF) and brightening (positive ΔF) patterns in cloud-free skies are closely correlated with increases and decreases in aerosol burden, respectively, which supports the SO_2-solar-dimming hypothesis. This result highlights the influence that humanity had on the climate over the 20th century.

2.2.4.2. Tropospheric sulphate

SO_4 is the most important component of the sulphur cycle in terms of climatic influence. It is useful to distinguish between tropospheric and stratospheric SO_4 because of their different compositions, origins and atmospheric roles. Tropospheric SO_4 exists as a mixture of H_2SO_4, ammonium bisulphate (NH_4HSO_4), and ammonium sulphate ($(NH_4)_2SO_4$), with the relative masses of these species determined by the ambient acidity and NH_3 availability [Seinfeld and Pandis, 1998]. Atmospheric aerosols are rarely composed of a single chemical constituent due to ageing processes; therefore, SO_4 often exists as a mixture with NH_3, NO_3, organic compounds and BC [Boucher *et al*., 2013]. SO_4 is highly soluble in water and therefore readily accumulates water vapour [d'Almeida *et al.*, 1991]. Additionally, this hygroscopic tendency allows SO_4 to act as CCN and thereby nucleate cloud particles. Although it is widely recognised that tropospheric SO_4 plays an important role in modulating cloud distributions and cloud microphysical properties [e.g. Carslaw *et al.*, 2010], determining the contribution of anthropogenic SO_4 to the total cloud radiative effect has proven difficult [Seinfeld *et al*., 2016].

Clouds influence the sulphur cycle by providing sites for aqueous-phase chemistry and by removing SO_4 within precipitation. The first process involves cloud droplets absorbing semivolatile organic and sulphur compounds, which can then condense onto the SO_4 CCN particle. If the cloud droplet evaporates, the aerosol is re-emitted to the atmosphere with a greater mass [Ervens *et al.*, 2011]. Precipitation removes SO_4 from the atmosphere via nucleation scavenging and impaction scavenging. Nucleation scavenging (or rainout) involves the removal of aerosol that was involved in the formation of the cloud droplet, while impaction scavenging (or washout) occurs

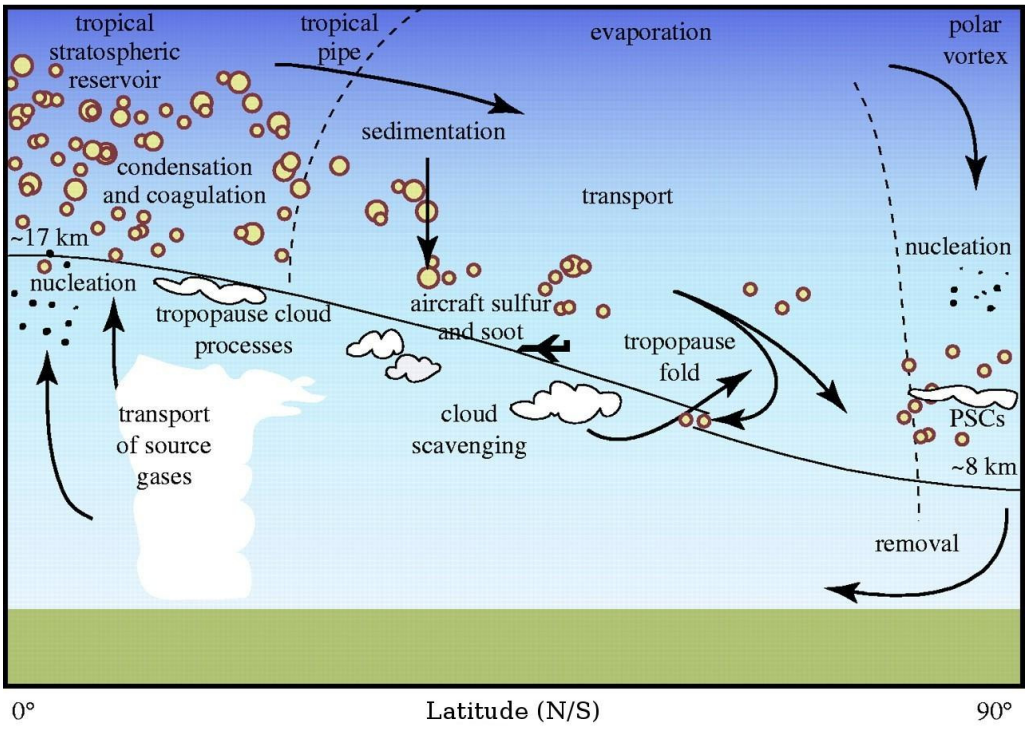

Figure 2.4. The key stratospheric SO_4 processes. Fig. 1.1 from Carslaw and Kärcher (2006)

when a falling hydrometeor collects aerosol during its descent [Lohmann *et al.*, 2016]. Croft *et al.* (2010) used a GCM to determine the contribution of rainout and washout to the total SO_4 deposition, finding relative contributions of 82 % and 14 % respectively. SO_4 is also deposited at the surface via dry deposition and gravitational settling (sedimentation). Aerosols are (dry) transported from the upper atmosphere toward the surface by eddy diffusion and gravitational settling. Subsequent transmission through the quasi-laminar sub-layer directly above the surface is dependent on the size of the aerosol and the surface topography. Sub-micron particles (<0.1 μm) are transmitted to the surface via Brownian diffusion, coarse mode particles (>2.5 μm) via gravitational settling, and intermediate sized particles via impaction and interception [Fuzzi *et al.*, 2015]. Observations and model studies indicate that dry deposition only plays a minor role in the removal of particulate-SO_4 from the troposphere compared to wet deposition [Croft *et al.*, 2010; Vet *et al.*, 2014].

2.2.4.3. Stratospheric sulphate

The transport of chemicals from the troposphere to the stratosphere occurs primarily in mid-latitude folds and in rising air masses in the tropics (Fig. 2.4) [Holton *et al.*, 1995]. The tropical tropopause layer marks the key entry point of sulphur gases such as OCS, SO_2 and H_2SO_4 into the stratosphere. Once in the stratosphere, OCS and

SO_2 are oxidised to form H_2SO_4 vapour, which is generally supersaturated in the lower tropical stratosphere [Rasch *et al.*, 2008b]. OCS oxidation prevails above 25 km altitude, while SO_2 oxidation is active at lower altitudes [Weisenstein and Bekki, 2006]. SO_4 aerosols form in the lower stratosphere from the binary homogeneous nucleation of gaseous H_2SO_4 and water vapour. These newly-nucleated particles then grow by condensation and coagulation [Carslaw and Kärcher, 2006]. Although stratospheric aerosol is primarily composed of aqueous H_2SO_4 (75% by weight), other chemicals such as meteoric smoke particles [e.g. Saunders *et al.*, 2012] and HNO_3 [Carslaw and Kärcher, 2006] also contribute to the aerosol mass.

Aerosol that forms in the lower tropical stratosphere is rapidly transported zonally by the strong stratospheric wind current [Bluth *et al.*, 1992]. Additionally, aerosol in the lower tropical stratosphere is transported poleward by the slow overturning BDC, which is partially impeded by a "leaky tropical pipe" between 15-30^o latitude. This 'leaky tropical pipe' restricts the mixing of tropical and subtropical air during the easterly phase of the QBO [Carslaw and Kärcher, 2006]. Stratospheric aerosols continue to evolve by microphysical processes throughout their residency. At the top of the stratospheric aerosol layer (~30 km altitude), SO_4 aerosols evaporate due to high ambient temperatures and low H_2SO_4 partial pressures. Within the aerosol layer, aerosols grow via coagulation and condensation and undergo gravitational settling which reduces the aerosol mass near the top of the aerosol layer [Weisenstein and Bekki, 2006]. Aerosols are removed from the stratosphere in extratropical tropopause folds and during the diabatic descent of air over the poles in winter and spring. Additionally, aerosols act as sites for PSC particle formation at high latitudes, with these PSC particles then rapidly growing to micrometre sizes and falling out of the stratosphere (Fig. 2.4) [Fahey *et al.*, 2001]. The average stratospheric lifetime for an aerosol particle is 1-2 years [Driscoll *et al.*, 2012].

Continuous volcanic degassing provides a constant source of SO_2 to the stratosphere and thereby modulates the background SO_4 layer [Vernier *et al.*, 2011]. Occasional cataclysmic volcanic eruptions can inject vast quantities of SO_2 into the stratosphere and transiently enhance the background SO_4 layer [Robock, 2000]. Stratospheric SO_4 influences O_3 chemistry by providing sites for catalytic heterogeneous reactions involving free radicals and O_3 [Solomon, 1999]. Additionally, an enhanced stratospheric SO_4 layer can lead to warming in the lower

tropical stratosphere, which then induces a positive mode of the Arctic oscillation (i.e. a stronger polar vortex) and results in high-latitude winter warming [Mao and Robock, 1998]. More importantly for this chapter, an enhanced stratospheric SO_4 layer efficiently backscatters solar radiation to space, which reduces the solar irradiance at the surface and results in global cooling. This effect was observed after Mt. Pinatubo [Soden *et al*., 2002], but was first posited by Benjamin Franklin in 1784 following the 1783 Lakagigar eruption [Franklin, 1784]. The interaction of aerosol with solar radiation is investigated in the next section.

2.3. Aerosol interactions with radiation

2.3.1. Mie theory: overview

When a beam of light traverses a medium (for instance, the atmosphere), particles in that medium attenuate the beam by scattering and absorbing a fraction of its energy. The degree of attenuation depends on the particle's radius (a) and refractive index (m), and on the wavelength of the incident radiation (λ). Mie theory formulates the scattering and absorption of light by spherical particles with sizes greater or approximately equal to the wavelength of the incident radiation [Mie, 1908]. Mie theory is applicable to light scattering by atmospheric aerosols. For smaller particles such as gases, the Rayleigh approximation is sufficient to describe the distribution of scattered radiation [Liou, 1977]. Mie theory solely depends on two properties of the particle – its radius and refractive index.

We do not give the complete mathematical formulation of Mie theory here [see e.g. Bohren and Huffman, 1983]. It is sufficient for our purposes to note that Mie theory provides a solution in spherical polar coordinates $[\hat{r}, \hat{\theta}, \hat{\phi}]$ to Maxwell's equations for the specific example of an electromagnetic wave scattered by a spherical particle in a homogeneous medium. Mie theory begins with a derivation of the scattering coefficients $\mathrm{a_n}$ and $\mathrm{b_n}$ (where n denotes the nth element of an infinite series, and the coefficients $\mathrm{a_n}$ and $\mathrm{b_n}$ are composed of harmonic Riccati-Bessel functions of the covariates m, a and λ). $\mathrm{a_n}$ and $\mathrm{b_n}$ are directly obtained from solving the wave equation with the boundary conditions that the incident, scattered and internal electric and magnetic fields are continuous on the particle's surface. To relate the scattered electromagnetic field to the incident field (which is the overarching aim of Mie theory), it is expedient to define two scattering functions: $S_1(\theta)$ and $S_2(\theta)$ (where θ is

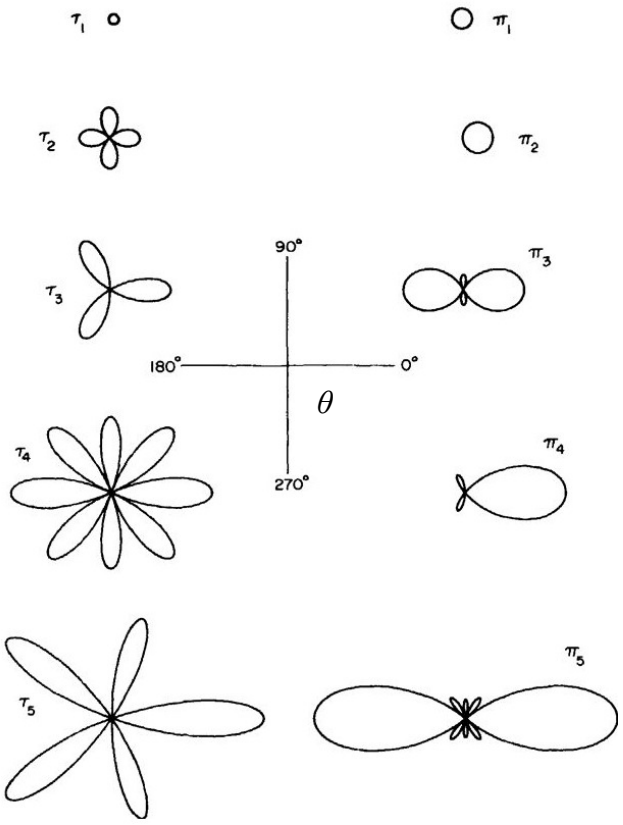

Figure 2.5. Polar plots of the first functions of π_n and τ_n. Fig. 4.3 from Bohren and Huffman (1983)

---

the angle of the scattered wave relative to the direction of propagation of the incident wave).

$$S_1(\theta) = \sum_{n=1}^{\infty} \frac{2n+1}{n(n+1)} [a_n \pi_n(\cos\theta) + b_n \tau_n(\cos\theta)] \tag{2.3a}$$

$$S_2(\theta) = \sum_{n=1}^{\infty} \frac{2n+1}{n(n+1)} [b_n \pi_n(\cos\theta) + a_n \tau_n(\cos\theta)] \tag{2.3b}$$

π_n and τ_n are functions of the associated Legendre polynomials of order 1, and the cosine of θ is 1 in the direction of propagation of the incident wave. The higher order terms of the infinite series in Eq. 2.3 become more important as the radius of the particle increases. Figure 2.5 shows polar plots (θ from 0^o to 360^o) of the first five terms of π_n and τ_n. The higher order terms of π_n and τ_n exhibit larger forward lobes (i.e. in the $\theta = 0^o$ direction), and smaller backward lobes ($\theta = 180^o$ direction) than the lower order terms. The physical interpretation of this result is that larger particles scatter more radiation in the forward direction than the backward direction.

It is customary when outlining Mie theory to decompose the scattered and electric fields into perpendicular (E_p) and parallel (E_l) components (Fig. 2.6). Under this

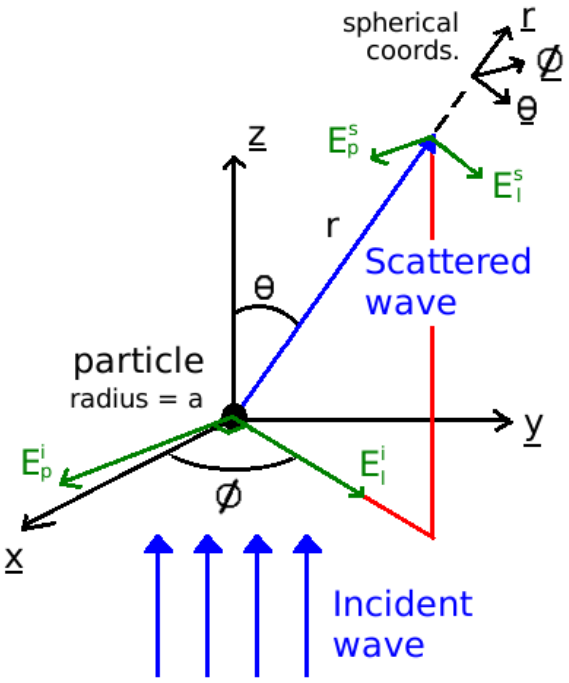

Figure 2.6. Schematic of the perpendicular (E_p) and parallel (E_l) components of the incident and scattered electric fields. Based on Fig. 2 from Liou (1977)

guise, the scattered electric field (E^s) is related to the incident electric field (E^i) according to Eq. 2.4 [Liou, 1977]. In Eq. 2.4, k is the wavenumber ($k = 2\pi / \lambda$) of the incident and scattered radiation, and i is the imaginary unit. Equation 2.4 is the fundamental result of Mie theory, and describes the amplitude and polarisation of the scattered wave as a function of its position in space, the properties of the incident wave, and the particle's optical properties.

$$\begin{pmatrix} E_p^s \\ E_l^s \end{pmatrix} = \frac{e^{ik(r-z)}}{-ikr} \begin{bmatrix} S_1(\theta) & 0 \\ 0 & S_2(\theta) \end{bmatrix} \begin{pmatrix} E_p^i \\ E_l^i \end{pmatrix} \tag{2.4}$$

2.3.2. Extinction, scattering, and absorption efficiencies

In terms of aerosol-radiation interactions, we are particularly interested in certain optical parameters that can be obtained from Mie theory. Firstly, it is useful to determine the fraction of the incident energy that is either absorbed or scattered by an individual aerosol particle. From Mie theory, this is achieved by integrating the Poynting vectors (i.e. the energy fluxes through a surface; determined from ½ Re{E×H} where H is the magnetic field and Re{} denotes the real part of a complex number) over the surface of an imaginary sphere with radius r that completely encloses the particle. From these integrals, we can obtain the total power that is scattered (W_s) and made extinct (W_e = absorbed + scattered) by the particle.

$$W_s = \frac{1}{2}\,\mathrm{Re}\left\{\int_0^{2\pi}\int_0^{\pi}(E_s \times H_s^*)\, r^2 \sin\theta\, d\theta\, d\phi\right\} \tag{2.5a}$$

$$W_e = \frac{1}{2}\,\mathrm{Re}\left\{\int_0^{2\pi}\int_0^{\pi}(E_i \times H_s^* + E_s \times H_i^*)\, r^2 \sin\theta\, d\theta\, d\phi\right\} \tag{2.5b}$$

Mie theory provides us with expressions for E_s, E_i, H_s^* and H_i^*, which represent the electric fields and the complex conjugates of the magnetic fields for the incident and scattered waves, respectively. The scattering and extinction cross sections (σ_s and σ_e in units of m^2) follow from dividing W_s and W_e by the intensity of the incident radiation (in units of W m^{-2}), once the integrals in Eq. 2.5 have been explicitly solved. Expressions for σ_s and σ_e in terms of the scattering coefficients a_n and b_n are provided below (Eq. 2.6).

$$\sigma_s = \frac{2\pi}{k^2}\sum_{n=1}^{\infty}(2n+1)(|a_n|^2 + |b_n|^2) \tag{2.6a}$$

$$\sigma_e = \frac{2\pi}{k^2}\sum_{n=1}^{\infty}(2n+1)\,\mathrm{Re}\{|a_n| + |b_n|\} \tag{2.6b}$$

The virtual cross-sections σ_s and σ_e represent the "shadows" of the particle, or the area of the incident irradiance that is attenuated by scattering or extinction. The absorption cross-section (σ_a) can be determined from the difference between the extinction and scattering cross-sections ($\sigma_a = \sigma_e - \sigma_s$). It is also useful to determine the scattering, absorption, and extinction efficiencies (Q_s, Q_a, Q_e), defined as the ratios of the virtual cross-sections (σ_s, σ_a, σ_e) to the particle's geometric cross-sectional area. For a spherical particle with radius a, the cross-sectional area of the particle is equal to πa^2. Expressions for the unitless scattering and extinction efficiencies (Q_s and Q_e, respectively) are given in Eq. 2.7.

$$Q_s = \frac{2}{x^2}\sum_{n=1}^{\infty}(2n+1)(|a_n|^2 + |b_n|^2) \tag{2.7a}$$

$$Q_e = \frac{2}{x^2}\sum_{n=1}^{\infty}(2n+1)\,\mathrm{Re}\{a_n + b_n\} \tag{2.7b}$$

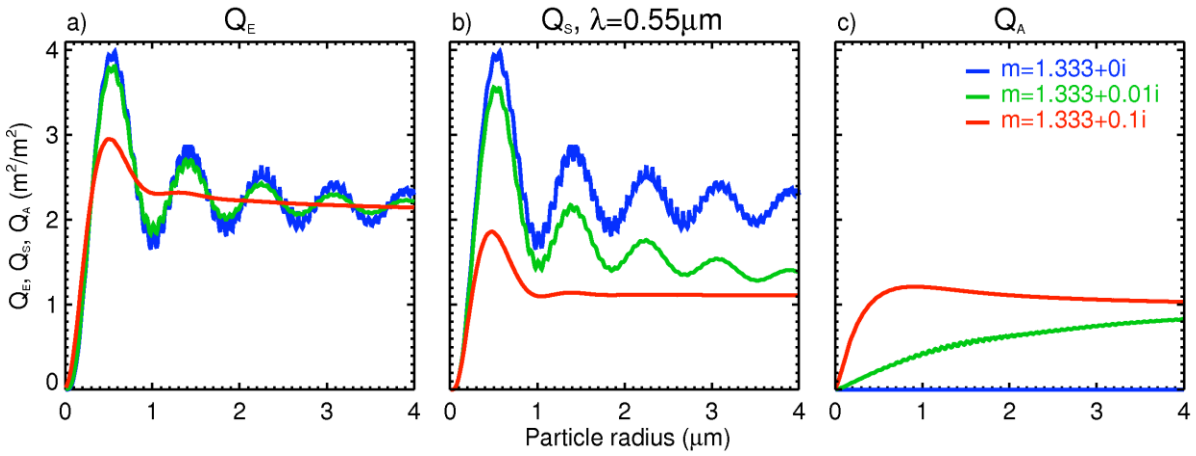

Figure 2.7 (a) extinction, (b) scattering, and (c) absorption efficiencies as a function of radius for λ = 0.55μm and various refractive indices

In Eq. 2.7, x denotes the size parameter (x = ka = $2\pi a$ / λ). As with the virtual cross-sections, the absorption efficiency Q_a is the difference between the extinction and scattering efficiencies ($Q_a = Q_e - Q_s$). Figure 2.7 shows the extinction, scattering and absorption efficiencies as a function of particle radius (0.01 < a < 4 μm) for λ = 0.55 μm and for three different values of m. For Fig 2.7, we have varied the imaginary part of m and kept the real part equal to 1.333; which is the real part of the refractive index of H_2O at λ = 0.55 μm. We calculated the optical parameters plotted in Fig. 2.7 using a Matlab® Mie code written by Christian Maetzler[6] and based on the algorithm of Bohren and Huffman (1983). In Fig. 2.7, the Q_e and Q_s values for m = 1.333+0*i* are identical because the imaginary component of m (i.e. the absorption component) is zero. Three aspects of Q_s(m =1.333+0i) are particularly interesting: (1) for a < λ, Q_s increases monotonically, (2) for a > λ, Q_s oscillates periodically around ~2, and (3) for a > λ, Q_s exhibits a pronounced ripple structure. Effect (1) is denoted the *Rayleigh effect* and is applicable to particles much smaller than the incident wavelength of light. Specifically, Rayleigh theory is valid for x << 1 and |m|x << 1. Under the Rayleigh criteria $Q_s \approx \lambda^{-4}$ and $Q_a \approx \lambda^{-1}$; this means that smaller particles scatter and absorb radiation more efficiently at shorter wavelengths. Effect (2) is denoted the *interference effect* and arises from interference of transmitted and diffracted waves incident on the centre of the particle. For Re{m} > 2.5, the periodicity of the interference effect disappears [Chýlek and Zhan, 1989]. Lastly, effect (3) is denoted the *ripple effect* and arises from the resonances of electromagnetic waves on the particle's surface. In mathematical terms, this arises from minima in the denominators of the a_n and b_n coefficients [van de Hulst, 1957]. Both the interference

[6] http://omlc.org/software/mie/ - last accessed 10/10/2016

and ripple structures are attenuated for partially absorbing particles (m = 1.333+0.01i and m = 1.333+0.1i in Fig. 2.7).

2.3.3. Single scattering albedo

A useful optical parameter for the aerosol sciences is the wavelength-dependent single scattering albedo (ω_0) which describes the ratio of a particle's scattering efficiency to its extinction efficiency (Eq. 2.8). A particle that purely scatters radiation at a specified wavelength (λ_0) would exhibit $\omega_0(\lambda_0) = 1$, while a purely absorbing particle would exhibit $\omega_0(\lambda_0) = 0$.

$$\omega_0(\lambda) = \frac{Q_s(\lambda)}{Q_e(\lambda)} = \frac{Q_s(\lambda)}{Q_s(\lambda) + Q_a(\lambda)} \tag{2.8}$$

2.3.4. Specific extinction coefficient

Another useful parameter for the aerosol sciences is the specific (i.e. mass-weighted) extinction coefficient (k_e in $m^2\ kg^{-1}$). Equation 2.9 formulates k_e for a spherical particle with radius a and density ρ (in units of $kg\ m^{-3}$). The specific absorption and scattering coefficients (k_a and k_s respectively) can be obtained by substituting σ_a and σ_s in place of σ_e in Eq. 2.9.

$$k_e(\lambda) = \frac{\sigma_e(\lambda)}{\rho\ \frac{4\pi a^3}{3}} = \frac{\pi a^2\ Q_e(\lambda)}{\rho\ \frac{4\pi a^3}{3}} \tag{2.9}$$

2.3.5. The scattering phase function and asymmetry parameter

The scattering phase function $\mathrm{P}(\theta)$ describes the angular distribution of the scattered light [Seinfeld and Pandis, 1998]. $\mathrm{P}(\theta)$ is equal to the flux density $\mathrm{F}(\theta)$ of the scattered radiation in a given direction (θ), normalised by the flux density integrated over all directions. For spherical particles, the phase function and flux density are independent of the azimuthal angle (ϕ – see Fig. 2.6). The phase function is related to the scattering functions $S_1(\theta)$ and $S_2(\theta)$ according to the following relation (Eq. 2.10).

$$P(\theta) = \frac{2\pi}{k^2\sigma_s}(|S_1(\theta)|^2 + |S_2(\theta)|^2) \tag{2.10}$$

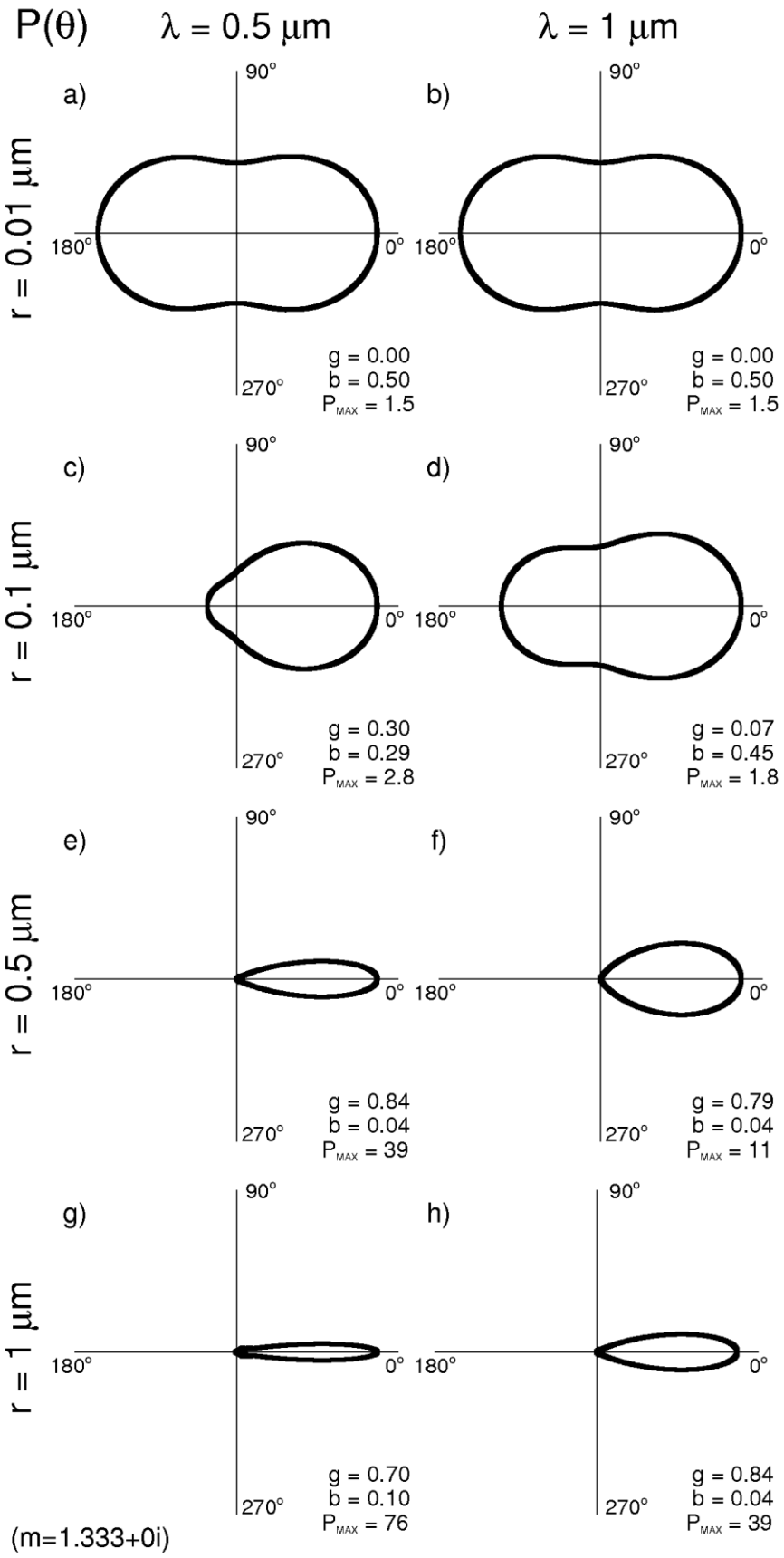

Figure 2.8 The scattering phase function $P(\theta)$ for 4 particle radii and 2 wavelengths, given a refractive index of m=1.333+0i. '*g*', 'b', and 'P_{MAX}' refer to the asymmetry parameter, the backscatter ratio and the maximum value of $P(\theta)$ respectively

Of particular interest to the aerosol sciences is the fraction of the scattered radiation that is scattered into the forward or backward directions. Although various parameters have been used to describe the angular distribution of the scattered light, the asymmetry parameter (g) is predominantly used. g is the intensity-weighted mean of the cosine of θ (Eq. 2.11). g = 1 for light scattered entirely into θ = 0° (i.e. forward scattering), g = -1 for light scattered entirely into θ = 180° (i.e. backward scattering), and g = 0 for isotropic scattering.

$$g = \frac{1}{2}\int_0^{\pi} \cos\theta \; P(\theta) \sin\theta \; d\theta \tag{2.11}$$

Another useful 'angular distribution' parameter is the hemispheric backscatter ratio b, which measures the fraction of the scattered wave that is scattered into the backward hemisphere.

$$b = \frac{\int_{\pi/2}^{\pi} P(\theta) \sin\theta \; d\theta}{\int_0^{\pi} P(\theta) \sin\theta \; d\theta} \tag{2.12}$$

Figure 2.8 shows the scattering phase functions and associated asymmetry parameter and hemispheric backscatter ratios for four different particle radii (a = 0.01, 0.1, 0.5, and 1 μm) and two wavelengths (λ = 0.5 and 1 μm), assuming a particle with constant refractive index m = 1.333+0i. It is clear that the larger particles preferentially scatter radiation into the forward direction (for instance, g = 0.84 for a = 0.5 μm and λ = 0.5 μm), while the smaller particles scatter evenly into the forward and backward directions (for instance, b = 0.50 for a = 0.01 μm and λ = 0.5 μm).

2.3.6. Optical parameters for various aerosols

2.3.6.1. Refractive Indices

We have shown that a particle's optical properties are dependent its radius and refractive index, and on the wavelength of the incident radiation. It is important to note that Mie theory as outlined in Section 2.3.1 is only exact for spherical particles; in reality, atmospheric particles assume a wide variety of shapes. Additionally, Mie theory only describes the elastic scattering of light, i.e. in which the scattered radiation has the same wavelength as the incident radiation. Inelastic light scattering,

in which the wavelength of the scattered radiation is different to that of the incident radiation, is not included within the Mie framework. Inelastic light scattering can occur when a particle changes its quantum state during interaction with light (the Raman effect). Inelastic light scattering is several orders of magnitude smaller than elastic scattering; therefore, we only consider elastic light scattering and the optical constants derived in Section 2.3.2 here.

It is interesting to note that Mie theory solely depends on two properties of the particle – its radius and refractive index. The refractive index of a substance is the ratio of the speed of light in a vacuum (*c*) to the speed of light in the substance [Mishchenko *et al*., 2002]. m is often decomposed into real and complex parts ($\mathrm{m} = \mathrm{n} + \mathrm{ik}$). The real part describes the dispersion (or phase lag), and the imaginary part the decrease of intensity of a wave as it propagates through the substance. The imaginary part contains detail of the light-absorptivity of the substance. The refractive index is a wavelength dependent quantity, i.e. $\mathrm{m}(\lambda) = \mathrm{n}(\lambda) + \mathrm{ik}(\lambda)$, and differs widely between materials. As an example, we shall look at the refractive indices for various aerosols that have been suggested for SAI (Section 1.3.3).

Figure 2.9 shows refractive indices for SO_4 as a H_2SO_4 (75% wt) solution, BC, and rutile TiO_2. The SO_4 and BC refractive indices are from a World Meteorological Organisation report [Deepak and Gerber, 1983] and the rutile TiO_2 indices are from Zeidler *et al.* (2011) and Ribarsky (1985). 'Rutile' refers to a specific tetragonal TiO_2 crystal; other (rarer) TiO_2 polymorphs include anatase and brookite. We have chosen rutile instead of the other TiO_2 polymorphs due to its greater refractive indices in the SW spectrum, which is an optimal property for an SAI candidate particle. Hereafter, any reference to TiO_2 can be regarded as exclusively pertaining to rutile. TiO_2 is birefringent, which means that a beam of light incident on a TiO_2 crystal is refracted in two different directions. The two refracted waves are polarised in the perpendicular or parallel planes relative to the c-axis (or the optic axis) of the TiO_2 crystal. Therefore, TiO_2 has two sets of wavelength-dependent refractive indices (denoted 'parallel' and 'perpendicular' in Fig. 2.9). Let $\mathrm{m}_{\parallel}$ denote the parallel refractive index and let $\mathrm{m}_{\perp}$ denote the perpendicular refractive index. For a uniaxial crystal such as rutile TiO_2, one of the refracted rays obeys Snell's law, such that the speed of light propagation in the crystal is constant for all angles of incidence (the 'ordinary' ray). The other refracted ray does not obey Snell's law and therefore has a

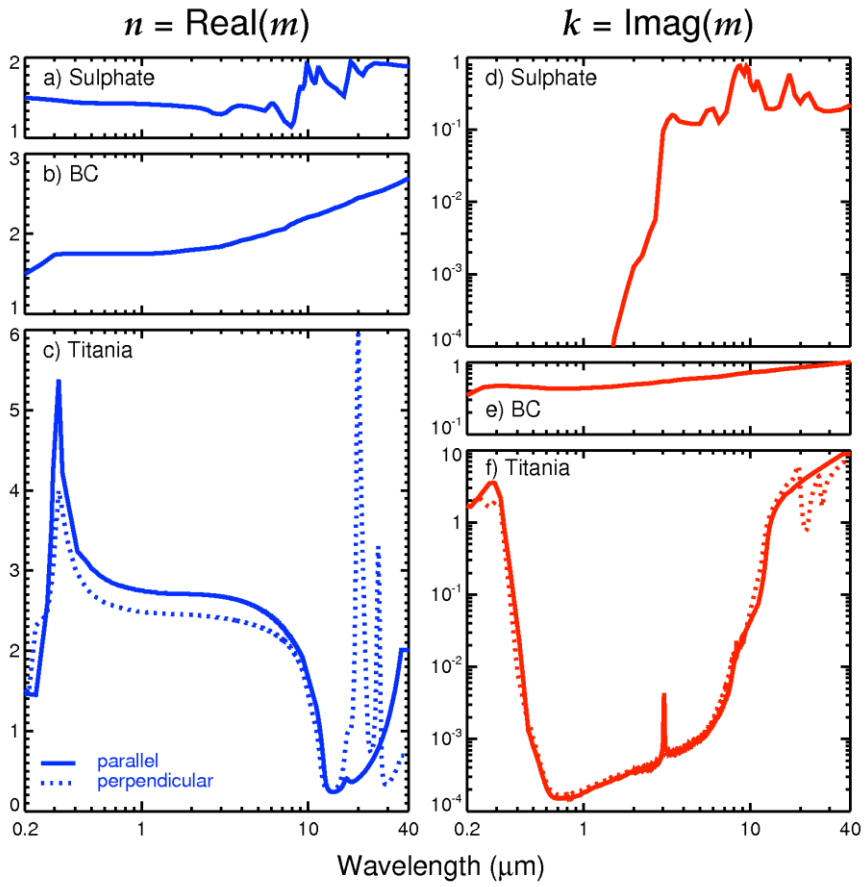

Figure 2.9 (a-c) real and (d-f) imaginary components of the refractive indices as a function of wavelength for SO_4, BC, and TiO_2

variable velocity that depends on the angle of incidence (the 'extraordinary ray'). The refractive index of the ordinary ray is $m_{\perp}$, while the refractive index of the extraordinary ray varies from $m_{\perp}$ for incident light parallel to the c-axis, to $m_{\parallel}$ for incident light perpendicular to the c-axis[7].

It is interesting (if slightly off topic) to relate the salient features of Fig. 2.9 to the structural and atomic properties of the individual substances. For instance, both the real and imaginary components of the refractive indices of BC are approximately spectrally invariant. This is due to the close proximity of energy levels between valence electrons in the graphitic (sp^2) bonds that make up the aromatic components of BC [Bond and Bergstrom, 2006]. The TiO_2 refractive indices are far more variable than for BC, for instance, $k(\lambda)$ for $0.3 < \lambda < 0.5$ μm spans five orders of magnitude. Tropf *et al.* (1995) discuss the dependency of n and k on lattice vibrations, electronic transitions and free-carrier density for the dielectric crystal yttria (Y_2O_3). While yttria has a cubic structure and rutile a tetragonal structure, the key modes of their

[7] https://www.microscopyu.com/techniques/polarized-light/principles-of-birefringence

refractive indices are comparable [e.g. Fig. 1 in Tropf *et al.*, 1995]. In Fig 2.9, the large values of $k(\lambda)$ when $\lambda < 0.3$ μm can be explained by the band theory of solids, i.e. by the difference between the low-energy valence band and the high-energy conduction band of TiO_2 [Yang *et al.*, 2004]. The large values of $n(\lambda)$ when $0.2 < \lambda < 5$ μm relate to the free-carrier (or specifically the valence electron) density of TiO_2 [Rocquefelte *et al.*, 2004]. The large fluctuations of $n(\lambda)$ when $15 < \lambda < 30$ μm can be attributed to TiO_2 lattice vibrations [Tropf *et al.*, 1995]. Lastly, aqueous H_2SO_4 is composed of a mixture of SO_4, HSO_4, and OH ions. The fluctuations in $k(\lambda)$ for $\lambda > 3$ μm relate to vibrations of various bonds within these ions, for instance the double S=O bond in SO_4 resonates at $\lambda > 8.5$ μm [Remsberg *et al.*, 1974]. These observations should highlight the inextricable relationship that exists between a substance's refractive indices and its atomic and structural properties.

2.3.6.2. Optical coefficients for a single particle

The optical coefficients $k_e(\lambda)$, $\omega_0(\lambda)$, and $g(\lambda)$ (Sections 2.3.3 - 2.3.5) can now be derived for SO_4, BC and TiO_2 particles using the refractive indices in Fig. 2.9. These optical coefficients collectively describe a substance's opacity, its relative scattering and absorption efficiencies, and the angular distribution of the scattered radiation. This is sufficient for modelling radiative transfer through an aerosol layer, which is the aim of Section 2.4. The optical coefficients $k_e(\lambda)$, $\omega_0(\lambda)$, and $g(\lambda)$ are all functions of the particle size parameter x and refractive index $m(\lambda)$. As x is a function of the particle's radius (a), we require a value of 'a' in order to derive the optical coefficients for various wavelengths. For this section we arbitrarily prescribe $a = 0.1$ μm, which is a typical size for Aitken or accumulation mode atmospheric aerosols (see Section 2.2.2) [Deepak and Gerber, 1983]. We use the average of the parallel and perpendicular refractive indices for TiO_2, and assume aerosol densities (ρ) of 1769, 4230, and 1000 kg m^{-3} for SO_4, TiO_2, and BC respectively.

Figure 2.10 shows the optical constants as a function of wavelength ($0.2 < \lambda < 20$ μm) for SO_4, TiO_2 and BC. It is clear that BC has a much greater k_e in the SW spectrum ($\lambda < 1$ μm) than TiO_2 or SO_4, but this is mostly through SW absorption rather than scattering ($\omega_0 < 0.5$ for BC). It is also clear that SO_4 has the lowest $k_e(\lambda)$ for $\lambda = 0.55$ μm (i.e. the peak wavelength of solar emission), while TiO_2 has a comparable $k_e(0.55\ \mu m)$ to BC despite being purely scattering at this wavelength (ω_0

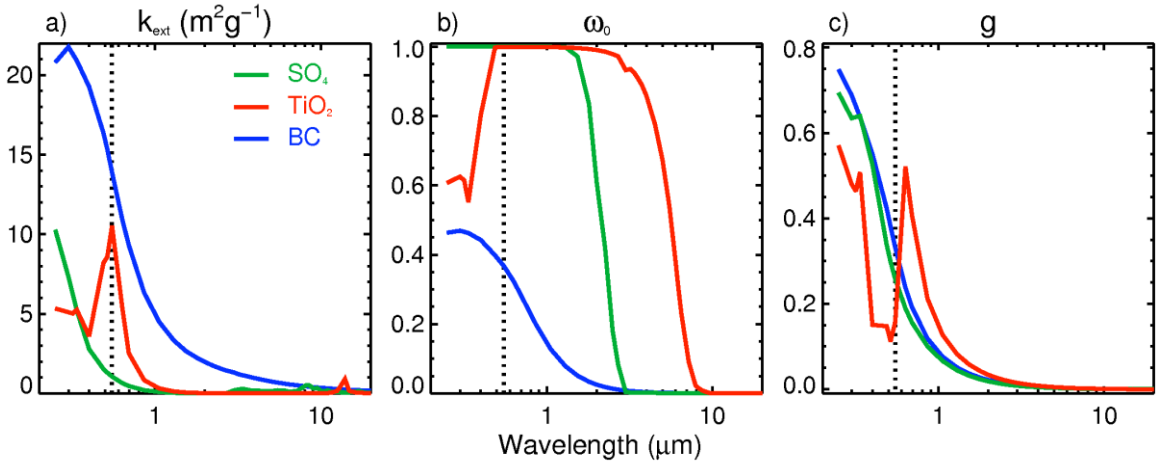

Figure 2.10 (a) specific extinction coefficient $k_e(\lambda)$, (b) single-scattering albedo $\omega_0(\lambda)$, and (c) asymmetry parameter $g(\lambda)$ for a spherical particle with a = 0.1 μm given SO_4, TiO_2 and BC refractive indices. Vertical dashed lines indicate λ = 0.55 μm.

= 1). However, TiO_2 also absorbs in the UV spectrum ($\omega_0 < 1$ for $\lambda < 0.3$ μm), as explained in Section 2.3.6.1. Therefore, while SO_4 produces less SW attenuation per mass than TiO_2, it does not exhibit TiO_2's SW absorptivity. The consequences of SW absorption by TiO_2 will be explored in Chapter 4. Lastly, SO_4 and BC exhibit a similar (uniform) decline of asymmetry parameter *g* with wavelength, which means that both substances scatter preferentially in the forward direction at smaller wavelengths. In contrast, TiO_2 exhibits a less uniform pattern of *g* with a greater backscattering capacity than SO_4 or BC for $\lambda < 0.55$ μm and a greater forward scattering capacity for $\lambda > 0.55$ μm.

2.3.6.3 Optical coefficients integrated over a size distribution

We noted in Section 2.2.2 that atmospheric aerosols undergo various ageing processes and thus exist as a distribution of different sizes. The lognormal distribution provides a close fit to observed aerosol size distributions; therefore, we will use this as the basis of this work. The optical parameters $\omega_0(\lambda)$, $k_e(\lambda)$, and $g(\lambda)$, as given in Eqs 2.8, 2.9 and 2.11 respectively, are only applicable to a single spherical particle with radius a. The specific extinction, scattering, and absorption coefficients, integrated over an aerosol size distribution with radii represented by r, are given in Eq. 2.13.

$$\overline{k_e}(\lambda) = \frac{\int_0^\infty \pi r^2 Q_e(\lambda, r, m(\lambda))\, n(r) dr}{\rho \int_0^\infty \frac{4\pi r^3}{3} n(r) dr} = \frac{E(\lambda)}{\rho \int_0^\infty \frac{4\pi r^3}{3} n(r) dr} \qquad (2.13a)$$

$$\overline{k_a}(\lambda) = \frac{\int_0^\infty \pi r^2 Q_a\big(\lambda, r, m(\lambda)\big)\, n(r) dr}{\rho \int_0^\infty \frac{4\pi r^3}{3} n(r) dr} = \frac{A(\lambda)}{\rho \int_0^\infty \frac{4\pi r^3}{3} n(r) dr} \tag{2.13b}$$

$$\overline{k_s}(\lambda) = \frac{\int_0^\infty \pi r^2 Q_s\big(\lambda, r, m(\lambda)\big)\, n(r) dr}{\rho \int_0^\infty \frac{4\pi r^3}{3} n(r) dr} = \frac{S(\lambda)}{\rho \int_0^\infty \frac{4\pi r^3}{3} n(r) dr} \tag{2.13c}$$

In Eq. 2.13, $E(\lambda)$, $A(\lambda)$, and $S(\lambda)$ are the 'volume' extinction, absorption and scattering coefficients (in units of m^{-1}). The 'volume' coefficients describe the light attenuation per unit metre through a homogeneous substance with an aerosol number concentration of N_0 (m^{-3} – where N_0 is a constant factor in $n(r)$). The coefficients $\overline{k_e}$, $\overline{k_a}$, and $\overline{k_s}$ describe the light attenuation per unit metre and unit mass of a substance. The size-integrated single-scattering albedo and asymmetry parameter are given in Eqs 2.14 and 2.15.

$$\overline{\omega_0}(\lambda) = \frac{\overline{k_s}(\lambda)}{\overline{k_e}(\lambda)} \tag{2.14}$$

$$\bar{g}(\lambda) = \frac{\int_0^\infty \pi r^2 Q_s\big(\lambda, r, m(\lambda)\big)\, g(\lambda, r)\, n(r) dr}{S(\lambda)} \tag{2.15}$$

The optical coefficients $\overline{k_e}(\lambda)$, $\overline{\omega_0}(\lambda)$, and $\bar{g}(\lambda)$ are all wavelength-dependent quantities. Often the radiative flux is given as the integrated flux over a spectrum of wavelengths. Formulae for the spectrally-weighted optical coefficients (for an arbitrary wavelength spectrum $\lambda_a < \lambda < \lambda_b$) are provided in Eqs 2.16 - 2.18 [Stenchikov *et al*., 1998].

$$\overline{\overline{k_e}} = \frac{\int_{\lambda_a}^{\lambda_b} \overline{k_e}(\lambda)\, f(\lambda) d\lambda}{\int_{\lambda_a}^{\lambda_b} f(\lambda) d\lambda} \tag{2.16}$$

$$\overline{\overline{\omega_0}} = \frac{\int_{\lambda_a}^{\lambda_b} \overline{k_s}(\lambda)\, f(\lambda) d\lambda}{\int_{\lambda_a}^{\lambda_b} \overline{k_e}(\lambda)\, f(\lambda) d\lambda} \tag{2.17}$$

$$\bar{\bar{g}} = \frac{\int_{\lambda_a}^{\lambda_b} \bar{g}(\lambda)\, \overline{k_s}(\lambda)\, f(\lambda) d\lambda}{\int_{\lambda_a}^{\lambda_b} \overline{k_s}(\lambda)\, f(\lambda) d\lambda} \tag{2.18}$$

In Eqs 2.16 - 2.18, $\mathrm{f}(\lambda)$ is the irradiance between λ and $\lambda + d\lambda$. For instance, Stenchikov *et al*. (1998) use the Planck function $F_B(\lambda, T)$ (Eq. 1.4 in this thesis) with T = 6000 K to represent the solar irradiance.

We can now determine the spectrally-weighted optical coefficients for SO_4, BC, and TiO_2 for a typical atmospheric size distribution. Specifically, we prescribe a dry median radius of $\mathrm{r_m}$ = 0.1 μm and standard deviation σ = 1.8 and use the lognormal distribution (Eq. 2.1). We use the Matlab Mie code to calculate the optical efficiencies (e.g. Q_e) and the asymmetry parameter and then integrate over the aerosol size distribution using Eqs 2.13-2.15. Finally, we utilise solar spectral irradiances from Kurucz (1995) for $\mathrm{f}(\lambda)$ in Eqs 2.16-2.18 to determine spectrally-integrated coefficients for the SW spectrum (Table 2.1).

(Solar) spectrally weighted coeffs.	SO_4	BC	TiO_2
k_e (m^2 kg^{-1})	2290	6580	2062
ω_0	0.997	0.434	0.956
g	0.703	0.654	0.677

Table 2.1 Spectrally weighted optical coefficients for SO_4, BC, and TiO_2 for a standard atmospheric size distribution. The values presented represent mean values integrated over the spectral region 0.3-3μm

2.4. Simple models of aerosol shortwave radiative forcing

2.4.1. Background

In Section 2.2, we established that aerosols are ubiquitous throughout the atmosphere. In particular, we noted that a semi-permanent and uniform SO_4 layer exists in the lower stratosphere. In Section 2.3, we showed that aerosols attenuate radiation via scattering and absorption and we derived optical coefficients for SO_4, BC, and TiO_2. We now combine these two sections in order to assess how a uniform aerosol layer would influence TOA SW radiative fluxes. We concentrate on the SW budget because the specific goal of the SAI geoengineering is to cool Earth by reflecting solar radiation. SO_4, BC, and TiO_2 will also influence LW radiation, as indicated by the non-zero optical coefficients for longer wavelengths (λ >> 1 μm) in Fig. 2.10. We will assess the LW effect of an aerosol layer in Chapter 3.

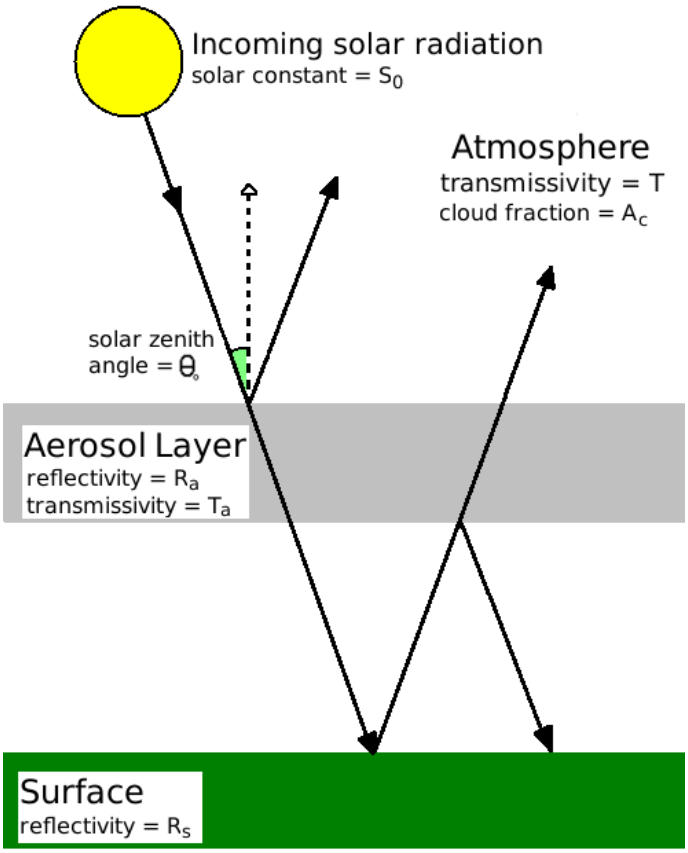

Figure 2.11 Schematic of a simple radiative transfer model for an aerosol layer

2.4.2. Atmospheric transmissivity

Figure 2.11 shows a schematic of a simple model for SW radiative transfer through an atmosphere, an underlying aerosol layer, and a surface. The integrated solar radiative flux at the top of the atmosphere is S_0. The angle that the sun makes with the normal to Earth's surface (the solar zenith angle) is denoted θ_0 and its cosine $\mu_0 = \cos(\theta_0)$ equals 1 for an overhead sun. As sunlight traverses the atmosphere, a fraction will be absorbed by O_3 and water and a fraction will be scattered by gas particles (Rayleigh scattering). Lacis and Hansen (1974) developed simple parameterisations for these processes, which we will use here to assess the atmospheric transmission at different solar zenith angles. Firstly, we relate the fraction of the incident sunlight that is absorbed by O_3 in the visible and UV spectra to the O_3 burden (x) (Eqs 2.19-2.20).

$$A_{O3}^{vis}(x) = \frac{0.02118\,x}{1 + 0.0042\,x + 0.000323\,x^2} \tag{2.19}$$

$$A_{O3}^{UV}(x) = \frac{1.082\,x}{(1 + 138.6\,x)^{0.805}} + \frac{0.0658\,x}{1 + (103.6\,x)^3} \tag{2.20}$$

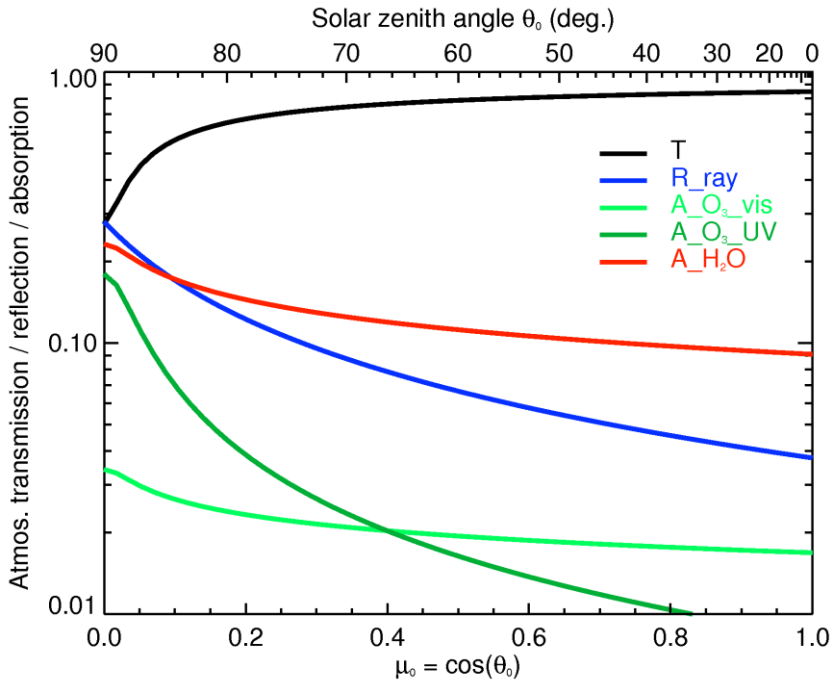

Figure 2.12 The SW transmissivity (T) of the atmosphere as a function of μ_0 using the Lacis and Hansen (1974) model with u = 0.4cm^{-1} and y = 0.7cm^{-1}

In Eqs 2.19-2.20, the covariate x is proportional to the vertical O_3 column burden u (in cm^{-3}) and a magnification factor (*M*), which is a function of μ_0 (Eq. 2.21).

$$x = uM = u\,\frac{35}{(1224\,\mu_0{}^2 + 1)^{0.5}} \tag{2.21}$$

We now relate the fraction of the incident sunlight that is absorbed by atmospheric water to the water column burden (y') (Eq. 2.22). In similar fashion to x in Eq. 2.21, y' is related to the vertical precipitable-water column burden (y in cm^{-3}) by the magnification factor (y′ = y *M*).

$$A_{H2O}(y') = \frac{2.9\,y'}{(1 + 141.5\,y')^{0.635} + 5.925\,y'} \tag{2.22}$$

We now relate the fraction of the incident sunlight that is scattered by gas particles to the cosine of the solar zenith (Eq. 2.23).

$$R_{ray} = \frac{0.28}{1 + 6.43\,\mu_0} \tag{2.23}$$

Finally, the atmospheric transmission (i.e. the fraction of the SW radiation that permeates the atmosphere) is unity minus the sum of the absorbed and scattered fractions (Eq. 2.24).

$$T(\mu_0, u, y) = 1 - A_{O3}^{vis}(\mu_0, u) - A_{O3}^{UV}(\mu_0, u) - A_{H2O}(\mu_0, y) - R_{ray}(\mu_0) \qquad (2.24)$$

Lacis and Hansen (1974) give typical values for u and y as 0.4 and 0.7 cm^{-1} respectively, which we adopt here. Fig. 2.12 shows the SW transmission (T) of the atmosphere as function of μ_0. For μ_0 = 0.5, the model gives T = 0.78 which is in close agreement with the value adopted by Charlson *et al.* (1991) (T = 0.76). The atmospheric transmission is greatest for small θ_0 (i.e. overhead sun) and decreases as θ_0 increases.

2.4.3. Charlson's model for a purely scattering aerosol layer

We return to Fig. 2.11 in order to assess the effect of a purely scattering aerosol (i.e. ω_0 = 1) layer on TOA SW fluxes. This derivation follows Charlson *et al*. (1991). An important property of an aerosol layer is the dimensionless aerosol optical depth (AOD, τ), which is defined as the specific extinction efficiency (k_e) multiplied by the aerosol mass concentration (ρ in kg m^{-3}) and integrated over the vertical depth of the aerosol layer (Eq. 2.25).

$$\tau = \int_{z_1}^{z_2} \bar{\bar{k}}_e \, \rho \, dz \qquad (2.25)$$

The AOD is the sum of the scattering and absorption optical depths ($\tau = \tau_s + \tau_a$). For a purely scattering aerosol, τ_a = 0 and $\tau = \tau_s$. If we assume that τ << 1 (i.e. a thin aerosol layer) then we can neglect multiple scattering. Under this assumption, the fundamental equation of radiative transfer for a plane-parallel atmosphere reduces to Beer's law (Eq 2.26).

$$\frac{F_s}{F_0} = 1 - e^{-\tau/\mu_0} \approx \tau/\mu_0 \qquad (2.26)$$

In Eq. 2.26, F_s is the scattered radiative flux and F_0 is the incident radiative flux. We now determine the fraction of the scattered radiation that is scattered in the upward direction. The hemispheric upscattered fraction for monodirectional incident radiation ($\beta(\mu_0)$) can be determined by integrating the aerosol phase function $P(\theta)$ (Eq. 2.10) over the upward hemisphere (i.e. -$\mu' \in [0,1]$ where μ' is the scattering angle relative to the downward normal) [Wiscombe and Grams, 1976].

$$\beta(\mu_0) = \frac{1}{2\pi}\int_0^1 \int_0^\pi P(\cos^{-1}(-\mu'\mu_0 + (1-\mu')^2(1-\mu_0)^2\cos\phi))\, d\phi\, d\mu' \quad (2.27)$$

The reflectivity of the aerosol layer, or the fraction of the incident radiation that is scattered in the upward direction, is $R_a = \beta\tau / \mu_0$ and the transmissivity of the aerosol layer is $T_a = 1 - R_a$. Given a surface reflectivity R_s, cloud fraction A_c, atmospheric transmissivity T, and TOA incident radiation $\mu_0 S_0$, Charlson *et al*. (1991) derived the following formula (Eq. 2.28) for the change in the outgoing TOA radiation (i.e. the SW radiative forcing) due to the addition of an aerosol layer (ΔF) :-

$$\Delta F = -\frac{1}{2} S_0 \bar{T}^2 (1 - \overline{A_c})(1 - \overline{R_s})^2 \bar{\beta}\tau \quad (2.28)$$

The over-bars in Eq. 2.28 denote an integration of the zenith angle dependent parameter over $\mu_0 \in [0, 1]$ (i.e. isotropic incident radiation), and the factor ½ denotes the sunlit fraction of Earth averaged over a year. The factor (1 - A_c) arises from the assumption that the aerosol radiative effect (ΔF) is negligible in cloudy regions. This model also assumes that the aerosol layer resides below the cloud layer and that all of the atmospheric absorption and reflection occurs above the aerosol layer. Therefore, this aerosol layer is assumed to reside near the surface. The application of this model to a stratospheric aerosol layer, such as would exist under SAI, is questionable due to these important assumptions. Nonetheless, this model is useful for garnering an impression of the qualitative outcome of a stratospheric aerosol layer.

In the SW spectrum, SO_4 is approximately purely scattering ($\omega_0 \approx 1$ in Table 2.1), therefore it is instructive to calculate ΔF for a typical SO_4 layer. We use the spectrally-integrated optical coefficients for SO_4 from Table 2.1. If we approximate the Mie phase function with the Henyey-Greenstein phase function [Wiscombe and Grams, 1976] then the hemispheric upscattered fraction for isotropic light ($\bar{\beta}$) can be related to the asymmetry parameter (g) according to the following formula (Eq. 2.29).

$$\bar{\beta} = \frac{1-g}{2g}\left[\frac{2}{\pi}(1+g)K(g^2) - 1\right] \quad (2.29)$$

In Eq. 2.29, $K()$ denotes the complete elliptic integral of the first kind. For g = 0.703 it follows that $\bar{\beta} = 0.21$. In order to determine the SO_4 optical depth (Eq. 2.25), we need an SO_4 column burden. From Fig. 2.2 (page 67), the global tropospheric SO_4 aerosol burden is 0.49 Tg[S], or ~2×10^9 kg[SO_4]. The average SO_4 column burden over Earth's surface is then 3.92×10^{-6} kg m^{-2}, given that Earth's surface area is 5.1×10^{14} m^2. Therefore the tropospheric sulphate optical depth averaged over Earth's surface is approximately $\tau = 2290 \times 3.92 \cdot 10^{-6} = 0.009$ (Eq. 2.25). We follow Charlson *et al*. (1991) and adopt A_c = 0.6, R_s = 0.15, S_0 = 1370 Wm^{-2}, and T = 0.78. If we apply these values to Eq. 2.28, we get ΔF = -0.22 Wm^{-2}. This can be compared to the anthropogenic SO_4 radiative forcing of -0.34 Wm^{-2} from AR5 [Boucher *et al*., 2013]. We have not included the effects of hygroscopic growth on the SO_4 optical properties, which would magnify the specific extinction coefficient and therefore make ΔF more negative than -0.22 Wm^{-2} [Charlson *et al*., 1991]. The Edwards and Slingo radiation code (Chapter 3) includes a hygroscopic growth module for SO_4 [Fitzgerald, 1975; d'Almeida *et al*., 1991] which can be used to assess the solar spectrally weighted optical coefficients for SO_4 under humid conditions. At a relative humidity of 70 % (i.e. the average relative humidity of the lower tropical troposphere [Vergados *et al*., 2015]), we find that k_e = 5578 m^2 kg^{-1}, ω_0 = 0.997, and g = 0.759. Using Eq. 2.29, the hemispheric upscattered fraction is $\bar{\beta} = 0.18$ (i.e. less upscattering than for dry SO_4) and the optical depth is τ = 0.022. If we apply these values to Eq 2.28, we derive a SW radiative forcing of ΔF = -0.48 Wm^{-2}. This implies that hygroscopic growth is an important factor in SO_4 SW forcing.

2.4.4. Haywood and Shine's model for a partially absorbing aerosol layer

Haywood and Shine (1995) extended Charlson's model to include consideration for partially- absorbing aerosols ($\omega_0 \neq 1$). Using a similar derivation to Charlson *et al.* (1991), but relaxing the ω_0 = 1 assumption, Haywood and Shine (1995) derived the following formula (Eq. 2.30) for the aerosol layer SW radiative forcing.

$$\Delta F = -DS_0\bar{T}^2(1-\overline{A_c})\left[(1-\overline{R_s})^2 - \frac{2\overline{R_s}}{\bar{\beta}}\left(\frac{1-\omega_0}{\omega_0}\right)\right]\omega_0\bar{\beta}\tau \qquad (2.30)$$

In Eq. 2.30, D is the fractional daylength (congruent to the factor ½ in Eq. 2.28) and ω_0 is the spectrally-weighted single scattering albedo (Eq. 2.17). In contrast to the

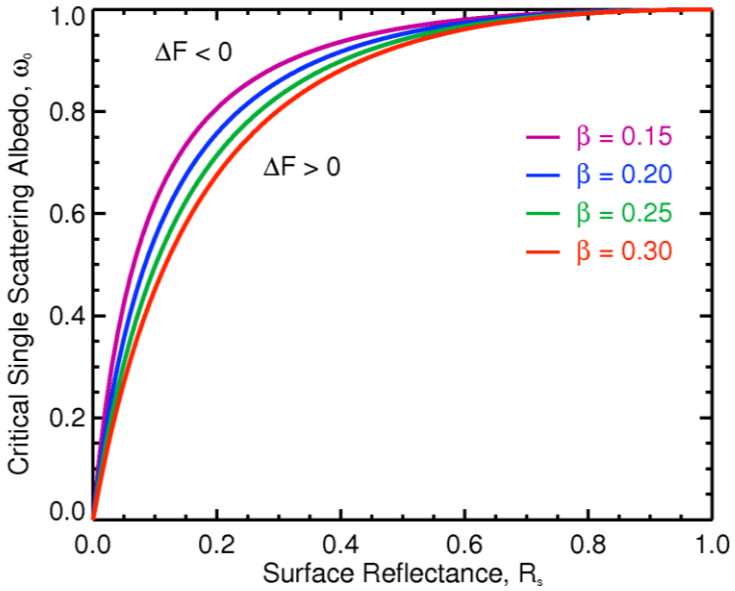

Figure 2.13 The critical single scattering albedo ω_0 at which the radiative forcing (ΔF) changes sign

model used by Charlson *et al.* (1991), it is possible to attain a positive radiative forcing using Haywood and Shine's model. This occurs when a partially absorbing aerosol layer resides above a reflective surface. Using Eq. 2.30, Haywood and Shine derived an inequality for the critical value of ω_0 at which the radiative forcing changes sign (Eq. 2.31).

$$\omega_0 < \frac{2\overline{R_s}}{\bar{\beta}(1-\overline{R_s})^2 + 2\overline{R_s}} \tag{2.31}$$

Figure 2.13 shows the critical single scattering albedo (Eq. 2.31) as a function of R_s and for various β. As β decreases (i.e. as the aerosol scatters more radiation toward Earth), the critical single scattering albedo increases, which means that forward-scattering aerosols are more likely to induce a positive radiative forcing than aerosols that scatter evenly into both hemispheres.

Using Eq. 2.30, we now use the optical coefficients in Table 2.1 to determine the SW radiative forcing for an idealised aerosol layer consisting of SO_4, BC, or TiO_2. We make the same assumptions as before, such that S_0 = 1370 Wm^{-2}, A_c = 0.6, and D = ½, and we prescribe an aerosol layer with τ = 0.1. Figure 2.14 shows the SW radiative forcing for these aerosol layers as function of R_s. For SO_4, ΔF < 0 for almost all values of R_s; this is due to SO_4's near unitary ω_0. In contrast, ΔF changes sign for TiO_2 at approximately R_s = 0.5 which suggests that TiO_2 would produce a positive radiative forcing over reflective surfaces. ΔF changes sign for BC at R_s =

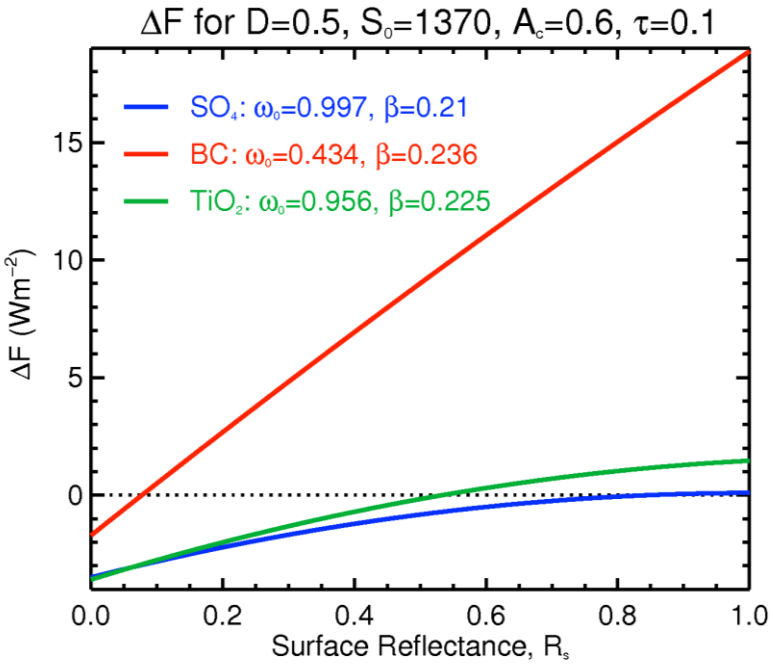

Figure 2.14 Radiative forcing (ΔF) as a function of surface reflectance R_s for SO_4, BC and TiO_2

0.075, which suggests that BC would only produce a negative radiative forcing over surfaces with low albedo.

2.4.5. Russell's model for solar zenith angle dependent radiative forcing

Russell et al. (1997) extended Haywood and Shine's model by considering the solar zenith angle dependency of the radiative forcing (Eqs 2.32-2.33).

$$\Delta F(\mu_0) = -\mu_0 S_0\, T(\mu_0)^2 (1 - A_c)\, \Delta R(\mu_0) \tag{2.32}$$

$$\Delta R(\mu_0) = \frac{\tau\omega_0\left[\beta(\mu_0)\left(1-R_s(\mu_0)\right) - 2\mu_0\bar{\beta}R_s(\mu_0)\left(1-\overline{R_s}\right)\right]}{\mu_0\left[1+\frac{\beta(\mu_0)\tau}{\mu_0}\right]} - \frac{\tau[(1-\omega_0)R_s(\mu_0)(1+2\mu_0)]}{\mu_0\left[1+\frac{\beta(\mu_0)\tau}{\mu_0}\right]} \tag{2.33}$$

$\Delta R(\mu_0)$ describes the change in planetary albedo due to the addition of an aerosol layer. The atmospheric transmission $T(\mu_0)$ can be approximated by using the Lacis and Hansen (1974) model (Eq. 2.24). The hemispheric upscattered fraction for monodirectional incident radiation $\beta(\mu_0)$ can be estimated by substituting the Mie phase function with the Henyey Greenstein phase function. $\beta(\mu_0)$ then becomes a single integral over the aerosol phase function [Eq. 22 in Wiscombe and Grams, 1976]. Figure 2.15 shows $\beta(\mu_0)$ as a function of g and for various μ_0. $\beta(\mu_0)$ decreases

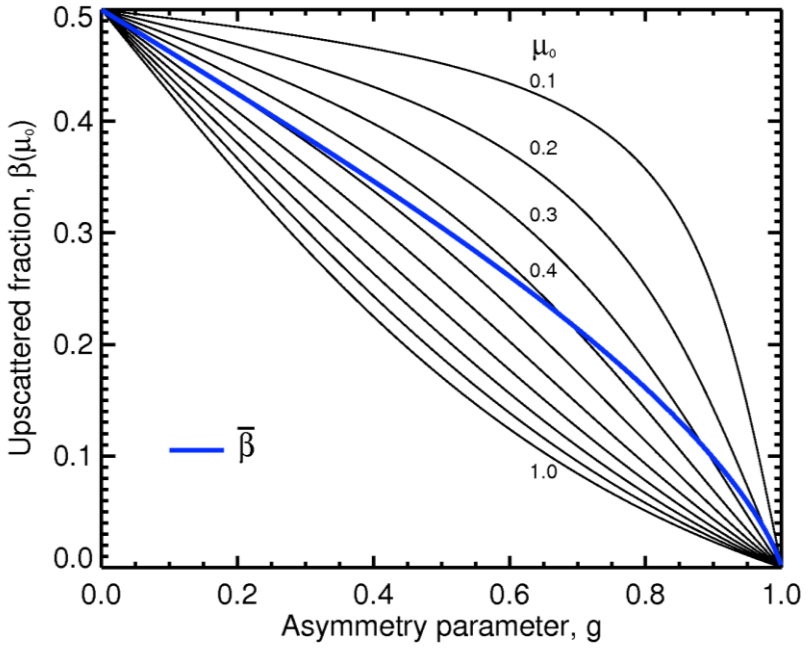

Figure 2.15 Upscattered fraction $\beta(\mu_0)$ as a function of the asymmetry parameter *g* for various μ_0. Also plotted is the upscattered fraction for isotropic incident radiation $\bar{\beta}$. Adapted from Fig. 3 of Wiscombe and Grams (1976)

with increasing μ_0, which means that the upscattered fraction is at a minimum for a directly overhead sun.

Figure 2.16 shows the radiative forcing (ΔF) as function of μ_0 for various parameter values. We assume $R_s(\mu_0) = \overline{R_s}$, such that the surface is a Lambertian reflector. In Fig. 2.16a, τ is varied while all other parameters are constant (see figure for details of values). It is clear that the magnitude of ΔF increases with τ. It is also clear that ΔF achieves its most negative value at $\mu_0 \approx 0.2$ (or $\theta_0 \approx 77^o$), i.e. when the sun is near the horizon. In Fig. 2.16b, ω_0 is varied while other parameters are held constant. For $\omega_0 = 1$, $\Delta F < 0$ for all values of μ_0, while for $\omega_0 = 0.75$, $\Delta F > 0$ for $\mu_0 > 0.55$. Partially-absorbing aerosols therefore induce a positive SW radiative forcing at small zenith angles. In Fig. 2.16c, R_s is varied while all other parameters are fixed with ω_0 prescribed as 0.9 (i.e. a partially-absorbing aerosol). Over a low-albedo surface ($R_s = 0.1$), $\Delta F < 0$ for all μ_0, while over a high-albedo surface ($R_s = 0.7$), $\Delta F > 0$ for all $\mu_0 > 0.1$. This means that a partially-absorbing aerosol may induce a positive or negative SW radiative forcing depending on the surface reflectivity. For instance, over highly-reflective clouds, partially-absorbing aerosols induce a positive radiative forcing. Finally, in Fig. 2.16d, *g* is varied while other parameters are fixed. For $g = 0.9$ (i.e. an aerosol that scatters light predominantly in the forward direction – see Fig. 2.8), $\Delta F >$

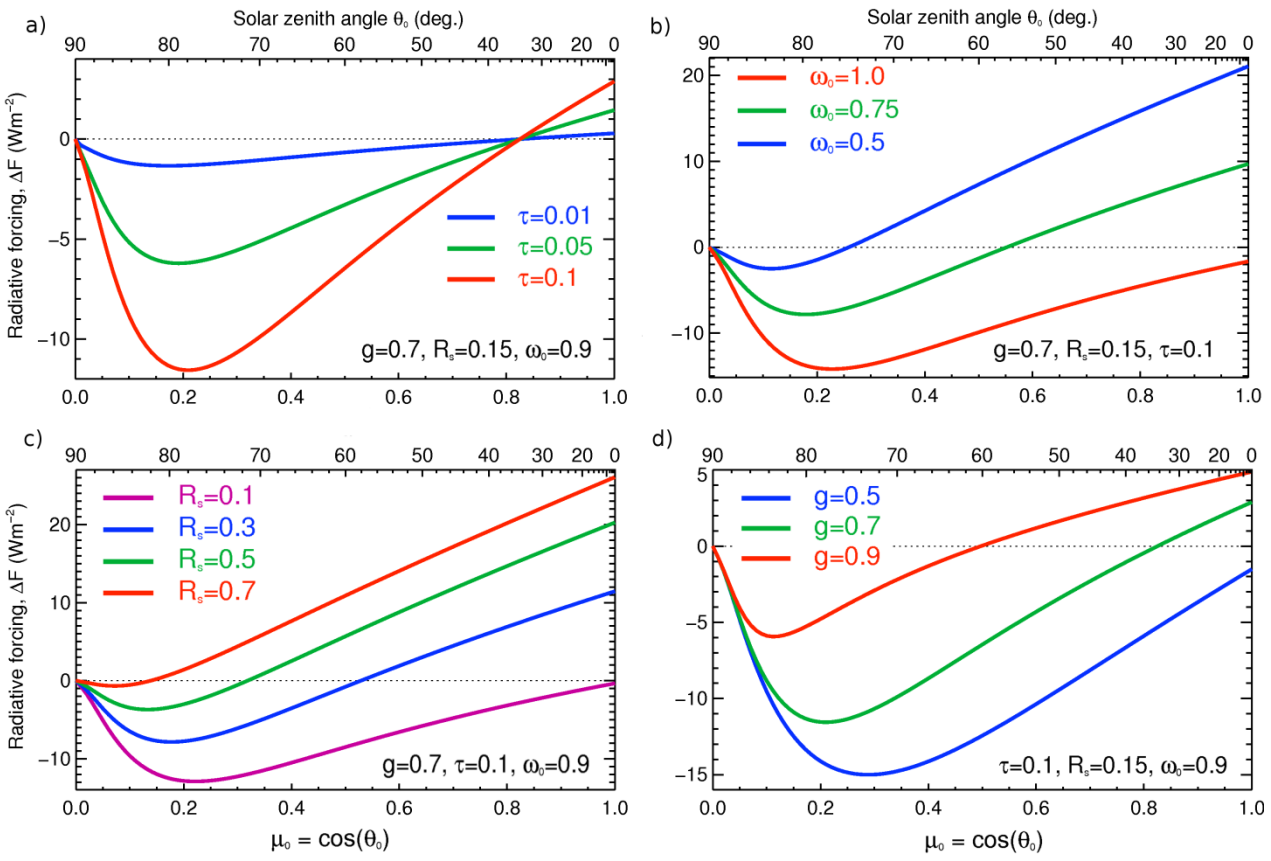

Figure 2.16 Russell's model for radiative forcing as a function of solar zenith angle for various (a) optical depths (τ = 0.01, 0.05, 0.1), (b) single scattering albedos (ω_0 = 1.0, 0.75, 0.5), (c) surface albedos (R_s = 0.1, 0.3, 0.5, 0.7) and (d) asymmetry parameters (g = 0.5, 0.7, 0.9). For all scenarios A_c = 0 and S_0 = 1370 Wm^{-2}

0 for $\mu_0 > 0.5$, while for g = 0.5 (i.e. an aerosol with comparatively more backward scattering), $\Delta F < 0$ for all μ_0. We recall from Section 2.3.5 that larger particles exhibit greater values of g than smaller particles. For SAI, smaller particles (i.e. with g closer to 0.5) will therefore be more effective at inducing a negative SW radiative forcing than larger particles. Figure 2.16 indicates that the SW radiative forcing induced by an aerosol layer would be highly sensitive to the aerosol layer's optical properties (i.e. τ, ω_0, g), the underlying surface albedo (R_s) and the solar zenith angle (μ_0).

2.4.6. Russell's model applied to SO_4, BC, and TiO_2 aerosol layers

It is instructive to apply the lessons learnt in the last section to idealised aerosol layers that are relevant to SAI. In Section 2.3.6, we derived spectrally weighted optical coefficients for SO_4, BC, and TiO_2 (Table 2.1). We apply these coefficients to Russell's model (Eq. 2.33) for the instance of a τ = 0.1 aerosol layer, with A_c = 0 and for three values of R_s (0.1, 0.5, 0.9). Figure 2.17 shows the TOA SW radiative forcing for these conditions and for the three aerosol species. For SO_4 and TiO_2, $\Delta F < 0$ for

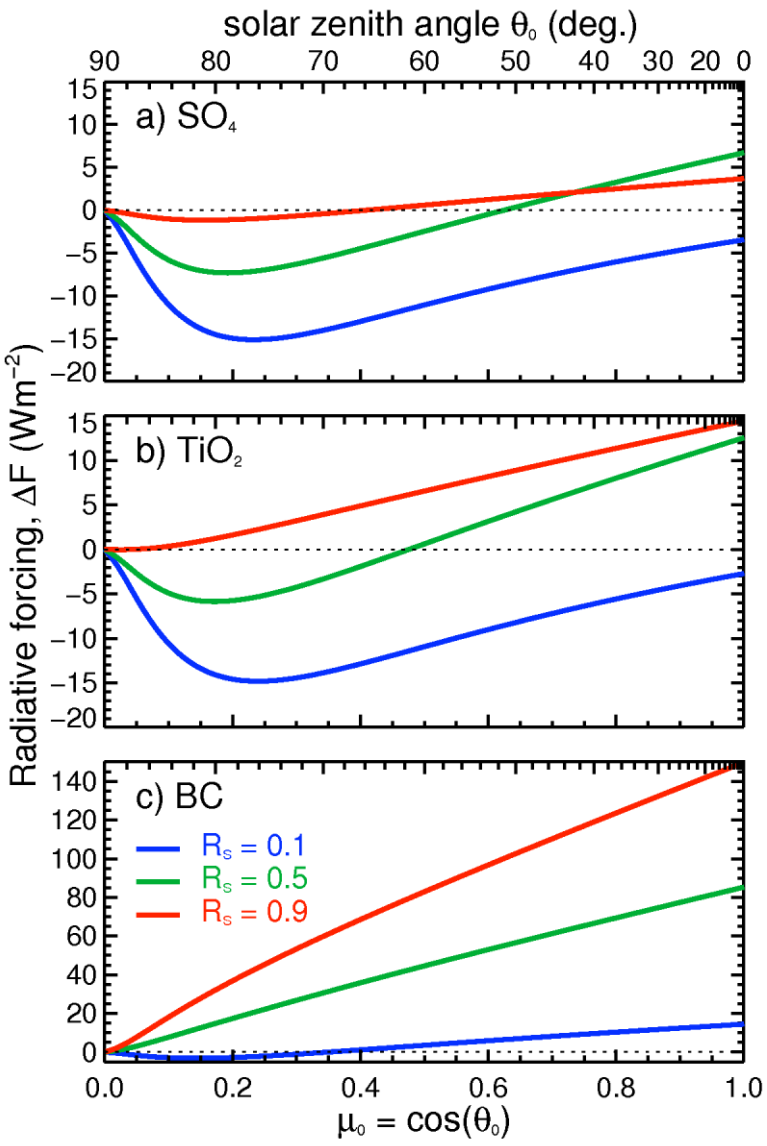

Figure 2.17 Russell's model for (a) SO_4, (b) TiO_2, and (c) BC layers with $\tau = 0.1$

all μ_0 for an absorbing underlying surface (R_s = 0.1), but for reflective surfaces (R_s = 0.5, 0.9), ΔF becomes positive for larger values of μ_0. Interestingly in the SO_4 case (Fig. 2.17a), ΔF is more positive at larger values of μ_0 for R_s = 0.5 than R_s = 0.9. This is because the first term in Eq. 2.33 (i.e. the scattering term) is a polynomial that is second order in R_s. If we assume $\omega_0 = 1$, $\mu_0 = 1$, and note that for $g = 0.7$, $\beta(1) \approx ½\,\bar{\beta}$ (Fig. 2.15), then Eq. 2.33 becomes a linear function of $(1 - R_s)(½ - 2R_s)$ which has maxima at R_s = 0.625. For TiO_2, the radiative forcing over a highly reflective surface (R_s = 0.9) is positive for all values of μ_0 (Fig. 2.17b); while for BC, $\Delta F < 0$ only for small μ_0 and low surface reflectivity (Fig. 2.17c).

The SO_4 ΔF at μ_0 = 0.5 and R_s = 0.1 is -11 Wm^{-2}. Donohoe and Battisti (2011) give a global-mean surface albedo from observations of ~0.12, therefore R_s = 0.1 is suitable for approximating Earth's surface albedo. If we assume A_c = 0.6 [Charlson *et al.*,

1991] in Eq. 2.32 and multiply $\Delta F(0.5)$ by a factor of ½ (i.e. factor D in Eq. 2.30), we obtain a rough estimate for the global and annual-mean radiative forcing of ΔF_{av} = -2.2 Wm^{-2}. Lacis *et al*. (1992) showed that the tropopause radiative forcing from a stratospheric SO_4 layer relates to the change in τ by $\Delta F \approx 30\Delta\tau$, which is similar to the ratio found here using a simple model and $\tau = 0.1$.

2.5. Summary

At the beginning of this chapter, we discussed the functions and origins of important atmospheric aerosols, with emphasis on SO_4 and the sulphur cycle. We identified two ways in which aerosols may interact with radiation: by altering cloud properties, and by directly absorbing or scattering radiation. We then proceeded to briefly outline Mie theory, which relates the radiation scattered by a spherical particle to the optical properties and size of the particle, and to the properties of the incident radiation. From Mie theory, we discussed certain useful wavelength-dependent optical coefficients such as the specific extinction coefficient, the single scattering albedo, and the asymmetry parameter. We then proceeded to integrate these optical coefficients over a wavelength spectrum (a waveband) and over a typical atmospheric aerosol size distribution, for the specific cases of SO_4, BC, and TiO_2 aerosols. These aerosols are potential candidates for SAI [Ferraro *et al.*, 2011]. We then discussed three simple SW radiative transfer models (a purely scattering aerosol model, a partially absorbing aerosol model, and a solar zenith angle dependent model) that can be used to estimate the TOA SW radiative forcing induced by a tropospheric aerosol layer. In Section 2.4, we applied these radiative transfer models to various idealised aerosol layers using the optical parameters derived in Section 2.3. An interesting result from Section 2.4 is that a SW-absorbing aerosol such as BC would only produce a negative SW radiative forcing over low-albedo surfaces (Figs 2.14 and 2.17). This suggests that a stratospheric BC layer would enhance the absorption of sunlight within the atmosphere, and therefore it will be interesting to assess whether this would still lead to a surface cooling (which is the primary goal of SAI).

It is important to note the limitations of the simple models utilised here. For instance, the assumption that clouds entirely reflect incident SW radiation is simplistic. Additionally, the models omit representation of the LW radiation changes that an

atmospheric aerosol layer would induce. Also, the spectrally-averaged optical properties presented in Table 2.1 were determined using the TOA $S_0(\lambda)$ distribution, when spectral-averaging over a post-atmospheric transmission solar distribution (i.e. $S_0(\lambda)T(\lambda)$) would be more appropriate for a tropospheric aerosol layer. In Chapter 3, we will use a complex radiative transfer code to investigate the radiative flux changes induced by atmospheric aerosol layer in greater detail and with greater accuracy than the models used in this chapter. Additionally, we will assess surface radiation changes for aerosol layers composed of SO_4, TiO_2 and BC.

Chapter 3 Investigating the radiative effects of a stratospheric aerosol layer using a detailed radiative transfer code

3.1. Introduction

The simple models employed in Chapter 2 were derived from the radiative transfer equation (RTE) for a plane-parallel atmosphere under the thin aerosol layer approximation. Additionally, these simple models were derived for tropospheric aerosol layers, i.e. it was assumed that the atmospheric attenuation of SW radiation by, for instance, atmospheric absorption and Rayleigh scattering occurs above the aerosol layer. The assumption of a tropospheric aerosol layer is clearly inappropriate for SAI, in which the enhanced aerosol layer would primarily reside above the tropopause, or above 80% of the mass of the atmosphere [Seinfeld and Pandis, 1998]. To determine the radiative effects of a stratospheric aerosol layer with greater fidelity, it is necessary to use a more detailed radiation code with explicit representation of the various constituents of the atmosphere. In this chapter, we will discuss the RTE for a plane-parallel atmosphere and derive approximate solutions. We will then use the Suite Of Community RAdiative Transfer Codes based on Edwards and Slingo (SOCRATES) radiation code [Edwards and Slingo, 1996] to evaluate radiative flux changes for stratospheric aerosol layers composed of various aerosols.

3.2. Radiative transfer through a plane-parallel atmosphere

3.2.1. The radiative transfer equation

The classical RTE for monochromatic (i.e. single wavelength) diffuse radiation in a plane-parallel atmosphere is given in Eq. 3.1. A full derivation of Eq. 3.1 is provided in Chapter 2 of Zdunkowski *et al.* (2007). We will adopt Zdunkowski's notations in this section.

$$\mu \frac{d}{d\tau} I(\tau,\mu) = I(\tau,\mu) - \frac{\omega_0}{2}\int_{-1}^{1} P(\mu,\mu')I(\tau,\mu')d\mu' - \frac{\omega_0}{4\pi} S_0 e^{-\frac{\tau}{\mu_0}} P(\mu,-\mu_0) - (1-\omega_0)B(\tau) \quad (3.1)$$

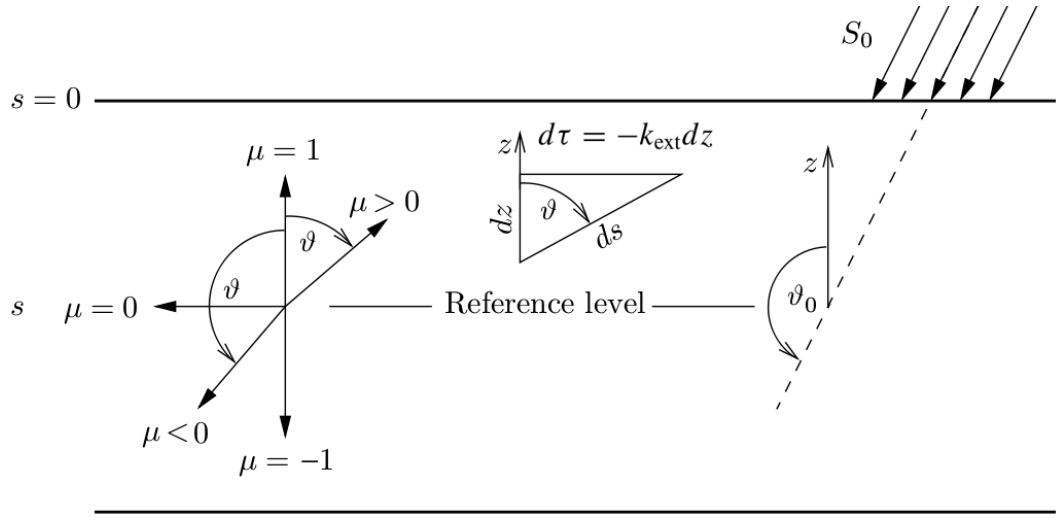

Figure 3.1 Schematic of the plane-parallel atmosphere geometry. $\mu > 0$ denotes upwelling radiation and $\mu < 0$ denotes downwelling radiation. θ_0 describes the incident direction of direct solar radiation. Fig. 2.3 from Zdunkowski et al. (2007)

In order to understand Eq. 3.1, it is necessary to discuss its individual components. The radiance (I) describes the diffuse radiation flowing through a surface (dσ) parallel to a plane, in a direction contained within a solid angle (dω) in a unit time (dt) and with frequencies in the range [ν, ν+dν]. $\mathrm{I}(\tau,\mu)$ has units of W m^{-2} sr^{-1} Hz^{-1}. The optical depth τ is the integral of atmospheric extinction coefficient over a vertical path from the top of the atmosphere (s = 0, Fig. 3.1) to a reference level (s, Fig. 3.1). The parameter μ_0 is the cosine of the solar zenith angle θ_0, which describes the incident direction of the direct solar radiation (S_0) relative to the horizontal plane, and the parameter μ describes the direction of the diffuse radiation. $\mathrm{I}(\tau,\mu)$ is therefore the monochromatic diffuse radiance at position τ (relative to the top of the atmosphere) and with direction μ.

Equation 3.1 is the azimuthally-averaged form of the RTE for a plane-parallel atmosphere. By 'plane-parallel', we mean that the model atmosphere is assumed to consist of horizontal layers in which the optical properties are uniform across each layer. By 'azimuthally-averaged', we mean that the optical properties have been integrated over the azimuthal angle $\phi \in [0, 2\pi]$ (see Fig. 2.6) to give a two dimensional field (θ, z), where z is measured from the lower boundary of the lowest atmospheric layer. The term 'diffuse radiation' refers to any radiation other than the direct solar radiation (S_0). Equation 3.1 relates the change in the diffuse radiation field to the sinks and sources of radiation within the atmosphere. The second term on the right hand side of Eq. 3.1 describes the diffuse radiation scattered from direction μ' into direction μ (where ω_0 is the single scattering albedo of the layer (Eq.

2.8) and $P(\mu,\mu')$ is the scattering phase function (Eq. 2.10)). The third term on the right hand side describes the fraction of S_0 that is converted via scattering into diffuse radiation, and the fourth term describes the addition of radiation from atmospheric emission (i.e. according to Planck's law, Eq. 1.4, for an atmosphere in local thermodynamic equilibrium).

3.2.2. Two-stream approximate solutions

In atmospheric sciences, it is most useful to use radiative fluxes (F) instead of radiances (I). F describes the rate at which radiation crosses a surface irrespective of the incident angle of the radiation. Thus F is obtained by integrating I over all solid angles ($d\omega$). The aim of this section is to obtain explicit formulae for F using Eq. 3.1. This derivation follows Zdunkowski *et al.* (2007). We will use the standard Schuster-Schwarzschild two-stream approximation [Schuster, 1905; Schwarzschild, 1906] in which Eq. 3.1 is evaluated for an upward flux (F_+) stream and a downward flux (F_-) stream, where the fluxes are determined from Eq. 3.2.

$$F_+ = 2\pi \int_0^1 \mu\, I(\tau,\mu) d\mu \;,\;\; F_- = 2\pi \int_0^1 \mu\, I(\tau,-\mu) d\mu \tag{3.2}$$

Firstly, we let $-\mu'$ and $-\mu_0$ refer to the direction of the downward diffuse radiation and direct solar radiation respectively, and we define the upscattered fraction $\beta(-\mu')$ as follows.

$$\beta(-\mu') = \frac{1}{2}\int_0^1 P(\mu,-\mu') d\mu \tag{3.3}$$

Note that Eq. 3.3 is identical to Eq. 2.27 but for a slight change of notation. Next, we will ignore the $B(\tau)$ term in Eq. 3.1 as there is negligible atmospheric emission in the solar (SW) spectrum which is of primary interest here, and we integrate over the upper and lower hemispheres ($\mu \in [0, 1]$ and $-\mu \in [0, 1]$ respectively). We then use the definitions Eq. 3.2-3.3 to obtain the following two-stream flux relations.

$$\begin{aligned}\frac{dF_+}{d\tau} = {} & 2\pi \int_0^1 I(\tau,\mu)\, d\mu - 2\pi\omega_0 \int_0^1 \big(1-\beta(-\mu')\big) I(\tau,\mu') d\mu' \\ & - 2\pi\omega_0 \int_0^1 \beta(-\mu')\, I(\tau,-\mu') d\mu' - \omega_0 S_0 e^{-\frac{\tau}{\mu_0}} \beta(-\mu_0)\end{aligned} \tag{3.4a}$$

$$\frac{dF_-}{d\tau} = 2\pi \int_0^1 I(\tau,-\mu)\,d\mu + 2\pi\omega_0 \int_0^1 \beta(-\mu')I(\tau,\mu')d\mu' \qquad (3.4b)$$
$$+ 2\pi\omega_0 \int_0^1 \big(1-\beta(-\mu')\big) I(\tau,-\mu')d\mu' + \omega_0 S_0 e^{-\frac{\tau}{\mu_0}}(1-\beta(-\mu_0))$$

Next, we average μ and $\beta(-\mu)$ with respect to the up and downwelling radiances $I(\tau,\mu_\pm)$ to obtain the parameters $\mu_\pm$ and $\beta_\pm$ (Eqs 3.5-3.6). For interest, Zdunkowski *et al.* (2007) defines $\mu_\pm$ as the mean directional cosines of the up and downwelling diffuse radiation.

$$\mu_+(\tau) = \frac{2\pi \int_0^1 \mu\, I(\tau,\mu)d\mu}{2\pi \int_0^1 I(\tau,\mu)\,d\mu} = \frac{F_+}{2\pi \int_0^1 I(\tau,\mu)\,d\mu} \qquad (3.5a)$$

$$\mu_-(\tau) = \frac{2\pi \int_0^1 \mu\, I(\tau,-\mu)d\mu}{2\pi \int_0^1 I(\tau,-\mu)\,d\mu} = \frac{F_-}{2\pi \int_0^1 I(\tau,-\mu)\,d\mu} \qquad (3.5b)$$

$$\beta_+(\tau) = \frac{2\pi \int_0^1 \beta(-\mu)\, I(\tau,\mu)d\mu}{2\pi \int_0^1 I(\tau,\mu)\,d\mu} \qquad (3.6a)$$

$$\beta_-(\tau) = \frac{2\pi \int_0^1 \beta(-\mu)\, I(\tau,-\mu)d\mu}{2\pi \int_0^1 I(\tau,-\mu)\,d\mu} \qquad (3.6b)$$

Finally, we insert the expressions Eqs 3.5-3.6 into Eq. 3.4 in order to remove any reference to the diffuse radiance (I) and we give the result in matrix form (Eq. 3.7).

$$\frac{d}{d\tau}\begin{pmatrix}F_+\\F_-\end{pmatrix} = \begin{pmatrix}\alpha_{11} & \alpha_{12}\\ \alpha_{21} & \alpha_{22}\end{pmatrix}\begin{pmatrix}F_+\\F_-\end{pmatrix} + S_0 e^{-\tau/\mu_0}\begin{pmatrix}-\omega_0\beta(-\mu_0)\\ \omega_0[1-\beta(-\mu_0)]\end{pmatrix} \qquad (3.7)$$

Explicit expressions for the coefficients α_{ij} are provided in Eq. 3.8.

$$\alpha_{11} = \frac{1-\omega_0(1-\beta_+)}{\mu_+} \quad \alpha_{21} = \frac{\omega_0\beta_+}{\mu_+}$$
$$\alpha_{12} = -\frac{\omega_0\beta_-}{\mu_-} \quad \alpha_{22} = -\frac{1-\omega_0(1-\beta_-)}{\mu_-} \qquad (3.8)$$

Various two-stream models based on Eq. 3.7 exist, each with their own values for the coefficients α_{ij}. Most of the models assume that $\mu_+ = \mu_- \equiv 1/D$ where the constant D is denoted the diffusivity factor, and $\beta_+ = \beta_- \equiv \beta(g)$ for some constant function of the

asymmetry factor *g*. With these assumptions, we can define α_1 and α_2 such that α_{11}= -α_{22}= α_1 and α_{21}= -α_{12}= α_2, and we can rewrite Eq. 3.7 in terms of α_1 and α_2.

$$\frac{d}{d\tau}\begin{pmatrix}F_+\\F_-\end{pmatrix} = \begin{pmatrix}\alpha_1 & -\alpha_2\\ \alpha_2 & -\alpha_1\end{pmatrix}\begin{pmatrix}F_+\\F_-\end{pmatrix} + S_0 e^{-\tau/\mu_0}\begin{pmatrix}-\omega_0\beta(-\mu_0)\\ \omega_0[1-\beta(-\mu_0)]\end{pmatrix} \quad (3.9)$$

	Classical Eddington scheme	Zdunkowski and Korb (1985) 'PIFM'	Zdunkowski *et al.* (1980)	Discrete ordinates method	Hemispheric-mean method
s	$\frac{3}{2}(1-\omega_0 g)$	$D-\frac{3}{2}\omega_0 g$	$2-\frac{3}{2}\omega_0 g-\frac{\omega_0}{2}$	$\sqrt{3}(1-\omega_0 g)$	$2(1-\omega_0 g)$
d	$2(1-\omega_0)$	$D(1-\omega_0)$	$2(1-\omega_0)$	$\sqrt{3}(1-\omega_0)$	$2(1-\omega_0)$

Table 3.1 Atmospheric optical parameters for the models used in SOCRATES

Additionally, we introduce the parameters s and d such that $s = \alpha_1 + \alpha_2$ and $d = \alpha_1 - \alpha_2$. Table 3.1 contains the values of s and d for the various models that are included within the SOCRATES code. Equation 3.9 is only valid for the SW spectrum, as the assumption of negligible atmospheric emission is invalid for LW radiation. On the other hand, there is little solar emission in the LW spectrum (λ > 3 μm), therefore it is appropriate to negate the S_0 term from the RTE when deriving Eq. 3.9 for the LW spectrum. An equivalent formula to Eq. 3.9 for the LW spectrum is given in Eq. 3.10 [Zdunkowski *et al.*, 2007].

$$\frac{d}{d\tau}\begin{pmatrix}F_+\\F_-\end{pmatrix} = \begin{pmatrix}\alpha_1 & -\alpha_2\\ \alpha_2 & -\alpha_1\end{pmatrix}\begin{pmatrix}F_+\\F_-\end{pmatrix} + D\pi(1-\omega)\begin{pmatrix}-B(\tau)\\ B(\tau)\end{pmatrix} \quad (3.10)$$

3.3. The SOCRATES radiation code

3.3.1. Background

SOCRATES uses the two-stream framework outlined in Section 3.2.2 to calculate radiative fluxes for a prescribed plane-parallel atmospheric column [Manners *et al.*, 2016]. Figure 3.2 shows the vertical resolution of such an atmosphere. Radiative fluxes are determined on model levels (with indices on the right hand side of Fig. 3.2), while optical properties are prescribed on model layers. For the SW spectrum, SOCRATES calculates the total upward flux (i.e. direct + diffuse) U, the total

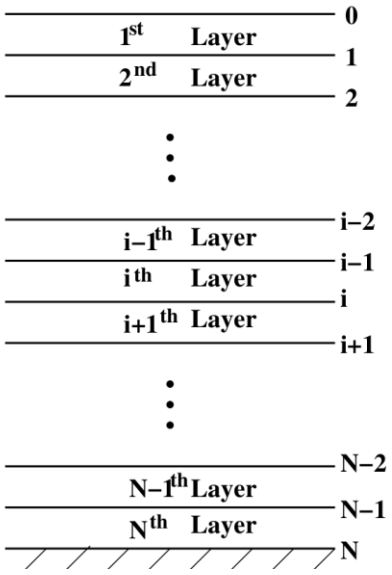

Figure 3.2 Vertical resolution of the plane-parallel atmosphere used by SOCRATES [Manners et al., 2016]

downward flux V, and the direct solar flux Z. For the LW spectrum SOCRATES defines U and V as differential (i.e. minus πB) upwelling and downwelling fluxes. Recurrence relations between successive fluxes are given in Eq. 3.11.

$$\begin{aligned} U_{i-1} &= T_i U_i + R_i V_{i-1} + S_i^+ \\ V_i &= T_i V_{i-1} + R_i U_i + S_i^- \\ Z_i &= T_{0i} Z_{i-1} \end{aligned} \tag{3.11}$$

The subscripts on U, V, and Z refer to levels, and the subscripts on T, R, T_0 and $S^{\pm}$ refer to layers. T and R represent a layer's transmissivity and reflectivity to diffuse radiation, respectively, and T_0 represents a layer's transmissivity to direct solar radiation. Formulae for T and R as a function of the layer's optical properties follow from finding the general solutions to the ordinary differential equations in Eq. 3.9. SOCRATES treats the source terms $S^{\pm}$ in Eq. 3.11 differently for the SW and LW spectra. As noted in Section 3.2.2, the primary source of diffuse radiation in the SW spectrum is from scattering of the direct solar beam (Eq. 3.12), while in the LW spectrum, atmospheric emission becomes the primary source. In the SW spectrum, $S^{\pm}$ is proportional to Z according to Eq. 3.12.

$$S_i^+ = c_{1i} Z_{i-1}, \; S_i^- = c_{2i} Z_{i-1} \tag{3.12}$$

The coefficients c_{1i} and c_{2i} are functions of the optical properties of the atmospheric layer, and follow from solving the particular integrals of the ordinary differential

equations in Eq. 3.9 whilst approximating $\beta(-\mu_0)$ with a suitable function of the asymmetry factor g [Zdunkowski *et al.*, 2007]. To complete the model for the SW spectrum, we require boundary conditions for U and V. At the top of the atmosphere, we set $V_0 = Z_0 = S_0\mu_0$ where S_0 is the solar radiative flux in a particular waveband. We use Eq. 3.13 for the lower boundary condition, with R_s and R_d the surface albedos for direct and diffuse radiation respectively. Note, that we will assume $R_s = R_d$ for the rest of this chapter.

$$U_N = (R_s - R_d)Z_N + R_d V_N \tag{3.13}$$

3.3.2. *δ*-rescaling of the optical properties

SOCRATES's SW model requires as input only three optical parameters for each atmospheric layer: the asymmetry parameter (g), the layer optical depth (τ), and the single scattering albedo (ω_0). We recall from Eq. 2.25 that τ is simply the specific extinction coefficient (k_e) multiplied by the column mass of the layer. Also, ω_0 is simply the ratio of the scattering coefficient and the extinction coefficient (k_s / k_e). Therefore, the basic optical parameters used by SOCRATES are k_s, k_e, and g. Of these parameters, only g contains information about the angular distribution of scattering. This simple treatment of the angular distribution of scattering can lead to large inaccuracies in the calculated radiative fluxes if an atmosphere contains highly-peaked forward-scattering particulates. A simple way to reduce these inaccuracies is to use the δ-rescaling transformation (Eq. 3.14), where the scaling parameter $f = g^2$ is introduced [Joseph *et al.*, 1976]. The optical parameters τ, ω_0, and g can now be replaced with their transformed parameters, τ^*, ω_0^*, and g^*.

$$\tau^* = \tau(1 - \omega_0 f) \tag{3.14a}$$

$$\omega_0^* = \frac{\omega_0(1-f)}{1-\omega f} \tag{3.14b}$$

$$g^* = \frac{g-f}{1-f} \tag{3.14c}$$

3.3.3. Optical properties for a prescribed atmosphere

SOCRATES requires as input, for each atmospheric layer and for each waveband, the optical parameters k_s, k_e, and g. If δ-rescaling is required then the parameter f will also be needed. In an individual atmospheric layer, multiple processes may act to

attenuate radiation. For instance, in Section 1.1.2 we discussed the absorption of LW radiation by atmospheric gases, and in Section 2.3.1 we discussed the scattering and absorption of SW radiation by gas and aerosol particles. Additionally, clouds attenuate both SW and LW radiation, with the specific cloud radiative effect dependent on the altitude of the cloud, its composition (i.e. liquid water / ice/ mixed-phase), and its optical thickness. Let the index *j* denote an individual light-attenuation process in a layer. Then the optical parameters for a given atmospheric layer and waveband (k_s, k_e, g, f) are related to the optical parameters for the individual processes ($k_s^{(j)}$, $k_e^{(j)}$, $g^{(j)}$, $f^{(j)}$) according to Eq. 3.15 [Manners *et al*., 2016].

$$k_e = \sum_j k_e^{(j)} \tag{3.15a}$$

$$k_s = \sum_j k_s^{(j)} \tag{3.15b}$$

$$g = \sum_j k_s^{(j)} g^{(j)} \Big/ \sum_j k_s^{(j)} \tag{3.15c}$$

$$f = \sum_j k_s^{(j)} f^{(j)} \Big/ \sum_j k_s^{(j)} \tag{3.15d}$$

For each process, $f^{(j)} = g^{(j)} \times g^{(j)}$. The optical depth of the layer is then $\tau = k_e \times \Delta m$, where Δm is the column mass of the layer which can be obtained from the equation of hydrostatic balance ($\Delta m = \rho \times dz = -dp/g$, where ρ, p, and g are the atmospheric density, pressure and the gravitational constant respectively). The single scattering albedo of the layer is obtained from $\omega_0 = k_s / k_e$.

For radiative absorption by gases, SOCRATES uses the correlated *k* approach, in which k_e^{gas} is weighted by the mass mixing ratio of the gas and by a temperature and pressure dependent scaling factor to account for Doppler broadening [Sun, 2011]. The 'mass mixing ratio' metric is defined as the concentration of a substance (in kg m^{-3}) divided by the density of dry air. For clouds, the optical parameters (k_s^{cloud}, k_e^{cloud}, g^{cloud}) are derived from parameterised functions of the cloud droplet effective radius (r_e) and the liquid and/or ice water content (L / I). These parameterisations were derived from single-column Mie calculations of light transfer through a cloudy atmosphere [e.g. Slingo and Schrecker, 1982]. Rayleigh scattering and other atmospheric radiative phenomena such as continuum absorption (i.e. the self-

broadening of the absorption lines of water vapour) are optional inclusions in a call to SOCRATES.

3.3.4. Optical properties for a prescribed aerosol layer

It is useful to relate the treatment of aerosols by SOCRATES to the optical parameters that were derived from the fundamental particle properties in Chapter 2. Firstly, for each aerosol we must prescribe a size distribution and density before proceeding to calculate the optical parameters for each waveband using Eqs 2.16-2.18. SOCRATES contains a Mie scattering module which is able to calculate the spectrally-weighted optical parameters using the method outlined in Section 2.3, given prescribed spectral weighting coefficients (i.e. $\mathrm{f}(\lambda)$ in Eqs 2.16-2.18) and for a given set of wavebands. As the SW and LW spectra are treated separately by SOCRATES, it is necessary to provide two sets of optical parameters for each aerosol (and more specifically, for all light-attenuating processes) – one for the SW spectrum and one for the LW spectrum. Therefore, we require two sets of spectral weighting coefficients. For the SW spectrum, it is customary to use either the observed TOA solar spectral irradiances [Kuruckz, 1995] or the Planckian function (Eq. 1.4) with T = 6000 K. For the LW spectrum, it is customary to use the Planckian function with T = 250 K, which is approximately equal to Earth's effective emission temperature ($T_e \approx 255$ K).

SOCRATES is able to account for multiple aerosol types in a single atmospheric layer. Let l and q_l denote the index and mass mixing ratio respectively for an individual aerosol type. Then the combined aerosol optical parameters (k_s^{aero}, k_e^{aero}, g^{aero}) follow from combining the individual aerosol optical parameters and weighting by the aerosol mass mixing ratio (Eq. 3.16). SOCRATES accounts for hygroscopic aerosol by calculating the layer-mean relative humidity and then interpolating the optical parameters from a prescribed lookup table.

$$k_s^{aero} = \sum_l k_s^{aero,l} q_l \tag{3.16a}$$

$$k_e^{aero} = \sum_l k_e^{aero,l} q_l \tag{3.16b}$$

$$g^{aero} = \sum_l k_s^{aero,l} q_l g_l / k_s^{aero,l} \tag{3.16c}$$

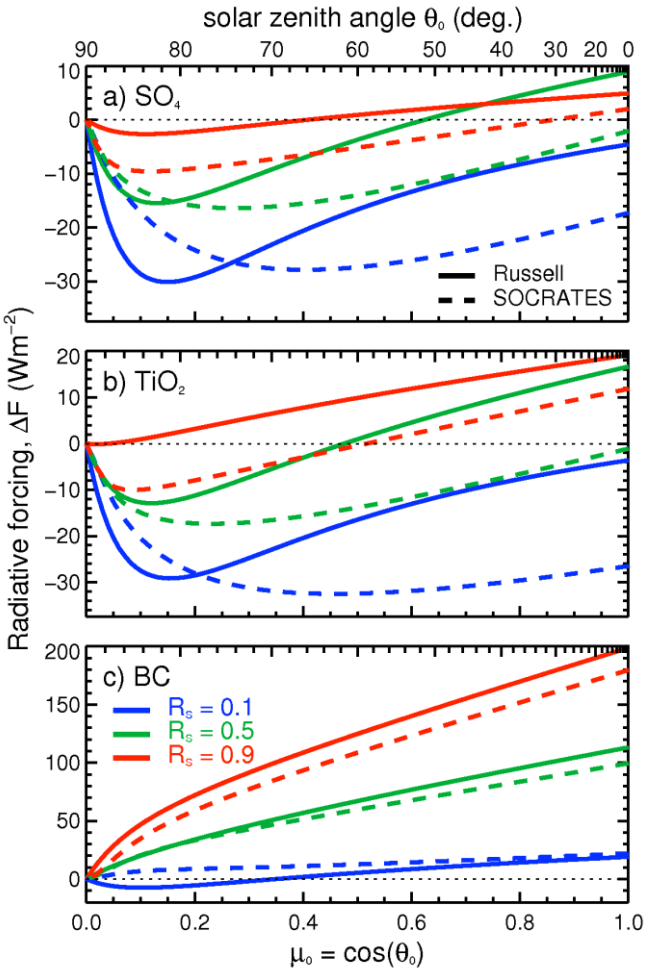

Figure 3.3 TOA radiative forcing for a $\tau = 0.1$ aerosol layer calculated using Russell's model (Eq. 2.32) and SOCRATES with a typical mid-latitude clear-sky atmospheric column and a lower stratospheric (15-20 km altitude) aerosol layer

3.4. Comparison of SOCRATES with Russell's model

As a preliminary exercise, we compare Russell's model for the SW radiative forcing of an aerosol layer with SOCRATES for an equivalent scenario. For SOCRATES, we use a mid-latitude atmospheric column (see Section 3.5.2) and prescribe a uniform aerosol mass mixing ratio between 15-20 km altitude such that the total aerosol optical depth is 0.1. Optical parameters for SO_4, TiO_2 and BC are determined using the method outlined in Section 2.3.6 for 6 wavebands in the SW spectrum and assuming a lognormal distribution with $r_m = 0.1$ μm and $\sigma = 1.8$. For Russell's model, we only account for the SW absorption by O_3 in the parameterisation of atmospheric transmission (i.e. T^2 in Eq. 2.32), and we use an O_3 column burden of 0.4 cm^{-1}. Figure 3.3 shows the SW radiative forcing as a function of solar zenith angle for Russell's model and SOCRATES assuming clear-sky conditions. Russell's model underestimates the negative radiative forcing induced by the SO_4 and TiO_2 over low-

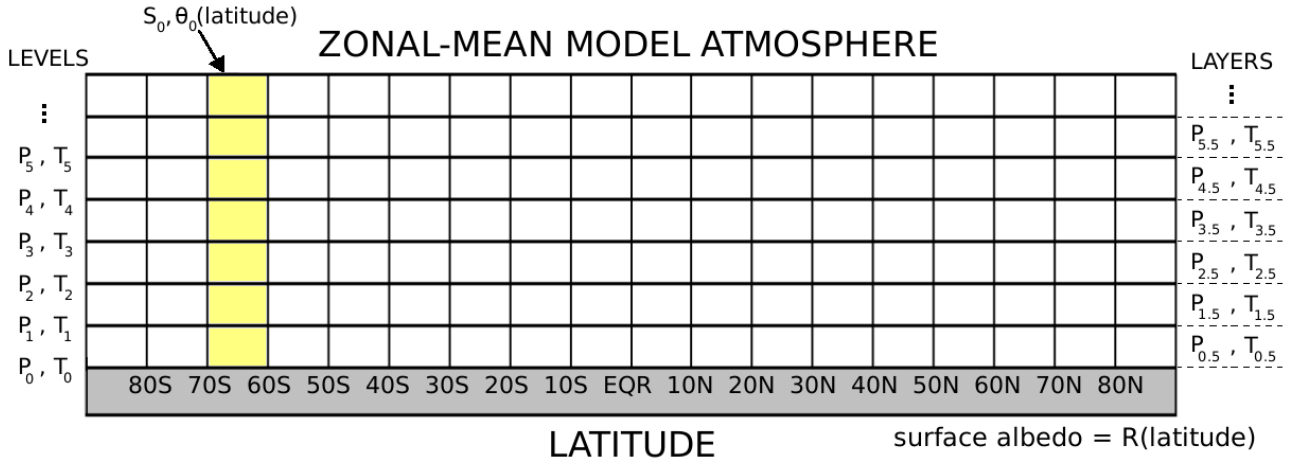

Figure 3.4 Schematic of a zonal-mean global atmosphere grid with horizontal increments of 10^{o} latitude. P and T on the vertical axes refer to the atmospheric pressure and temperature respectively

albedo surfaces at small zenith angles, and gives a positive radiative forcing at mid-range zenith angles ($\mu_0 \approx 0.6$) over high-albedo surfaces, where SOCRATES gives a positive radiative forcing (Fig. 3.3a,b). These differences might have been reduced had we accounted for the spectral distribution of optical coefficients in Russell's model, rather than specifying a single optical coefficient to represent the entire SW spectrum (Section 2.4.6). Boucher *et al.* (1998) and Russell *et al.* (1997) have compared simple and detailed SW radiative transfer models in some detail.

3.5. Development of a model atmosphere

3.5.1. Background

To assess the annual and seasonal radiative effects of a global aerosol layer in detail, it is necessary to develop a background global atmosphere that sufficiently represents Earth's atmosphere. We limit the scope of this exercise to the development of a zonal-mean model atmosphere that is acceptably representative of Earth's atmosphere. Figure 3.4 shows a schematic of the atmospheric grid, where we have chosen (horizontal) latitude increments of 10^{o} from 90^{o}S to 90^{o}N. Aerosol and gaseous mass mixing ratios, cloud properties and water vapour mass mixing ratios are all defined on layers and are assumed uniform across each grid-cell. We derive suitable values for the zonal-mean surface albedo as a function of latitude from the literature. Additionally, we will consider the monthly variations of the solar zenith angle as a function of latitude.

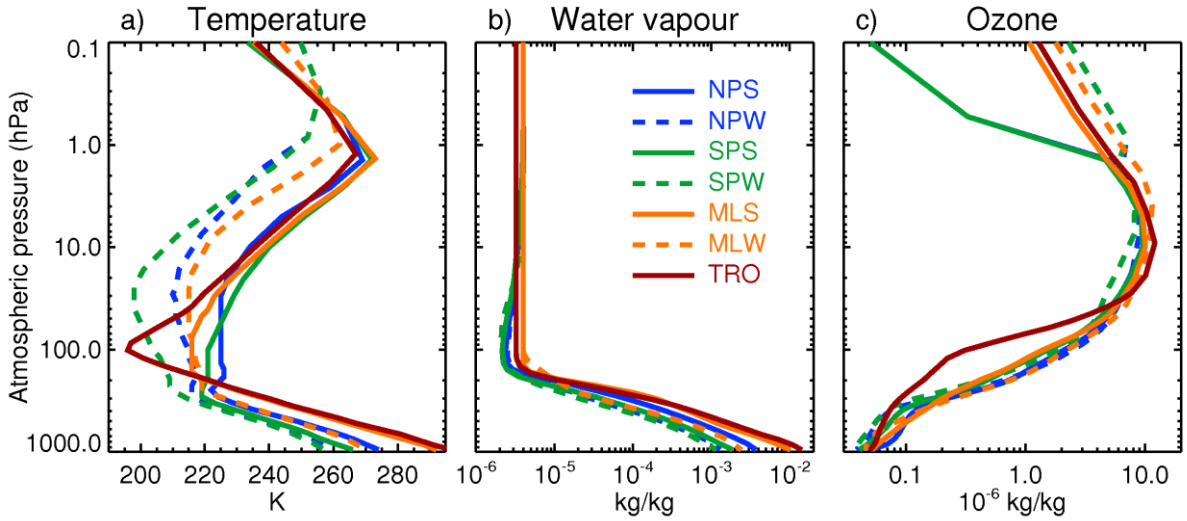

Figure 3.5 Atmospheric single-column profiles for the tropics (TRO), mid-latitude region summer and winter (MLS, MLW), and North/South Polar region summer and winter (NPS, NPW, SPS, SPW) from McClatchey *et al.* (1972) and ERA-I [Dee *et al.,* 2011]

3.5.2. Temperature, pressure, water vapour, and ozone

The offline SOCRATES code comes provisionally equipped with standard atmospheric profiles from McClatchey *et al.* (1972). Single column profiles are provided for the tropics (TRO), the mid-latitude region for winter and summer (MLW and MLS respectively), and the sub-Arctic region for winter and summer. Each profile includes the temperature (T), pressure (P), water vapour mass mixing ratio (q_{H2O}) and O_3 mass mixing ratio (q_{O3}) on 1 km levels from the surface to 25 km altitude, then on 5 km levels from 25 km to 50 km altitude, and finally evaluated at 70 and 100 km altitudes. In total, therefore, each profile has 33 levels. We linearly interpolate T, q_{H2O}, and q_{O3} with the logarithm of P to obtain values at the mid-points of layers.

During the model-evaluation stage of this chapter (Section 3.5.7), we found that the McClatchey sub-Arctic profiles do not provide a good representation of the high latitude climates. Therefore, we instead use ERA-Interim (ERA-I) data, averaged over the period 1979-2015 and interpolated onto the McClatchey pressure grid, for the high latitudes in our model atmosphere [Dee *et al.*, 2011]. Specifically, we have created single-column profiles for the South Polar Region (60°S-90°S) summer and winter (SPS and SPW), and for the North Polar Region (60°N-90°N) summer and winter (NPS and NPW). Table 3.2 shows the atmospheric profiles designated for each month and latitude and Fig. 3.5 shows the vertical profiles of T, q_{H2O}, and q_{O3}.

Latitude → Month ↓	85S, 75S, 65S	55S, 45S, 35S	25S, 15S, 5S	5N, 15N, 25N	35N, 45N, 55N	65N, 75N, 85N
JAN-MAR	SPS*	MLS	TRO	TRO	MLW	NPW*
APR-JUN	SPW*	MLW	TRO	TRO	MLS	NPS*
JUL-SEP	SPW*	MLW	TRO	TRO	MLS	NPS*
OCT-DEC	SPS*	MLS	TRO	TRO	MLW	NPW*

Table 3.2 The atmospheric profiles designated for each season and latitude band. * indicates the data is from ERA-I

3.5.3. Atmospheric gases

SOCRATES uses mass mixing ratios (q) as input for gases and aerosols. However, atmospheric gases are often expressed in terms of a molar mixing ratio with respect to dry air (mol mol^{-1}). The observed global-mean molar mixing ratios of the long-lived GHGs CO_2, CH_4 and N_2O in the year 2000 were 3.69×10^{-4}, 1.75×10^{-6}, and 3.16×10^{-7} mol mol^{-1} respectively[8]. The atmosphere also contains various halocarbon gases which are primarily of anthropogenic origin. It is common practice to subsume all CFC gases into a CFC-12 equivalent quantity (CFC-12eq), and all hydrofluorocarbon (HFC) gases into a HFC-134A equivalent quantity (HFC-134Aeq). The molar mixing ratios of CFC-12eq and HFC-134Aeq in the year 2000 were 9.99×10^{-10} and 8.09×10^{-11} mol mol^{-1}. Mass mixing ratios can be determined from the product of the molar mixing ratio and the ratio of the gas' molar mass to the molar mass of dry air (28.964 g mol^{-1}). Hence, mass mixing ratios for CO_2, CH_4, N_2O, CFC-12eq, and HFC-134Aeq in the year 2000 were 5.6×10^{-4}, 9.67×10^{-7}, 4.8×10^{-7}, 4.17×10^{-9}, and 2.85×10^{-10} kg kg^{-1} respectively. The mass mixing ratio of oxygen (O_2) is 0.2314. We apply these mass mixing ratios uniformly in our model atmosphere. In the spectral files used for this work, CO_2, O_2, H_2O and O_3 absorb in the SW spectrum, while CO_2, H_2O, O_3, CH_4, N_2O, CFC-12 and HFC-134A absorb in the LW spectrum.

3.5.4. Surface albedo

We use the zonal-mean surface albedo (R_s) model of Donohoe and Battisti (2011) (Fig 3.6). The global-mean R_s in this model is 0.14. R_s is highest at the poles due to the prevalence of sea ice and ice sheets at high latitudes. In the tropics, R_s is much lower ($R_s < 0.1$) due to the significant oceanic surface area. We have made the

[8] Data from http://www.pik-potsdam.de/~mmalte/rcps/

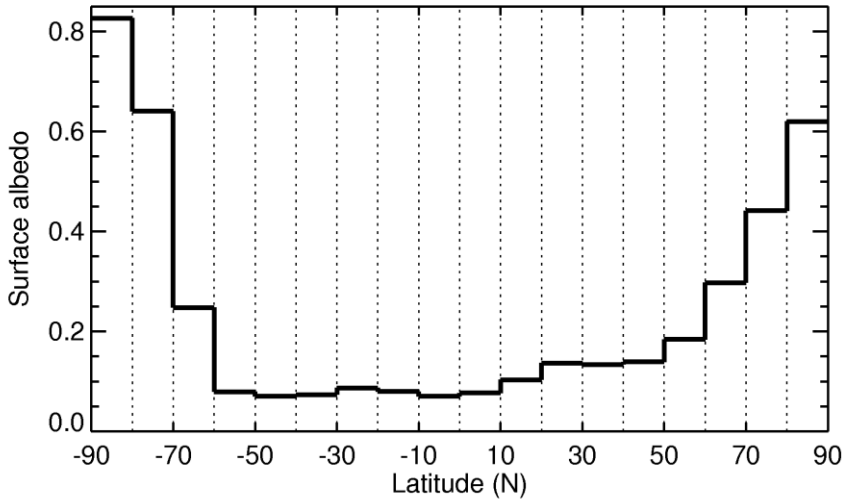

Figure 3.6 Zonal-mean surface albedos from Donohoe and Battisti (2011)

assumption that R_s is seasonally invariant here, which may be inappropriate at high latitudes due to the seasonality of sea ice. We have also made the assumption that R_s is spectrally invariant (i.e. $R_s(\lambda) \equiv R_s$). Varotsos *et al.* (2014) found from airborne observations that water albedo decreases with wavelength in the solar spectrum, while sand albedo increases with wavelength in the solar spectrum. Therefore the use of a spectrally invariant R_s may also lead to inaccuracies in the calculated radiation field.

3.5.5. Clouds

SOCRATES includes a detailed cloud radiation scheme which is able to accommodate liquid, ice, and mixed phase clouds. Therefore, it is judicious to represent the cloud phase when creating a zonal-mean cloud distribution. For this work, we use a subset of the ERA-I reanalysis data to develop a cloud distribution [Dee *et al.*, 2011]. Specifically, we use the ERA-I cloud fractional cover (CLFR), ice water content (IWC), and liquid water content (LWC) for the period December 1994 to November 1999, averaged over the December-February (DJF), March-May (MAM), June-August (JJA), and September-November (SON) seasons. For the individual months in the model atmosphere, we use the appropriate seasonal cloud field (for instance, for January we use the DJF field). Figure 3.7 shows the gridded seasonal cloud data. The low temperatures at high tropospheric altitudes provide a limit to the LWC above 5 km altitude (Fig. 3.7e-h). In the upper troposphere, clouds are instead predominantly composed of ice crystals. The highest cloud layer is in the tropics, while a persistent cloud layer exists near the surface at high latitudes.

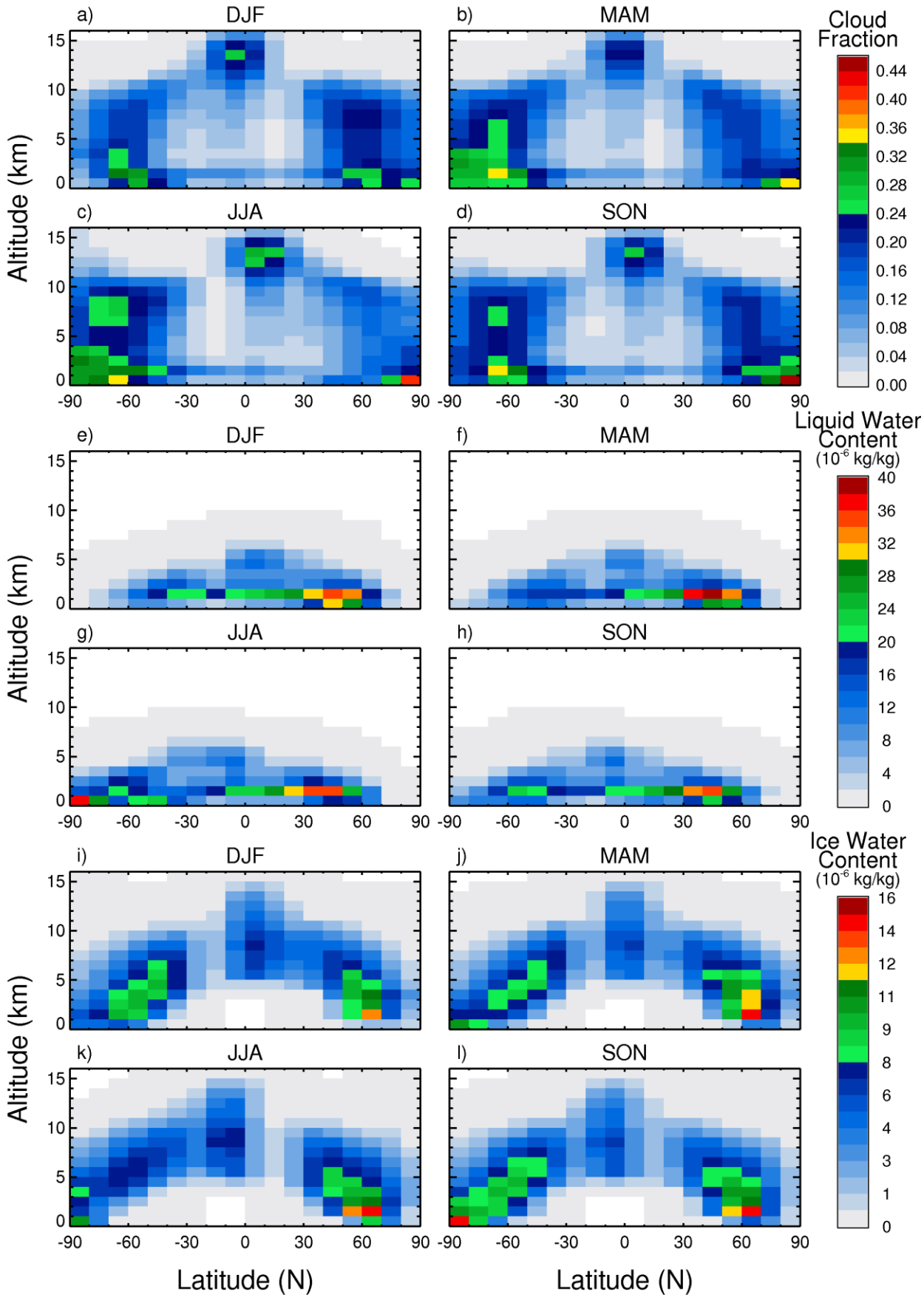

Figure 3.7 Seasonally-averaged zonal-mean cloud distributions from ERA-I (Dec 1994 – Nov 1999). (a-d) cloud fraction, (e-h) cloud liquid water content (10^6 kg per kg of dry air), (i-l) cloud ice water content (10^6 kg per kg of dry air)

3.5.6. Solar zenith angle

In order to calculate the SW radiative fluxes for each season and latitude it is necessary to determine the monthly-mean daytime solar zenith angles θ_0 and the daylength D (i.e. the time interval between sunrise and sunset). Let n = 1, …, 12 denote the month index, where for January we let n = 1. Then the solar declination angle Δ in unit radians can be determined from Eq. 3.17.

$$\Delta(n) = \frac{23.5\pi}{180}\cos\left(\frac{(n-6)\pi}{6}\right) \tag{3.17}$$

The solar declination angle is at a minimum and maximum during the summer and winter solstices respectively. Now, let t = 0, ..., 23 denote the time lapse in unit hours relative to the solar noon. Then the hour angle can be determined from Eq. 3.18.

$$h(t) = \frac{2\pi}{24}t \tag{3.18}$$

Finally, the solar zenith angle as a function of hour angle, latitude (ψ, in radians), and month can be determined from Eq. 3.19.

$$\theta_0(\psi, \Delta, h) = \cos^{-1}(\sin(\psi)\sin(\Delta) + \cos(\psi)\cos(\Delta)\cos(h)) \tag{3.19}$$

The monthly-mean daylength D in unit hours can be obtained by multiplying the hour angle at sunrise (h^*) by 24/π (Eq. 3.20).

$$D(\psi, \Delta) = \frac{24}{\pi}h^* = \frac{24}{\pi}\cos^{-1}(-\tan(\psi)\tan(\Delta)) \tag{3.20}$$

We require θ_0 at regular time intervals during daytime hours ($\theta_0 < 90^o$) for each latitude and month. It is therefore necessary to choose suitable daytime hour angles at which to calculate θ_0. We choose hour angle increments of $h^*/6$ and define h_{day} = $\{-h^*, -h^*+h^*/6, \ldots, h^*\}$, which equates to 13 time-steps. The daytime θ_0 follow from substituting h_{day} for h in Eq. 3.19.

3.5.7. Evaluation of the model atmosphere

3.5.7.1. Model configuration

It is important to evaluate the radiative fluxes in the model atmosphere before assessing stratospheric aerosol layers, in order to gain confidence in our model. It is firstly necessary to specify a microphysical cloud representation. For this investigation, we prescribe constant liquid cloud droplet and ice crystal effective radii of 6 μm and 30 μm respectively [Manners *et al*., 2016]. Additionally, we use SOCRATES's liquid droplet and ice crystal types 4 and 8, which relate the cloud optical coefficients to the effective radius using a Padé approximation with thin averaging for liquid droplets, and a parameterisation following Baran *et al.* (2001) for the ice crystals [Edwards and Slingo, 1996]. For this investigation, we uniformly apply δ-rescaling and we represent the vertical cloud distribution using the maximum random overlap option [see Manners *et al*., 2016, for details]. All of these options are the default values for SOCRATES when coupled to the Met Office Unified Model (MetUM), which provides the motivation for their use in this work [e.g. Johns *et al.*, 1997]. However, it is important to note the simplicity of this treatment of cloud microphysics – in reality cloud effective radii vary spatiotemporally; clouds can be decomposed into stratiform and convective types (depending on how they are formed); and the use of thin averaging for water droplets assumes an optically thin cloud which is often not the case. Additionally SOCRATES does not delineate between cloud types when implementing the cloud-overlap scheme and the choice of maximum random overlap will affect the radiative fluxes between successive model levels. All of these choices will affect the cloud radiative properties. Finally, the ERA-I LWC and IWC data are provided as grid box mean values, whereas SOCRATES requires in-cloud mean values. Therefore, we must divide the LWC and IWC by the CLFR before inputting to the radiation code.

Using the zonal-mean model atmosphere with no aerosol representation, we now use SOCRATES to calculate the SW and LW radiative fluxes at every altitude, latitude (ψ), month (n), and monthly-mean daytime solar zenith angle (θ_0) for the case of cloudy and clear skies. For SW radiation, we use a 6-waveband spectral file that spans $0.2 < \lambda < 10$ μm. For LW radiation, we use a 9 waveband spectral file that spans 3 μm $< \lambda <$ 1 cm. These spectral files are the default spectral files used by the operational MetUM. The cloud SW radiative effect $CRE_{SW}(\psi,n,\theta_0)$ and LW radiative

effect $CRE_{LW}(\psi,n,\theta_0)$ are obtained from the difference in outgoing SW and LW radiative fluxes, respectively, at the top of the atmosphere between the cloudy and clear-sky scenarios. To obtain the monthly-mean CRE_{SW} (where we have used a single day to represent average monthly conditions), we must integrate the daytime CRE_{SW} over the 24 hour day (Eq. 3.21).

$$CRE_{SW}(\psi,n) = \frac{D(\psi,n)}{24}\left(\frac{1}{12}\sum_{i=1}^{12}\frac{CRE_{SW}(\psi,n,\theta_{0,i}) + CRE_{SW}(\psi,n,\theta_{0,i+1})}{2}\right) \quad (3.21)$$

In Eq. 3.21, $\theta_{0,1} = \theta_{0,13}$ is the greatest daytime solar zenith angle (i.e. equal to 90° for all low and mid latitudes throughout the year) and $\theta_{0,7}$ is the noon-time solar zenith angle. LW emission is independent of θ_0; therefore we only need to calculate CRE_{LW} once for each month. For simplicity, we assume all months are of equal length, and therefore the annual-mean *CRE* is the average of the monthly-means (Eq 3.22).

$$CRE(\psi) = \frac{1}{12}\sum_{n=1}^{12} CRE(\psi,n) \quad (3.22)$$

In Eq. 3.22, *CRE* may refer to either CRE_{SW} or CRE_{LW}. Finally, to obtain the global and annual-mean cloud radiative effect, we weight the zonal-mean *CRE* by the fraction of Earth's total surface area within the respective latitude-bands (Eq. 3.23).

$$\overline{CRE} = \sum_{\psi} CRE(\psi) \times \left[\frac{\sin(\psi + 5^o) - \sin(\psi - 5^0)}{2}\right] \quad (3.23)$$

3.5.7.2. Cloud radiative effect and TOA radiation

We now compare the annual-mean radiative fluxes in the model atmosphere to observations. Table 3.3 shows the global and annual-mean *CRE* and TOA radiative fluxes for the model and from satellite observations. To test the sensitivity of the model to changes in cloud cover, we have also calculated the radiative quantities for scenarios in which the CLFR is uniformly multiplied by 1.5 and 2 ('CLFR × 1.5' and 'CLFR × 2' respectively) whilst all other factors, including the in-cloud LWC and IWC, are held constant. The CRE_{SW} and CRE_{LW} observations are from the Clouds and the Earth's Radiant Energy System (CERES) dataset averaged over the years 2001-2007 [Allan *et al.*, 2011], while the TOA radiative flux observations are taken from

Trenberth *et al.* (2009). It is clear that the 'CLFR × 1.5' model provides the best fit to the *CRE* observations, whilst 'CLFR × 2' provides the best fit to the TOA radiative flux observations.

[Wm^{-2}]	Clear sky	Model	CLFR × 1.5	CLFR × 2	Observations
CRE_{SW}	N/A	-30	-44	-58	-47
CRE_{LW}	N/A	17	25	33	28
CRE_{SW} + CRE_{LW}	N/A	-13	-19	-25	-19
TOA SW ↓	339	339	339	339	341
TOA SW ↑	48	78	91	106	102
TOA LW ↑	261	244	235	227	239

Table 3.3 Global and annual-mean cloud radiative effects and TOA radiative fluxes for clear sky conditions, cloudy skies, and from observations. CRE_{SW} and CRE_{LW} observations are from Allan *et al.* (2011) and TOA fluxes are from Trenberth *et al.* (2009)

Figure 3.8a shows the annual-mean *CRE* for the 'CLFR × 1.5' model and for CERES observations as a function of latitude. It is clear that 'CLFR × 1.5' adequately captures the spatial distribution of *CRE*, with a peak negative CRE_{SW} at ~60°S and peak CRE_{LW} over the equator and at 60°S/N. Figure 3.8b shows the annual-mean all-sky incoming SW radiation and outgoing SW and LW radiation as a function of latitude for 'CLFR × 1.5' and CERES observations. The model proficiently captures the spatial distribution of outgoing SW and LW radiation. Figure 3.8c shows the annual-mean all-sky (ALL) and clear-sky (CLR) downward SW and LW fluxes at the surface. Again, the model proficiently captures the radiative fluxes in the tropics and mid-latitudes. However, in the SH at high latitudes, significantly more LW radiation is reaching the surface in the model (~200 Wm^{-2}) than in the observations (~100 Wm^{-2}). This indicates that we should treat results from the model at high latitudes with a degree of caution. However, as only ~13 % of Earth's surface area is contained at latitudes > 60°, the global-mean values should be adequately represented by the 'CLFR × 1.5' model. We will therefore adopt 'CLFR × 1.5' as the background model atmosphere. We recognise that the use of zonal-mean profiles such as those presented in this work ignore certain specific correlations that may influence the TOA radiative fluxes and cloud radiative effect. For example, cloud fraction is generally higher over oceanic areas where the supply of moisture from the

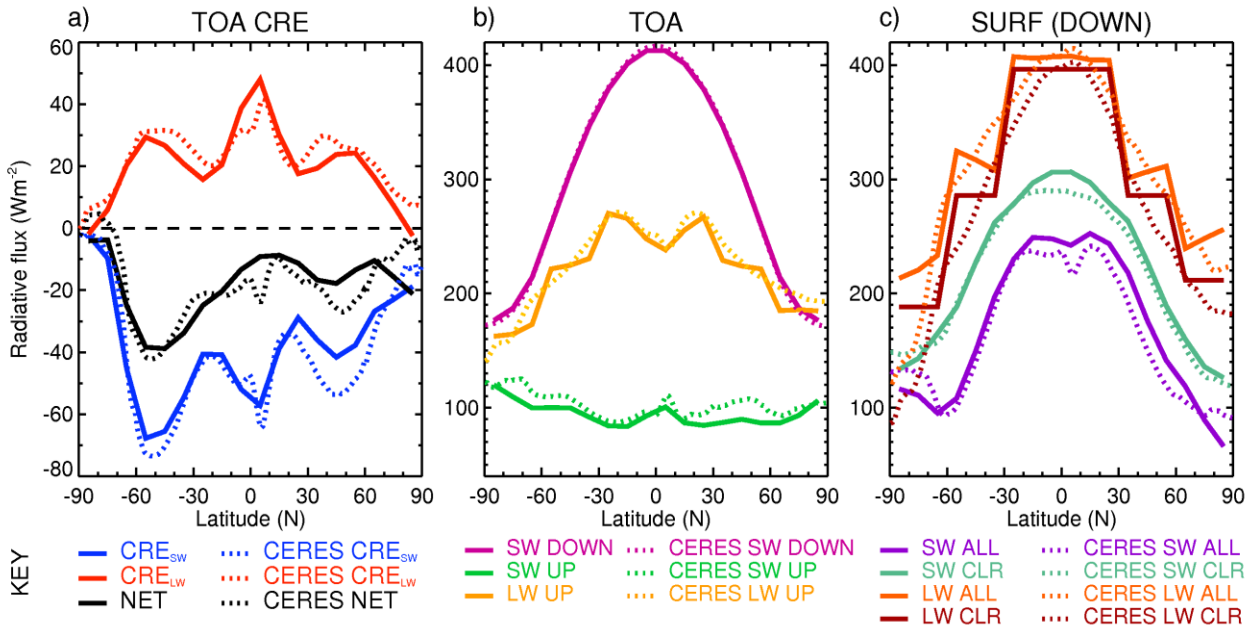

Figure 3.8 (a) TOA annual-mean cloud radiative effect for the 'CLFR × 1.5' model and CERES (2001-2007) observations, (b) TOA incoming and outgoing radiative fluxes, (c) downwelling radiative fluxes at the surface for all-sky (ALL) and clear-sky (CLR) conditions

surface is more abundant than over land regions. Thus there will be higher cloud fractions over relatively dark surfaces and lower cloud fraction over relatively bright surfaces. Other factors will also impact on the fidelity of the results include e.g. land/ocean variations in column water vapour which affects the SW and LW radiation budget [Heng *et al.*, 2014]. These kinds of correlations necessitate a pragmatic approach where we simply scale the cloud fraction in order that the zonal-model is reasonably representative of observations.

3.6. Stratospheric aerosol layer radiative forcing

The purpose of Section 3.5 was to develop a model atmosphere which could be used to investigate the radiative effects of various stratospheric aerosol layers. We will now combine a realistic representation of a stratospheric aerosol layer with the reasonably representative model atmosphere to evaluate the radiative flux changes induced by various stratospheric aerosols. Note that, for simplicity, we do not include tropospheric aerosol or background stratospheric aerosol in our model.

3.6.1. A stratospheric aerosol layer model

Firstly, it is necessary to specify realistic zonal and monthly-mean stratospheric aerosol fields. Our approach differs from Ferraro *et al.* (2011), who applied a globally-uniform aerosol layer between the tropopause and 22 km altitude. Instead, we use the difference of the zonal and monthly-mean *volc2* and *bgd* SO_4 fields from

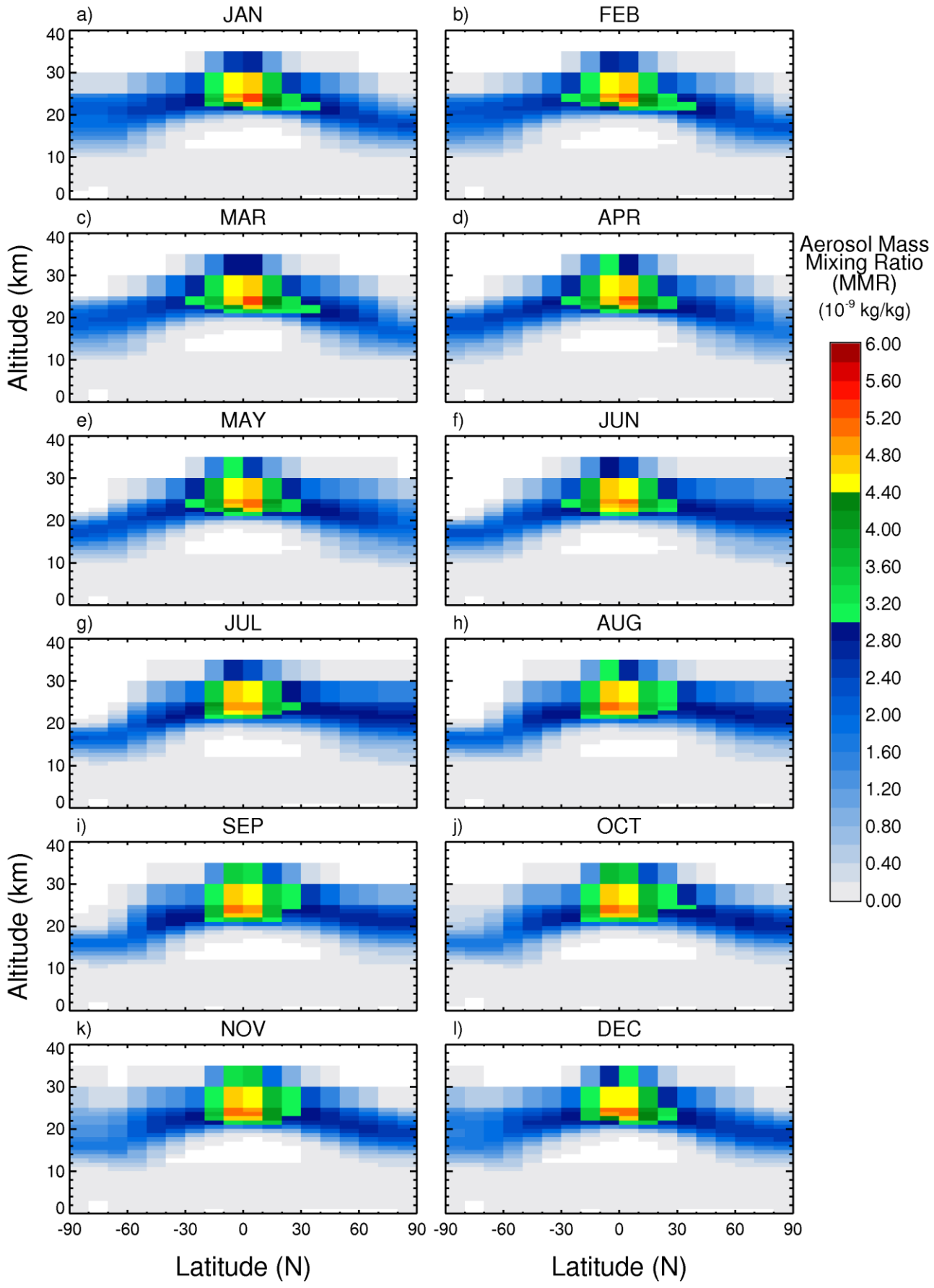

Figure 3.9 Monthly and zonal-mean aerosol mass mixing ratios (MMR in 10^{-9} kg/kg) from Rasch et al. (2008a), normalised so that the global aerosol burden is 1 Tg

Rasch *et al.* (2008a) to obtain realistic stratospheric aerosol layers. *volc2* is based on a constant 2 Tg[S] yr^{-1} injection scenario with a prescribed SO_4 aerosol lognormal distribution with r_m = 0.376 μm and σ = 1.25 (‘*volc’* refers to the use of a post-volcanic stratospheric aerosol size distribution and *‘2’* denotes the injection rate), and *bgd* (i.e. *background*) is the equivalent scenario with no geoengineering (i.e. with SO_4 from other sources). In the *volc2* simulation, SO_2 was injected at a constant rate evenly between 10^oS-10^oN and in a 2 km thick region at 25 km altitude [Rasch *et al.*, 2008a]. The *volc2* and *bgd* aerosol fields were provided to us in terms of zonal and monthly-mean aerosol surface-area concentrations S_A (μm^{-2} cm^{-3}). To obtain mass-mixing ratios (q_A) from S_A, we must use Eq. 3.24.

$$q_A = \frac{[S_A \times 10^{-6}] \times r_e \rho_s}{3\rho_{air}} \tag{3.24}$$

In Eq. 3.24, ρ_s is the aerosol density (kg m^{-3}), ρ_{air} is the atmospheric density (kg m^{-3}), and r_e (m) is the effective radius of the aerosol size distribution [Stenchikov *et al.*, 1998]. For the *volc2* size distribution, the effective radius is 4.3×10^{-7} m and we assume ρ_s = 1769 kg m^{-3} for SO_4. In order to obtain ρ_{air}, we must apply the ideal gas law to the temperatures and pressures from the appropriate atmospheric profile for each month and latitude band (Table 3.2). After calculating q_A for *volc2* and *bgd*, we then subtract the *bgd* q_A from the *volc2* q_A to obtain the desired stratospheric aerosol profiles. The *volc2-bgd* global stratospheric aerosol burden is found to be approximately 22 Tg. Figure 3.9 shows the gridded monthly *volc2-bgd* aerosol mass mixing ratios normalised such that the global atmospheric aerosol burden is 1 Tg. A persistent tropical aerosol reservoir is clearly present, which may be due to the tropical SO_2 injection design employed by Rasch *et al.* (2008a). The stratospheric aerosol is contained within a ~20 km vertical layer above the tropopause for all latitudes and months.

3.6.2. Radiative forcing definitions

The ‘adjusted radiative forcing’ (*ARF*) was defined in Section 1.1.3 as the change in net downwelling radiation at the tropopause induced by a climate forcing agent, after allowing for stratospheric temperature adjustment [Myhre *et al.*, 2013]. The ‘instantaneous radiative forcing’ (*IRF*) is defined as the change in net radiation at the

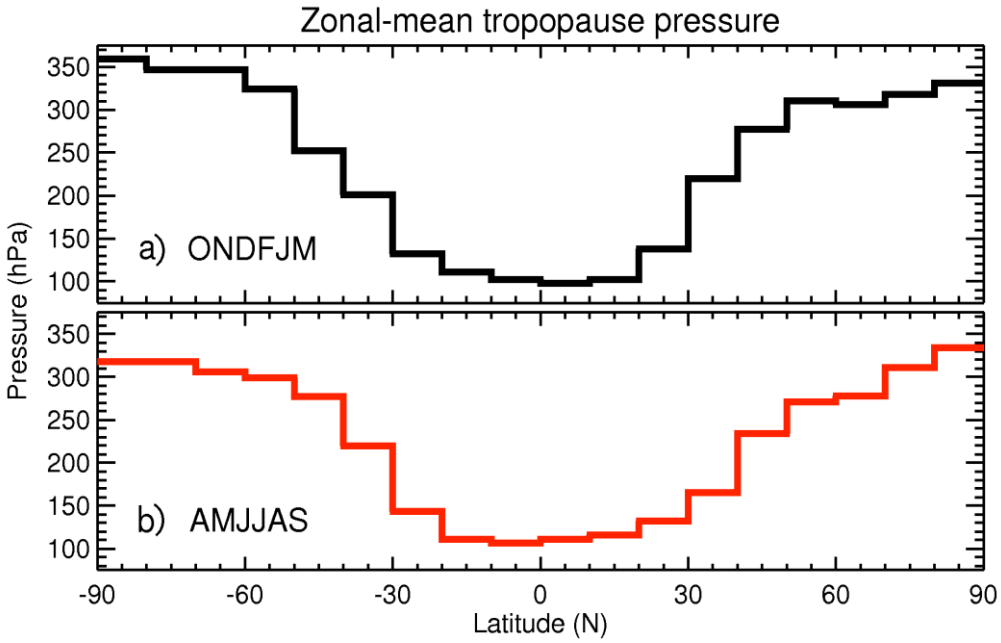

Figure 3.10 Zonal-mean tropopause pressure for (a) October-March and (b) April-September seasons. Values are from Wilcox et al. (2012) based on ERA-I data

tropopause without stratospheric temperature adjustment. The purpose of calculating the *RF* derives from the fact that climate change is a direct consequence of energy changes in the atmosphere. In equilibrium climate model studies, the change in GMST (ΔT) following the addition of a forcing agent can be related to the *RF* by $\Delta T = \lambda \times RF$, where λ is the climate sensitivity parameter (K / Wm^{-2}). The *ARF* metric has a stronger linear relationship with ΔT than the *IRF* as the troposphere and stratosphere are only weakly coupled [Mhyre *et al.*, 2013]. *ARF* and *IRF* are both historical concepts and have generally been superseded by the 'effective radiative forcing' (*ERF*) which also accounts for rapid tropospheric adjustments. Aerosol radiative effects can be further grouped into direct aerosol-radiation interactions (ari) and indirect aerosol-cloud interactions (aci). In this section, we will evaluate the *IRF*ari (i.e. the instantaneous radiative forcing for an aerosol layer, evaluated at the tropopause) as our background atmosphere is fixed. Additionally, we will evaluate the annual-mean net radiation changes at the surface and TOA. In order to evaluate *IRF*ari, it is necessary to specify a zonal-mean tropopause model. We use the JJA (Jan-Aug) and DJFM (Dec-Mar) zonal-mean tropopause heights from Wilcox *et al.* (2012) which were derived from ERA-I dataset for the period 1989-2007. We use the JJA tropopause for the Apr-Sep months and the DJFM tropopause for the Oct-Nov months (Fig. 3.10).

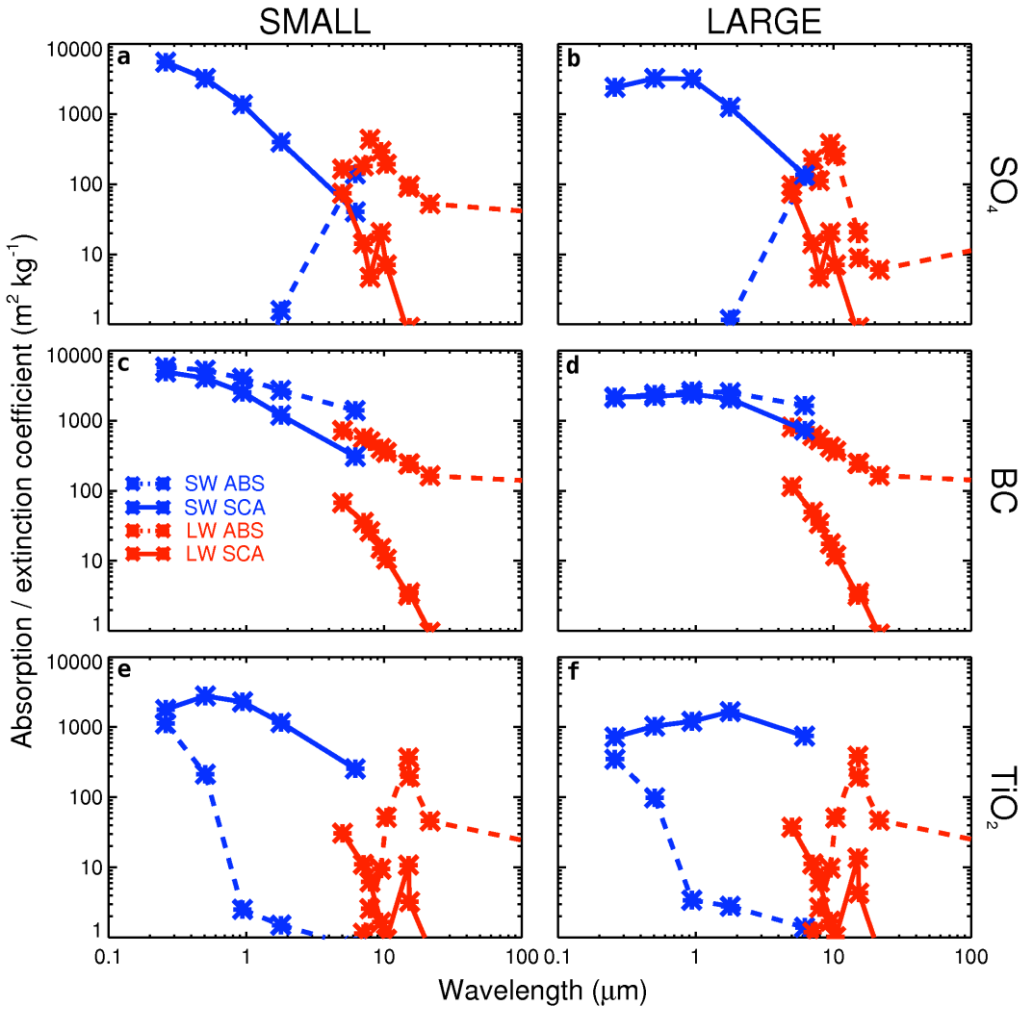

Figure 3.11 Aerosol optical properties for (a,c,e) SMALL and (b,d,f) LARGE size-distributions as a function of wavelength. Points are plotted at the middle of each waveband, as detailed in Bellouin et al. (2007)

3.6.3. Aerosol microphysical properties

We are interested in the SAI candidate aerosols SO_4, TiO_2, and BC in this thesis. Refractive indices and densities for these aerosols were given in Section 2.3.6. To assess the importance of aerosol size on *IRF*ari, two lognormal size distributions will be investigated for each aerosol: a LARGE particle mode with r_m = 0.376 μm and σ = 1.25 and a SMALL particle mode with r_m = 0.05 μm and σ = 2.03. These size distributions are the volcanic (*volc2*) and background aerosol distributions of Rasch *et al.* (2008a). Although Rasch *et al.* (2008) derived these distributions from SO_4 observations, the SMALL size distribution is similar to the optimised TiO_2 distribution of Pope *et al.* (2012) (i.e. r_m = 0.045 μm and σ = 1.8). The applicability of assuming spherical particles for the solid aerosols BC and TiO_2 is questionable due to their tendency to form long-chain agglomerates in the atmosphere [Dykema *et al.*, 2016],

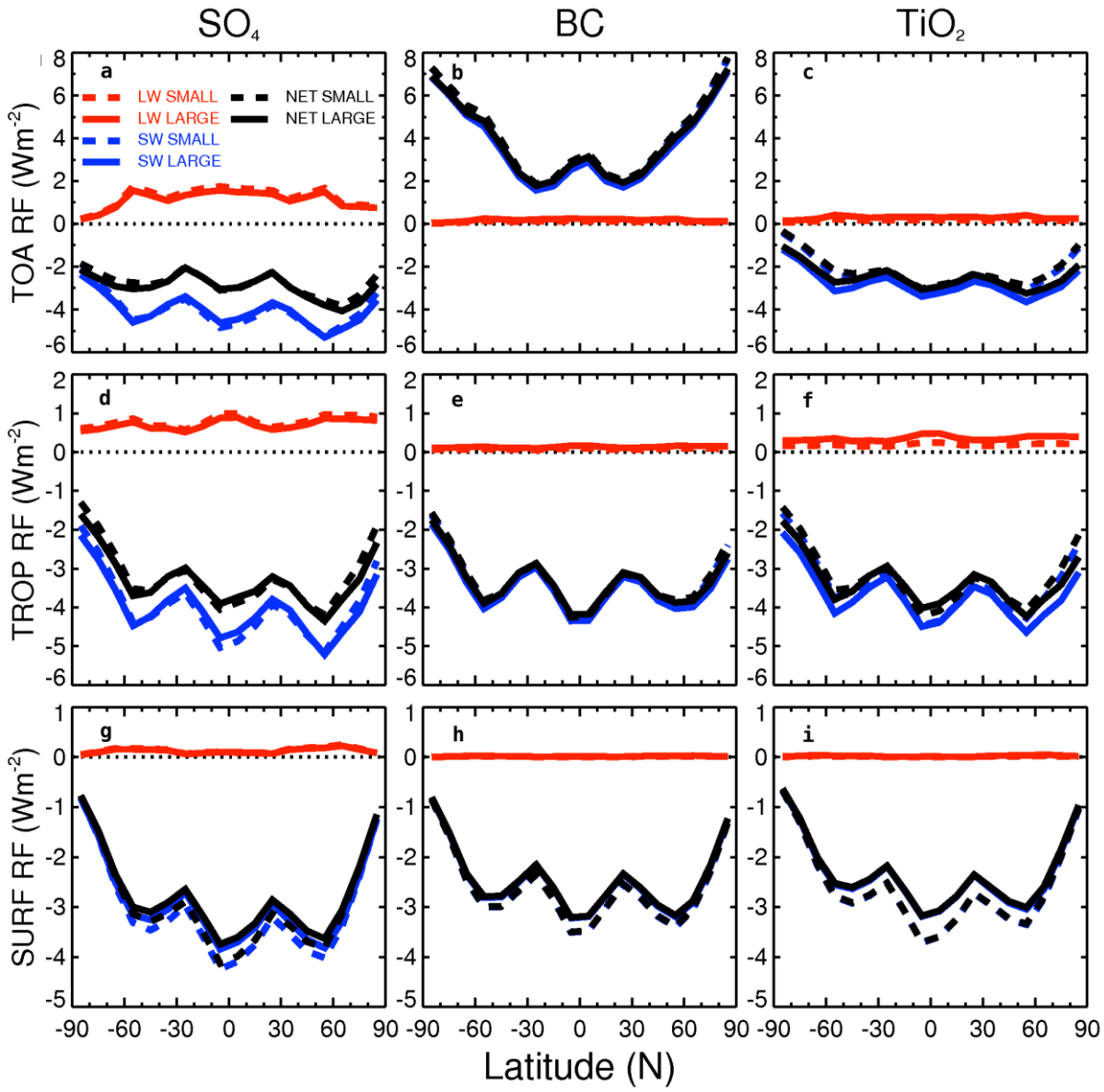

Figure 3.12 Annual-mean net IRF at the (a-c) TOA, (d-f) tropopause (TROP), and (g-i) surface (SURF) for SMALL/LARGE SO_4, BC, and TiO_2 as a function of latitude

which will be discussed more in Chapter 4. Additionally, the use of a uni-modal size distribution is a simplification – in reality atmospheric aerosols exist in various size modes depending their age and composition (Section 2.1). We use a uni-modal size distribution in this work to reflect the dominant stratospheric aerosol size mode in terms of radiative interactions for background and post-volcanic conditions [Rasch *et al*., 2008]. Figure 3.11 shows the specific absorption and scattering coefficients for the SMALL and LARGE size modes. It is clear the SW coefficients are more sensitive than the LW coefficients to the change in aerosol size.

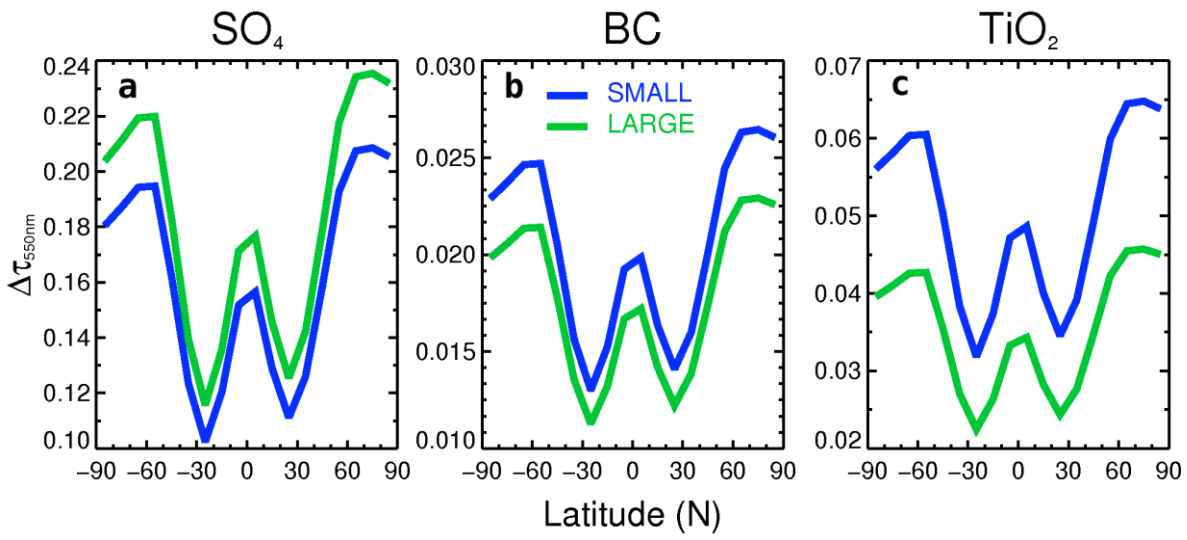

Figure 3.13 Annual-mean 550nm aerosol optical depth required for a net IRFari of -3.5 Wm^{-2}

3.6.4. Instantaneous radiative forcing

To assess the radiative effects of various aerosol layers, we adopt the approach of Ferraro *et al.* (2011) and prescribe an aerosol mass burden such that the annual-mean net (SW+LW) *IRF*ari at the tropopause is -3.5 Wm^{-2} for each aerosol type and size mode. To achieve this, we firstly calculated the *IRF*ari for a global aerosol mass burden of 1 Tg (i.e. Fig. 3.9) using the same approach as for the *CRE* (Eqs 3.21-3.23) but with the *CRE* replaced with the net downwelling radiation difference between the scenarios with and without the aerosol layer. This double call to the radiation code is a commonly used approach to calculate *RF*. After calculating *IRF*ari(1Tg), we assumed that the *IRF*ari is a linear function of aerosol mass burden and hence derived a new estimate for the aerosol mass burden using 1 Tg × -3.5 Wm^{-2} ÷ *IRF*ari(1Tg). Figure 3.12 shows the annual-mean radiative forcing evaluated at the TOA, the tropopause (i.e. the *IRF*ari), and the surface, given a global and annual-mean net *IRF*ari of -3.5 Wm^{-2}. SO_4 induces the greatest LW *IRF*ari (Fig. 3.12d), and hence the SO_4 SW *IRF*ari must also be greater than for BC and TiO_2 to produce an equal net *IRF*ari. The BC SW *RF* at the TOA is positive (Fig. 3.12b) while the BC SW *IRF*ari is negative (Fig. 3.12e), which suggests that the stratosphere in that scenario is absorbing SW radiation. The TiO_2 TOA SW anomaly is also less than the TiO_2 SW *IRF*ari, which also suggests that the stratosphere in that scenario is predominantly absorbing SW radiation.

Figure 3.13 shows the annual-mean aerosol optical depth anomaly ($\Delta\tau$) evaluated at wavelength λ = 550 nm. Although the aerosol mass-mixing ratio is largest in the

tropics (Fig. 3.9), the $\Delta\tau$ peaks at high latitudes. The $\Delta\tau$ pattern closely matches the *IRF*ari pattern in Fig. 3.12 except at high latitudes where there is much less sunlight incident at the TOA (Fig. 3.8b), hence the *IRF*ari here is at a minimum. Table 3.4 shows the $\Delta\tau$, aerosol mass burden, and global and annual-mean SW and LW *IRF*ari. The SO_4 mass burden required to produce a net *IRF*ari of -3.5 Wm^{-2} is much greater than the TiO_2 and BC mass burdens [Ferraro *et al.*, 2011]. Interestingly, the mass burden and LW *IRF*ari for LARGE SO_4 are both less than for SMALL SO_4. This result is counterintuitive as smaller aerosols reflect SW radiation more effectively than larger aerosols (Section 2.3.5) and therefore less mass should be needed for an equal radiative effect, while larger aerosols absorb more effectively in the LW spectrum. Table 3.4 suggests that the LARGE SO_4 distribution is a more optimal aerosol than SMALL SO_4 for SAI. The opposite is true for BC and TiO_2, in which the SMALL modes require less mass and induce less LW *IRF*ari than the LARGE modes.

Aerosol	Size mode	$\Delta\tau$(550nm)	Mass burden (Tg)	SW *IRF*ari (Wm^{-2})	LW *IRF*ari (Wm^{-2})
SO_4	SMALL	0.15	27	-4.27	0.79
	LARGE	0.17	23.6	-4.19	0.71
BC	SMALL	0.019	1.1	-3.58	0.07
	LARGE	0.016	1.8	-3.64	0.13
TiO_2	SMALL	0.046	7.9	-3.68	0.19
	LARGE	0.032	14.8	-3.86	0.36

Table 3.4 Global-mean 550nm aerosol optical depth anomaly, aerosol mass burden, and SW/LW net radiation changes at the tropopause for each aerosol and size mode

3.6.5. Adjusted radiative forcing

3.6.5.1. A fixed dynamical heating model

In Section 3.6.2, we noted that the GMST response to an imposed radiative forcing exhibits a stronger linear relationship with the *ARF* than with the *IRF* as the troposphere and stratosphere are weakly coupled. The *ARF* differs from the *IRF* by accounting for stratospheric temperature adjustment. As the SW *IRF*ari for TiO_2 and BC are significantly different to the respective SW perturbations at the TOA (Fig. 3.12), stratospheric temperature changes are likely to be important in these

scenarios. Therefore, it is instructive to evaluate the stratospheric temperature changes, and furthermore the *ARF*ari, for these scenarios in order to predict the climate response. A simple method for determining stratospheric temperature adjustment is to use a Fixed Dynamical Heating (FDH) model, which assumes that heating rate perturbations are solely counterbalanced by radiative processes [Maycock *et al.*, 2011]. Although FDH does not account for dynamical temperature changes, comparisons with GCMs have shown that FDH produces a qualitatively similar stratospheric temperature response [e.g. Gray *et al.*, 2009].

The instantaneous SW and LW heating rates (Q_s and Q_l in Ks^{-1}) on model layers can be calculated from the net SW and LW radiation leaving the atmospheric layer (Wm^{-2}) divided by the product of the column mass burden of the layer (kg m^{-2}) and the specific heat capacity c_p (J kg^{-1} K^{-1}). If an atmospheric layer experiences a net radiation gain then the corresponding heating rate will be positive. In a quasi-steady state, the SW and LW heating rates are balanced by dynamical heating rate (Q_d such that $Q_s + Q_l = -Q_d$). If a climate forcing agent is introduced to the atmosphere then the radiative heating rates will change (let Q_s' and Q_l' denote the perturbed heating rates). The FDH approach relates the temperature tendency to the perturbed heating rates. Specifically, we will assume that Q_d remains unchanged, we let T_0 denote the original temperature and we let T denote the adjusted temperature. Then the atmospheric temperature tendency (dT/dt) can be related to the heating rates according to Eq. 3.25 [Forster and Shine, 1997].

$$\frac{dT}{dt} = Q_s' + Q_l'(T) + Q_d = Q_s' + Q_l'(T) - \left(Q_s + Q_l(T_0)\right) \neq 0 \qquad (3.25)$$

The FDH approach incrementally advances Eq. 3.25 in time (Eq. 3.26), until the perturbed heating rates ($Q_s' + Q_l'$) are balanced by the dynamical heating rate ($Q_s + Q_l$).

$$T(t + \Delta t) = \left[Q_s' + Q_l'(T(t)) - \left(Q_s + Q_l(T_0)\right)\right] \times \Delta t \qquad (3.26)$$

The FDH code used for this investigation is based on the model developed by Forster and Shine (1997), which has subsequently been used by Maycock *et al.* (2011), Ferraro *et al.* (2011) and others. In this model, temperature changes are only applied above a specified tropopause level and a constant time increment of Δt = 6

hr is used. Temperatures are assumed equilibrated when $|\Delta T| = |T(t + \Delta t) - T(t)| < 0.001$ K. We evaluate the stratospheric temperature adjustment for each month and latitude. The SW heating rates are calculated for each daytime solar zenith angle and then integrated over a month using an equivalent formula to Eq. 3.21. The LW heating rates are determined for a single daytime solar zenith angle in similar fashion to the CRE_{LW} in Section 3.5.7. The unperturbed heating rates (Q_s and Q_l) are firstly determined for the background atmosphere on model layers. Heating rates are then linearly interpolated onto model levels using the logarithm of atmospheric pressure. The perturbed SW heating rates (Q_s') are not sensitive to atmospheric temperature changes and therefore we only need to calculate the monthly-mean Q_s' once for each atmospheric column. The perturbed LW heating rates (Q_l') are sensitive to atmospheric temperature changes and must be re-calculated at each timestep (Eq. 3.26).

3.6.5.2. Aerosol-induced stratospheric temperature changes

Figures 3.14-3.16 show the DJF and JJA seasonal-mean temperature anomalies for SMALL and LARGE mode (3.14) SO_4, (3.15) TiO_2, and (3.16) BC. These figures can be compared to Fig. 2 of Ferraro *et al.* (2011). Our work differs from Ferraro's as we have used a different aerosol layer representation, aerosol size distributions, and background climatology. Nevertheless, the stratospheric temperature changes in our work are qualitatively similar to those of Ferraro. In particular, we find a peak warming in the lower tropical stratosphere for all aerosols and both seasons. In the case of SO_4, this is primarily induced by terrestrial LW absorption and then minimal LW emission to space from the cold tropical tropopause layer (i.e. a LW flux convergence) [Ferraro *et al.*, 2011]. BC and TiO_2 both exhibit strong stratospheric warming in the summer hemisphere (Figs 3.15-3.16), which results from the absorption of solar radiation within the aerosol layer. BC exhibits a much greater maximum stratospheric warming (25.6 / 24.6 K for SMALL / LARGE) than either SO_4 (3.7 / 3.4 K) or TiO_2 (4.8 / 3.8 K), which is due to its greater SW absorption coefficient (Fig. 3.11). Note that the colour bar ranges in Figs 3.14-3.16 vary due to the significantly greater stratospheric heating in the BC scenario (Fig. 3.15) than in the SO_4 and TiO_2 scenarios (Figs 3.14 and 3.16).

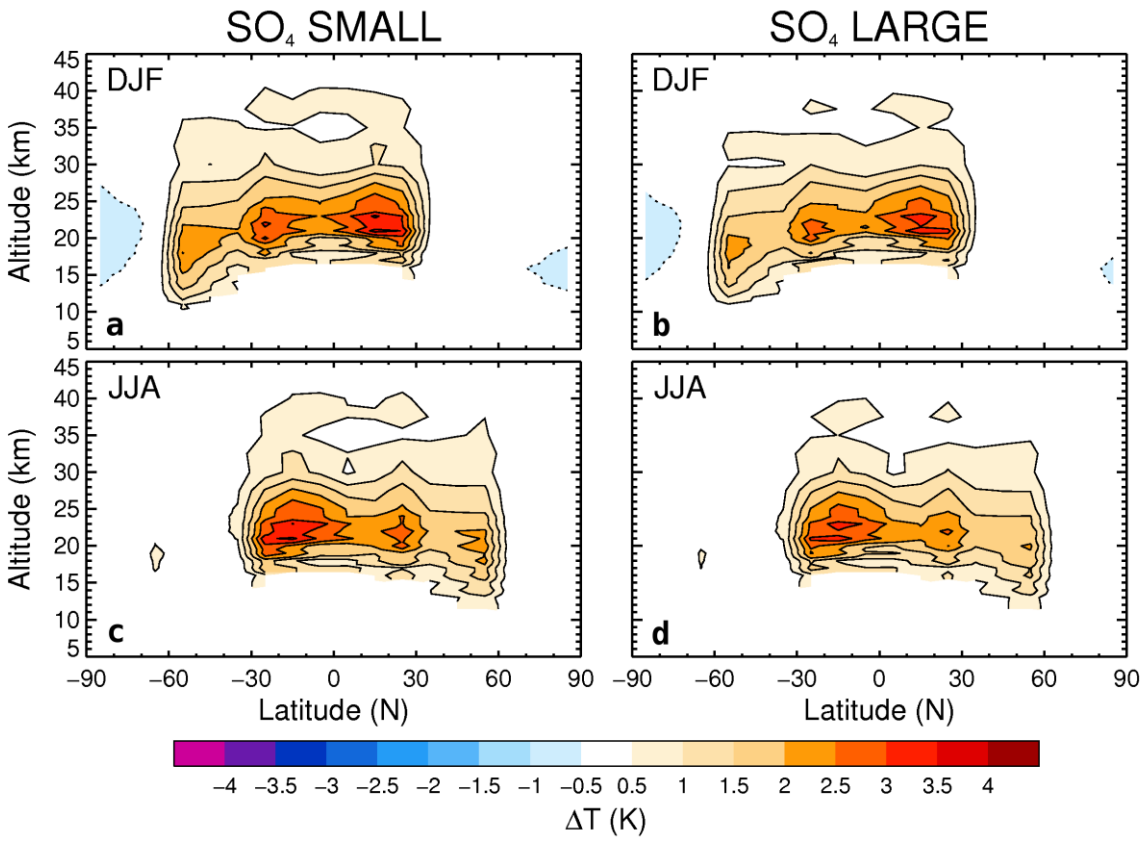

Figure 3.14 (a,b) December-February (DJF) and (c,d) June-August (JJA) stratospheric temperature adjustment for SMALL/LARGE mode SO_4

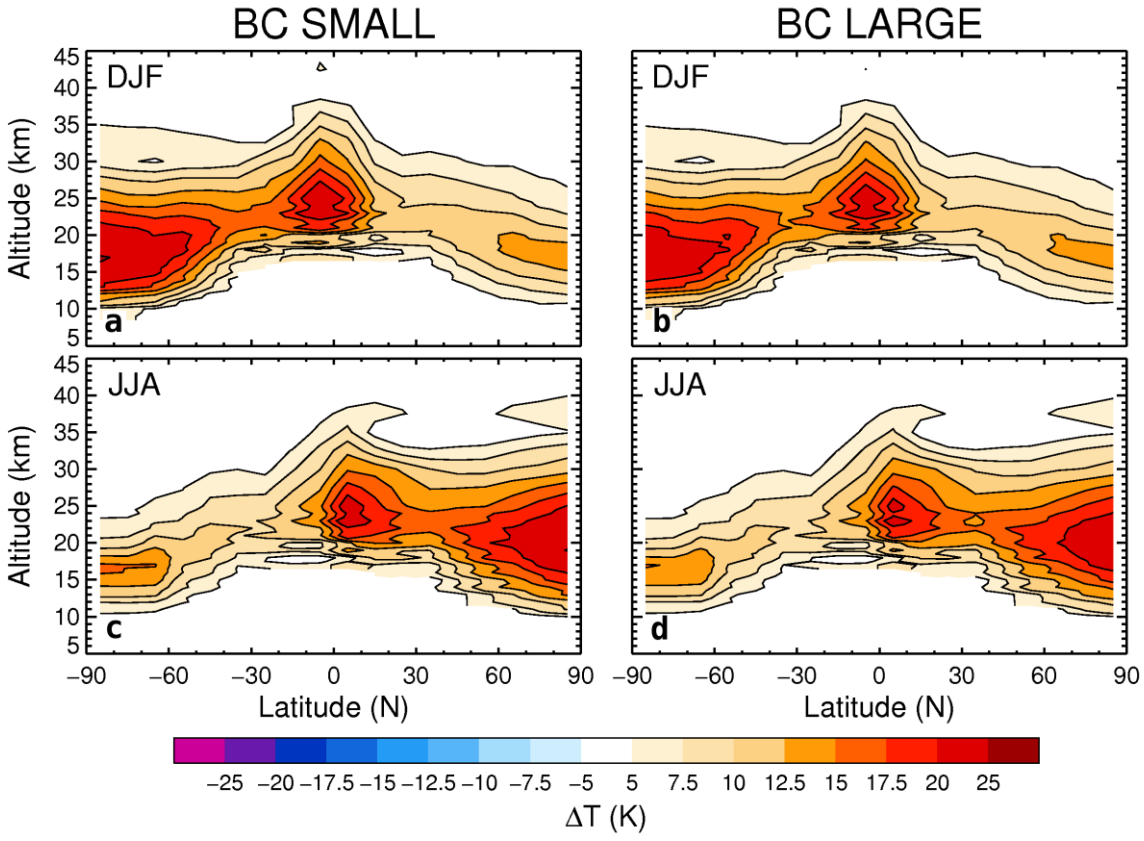

Figure 3.15 The same as Fig. 3.14 but for BC

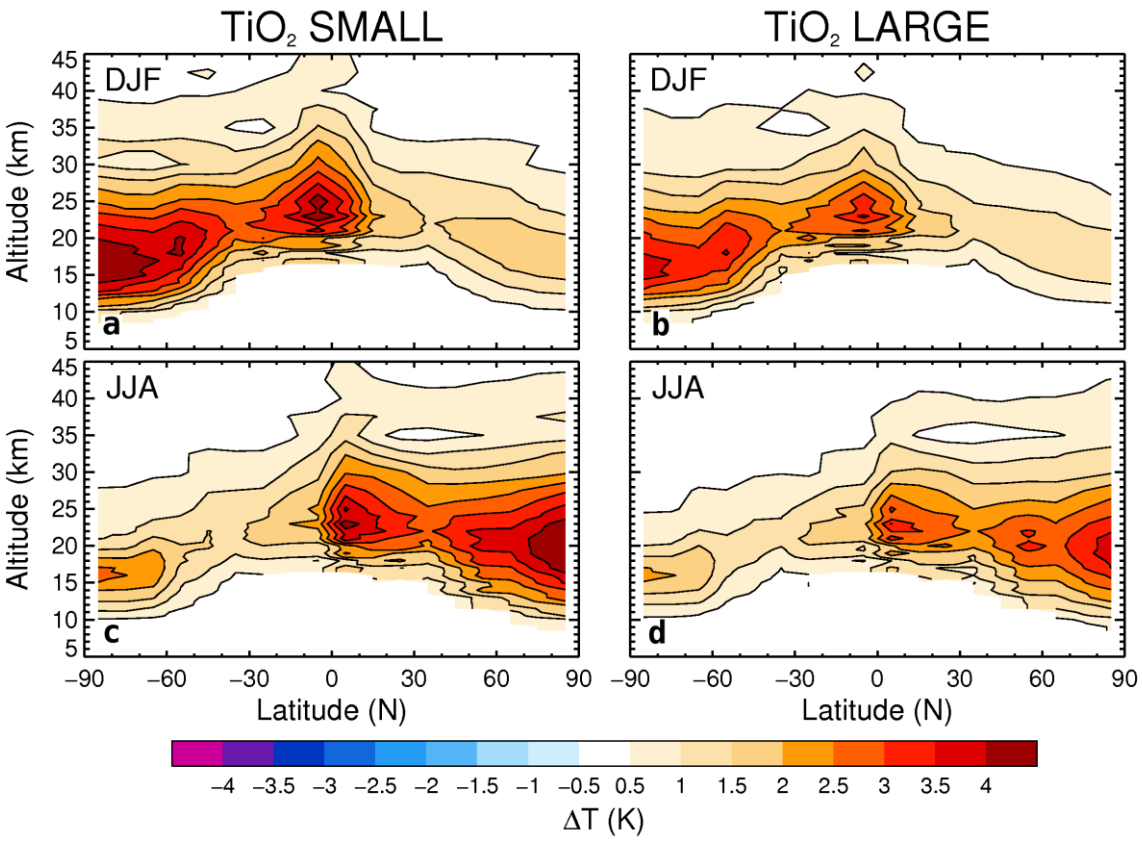

Figure 3.16 The same as Fig. 3.14 but for TiO_2

			TROP RF (Wm^{-2})			TOA RF (Wm^{-2})		
	Aerosol	Size	SW	LW	NET	SW	LW	NET
*IRF*ari	SO_4	SMALL	-4.3	+0.8	-3.5	-4.2	+1.4	-2.8
		LARGE	-4.2	+0.7	-3.5	-4.2	+1.3	-2.9
	BC	SMALL	-3.6	+0.1	-3.5	+3.2	+0.1	+3.3
		LARGE	-3.6	+0.1	-3.5	+2.9	+0.2	+3.1
	TiO_2	SMALL	-3.7	+0.2	-3.5	-2.6	+0.2	-2.4
		LARGE	-3.9	+0.4	-3.5	-3	+0.3	-2.6
*ARF*ari	SO_4	SMALL	-4.3	+1.1	-3.2	-4.2	+1	-3.2
		LARGE	-4.2	+0.9	-3.2	-4.2	+0.9	-3.2
	BC	SMALL	-3.6	+2.4	-1.2	+3.2	-4.3	-1.1
		LARGE	-3.6	+2.4	-1.3	+2.9	-4.1	-1.2
	TiO_2	SMALL	-3.7	+0.6	-3.1	-2.6	-0.5	-3.1
		LARGE	-3.9	+0.7	-3.2	-3	-0.2	-3.2

Table 3.5 Annual and global-mean radiative forcing at the tropopause (TROP) and TOA before and after accounting for stratospheric temperature adjustment (IRF and ARF respectively)

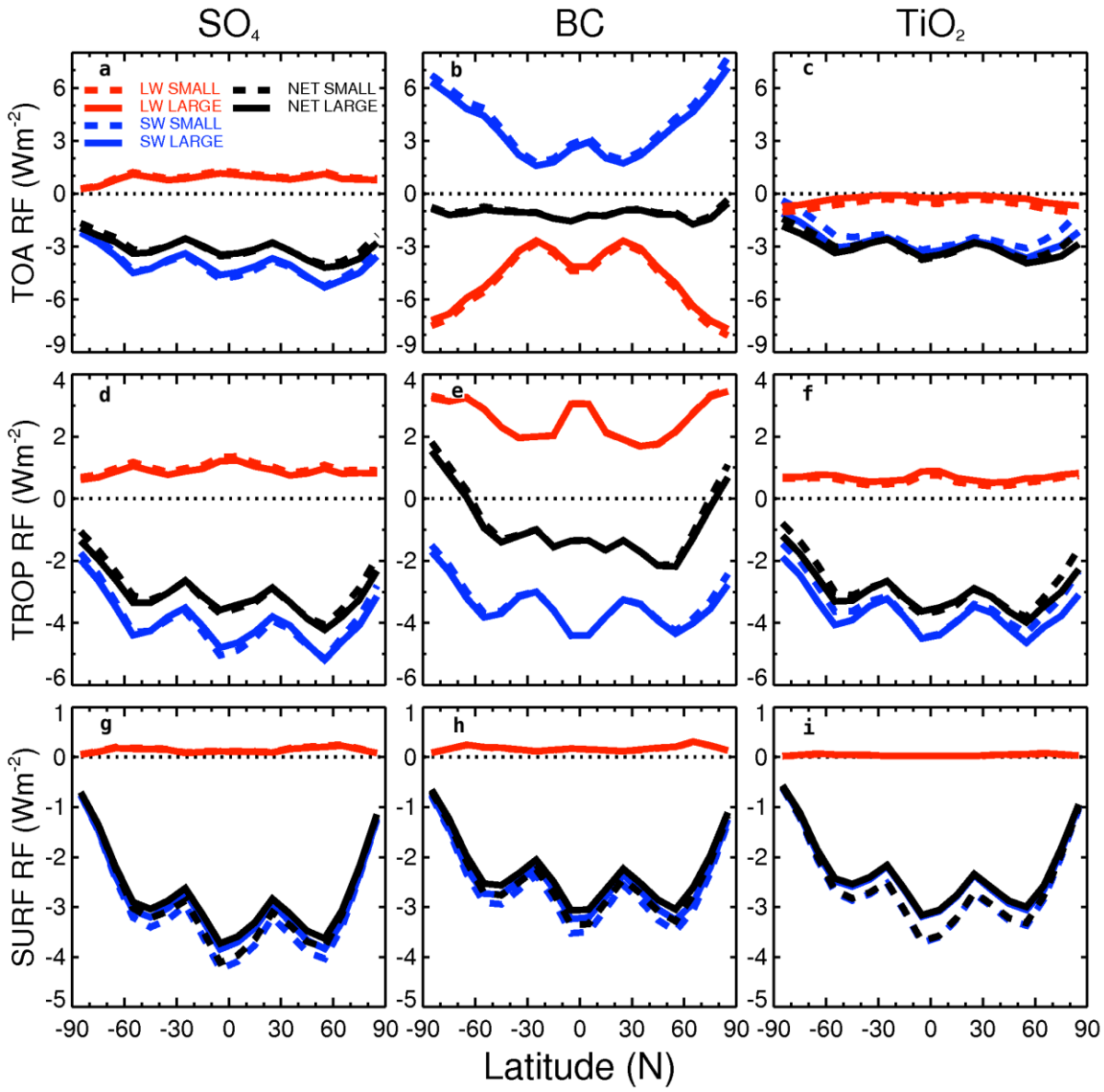

Figure 3.17 Annual-mean ARF at the TOA, tropopause (TROP) and surface (SURF) for SMALL/LARGE SO_4, BC, and TiO_2 after stratospheric temperature adjustment

---

Table 3.5 shows the annual and global-mean net radiation changes at the tropopause (TROP) and TOA, before and after accounting for stratospheric temperature adjustment (*IRF*ari and *ARF*ari respectively). It is clear that the effect of stratospheric temperature adjustment is to equilibrate the radiative fluxes at the tropopause (TROP) and the TOA. The resultant *ARF*ari for BC (-1.2 Wm^{-2}) is smaller than for SO_4 or TiO_2 (-3.2 Wm^{-2}) as the stratospheric temperature changes are much greater for BC (Fig. 3.14). Figure 3.17 shows the annual-mean net radiation changes at the TOA, TROP and SURF as a function of latitude when stratospheric temperature adjustment is accounted for. The stratospheric warming in the BC scenario results in a positive TROP *ARF*ari at high latitudes. For SO_4 and TiO_2, the

spatial distribution of *ARF*ari is similar to the *IRF*ari (Fig 3.12). It is clear that for a light-absorbing aerosol such as BC, the *IRF*ari is not a useful proxy for the *ARF*ari. Hansen *et al.* (1997) found a similar result for stratospheric O_3 changes. As the *ARF*ari is linearly proportional to GMST response it follows that, for an equivalent *IRF*ari, BC would produce the least surface temperature change of the aerosols assessed here.

3.7. Diffuse radiation at the surface

Vegetation requires sunlight for photosynthesis; therefore, the distribution of sunlight over Earth's surface is of vital importance for the regulation of life. Diffuse sunlight is able to penetrate deeper into plant canopies than direct sunlight; therefore plant canopies as a whole use diffuse sunlight more efficiently than direct sunlight [Gu *et al*., 2003]. However, the total intensity of sunlight at the surface is diminished by a scattering atmosphere. Therefore photosynthesis may either be enhanced by the presence of stratospheric aerosol due to elevated diffuse radiation, or diminished due to reduced sunlight intensity. Plant photosynthesis results in the conversion of atmospheric CO_2 into biomass, therefore the atmospheric CO_2 concentration is sensitive to changes in photosynthetic activity.

Atmospheric aerosols scatter radiation into the forward and backward directions, and thereby increase the diffuse/direct ratio at the surface [Kalidindi *et al.*, 2015]. Mercado *et al.* (2009) showed that the global land carbon sink was enhanced over the period 1960-1999 due to an enhanced diffuse fertilisation effect caused by aerosol and cloud changes. Gu *et al.* (2003) investigated the diffuse fertilisation effect for a single deciduous forest following the 1991 Mt. Pinatubo eruption, finding that the Pinatubo aerosol enhanced the clear-sky noon-time photosynthesis rates in 1992 by 23% relative to background levels. Kalidindi *et al.* (2015) used a GCM to assess the diffuse and direct sunlight changes at the surface for an SAI scenario with a 20 Tg[SO_4] stratospheric aerosol layer. They found global-mean diffuse and direct anomalies at the surface of +10 and -12 Wm^{-2} respectively; and that the diffuse fertilisation effect was completely offset by the reduced direct sunlight at the surface. Figure 3.18 shows the annual-mean direct, diffuse and net (direct+diffuse) solar radiation anomalies at the surface for our model, and the diffuse/direct ratio for each aerosol type/size and for the background atmosphere ('BGD'). The global-

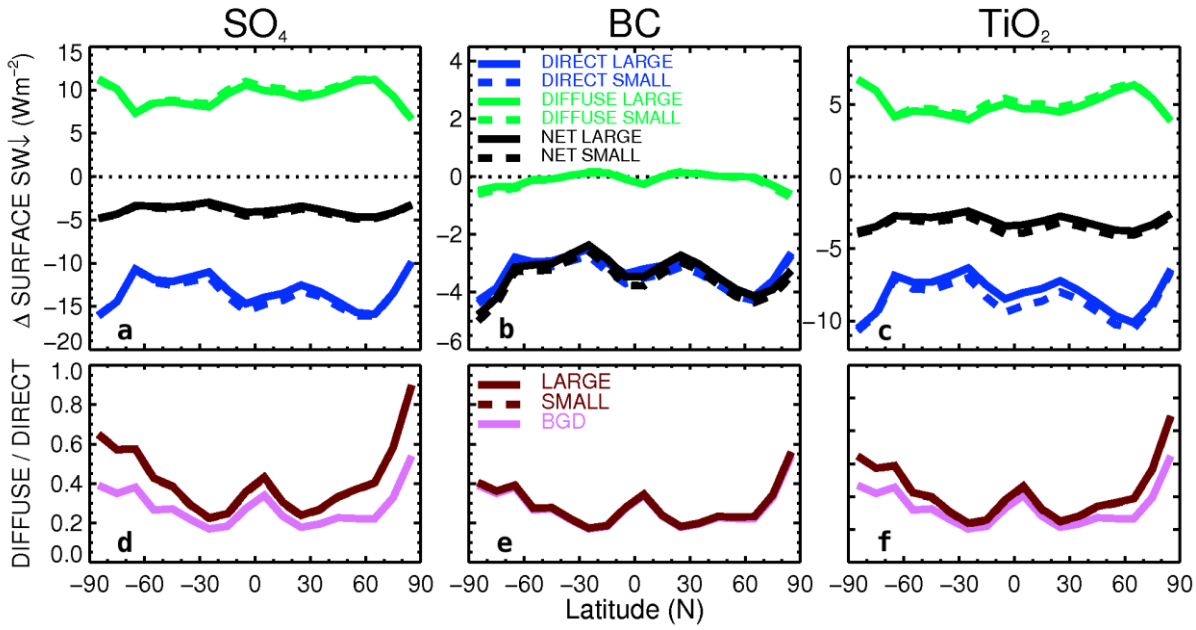

Figure 3.18 (a-c) Annual-mean changes to the downwelling direct and diffuse solar radiation at the surface as a function of latitude; (d-f) the ratio of diffuse to direct solar radiation

mean diffuse and direct radiation anomalies at the surface for the SO_4 LARGE scenario are +9.4 and -13 Wm^{-2} respectively, which are comparable to Kalidindi *et al.* (2015). SO_4 clearly produces the largest diffuse and direct changes at the surface (per equivalent *IRF*ari) of the aerosols considered here, and the SO_4 diffuse/direct ratio is most enhanced at high latitudes. The diffuse radiation anomaly at the surface for BC is minimal, which suggests that BC would not induce a strong diffuse fertilisation effect. Note that the model employed here does not allow for changes to cloud properties, which would also alter the distribution of sunlight at the surface. Also the model does not account for changes to humidity, ozone, and gas / aerosol concentrations; nor does the model account for spatiotemporal heterogeneity in the stratospheric aerosol size distribution, all of which would affect the diffuse/direct ratio.

3.8. Ultraviolet radiation at the surface

3.8.1. Background

The solar radiation spectrum can be divided into UV ($0.1 < \lambda < 0.4$ μm), visible ($0.4 < \lambda < 0.77$ μm) and infra-red light ($\lambda > 0.77$ μm). Approximately 8% of the total solar power at the top of the atmosphere is contained within the UV spectrum, 46% is in the visible spectrum and 46% is in the infra-red spectrum [Iqbal, 1983]. The UV spectrum can be further divided into UV-C ($0.1 < \lambda < 0.28$ μm), UV-B ($0.28 < \lambda <$

0.315 μm), and UV-A (0.315 < λ < 0.4 μm) sub-spectra. UV-C contains more energy per quanta than either UV-B or UV-A, but solar UV-C is almost completely absorbed by atmospheric O_3, O_2 and trace gases and thus very little reaches Earth's surface [Casale *et al.*, 2003]. In contrast, UV-B is only 'strongly' absorbed by O_3, while UV-A is weakly absorbed by O_3 and thus readily transverses a cloud-free atmosphere. The distribution of UV radiation at the surface depends on the solar zenith angle, O_3 column burden, cloudiness, aerosol concentrations, and surface reflectivity [Sabziparvar *et al.*, 1999]. The path-length through the stratospheric O_3 layer is at a minimum for directly overhead sun, hence surface UV is more abundant at low latitudes than at high latitudes [d'Orazio *et al.*, 2013].

Although most of the UV that reaches the surface is in the UV-A spectrum, UV-B is far more environmentally damaging. The environmental consequences of increases in surface UV-B are far-reaching and include: increases in skin cancer incidence; ocular (eye) damage, damage to vegetation by plant DNA mutations, damage to outdoor materials, and changes to tropospheric photochemistry (such as enhanced smog formation) [Madronich *et al.*, 1998]. Although enhanced UV-B exposure increases the risk of skin cancer, UV-B is also essential for vitamin D synthesis in humans. Vitamin D deficiency increases the risk of internal cancers, auto-immune diseases and psychiatric diseases [Williamson *et al.*, 2014]. Therefore, changes in UV-B at the surface may act to promote and/or damage human health. The specific risk of sun burn (erythema) or skin cancer depends on an individual's skin-pigment. Individuals with very fair skin (Fitzpatrick phototype I) are likely to experience erythema after receiving a UV-B dosage of 15-30 mJ/cm^2, whereas for dark-skinned individuals (Fitzpatrick phototype VI,) the minimium UV-B dosage that causes erythema is 90-150 mJ/cm^2 [d'Orazio *et al.*, 2013].

Historical surface UV-B trends were closely aligned to contemporaneous atmospheric O_3 changes [Madronich *et al.*, 1998]. In a seminal paper, Molina and Rowland (1974) proposed that anthropogenic emissions of CFC gases would result in unprecedented stratospheric O_3 depletion; which was later verified as manifest from Antarctic observations [Farman *et al.*, 1985]. Subsequent concern over the consequences of O_3 depletion (for instance, UV-B increases at the surface) resulted in the signing of the 'Montreal Protocol on Substances that Deplete the Ozone Layer' in 1987; an international treaty to phase out emissions of CFCs and other O_3

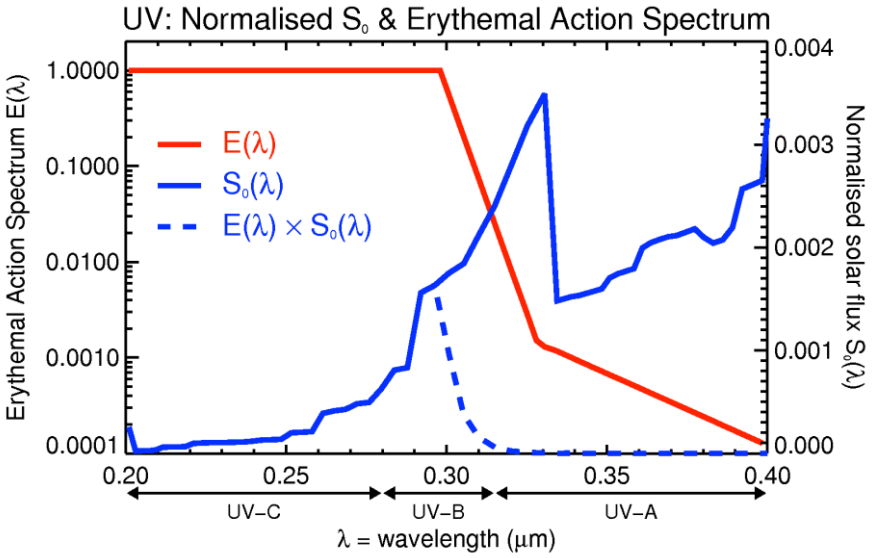

Figure 3.19 The normalised solar irradiance as a function of wavelength (blue) [Kuruckz., 1995], plotted with the erythemal action spectrum (red) [McKinlay and Diffey, 1987]

depleting substances (ODS). The Montreal Protocol has largely been successful at phasing out ODS emissions, and stratospheric O_3 levels are predicted to return to 1980s values between the years 2040 and 2060 [Eyring *et al.*, 2010]. There is strong evidence to suggest that UV-B irradiance at Earth's surface has increased in recent decades as a result of O_3 depletion [McKenzie *et al.*, 2007]. Consequently, surface UV-B irradiance is predicted to decrease over the next 50 years as stratospheric O_3 levels return to 1980s values [Williamson *et al.*, 2014].

Transient stratospheric O_3 depletion events have been observed in the aftermath of large volcanic eruptions. In 1992, following the 1991 Mt Pinatubo eruption, the global and annual-mean O_3 burden was 2% lower than any of the preceding 12 years, and column O_3 burden reductions of 50% were recorded in the Antarctic spring [Gleason *et al.*, 1993]. Ozone destruction is catalysed by heterogeneous chemistry on the surface of liquid SO_4 particles in the presence of free radicals such as reactive chlorine [Tilmes *et al.*, 2012]. Aerosols are removed from the stratosphere within 1-2 years; hence the catalysis of O_3 destruction by volcanic aerosol is a short-term phenomenon. The same would not be true for SAI, as the geoengineered stratospheric aerosol layer would have to be regularly replenished to avoid the termination effect [Jones *et al.*, 2013]. Tilmes *et al.* (2009) simulated SAI with a GCM, and found that a constant 4 Tg[SO_2] yr^{-1} tropical injection scenario would delay the recovery of the Antarctic O_3 layer by approximately 30 years, due to enhanced heterogeneous chemistry on the aerosol surfaces and changes to stratospheric

dynamics. Tilmes *et al*. (2012) expanded the work of Tilmes *et al.* (2009) by investigating UV changes at the surface using the same SAI scenario, and then comparing against a 'no-geoengineering' simulation. Stratospheric aerosols influence UV radiation directly via scattering and absorption, and indirectly via perturbing O_3 concentrations [Vogelmann *et al*., 1992]. These effects tend to be of the opposite sign, with UV increases at the surface from aerosol-induced O_3 depletion counteracted by increased UV shielding from the aerosol layer. Tilmes *et al*. (2012) found that in the tropics, the surface UV irradiance was reduced under SAI as a result of a dominant aerosol scattering effect, but at high-latitudes surface UV increased as a consequence of O_3 depletion.

3.8.2. Erythemal UV changes at the surface

3.8.2.1. Aerosol optical properties in the UV spectrum

In this section, we will evaluate the changes in UV radiation at the surface for the SO_4, BC, and TiO_2 aerosol layers described in Section 3.6. Specifically, we adopt the approach used in Tilmes *et al*. (2012) and calculate the noon-time erythemal UV radiation (UV_{ERY}) changes at the surface under SAI. UV_{ERY} is defined as the UV irradiance at the surface $S_0(\lambda)$ weighted by the erythemal action spectrum $E(\lambda)$ and integrated over λ (Fig. 3.19) [McKinlay and Diffey, 1987]. $E(\lambda)$ describes the relative risk of developing erythema in human skin as a function of wavelength. Skin exposed to UV-C or UV-B light will burn faster than skin exposed to UV-A, which is reflected in $E(\lambda)$. For this investigation, we use a SW spectral file with 220

Aerosol	Size	Absorption (m^2 kg^{-1})	Scattering (m^2 kg^{-1})	Asymmetry parameter g
SO_4	SMALL	4×10^{-4}	4890	0.71
	LARGE	4×10^{-4}	2610	0.67
BC	SMALL	5733	4765	0.71
	LARGE	2171	2173	0.87
TiO_2	SMALL	1018	1945	0.45
	LARGE	360	711	0.68

Table 3.6 Aerosol optical properties weighted by solar irradiance [Kuruckz, 1995] and integrated over the UV spectrum

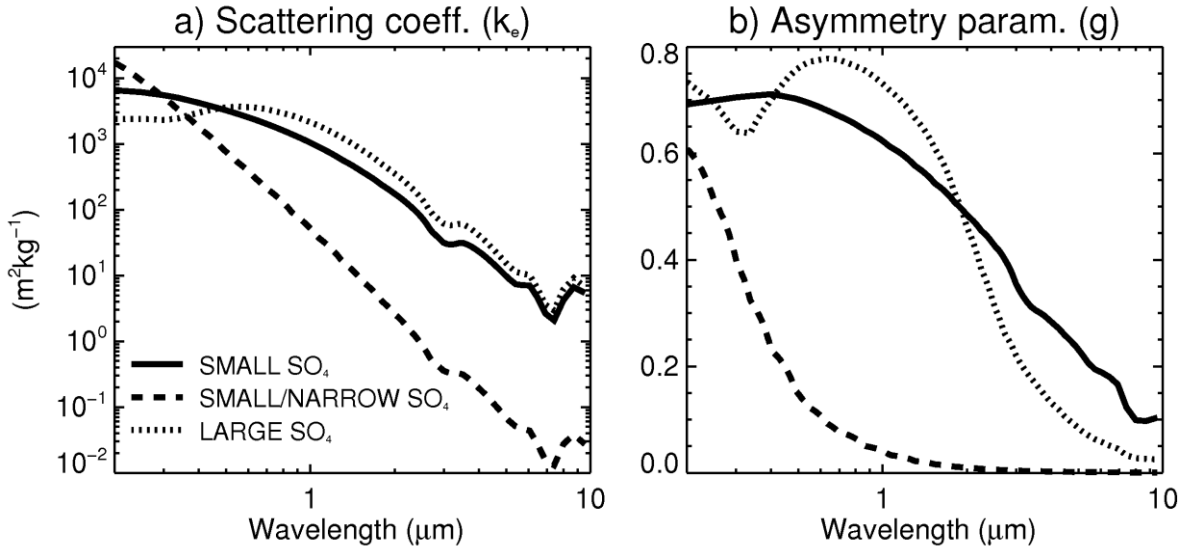

Figure 3.20 (a) scattering efficiency and (b) asymmetry parameter in the SW spectrum for SMALL (r_m=0.05,σ=2.03), SMALL/NARROW (r_m=0.05,σ=1.25) and LARGE (r_m=0.376,σ=1.25) mode SO_4

wavebands, rather than the 6 wavebands used in previous sections. This spectral file includes 66 wavebands in the UV spectrum (0.2 < λ < 0.4 μm). Table 3.6 shows the aerosol optical properties averaged over the UV spectrum.

From Table 3.6, although SMALL SO_4 exhibits a greater UV scattering coefficient than LARGE SO_4, it also scatters more in the forward direction (g = 0.71 compared to g = 0.67). This is a surprising result as smaller aerosols should scatter more in the backward direction than larger aerosols (Section 2.3.5), which warrants further investigation. Figure 3.20 shows the scattering efficiency (k_e) and asymmetry parameter (g) for SO_4 for the SMALL and LARGE size distributions and for a narrow SMALL distribution (r_m = 0.05 μm and σ = 1.25). For the SMALL/NARROW distribution, k_e and g decrease monotonically with wavelength. In contrast, for the SMALL distribution, g increases slightly over the UV spectrum and actually exceeds g for the LARGE distribution between 0.25 μm and 0.4 μm. This suggests that the SMALL distribution's anomalously large g in the UV spectrum is due to the large spread of the SMALL distribution (σ = 2.03). Returning to Table 3.6, the SMALL-mode BC and TiO_2 particles scatter more into the backward direction than their respective LARGE-mode particles. BC and TiO_2 also absorb strongly in the UV spectrum.

The SO_4 LARGE scenario uses a similar SO_4 mass burden (~20 Tg) to that used by Tilmes *et al.* (2012). As we are also using the same aerosol size distribution, we feel

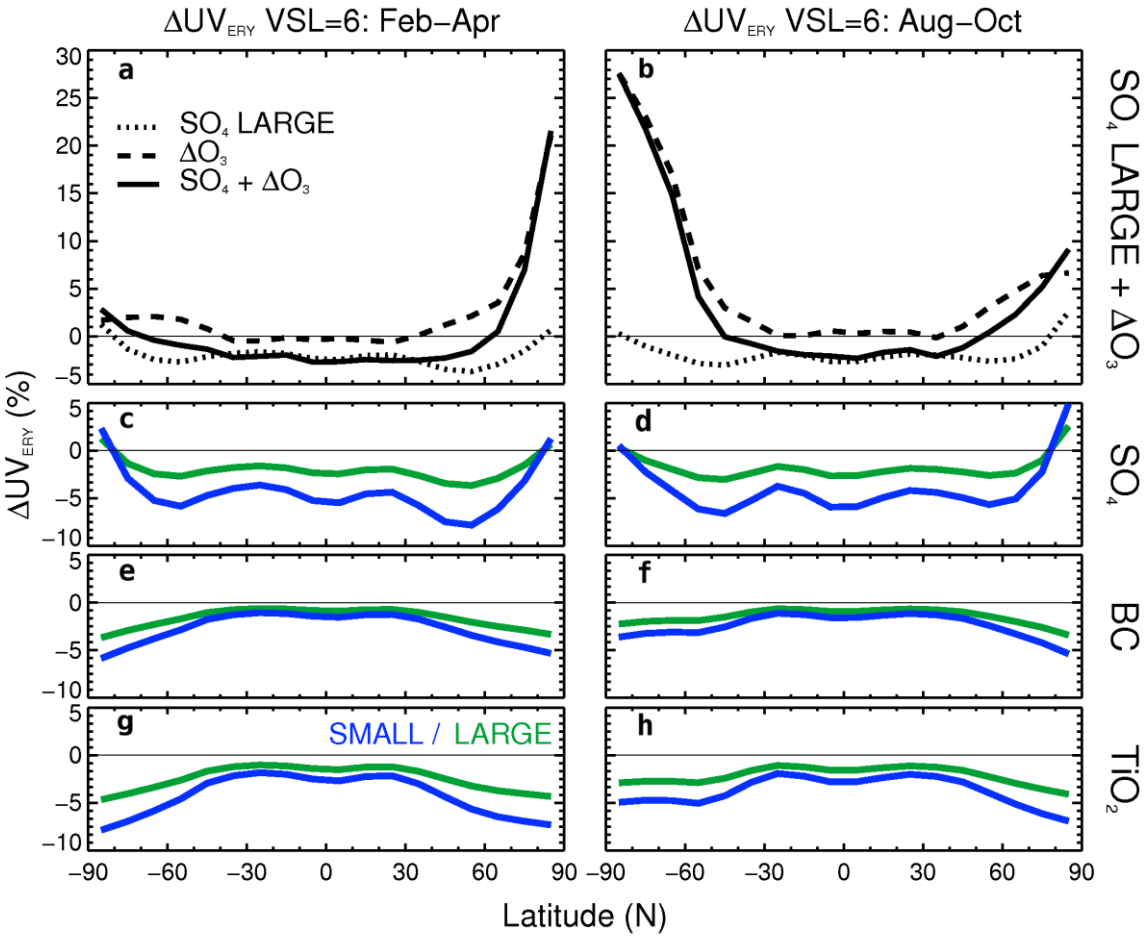

Figure 3.21 UV_{ERY} changes (%) at the surface for the (a,c,e,g) Feb-Apr and (b,d,f,h) Aug-Oct seasons. (a,b) UV_{ERY} changes due to O_3 depletion in the VSL=6 scenario of Tilmes et al. (2012), (c-h) UV_{ERY} changes due to aerosols alone

justified in presenting here the UV_{ERY} changes at the surface due to the aerosol-induced O_3 depletion (ΔO_3) as calculated by Tilmes *et al* in their VSL=6 scenario. 'VSL=6' refers to the fact that Tilmes *et al.* tested the sensitivity of SAI-induced ΔO_3 for various levels of very-short lived (VSL) halogen concentrations. The 'VSL=6' scenario specified a uniform stratospheric increase of reactive bromine (Br_y) by 6 parts per trillion (ppt), and represented a mid-range estimate of stratospheric VSL halogen concentrations.

3.8.2.2. Aerosol-induced surface UV changes

Figure 3.21 shows the noontime surface UV_{ERY} changes (%) as a function of latitude for the SMALL/LARGE SAI scenarios for the (left) February-April and (right) August-October seasons. Figures 3.21a,b show the UV_{ERY} changes for SO_4 LARGE and for the associated ΔO_3-induced UV_{ERY} changes in the VSL=6 scenario of Tilmes *et al.* (2012). Fig. 3.21 can be compared to Fig. 4 of Tilmes *et al.* (2012). For each of the

aerosols considered here, the UV_{ERY} changes are greater for the SMALL mode than the LARGE mode, which suggests that smaller aerosols would be more efficient at blocking UV radiation than larger aerosols. However, smaller aerosols also have a greater surface area concentration than larger aerosols, which results in more sites for heterogeneous chemistry and concomitant O_3 depletion [Pope *et al.,* 2012]. Therefore, the UV_{ERY} changes due to ΔO_3 for the SO_4 SMALL scenario would likely be greater than the UV_{ERY} changes plotted in Figs 3.21a,b. The peak UV_{ERY} reductions in the SO_4 scenarios occur at low latitudes (Fig. 3.21c,d), with negligible UV_{ERY} changes at high latitudes. In contrast, the UV-absorbing aerosols BC and TiO_2 exhibit peak UV_{ERY} reductions at high latitudes (Fig. 3.21e-h). For perspective, observed surface UV_{ERY} irradiances are greater in the tropics (~250 mWm^{-2}) than at high latitudes (<50 mWm^{-2}). As vitamin D deficiency is a particular problem at high latitudes [e.g. Casswall, 2013], it is ambiguous whether surface UV_{ERY} increases at high latitudes (such as seen in the ΔO_3 scenario in Fig. 3.21) would be harmful or beneficial to humans [Nowack *et al.*, 2016].

In order to perform a thorough assessment of the UV_{ERY} impacts of SAI, additional work would be needed to assess the ΔO_3 for BC and TiO_2 injections [Tang *et al.*, 2014]. Ozone changes may directly occur on the surface of aerosol particles, or may be instigated indirectly by changes to the ambient stratosphere [Kravitz *et al.*, 2012]. Kravitz *et al.* (2012) found that a 1 Tg yr^{-1} stratospheric injection of small-radius BC particles caused global-mean O_3 depletion of 50%, which was an indirect consequence of stratospheric warming. Stratospheric warming increases the moisture content of air entering the stratosphere, which results in enhanced OH-catalysed O_3 depletion. Research into the heterogeneous chemistry on the surface of TiO_2 particles has already started with Tang *et al.* (2014).

3.9. Summary

At the start of this chapter, we discussed the radiative transfer equation for a plane-parallel atmosphere and its use within the SOCRATES radiative transfer code. We then created a zonal-mean model atmosphere which included explicit representation of atmospheric gases, seasonal cloud distributions and surface reflectivity as a function of latitude. Using the model atmosphere, we have evaluated the radiative effects of stratospheric aerosol layers composed of SO_4, TiO_2, and BC. For each

aerosol, and for small and large size distributions, we have determined the global aerosol burden required to induce an annual-mean instantaneous radiative forcing at the tropopause of -3.5 Wm^{-2}. Using the resultant aerosol layers, we have investigated the effects of SAI on the stratospheric temperature profile, diffuse radiation at the surface and UV radiation at the surface.

An interesting finding of this chapter is that the adjusted radiative forcing for the SW-absorbing BC is a factor of 3 smaller than the instantaneous radiative forcing. This is because the SW absorption within the BC layer results in a lower-stratospheric warming and a thermal heating of the tropopause. This effect is less apparent for SO_4 and TiO_2, for which the instantaneous and adjusted radiative forcings are similar (-3.5 and -3.2 Wm^{-2} respectively). Another finding of this work is that the RF perturbations are more sensitive to changes in aerosol composition than size. For instance, the stratospheric temperature changes (Figs 3.14-3.16) are markedly different for the aerosol species, but differ little between the two size modes. However, due to the limited scope of the sensitivity tests performed here (i.e. only two size distributions are assessed) and due to the simplicity of the model atmosphere (Section 3.5) which doesn't account for aerosol-cloud interactions, further research would be needed to robustly determine the sensitivity of RF to aerosol size. It may be that the SMALL and LARGE distributions selected here are too similar to each other to gage the true sensitivity of radiative flux perturbation to aerosol size. Indeed, in Fig. 3.20, we have shown that the SMALL SO_4 distribution exhibits significantly different optical properties to a SMALL *and* NARROW SO_4 distribution. As the aerosol sizes that would eventuate from SAI are unknown, and would be dependent on the injection scenario and would vary spatiotemporally [Heckendorn *et al*., 2009], we feel justified in using the SMALL/ LARGE distributions in this work. Two important aerosol effects have not been accounted for in this chapter: the impact on clouds (and associated radiation) changes, and the hygroscopic growth of aerosols. We shall consider both effects implicitly in Chapter 4.

Chapter 4 Climatic impacts of stratospheric geoengineering with sulphate, black carbon and titania injection*

4.1. Introduction

Geoengineering strategies, or large-scale climate interventions that aim to reduce global warming, include strategies to sequester atmospheric CO_2 (CDR), and strategies to reduce solar irradiance at Earth's surface (SRM) [Shepherd, 2009]. CDR and SRM were briefly discussed in Chapter 1. SAI, an SRM scheme which has received significant attention, involves the enhancement of the stratospheric aerosol layer in order to reflect more sunlight back to space. This scheme mimics large volcanic eruptions such as Mt Pinatubo in 1991, which injected approximately 15 to 20 Tg of SO_2 into the tropical stratosphere and induced a globally averaged surface cooling of around 0.3 K for the following two years [Stenchikov *et al.*, 2002]. Further details of the Pinatubo eruption will be given in Chapter 5.

SO_4 aerosols have featured predominantly in SAI research because of the volcanic analogue [e.g. Kravitz *et al.*, 2011]. GCM simulations suggest that, while sufficient SO_4 injection could effectively reduce global-mean temperature, possible side effects include changes to regional temperature and precipitation [Bala *et al.*, 2008; Tilmes *et al.*, 2013], O_3 [e.g. Tilmes *et al.*, 2009; Pitari *et al.*, 2014], stratospheric dynamics [Aquila *et al.*, 2014] and sea-ice extent [Berdahl *et al.*, 2014]. SAI would likely produce a tropical overcooling and high-latitude residual warming if the global-mean temperature were stabilised, due to an imperfect mitigation of the TOA radiative fluxes [Kravitz *et al.*, 2013]. Precipitation changes could result from changes to the moist static stability of the atmosphere and a concomitant weakening of the hydrological cycle [Bala *et al.*, 2008], and the regional precipitation changes under GeoMIP simulations have been shown to be reasonably consistent across a range of climate models [Tilmes *et al.*, 2013]. Stratospheric O_3 concentrations could be

*This chapter is based on the following publication, a copy of which is provided in Appendix 1.

Jones, A. C., J. M. Haywood, and A. Jones (2016a), Climatic impacts of stratospheric geoengineering with sulphate, black carbon and titania injection, *Atmos. Chem. Phys.*, 16, 2843-2862, doi:10.5194/acp-16-2843-2016

depleted as a result of enhanced heterogeneous chemistry on the surface of SO_4 aerosols or as a result of changes to the stratospheric dynamics and chemistry [e.g. Tilmes *et al.*, 2009]. Stratospheric dynamical changes could occur as the result of tropical heating in the SO_4 layer and by changes to wave propagation from the troposphere [e.g. Aquila *et al.*, 2014].

In order to ameliorate the known side effects of SO_4 injection, some authors have proposed alternative aerosols to SO_4 [e.g. Teller *et al.*, 1997]. Crutzen (2006) suggested the possible injection of BC, which would mimic hypothetical nuclear winter scenarios. One advantage of BC over SO_4 is that less mass would be needed for an equivalent radiative forcing [Crutzen, 2006]. BC particles efficiently absorb solar radiation, unlike SO_4 which primarily reflects solar radiation [Ferraro *et al.*, 2011]. Alternatively, minerals such as TiO_2, silica (SiO_2) and Al_2O_3, which have a high refractive index at wavelengths of peak solar radiative flux (~550 nm), have also been suggested [Pope *et al.*, 2012]. Although the use of alternative aerosols is not a new suggestion [e.g. Teller *et al.*, 1997], comparatively little research has been conducted on their potential utility. Kravitz *et al.* (2012) simulated a constant BC injection scenario of 1 Tg yr^{-1} in the tropics for small radius (0.03 μm) and large radius (0.15 μm) aerosols. They found that the small particle BC aerosol scenario produced a global-mean surface cooling of 9.45 K, but also induced stratospheric warming of >60 K and global O_3 loss of ~50 %. The large particle BC aerosol scenario had a negligible climatic impact. Using an FDH code, Ferraro *et al.* (2011) compared the stratospheric heating of SO_4, TiO_2, and BC layers for an equivalent instantaneous radiative forcing. Their results showed a tropical stratospheric warming signal for all the aerosols, though much greater in the case of BC. To date, no work has used a comprehensive fully coupled atmosphere-ocean GCM to directly compare the possible climatic impacts of SAI with alternative aerosols to SO_4, which is the motivation for the research documented in this chapter.

In this chapter, we show the results from GCM simulations of the stratospheric injection of SO_4, TiO_2 and BC against a baseline RCP8.5 scenario. TiO_2 is selected to represent an efficient light-scattering aerosol and BC is selected as a light-absorbing aerosol. Further details of the physical and optical properties of BC and TiO_2 are given in Chapter 2. RCP8.5, which is the high-end carbon-intensive CMIP5 scenario, is selected to give a significant greenhouse effect against which to

employ geoengineering, in order to distinguish the climatic impacts specific to each aerosol. Observations have shown that the current global GHG emissions exceed the emissions inherent in RCP8.5 [Peters *et al.*, 2013]; therefore this work could be considered as geoengineering against a business-as-usual scenario. Additionally, the next generation of GeoMIP simulations (GeoMIP6) will utilise a carbon-intensive scenario [Kravitz *et al.*, 2015], hence the research described in this chapter will provide a useful supplement to those results. We chose to inject aerosol at a sufficient rate to counterbalance the TOA annual and global-mean radiative flux imbalance caused by increasing atmospheric GHGs. Our simulation design is similar to GeoMIP's G3 scenario, which instead used the RCP4.5 concentrations scenario as its baseline and injected SO_2 at a sufficient rate to counterbalance GHG radiative forcing [Kravitz *et al.*, 2011]. In Section 4.2, we describe the specifications of the GCM employed, including the aerosol optical properties utilised. In Section 4.3, we describe the geoengineering strategy incorporated. We then analyse the climate changes in the 2090s with respect to a simulated historical period in Section 4.4, and discuss impacts on a wide range of meteorological parameters in Section 4.5.

4.2. Model

4.2.1. The HadGEM2-CCS model

For this investigation, we use the Hadley Centre Global Environment Model version 2-Carbon Cycle Stratosphere (HadGEM2-CCS) model in a fully coupled atmosphere-ocean mode. HadGEM2-CCS is the high-top configuration of the HadGEM2 family of models, and includes a well-resolved stratosphere that is capable of internally generating a realistic QBO [Martin *et al.*, 2011]. The atmosphere component comprises 60 vertical levels extending to 84 km and a horizontal resolution of 1.25^o x 1.875^o latitude by longitude respectively. The 40-level ocean component has a horizontal resolution of 1^o by 1^o from the poles to 30^o N/S, with the latitudinal resolution then increasing smoothly to 0.33^o at the equator [Martin *et al.*, 2011]. For this investigation, GHG concentrations, stratospheric O_3, anthropogenic aerosols and aerosol precursor gases are prescribed following the CMIP5 protocol [Taylor *et al.*, 2012], with historical data from 1860-2005 and RCP8.5 concentrations from 2005-2100. HadGEM2-CCS contains the aerosol module: Coupled Large-scale Aerosol Simulator for Studies in Climate (CLASSIC). The module's sulphur cycle is

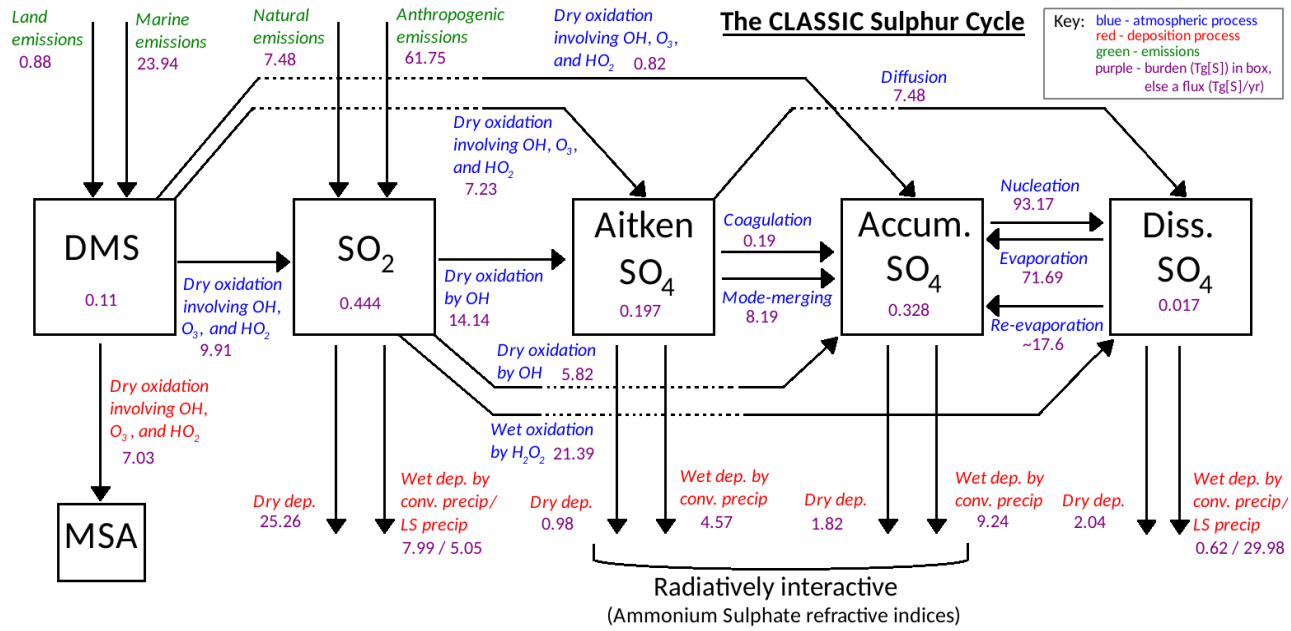

Figure 4.1 Schematic of the CLASSIC sulphur cycle. Processes that transfer mass between sulphur species are in blue, sources are in green, and sinks are in red. Purple numbers next to arrows denote approximate annual-mean fluxes (Tg[S]/yr) and in boxes denote global burdens (Tg[S]) Adapted from Fig. 5 in Bellouin *et al*. (2007)

described in detail in Bellouin *et al.* (2011) and is schematically shown in Fig. 4.1. Briefly, it includes the oxidation of SO_2 and DMS to form SO_4 aerosol in aqueous and gas phase reactions. SO_4 is represented by ammonium sulphate refractive indices (typical of tropospheric sulphate – Section 2.2.4.2), and is partitioned into Aitken, accumulation and dissolved modes, with hygroscopic growth in the accumulation mode following d'Almeida *et al.* (1991). Mass transfer from the Aitken to accumulation mode occurs through coagulation (Aitken-accumulation collisions) and mode-merging (Aitken-Aitken collisions). The Aitken and accumulation modes are represented by lognormal size-distributions with a prescribed dry-mode median radius (r_m) and geometric standard deviation (σ). Aerosol is removed from the atmosphere via wet and dry deposition (important in the troposphere) and sedimentation (important in the stratosphere) with sedimentation rates calculated by applying Stokes' Law. SO_2 and DMS are primarily emitted into the first model layer (i.e. at the surface), except for anthropogenic "chimney stack" SO_2 emissions which are emitted into the fifth model layer (~0.5 km altitude). Atmospheric concentrations of chemical oxidants (e.g. OH) are prescribed for the duration of the simulations [Martin *et al.*, 2011].

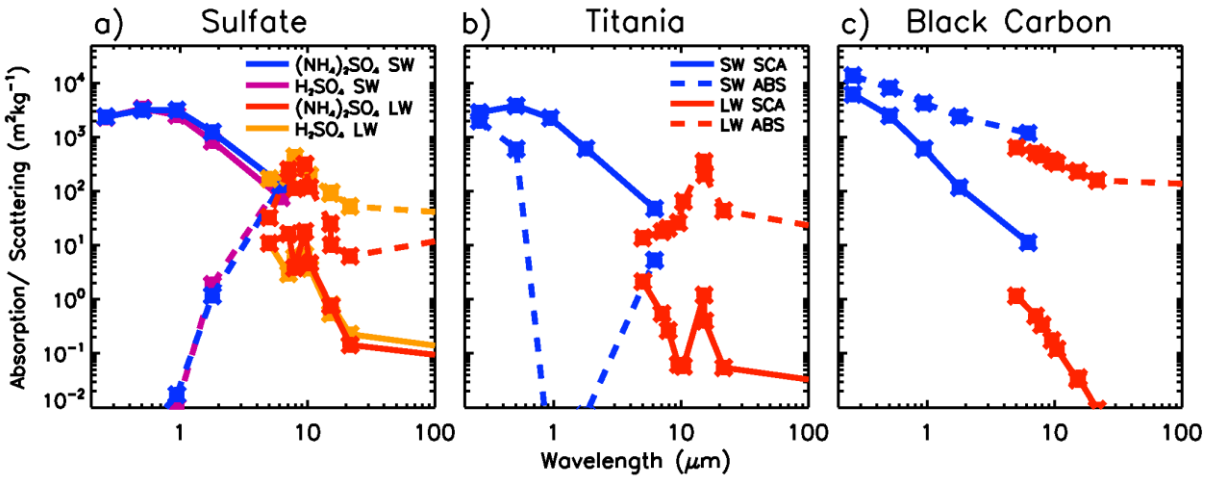

Figure 4.2 Optical properties as a function of wavelength for (a) accumulation mode SO_4 as ammonium sulphate ($(NH_4)_2SO_4$ - blue/red – used in the simulations) and sulphuric acid (H_2SO_4 - purple/orange), (b) TiO_2, (c) BC. Points are plotted at the middle of each spectral waveband, as detailed in Bellouin et al. (2007)

4.2.2. Stratospheric aerosol microphysical and optical properties

In the geoengineering simulations, we inject SO_2 into the model stratosphere and allow CLASSIC to oxidise the SO_2 to form SO_4, which is then able to interact with radiation (Fig. 4.1). For this investigation we have modified the size distribution of accumulation-mode SO_4 in CLASSIC in order to better represent the optical and physical properties exhibited by larger aerosols in high stratospheric aerosol burdens. CLASSIC's default size distribution for accumulation-mode SO_4 assumes a dry mode median radius of r_m = 0.095 μm and a geometric standard deviation of σ = 1.4. In this study, we instead represent accumulation-mode SO_4 using the *volc2* size distribution from Rasch *et al.* (2008a) with r_m = 0.376 μm and σ = 1.25, and apply this change ubiquitously (i.e in the troposphere and stratosphere). Although stratospheric SO_4 predominantly exists as a sulphuric acid solution (see Section 2.2.4.3), for consistency with the control simulations we represent SO_4 with ammonium sulphate refractive indices in the geoengineering runs. This contrasts with our use of sulphuric acid refractive indices in Chapters 2 and 3. Fig 4.2a shows the specific absorption and scattering coefficients in the SW and LW spectra for dry-mode ammonium sulphate (blue/red) and for sulphuric acid (purple/orange), using the *volc2* size distribution. The SW coefficients are very similar for the two species. In the LW spectrum, the dry-mode ammonium sulphate absorbs less radiation for wavelengths > 10 μm, for instance, having an absorption coefficient of 10 m^2kg^{-1} at λ = 15 μm compared to 96 m^2kg^{-1} for sulphuric acid. However, at a relative humidity of

50 %, ammonium sulphate's absorption coefficient increases to 104 m^2kg^{-1} due to hygroscopic growth, which is more consistent with sulphuric acid.

CLASSIC includes a tropospheric BC scheme with fresh, aged and in-cloud modes [Bellouin *et al.*, 2011]. We introduce an additional non-hygroscopic stratospheric BC component and prescribe a uni-modal lognormal size distribution with r_m = 0.0118 μm and σ = 2.0, which is taken from tropospheric BC observations [Deepak and Gerber, 1983]. We prescribe a density for BC of 1000 kg m^{-3} and take refractive indices from a World Meteorological Organisation report [Deepak and Gerber, 1983]. For stratospheric TiO_2, we assume the non-hygroscopic uni-modal lognormal size distribution of Pope *et al.* (2012) with r_m = 0.045 μm and σ = 1.8. This size distribution was selected to give the TiO_2 aerosol a high scattering efficiency, as shown by Pope *et al.* (2012). We prescribe a density for TiO_2 of 4230 kg m^{-3} [Pope *et al.*, 2012], and for the refractive indices we follow Ferraro *et al.* (2011) and use the average of the extraordinary and ordinary values from Ribarsky (1985).

The specific absorption (k_a) and scattering (k_s) coefficients for SO_4 (accumulation/dry-mode), TiO_2 and BC are plotted as a function of wavelength in Fig. 4.2. For SO_4, the specific extinction coefficient (k_e) at 500nm of 3200 m^2kg^{-1} and single scattering albedo (ω_0) of 1 reflects the non-absorbing properties of SO_4. Although TiO_2's 500nm scattering efficiency (k_s = 3850 m^2kg^{-1}) is greater than SO_4's in this instance, TiO_2 additionally absorbs SW radiation (k_a = 2000 m^2kg^{-1} at 250 nm, and k_a = 600 m^2kg^{-1} at 500 nm) which can be explained by the band-theory of solids [Yang *et al.*, 2003]. Thus TiO_2 is partially absorbing at solar wavelengths. Our modelled BC efficiently absorbs SW radiation (k_a = 8300 m^2kg^{-1} at 500 nm) but also produces a non-negligible SW scattering effect (k_s = 2500 m^2kg^{-1} at 500 nm) which is comparable in magnitude to the equivalent scattering efficiency of both TiO_2 and SO_4. Therefore, to describe TiO_2 as an efficient light-scatterer and/or BC as an efficient light-absorber is an over-simplification.

Our choice of particle size and density will impact the aerosol's gravitational sedimentation rate and therefore its atmospheric residence time (the sedimentation rate is also a property of the local atmospheric conditions) [Rasch *et al.*, 2008a]. To respective gravitational sedimentation rates by using the method of Pruppacher and Klett (1979) (which utilises Stoke's law) and incorporating temperature and pressure

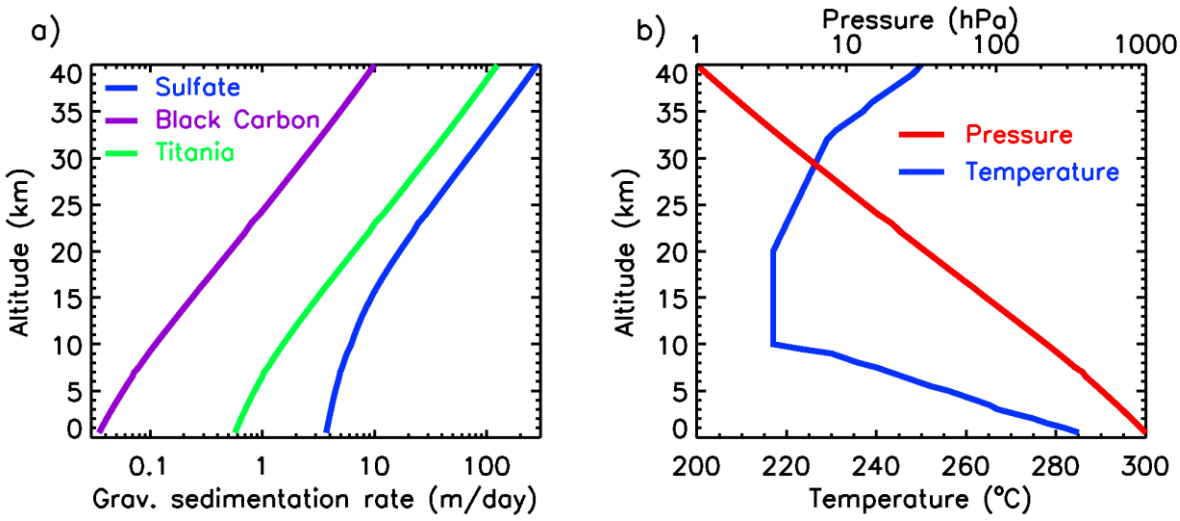

Figure 4.3 (a) Gravitational sedimentation rates for SO_4, TiO_2 and BC, calculated using densities of 1769, 4230 and 1000 kg/m^3 respectively, the mass-weighted radii of the specified log-normal distributions and the method of Pruppacher and Klett (1979) (b) We use the International Standard Atmosphere [ICAO, 1993] for temperature and pressure as a function of altitude

values from the International Standard Atmosphere [ICAO, 1993] (Fig. 4.3). The method for determining the gravitational sedimentation rate as a function of temperature (T in °C), pressure (P), and aerosol radius (r_m) and density (ρ) is as follows. Firstly, the dynamic viscosity of air (η_a) as a function of the air temperature is calculated using the implicit relationship given in Eq. 4.1, which is derived from Smithsonian tables [p. 323, Pruppacher and Klett, 1979].

$$\begin{aligned} \eta_a &= (1.718 + 4.9 \cdot 10^{-3}\ T) \cdot 10^{-5} && | \ T \geq 0 \\ &= (1.718 + 4.9 \cdot 10^{-3}\ T - 1.2 \cdot 10^{-5}\ T^2) \cdot 10^{-5} && | \ T < 0 \end{aligned} \tag{4.1}$$

The mean free path of air particles λ (the average distance travelled by a moving air particle between successive impacts) is then determined as a function of the temperature and pressure, and reference temperature T_0 = 20 °C and reference pressure P_0 = 101,325 Pa (Eq. 4.2).

$$\lambda = \frac{6.6 \cdot 10^{-8}\ P_0\ T}{P\ T_0} \tag{4.2}$$

Finally, the Cunningham correction factor (C_f) and the sedimentation velocity (v) are calculated using Eq. 4.3 - 4.5 [p. 362, Pruppacher and Klett, 1979].

$$\alpha_c = 1.257 + 0.4 \cdot e^{\left(-r_m \cdot \frac{1.1}{\lambda}\right)} \tag{4.3}$$

$$C_f = 1 + \frac{\alpha_c \times \lambda}{r_m} \quad (4.4)$$

$$v = \frac{2\, C_f\, {r_m}^2\, g\, \rho_s}{9\, \eta_a} \quad (4.5)$$

Where g = 9.8 m s^{-1} is the acceleration due to gravity. We find that the average sedimentation rates between 18-26 km altitude for our prescribed SO_4, TiO_2, and BC are 23, 9.5 and 0.75 m day^{-1} respectively, and the equivalent rates between 26-30 km are 52, 22, and 1.8 m day^{-1}. Therefore, one would expect BC to be advected to much higher altitudes than SO_4 in these simulations. For perspective, Schoeberl *et al.* (2008) deduced from observations that the atmospheric tropical vertical velocity between 18 and 26 km has an upper limit of 35 m day^{-1}, and the equivalent velocity between 26 and 30 km is below 61 m day^{-1}.

4.3. Method

4.3.1. Model validation

We first validated the model's stratospheric SO_4 scheme by simulating the 1991 Mt Pinatubo eruption and then comparing the results with observations. These simulations comprised a 10-member ensemble in which 20 Tg[SO_2] is injected between 16-18 km over a 24-hour period in June 1991, which was the method adopted by Aquila *et al.* (2012). Figure 4.4a shows the annual and global-mean SO_4 AOD anomaly for the HadGEM2 ensemble and for AVHRR and SAGE II observations. The model clearly captures the peak AOD from the AVHRR data, and the exponential decline thereafter. SAGE II was unable to capture the peak AOD for the first few months after Pinatubo due to saturation at AODs > 0.15, which is clear from Fig. 4.4a. Figures 4.4b-d show the zonal-mean AOD anomaly for the same time period. The agreement between the model and observed AOD is reasonable. Some differences in the temporal evolution of the AODs in the model and the observations are due to the almost concurrent eruption of Cerro Hudson which injected approximately 3.3 Tg[SO_2] into the southern hemisphere [Deshler and Anderson-Sprecher, 2006]. This relatively close agreement between observations and HadGEM2 estimates, together with other modelling studies of other volcanic eruptions [Haywood *et al.*, 2010] suggests that the model is a useful tool for SAI simulations.

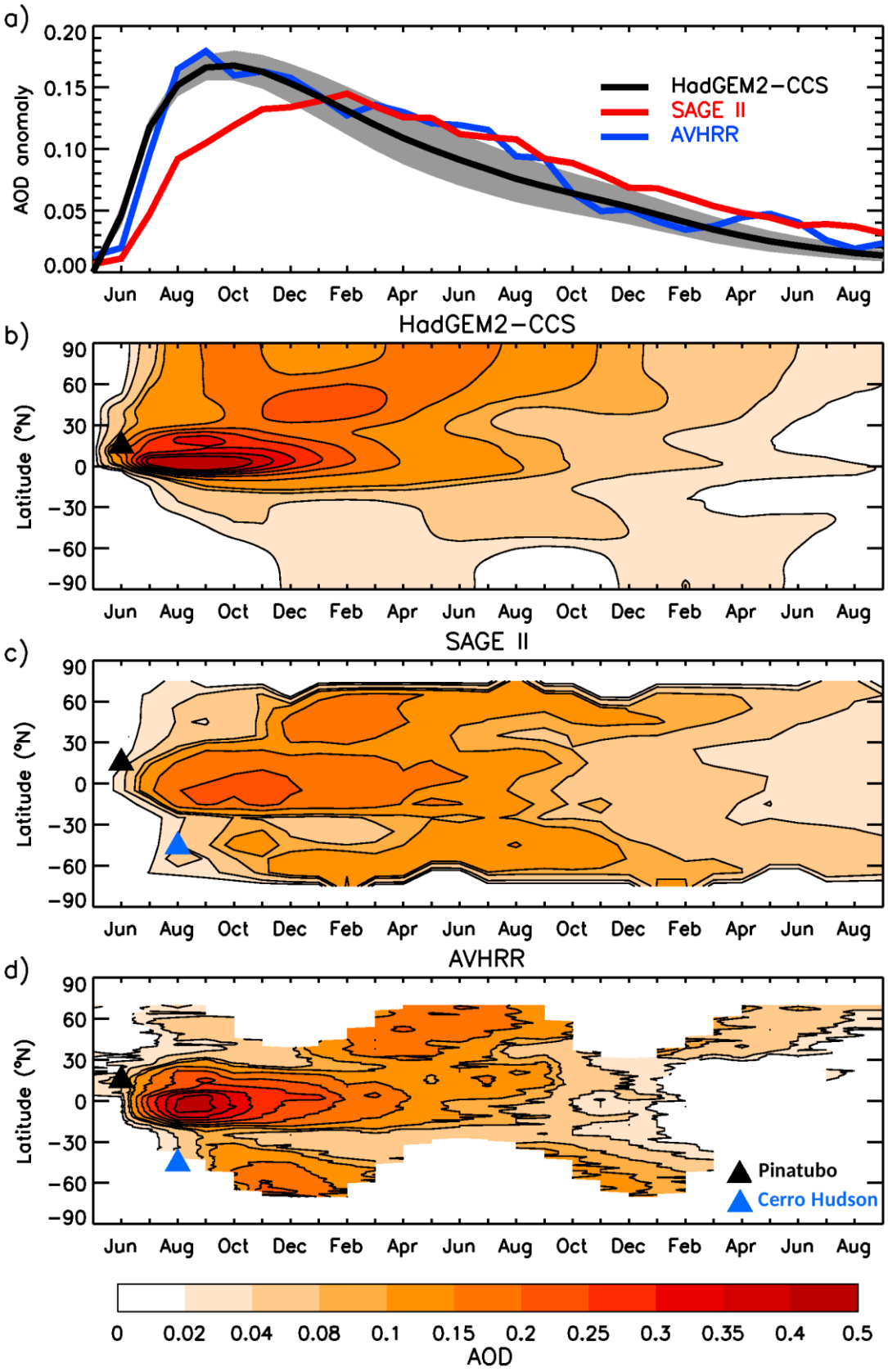

Figure 4.4 (a) 75°S-75°N-mean 550nm SO_4 AOD anomaly for the Pinatubo simulations and observations, (b-d) timeseries of zonal-mean 550nm SO_4 AOD anomaly. The grey shaded area in (a) shows +/- 1 standard deviation for the simulations

Scenario name	Description	Time period	Ensemble size	CMIP5?
piControl	Constant pre-industrial conditions	1860 (240 yrs)	1	Yes
Historical	Historical GHG/aerosol forcing	1860-2005	3	Yes
RCP8.5	High GHG concentrations scenario	2005-2100	3	Yes
geoSulf	SO_2 injection to counteract RCP8.5 forcing	2020-2100	3	No
geoBC	BC injection to counteract RCP8.5 forcing	2020-2100	3	No
geoTiO_2	TiO_2 injection to counteract RCP8.5 forcing	2020-2100	3	No

Table 4.1 Specifications of the experiments used in this study

4.3.2. Geoengineering specifications

For this work, we firstly utilised HadGEM2-CCS simulations that had already been performed for CMIP5 [Jones *et* al., 2011; Taylor *et al.*, 2012]. These included a 240-year pre-industrial control (piControl) simulation (forced by constant 1860's GHGs and aerosol emissions) and a 3-member 'initial value' ensemble for the recent historical period (1860-2005). For the future period (2005-2100) we decided to use the 'carbon-intensive' RCP8.5 scenario (following CMIP5 protocol); with the 3-member ensemble directly following on from the historical simulations [Taylor *et al*., 2012]. We then extracted the climatologies at the start of year 2020 from the RCP8.5 simulations and used these as the basis of our geoengineering simulations. Specifically, the geoengineering simulations comprised 3-member ensembles of: RCP8.5 with SO_2 injection (geoSulf), RCP8.5 with TiO_2 injection (geoTiO_2), and RCP8.5 with BC injection (geoBC). Aerosol (or gaseous SO_2 for the geoSulf scenario) was injected continuously from 2020 to 2100, and at a constant rate between 23 and 28 km altitude (4 model levels) in a single vertical column at the equator. The injection altitude and location were chosen to ensure a long stratospheric lifetime of the aerosol, which is transported poleward by the upper branch of the BDC [Niemeier *et al.*, 2011], and therefore make the geoengineering approach reasonably efficient. Table 4.1 contains a summary of the simulations.

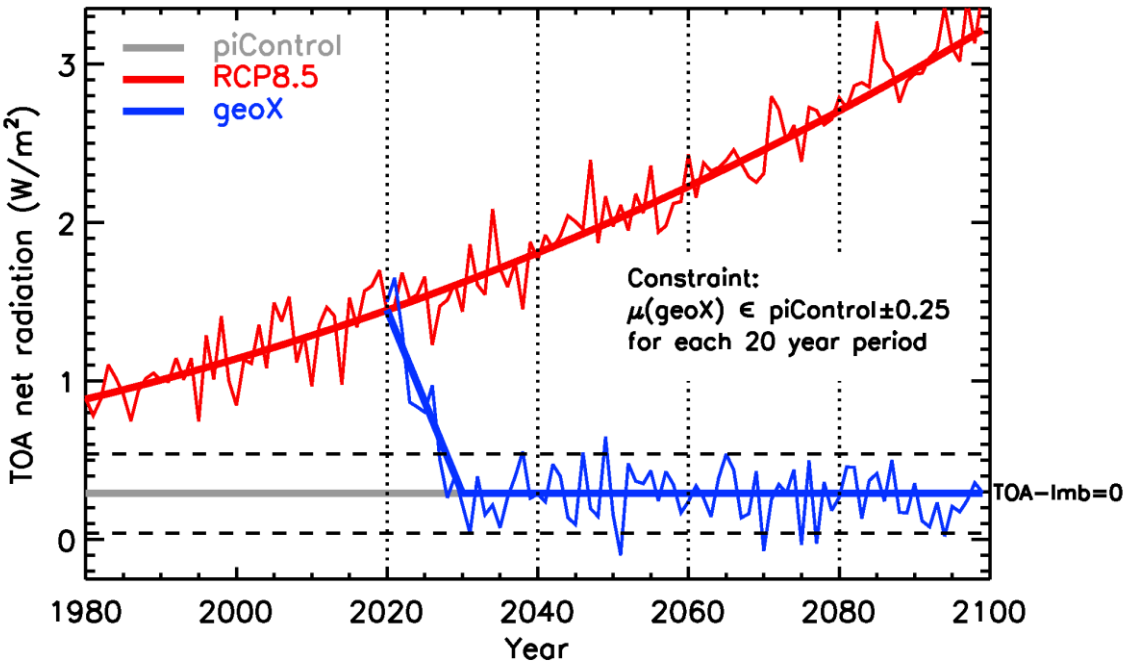

Figure 4.5 Schematic showing the goal of the geoengineering strategy

---

We inject aerosol at such a rate as to maintain the TOA net radiative flux at piControl levels. Specifically, we define the TOA radiative flux Imbalance (TOA-Imb) as the annual and global-mean TOA net radiative flux (incoming SW minus outgoing LW+SW) minus the average TOA net radiative flux of the piControl period. The piControl TOA net radiative flux is positive (+0.27 Wm^{-2}) as anthropogenic GHGs were emitted prior to 1860 (the piControl reference period). By sufficient aerosol injection, we aim to maintain TOA-Imb = 0. A schematic of this strategy is shown in Fig. 4.5. This scenario represents our interpretation of 'equal amount of geoengineering' for each aerosol. The advantage of returning net radiation to piControl levels (rather than completely equilibrating TOA fluxes) is that piControl had already been simulated comprehensively for CMIP5 (240 model years), hence permitting robust statistics to be calculated. The TOA radiative imbalance is a metric that satellites are able to measure (e.g. CERES [L'Ecuyer *et al.*, 2015] and EarthCare [Illingworth *et al.*, 2015]), albeit with +/- 3 Wm^{-2} accuracy at present [Priestley *et al.*, 2011; von Schuckmann *et al.*, 2016]. Therefore our target could be applicable to an actual SAI scenario. In contrast, the ARF (the net radiation perturbation at the tropopause from some external forcing, after stratospheric adjustment) cannot be directly measured by satellites and therefore it would be difficult to obtain a specified radiative forcing in an

actual SAI scenario. Of course, other metrics could be chosen [e.g. MacMartin *et al.*, 2013], with each metric having its own signal/noise characteristic.

4.3.3. Conducting the simulations

We now describe the process by which we carried out the simulations. The RCP8.5 and piControl simulations had already been conducted prior to this investigation as part of CMIP5. The geoengineering simulations took place in 3 phases: (a) we performed atmosphere-only simulations of 1 Tg yr^{-1} aerosol injection to determine the aerosol TOA radiative effect; (b) we used the aerosol radiative effect to calculate initial injection rate estimates; (c) we began the 80-year GCM integrations, calibrating the injection rates en route.

a. We performed atmosphere-only simulations with a constant 1 Tg yr^{-1} aerosol injection rate using historical background-conditions (1990-2005). We then determined the steady-state annual and global-mean aerosol radiative effect (the difference in TOA net radiation between the aerosol simulation and the control, per injection rate), which is given in Table 4.2. For SO_4, because the radiative effect was small, we performed an additional simulation with 5 Tg[SO_2] yr^{-1} and then divided the results by 5 for precision. Similarly, the BC simulation failed to converge to steady state within 15 years and was therefore run for a further 15 years.

	SO_4	TiO_2	BC
TOA radiative effect (Wm^{-2} / Tg yr^{-1})	0.46	1.1	7.4

Table 4.2 TOA radiative effect per injection rate

b. Rather than use the TOA-Imb from the RCP8.5 simulations to estimate the required aerosol injection rates, we instead used the Anthropogenic Radiative Forcing (AnthroRF)[9] [Meinshausen *et al*, 2011]. Specifically, we deducted the 1860 AnthroRF (0.17 Wm^{-2}) from the AnthroRF s for 2020, 2040, 2060, 2080, and 2100, and then calculated the injection rates required to offset these adjusted AnthroRFs by dividing by the TOA aerosol radiative effect. We used the

[9] http://www.pik-potsdam.de/~mmalte/rcps/

AnthroRF to estimate the injection rates required to produce TOA-Imb = 0 as this seemed a sensible method for approximating the necessary aerosol injection. Because each model will have an AnthroRF which is different from Meinshausen *et al.* (2011) it is possible that our initial estimate is in error. However, our method uses this only as an initial 1st guess for the injection rates, which are iteratively adjusted as described in c). The model then linearly interpolates the injection rates between these years.

	AnthroRF (Wm^{-2})		SO_2 injection rate (Tg/yr)		TiO_2 injection rate (Tg/yr)		BC injection rate (Tg/yr)	
Year	Actual	Adjusted	Initial	Final	Initial	Final	Initial	Final
2020	2.56	2.39	5.2	4.4	2.2	1.4	0.32	0.21
2040	3.83	3.66	8.0	7.4	3.3	2.5	0.49	0.29
2060	5.34	5.17	11.2	11.6	4.7	4.1	0.70	0.45
2080	6.79	6.62	14.4	13.6	6.0	4.8	0.89	0.62
2100	8.15	7.98	17.4	14.2	7.3	6.2	1.08	0.88

Table 4.3 Anthropogenic radiative forcing (AnthroRF) [Meinshausen *et al.*, 2011]; AnthoRF minus AnthroRF(year = 1860); estimated injection rates; and final injection rates

c. A single simulation was then initiated for each aerosol, with initial injection rates as specified in Table 4.3. After every 20 year interval, the simulation was stopped and the TOA-Imb was calculated for that time period. If there was significant deviation from zero (we adopted |mean(TOA-Imb)|> 0.25 Wm^{-2} as the criterion), then we recalculated the amount of injection required. The recalibration was conducted as follows: the TOA-Imb at the end of the 20 year period (time = t_{20}) was calculated for the mean of the RCP8.5 ensemble, denote this R_{rcp}. The injection of aerosol at time t_{20} at rate I_{geo} produced TOA-Imb R_{geo} which we wish to be zero. Therefore an improved injection rate at t_{20} would be $I'_{geo} = I_{geo} \times R_{rcp} / (R_{rcp} - R_{geo})$. Additionally, at all specified timesteps after t_{20} ($t_n = t_{20}+20n$, $n = 1,...$), we modify the injection rate as such: $I'_{geo}(t_n) = I_{geo}(t_n) \cdot R_{rcp}/(R_{rcp} - R_{geo})$. After resetting the injection rates, we restarted the simulation from the start of the last

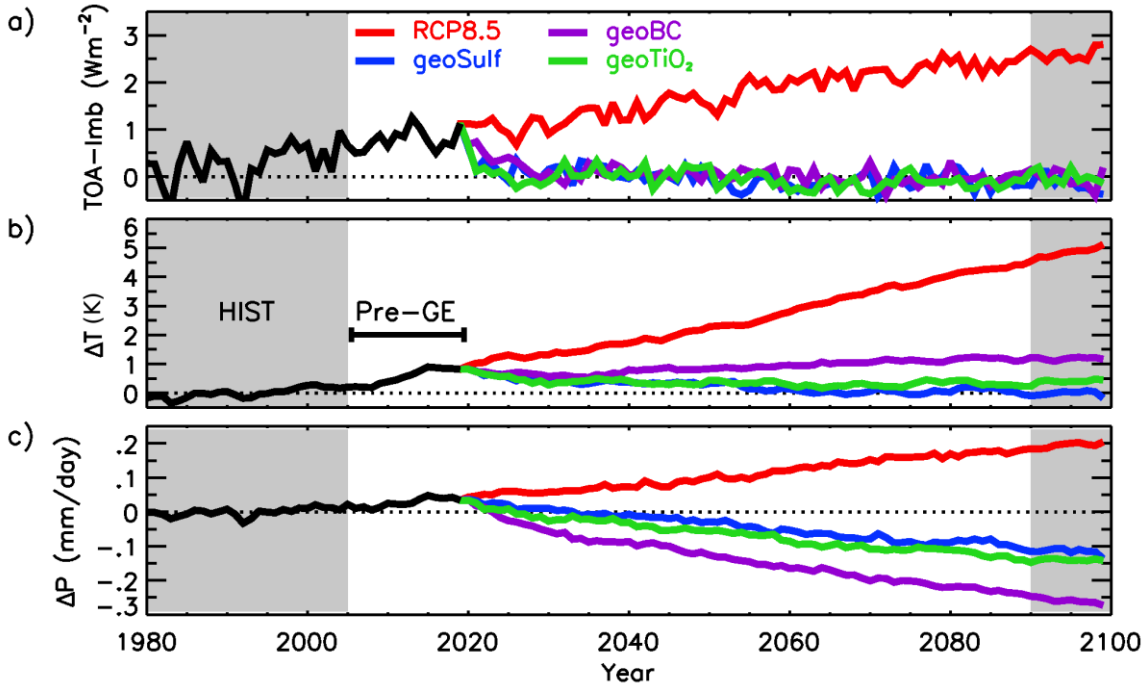

Figure 4.6 Timeseries of annual and global-mean a) TOA radiative flux anomaly with respect to the piControl simulation b) near-surface air temperature anomaly with respect to the HIST period c) global-mean precipitation anomaly with respect to HIST

time period. Final injection rates are given in Table 4.3. We then used the final injection rates to run two more ensemble members for each aerosol. This feedback-orientated method is similar to the methods suggested by MacMartin *et al.* (2014) and Kravitz *et al.* (2014b).

4.3.4. Conducting the analysis

Our analysis focuses initially on the temporal evolution of the TOA-Imb and global-mean temperature changes to show that our simulations provide plausible counterbalances to global-mean temperature changes under RCP8.5. However, our main focus is on the differences between a recent historical period (1980-2005) (hereafter denoted HIST) and the geoengineering experiments during the period 2090-2100, with an emphasis on different geographical patterns. As we were not explicitly attempting to reach a specific global-mean temperature, the choice of reference period was left until after the geoengineering simulations had been completed. We then selected a recent historical period from which the 2090s global-mean temperature anomaly for geoSulf was negligible (Fig. 4.6b). The HIST period selected is close to the historical control period used in the IPCC

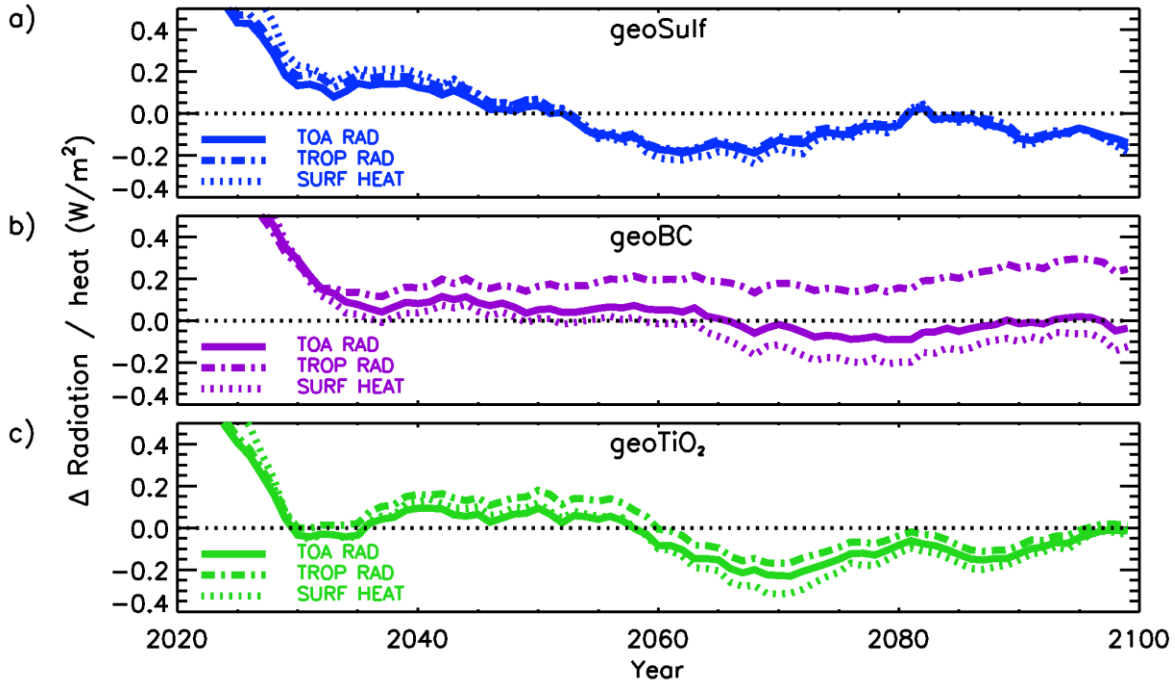

Figure 4.7 10-year running-average annual and global-mean net radiation anomaly at the tropopause and TOA, and net downward heat flux anomaly at the surface, with respect to piControl. Positive values indicate an increase in net downward flux

AR5 report (1986-2005) [e.g. Fig. 12.10 from Collins *et al.*, 2013] which facilitates comparison of our RCP8.5 climate changes with the CMIP5 multi-model means.

4.4. Results

4.4.1. Effectiveness at maintaining the global-mean climate

Figure 4.6 shows the annual and global-mean TOA-Imb and near-surface air temperature anomaly for the geoengineering and RCP8.5 simulations, with respect to the HIST period. For all of the geoengineering simulations we were able to maintain TOA-Imb ≈ 0 for the entirety of the 80-year period (Fig. 4.6a). For geoSulf, geoTiO_2 and geoBC, the TOA-Imb was maintained within +/- 0.21, +/- 0.18 and +/- 0.20 Wm^{-2}, respectively (1 standard deviation throughout the 2020-2100 period). The near-surface global temperature response differs between the aerosols with a greater cooling trend for SO_4 than for TiO_2 or BC (Fig. 4.6b).

To determine the cause of the anomalous warming in geoBC, we assess the net radiative flux at the top of the atmosphere for 2020-2100. Figure 4.7 shows the global-mean net-downward radiative flux anomaly for the geoengineering experiments, evaluated at the TOA and the tropopause; and the global-mean net-downward heat flux anomaly at the surface. The radiative flux changes at the

TOA and tropopause, and the heat flux anomaly at the surface, are comparable for the geoSulf and geoTiO_2 experiments for the duration of 2020-2100. In contrast, geoBC exhibits an increasingly positive net radiative flux anomaly at the tropopause (+0.2 Wm^{-2} averaged over 2020-2100) despite the negligible TOA radiative flux anomaly. After stratospheric temperature adjustment, radiative perturbations at the TOA and tropopause are equal for a given climate forcing, which implies that the consistently non-adjusted stratosphere (due primarily to increasing aerosol injection rates) is responsible for the differences in TOA and tropopause radiative perturbations in geoBC. Hansen *et al.* (1997) also found that instantaneous and adjusted radiative forcing differ most when there is a large heating affecting the tropopause. This implies that if we had injected aerosol sufficiently to produce an equal radiative effect at the tropopause, the temperature trends for the geoengineering experiments in Fig. 4.6 would have been more comparable. If we were to choose stabilisation of temperature as our basic metric, then one could approximate the results by simply scaling the results by the ratio of the temperature perturbation relative to 1980-2005 to that for geoSulf. The scaling would be 1 (by design) for geoSulf, 1.1 for geoTiO_2 and 1.28 for geoBC. If the metric chosen were instead to keep the global-mean precipitation the same, then the scaling would be 1 (by design) for geoSulf, 0.91 geoTiO_2 and 0.68 for geoBC. However, we shall see that the changes in many of the variables we consider are dominated by large scale changes in the spatial patterns of response rather than the 10-30 % changes in magnitude of the response that applying such a scaling would induce. We therefore choose to present un-scaled results here but caveat that such a scaling could be applied should we wish to apply a different metric. From Fig. 4.6b, geoSulf exhibits a near-surface air cooling trend with respect to 2020 despite a net gain of atmospheric energy, which is likely due to an uneven vertical distribution of this energy gain.

Fig. 4.6c shows the global-mean precipitation anomaly with respect to the HIST period. The precipitation reduction is greater for BC than for SO_4 and TiO_2, despite the positive temperature trend in geoBC. The hydrological sensitivity to geoengineering, defined as the global-mean precipitation change per unit temperature change, is 2 % K^{-1} for SO_4, 2.5 % K^{-1} for TiO_2, and 4.6 % K^{-1} for BC. The hydrological sensitivity for RCP8.5 is 1.32 % K^{-1}, which is close to the CMIP5

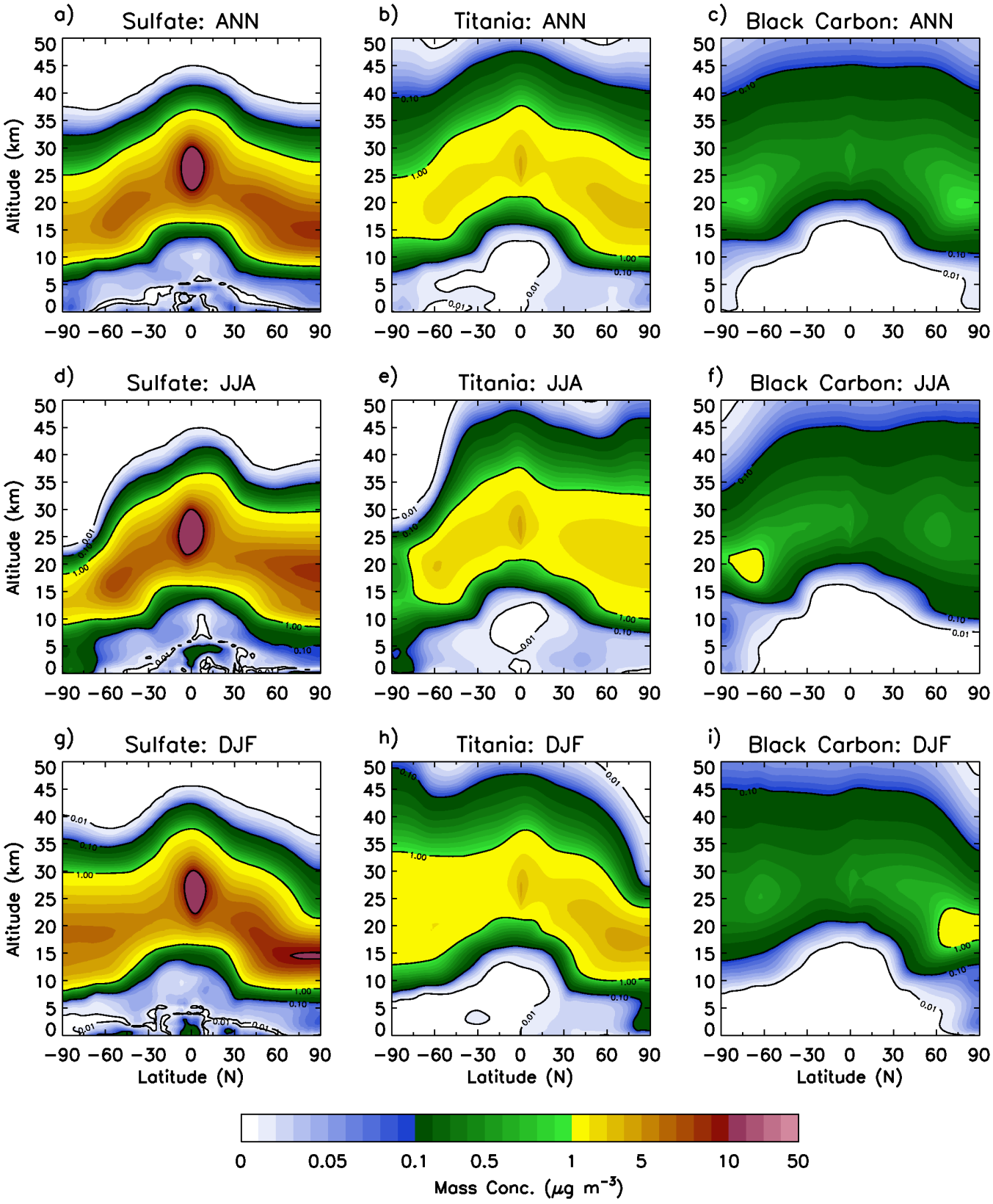

Figure 4.8 Annual and seasonal zonal-mean mass concentration anomalies for sulphate (geoSulf – a,d,g), TiO_2 (geoTiO_2 – b,e,h) and black carbon (geoBC – c,f,i)

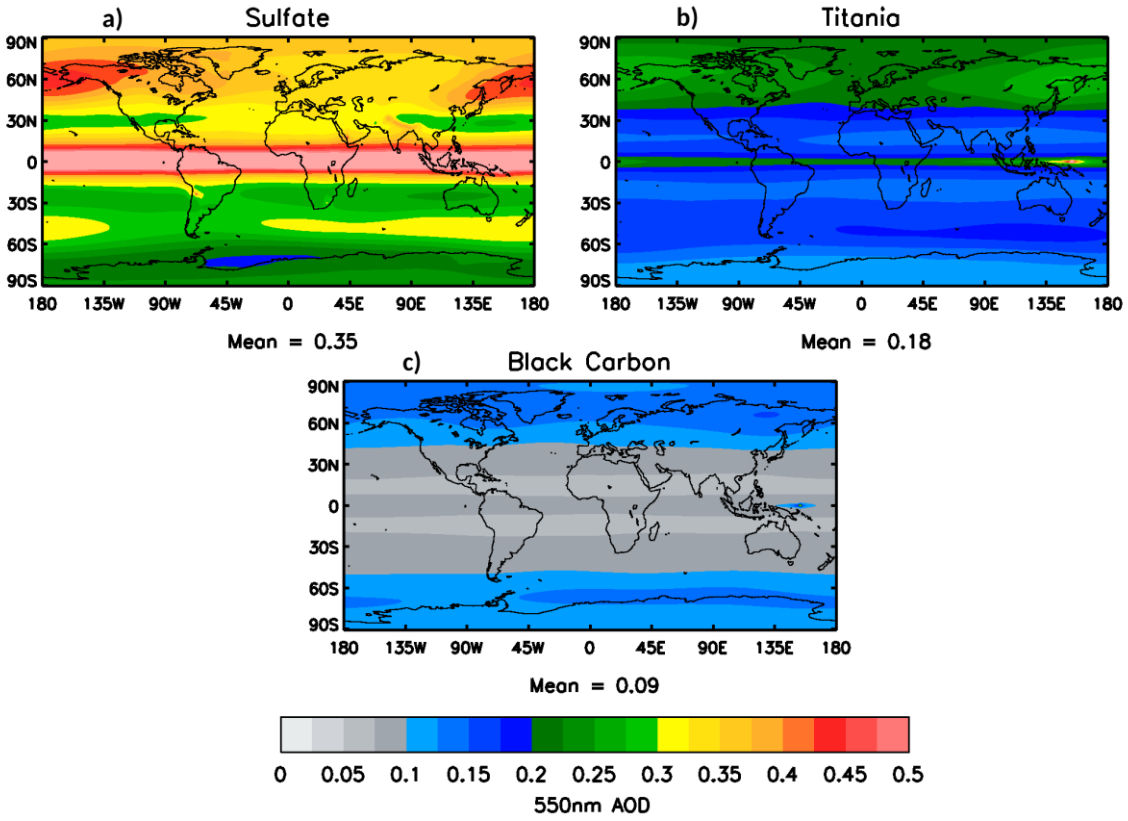

Figure 4.9 Annual-mean 550nm optical depth anomaly for (a) sulphate (geoSulf), (b) TiO_2 (geoTiO_2) and (c) black carbon (geoBC)

ensemble-mean [Fig. 12.7 from Collins *et al.*, 2013]. For comparison, Bala *et al.* (2008) found a hydrological sensitivity of 2.4 % K^{-1} for solar irradiance reduction and 1.4 % K^{-1} for CO_2 increase.

4.4.2 Aerosol distribution

The time-averaged injection rates for the 2090s period are 14 Tg[SO_2] yr^{-1}, 5.8 Tg yr^{-1} and 0.81 Tg yr^{-1} for geoSulf, geoTiO_2 and geoBC, respectively. This SO_2 injection rate is approximately equivalent to 1 Mt Pinatubo eruption per year [Dhomse *et al.*, 2014]. These injection rates equate to global aerosol mass-burden anomalies of 49.5, 20.2, and 5.1 Tg for geoSulf, geoTiO_2 and geoBC, respectively. The geoBC mass burden is comparable to the equilibrium burdens of the high-altitude (HA) and small-radius (SmR) experiments from Kravitz *et al.* (2012), although they injected BC at a constant rate of 1 Tg yr^{-1}, around 20% higher than in our study. The SmR experiment involved a 10-year injection of BC particles with a uniform radius of 0.03 μm, into a region between 100-150 mb altitude and over the latitude range 10°S-10°N, against baseline perpetual year 2000 conditions. Figure 4.8 shows the 2090s annual, June-July-August (JJA) and December-January-

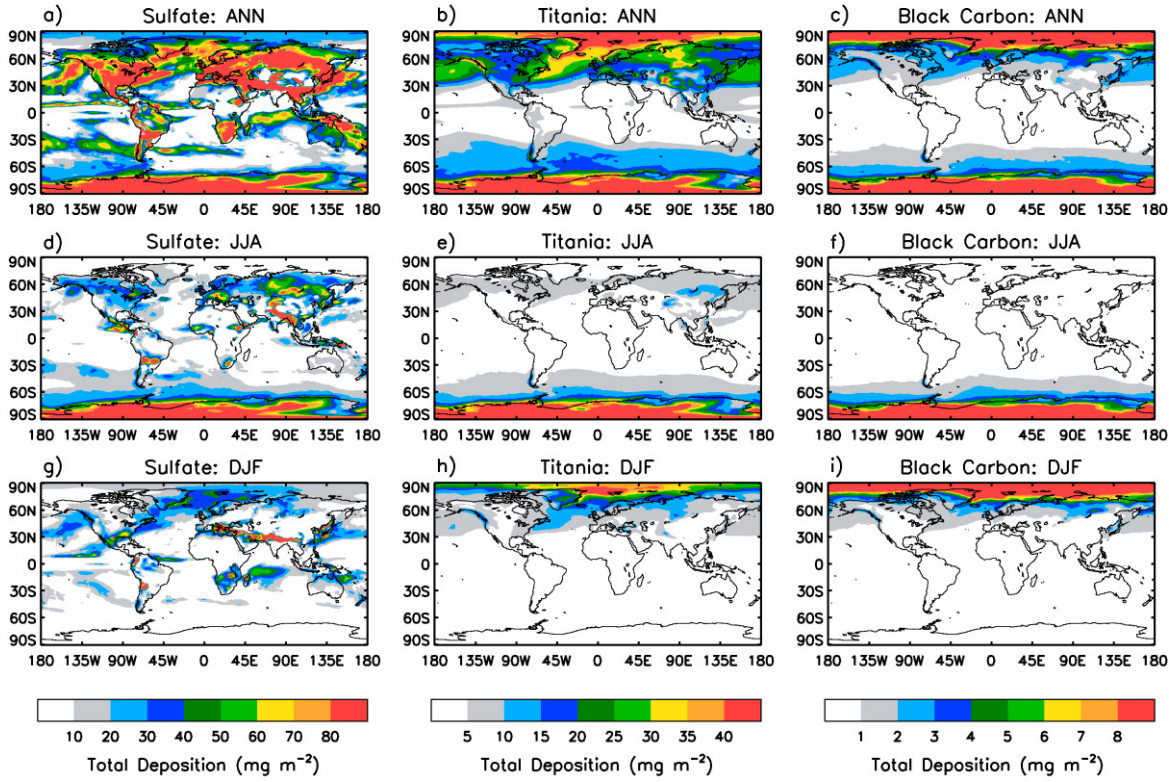

Figure 4.10 Annual and seasonal total deposition anomalies (in units of mg m^{-2} yr^{-1} and 0.25× mg m^{-2} yr^{-1} respectively)

February (DJF) aerosol mass concentration anomalies. Peak SO_4 concentrations are found at the injection region at the equator (Figs. 4.8a,d,g) and over the winter pole. TiO_2 and BC reach greater altitudes than SO_4 (>50 km), which is due to their smaller size-distributions and self-lofting from SW absorption [Kravitz *et al.*, 2012]. While SO_4 aerosol concentrations are highest at the equator, the highest concentrations of BC are found in the polar stratosphere. This is because the larger particle size of the SO_4 aerosol is subject to a larger sedimentation velocity (Fig. 4.3) and thus a greater fraction of aerosol is removed close to the source region. The results from TiO_2 suggest a spatial distribution intermediate between SO_4 and BC owing to the intermediate size distribution. Figure 4.9 shows the annual-mean 550nm aerosol optical depth anomaly, which corroborates our inference of a tropical aerosol reservoir for SO_4.

Figure 4.10 shows the total annual, JJA and DJF aerosol deposition anomalies averaged over the 2090s. SO_4 is predominantly deposited in the NH extratropics in the boreal spring and summer (Fig. 4.10d) which is likely attributable to tropopause fold events in the lower branch of the BDC [Kravitz *et al.*, 2012]. In contrast, TiO_2 and BC are primarily deposited at high latitudes in the polar winter, which is attributable

to the diabatic descent of air in the deep branch of the BDC [e.g. Tegtmeier *et al.*, 2008]. Kravitz *et al.* (2012) also found in their SmR experiment that BC deposition was limited to the Polar Regions, but their maximum deposition was during polar summer rather than polar winter. The annual and global-mean deposition rates of SO_4 and BC from geoengineering are 37 and 1.5 mg m^{-2} yr^{-1} respectively. These amounts may be compared with 231 and 12.7 mg m^{-2} yr^{-1} from non-geoengineering sources, amounting to increases of 16 % and 12 % respectively. The annual and global-mean deposition rate for TiO_2 is 11 mg m^{-2} yr^{-1}.

4.4.3 Temperature and precipitation

Figure 4.11 shows the annual-mean near-surface air temperature (Figs. 4.11a-d) and precipitation anomalies (Fig. 4.11e-h) with respect to HIST. RCP8.5 (Fig 4.11a) shows the typical global warming signal of amplified warming at high latitudes due to temperature feedbacks [e.g. Pithan and Mauritsen, 2014] and the surface-albedo feedback [e.g. Kharin *et al.*, 2013]. This results in an annual-mean warming of 11.3 K averaged over the Arctic region (> 60 ^{o}N) and an average NH land warming of 7.3 K. This figure provides an alarming picture of the change in global-mean temperature by the end of this century should global society follow the RCP8.5 pathway. All 3 SAI experiments produce a surface-cooling with respect to RCP8.5, with geoSulf exhibiting the greatest global-mean cooling effect of -4.85 K, considering TOA-Imb is balanced for each geoengineering experiment. The latitudinal distribution of cooling varies markedly between the SAI experiments, with relative tropical cooling for geoSulf and geoTiO_2 (Figs. 4.11b,d) and polar cooling for geoBC (Fig. 4.11c). Defining the 'SAI cooling effect' as the temperature difference between SAI and RCP8.5, the ratio of cooling effect at high latitudes (> 60^{o}) between geoBC and geoSulf is 1.19 and between geoBC and geoTiO_2 is 1.23. In the tropics and mid-latitudes (< 60^{o}) the equivalent ratios are 0.64 and 0.71 respectively. The high-latitude cooling in the case of geoBC is attributable to the zonal distribution of BC (Figs. 4.8c,f,i) which is more evenly spread over the stratosphere than for geoSulf and geoTiO_2. The result is a greater surface SW forcing at high-latitudes in the summer hemisphere for geoBC. For instance, in the Arctic (>60^{o}N) in JJA, the surface SW forcing is -25.7 Wm^{-2} in geoBC and -3.3 and -6.6 Wm^{-2} in geoSulf and geoTiO_2 respectively. Although the global-mean precipitation rate increases in the

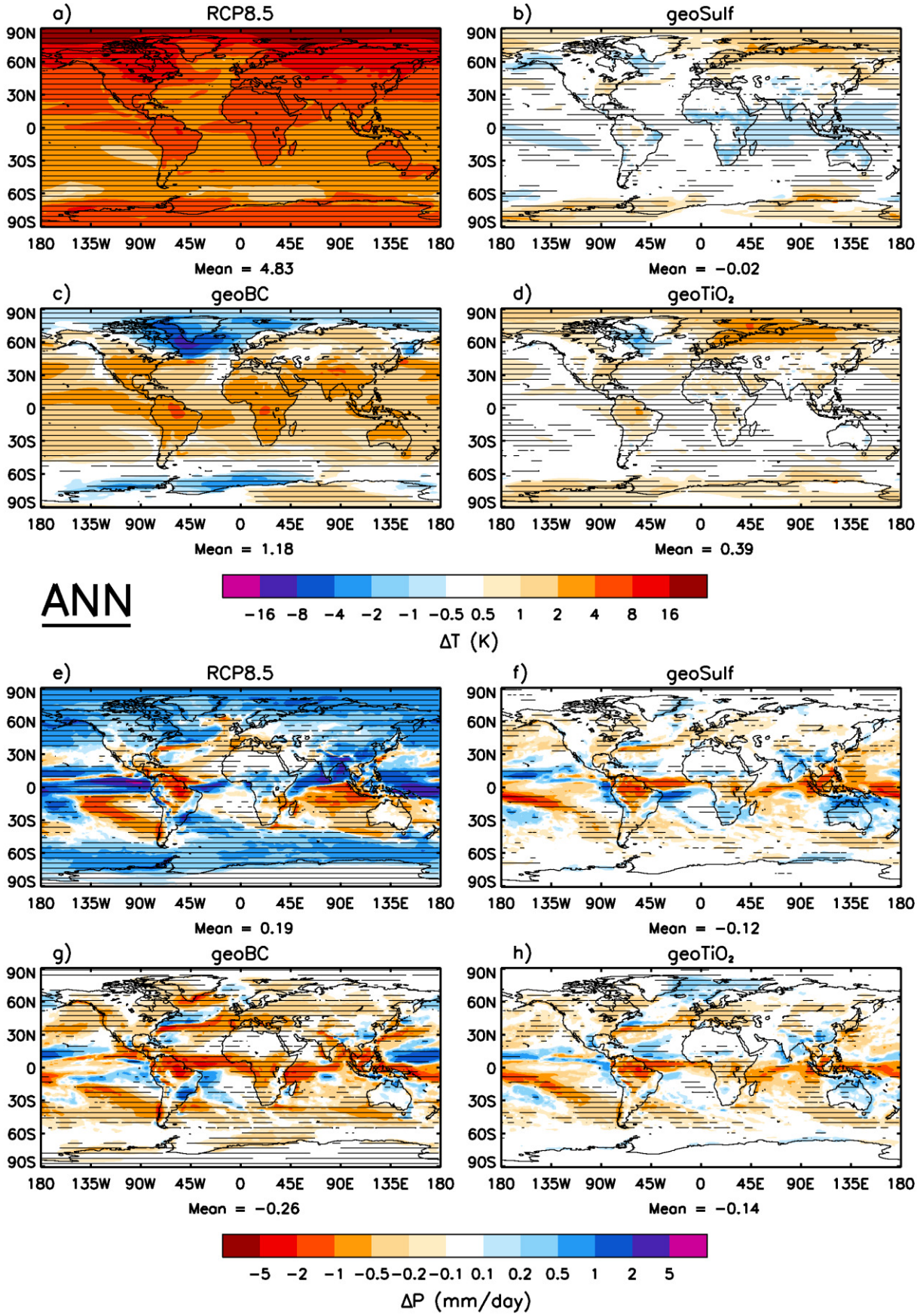

Figure 4.11 Annual-mean near-surface air temperature (top) and precipitation rate (bottom) anomalies with respect to HIST. Stippling indicates where changes are significant at the 5% level using a two-tailed Student's t-test

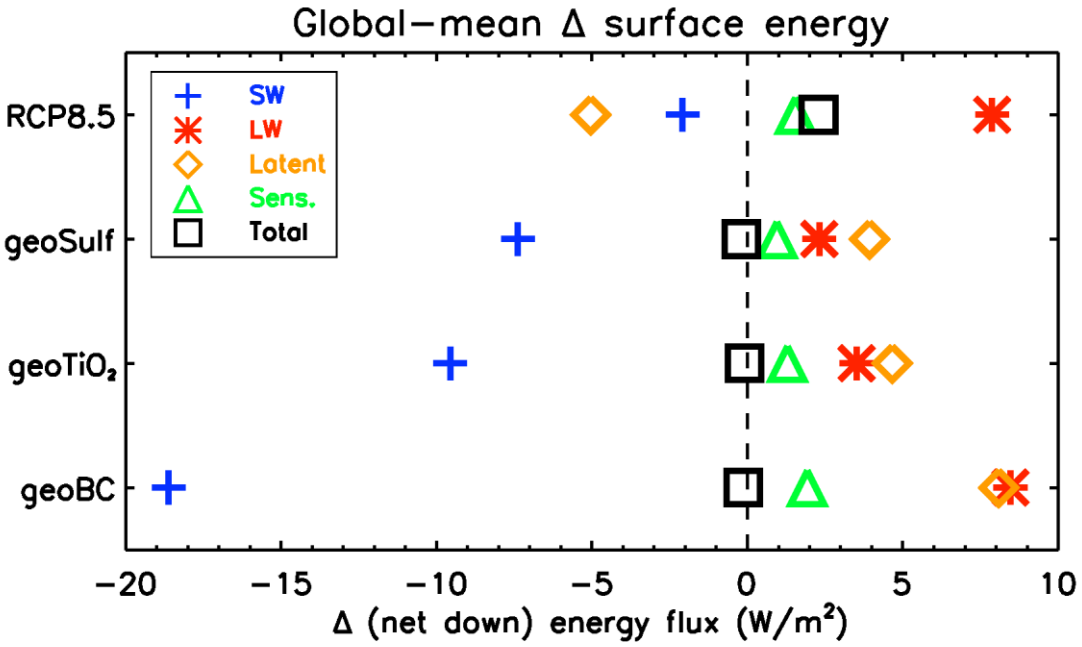

Figure 4.12 2090's annual and global-mean net downward energy flux anomalies at the surface (Wm^{-2}). Calculated with respect to piControl

---

RCP8.5 scenario (Fig. 4.11e), certain regions such as the Amazon basin exhibit a drying trend. This is in line with the CMIP5 multi-model projections documented in AR5 [e.g. Fig. 12.10 from Collins *et al.*, 2013]. All of the SAI experiments show a global-mean precipitation reduction with respect to both HIST and RCP8.5 (Figs. 4.11f-h), which is due to the deceleration of the hydrological cycle and is a robust model response to SAI [e.g. Yu *et al.*, 2015; Tilmes *et al.*, 2013; Bala *et al.*, 2008]. The magnitudes of the precipitation changes are greater for geoBC than for geoSulf or $geoTiO_2$, for instance, the global-mean precipitation anomaly is -0.26 mm day^{-1} for geoBC compared to -0.12 mm day^{-1} for geoSulf and -0.14 mm day^{-1} for $geoTiO_2$. In order to maintain TOA-Imb=0, BC must produce a greater SW perturbation at the tropopause and at the TOA than SO_4 or TiO_2, which is compensated by the increased LW perturbation resulting from stratospheric warming. The troposphere is relatively transparent to SW radiation but absorbs efficiently in the LW spectrum, therefore the annual-mean surface radiative forcing in the geoBC experiment is greater (−18.6 W m^{-2}) than for geoSulf or $geoTiO_2$ (−7.4 and −9.6 Wm^{-2} respectively – see Fig. 4.12). Bala *et al.* (2008) and Muller and O'Gorman (2011) have shown that the magnitude of the global-mean precipitation response to an imposed forcing is dependent on the energy flux entering/leaving the atmosphere (the radiative forcing of the atmosphere). The radiative forcing of the atmosphere is

the difference between net radiative fluxes at the TOA and at the surface. As the net radiative flux anomaly at the TOA is, by design, equal for the different geoengineering scenarios here and the net radiative flux anomaly at the surface is greater for geoBC (Fig. 4.12), the precipitation reduction is therefore amplified in the geoBC scenario.

It is important to note that if the RCP8.5 warming relative to HIST was completely offset in the geoBC and geoTiO_2 experiments, the hydrological response would be greater than in Fig. 4.11. Using the hydrological sensitivities calculated in Section 4.4.1, the precipitation changes relative to HIST would be -0.34 mm day^{-1} for geoBC and -0.16 mm day^{-1} for geoTiO_2. From Fig. 4.12, the reduction in surface SW flux in the RCP8.5 scenario is due to increases in water vapour [Haywood *et al.*, 2011]. Haywood *et al.* (2011) report a clear-sky reduction of -5.7 Wm^{-2} in RCP8.5 2090s with respect to a recent historical period, while our study is consistent at a value of -5.4 Wm^{-2} (not plotted). However, in all geoengineering cases, this reduction is comprehensively overwhelmed by aerosol direct effects. Figure 4.13 shows the JJA temperature (Figs. 4.13a-d) and precipitation (Figs. 4.13e-h) anomalies. In the geoSulf and geoTiO_2 scenarios, the temperature is effectively maintained at HIST levels (Figs. 4.13b,d). However, a slight bias towards high-latitude NH warming in geoSulf and geoTiO_2 results in a northward displacement of the ITCZ, which is exemplified by the Sahelian precipitation increase in Figs. 4.13f,h. This phenomenon was noted by Haywood *et al.* (2013) and has been observed after large hemispherically-asymmetric volcanic eruptions [Oman *et al.*, 2006a]. Although the general pattern of precipitation change is similar for the 3 SAI scenarios, geoBC again displays a greater drying signal, with 80% of the total land area experiencing a JJA precipitation reduction in geoBC compared to 70% for geoTiO_2, 57 % for geoSulf and 52 % for RCP8.5.

Figure 4.14 shows the DJF temperature (Figs. 4.14a-d) and precipitation (Figs. 4.14e-h) anomalies. The temperature reduction over Greenland in geoBC (Fig. 4.14c) is due to the significant decrease in downwelling SW radiation at the surface during the Arctic sea-ice formation season (September-October-November), which leads to a positive sea-ice albedo feedback and further localised cooling. This inference is corroborated by Fig. 4.15, which shows the Arctic DJF sea-ice extent in terms of the average DJF sea-ice boundary. The sea-ice boundary in geoBC (Fig.

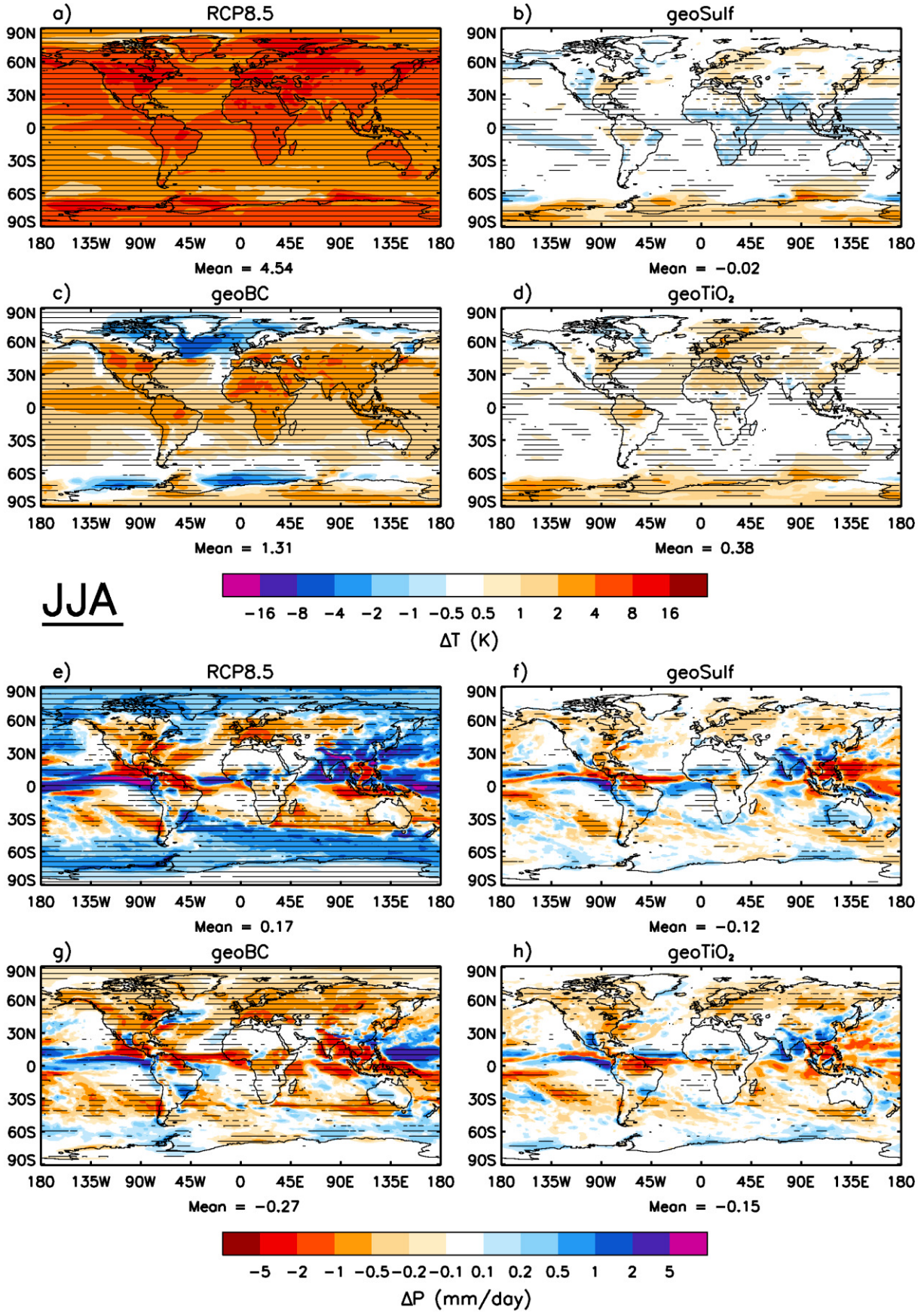

Figure 4.13 JJA near-surface air temperature (top) and precipitation rate (bottom) anomalies with respect to HIST

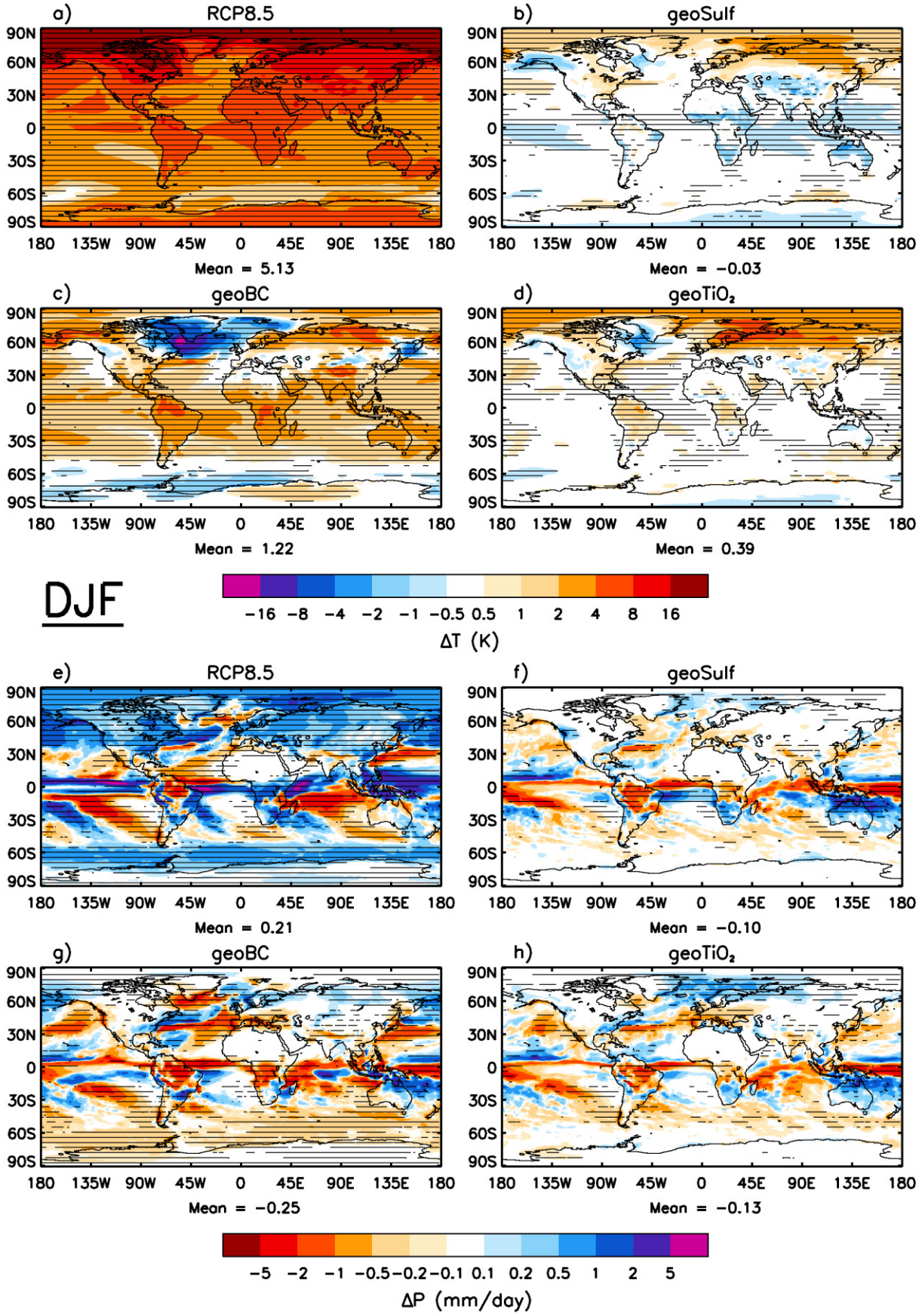

Figure 4.14 DJF near-surface air temperature (top) and precipitation rate (bottom) anomalies with respect to HIST

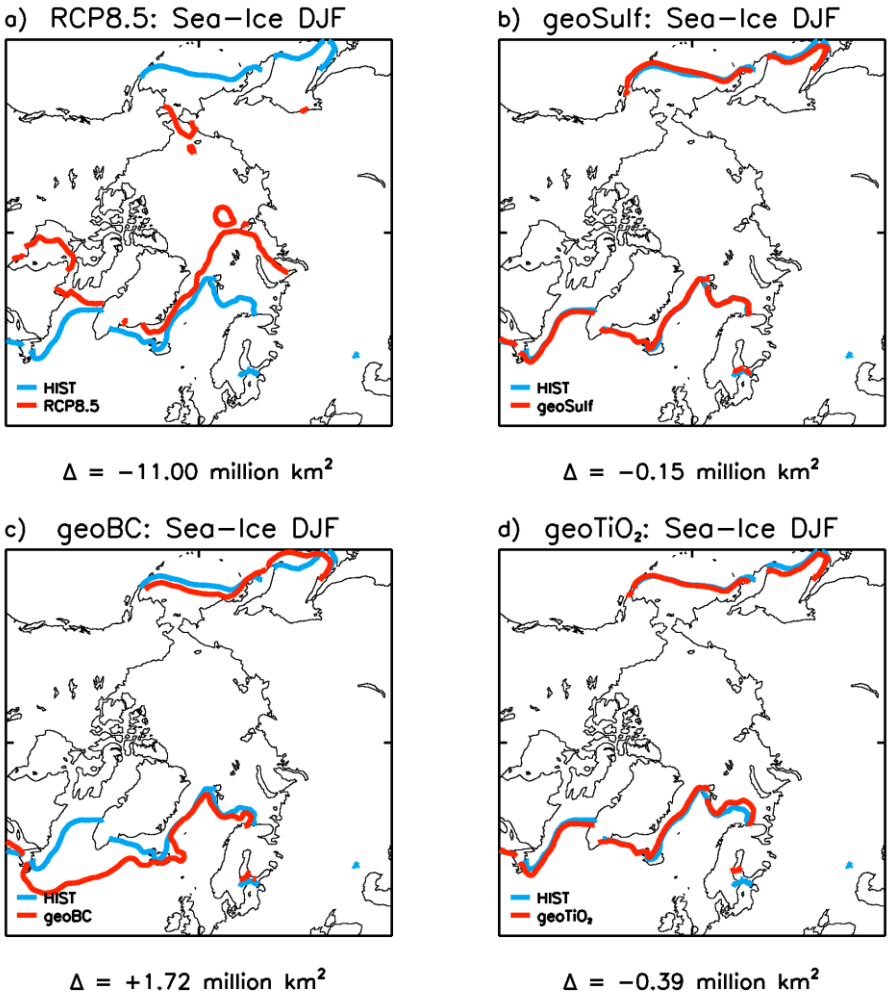

Figure 4.15 DJF NH sea-ice edge plotted with the HIST extent

4.15c) extends to well below Greenland, and the total sea-ice extent anomaly is +1.72 million km^2 which vastly exceeds the HIST standard deviation of +/- 0.52 million km^2. In comparison, the sea-ice extent anomaly of -11 million km^2 for RCP8.5 (Fig. 4.15a) marks a reduction by 43% of the total HIST sea-ice extent. Returning to Fig. 4.14, the poleward shift in the NH extratropical rain-belt over the Atlantic in RCP8.5 (Fig. 4.14e) is a robust result of GHG-induced global warming and is related to storm track displacement [Lombardo *et al.*, 2015]. This same response is evident in the geoengineering simulations (Figs. 4.14f-h), although to a much lesser extent in geoSulf and geoTiO$_2$.

4.4.4. Stratospheric changes

Figure 4.16 shows the zonal-mean temperature change as a function of latitude and altitude for the JJA and DJF seasons. The stratospheric cooling in conjunction with tropospheric warming in RCP8.5 (Figs. 4.16a,e) is a robust result of increasing GHG concentrations [e.g. Schmidt *et al.*, 2013b]. Stratospheric cooling is the result of

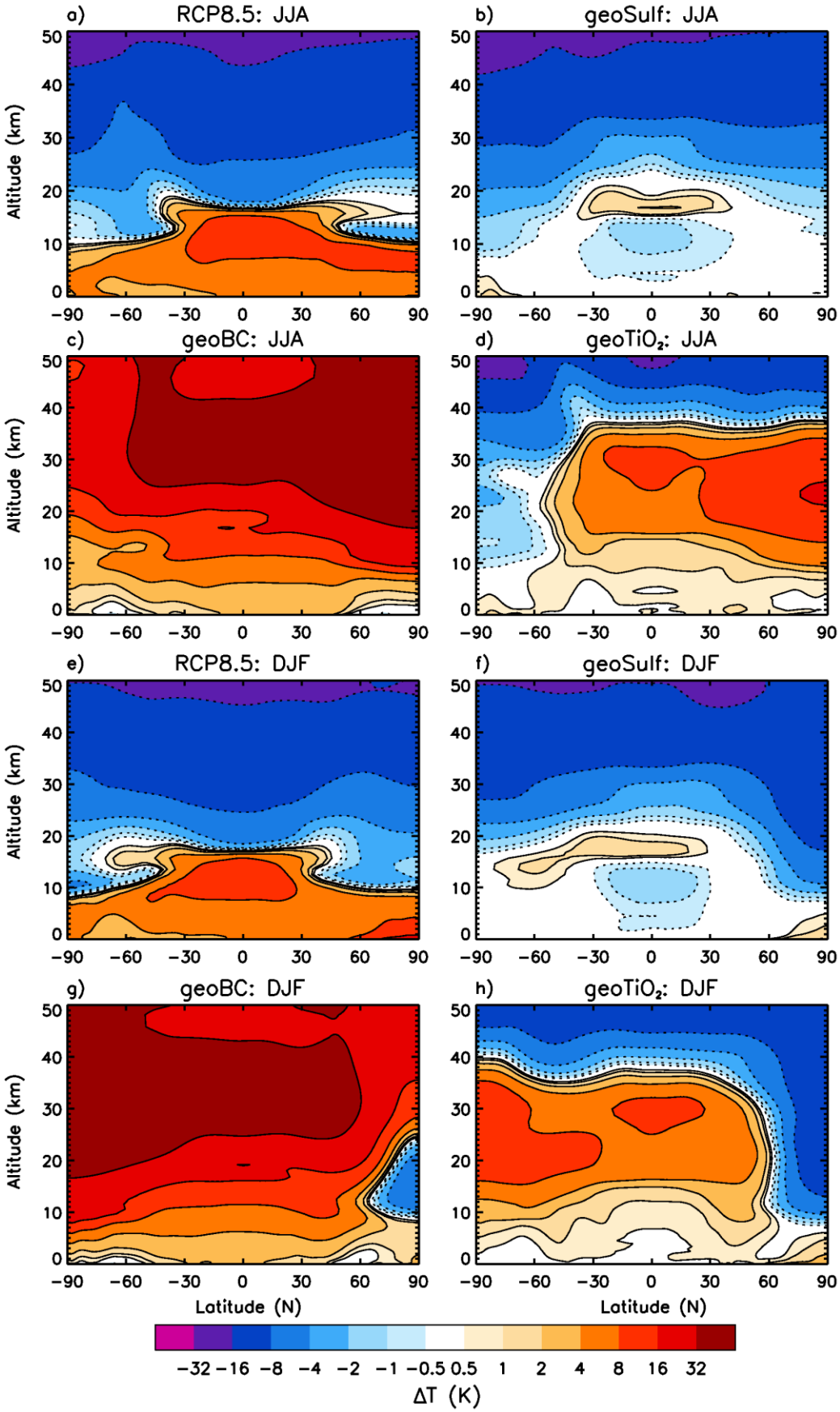

Figure 4.16 JJA (a-d) and DJF (e-h) zonal-mean temperature anomaly with altitude, with respect to HIST

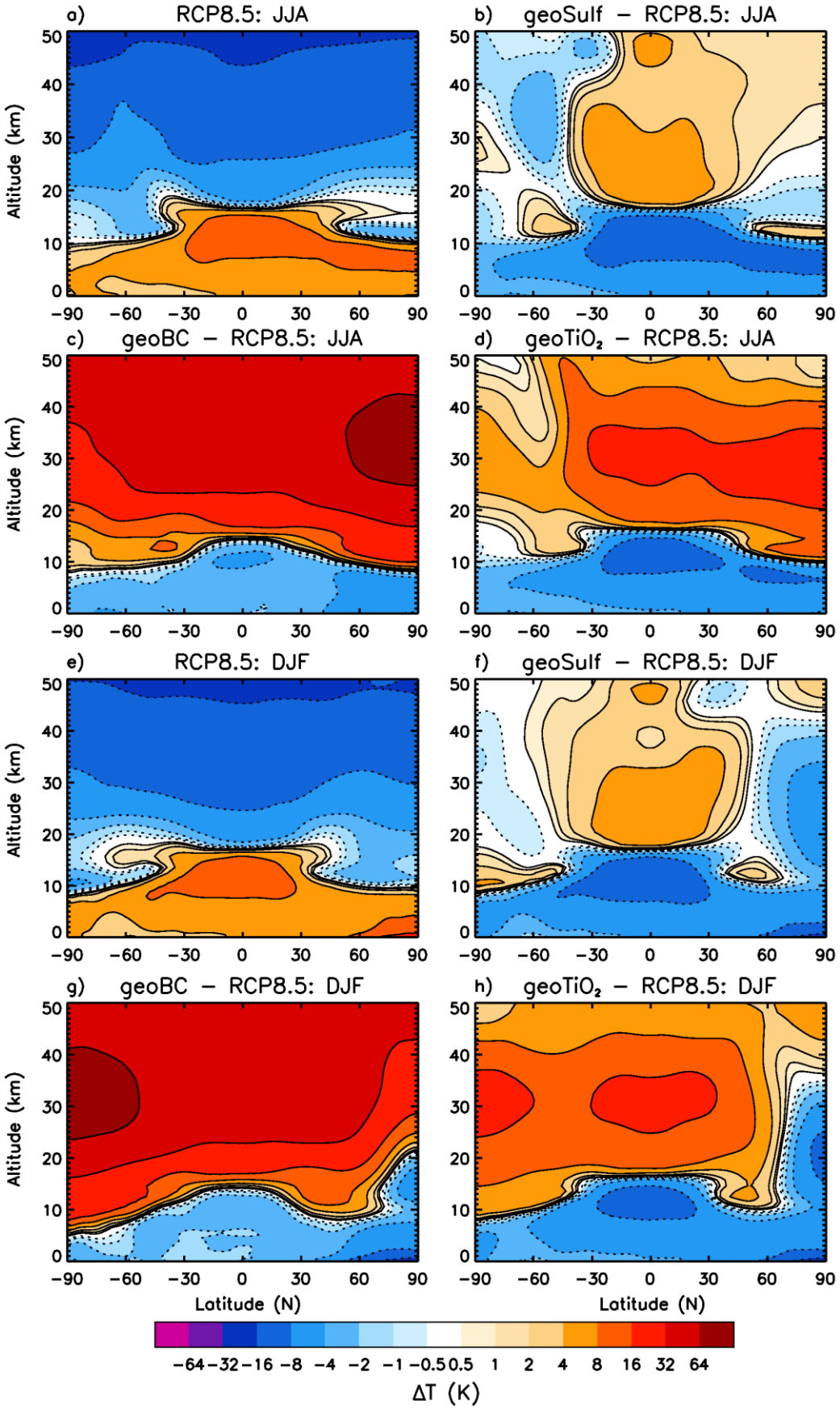

Figure 4.17 JJA (a-d) and DJF (e-h) zonal-mean temperature anomaly with altitude, with respect to the HIST temperature profile for RCP8.5 (a,e), and with respect to RCP8.5 for geoSulf, geoBC and geoTiO$_2$

enhanced GHG concentrations increasing the emissivity (ε in Eq. 1.3) of the atmosphere above the level of effective LW emission to space. Aerosols directly affect temperature by absorbing radiation, and indirectly by scattering radiation and by ambient dynamical and chemical changes [Carslaw and Kärcher, 2006]. SO_4 predominantly absorbs in the LW and near-infrared spectra (Fig. 4.2a). The stratospheric radiative heating in geoSulf is therefore most pronounced in the tropical region, where SO_4 absorbs outgoing LW radiation from the warm troposphere below and then emits comparatively less radiation from the cold stratosphere. In contrast, TiO_2 and BC absorb in both the SW and LW spectrum (Figs. 4.2b,c), and therefore preferentially warm the summer hemisphere and tropical stratosphere where solar radiation is most prevalent. geoBC produces the most significant warming effect, with an average stratospheric (15-50 km altitude) temperature increase of 33 K and a maximum temperature increase of 68 K (Figs. 4.16c,g). Figure 4.17 shows the zonal-mean temperature changes for RCP8.5 with respect to HIST (the same as in Fig. 4.16) and for geoSulf, geoTiO_2, and geoBC with respect to 2090s RCP8.5. The maximum BC-induced heating relative to the baseline RCP8.5 scenario is 76 K (Figs. 4.17c,g). This is comparable to the ~80 K temperature change that Kravitz *et al.* (2012) found in their SmR scenario. For comparison, the maximum SO_4-induced and TiO_2-induced heating relative to RCP8.5 are far more modest at 7 K and 22 K, respectively (Figs. 4.17b,d,f,h).

A warming of the lower tropical stratosphere could have multiple climatic repercussions such as a weakening of the tropospheric tropical circulation [Ferraro *et al.*, 2014], strengthening of the polar vortex [Driscoll *et al.*, 2012] and modification of the QBO [Aquila *et al.*, 2014]. Additionally, an increase in the tropical tropopause layer temperature would increase the specific humidity of air entering the stratosphere [Dessler *et al.*, 2013]. Changes to the stratospheric water vapour content could have significant chemical and radiative impacts, contributing to O_3 depletion via the HO_x cycle and stratospheric warming via LW absorption [Kravitz *et al.*, 2012]. To assess the effects of geoengineering on stratospheric water vapour, we calculate the time-averaged H_2O mixing ratio averaged between 20^oS-20^oN and 16-20 km altitude. In the HIST era, the H_2O MMR is 4.2 ppmv, in close agreement with Halogen Occultation Experiment (HALOE) HALOE observations [Gettelman *et al.*, 2010]. In the 2090s, the average H_2O MMR is 6.3

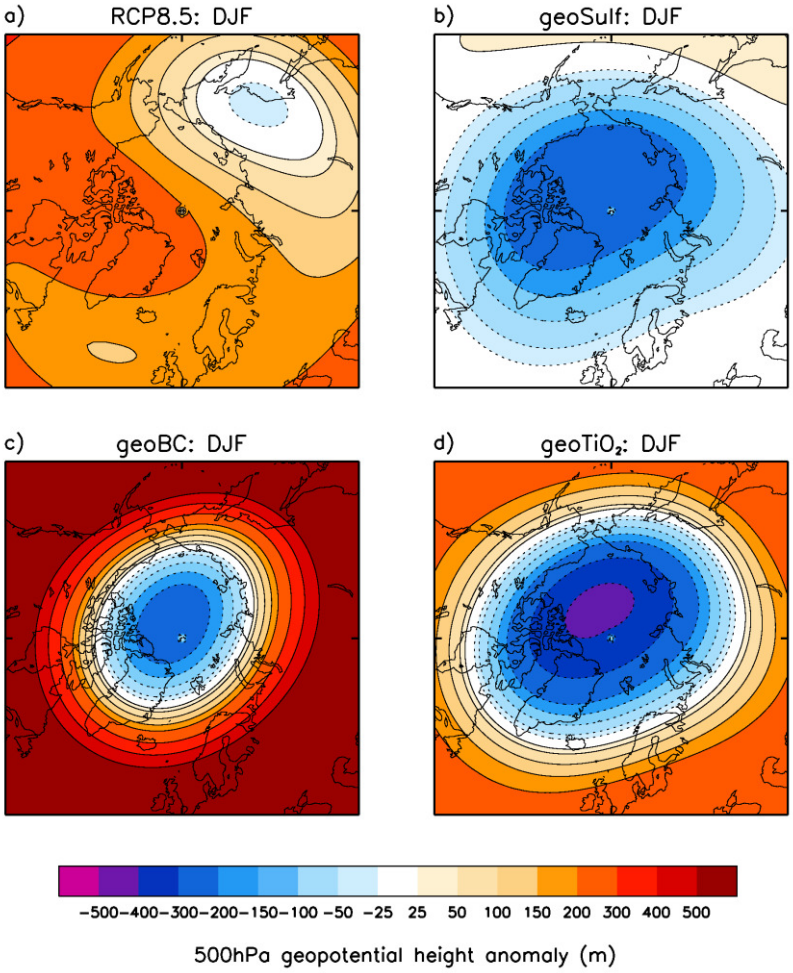

Figure 4.18 DJF 50hPa geopotential height anomaly

ppmv for RCP8.5, 4.8 ppmv for geoSulf, 7.1 ppmv for geoTiO$_2$, and 32.7 ppmv for geoBC. The stratospheric water vapour feedback is therefore greater for geoBC and geoTiO2 than for geoSulf.

A strengthening of the polar vortex could be instigated by an increased temperature gradient between the tropical/mid-latitude and polar stratospheres, a phenomenon which was observed after the Pinatubo eruption [Stenchikov *et al.*, 2002]. We concentrate on the Arctic wintertime (DJF) response to SAI, and adopt a similar metric to that used by Ferraro *et al.* (2011) to determine the stratospheric temperature gradient. Specifically, we determine the difference in temperature between 20^{o}N-20^{o}S (Tropics) and 50^{o}N-90^{o}N (North Pole) at 17-22 km altitude in the DJF season. Using this metric, the change in temperature gradients for geoBC, geoSulf and geoTiO$_2$ are +10.4, +7, and +10.1 K, respectively; with all experiments indicating a steeper temperature gradient between the tropics and poles. Fig. 4.18 shows the 50hPa DJF geopotential height anomalies over the Arctic for RCP8.5 and

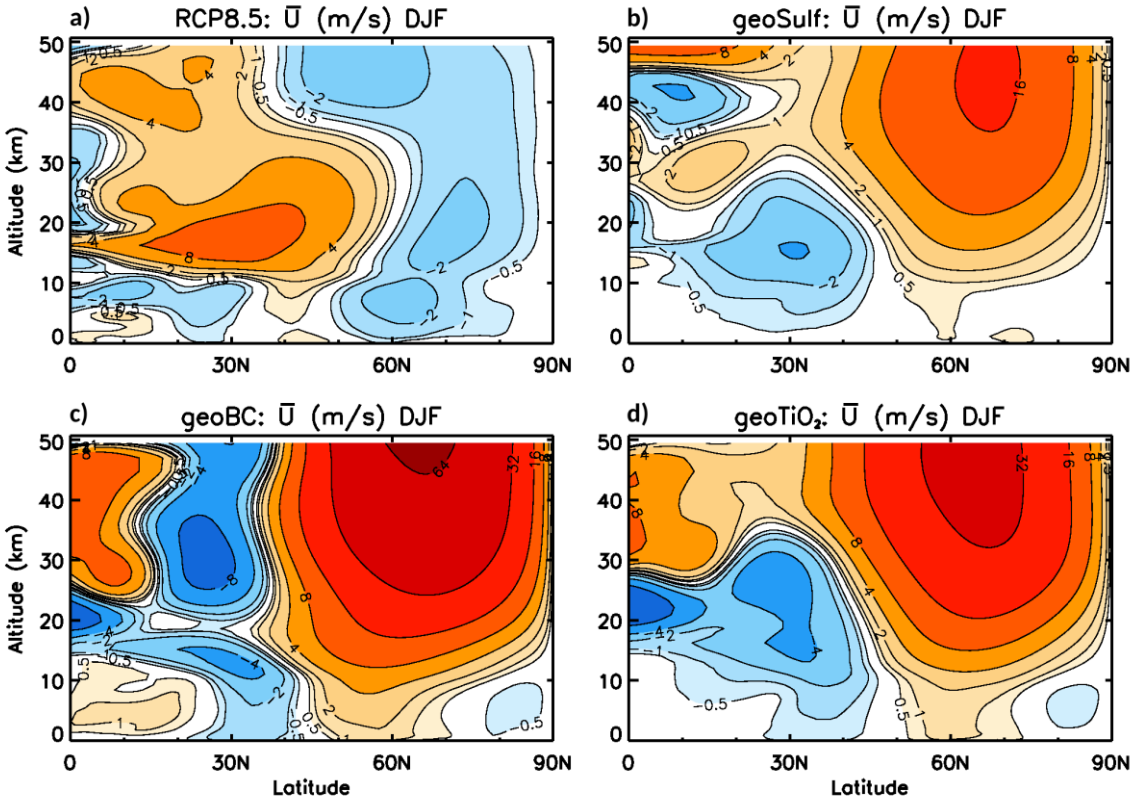

Figure 4.19 DJF zonal-mean zonal wind anomaly relative to HIST

the 3 SAI experiments. The negative geopotential height anomaly centered over the North Pole in all the SAI experiments is indicative of a strengthened polar night jet and a positive Arctic Oscillation phase [Stenchikov *et al.*, 2002]. The DJF zonal-mean zonal-wind anomaly (Fig. 4.19) substantiates our inference of a strengthened polar-night jet under SAI, with increased zonal windspeeds at 65^{o}N and 40 km altitude of 62 m s^{-1}, 17 m s^{-1}, and 37 m s^{-1} for geoBC, geoSulf and geoTiO$_2$ respectively.

The QBO is a periodic change in the equatorial zonal wind pattern in the stratosphere, which fluctuates between easterly and westerly phases [Baldwin *et al.*, 2001]. Aquila *et al.* (2014) showed that radiative heating in the aerosol layer could prolong the westerly phase of the QBO (where the phase is defined at 40 hPa) by enhancing the residual-mean upwelling motion and strengthening the westerly winds. HadGEM2-CCS includes a non-orographic gravity wave scheme that permits the model to internally generate a QBO and is therefore capable of assessing QBO changes [Martin *et al.*, 2011]. The average QBO period for the HIST ensemble is 27 months which agrees closely with observations [e.g. Baldwin *et al.*, 2001]. Figure 4.20 shows the 2090s QBO timeseries for one ensemble member of the RCP8.5 and

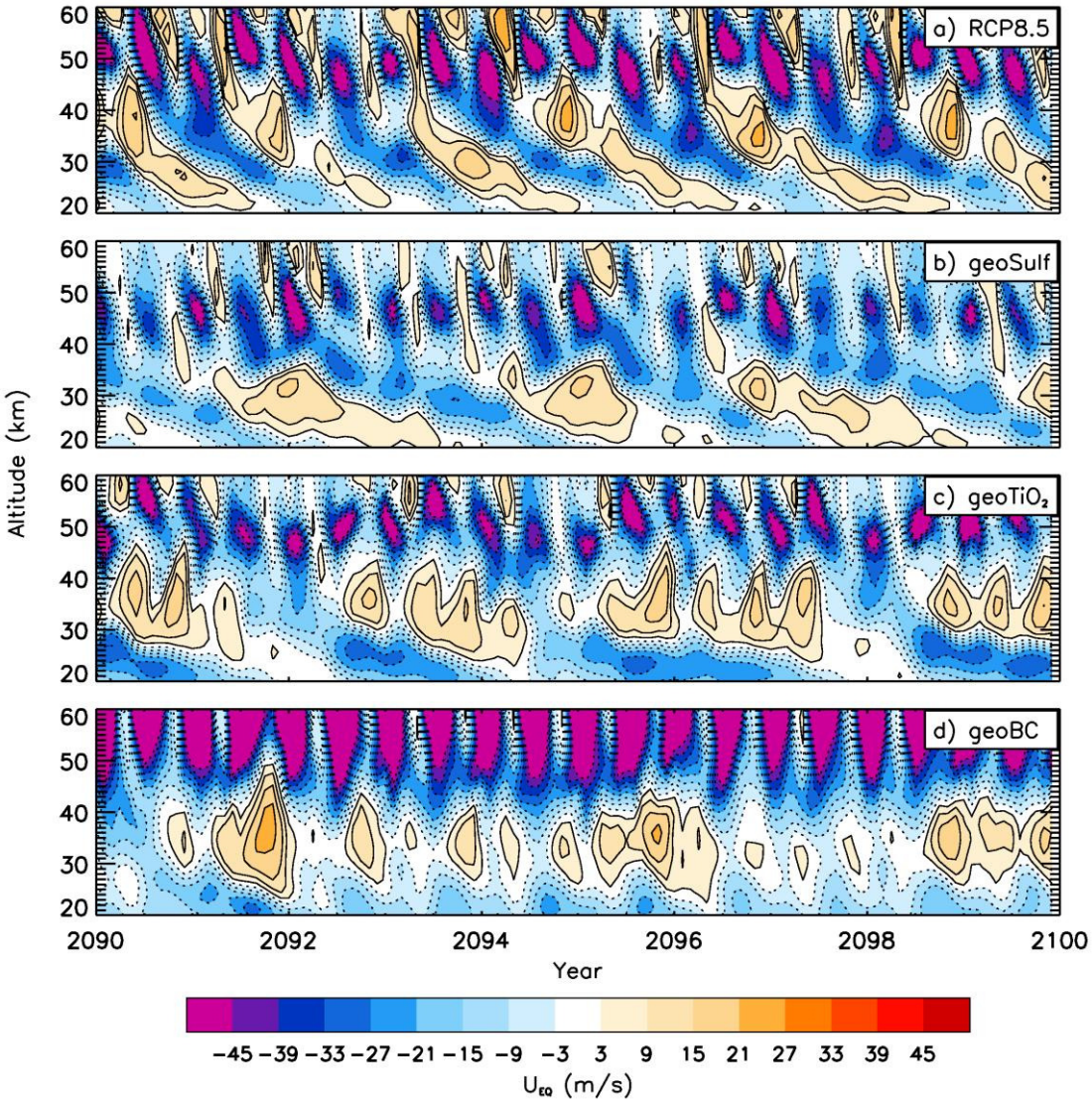

Figure 4.20 Time series of equatorial (5S-5N) zonal-mean zonal wind profile

SAI experiments. The average QBO periods for this time span, which are determined using all 3 ensemble members, are 20 months for RCP8.5, 31 months for geoSulf and 36 months for geoTiO$_2$. For geoBC, no QBO-like oscillation can be detected in the 10-year time span, suggesting a persistent westerly phase such as observed by Aquila *et al.* (2014) in their 5 Tg[SO_2] yr^{-1} injection scenario ($G_5^{22\text{-}25km}$- where '5' indicates the SO_2 injection rate and '22-25 km' indicates the injection altitude). In their HadGEM2-CC simulations, Kawatani and Hamilton (2013) also observed a decline in the QBO period for the RCP8.5 scenario, although they were unable to provide a reason for this. A robust inference from this work is that the magnitude of SAI's impact on stratospheric zonal winds correlates with the magnitude of the stratospheric warming (Fig. 4.17 for temperature, and Figs 4.19, and 4.20 for wind anomalies).

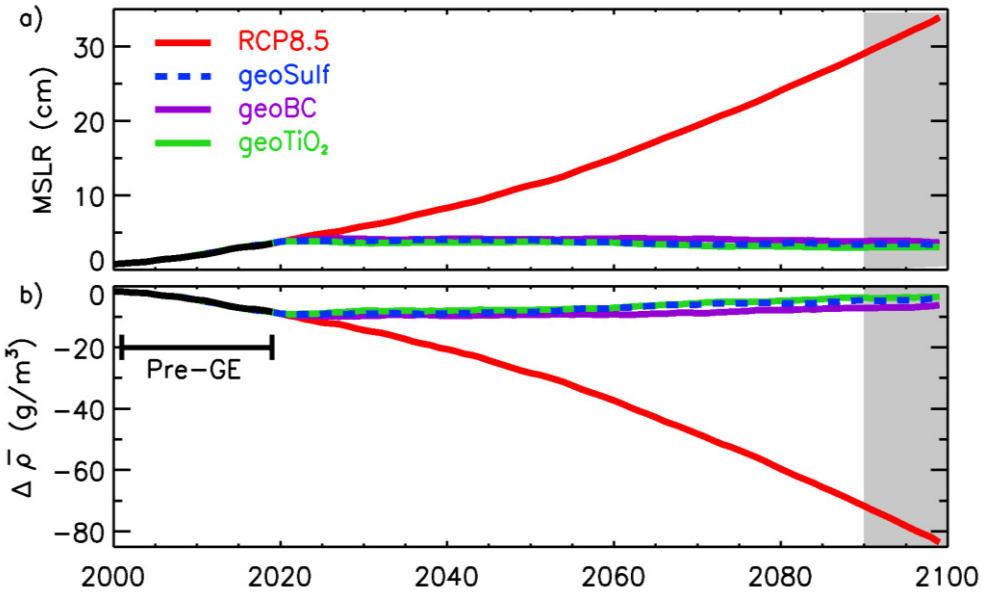

Figure 4.21 Timeseries of thermosteric GMSL rise (i.e. global MSLR), calculated using changes in oceanic temperature and salinity. (a) thermosteric GMSL rise (b) oceanic density anomaly

4.4.5 Sea level and permafrost changes

As noted in Chapter 1, 90 % of the energy accumulated by the Earth system as a result of anthropogenic GHGs has been absorbed by the oceans. As a result, the oceans have warmed and the GMSL has risen in recent decades by +1.1 mm yr^{-1} from thermal expansion alone. Although other processes influence the GMSL, such as ice-sheet and glacial melt and land water storage changes, thermosteric (salinity and temperature related) changes are projected to contribute 30-50 % of the total GMSL rise in the 21st century in all of the RCP scenarios [Church *et al.*, 2013]. It is straightforward to calculate the thermosteric component of GMSL rise using the UNESCO equation, which relates the density of seawater to its temperature and salinity, and then by integrating the density anomalies over the ocean depth [UNESCO, 1981; Gill, 1982]. Figure 4.21 shows the thermosteric GMSL rise for the RCP8.5 and geoengineering simulations and the average change in ocean water density, both relative to the HIST era. The GMSL rise in the RCP8.5 scenario of ~30 cm in 2100 relative to HIST is in close agreement with the CMIP5 ensemble [Fig. 13.10 in Church *et al.*, 2013]. The geoengineering scenarios exhibit an insignificant negative trend in GMSL rise (Fig. 4.21a), which suggests that SAI at a sufficient rate to balance TOA energy fluxes would be effective at counteracting thermosteric sea level rise regardless of the aerosol injected. This is despite geoBC exhibiting a significant Arctic sea-ice increase (Fig. 4.15), although global-mean surface energy

NH permafrost area (10^6 km^2)	NH [180W → 180E, EQ → 90N]	N. America [170W → 25W, 43.5N → 90N]	N. Eurasia [25W → 170W, 43.5N → 90N]	Tibet [65E → 110E, 25N → 43.5N]
HIST 1980-2005	26.44	9.10	15.37	1.97
RCP8.5 2090s	7.97	3.44	4.09	0.44
geoSulf 2090s	25.29	9.03	14.17	2.10
geoTiO_2 2090s	24.92	8.97	13.91	2.03
geoBC 2090s	24.32	8.79	14.31	1.21

Table 4.4 NH total permafrost area (10^6 km^2) for the HIST and 2090s periods

fluxes are effectively stabilised in geoBC despite the sea-ice change (Fig. 4.12). Our results substantiate the findings of Irvine *et al.* (2012) and Moore *et al.* (2010).

Permafrost refers to permanently frozen soil layers found at high latitudes and in mountainous regions [Caesar *et al.*, 2013]. As discussed in Chapter 1, permafrost changes are important for climate due to the large amount of OC stored in the frozen soil which, if emitted to the atmosphere as CH_4 or CO_2, could exacerbate global warming. We assess the terrestrial permafrost changes in these simulations by specifying permafrost-laden gridcells as gridcells in which the deep soil (3 m depth) temperature is below freezing point for 2 consecutive years. As also found by Caesar *et al.* (2013), Koven *et al.* (2013) and Slater and Lawrence (2013), HadGEM2 overestimates the total global permafrost extent (GPE), with a year 2000 value of 26 million km^2 (Fig 4.22) compared to an observed area of ~18 million km^2 [Hugelius *et al.*, 2014]. The HIST permafrost areal extent over the Tibetan plateau (1.97 million km^2) also slightly exceeds the observed extent (~1.6 million km^2 [Ran *et al.*, 2012]).

The GPE in the HIST/RCP8.5 scenario decreases from 27 to 23 million km^2 between 1980 and 2020, and then continues to rapidly diminish to reach 7 million km^2 by year 2100, as also found by Caesar *et al.* (2013). All three geoengineering scenarios exhibit a 10-year GPE rebound following the initiation of aerosol injection (2020-2030), after which GPE is then essentially stabilised at ~25 million km^2 (Fig. 4.22). Figure 4.23 shows the spatial maps of NH permafrost boundaries in the HIST period (thick black lines) and 2090s periods. It is clear that all three SAI scenarios

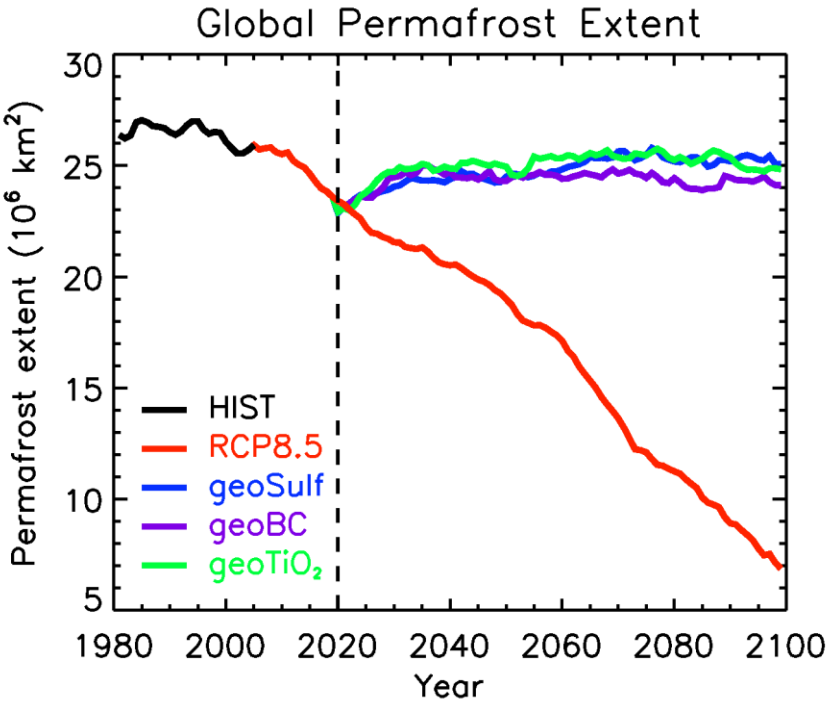

Fig 4.22 Global permafrost areal extent (10^6 km^2) for the ensemble-means of HG2 simulations

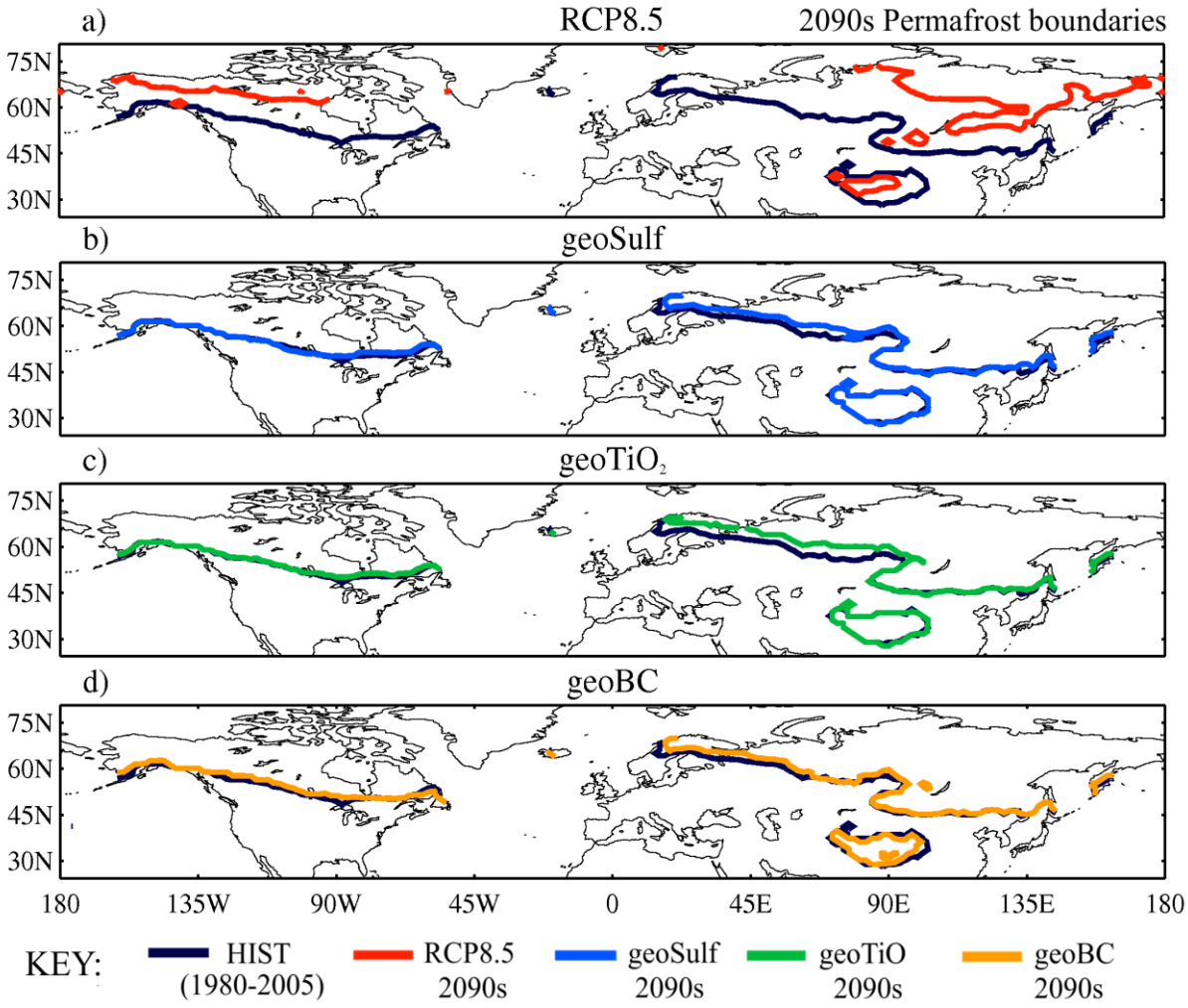

Fig 4.23 Permafrost boundaries for the HIST (1980-2005) and 2090s periods

effectively mitigate changes to the northern circumpolar (latitudes > 43.5N) permafrost boundary. However, the geoBC scenario exhibits a 39 % decrease of permafrost extent over the Tibetan Plateau relative to HIST (Fig 4.23d; Table 4.4). This relates to the residual atmospheric warming at low latitudes in the geoBC scenario (Fig. 4.11c). Conversely, the geoSulf and geoTiO_2 scenarios exhibit permafrost area gains over the Tibetan Plateau of 7 % and 3 % relative to HIST respectively (Table 4.4).

HadGEM2-CCS does not include the permafrost carbon feedback therefore it is prudent to estimate it. Approximately 1300 (+/- 200) GtC of OC is stored in the northern circumpolar permafrost region [Hugelius *et al.*, 2014], while the Tibetan Plateau permafrost contains ~160 (+/- 90) GtC of OC [Mu *et al.*, 2015]. Schneider von Deimling *et al.* (2012) used a GCM coupled to a detailed permafrost model to investigate the PCF for the RCP8.5 scenario. By 2100, they found a 57 % permafrost areal decrease with respect to present day, and cumulative CO_2 and CH_4 emissions over the 21st century from permafrost thawing of +30 [16, 55] and +0.19 [0.07, 0.45] GtC respectively. This can be compared to present day anthropogenic emissions CO_2 and CH_4 emissions of +10 and +0.4 GtC yr^{-1}, respectively. Therefore, it is unlikely that the PCF will significantly alter global-mean temperature by 2100, even in the RCP8.5 scenario [Collins *et al.*, 2013]. As SAI obviates much of the permafrost thawing (Fig. 4.22-4.23), we estimate that it would additionally inhibit the PCF response.

4.5. Summary and Discussion

In this chapter, we have assessed the climatic impacts of SO_4, BC and TiO_2 injection against a baseline RCP8.5 scenario, by comparing the 2090s climate with a simulated historical period. We have shown that, although the distribution of climate changes are similar for the three SAI scenarios, certain changes differ, for instance BC produces a substantially greater stratospheric warming signal with concomitantly greater changes to stratospheric dynamics. The severity of the stratospheric temperature changes effectively excludes BC from being a viable option for geoengineering. Additionally, we have shown that producing an equivalent top of the atmosphere radiative perturbation with a SW-absorbing aerosol such as BC (or to a lesser extent TiO_2) compared to a SW-scattering aerosol such as SO_4, induces

a comparatively greater SW forcing at the surface. Bala *et al.* (2008) showed that reduced latent heat fluxes compensate for the SW reduction at the surface, instigating a deceleration of the hydrological cycle that is proportional to the magnitude of the SW reduction. This explains the comparatively greater precipitation reduction exhibited by geoBC in Figs. 4.11, 4.13, and 4.14. Our results complement Niemeier *et al.* (2013), who showed that a LW-absorbing SO_4 layer would produce a greater hydrological perturbation per TOA SW forcing than a simple solar irradiance reduction scenario. The geoBC scenario displays a greater cooling at high latitudes than the geoSulf and geoTiO_2 scenarios (Figs. 4.11, 4.13, and 4.14), which comparatively exhibit a net tropical cooling. This raises the question of whether a combination of aerosols could potentially be injected to produce a cooling that is uniform with latitude if necessary. Although SAI with SO_4 and TiO_2 effectively maintains the regional distribution of temperature at HIST levels, with a slight residual warming at high latitudes, the hydrological cycle decelerates substantially in all SAI scenarios which is exemplified by a global-mean reduction in precipitation. However, annual-minimum sea-ice extent in both hemispheres and global-mean thermosteric sea-level (Fig. 4.21) are almost entirely maintained at HIST levels for all SAI scenarios.

We find that SO_4 induces less stratospheric warming than TiO_2. In contrast, Ferraro *et al.* (2011) found that the peak stratospheric warming for TiO_2 was approximately a third of that from SO_4. Although the different climatologies, model configurations, and aerosol spatial distributions will contribute to the difference in stratospheric temperature adjustment between our work and Ferraro *et al.* (2011), the primary reason for the disparity is likely to be the aerosol size distributions. Our TiO_2 is smaller (r_m = 0.045 μm compared to 0.1 μm for Ferraro *et al.* (2011)) and therefore scatters and absorbs SW more efficiently, producing a greater localised 'solar' warming. Their SO_4 distribution contains a larger spread (σ = 2.0 for Ferraro *et al.* (2011) compared to σ = 1.25 here), resulting in more coarse-mode particles and greater LW absorption. This disparity highlights the sensitivity of climatic effects to the specified aerosol size distribution. On a separate note, Ferraro *et al.* (2011) neglected to alter the TiO_2 density component in the calculation of their aerosol mass and specific optical properties [A. Ferraro, personal communication]. The density that they used for TiO_2 of 1600 kg m^{-3} is appropriate for SO_4, but should have been

altered to ~4000 kg m^{-3} for TiO_2. Therefore, their TiO_2 aerosol burden should be multiplied by 2.5 to give 7.5 Tg, and their optical coefficients divided by 2.5, to obtain appropriate values.

It is important to note that the climate impacts described in Section 4.4 are dependent on the optical properties of the aerosol, which are further dependent on the aerosol particle's size, shape, and composition [e.g. Kravitz *et al.*, 2012]. In this investigation, the dry-mode size distribution of the aerosol species is held constant and hygroscopic growth is not represented in the BC and TiO_2 schemes (Section 4.2.2), nor are the effects of internal mixing represented. Observations have shown that fresh BC aerosol is predominantly hydrophobic, but the uptake of soluble particulates (e.g. secondary organics) results in increased hygroscopicity [Liu *et al.*, 2013]. Mineral dust, which contains 1-10 % TiO_2 by mass [Ndour *et al.*, 2008], exhibits low hygroscopicity for radii < 0.1 μm and similar growth to equivalently-sized SO_4 aerosol thereafter [Koehler *et al.*, 2009]. Although the historical stratospheric water vapour content is low (~4.2 ppmv in the tropical lower stratosphere during the HIST period), aerosol-induced stratospheric warming in the tropical tropopause layer would increase the specific humidity of air entering the stratosphere, therefore impacting hygroscopic growth. The injection of aerosol into pre-existing aerosol layers would lead to larger particles through coagulation and condensation, which would further alter the aerosol's optical and physical properties. The actual size of the aerosol in an SAI scheme would therefore depend on the injection strategy (e.g. location/ season) and the size and composition of the injected species [e.g. Carslaw and Kärcher, 2006; Heckendorn *et al.*, 2009]. Recent research from Heckendorn *et al.* (2009), Pierce *et al.* (2010), English *et al.* (2012), and Weisenstein *et al.* (2015) have highlighted the importance of representing aerosol growth in SAI simulations. Incorporating aerosol microphysics would result in a better representation of the aerosol's optical properties; this is particularly important for solid aerosols that form chain-like fractals. However, it is also important that the model's climatology is able to respond radiative changes induced by the aerosol. A more detailed assessment would couple a 3D GCM with a detailed aerosol microphysics module, but such experiments over the centennial timescales of this work are computationally expensive. The next-generation Hadley Centre model (UKESM-1) will incorporate the GLOMAP-mode two-moment aerosol module [Mann

et al., 2010] and the UKCA chemistry scheme, which would allow for such an assessment [Morgenstern *et al.*, 2009]. A detailed assessment of the aerosol microphysics for SO_4, BC, and TiO_2 injection is therefore not within the scope of this work, but presents an important subject for future work.

Another interesting aspect of SAI which we have not directly assessed in this work is the impacts to tropospheric climatology once the aerosol is removed from the stratosphere. In particular, we identified SO_4 and aged BC aerosol as being hygroscopic in Section 2.2, and therefore able to act as CCN and form cloud droplets. Additionally, stratospheric SO_4 aerosol is able to nucleate cirrus cloud droplets, such as observed following the Mt Pinatubo eruption [Lohmann *et al.*, 2003], which would enhance LW absorption in the upper atmosphere. Aerosol-cloud interactions are coarsely parameterised by current GCMs such as HadGEM2, and contribute the largest source of uncertainty to past and future climate forcing [Boucher *et al.*, 2013]. Therefore we defer a detailed analysis of the impacts of SAI on cloud properties to a future piece of work with UKESM-1. Nevertheless, it interesting to note from Fig. 4.10 that much of the aerosol deposition from these simulations is over pristine environments (e.g. the open ocean) where marine cloud brightening would be most effective [e.g. Jones and Haywood, 2012].

The climatic impacts described in Section 4.4 are specific to geoengineering against a baseline RCP8.5 scenario. If instead we had used a middle-of-the-road GHG-concentrations scenario such as RCP4.5 [Taylor *et al.*, 2012], as used in the first tier of GeoMIP scenarios [Kravitz *et al.*, 2011], then less aerosol-injection would be needed to obtain TOA-Imb=0 and therefore the aerosol deposition rates and atmospheric mass concentrations would be less than those reported in Section 4.4. One would expect that the magnitude of stratospheric temperature changes (Fig. 4.17) and therefore zonal-mean zonal wind changes (Fig. 4.20) would be much less for each of the aerosols, possibly confounding the conclusions given here relating to their comparative efficacy. An estimate for the amount of SAI required for RCP4.5 can be garnered from integrating the temperature anomalies for RCP8.5 and RCP4.5 for the period 2020-2100. The ratio of the integrated temperature anomalies for RCP4.5 to RCP8.5 is 0.43, hence we can assume that the injection rates required for RCP4.5 are ~0.43 of those for RCP8.5, producing a climate perturbation ~0.43 times as great. A

further set of simulations, which instead utilise RCP4.5 as the baseline scenario, would be required to test this hypothesis.

We have used prescribed O_3 fields in these simulations because representing stratospheric chemistry is prohibitively computationally expensive for the multiple centennial simulations performed here [Martins *et al.*, 2011]. Kravitz *et al.* (2012) showed in their SmR scenario that BC injection could potentially result in global O_3 depletion of >50 %, therefore the chemistry changes in SAI could potentially exceed the importance of the physical changes in terms of climatic impacts (e.g. UV radiation at the surface). Tilmes *et al.* (2012) showed that SW scattering by geoengineered SO_4 could potentially compensate for O_3 loss by back-scattering UV radiation in the tropics, but that this effect was insufficiently compensatory at high latitudes. Their result was scenario-dependent; O_3 loss due to heterogeneous chemistry is enhanced for smaller particles and in the presence of higher free-radical concentrations. Therefore, additional research is needed in order to understand the effects on atmospheric chemistry of injecting alternative aerosols. This work has already been started for TiO_2 by Tang *et al.* (2014).

Another important aspect of SAI which is comparatively under-researched is the potential for impacts on human health. Aerosol concentrations in the air near the surface are of interest because of potential human respiratory impacts [Robock, 2008]. For instance, the USA's National Institute for Occupational Safety and Health (NIOSH) recommends maximum exposure limits of 0.3 mg m^{-3} for ultrafine TiO_2 particles (radius <0.05 μm) and 2.4 mg m^{-3} for fine particles (radius < 1.5 μm) [Dankovic *et al.*, 2011]. After undergoing coagulation and ageing in the atmosphere, it is likely that the second exposure limit is more applicable to this work. In our simulations, the maximum 2090's near-surface air concentration of TiO_2 (e.g. Fig. 4.8) for land regions between 60^oS-60^oN is 254 ng m^{-3}, which is of the order of 10^2 less than the NIOSH 'fine-particle' exposure limit. The equivalent maximum concentration anomalies of BC in geoBC and SO_4 in geoSulf are 10 ng m^{-3} and 1851 ng m^{-3} respectively. More work is needed to assess the potential impacts of SAI on air quality and human health.

Another thus far unmentioned aspect of this research is the potential for surface albedo modification by aerosol deposition. In particular, BC deposition on snow

reduces the snow albedo through enhanced snow-melt and the coarsening of snow grains, which results in amplified high-latitude warming [Marks and King, 2013]. HadGEM2-CCS does not include the BC-on-snow feedback; therefore we estimate it by comparing the deposition rates for 2090s geoBC with the historical period. Jiao *et al.* (2014) report that the simulated annual-mean Arctic (>60^{o}N) BC deposition for the 2006-2009 period ranges from 13-35 $\times 10^{7}$ kg yr^{-1} for the AEROCOM Phase II models. The annual-mean Arctic BC deposition for the 2006-2009 period from our HadGEM2-CCS simulations is 23×10^{7} kg yr^{-1}, which is within the AEROCOM range. The annual-mean Arctic BC deposition anomaly for the 2090s period in geoBC is 19.6×10^{7} kg yr^{-1}. Therefore, the effects of dirty snow in such an SAI scenario would likely be significant, which would have impacts on the distribution of temperature, particularly at high latitudes, potentially confounding some of our conclusions. Although we have emphasized this issue with respect to BC, it is important to note that any particle that absorbs SW radiation will instil this forcing. Therefore TiO_2, which has a non-unitary single scattering albedo at short wavelengths, will also cause snow-grain coarsening and snow-melt by absorbing solar radiation and warming the top layer of the snow pack.

This research has highlighted potential climate impacts of injecting various stratospheric aerosols in order to ameliorate global warming. However, additional research is needed to further assess the climatic impacts of stratospheric aerosol injection such as the impacts on O_3. Whilst research indicates that SAI is capable of averting certain climate changes such as surface-warming, SAI provides no amelioration for other climate impacts, such as ocean acidification. It is therefore important to note that the safest possible solution to avoiding the sort of climate change instantiated by (e.g.) Fig. 4.11a of this thesis is to effectively mitigate GHG emissions.

Chapter 5 Sensitivity of volcanic aerosol dispersion to meteorological conditions: A Pinatubo case study*

5.1. Introduction

In Chapter 4 we used HadGEM2-CCS to investigate the climatic impacts of SAI. It is important to note that the conception of SAI as a geoengineering proposal was motivated by large-scale volcanic eruptions [Budyko, 1977]. As a precursor to the SAI simulations performed for Chapter 4, we simulated the 1991 Pinatubo eruption to validate HadGEM2-CCS's aerosol transport module (Section 4.3.1). An interesting result of these simulations was the high variability of the AOD exhibited by the 10-member 1-day eruption simulations (Fig. 4.4). In this chapter, we assess the sensitivity of volcanic aerosol dispersion to ambient meteorological conditions by simulating Pinatubo-like eruption scenarios.

5.2. The 1991 Mt. Pinatubo eruption

After weeks of precursory activity, Mt. Pinatubo in the Philippines (15^{o}N, 121^{o}E) erupted on 15th June 1991 in a volcanic episode that lasted ~9 hours starting at 14:00 (local time), although 90% of the total magmatic injecta was emitted in an intense phase that lasted ~3 hours [Holasek *et al.*, 1996, Guo *et al.*, 2004; Self *et al.*, 2004]. The Pinatubo eruption was significant for multiple reasons. It was the first major volcanic eruption to be comprehensively documented by satellite instruments, lidars and airborne aerosol counters [McCormick *et al.*, 1995]; it likely produced the greatest volume of volcanic material injected into the atmosphere of any 20th century eruption [Bluth *et al.*, 1992; Robock, 2000]; and it had a broad climatic influence that would prove a vital validation tool for the burgeoning GCM development community. The Pinatubo eruption induced a global-mean lower-tropospheric cooling of 0.3^{o}C (averaged over the subsequent 4 years) [Soden *et al.*, 2002]; enhanced O_3 reaction

*This chapter is based on the following publication, a copy of which is provided in Appendix 2.

Jones, A. C., J. M. Haywood, A. Jones, and V. Aquila (2016b), Sensitivity of volcanic aerosol dispersion to meteorological conditions: A Pinatubo case study, *J. Geophys. Res. Atmos.*, 121, 6892–6908, doi:10.1002/2016JD025001.

catalysis for 1-2 years [Hofmann *et al.*, 1992; McCormick *et al.*, 1995]; disrupted the hydrological cycle [Spencer *et al.*, 1998; Trenberth and Dai, 2007]; induced a tropical stratospheric warming [Labitzke and McCormick, 1992]; and instigated a wealth of other climatic perturbations [e.g. McCormick *et al.*, 1995; Robock, 2000].

The primary driver of these climatic impacts was the volcanic aerosol that resided in the stratosphere for multiple years and influenced both the incoming SW radiation and outgoing LW radiation [Stenchikov *et al.*, 1998]. This aerosol plume was primarily composed of SO_4 in the form of liquid H_2SO_4 droplets (60-80 % by mass) in aqueous solution, formed from the oxidation of gaseous SO_2 which was oxidised to SO_4 with an e-folding time of ~35 days [Bluth *et al*., 1992]. Heavier constituents of the initial plume such as ash were removed from the atmosphere within weeks and therefore provided a short-term, localised climatic forcing [Russell *et al.*, 1996; Niemeier *et al.*, 2009]. Early observations from the Total Ozone Mapping Spectrometer (TOMS) instrument suggested that Pinatubo emitted ~20 Tg of SO_2 [Bluth *et al*., 1992], although a later, revised estimate suggested 14-23 Tg [Guo *et al.*, 2004]. Recent Pinatubo simulations with models that incorporate aerosol microphysics suggest that an SO_2 emission of nearer 14 Tg produces better agreement with observations [Sheng *et al.*, 2015b].

The evolution of the aerosol cloud was observed by the Advanced very-high-resolution radiometer (AVHRR) and Stratospheric Aerosol and Gas Experiment version 2 (SAGE II) satellite-borne instruments [Stowe *et al.*, 1992; McCormick and Veiga, 1992]. After the eruption, the aerosol plume was rapidly transported westward via zonal stratospheric winds and encircled Earth within 22 days [Bluth *et al.*, 1992]. Additionally, the aerosol cloud was initially advected both northward and southward, crossing the equator within 1 week [Young *et al*., 1994]. Subsequent meridional transport was impeded by the “leaky tropical pipe” – a sharp latitudinal potential vorticity gradient in the subtropical stratosphere – and later by the strong polar night jet in the SH [Boville *et al.*, 1991]. For the first couple of months after the eruption, the aerosol cloud was primarily confined to the tropical stratosphere (20^oS-30^oN), within altitudes of 20-30 km [McCormick *et al.*, 1995]. The contemporaneous descending easterly-shear phase of the QBO, coupled with a strong lower-stratospheric meridional wind gradient in the subtropics, contributed to the initial confinement of the aerosol to the tropics [Trepte and Hitchman, 1992; Trepte *et al.*,

1993; Choi *et al.*, 1998]. By July 1991, aerosol in the lower stratosphere (~16 km/ 100 hPa altitude) had been transported to high NH latitudes (>50^{o}N), primarily through advection by a tropospheric quasi-stationary anticyclone over Asia [McCormick *et al.*, 1995; Trepte *et al.*, 1993; Timmreck *et al.*, 1999b]. Additionally, aerosol was later transported to the NH at higher altitudes (~25 km/ 30 hPa altitude) in the months following the shift from summer to winter stratospheric dynamics in October 1991 [Trepte *et al.*, 1993]. Significant aerosol transport into the SH occurred during September 1991 in the high altitude regime (~22 km/ 40 hPa altitude), primarily as the result of transient subtropical anticyclones [Trepte *et al.*, 1993]. The global sulphate cloud decayed exponentially with an e-folding time of ~1-2 years [Kirchner *et al.*, 1999; Driscoll *et al.*, 2012].

Various GCMs have been used to simulate the dispersal of the Pinatubo aerosol cloud. Early experiments treated the aerosol as a passive tracer, which disregards the radiative feedbacks of the aerosol [Boville *et al.*, 1991; Pudykiewicz and Dastoor, 1995; Timmreck *et al.*, 1999b]. Young *et al.* (1994) combined a 3D circulation model with an aerosol transport/radiation code to show the importance of including the radiative feedbacks on the resultant dispersion of the aerosol. Timmreck *et al.* (1999a) showed that the stratospheric dynamical adjustments from aerosol-induced radiative heating could induce a strengthening of the polar vortex, in agreement with observations from 1991/1992 [e.g. Robock and Mao, 1995]. However, the simulated tropical aerosol reservoir in Timmreck *et al.* (1999a) was short-lived compared with observations, which the authors attributed to the absence of a QBO in their GCM. The QBO is a periodic oscillation of the equatorial, stratospheric zonal-mean zonal-wind direction at ~40 hPa altitude [Baldwin *et al.*, 2001]. Pinatubo simulations with GCMs that do not include a QBO have generally exhibited a short-lived tropical aerosol reservoir [Oman *et al.*, 2006b; Niemeier *et al.*, 2009; Toohey *et al.*, 2011]. Niemeier *et al.* (2009) coupled an aerosol microphysics module with a GCM to show that radiative heating induced by the short-lived ash ejected by Pinatubo could alter the initial trajectory of the sulphate plume. Toohey *et al.* (2011) showed that the Pinatubo AOD evolution is sensitive to the season of eruption (particularly in the NH), which they attributed to the state of the BDC in the stratosphere. Aquila *et al.* (2012) (hereafter, *AQ12*) simulated Pinatubo using the GEOS-5 GCM, which included a single-moment sulphate-transport scheme and radiatively-interactive

aerosol, but no QBO representation. They injected 20 Tg[SO_2] at the comparatively low altitudes of 16-18 km over a single day in 8 consecutive '15th Junes' and with perpetual year-2000 conditions. The low-altitude specification was selected because sensitivity tests with high-altitude eruptions (16-25, 17-27, 20-27, 20-30 km) had elevated the aerosol to altitudes that exceeded observations [e.g. McCormick and Veiga, 1992]. Their ensemble-mean 550nm AOD evolution (Fig. 2 of *AQ12*) compared well to AVHRR and SAGE II observations. English *et al.* (2013) coupled a 3D sectional aerosol model to a GCM to study the linearity of atmospheric aerosol burdens to increasing levels of SO_2 emissions, finding a non-linear relationship due to enhanced aerosol growth and sedimentation. To compensate for the omission of radiatively-interactive aerosol and a QBO, English *et al.* (2013) injected over a wide-area (2^{o}S-14^{o}N, 95^{o}E-115^{o}E) and vertical span (15-29 km altitude), a technique also utilised by Timmreck *et al.* (1999a), Weisenstein *et al.* (2007), and Dhomse *et al.* (2014). This 'wide-injection' method sidesteps the necessary radiatively-induced dynamical changes required to transport the aerosol southward and upward [*AQ12*]. Dhomse *et al.* (2014) used a detailed aerosol microphysics module coupled to a GCM with an internally-generated QBO, to show that a simulated 10 Tg[SO_2] Pinatubo-like eruption produced aerosol size distributions that matched observations better than the ubiquitously utilised 20 Tg[SO_2] emission rate. Mills *et al.* (2016) also found that a 10 Tg[SO_2] injection produced the best fit to Pinatubo observations, while Sheng *et al.* (2015b) found that 14 Tg[SO_2] produced the best fit. However, climate models are imperfect tools for inferring the quantity of SO_2 emitted by a volcanic eruption due to scenario-based uncertainties such as the altitude and composition of the volcanic plume; model-specific limitations such as coarse spatiotemporal resolutions and parameterised processes; missing processes such as the co-injection of volcanic ash, and internal variability such as meteorological conditions.

A previously unexplored aspect of the Pinatubo eruption is the role of meteorology in the evolution of the aerosol plume; although the ensemble standard-deviations in Fig. 1 and Fig. 3 of *AQ12* and Figs 5d,e,f of Toohey *et al.* (2011) suggest a high meteorological sensitivity in previous simulations. The spread of the aerosol plume has implications for the climatic impacts of volcanic eruptions. For instance, Haywood *et al.* (2013) showed that enhancement of the stratospheric sulphate

burden in a single hemisphere could alter the position of the ITCZ and associated monsoon precipitation. The aim of this investigation is to explicitly assess the sensitivity of the Pinatubo aerosol dispersion to the ambient meteorology. Additionally, we compare the aerosol dispersion from a 10-day eruption to the ensemble-mean of ten 1-day eruptions, which represent two intuitive methods of overcoming meteorological variability whilst simulating a volcanic eruption. In Section 5.3 we describe the GCM (HadGEM2-CCS) used for this investigation and the Pinatubo simulation suite. In Section 5.4.1 we compare the global-mean sulphate optical depth anomalies for the Pinatubo simulations to observations. In Section 5.4.2 we compare the aerosol dispersion for the ensemble-mean of the 1-day eruptions with the 10-day eruption. In Section 5.4.3 we compare the aerosol dispersion for individual 1-day eruption simulations to assess the importance of meteorology. We discuss the significance of our results in the context of potential climatic impacts of future volcanic eruptions and future GCM Pinatubo simulations in Section 5.5.

5.3. Method

5.3.1. Model specifications

For this work, we use the HadGEM2-CCS GCM in atmosphere-only mode with prescribed climatological sea-surface temperature and sea-ice fields. We use perpetual piControl baseline conditions derived from CMIP5 specifications [Jones *et al.*, 2011; Taylor *et al.*, 2012]. This includes prescribed O_3 fields following Cionni *et al.* (2011) and fixed atmospheric concentrations of CO_2, CH_4, and N_2O. Except for the process of CH_4 oxidation, HadGEM2-CCS does not include stratospheric chemistry, but does include a well-resolved stratosphere capable of internally generating a realistic QBO [Hardiman *et al.*, 2012; Watson and Gray, 2014]. The internal QBO is forced by parameterised orographic and non-orographic gravity wave drag schemes [Martin *et al.*, 2011]. HadGEM2-CCS has been used for assessing the impacts of climate change on the stratospheric polar vortex strength [Mitchell *et al.*, 2012], the climatic impacts of stratospheric geoengineering schemes [Jackson *et al.*, 2015; Jones *et al.*, 2016a], and the influence of solar variability on surface climate [Gray *et al.*, 2013]. Additionally, Haywood *et al.* (2010) simulated the 2008 Sarychev volcanic eruption with an atmosphere-only configuration of

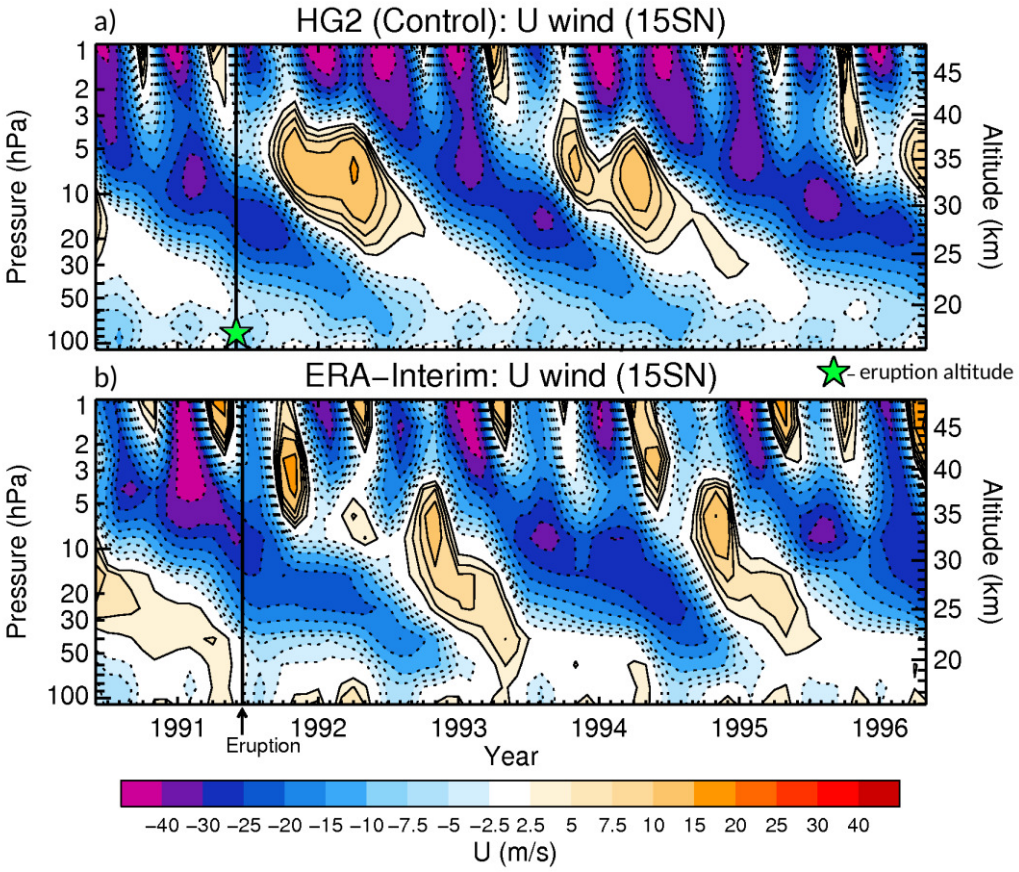

Figure 5.1. Zonal-mean zonal-wind during the Pinatubo-eruption era for a) the HadGEM2-CCS control simulation, b) ERA-I reanalysis data [Dee et al., 2011]

HadGEM2-CCS (as used here). Haywood *et al.* (2010) found that the simulated SO_2 dispersion closely resembled Infrared Atmospheric Sounding Interferometer (IASI) observations and the SO_4 showed reasonable agreement with that derived from the Optical Spectrograph and Infrared Imager System (OSIRIS) limb-sounding instrument.

We discussed HadGEM2-CCS's aerosol scheme in Section 4.2. As in Chapter 4, CLASSIC's sulphate accumulation mode is modified for this investigation in order to reflect the larger aerosols observed after volcanic eruptions [Russell *et al.*, 1996]. The modified accumulation mode is represented by a lognormal distribution with geometric mean radius of r_m = 0.376 μm and standard deviation of σ = 1.25 [Rasch *et al.*, 2008a], with the corresponding optical properties shown in Fig. 4.2a. This size distribution is applied throughout the atmosphere, which will have some influence on the tropospheric sulphur cycle and the associated aerosol-radiation and aerosol-cloud interactions. For instance, increasing the size of particles in the accumulation mode will enhance the rate of coagulation (transferring more mass from the Aitken to accumulation mode), which will concomitantly accelerate wet deposition from the

Name	Injection height (km)	Duration of eruption	Total SO_2 emitted (Tg)	Ensemble members	Ensemble-mean name
CONTROL	N/A	N/A	N/A	1	N/A
10D_HIGH	19-29	10 days	14	1	N/A
1D_HIGH	19-29	1 day	14	10	1D_HIGH_AV
10D_LOW	16-18	10 days	20	1	N/A
1D_LOW	16-18	1 day	20	10	1D_LOW_AV
1D_LOW+CH	16-18 (P) 11-16 (CH)	1 day (P) 8 hours (CH)	20 (P) 3.3 (CH)	2	N/A
3H_LOW	16-18	3 hours	20	10	3H_LOW_AV

Table 5.1. List of experiments. For the 1D_LOW+CH simulations, 'P' refers to Pinatubo and 'CH' refers to Cerro Hudson

boundary layer (Section 4.2.1). By prescribing a fixed radius, the model is unable to accurately represent the physical and optical properties of the evolving aerosol size distribution within the aerosol plume [Dhomse *et al.*, 2014]. The dry-mode effective radius of this distribution (0.42 μm) is similar to the peak effective radius between 1 to 200 hPa from the Pinatubo simulations of English *et al.* (2013). The model's radiation scheme [Edwards and Slingo, 1996] is coupled to the dynamics, allowing for radiatively-induced aerosol self-lofting [Young *et al.*, 1994].

5.3.2. Pinatubo simulation design

A 40-year piControl simulation was initially conducted, from which we selected a model-year in which the simulated QBO in June resembled the Pinatubo-concurrent QBO conditions. Specifically, Mt. Pinatubo erupted in June 1991, at which time the QBO had entered an easterly phase 2 months previously [Hansen *et al.*, 1992]. Trepte *et al.* (1993) showed that the transport of aerosol after large tropical volcanic eruptions is highly sensitive to the contemporaneous QBO phase. A time-series of our simulated QBO compared with the ERA-I re-analyses for the Pinatubo period is shown in Fig. 5.1. Our Pinatubo simulations were initiated from June in the selected model-year (time/altitude indicated in Fig. 5.1 by a green star). We performed a single control simulation with no additional SO_2 emission, a single simulation with a continuous 10-day eruption (*10D*) in which SO_2 is emitted evenly between 1^{st}-10^{th} June, ten simulations with 1-day eruptions (*1D*) in which SO_2 is emitted evenly over

a 24-hour period on 1st, ..., 10th June, and ten simulations with 3-hour eruptions (*3H*) in which SO_2 is emitted evenly over a 3-hour period from 14:00-17:00 on 1st, ..., 10th June. The *1D* scenario was chosen following the simulation design of *AQ12*. However, as 90 % of the total mass injected by Pinatubo on June 15th occurred during a ~3 hour phase from 14:00-17:00 [Holasek *et al.*, 1996, Self *et al.*, 2004], we also examine any differences that may occur when representing Pinatubo emissions with a 3-hour eruption. For each of the Pinatubo simulations, SO_2 is injected into a single horizontal grid-cell at (15°N, 120°E). We test two Pinatubo-like eruption scenarios that have been used in the literature. Firstly, we adopt a similar eruption design to *AQ12*, in which 20 Tg[SO_2] is injected evenly between 16-18 km (100-70 hPa) altitude (2 vertical model-levels), and denote these experiments *LOW*. Secondly, we adopt a similar eruption design to Dhomse *et al.* (2014) and inject 14 Tg[SO_2] evenly between 19-29 km (65-15 hPa) altitude (9 vertical model-levels), and denote these experiments *HIGH*. The *HIGH* scenario differs slightly from Dhomse *et al.* (2014) who injected 10 and 20 Tg[SO_2] between 19-27 km altitude. Sheng *et al.* (2015b) found that 14 Tg[SO_2] injection at high altitudes produces a close match to observations. The experiments are listed in Table 5.1. Although the simulated climatology is 'perpetual piControl', we use the equivalent Pinatubo year for plotting/references to facilitate comparison with observations.

5.4. Results

5.4.1. Global-mean sulphate optical depth

The primary climatological field assessed in this research is the 550 nm sulphate AOD, which was diagnosed in the aftermath of the Pinatubo eruption by the AVHRR and SAGE II satellite-borne instruments, albeit at slightly different wavelengths of 630 nm and 525 nm respectively [Stowe *et al.*, 1992; McCormick and Veiga, 1992]. Figure 5.2 shows the monthly-mean 550nm AOD anomaly, averaged between 75°S-75°N, for the HadGEM2-CCS (HG2) *1D* and *10D* simulations and the AVHRR and SAGE II observations. This plot is similar to Fig. 4.4a in Chapter 4, but differs for the SAGE II and AVHRR observations as we have chosen to use updated datasets for this investigation. AVHRR data is only collected over the cloud-free global oceans and is based on the updated dataset of Zhao *et al.* (2013). For SAGE II, we use the updated gap-filled aerosol-extinction climatology developed for Chemistry-Climate

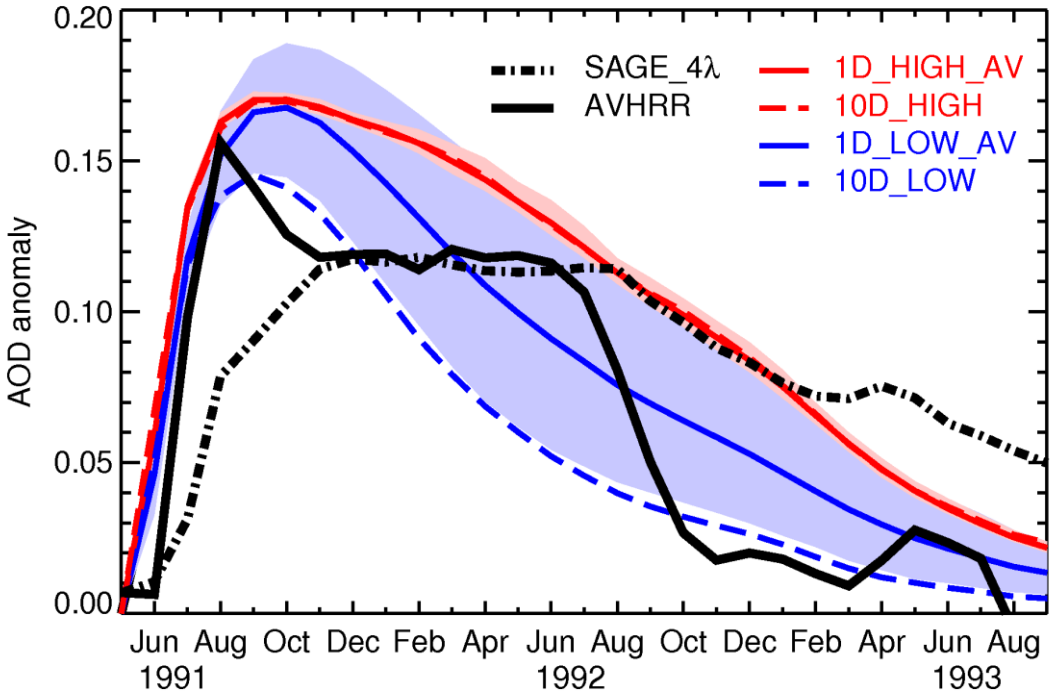

Figure 5.2. 75°S-75°N mean sulphate 550nm AOD anomaly for the HadGEM2-CCS simulations and SAGE II (black, thick) and AVHHR (black, dashed) observations. The blue shaded area shows the range of the 1D_LOW ensemble, the light-red shaded area shows the range of the 1D_HIGH ensemble

Model Initiative (CCMI) simulations based on the SAGE_4λ method [Arfeuille *et al.*, 2013]. The SAGE_4λ dataset uses observations from the Cryogenic Limb Array Etalon Spectrometer (CLAES) and Halogen Occultation Experiment (HALOE) instruments when SAGE II data is unavailable [L. Thomason, personal communication, 2016]. To retrieve SAGE_4λ AODs, we integrate aerosol extinctions above the tropopause height, where the tropopause is derived from our HG2 simulations as in Mills *et al.* (2016). For AVHRR, we subtract the monthly-mean AODs from the year 1990 to calculate anomalies, which was the approach used by *AQ12* and Mills *et al.* (2016). For HG2, we subtract the parallel AOD of the *CONTROL* simulation to calculate anomalies. The blue and orange shaded areas in Fig. 5.2 show the range for the *1D_LOW* and *1D_HIGH* experiments, respectively. From Fig. 5.2, it is clear that both the *1D_LOW_AV* and the *1D_HIGH_AV* AODs are initially in close agreement with the AVHRR values, with a peak in October 1991 of ~0.17 and exponential decline thereafter. As discussed by multiple authors, SAGE II was unable to capture the peak AOD for the first few months after Pinatubo due to saturation at AODs > 0.15 [Russell *et al.*, 1996]. Despite the integration of CLAES

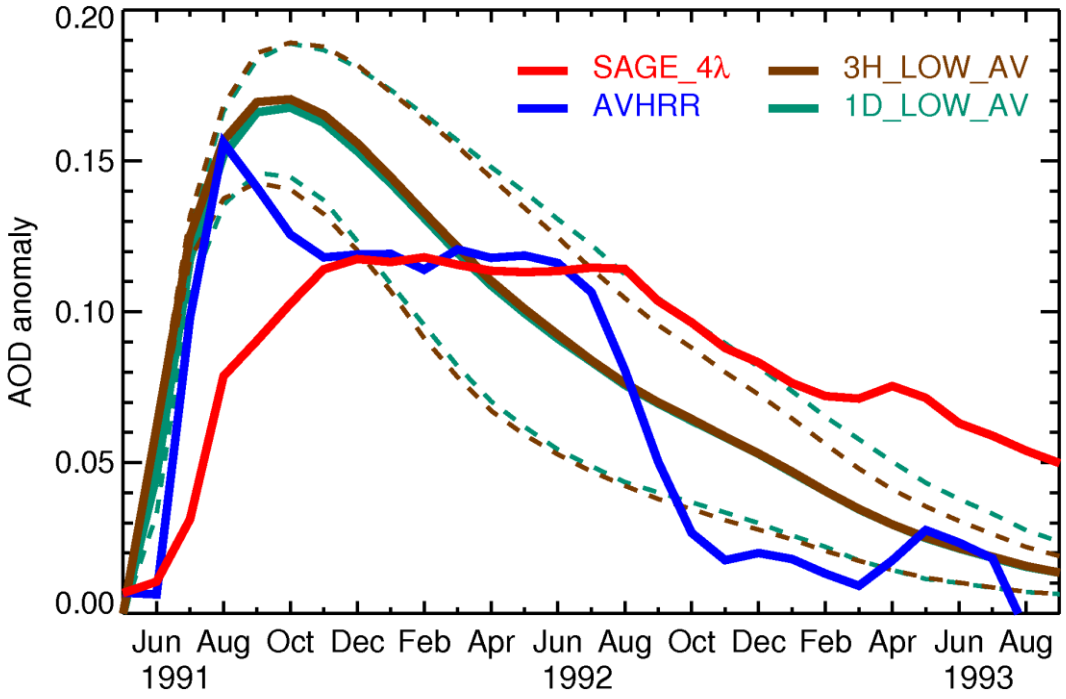

Figure 5.3. 75°S-75°N mean sulphate 550nm AOD anomaly for the 3H_LOW_AV ensemble-mean (brown) and 1D_LOW_AV ensemble-mean (green) and observations. Dashed lines indicate the range of the ensemble

data with SAGE II data to overcome this saturation issue [L. Thomason, personal communication, 2016]; the updated SAGE_4λ dataset is still unable to capture the peak aerosol extinctions in the immediate aftermath of the eruption. However, the greater coverage of the SAGE II observations and the instrument's ability to detect lower AODs than AVHRR (< 0.02) [Stowe *et al.*, 1992] make it useful for later AOD values. In particular, from January 1992 the aerosol plume had diminished sufficiently for SAGE_4λ and AVHRR AODs to be similar on the global-mean scale (Fig. 5.2). A few aspects of the HG2 AODs in Fig. 5.2 are salient: (1) *10D_LOW* is significantly less than *1D_LOW_AV* and peaks in September 1991 at ~0.145 rather than October 1991 with a peak of ~0.17; (2) the *1D_LOW* ensemble spread is broad, for instance, the maximum AOD in April 1992 is ~0.15 compared a minimum of ~0.065; (3) the *1D_HIGH* ensemble spread is small, suggesting that the aerosol dispersion after a high-altitude SO_2 emission would be less sensitive to the ambient meteorology.

Figure 5.3 compares the global 550 nm sulphate AOD anomaly for the *3H_LOW* and *1D_LOW* simulations. It is clear that the 3-hour and 1-day eruptions produce very similar AODs, both in terms of ensemble-mean and the ensemble-range. This result

could be an artefact of our model; a better representation of the aerosol microphysics within the evolving aerosol plume might yield greater differences between the 3-hour and 24-hour eruptions scenarios than shown here due to differing feedbacks between the aerosol and the meteorology. However, for the basis of this investigation and due to the similarity between the AOD evolutions, we present results from the aerosol dispersion from the *1D_LOW* simulations instead of the *3H_LOW* simulations for consistency with *AQ12*.

5.4.2. 10-day eruption against 1-day eruption ensemble-mean

Figure 5.4 shows the time-series of zonal-mean AOD anomaly for the *10D* experiments and the ensemble-means of the *1D* experiments, and for SAGE_4λ and AVHRR observations. For the HG2 experiments, we use the zonal-mean AOD over oceans from 05/91-12/91 for best comparison with AVHRR. The R^2 values given in Fig. 5.4 for the HG2 AOD fields are calculated with respect to AVHRR from July – December 1991 and SAGE_4λ thereafter. R^2, the coefficient of determination, describes the proportion of the variance in the observations that can be explained by the model (ranging from 0 to 1, with higher values indicating better agreement) [Legates and McCabe, 1999]. Note that Figs 5.4d,e,f are almost identical to Figs 4.4b,c,d, except that we have used the updated AVHRR and SAGE II datasets in this section. While *1D_LOW_AV* captures the transport of aerosol into the SH as observed by SAGE II and AVHRR, the *10D_LOW* volcanic aerosol is entirely confined to the NH. It is clear from the R^2 values that *1D_LOW_AV* describes slightly more of the variability in the observations than *1D_HIGH_AV* (R^2 of 0.31 compared to 0.27), and that *1D_LOW_AV* is a much better fit to the observations than *10D_LOW*. The difference in AOD in the SH between *1D_LOW_AV* and the observations is partially attributable to the Cerro Hudson eruption in August 1991 at (46^{o}S, 73^{o}W) which injected 3.3 Tg[SO_2] into the stratosphere [Deshler and Anderson-Sprecher, 2006] and is not represented in these simulations. The Cerro Hudson aerosol was able to penetrate deep into the SH immediately (because of the volcano's location), whilst the Pinatubo aerosol was contemporaneously confined to the tropical vortex [McCormick *et al.*, 1995; Legrand and Wagenback, 1999]. We chose not to represent the Cerro Hudson eruption in these simulations as the primary purpose is to investigate the influence of meteorological variability on the evolution of the plume from Pinatubo from HG2. By omitting representation of Cerro

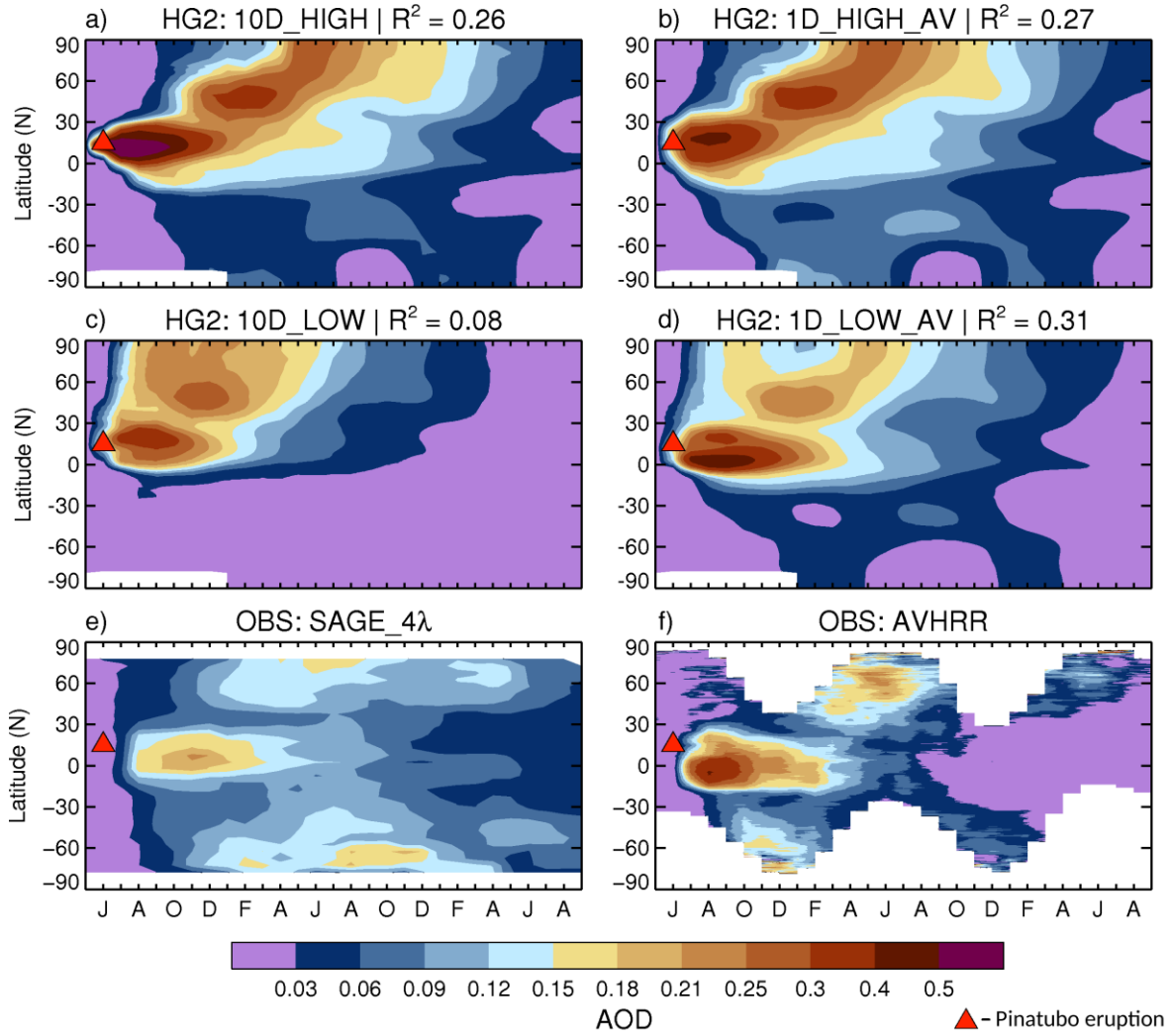

Figure 5.4. Latitude vs time plot of monthly/zonal-mean sulphate 550nm AOD anomaly for a) 10D_HIGH, b) 1D_HIGH_AV, c) 10D_LOW, d) 1D_LOW_AV, e) SAGE II, f) AVHRR. Red triangles indicate the Pinatubo eruption

Hudson, a 'perfect' Pinatubo simulation would not produce R^2 = 1, because the AVHRR/ SAGE_4λ observations also include the Cerro Hudson aerosol. Therefore R^2 as used in Fig. 5.4 only provides an approximate measure of "goodness of fit" between the model and observations.

Figure 5.5 shows the equatorial SO_2 concentration anomaly plotted against altitude in September 1991 for *10D_HIGH*, *1D_HIGH_AV*, *10D_LOW*, and *1D_LOW_AV*. Observations from the Microwave Limb Sounder (MLS) [Read *et al.*, 1993] are indicated by black circles in Fig. 5.5. It is clear that *1D_LOW_AV* best captures the peak of the SO_2 plume as observed by the MLS at ~22 hPa altitude. However, *1D_LOW_AV* overestimates the SO_2 concentrations at ~50 hPa compared to the MLS observations, which could be due to SO_2 removal processes that are not represented in the model such as deposition on ash or ice, or it could be due to the

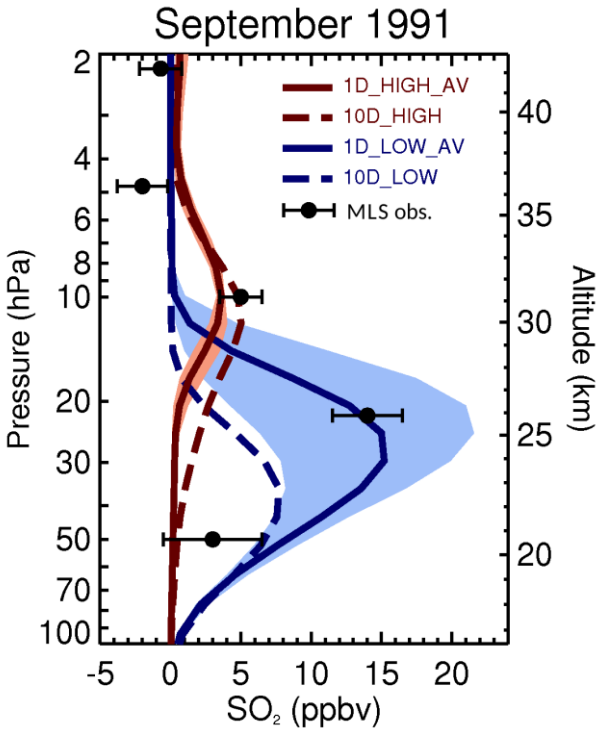

Figure 5.5. Equatorial (10°S-10°N) mean SO_2 concentration anomaly in September 1991 for 1D_HIGH_AV, 10D_HIGH, 1D_LOW_AV, and 10D_LOW. Black circles indicate Microwave Limb Sounder (MLS) observations as reported in Read et al. (1993)

fixed aerosol radius used here. The 14 Tg[SO_2] *HIGH* simulations fail to capture the peak of the SO_2 plume, however the *HIGH* simulations do provide a better fit to the MLS observations at ~10 hPa than the *LOW* simulations. This suggests that our simulations of Pinatubo with HG2 are better represented by *LOW* than *HIGH* injection profiles although we recognise that the best representation of injection profile would be somewhat higher than *LOW* but considerably lower than *HIGH*. For the rest of this analysis, we focus on the *LOW* experiments as the *1D_LOW* ensemble-mean provides the best fit to the observations such that *1D_LOW_AV* has a similar global-mean AOD evolution to *1D_HIGH_AV* (Fig. 5.2); a better R^2 in the horizontal (Fig. 5.4) and a better vertical SO_2 distribution when compared to observations (Fig. 5.5).

From Fig. 5.5, the *10D_LOW* SO_2 concentrations are much smaller than the MLS measurements reported by Read *et al.* (1993) and peak at 40 hPa altitude rather than the ~25 hPa altitude from observations. Conversely, the *1D_LOW_AV* and most of the *1D_LOW* ensemble's SO_2 concentrations are similar to observations (e.g. ~14 ppbv at 22 hPa). Figure 5.6 shows the atmospheric zonal-mean SO_4 mass mixing ratio anomalies for *1D_LOW_AV* and *10D_LOW* for July, September, November, and December 1991. From Fig. 5.6, the sulphate reservoir in the tropics in July is at

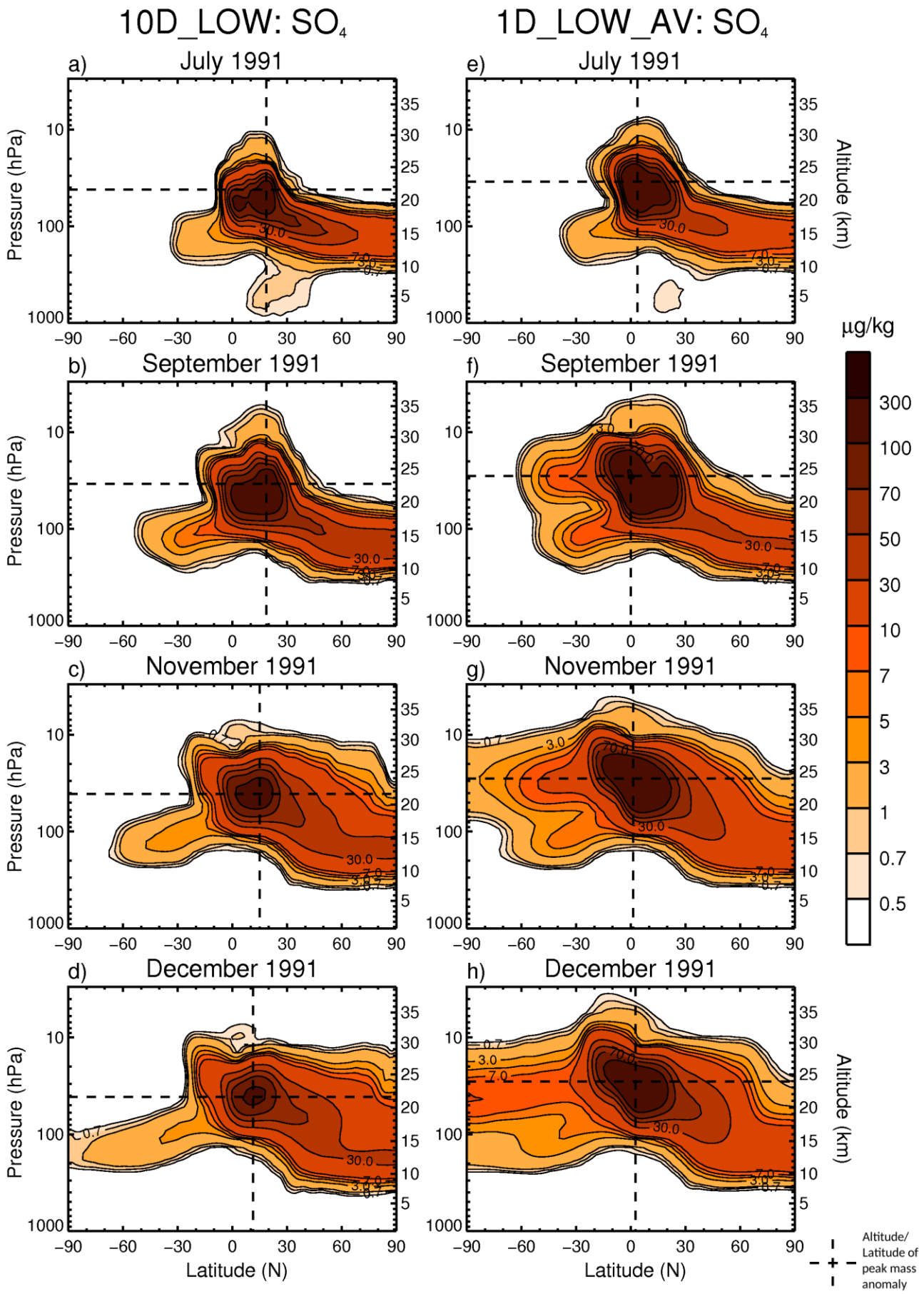

Figure 5.6. Latitude vs altitude plot of zonal-mean sulphate mass concentration anomaly for 10D_LOW and 1D_LOW_AV

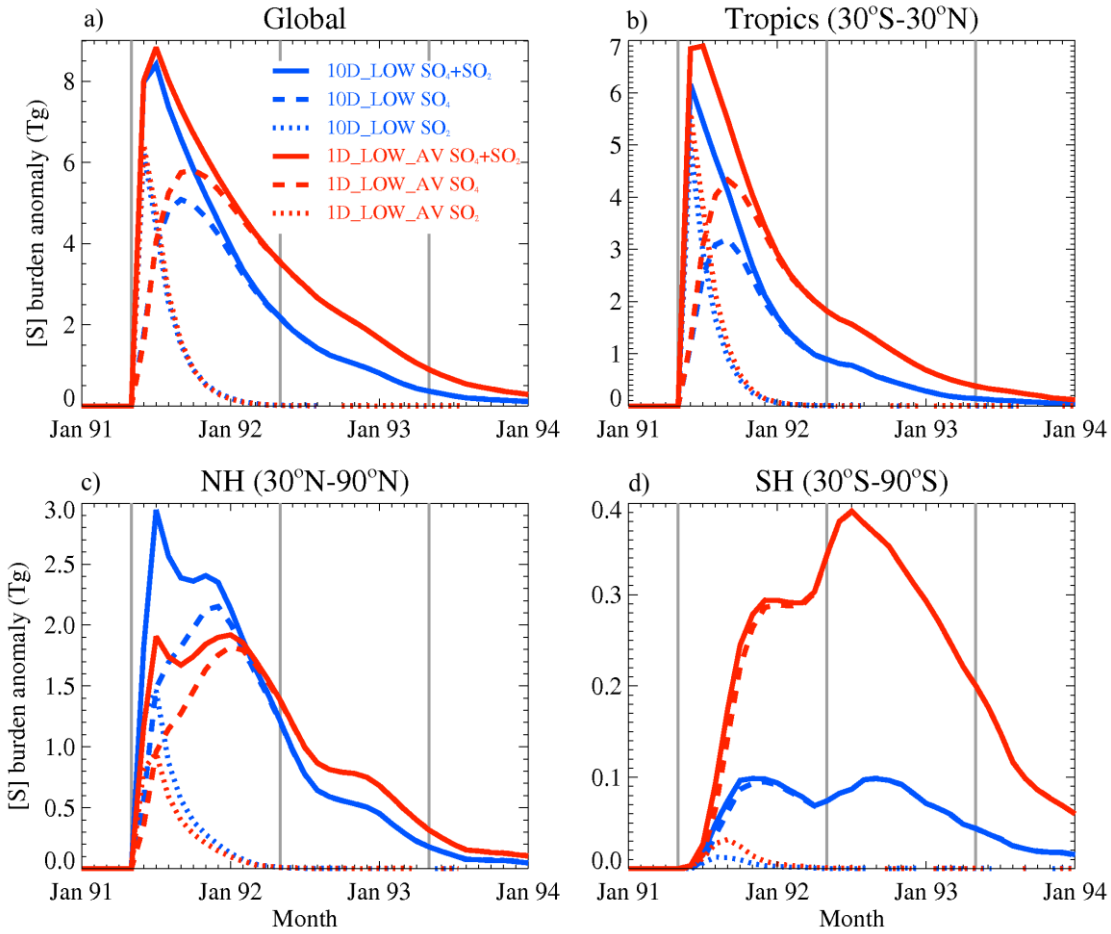

Figure 5.7. (a) Global, (b) tropical (30°S-30°N), (c) extratropical NH (30°N-90°N), and (d) extratropical SH (30°S-90°S) atmospheric sulphur burden (Tg[S]) anomalies for 10D_LOW (blue lines) and 1D_LOW_AV (red lines). Continuous lines correspond to total sulphur, dashed lines to SO_4, and dotted lines to SO_2

a higher altitude for *1D_LOW_AV* than for *10D_LOW* and closer to the equator, for instance the peak mass mixing ratio anomaly (indicated by dashed lines in Fig. 5.6) in July for *1D_LOW_AV* is at (34hPa, 4°N) and for *10D_LOW* is at (41hPa, 19°N). Trepte and Hitchman (1992) showed that aerosol in the lower tropical stratosphere (>40 hPa altitude) is rapidly transported towards high latitudes, whilst aerosol at higher altitudes (40-10 hPa altitude) is confined to the tropical pipe. By July, 3 Tg[S] of combined SO_2 and SO_4 has been transported to mid/high NH latitudes (>30°N) in *10D*, compared to 1.9 Tg[S] in *1D_LOW_AV* (Fig. 5.7). The sulphate in the tropical reservoir in *1D_LOW_AV* is predominantly transported to the SH in the upper branch of the BDC (~30 hPa altitude) in September (Fig. 5.6f), reaching the South Pole by November (Fig. 5.6g), in line with observations [Trepte *et al.*, 1993]. However, the *10D_LOW* aerosol is only transported to the SH in a lower stratospheric pathway at ~100 hPa altitude (Fig. 5.6d).

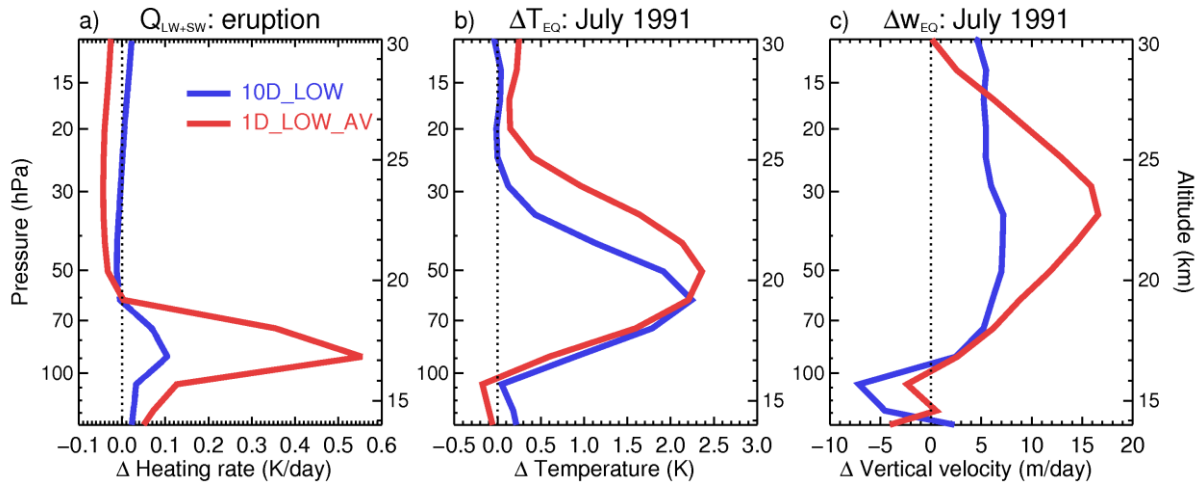

Figure 5.8. (a) Instantaneous clear-sky heating rate anomaly for the duration of the eruption at [15°N, 120°E], (b) July 1991 zonal-mean temperature anomaly averaged between 5°S and 15°N, (c) July 1991 zonal-mean vertical velocity anomaly averaged between 5°S and 15°N

To explain the difference in meridional transport between *1D_LOW_AV* and *10D_LOW*, it is necessary to compare the radiative heating perturbations. Figure 5.8 shows (a) the initial clear-sky heating rate anomaly for the duration of the eruption (i.e. 10 days for *10D_LOW* and 1 day for *1D_LOW_AV*) at the eruption location, (b) the equatorial (5°S-5°N) temperature anomaly in July, and (c) the equatorial vertical velocity anomaly in July. The *1D_LOW* simulations clearly exhibit a greater radiative-heating perturbation than for *10D_LOW* (Fig. 5.8a), which is due to the difference in initial mass-loading of SO_2. Although the radiative properties of SO_2 are not represented in this model, the SO_4 plume, which immediately begins to form from oxidation of the volcanic SO_2, is also denser for *1D_LOW* than *10D_LOW*, thus inducing a greater radiative heating perturbation which is counterbalanced by adiabatic cooling from enhanced vertical motion and by temperature tendencies [e.g. Eq. 3 in Holton *et al.*, 1995]. This is exemplified by the greater equatorial heating (Fig. 5.8b) and vertical velocity perturbation (Fig. 5.8c) in *1D_LOW_AV* than *10D_LOW*. The *1D_LOW* aerosol is therefore 'self-lofted' to higher altitudes than the *10D_LOW* aerosol, and is concomitantly transported in the upper stratospheric pathway in the SH.

The peak aerosol burden anomaly in the *1D_LOW_AV* experiment is 5.8 Tg[S] (Fig. 5.7), which falls within the observed uncertainty range of 3.7 to 6.7 Tg[S] given by Dhomse *et al.* (2014). By December 1991, 40% of the 10 Tg[S] volcanic sulphur in *1D_LOW_AV* has been removed from the atmosphere (Fig. 5.7a). Figure 5.9 shows the relative contributions to the total sulphur deposition at the surface from the

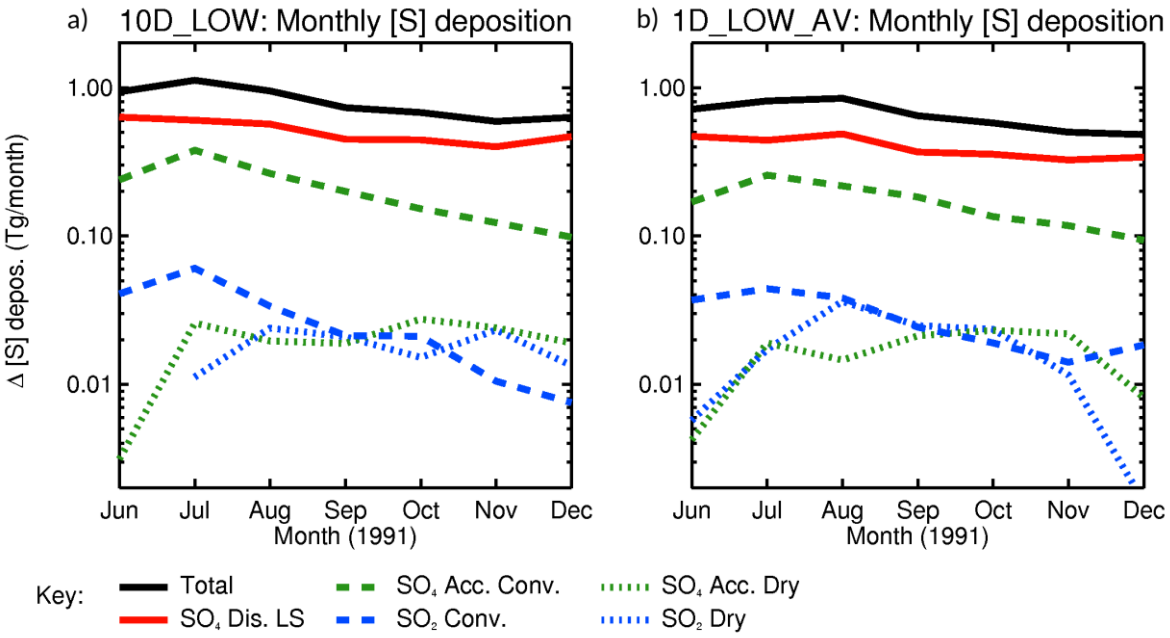

Figure 5.9. Monthly-mean sulphur deposition anomaly partitioned into the key loss pathways for (a) 10D_LOW and (b) 1D_LOW_AV. Acc. and Dis. stand for accumulation and dissolved, LS refers to large-scale precipitation, Conv. refers to convective scavenging, and Dry refers to dry deposition

primary removal processes for the first 7 months after the eruption for *10D_LOW* and *1D_LOW_AV*. It is clear that the wet deposition of dissolved sulphate by large-scale precipitation events contributes the largest deposition of sulphur (~60 %), followed by convective scavenging of accumulation-mode sulphate (~25 %). SO_2 deposition by convective scavenging contributes ~4% of the total sulphur deposition, which decreases over time as SO_2 is oxidised to form sulphate.

5.4.3. 'Day 1' eruption against 'Day 10' eruption

Figure 5.10 shows the zonal-mean AOD evolution for the individual *1D_LOW* simulations. The first 8 ensemble members show reasonable conformity with AVHRR / SAGE_4λ observations (Fig. 5.4e,f), which is quantitatively corroborated by their similar R^2 values (~0.3-0.5). However, the last 2 simulations (*1D_LOW_9* and *1D_LOW_10*) exhibit minimal transport of aerosol into the SH, in disagreement with the observations (reflected in R^2 values <0.1). The only difference between the simulations is the meteorology encountered by the aerosol plume. Figure 5.11 shows the zonal-mean AOD evolution from *AQ12*'s 8 ensemble members (equivalent to our Fig. 5.10). Despite the fact that the meteorology is independent of that in *AQ12*, we have obtained very similar results – for instance the difference between their simulations Pin45act4d and Pin45act3d, with the latter showing a persistent-NH

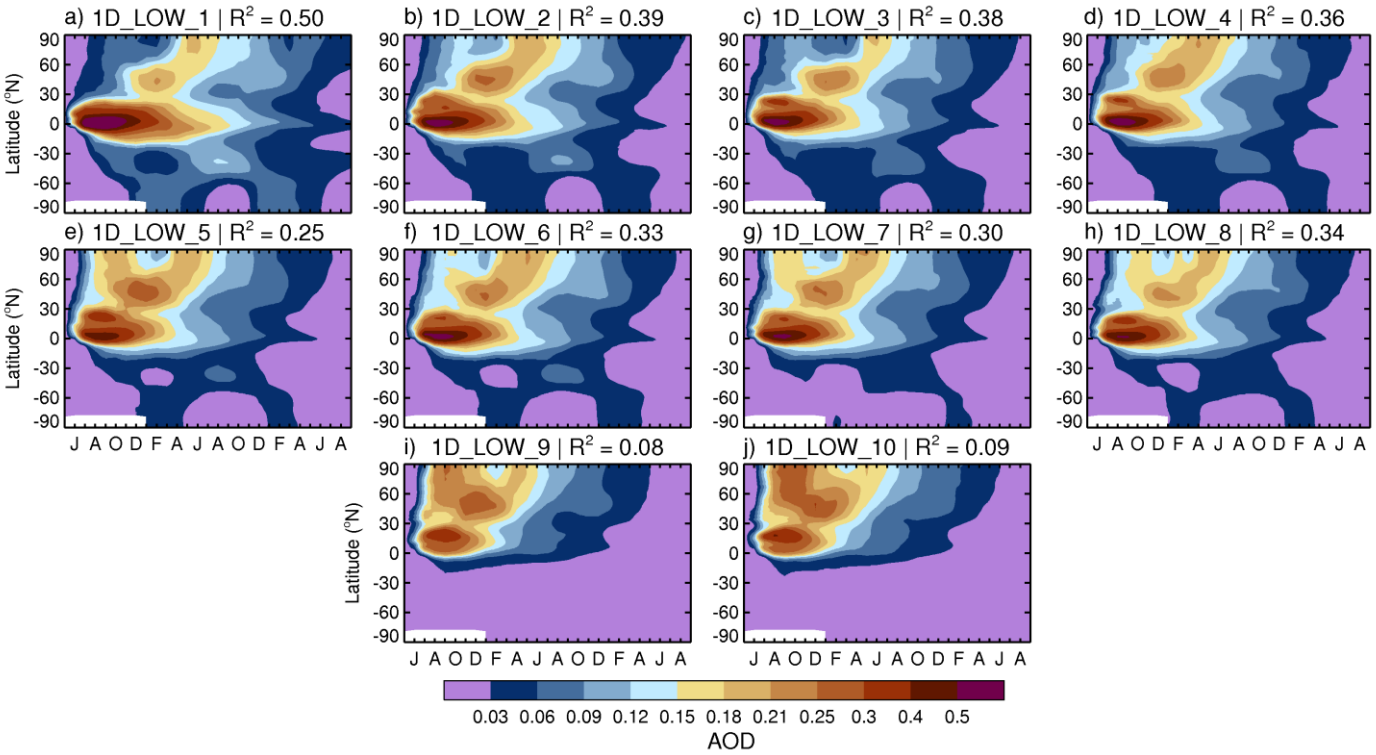

Figure 5.10. Latitude vs time plot of monthly/zonal-mean sulphate 550nm AOD anomaly for the 1D_LOW ensemble

aerosol plume, is similar to the difference between our *1D_LOW_1* and *1D_LOW_10*. Figure 5.12 shows the zonal-mean AOD evolution for the *3H_LOW* simulations. It is clear that the individual *3H_LOW* simulations are very similar to their counterpart *1D_LOW* simulations, for instance *1D_LOW_1* and *3H_LOW_1* have R^2 values of 0.50 and 0.48 respectively.

As mentioned in Section 5.4.2, the absence of SH aerosol in the HG2 simulations could partially be attributed to the lack of representation of the Cerro Hudson (CH) eruption, which occurred on the 15th August 1991. In order to assess the importance of the CH eruption on SH aerosol in the aftermath of the Pinatubo eruption, we have rerun the 1st and 10th *1D* ensemble members (*1D_LOW_1* and *1D_LOW_10*) with a CH-like eruption included. CH is represented by a 3.3 Tg[SO_2] injection, with SO_2 emitted uniformly between 11-16 km altitude from 04:00-12:00 on August 1st (2 months after Pinatubo) at (46°S, 73°W) [Schoeberl *et al.*, 1993b; Deshler and Anderson-Sprecher, 2006]. Figure 5.13 shows the zonal-mean 550nm AOD evolution for the *1D_LOW_1+CH* and *1D_LOW_10+CH* experiments. It is clear that the inclusion of CH in the simulations has not significantly affected the AOD distribution, for instance, the R^2 values for the *1D_LOW_10* and *1D_LOW_10+CH* experiments are the same (0.09).

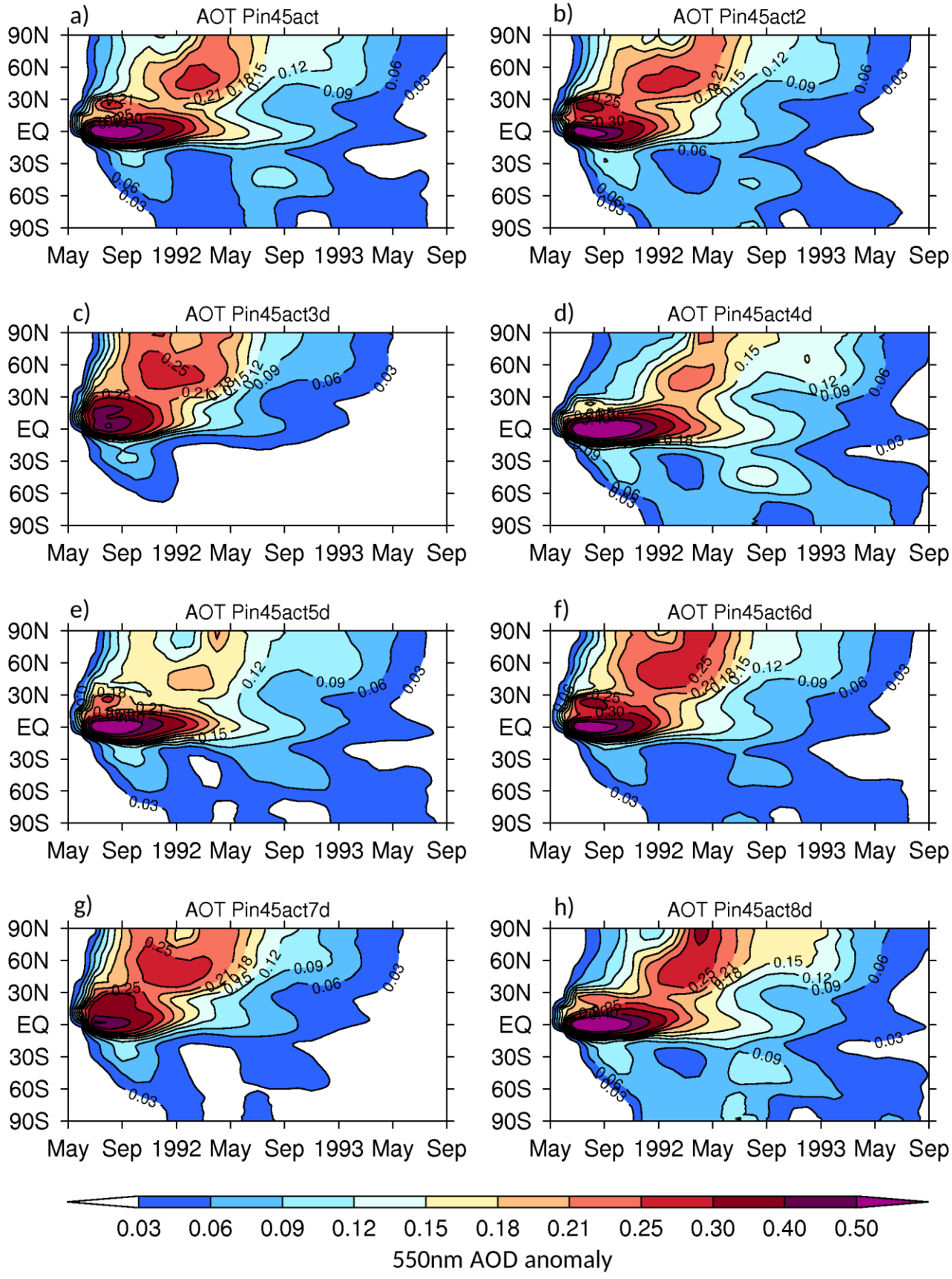

Figure 5.11. Latitude vs time plot of monthly/zonal-mean sulphate 550nm AOD anomaly for the 8-member Pinatubo ensemble from Aquila *et al.* (2012)

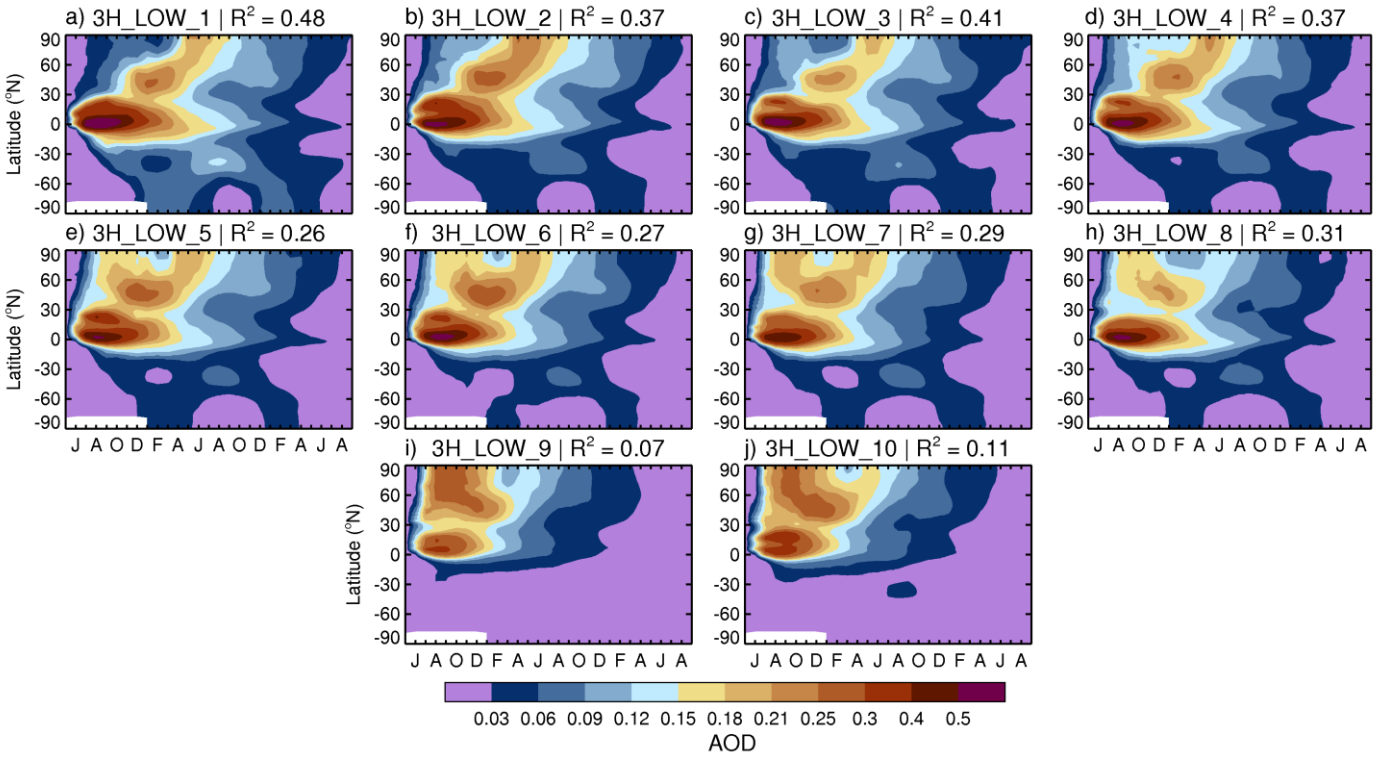

Figure 5.12. Latitude vs time plot of monthly/zonal-mean sulphate 550nm AOD anomaly for the 3H_LOW ensemble

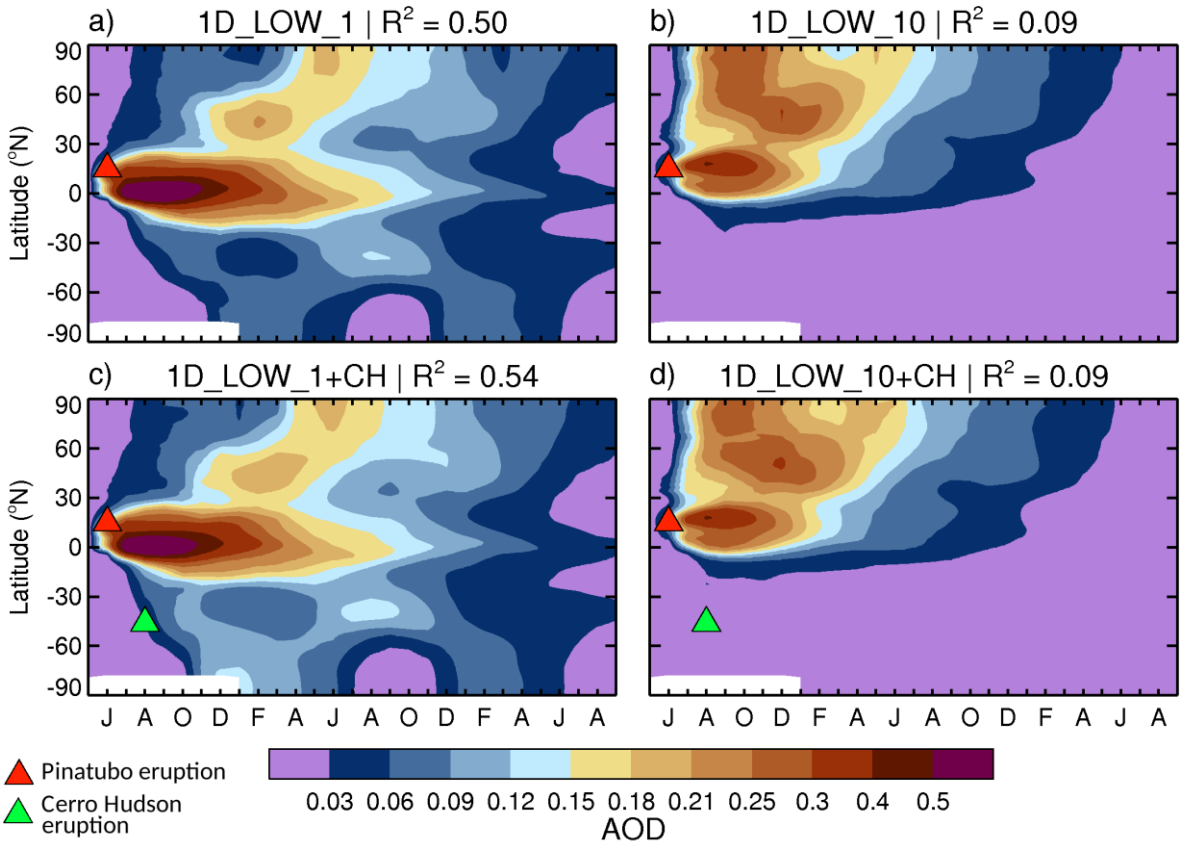

Figure 5.13. Latitude vs time plot of monthly/zonal-mean sulphate 550nm AOD anomaly for (a) 1D_LOW_1, (b) 1D_LOW_10, (c) 1D_LOW_1 plus Cerro Hudson, and (d) 1D_LOW_10 plus Cerro Hudson. Red and green triangles indicate the Pinatubo and Cerro Hudson eruptions respectively

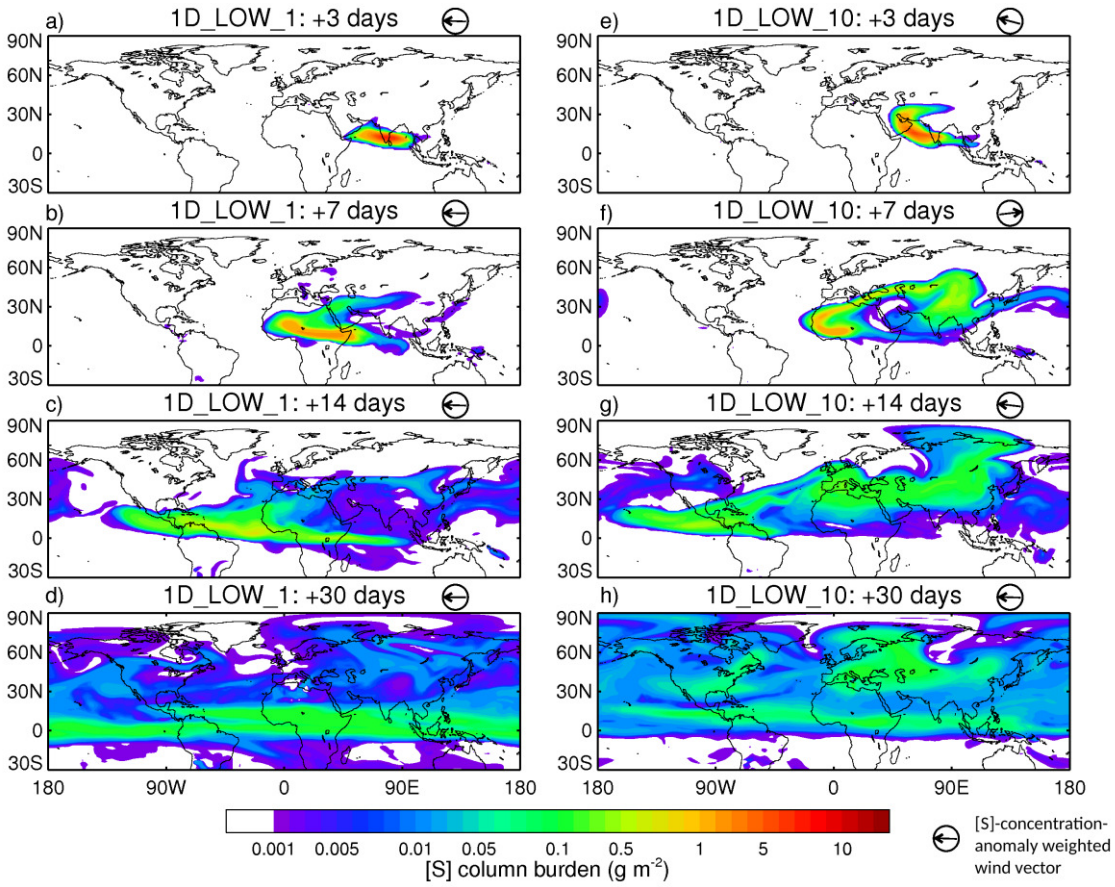

Figure 5.14. Sulphur ([S]) column burden anomaly for 1D_LOW_1 and 1D_LOW_10 for 3, 7, 14 and 30 days after the eruption. Circled-arrows show the direction of the [S]-concentration-anomaly weighted wind vector $[\hat{u}, \hat{v}]$

Figure 5.14 shows the total sulphur (SO_2+SO_4) column burden anomaly (g[S]/m^2) for the most disparate *1D_LOW* simulations, *1D_LOW_1* and *1D_LOW_10*, at intervals of 3, 7, 14 and 30 days after the initiation of the eruption. The circled-arrows in Fig. 5.14 show the direction of the [S]-concentration-anomaly weighted wind vector. During the first 3 days following the eruption, the *1D_LOW_10* aerosol exhibits a more northward progression as indicated by the significant aerosol burden at 30°N in Fig. 5.14e. The *1D_LOW_10* aerosol is advected northward by the prevailing southerly wind at ~45°E (Fig. 5.14e), whilst the *1D_LOW_1* aerosol remains concentrated between 10°-20°N. The most dramatic difference in the [S]-weighted wind vector between *1D_LOW_1* and *1D_LOW_10* simulations occurs at day 7. Here, *1D_LOW_1* indicates a continued progression westward in the easterly winds while *1D_LOW_10* shows an almost complete reversal in the direction of advection owing to the influence of the anticyclone over Asia in this simulation. Figure 5.15 shows the 100 hPa wind-vector superimposed on the 100hPa wind-speeds for *1D_LOW_1* and *1D_LOW_10*, evaluated 3 days after the eruption, and for ERA-I

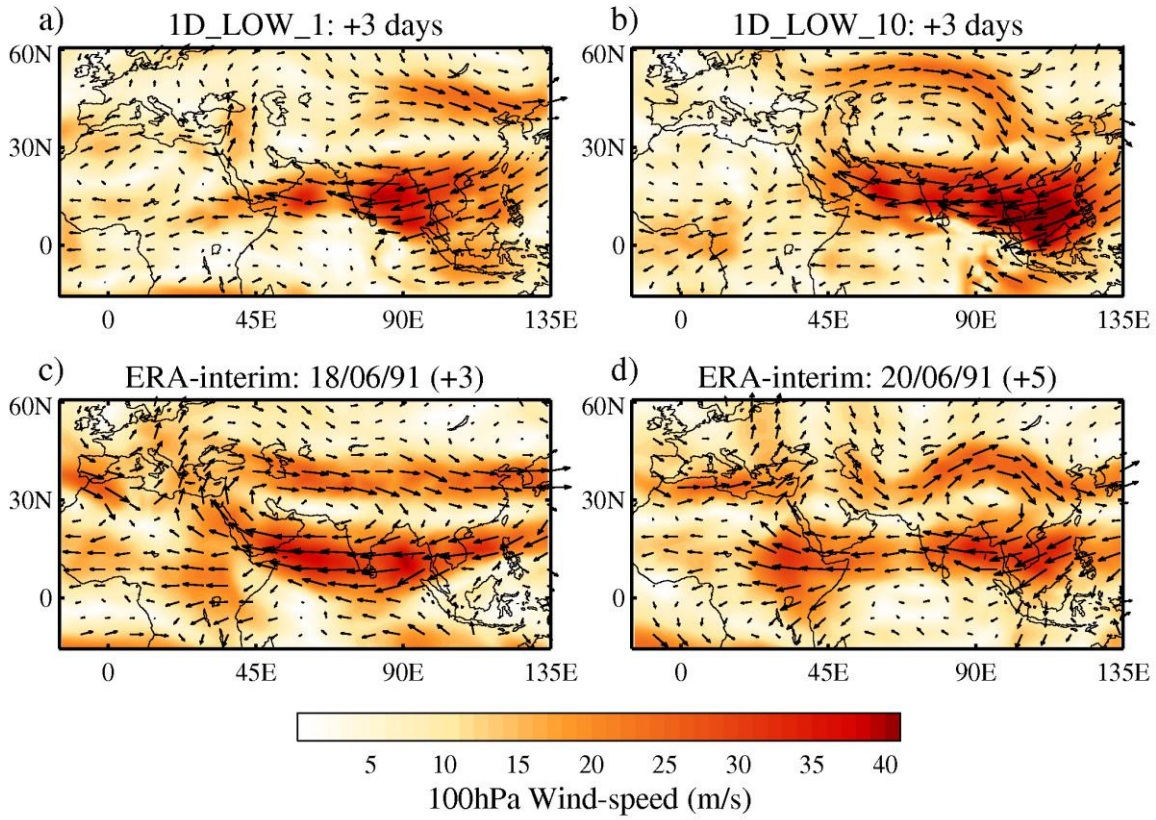

Figure 5.15. 100 hPa horizontal windvector plotted on 100 hPa horizontal windspeed for (a) 1D_1 eruption + 3 days, (b) 1D_10 eruption + 3days, (c) ERA-I 18/06/1991, (d) ERA-I 20/06/1991 [Dee et al., 2011]

reanalysis on June 18th and June 20th 1991 [Dee *et al.*, 2011]. It is clear that the northward advection of aerosol in *1D_LOW_10* is driven by the anticyclonic vortex centred over North India [30°N, 75°E] (Fig. 5.15b), which is not present in *1D_LOW_1* at the equivalent time (Fig. 5.15a). Although a similar southerly wind at ~45°E is present on June 18th in the reanalysis data (Fig. 5.15c), it had dissipated by the 20th June (Fig. 5.15d). Anticyclogenesis over Asia in June is the result of warming over a region spanning Iraq to Tibet [Yanai *et al.*, 1992], with anticyclonic anomalies then propagating eastward along the subtropical jet [Watanabe and Yamazaki, 2012] and eventually weakening by August [Bourassa *et al.*, 2012]. Bourassa *et al.* (2012) suggested that an anticyclonic vortex over Asia was fundamental in the transport of the volcanic plume immediately after the 2011 Nabro [13°N, 41°E] eruption although these findings have been contested [Fromm *et al.*, 2014]. What is clear is that the precise meteorological conditions that prevail during the eruption strongly influence the poleward progression of the aerosol. From Fig. 5.14 and Fig. 5.15 we have shown that the aerosol transport out of the tropics is

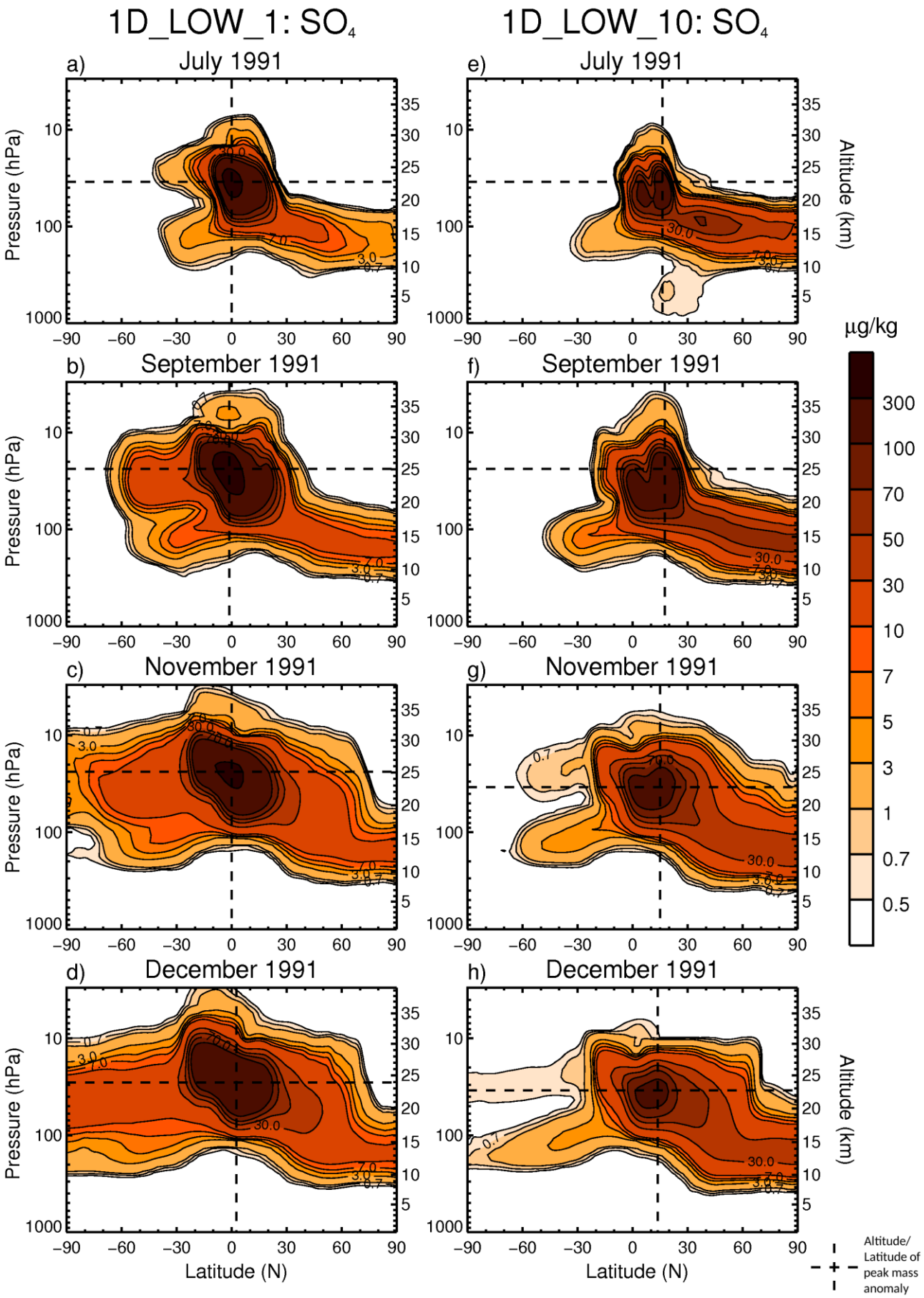

Figure 5.16. Latitude vs altitude plot of zonal-mean sulphate mass concentration anomaly for 1D_LOW_1 and 1D_LOW_10

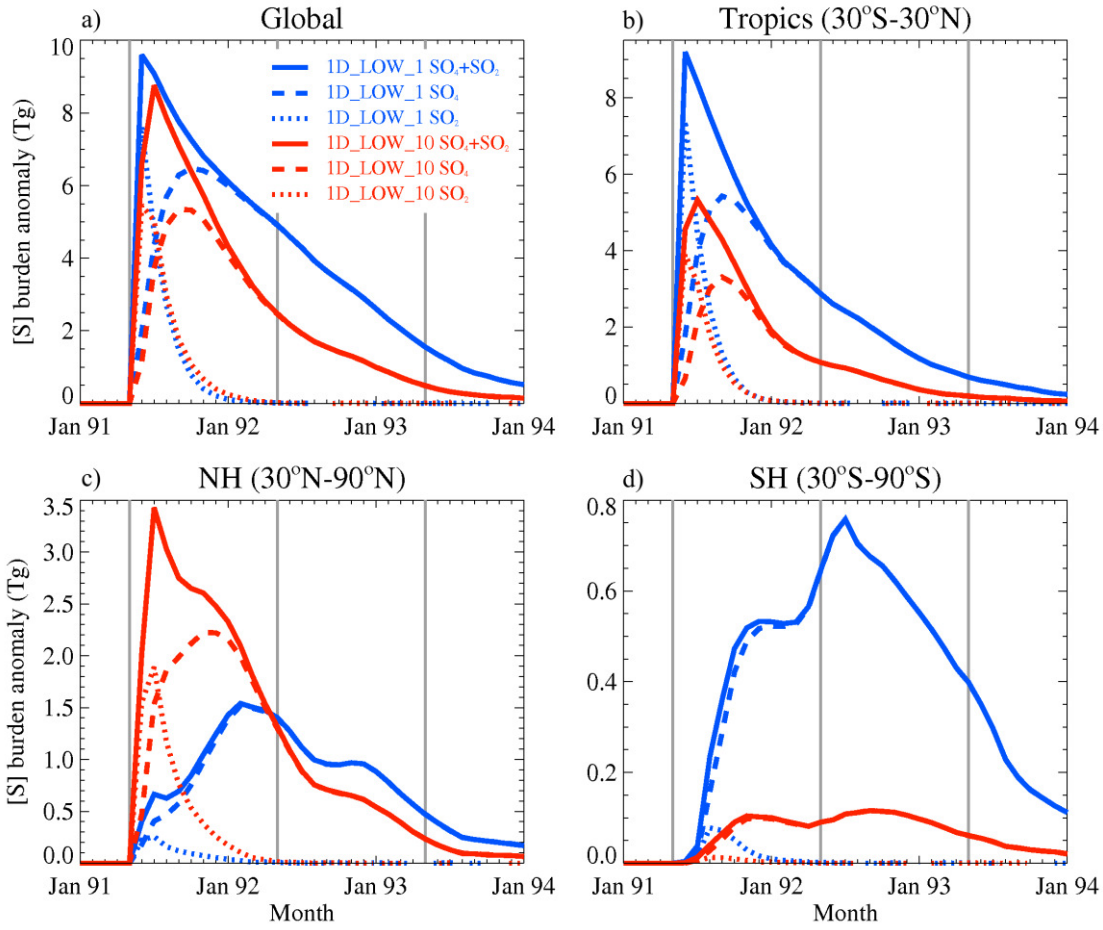

Figure 5.17. Equivalent to Fig. 5.7 but for 1D_LOW_1 and 1D_LOW_10

inextricably linked to the ambient wind direction, with the *1D_LOW_1* aerosol encountering a zonally-dominant transport regime (Fig. 5.14a). As a result, by day 30 the *1D_LOW_1* aerosol is primarily confined to the tropics (Fig. 5.14d) at altitudes of ~40 hPa, while the *1D_LOW_10* aerosol is primarily confined to the NH (Fig. 5.14h). Consequently, *1D_LOW_1* aerosol is transported into the SH within the upper branch of the BDC (Fig. 5.16). By January 1992, 0.54Tg[S] of combined SO_2 and SO_4 has been transported to the SH in *1D_LOW_1*, compared to 0.1 Tg[S] in *1D_LOW_10* (Fig. 5.17).

5.4.4. Potential climatic consequences

The spatial distribution of the volcanic aerosol has important implications for the resultant climate impacts. Haywood *et al.* (2013) showed that hemispherically-asymmetrical aerosol forcing is causally related to the displacement of the ITCZ. For instance, the 20th century NH volcanic eruptions of Novarupta-Katmai (June 1912) and El Chichón (March-April 1982) produced peak sulphate AOD hemispheric-asymmetries (AOD_{NH-SH}) of 0.08 and 0.07 respectively [Sato *et al.*, 1993; Haywood

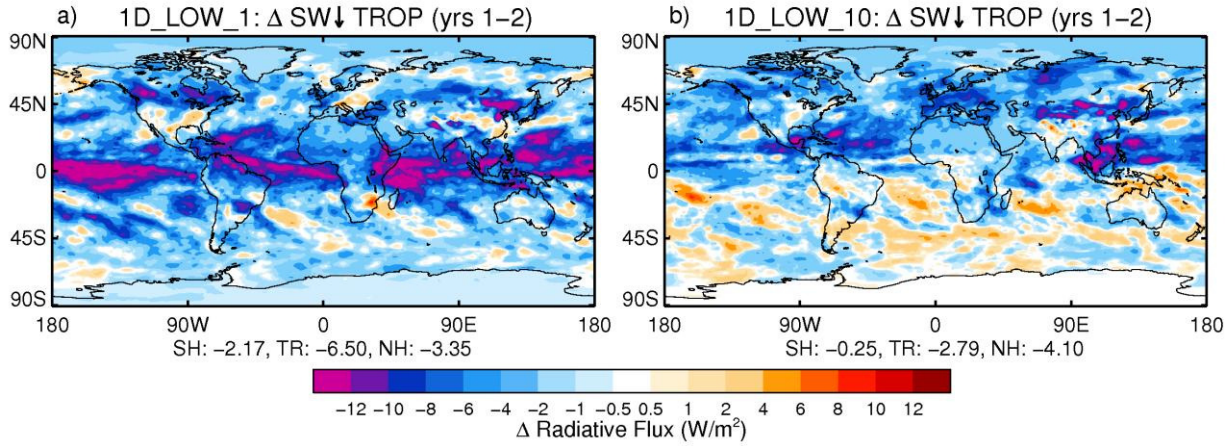

Figure 5.18 Tropopause short wave net-downward radiation anomaly for 1D_LOW_1 and 1D_LOW_10 simulations averaged over 2 subsequent years following the eruption

et al., 2013], resulting in significant negative Sahelian precipitation anomalies in the subsequent year. In contrast, Pinatubo produced a peak AOD_{NH-SH} of 0.04 and no significant shift in the ITCZ [Haywood *et al.*, 2013], although precipitation is generally suppressed subsequent to large volcanic eruptions owing to reductions in surface irradiances leading to reductions in latent heat fluxes and a slowing down of the hydrological cycle [Trenberth and Dai, 2007]. In these experiments, *1D_LOW_1* produces a peak AOD_{NH-SH} of 0.05, which is close to the Pinatubo observations, while *1D_LOW_10* produces a peak AOD_{NH-SH} of 0.10, which exceeds the observed AOD_{NH-SH} for Novarupta-Katmai and El Chichón. Figure 5.18 shows the SW radiative flux anomalies at the tropopause for *1D_LOW_1* and *1D_LOW_10*, averaged over the 2 complete calendar years (Jan-Dec) following the eruption. The SW forcing is more spatially uniform for *1D_LOW_1* than for *1D_LOW_10*, which is a direct result of the location of the aerosol plume. For instance, the SW forcing in *1D_LOW_10* in the SH is negligible (-0.25 Wm^{-2}), while the SW forcing in the NH is significant (-4.1 Wm^{-2}). The standard deviation of the NH (30°N-90°N) mean net SW flux at the tropopause in the Control simulation is 0.26; therefore this SW forcing is significant at the 2σ level.

The aerosol burden in the tropical reservoir has implications for stratospheric dynamics and therefore stratospheric O_3 concentrations [Aquila *et al.*, 2014]. Stratospheric sulphate aerosols provide surfaces for heterogeneous reactions between free radicals and O_3 which can result in O_3 depletion [Aquila *et al.*, 2013]. Additionally, tropical stratospheric warming due to LW and near-infrared absorption within the aerosol layer would increase the local upwelling velocity and transport O_3-

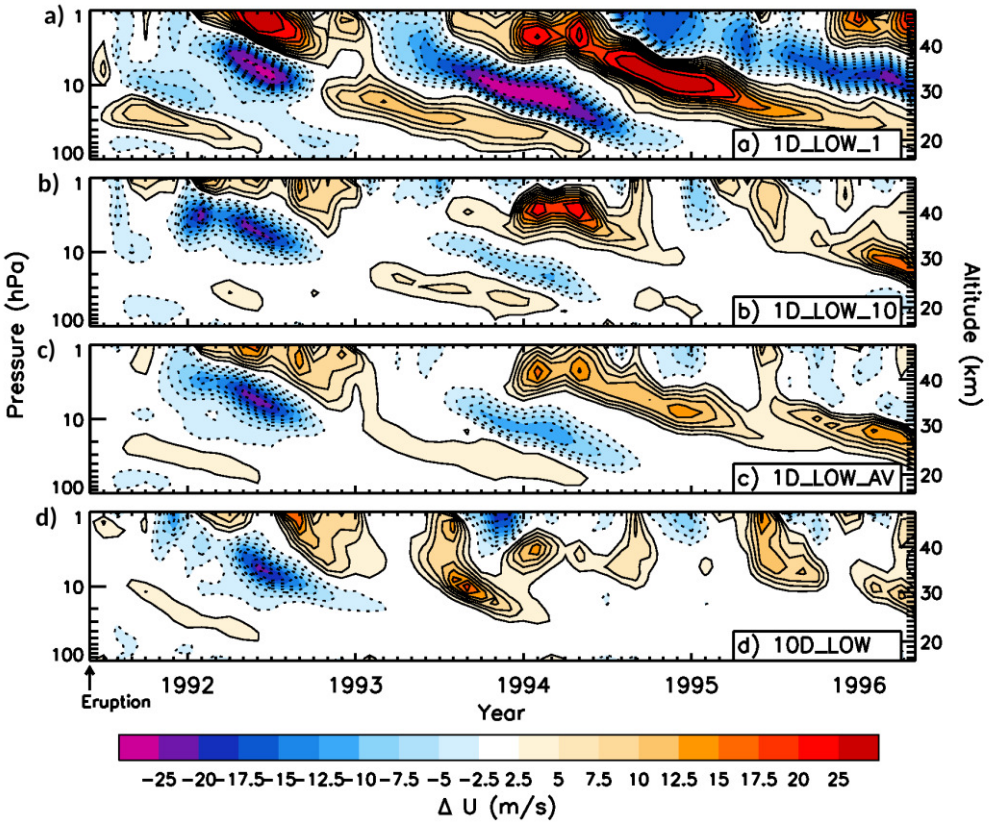

Figure 5.19 Stratospheric equatorial (5°S-5°N) zonal-mean zonal wind anomaly with respect to CONTROL, for 1D_LOW_1, 1D_LOW_10, 1D_LOW_AV, and 10D_LOW

poor air in the lower stratosphere to higher altitudes where O_3 is more easily destroyed [Schoeberl *et al.*, 1993a]. Figure 5.19 shows the equatorial zonal-mean zonal-wind perturbation for *1D_LOW_1*, *1D_LOW_10*, *1D_LOW_AV*, and *10D_LOW*. Tropical stratospheric aerosols promote a prolonged westerly QBO phase [Aquila *et al.*, 2014]. The greater tropical sulphate reservoir in *1D_LOW_1* causes a delay to the downward propagation of the easterly winds, which is exemplified by the positive (westerly) anomaly in *1D_LOW_1* at ~40 hPa following the eruption (Fig. 5.19). Labitzke (1994) reports that after Pinatubo observations showed a warming of the lower stratosphere of about 3 K and a delay in the downward propagation of the easterly winds. Figure 5.20 shows the equatorial zonal-mean zonal-wind profiles for the Control and *1D_LOW_1* simulations. QBO phase changes are indicated in Fig. 5.20 by vertical black lines along 40 hPa altitude (where the QBO phase is defined by the zonal-wind direction at 40 hPa) [Baldwin *et al.*, 2001]. From Fig. 5.20, the first QBO phase change following Pinatubo is delayed by 1-2 months in the *1D_LOW_1* simulation compared to the *CONTROL*. Additionally, the significant aerosol concentration anomaly at the South Pole in

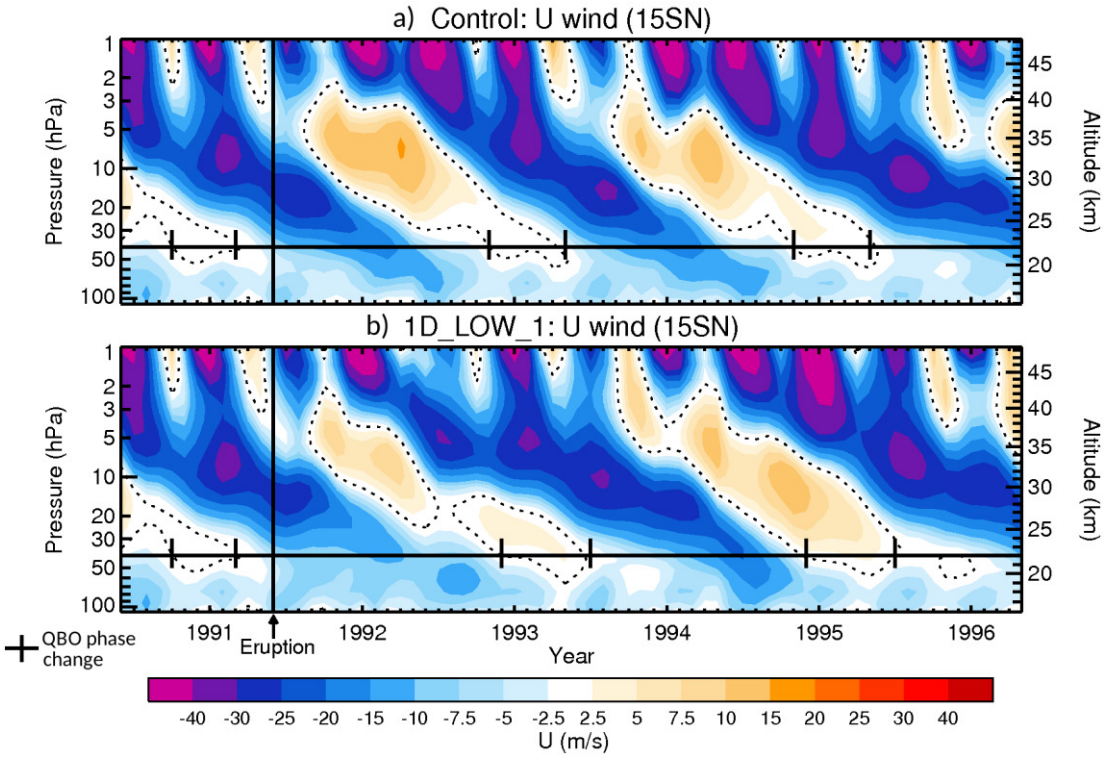

Figure 5.20 QBO for the (a) CONTROL and (b) 1D_LOW_1 simulations. The vertical black line indicates the Pinatubo eruption, the horizontal black line indicates the 40 hPa level, and vertical black lines (between 50-30 hPa) indicate the QBO phase changes. Dashed lines indicate U = 0 m/s

November 1991 for *1D_LOW_1* (Fig. 5.16c) would enhance heterogeneous O_3 chemistry within the Antarctic vortex, as observed after the Pinatubo eruption [McCormick *et al.*, 1995].

5.5. Summary and Discussion

We have shown that the dispersion of volcanic aerosol can be highly sensitive to the ambient meteorology, with this sensitivity dependent on the altitude of SO_2 emission. While simulations using the 20 Tg[SO_2] *LOW* injection scenarios show a lot of sensitivity to meteorological conditions, simulations using the 14 Tg[SO_2] *HIGH* scenarios show little sensitivity. While it is difficult to determine whether the 20 Tg[SO_2] *LOW* or the 14 Tg[SO_2] HIGH simulations provide simulations that are more consistent with observations from global-mean assessments of the AOD alone, assessment of the spatial distribution in both the horizontal and vertical suggests that, for our modelling study at least, members of the 20 Tg[SO_2] *LOW* ensemble are most consistent with observations. We find that the mean of the ten 1-day eruptions where 20 Tg[SO_2] is emitted between 16-18 km altitude provides a reasonable consistency with observations, but there is significant variability between the ensemble members. This variability is related to anomalous anticyclonic activity

along the subtropical jet, which affects the “leakiness” of the tropical pipe and therefore the amount of aerosol that is retained within the tropical reservoir. We have discussed the implications of our results with respect to resultant climate changes, for instance, the possible effects of hemispherically-asymmetric aerosol burdens on Sahelian precipitation, but note that a GCM with an interactive ocean model would be needed to comprehensively evaluate the climatic impacts of the different Pinatubo realisations. We have also compared the aerosol dispersion from a simulated 10-day eruption with the ensemble-mean of the ten 1-day eruptions. These simulation designs represent two intuitive methods of overcoming the problem of variable meteorology. We have shown that the 10-day eruption is unable to produce the radiative heating and concomitant aerosol self-lofting required to transport aerosol to the SH, hence the resultant spatial distribution of sulphate AOD compares inadequately to observations (Fig. 5.4c). In contrast, the 1-day ensemble-mean AOD anomaly is much closer to observations (Fig. 5.4d); therefore performing a 1-day eruption ensemble presents a better solution to overcoming variable meteorology. However, the intra-ensemble variability in the *1D_LOW* experiments is significant; for instance, *1D_LOW_9* and *1D_LOW_10* fail to capture the SH transport of aerosol observed after Pinatubo (Figs 5.10i,j). Assuming that the *1D_LOW* results represent the complete set of possible realisations of the Pinatubo eruption, this would mean a 20% chance of obtaining a ‘failed’ simulation for the specific goal of obtaining SH transport.

We have also performed simulations in which 20 Tg[SO_2] is emitted within a 3-hour span between 16-18 km altitude (*3H_LOW*). The 3 hour duration was selected to represent the cataclysmic Pinatubo eruption that occurred on the 15th June 1991 [Holasek *et al.*, 1996]. We find that our results from a 24-hour period are equivalent to those from a 3-hour eruption. However, we qualify this result by noting the limitations of the aerosol microphysics scheme employed here which only consists of two sulphate size modes. Additionally, SO_2 is not the only substance emitted by volcanic eruptions - volcanic ash is co-emitted and would very likely change the heating rates due to the predominance of coarse mode aerosols [e.g. Niemeier *et al.*, 2009] that are effective absorbers of infra-red radiation. We have also performed simulations in which the Cerro Hudson eruption that occurred on 15th August 1991 is represented by a 3.3 Tg[SO_2] injection between 11-15 km altitude at [46^{o}S, 73^{o}W], in

an eruption that lasts 8 hours. We find little difference in zonal-mean AOD between simulations with and without the Cerro Hudson eruption (Fig. 5.13).

Our results are conditional on the selected specifications of the eruption and the specifications of HadGEM2-CCS. For instance, we have shown that the aerosol dispersion after a high altitude SO_2 emission scenario (19-29 km) is substantially less sensitive to the existing meteorological state which is due to the limited meteorological variability in the middle stratosphere. It is therefore imperative to precisely identify the initial location of the volcanic plume in order to accurately model the concomitant aerosol transport. An eruption during a different month might also avoid the variability associated with the Asian anticyclone, which is a seasonal (June-August) phenomenon [Park *et al.*, 2007], and an eruption during a different QBO phase would alter the permeability of the tropical pipe [Trepte *et al.*, 1993].

The transport of volcanic aerosol and gases from the troposphere to the stratosphere is primarily mediated by deep and shallow convection cells in the tropics, and along isotopes in mid-latitude tropopause folds [Carslaw and Karcher, 2006; Kremser *et al.*, 2016]. This emphasises the importance of convection in controlling the vertical distribution and stratospheric budget of SO_4. Kipling *et al.* (2016) used HadGEM3-UKCA to investigate which processes are most important in controlling the vertical profiles of various atmospheric aerosols. They found that the vertical SO_4 profile was particularly sensitive to convection and large-scale rainout (the dominant SO_4 removal process from the troposphere – Fig. 5.9). An interesting question is how sensitive is tropical convection and volcanic aerosol dispersion to the contemporaneous mode of the El Niño Southern Oscillation (ENSO) index (a periodic oscillation in warm and cold ocean surfaces on opposite sides of the Pacific Ocean). For instance, ENSO mediates the vertical propagation of planetary waves from the tropical troposphere to the stratosphere which determines the QBO phase and concomitantly, the leakiness of the tropical pipe [Schirber, 2015]. Additionally ENSO affects the stratosphere-troposphere exchange of ozone [Zeng and Pyle, 2005] and the general dynamics of the lower stratosphere [Simpson *et al*., 2011], both of which affect the meteorological variability of the lower stratosphere.

Additionally, the representation of sulphate aerosol in HadGEM2-CCS is limited to 2 hygroscopic modes with fixed dry-mode radii [Bellouin *et al.*, 2007]. Observations

from the post-Pinatubo era showed that the global sulphate size distribution continued to grow for 1.5 years after the eruption to attain effective radii of approximately 0.6-0.8 μm [Stenchikov *et al.*, 1998; Russell *et al.*, 1996], whereas the accumulation-mode aerosol in these simulations is fixed at a geometric mean radius of a lognormal mode of 0.376 μm. Larger particles experience greater fall velocities [Rasch *et al.*, 2008a] and absorb more efficiently in the LW and near-infrared spectrum, and scatter less efficiently in the SW spectrum. Our model might therefore underestimate the gravitational sedimentation rates and LW heating rates exhibited by the volcanic aerosol. Inevitably, the sea-surface temperature and meteorological state in our atmosphere-only simulations are unrelated to the observed post-Pinatubo conditions. Our simulations, therefore, include a subset of possible meteorological conditions that could be encountered by a volcanic-aerosol plume; conditions which would also differ with season and latitude of eruption. For interest, the ongoing model intercomparison project VolMIP[10] also selected to use pre-industrial baseline conditions for their eruption simulations. VolMIP's VolLongS60EQ scenario is comparable in design to our simulations (but with a significantly greater SO_2 emission of 100 Tg); therefore a direct evaluation of the aerosol plume evolution in that scenario could prove elucidative. One final caveat is that we prescribed O_3 concentrations for the duration of these simulations; therefore the model excludes simulation of the O_3 changes from heterogeneous reactions on the aerosol surfaces (and the resultant feedbacks) such as observed after Pinatubo [McCormick *et al.*, 1995]. We believe that these caveats, however, do not alter the primary result of this research: that volcanic aerosol plume evolution can be highly sensitive to the existing meteorological state.

With the improved representation of stratospheric aerosol in climate models it is tempting to suggest the models might disregard the imposition of climatologies of stratospheric aerosol concentrations in favour of simply injecting SO_2 and relying on the aerosol scheme to provide sulphate aerosol concentrations that are self-consistent with the meteorology. However, the extreme variability evidenced by the factor of two difference between the AOD in the *1D_LOW_1* and *1D_LOW_10* scenarios (Fig. 5.2) suggests that the meteorological variability may compromise results: studies may "get lucky" and represent a particular volcanic eruption with

[10] http://volmip.org/experiments.html

reasonable fidelity, but they may not. Indeed the chances of successfully representing all significant volcanic eruptions in the 20th century (Novarupta-Katmai, Agung (March, May 1963), El Chichón, and Pinatubo) can be estimated from our statistics as around 0.8^4 or ~0.4, indicating that the chances of simulating all volcanoes with reasonable fidelity is less than 50:50. Our results also suggest that simply averaging by simulating a multiple-day eruption cannot represent the heating rates in the atmosphere and hence correctly model aerosol-dispersion. Our study suggests that centennial scale modelling such as the CMIP6 “deck” may wish to stick to tried and tested climatological stratospheric aerosol concentrations. Our study also suggests that future climate model simulations should account for meteorological variability when simulating volcanic eruptions.

Chapter 6 Solar geoengineering and North Atlantic tropical cyclone frequency*

6.1 Introduction

Solar geoengineering (SG) refers to a wide range of proposed methods for counteracting global warming by artificially reducing solar insolation at Earth's surface [Shepherd, 2009]. The most widely known SG proposal is SAI which has impacts analogous to those from large-scale volcanic eruptions [Crutzen, 2006]. Studies with GCMs indicate that SG could effectively cool Earth's surface, at the expense of regional climate changes [Ricke *et al.*, 2010], but these regional changes are less severe than those in a non-geoengineered world [Jones *et al.*, 2016a]. Some studies have investigated regional SG application scenarios, which could prove preferential to a global application by restricting the geospatial magnitude of the climate response, or by being used to target specific climate changes [Robock *et al.*, 2008; MacCracken *et al.*, 2009; MacMartin *et al.*, 2013; Haywood *et al.*, 2013]. SAI does not easily lend itself to regional impositions due to the rapid dispersion of aerosols in the stratosphere. In contrast, other SG proposals such as MCB might be entirely confined to specific regions that are the most sensitive to that technique [Shepherd, 2009]. Nevertheless, SAI could be contained or promoted in a single hemisphere due to the general poleward transport tendency of the stratospheric circulation [Robock *et al.*, 2008, Haywood *et al*., 2013]. Preferential aerosol injection in a single hemisphere would alter tropical sea-surface temperature (SST) gradients and displace the ITCZ toward the opposite hemisphere as observed following the 20th century Katmai (1912) and El Chichón (1982) volcanic eruptions [Haywood *et al.*, 2013, 2016]. Consequentially, SAI concentrated in the NH would likely reduce rainfall over the Sahel and vice versa for SAI in the SH [Haywood *et al.*, 2013].

---

*A paper based on this chapter has been submitted to Nature Climate Change:

A. C. Jones, J. M. Haywood, N. Dunstone, M. K. Hawcroft, K. I. Hodges, and A. Jones (2017), Solar geoengineering and North Atlantic tropical cyclone frequency, *submitted to Nature Climate Change*

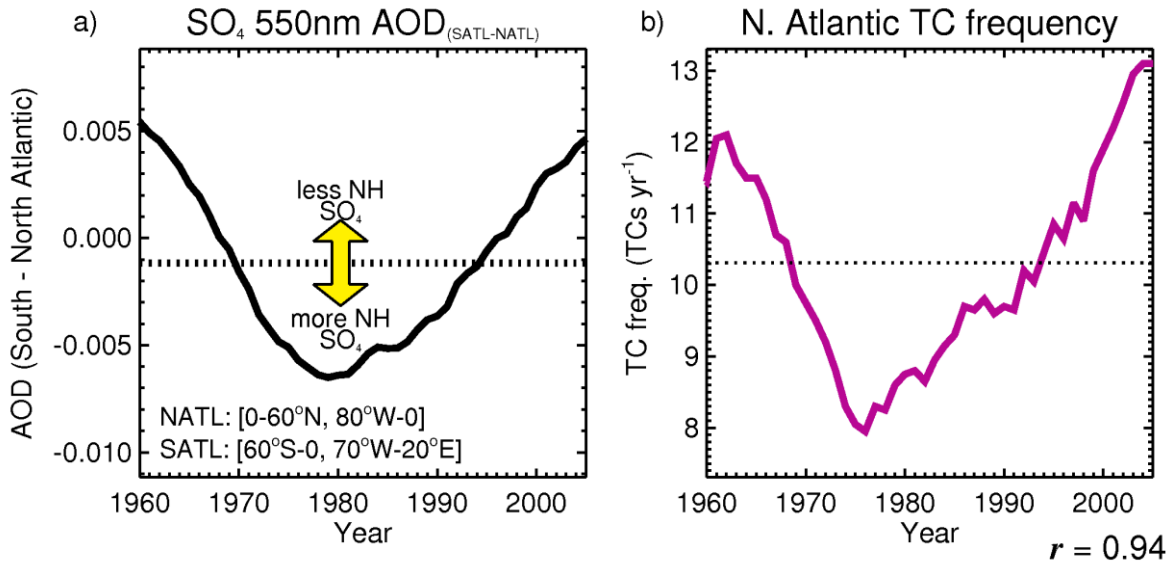

Figure 6.1. (a) SO_4 550nm AOD: time-series of difference between the North Atlantic basin and South Atlantic basin in HadGEM2-ES HIST simulations, (b) modelled North Atlantic TC frequency. Both indices smoothed by 10 y running mean.

Another phenomenon related to the location (latitude) of the ITCZ is North Atlantic tropical cyclone (TC) frequency [Dunstone *et al.,* 2013]. An ITCZ displaced to the north provides optimal conditions for cyclogenesis promotion from African easterly waves (AEWs) in the hurricane main development region (MDR, [5-25N, 15-85W]), which results in anomalously high TC activity [Goldenberg *et al.*, 2001; Dunstone *et al.*, 2013]. In contrast, an ITCZ displaced to the south is associated with increased wind shear over the MDR and attenuated TC activity. A significant attenuation of TC activity followed the El Chichón (1982) and Pinatubo (1991) volcanic eruptions, both of which primarily enhanced the NH aerosol burden [Evan, 2012; Guevara-Murua *et al.*, 2015]. Conversely, the Tambora (1815) and Agung (1963) volcanic eruptions primarily enhanced the SH aerosol burden, and were subsequently followed by periods of enhanced TC activity [Guevara-Murua *et al.*, 2015].

GCM studies have implicated periods of high (low) NH-centric anthropogenic aerosol emissions with attenuated (enhanced) TC activity in the 20th century [Emanuel and Mann, 2006; Wang *et al.*, 2012; Dunstone *et al.*, 2013; Chiacchio *et al.*, 2017]. Dunstone *et al.* (2013) in particular found a strong correlation between active (inactive) TC periods and periods of abated (enhanced) anthropogenic aerosol emissions over the 20th century. Figure 6.1 shows the difference between SO_4 550nm AOD in the South Atlantic ocean basin [0-60S, 70W-20E] and the North

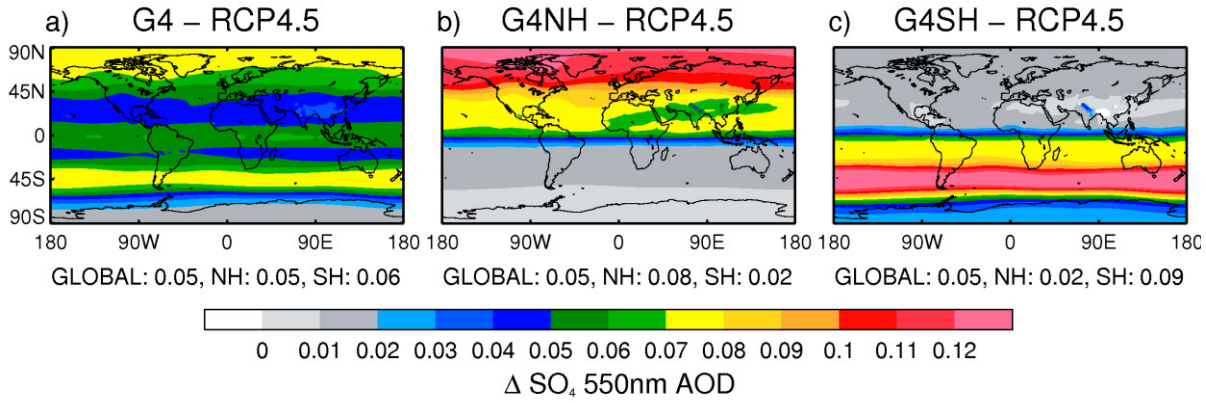

Figure 6.2. SO_4 550nm optical depth anomaly 2020-2070 for (a) G4, (b) G4NH and (c) G4SH relative to RCP4.5

Atlantic ocean basin [0-60N, 80W-0] for the period 1960-2005 (Fig. 6.1a) and the corresponding North Atlantic annual TC frequency (Fig. 6.1b), as derived from the 'historical' simulations in Dunstone *et al.* (2013). Both sets of data are have been smoothed by 10-year running-means. The correlation between the variables is striking at 0.95, suggesting a strong positive linear relationship. However, correlation does not prove causality. This result strongly suggests that periods of high aerosol concentrations over the North Atlantic Ocean (associated with elevated anthropogenic emissions) acted to partially attenuate North Atlantic TC frequency in the recent historical period [Dunstone *et al.*, 2013].

The strong relationship between asymmetric aerosol burdens and North Atlantic TC activity raises the question of whether SAI could be used to modulate North Atlantic TC activity. In this chapter, we investigate the effects of both single-hemisphere and global SAI scenarios on North Atlantic TC activity using simulations performed with HadGEM2-ES. For verification and optimisation purposes, we also track TCs in the ERA-I re-analyses for the period 1979-2014 [Dee *et al.*, 2011] and compare the ERA-I and simulated TC frequency with observations from the HURDAT2 "Best Tracks" dataset [Landsea and Franklin, 2013].

6.2 Model and simulations

HadGEM2-ES is a fully coupled atmosphere–ocean climate model developed by the UK Met Office [Collins *et al.*, 2011]. The atmospheric sub-model has 38 levels extending to ~40 km, with a horizontal resolution of $1.25^{o} \times 1.875^{o}$ latitude and longitude, respectively. The model includes the CLASSIC aerosol scheme [Bellouin *et al.*, 2011] and an interactive carbon cycle. HadGEM2-ES is forced following the

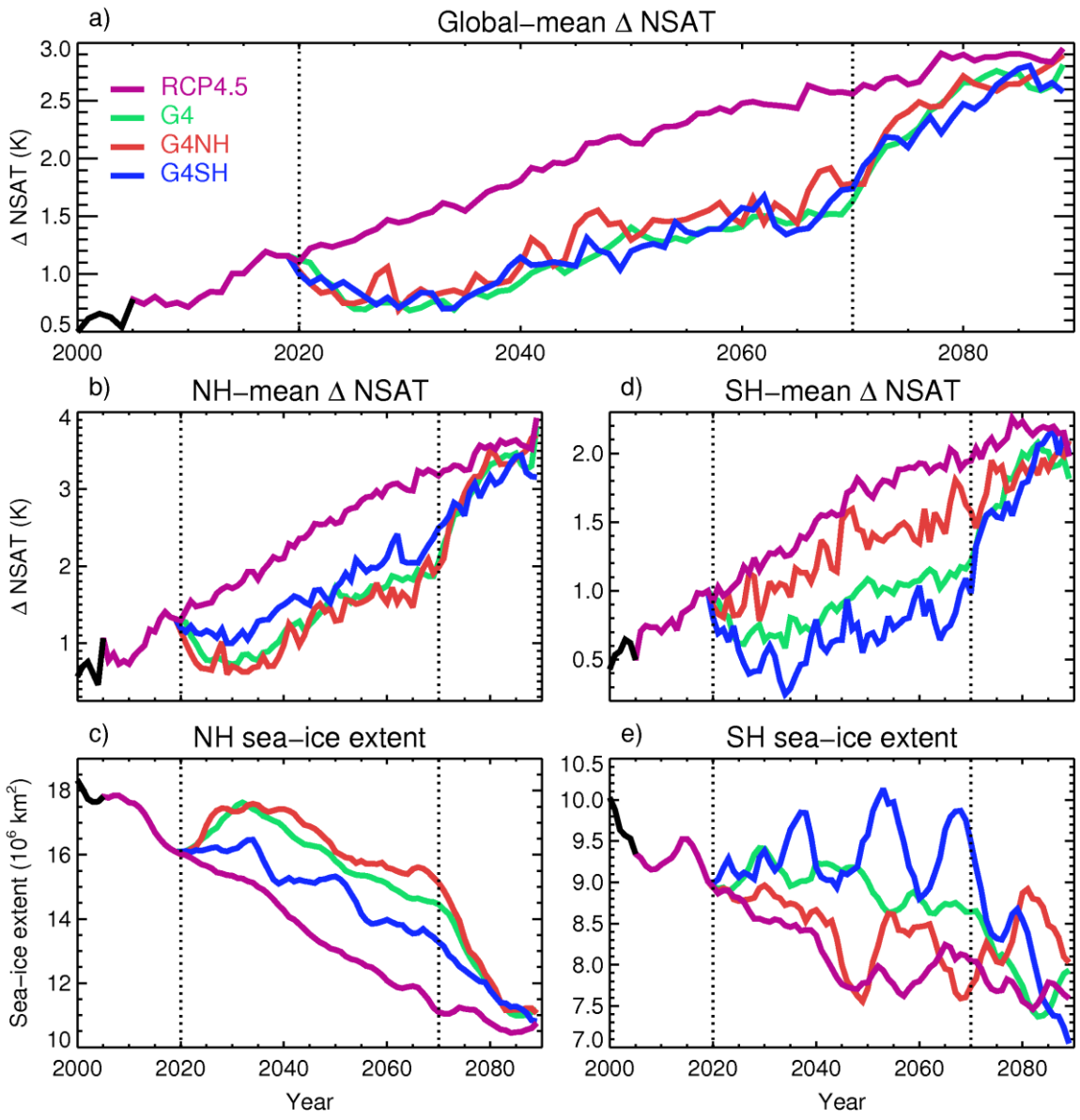

Figure 6.3. (a) Global-mean near-surface air temperature (NSAT) anomaly relative to a 240 y pre-industrial control simulation for RCP4.5/G4/G4NH/G4SH; (b,c) NH NSAT anomaly and total sea-ice extent (10^6 km^2); (d,e) SH NSAT anomaly and total sea-ice extent. Sea-ice extents are smoothed by a 5-year running mean

---

CMIP5 protocol using historical data from 1860 to 2005 and RCP scenarios up to 2100 [Jones *et al.*, 2011; Taylor *et al.*, 2012]. Further details of the model configuration are provided by Haywood *et al.* (2013). Note that HadGEM2-ES differs from HadGEM2-CCS (Chapters 4 and 5) by incorporating an interactive tropospheric chemistry module (UKCA) at the expense of HadGEM2-CCS's well-resolved stratosphere [Martin *et al.*, 2011]. SO_4 aerosol is represented by ammonium sulphate refractive indices and the standard aerosol size distributions for CLASSIC [Bellouin *et al.*, 2007], rather than the *volc2* size distribution used in Chapters 4 and 5.

We assess two ensemble members for the recent historical period (1950-2005, hereafter denoted HIST) and 3 ensemble members for the RCP4.5 scenario (2006-2089). For SAI, we assess 3 ensemble members for a global SAI scenario (G4) in which a constant injection rate of 5 Tg[SO_2] yr^{-1} is applied uniformly over the globe from 2020-2070, and 1 ensemble member each for NH-only (G4NH) and SH-only (G4SH) SAI scenarios in which 5 Tg[SO_2] yr^{-1} is injected evenly over the hemisphere from 2020-2070 [Haywood *et al.*, 2013]. We assess the impact of SAI-cessation by abruptly suspending aerosol injection in year 2070 in G4/G4NH/G4SH and allowing the model to run for a further 20 years. The G4 scenario follows the GeoMIP protocol [Kravitz *et al*., 2011], while the G4NH and G4SH scenarios were conducted by Haywood *et al.* (2013). Figure 6.2 shows the spatial maps of the SO_4 550nm optical depth anomalies in the SAI simulations relative to RCP4.5. It is clear from Fig. 6.2 that the geoengineered aerosol is concentrated primarily in the hemisphere(s) of injection. Figure 6.3 shows the global and hemispheric-mean temperature and sea-ice changes for the ensemble-means of the simulations. SAI does much to ameliorate changes in standalone RCP4.5, with the principal counteractive effect occurring in the hemisphere(s) of injection. However, the impacts in the unaltered hemisphere are significant, for instance, an NH cooling of 0.7 K in G4SH relative to RCP4.5 (2020-2070), compared to 1 K in G4 and 1.1 K in G4NH (Fig. 6.3b).

6.3 Storm tracking

TC tracking is conducted using Kevin Hodges' TRACK code (vn. 1.4.7), which has also been used for a variety of similar investigations [e.g. Hodges, 1995, 1996, 1999; Hoskins and Hodges, 2002; Bengtsson *et al.,* 2007; Strachan *et al.*, 2013; Roberts et al., 2015]. Hodges (1995) provides a detailed account of TRACK's core functionality. We adopt the approach of Bengtsson *et al.* (2007) (hereafter *BE07*) here. Firstly, we determine the relative vorticity (ξ) on 850, 500, and 250 hPa vertical pressure levels from the zonal (U) and meridional (V) wind using: $\xi = (1/a \times \cos(\theta)) \times (dV/d\lambda - dU\cos(\theta)/d\theta)$, where a is Earth's radius, and θ and λ are latitude and longitude in radians respectively. U and V are provided on 6 hour time-steps, and we only consider the June-November (JJASON) season, in which most of the North Atlantic TC activity occurs. For ERA-I [Dee *et al.*, 2011] we use the full Gaussian resolution (H512×256) datasets on 6 hour time-steps for the period 1979-2014.

The data is firstly spectrally filtered using spherical harmonic decomposition, which translates the HadGEM2-ES and ERA-I data onto a consistent Gaussian grid (128 × 64 longitudes by latitudes) and truncates wavenumbers less than 5 and greater than 42 (i.e. T42) [e.g. Hoskins and Hodges, 1992]. Additionally, we employ a Hoskins filter to smooth the data and reduce the Gibbs effect [Sardeshmukh and Hoskins, 1984]. For each simulation and for each year, we run TRACK using the same criteria as *BE07* to identify and track vortices. As we are only interested in North Atlantic TCs in this work, we restrict the storm tracking to the NH. Storms are initially identified as local maxima in the 850 hPa relative vorticity field that exceed 0.5×10^{-5} s^{-1} at a spectral resolution of T42. All vortices are retained at this stage, providing that their lifetimes exceed 2 days. As noted by *BE07*, while this method necessitates the tracking of many systems, it is a necessary approach to capture as much of the TC lifetime as possible. To identify the vortices with a warm core structure (i.e. TCs), we reference the tracks to the vorticity field at the 850, 500, and 250 hPa levels at a resolution of T63, using the steepest ascent maximization approach described in *BE07.* The criteria used to identify the TC are as follows:-

1. Lifetime ≥ 2 days (i.e. 8 time steps)
2. Cyclogenesis, defined by first identification, must occur within 0-30 ^{o}N
3. The maximum T63 intensity of relative vorticity at 850 hPa during the lifetime ≥ ξ_1 for some chosen value of ξ_1
4. There must be a T63 vorticity maxima at each level up to 250 hPa and the difference in vorticity between 850 hPa and 250 hPa (850-250) ≥ ξ_V for some chosen value of ξ_V (the *warm core* criterion)
5. Criteria 3 and 4 must be achieved for at least *n* consecutive time steps

Finally, we impose the spatial criterion that storms must traverse the North Atlantic hurricane main development region (MDR, [5-25^{o}N, 15-85^{o}W]). This criterion should help us avoid falsely identifying extratropical storms as TCs. For the HURDAT2 “Best Track” observations [Landsea and Franklin, 2013], we impose the following TC selection criteria:-

1. Lifetime ≥ 2 days, with at least one day within JJASON
2. Maximum sustained wind-speed ≥ 34 knots (i.e. attains TC status)
3. Must pass through 0-30 ^{o}N and within the North Atlantic basin

As with *BE07*, we test different permutations of (ξ_1, ξ_V, n = 4) for ERA-I and HadGEM2-ES against HURDAT2. For ERA-I, we find that a TC selection criterion of (6, 5.5, 4) provides the best fit to HURDAT2. This criterion closely resembles the *BE07* criterion of (6, 6, 4). Previous studies have found that HadGEM2-ES has a low bias in terms of TC intensity/frequency in the North Atlantic basin, which is possibly attributable to the coarse spatial resolution of the model [e.g. Fig. 1g of Camargo, 2012; Williams *et al.*, 2012; Haywood *et al.*, 2016]. In this study, we also observe this bias when using the ERA-I criterion (6, 5.5, 4) to identify TCs in the HadGEM2-ES simulations. Smith *et al.* (2010) and Dunstone *et al.* (2013) found that HadGEM2-ES is able to skilfully predict TC frequency trends when the TC intensity thresholds are relaxed. As we are primarily interested in how TC frequency responds to SAI, we use a similarly pragmatic approach here. Specifically, we relax the TC criterion to (4.5, 3.5, 4) for the HadGEM2-ES simulations, which produces a similar number of TCs in HIST to the HURDAT2 observations (Fig. 6.4 and Tables 6.1 and 6.2). It is important to note that the characteristics (e.g. the intensity) of the simulated TCs that fulfil the criteria (4.5, 3.5, 5) will differ from those of the ERA-I TCs due to the different selection criteria applied. Nevertheless, the model capably produces historical TC trends (Fig. 6.4), which gives us confidence that this approach allows us insight into future TC frequency trends under the RCP4.5 and SAI scenarios. The correlation coefficients between the TC frequencies using the two different TC selection criteria (i.e. *r* in Tables 6.1 and 6.2) indicate strong positive correlations. This suggests that the results of this study might be resistant to our choice of TC selection criteria.

			(4.5, 3.5, 4)		(6, 5.5, 4)		
Expt.	Ens.	Year	Mean	St. Dev.	Mean	St. Dev.	*r*
HURDAT	-	1979-2005	10.2*	4.5*	-	-	-
ERA-I	-	1979-2005	22.4	6.4	10.6	4.2	0.81
HIST	1	1979-2005	10.9	3.6	4.7	2.6	0.80
	2	1979-2005	11.9	3.6	4.4	2	0.62

Table 6.1. TC frequency in the ERA-I era for HadGEM2, ERA-I and HURDAT2. *Note that the specified configuration of TRACK is not relevant to the HURDAT observations

			(4.5, 3.5, 4)		(6, 5.5, 4)		
Expt.	Ens.	Year	Mean	St. Dev.	Mean	St. Dev.	*r*
HURDAT	-	1950-2000	9*	3.2*	-	-	-
HIST	1	1950-2000	10	2.9	3.9	2.2	0.62
	2	1950-2000	10.8	3.6	4.2	2.1	0.66
RCP4.5	1	2020-2070	9.7	3.3	3.7	1.9	0.5
	2	2020-2070	9.9	3	3.7	2.1	0.68
	3	2020-2070	9.6	3.5	3.4	2.1	0.69
G4	1	2020-2070	11.3	3.2	4.3	2.3	0.66
	2	2020-2070	11.9	4	4.9	2.1	0.77
	3	2020-2070	10.4	3.8	3.7	2.2	0.59
G4NH	-	2020-2070	7.6	2.9	3.1	1.7	0.69
G4SH	-	2020-2070	14.3	3.6	6	2.7	0.63

Table 6.2. TC frequency in the 1950-2000 (HIST) and 2020-2070 periods. *Note that the specified configuration of TRACK is not relevant to the HURDAT observations

6.4 Results

6.4.1 Annual TC frequency

Figure 6.4 shows the JJASON, 10-year running-mean TC frequency over the historical period in the model, reanalyses and HURDAT2 observations (Fig. 6.4a), and the simulated TC frequency in the RCP4.5 and SAI scenarios (Fig. 6.4b). In the historical period, the model skilfully captures observed TC frequency trends (r = 0.71 with HURDAT) including the decline in activity through ~1960 to ~1980 and the increase in activity since ~1980. In RCP4.5, TC frequency decreases steadily between 2020 and 2070 (-0.3 TCs dec^{-1}), while in G4 TC frequency increases slightly relative to HIST (annual-mean TCs y^{-1} = 11.2 compared to 10.4). G4SH exhibits a marked increase in TC frequency relative to HIST (annual-mean TCs y^{-1} = 14.3), while G4NH conversely exhibits a pronounced reduction (annual-mean TCs y^{-1} = 7.6). The G4NH and G4SH results are consistent with observed TC activity changes following volcanic aerosol enhancements confined to a single hemisphere [Evan, 2012; Guevara-Murua *et al.*, 2015]. TC frequency swiftly rebounds to concurrent RCP4.5 levels following the cessation of SAI in G4, G4NH, and G4SH in

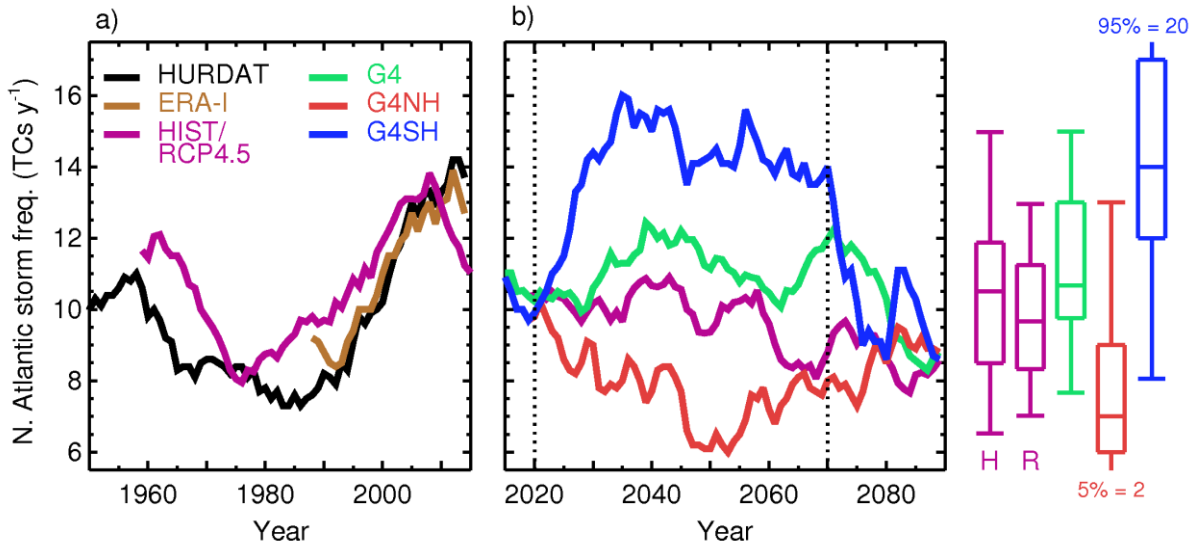

Figure 6.4 (a) Historical TC frequencies, smoothed by 10-year running means, for ERA-I [Dee et al., 2011], the ensemble mean of the HadGEM2-ES HIST simulations and HURDAT2 observations [Landsea and Franklin, 2013]. (b) the same as (a) but for the RCP4.5 and SAI simulations. Vertical dotted lines in (b) indicate the start and end of SAI in G4, G4NH, and G4SH. The box and whisker plots (right) show the 5, 25, 50, 75, and 95% quantiles of the HIST ('H', 1950-2000) and RCP4.5/ SAI (2020-2070) raw annual TC counts

		Raw TC counts (Fig. 6.5) 1950-2000	10-yr mov. av. TC counts (Fig. 6.4) 1960-2000
RCP4.5	2020-2070	**0.17**	**0.80**
	2050-2070	**0.07**	0.044
	2060-2070	0.018	6.3×10^{-4}
G4	2020-2070	**0.12**	9.1×10^{-6}
	2050-2070	**0.22**	1.9×10^{-3}
	2060-2070	**0.07**	0.016
G4NH	2020-2070	3.6×10^{-6}	0
	2050-2070	2.3×10^{-4}	0
	2060-2070	1.8×10^{-3}	8.3×10^{-7}
G4SH	2020-2070	1.2×10^{-7}	0
	2050-2070	9.4×10^{-4}	0
	2060-2070	0.042	4.8×10^{-7}

Table 6.3. p-values calculated from a 2-sided Wilcoxon rank sum test on annual TC frequency for TRACK configuration (4.5, 3.5, 4). Bold font indicates the values that are not significant at the 5% level (i.e. > 0.05).

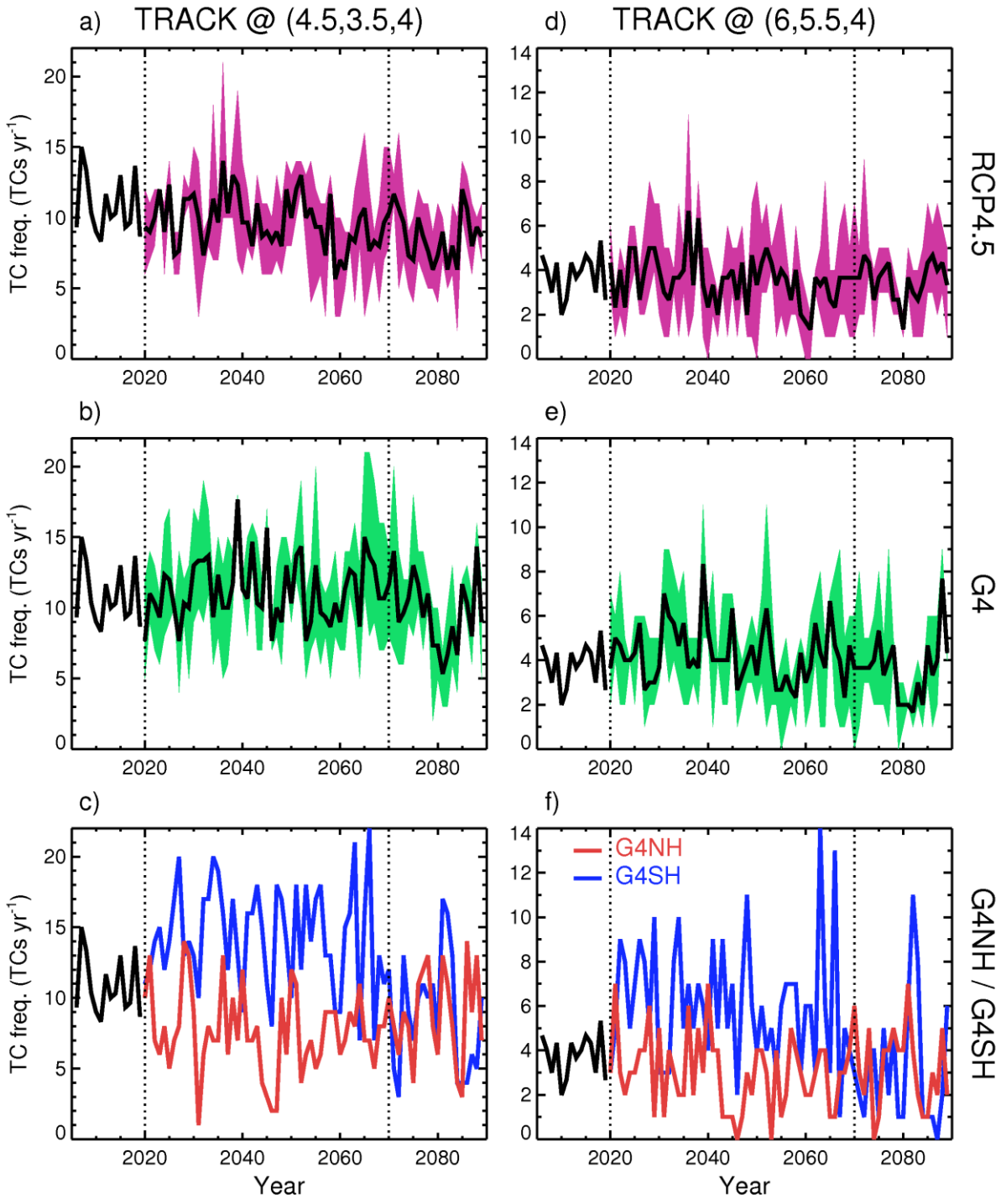

Figure 6.5. Annual TC frequency determined using TC selection criteria: (a-c) (4.5,3.5,4) and (d-f) (6, 5.5, 4). Purple and green shading indicate the range of RCP4.5 and G4 values

year 2070 (Fig. 6.4b), which confirms that the "termination effect" [Jones *et al.*, 2013] extends to North Atlantic storm activity.

To determine whether TC changes are statistically significant with respect to HIST, we employ a Wilcoxon rank sum test (WRST) [Wilcoxon, 1945], which is similar to a Student's t-test but without the underlying assumption of normally distributed data.

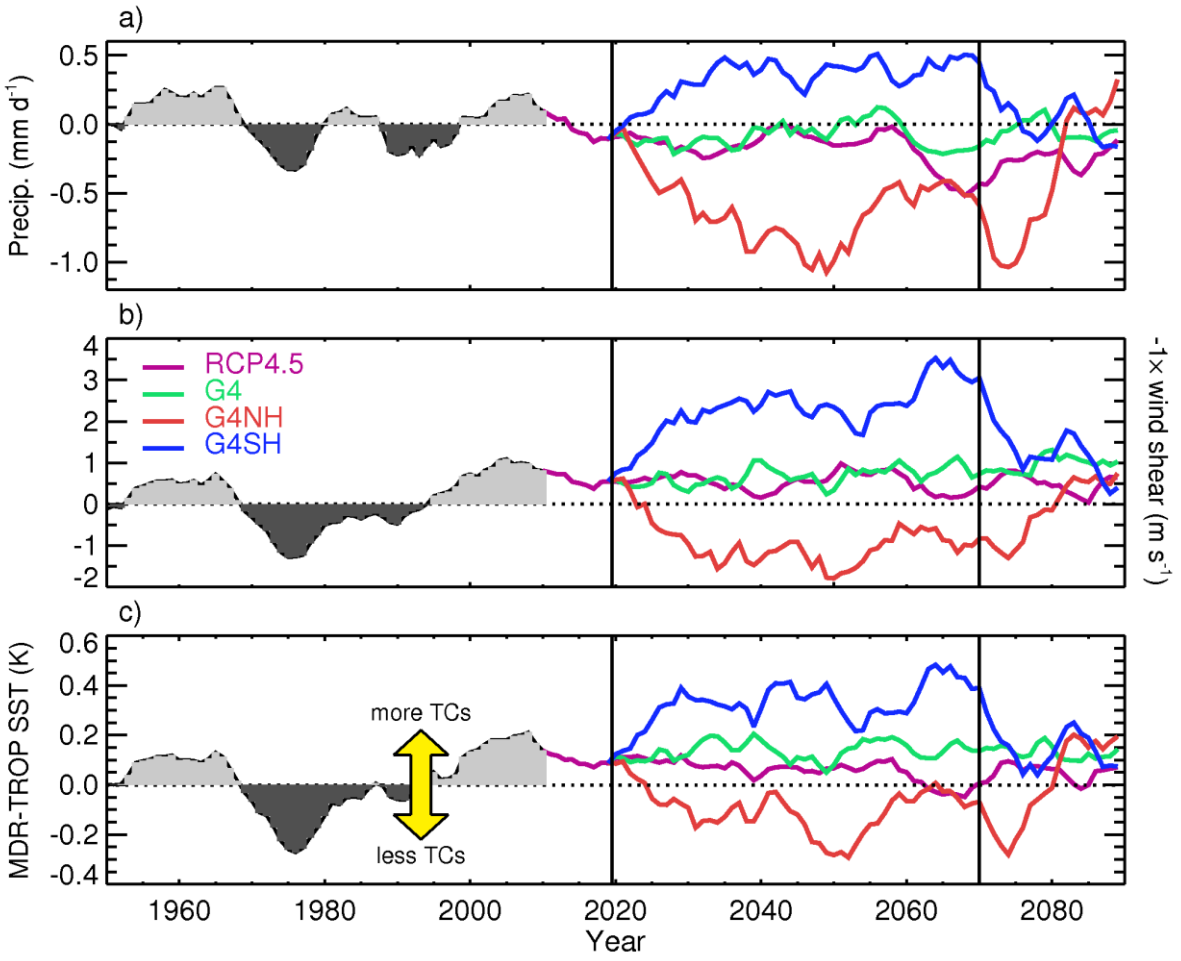

Figure 6.6. (a) JJASON precipitation anomaly (relative to 1950-2000) averaged over the MDR [5-20N, 15-85W]. (b) the same as (a) but for inverse vertical zonal-wind shear (U(850 hPa) – U(250 hPa)). (c) the same as (a) but for relative SSTs (i.e. MDR minus the tropical mean SST)

We apply the WRST to raw TC frequency (Fig. 6.5) and the 10-year running-means (Fig. 6.4), and compare the HIST period with various subsets of the RCP4.5 and SAI time periods (Table 6.3). It is clear from the *p*-values in Table 6.3 that the G4NH and G4SH TC changes are significant at the 5% level for every test applied. Conversely, the raw TC frequency changes in the G4 scenario are not statistically significant at the 5% level, but the smoothed values are. Interestingly, the TC frequency decline in the RCP4.5 scenario (relative to HIST) eventually becomes significant between 2060 and 2070.

6.4.2 TC-related indices and climate anomalies

The progression of AEWs to TCs is contingent on the ambient meteorological conditions, which may act to induce or dissipate the storm. For instance, enhanced zonal-wind shear over the MDR counteracts cyclogenesis [Latif *et al.*, 2007],

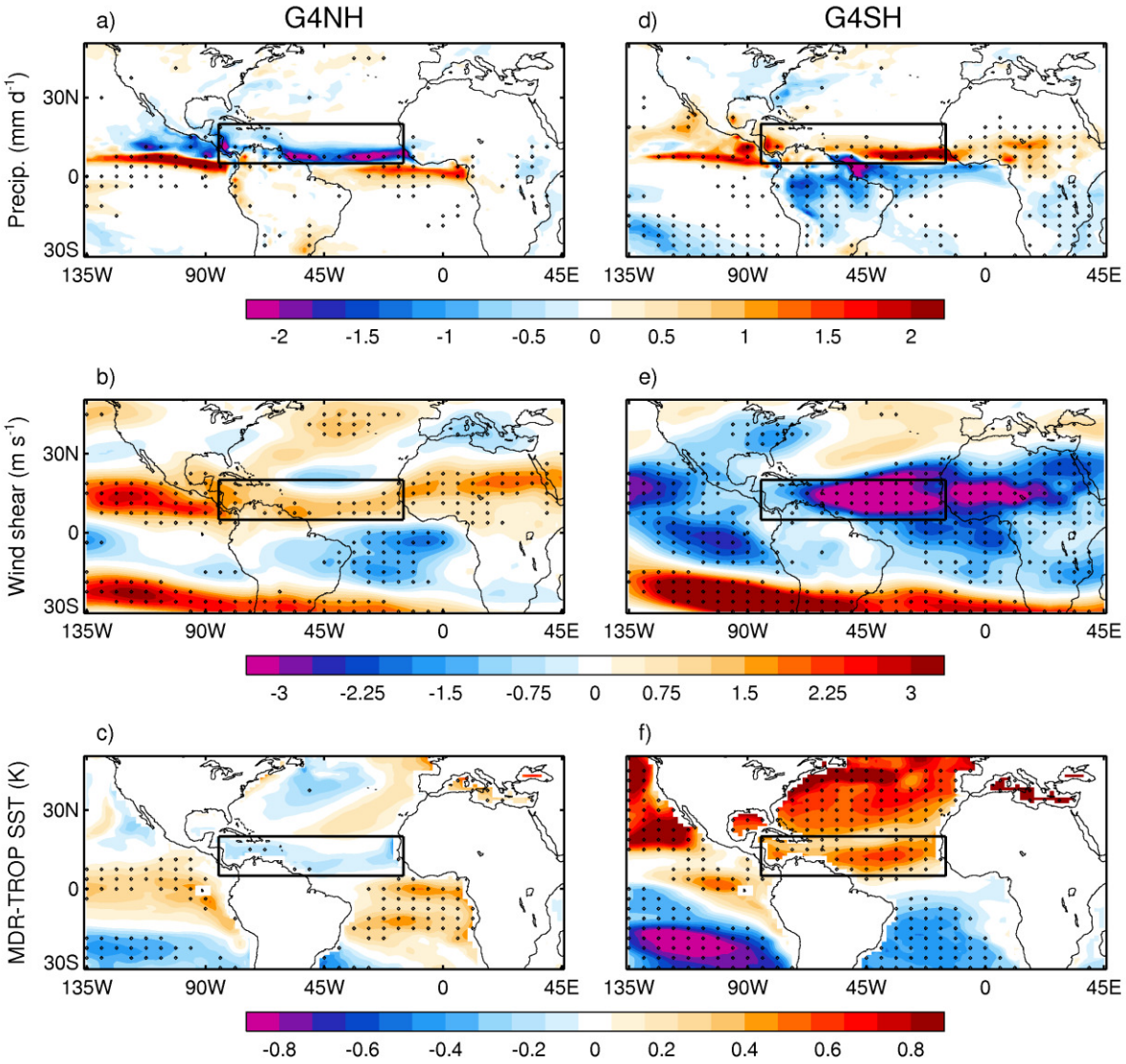

Figure 6.7. (a) G4NH JJASON precipitation anomaly relative to 1950-2000. (b) the same as (a) but for inverse vertical zonal-wind shear. (c) the same as (a) but for relative SSTs. (d-f) the same as (a-c) but for G4SH. Stippled regions on the maps show where differences are outside the 90% variability of a 240 y pre-industrial control ensemble mean [Dunstone et al., 2013]. The MDR, as used in Fig. 2, is marked by black rectangles.

whereas a warm ocean surface provides the storm vortex with energy [Villarini and Vecchi, 2012]. Historical trends in wind shear (U_{850}-U_{250}), precipitation and relative SST (MDR minus tropical-mean) in the MDR closely correlate with North Atlantic TC activity [Fig 1. in Dunstone *et al.*, 2013] and these indices offer an alternative tool to counting vortices for predicting future TC trends. Figure 6.6 shows various North Atlantic TC indices as extracted from the HadGEM2-ES simulations. It is clear that active (1950-1965, 1995-2014) and inactive (1965-1995) TC periods in the HIST simulation (Fig. 6.4a) were commensurate with active and inactive periods in the indices (Fig. 6.6). The same correlations between indices and TC frequency persist

in the RCP4.5 and SAI simulations, with G4SH and G4NH exhibiting continuously positive and negative indices respectively (Fig. 6.6). This suggests that meteorological conditions presently conducive to cyclogenesis remain conducive in these scenarios. Figure 6.7 shows spatial maps of precipitation, wind shear and relative SST anomalies in the G4NH and G4SH scenarios. In G4NH, aerosol-induced cooling of the North Atlantic sea-surface (>30N) results in a southward shift and strengthening of the African easterly jet (AEJ), increasing wind-shear in the MDR, and anomalous descent and precipitation reduction over the MDR (Fig. 6.7a-c) [Dunstone *et al.*, 2013]. Conversely, preferential cooling of the South Atlantic in G4SH enhances ascent and precipitation in the MDR and shifts the AEJ north, reducing zonal-wind shear over the MDR and producing favourable conditions for cyclogenesis (Fig. 6.7d-f).

6.4.3 TC spatial statistics

HadGEM2-ES generates too few (many) TCs in the east (west) MDR compared with ERA-I (Fig. 6.8). This might be attributable to a low bias in the albedo over the Southern Ocean; Haywood *et al.* (2016) found that persistent biases in TC indices (Fig. 6.6) in the model were significantly reduced when the SH was artificially brightened by various mechanisms including SAI.

Regardless of source, the low genesis bias in the east results in too few TCs migrating north and transitioning to extratropical storms (Fig. 6.8e). Nevertheless, it is interesting to note that in G4SH (G4NH) cyclogenesis is enhanced (attenuated) on both sides of the MDR (Fig. 6.9c,d). In the unperturbed RCP4.5 simulation, a disjointed picture emerges of weakened TC genesis in the Caribbean Sea and a northward shift in the primary genesis region over West Africa (Fig. 6.9a). A global SAI application (G4) appears to counteract cyclogenesis changes over the Caribbean in RCP4.5, but does little to ameliorate changes in the east (Fig. 6.9b). We qualify these inferences by reiterating that the TC frequency changes are not significant in RCP4.5 and G4 (Table 6.3), and noting that North Atlantic TC projections in the RCP4.5 scenario from the CMIP5 ensemble have proven inconclusive [Villarini and Vecchi, 2012; Camargo, 2013].

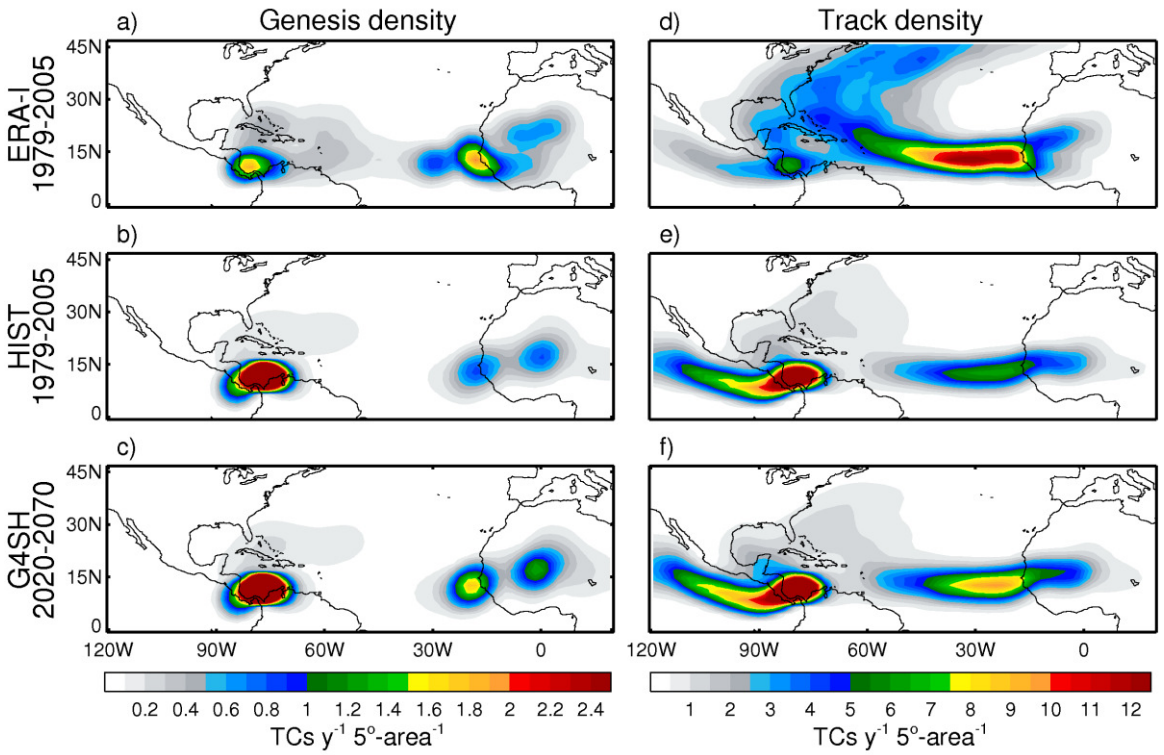

Figure 6.8 (a-c) TC genesis density and (d-f) track density for: (a,d) ERA-I with TRACK at (6,5.5,4), (b,e) HIST, and (c,f) G4SH both with TRACK at (4.5,3.5,4)

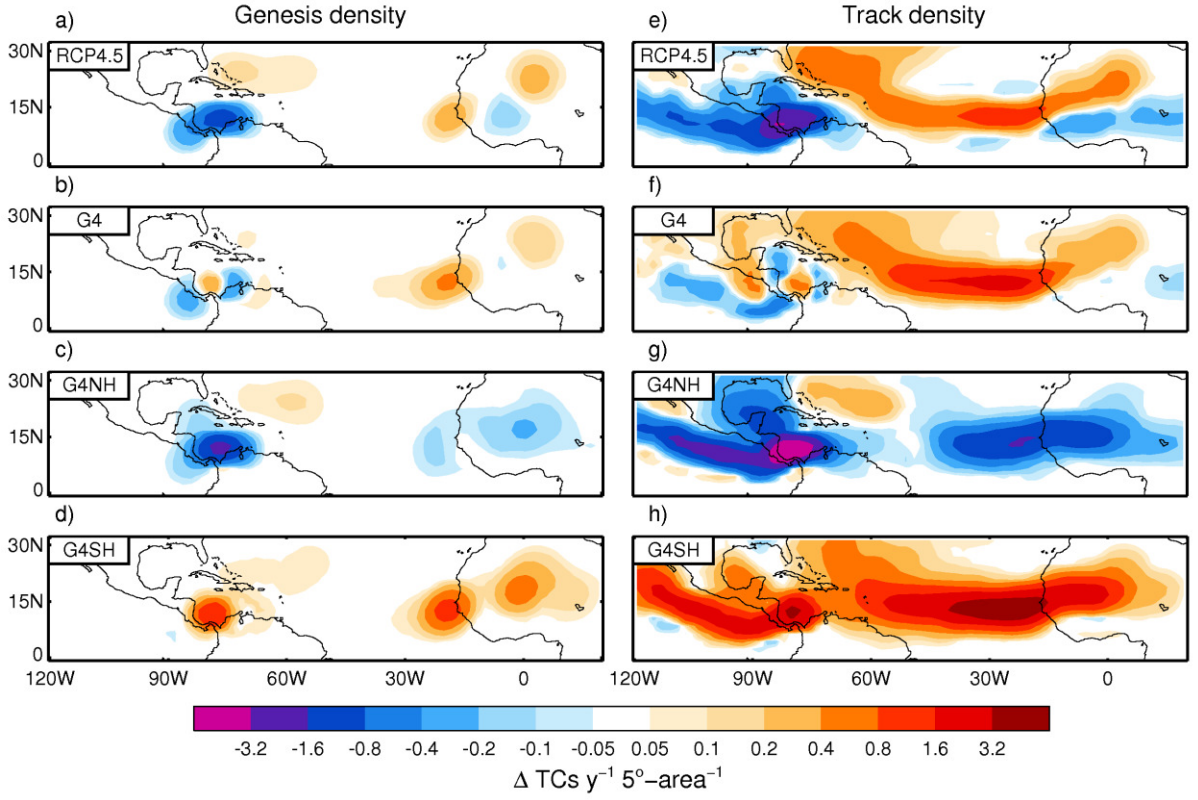

Figure 6.9 (a-h) TC genesis and track density anomalies (2020-2070 relative to 1950-2000) in units of TC number density per year per unit area, where the unit area is equivalent to a 5° spherical cap [Bengtsson et al., 2007; Hodges, 2008]

6.5 Summary and Discussion

The primary result of this research is to demonstrate that single-hemisphere SAI could be applied to modulate North Atlantic TC frequency. However, a scenario in which TC frequency is suppressed by NH SAI would unavoidably induce droughts in the Sahel, and vice versa for SH SAI [Haywood *et al.*, 2013]. TC frequency is causally related to local SSTs, which in turn are sensitive to changes in solar irradiance at the surface; therefore it is likely that the results of this research are applicable to any SG method [Haywood *et al.*, 2016]. This work reemphasizes the perils of unilateral geoengineering, which might prove attractive to individual actors due to a greater controllability of local climate responses; but with inherent additional risk elsewhere [Robock *et al.*, 2008; Ricke *et al.*, 2010]. For instance, the COP21 target of stabilising global-mean warming at 1.5 K above pre-industrial levels [UNFCCC, 2015] appears extremely difficult to achieve even with measures well beyond what would be considered under conventional mitigation scenarios [Jones *et al.*, *submitted*]. The overshoot of 1.5 K could theoretically be combated using SAI (Fig. 6.3), but if applied just to cool the northern hemisphere, which might have preferential local climate responses (e.g. less Atlantic TCs) for the geoengineering parties, there could be potentially devastating impacts (e.g. Sahelian drought) in other regions. We therefore recommend the expeditious implementation of international regulation to control large-scale SG deployment, in order to develop a truly global approach and deter large-scale unilateral deployment.

A second observation from this work concerns the inability of HadGEM2-ES to generate North Atlantic TCs of a sufficient intensity and lifetime to migrate north and transition into extra-tropical storms (Fig. 6.8). This is a persistent bias of the HadGEM family of models (and, in general, the current generation of GCMs) [e.g. Strachan *et al.*, 2013] which might relate to the coarse-spatial resolution of the model, to a low bias in the albedo of the Southern Ocean, or to presently unknown factors [Haywood *et al.*, 2016]. It will be interesting to see whether the TC intensity/frequency bias improves in the next generation Hadley Centre GCM (UKESM1), which will have a greater spatial resolution (N216) than HadGEM2 (N96).

Chapter 7 Summary and Discussion

7.1. Summary

Ineffective international efforts to mitigate GHG emissions and related concerns over the climatic impacts of unabated GHG emissions have galvanised the scientific community to develop alternative strategies (i.e. geoengineering) for counteracting global warming. SAI, which mimics large scale volcanic eruptions, is the most widely-researched geoengineering proposal [Irvine *et al*., 2016]. The pre-eminence of SAI over other geoengineering proposals is most likely due to the volcanic analogue, with volcanic eruptions providing invaluable observations that have been utilised for GCM verification purposes. Consequently, GCM-based studies have identified various robust climate responses to SAI that can also be seen in the volcanic signal (e.g. changes to the hydrological cycle [Trenberth and Dai, 2007; Tilmes *et al*., 2013]). One area of SAI research that is yet to receive significant traction is the potential utility of alternative aerosols to SO_4, with SO_4's predominance relating to the volcanic analogue and the abundance of natural sulphur resources [Keith *et al.*, 2010]. Alternative aerosols may have greater light-scattering properties than SO_4, which would reduce the mass injection needed to achieve a certain radiative effect, or might be chemically inert and thus preserve stratospheric O_3 [Ferraro *et al.*, 2011; Pope *et al.*, 2012]. In fact, Keith *et al.* (2016) suggest that SAI with calcite ($CaCO_3$) could neutralise the background stratospheric aerosol and resultantly enhance O_3 concentrations whilst still inducing a global cooling effect. With SAI rapidly garnering scientific credibility (exemplified by its inclusion within AR5 [IPCC, 2013]) and with SO_4 an imperfect aerosol choice, it is instructive to assess the potential climatic impacts of injecting alternative aerosols to SO_4, which has provided the motivation for work presented in this thesis.

In this thesis, we have concentrated on two alternative aerosols: BC (which efficiently absorbs sunlight) and TiO_2 (which efficiently scatters sunlight), as well as conventional SO_4. In Chapter 2, we outlined Mie theory, which describes the interaction of light with spherical particles, and we introduced three key optical parameters (k_e, ω_0, g) which collectively describe the light extinction properties of a particle. We then used simple SW radiative transfer models to explore the radiative

impacts of aerosol layers composed of SO_4, BC, and TiO_2. This preliminary analysis was extended in Chapter 3, in which we employed a detailed radiative transfer code (SOCRATES), a custom-made model atmosphere, and a stratospheric aerosol layer model to investigate the radiative impacts of SO_4, BC, and TiO_2 aerosol layers. We found that to produce an instantaneous net (SW+LW) radiative forcing at the tropopause of -3.5 Wm^{-2}, which is equivalent to a doubling of CO_2 concentrations above pre-industrial levels [Ferraro *et al.*, 2011], would require a greater SO_4 mass burden (23-27 Tg) than for TiO_2 (8-14 Tg) or BC (1-2 Tg). We then investigated the stratospheric temperature response to SAI using an FDH code, and found that the stratospheric heating due to SW absorption for BC would be much greater (max ≈ 25 K) than for either SO_4 or TiO_2 (max ≈ 5 K), in agreement with the results of Ferraro *et al*. (2011). Consequently, the adjusted radiative forcing for a given instantaneous radiative forcing was found to be smaller for BC than for SO_4 or TiO_2. We also found that SO_4's forward-scattering properties resulted in an enhanced diffuse to direct ratio of sunlight at Earth's surface, an effect which was minimal for TiO_2 and BC, which could have consequences for plant productivity [Kalidindi *et al*., 2015].

In Chapter 4, we performed SAI simulations with HadGEM2-CCS in which SO_4, TiO_2, and BC were injected at such a rate as to counterbalance TOA energy changes in a high-end GHG concentrations scenario (RCP8.5). RCP8.5 was selected to give a significant greenhouse effect against which to employ geoengineering, in order to distinguish the climatic impacts specific to each aerosol. We found that BC injection resulted in the greatest hydrological cycle perturbation, despite also producing the weakest global cooling signal (Fig. 4.6). Combined with drastic stratospheric warming (max > 70 K, Fig. 4.17) that would induce significant ozone depletion, this result effectively excludes BC from being a realistic candidate for SAI. A novel result of these simulations was to show that TiO_2 also produces a significant stratospheric warming signal (max ≈ 22 K, Fig. 4.17) due to its absorption of solar UV radiation. It is important to note that this result pertains exclusively to rutile TiO_2; in contrast anatase TiO_2 would produce considerably less stratospheric warming [Dykema *et al*., 2016]. In Chapter 4, we investigated a comprehensive array of climatic variables – temperature, precipitation, sea-ice extent, stratospheric winds, thermosteric sea-level changes and permafrost – in order to elicit a nuanced perception of the climatic implications of SAI. A clear result of these simulations was to demonstrate the

myriad of climate change risks that could be offset by SAI, for instance, by comparing the end-of-century temperature changes in RCP8.5 (Fig. 4.11a) with geoSulf (Fig. 4.11b). It is tempting to view SAI research (and more generally, geoengineering research) as a moral hazard, as it divests time and resources from conventional climate change research [Crutzen, 2006]. However, if society fails to transition onto a sustainable energy pathway and GHG emissions continue unabated, then SAI might eventually become the only available tool capable of rapidly counteracting global warming and offsetting climate change risk. In this entirely conceivable scenario, SAI research becomes a moral and ethical imperative, in order to ensure that any SAI deployment is not implemented hastily and without suitable risk management.

SAI, as a geoengineering method, is fundamentally related to large-scale volcanic eruptions which transiently alter the stratospheric aerosol budget and induce a wealth of other climatic perturbations. In Chapter 5, we investigated a thus far sparsely-explored area of volcanology – the role of ambient meteorology in the dispersion of the volcanic aerosol plume. This study was serendipitously motivated by the results of preliminary model verification simulations performed for Chapter 4 (Fig. 4.4a), which showed that the AOD evolution for 10 1-day eruptions initiated on consecutive days exhibited high variability (the grey area in Fig. 4.4a). In Chapter 5, we found that this high AOD variability was particularly manifest in low-altitude (16-18 km) Pinatubo-like volcanic aerosol eruptions (Figs 5.2, 5.10, 5.11), whereas higher altitude eruptions (19-29 km) exhibited considerably less day-to-day variability (Fig. 5.2). A particularly interesting result of this study was the confinement of aerosol to the NH in some of the realisations (e.g. Fig. 5.10i) but much less so in others (e.g. Fig. 5.10a). Single hemisphere aerosol enhancements induce SST gradients which concomitantly shift the ITCZ toward the opposite hemisphere resulting in, e.g., Sahelian drought or greening [Haywood *et al.*, 2013]. Thus the ambient weather conditions during a large-scale volcanic eruption could have important climatic and societal implications in remote regions. It is therefore important that satellites are able to measure the precise altitude of the initial volcanic aerosol injection, in order to discern the significance of meteorological variability on the subsequent aerosol dispersion. Also, future GCM-based studies of volcanic eruptions should account for meteorological variability when designing their

simulations. Failure to account for meteorological variability might lead to false conclusions about model performance.

Conducting or promoting SAI in a single hemisphere in order to restrict the spatial magnitude of the climate response has been the subject of previous GCM-based studies [e.g. Robock *et al.*, 2008; MacMartin *et al.*, 2013; Haywood *et al.*, 2013]. Haywood *et al.* (2013) in particular found that single hemisphere SAI could produce diametrically opposed results, with NH (SH) SAI applications resulting in Sahelian drought (greening). This result alone could spur an individual actor (i.e. state or multinational organisation) to initiate unilateral SAI deployment for either benevolent or malevolent purposes. In Chapter 6, we have investigated whether single hemisphere SAI applications could be used to modulate North Atlantic tropical cyclone frequency. Our study was motivated by previous research that implicated hemispherically-asymmetric aerosol enhancements (of anthropogenic and volcanic origin) with low-frequency North Atlantic TC trends in the 20th century [Evan, 2012; Dunstone *et al.*, 2013; Guevara-Murua *et al.*, 2015]. This study was also motivated by the results of Chapter 5, in which we found that aerosol could remain trapped in a single hemisphere or be transported to both hemispheres depending solely on meteorological conditions. In Chapter 6, we utilised simulations that were performed for the Haywood *et al.* (2013) study with HadGEM2-ES, and tracked vortices in the tropical North Atlantic basin using the feature tracking software 'TRACK' [Hodges, 1995]. The primary result of this study was to demonstrate that SAI promoted in the SH would enhance North Atlantic TC activity, while SAI in the NH would attenuate TC activity (Fig. 6.4). Periods of heightened TC activity in the North Atlantic basin are historically associated with increased risk of intense hurricane landfall on the US coast, which can result in humanitarian and economical disasters [Rappaport, 2000]. In conjunction with the results of Haywood *et al.* (2013) and Ricke *et al.* (2010), our results demonstrate that regional or unilateral SAI applications would unavoidably produce winners and losers, or countries/regions that benefit from SAI implementation and countries/regions that would be put at a disadvantage. Therefore, SAI could be weaponized as readily as it could be utilised for local climate remediation, especially due to the non-localised climate response of a regional application. It is essential that policymakers begin implementing measures to deter unilateral SAI deployments; in order that any SAI deployment is to be used for the

general public good, and in a controlled and coordinated manner with suitable detection and attribution mechanisms installed (e.g. instruments aboard satellites).

7.2. Evaluation

It is useful to return to the thesis goals from Section 1.4 to assess whether this PhD has been successful. The first goal was to compare the climatic changes for scenarios in which SO_4, BC, and TiO_2 are injected at a sufficient rate as to achieve an equal amount of geoengineering. For the purpose of this work, we interpreted 'amount of geoengineering' to mean the energy perturbation at the top of the atmosphere and we devised an explicit goal of injecting aerosol at a sufficient rate as to stabilise annual and global mean TOA energy fluxes at pre-industrial levels. In order to compare SAI with alternative aerosols (and hence to answer Goal 1), we shall use the approach adopted by the Royal Society in their intercomparison of geoengineering proposals (Fig. 1.7). Firstly, we define 'effectiveness' as the ability to offset TOA energy fluxes, 'timeliness' as the speed with which the global-mean temperature responds to SAI in our simulations, 'safety' as the ability to offset all regional climate changes, and 'cost' as the relative cost of achieving a certain TOA radiative effect.

In terms of effectiveness, all 3 aerosols rapidly stabilise TOA energy fluxes following injection (Fig. 4.6a), although the stratospheric warming in the BC scenario (and, to a lesser extent, the TiO_2 scenario) reduces its efficacy (effectiveness: SO_4 = 4, TiO_2 = 3.75, BC = 3.5). In terms of cost, we must account for the relative price of materials and the amount of material that would need to be injected, as well as deployment and operating costs. Present day material costs are £2 bn/Tg for TiO_2 [Davidson *et al*., 2012], £0.8 bn/Tg for BC as carbon black [Kravitz *et al.*, 2012], and £0.2 bn/Tg for SO_2 [Robock *et al*., 2009]. To transport 1 Tg of a material per year to the stratosphere would initially cost ~£5 bn, with annual operating costs of ~£3.2 bn/yr [Robock *et al*., 2009]. If we multiply the 2100 aerosol injection rates from Chapter 4 (Table 4.3) by 1÷8.5 to approximate the injection rates necessary to attain 1 Wm^{-2}, we derive: 1.67 Tg[SO_2]/yr, 0.73 Tg[TiO_2]/yr, and 0.11 Tg[BC]/yr. The initial costs required to meet these injection rates are then: £8.5 bn for SO_2, £3.65 bn for TiO_2 and £0.55 bn for BC and annual operating costs are: £5.7 bn for SO_2, £3.8 bn for TiO_2 and

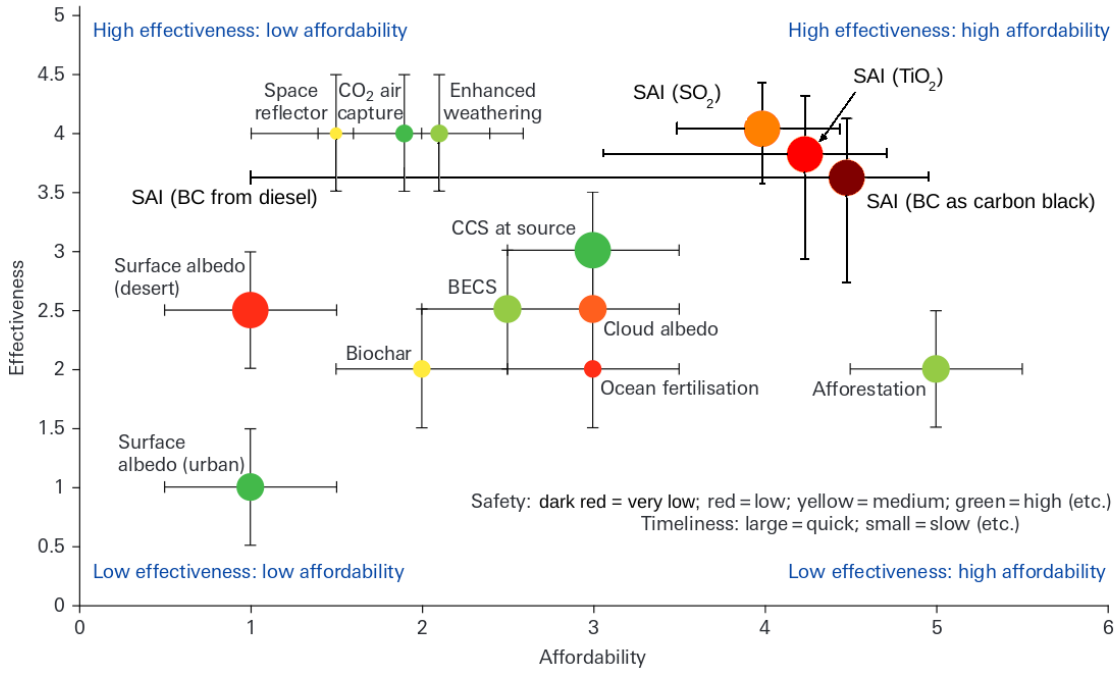

Figure 7.1 An update of the Royal Society's intercomparison of various geoengineering proposals (Fig. 1.7) which now includes SAI with SO_2, BC and TiO_2 injection (using the values derived from Chapter 4 results)

£0.44 bn for BC. From this tentative analysis, BC injection appears to be an order of magnitude cheaper than TiO_2 or SO_2. However, carbon black would have to be refined to create suitably sized BC particles for SAI (which might be prohibitively expensive). If diesel combustion were instead used to produce BC, then the overall cost of deployment would increase by 2 orders of magnitude [Kravitz et al., 2012] (affordability: SO_4 = 4, TiO_2 = 4.25, BC = 4.5). In terms of safety, geoBC exhibited the largest residual and aerosol-induced climate changes (including stratospheric warming of >70 K which would cause significant ozone depletion [Kravitz *et al.*, 2012]) and is therefore inherently more risky than either SO_2 or TiO_2 injection, or indeed most other geoengineering proposals (safety: SO_4 = orange, TiO_2 = red, BC = dark red). Finally, all 3 aerosols would reduce global-mean temperature within 1-2 years (Fig 4.6) (Timeliness: SO_4 = large, TiO_2 = large, BC = large). Figure 7.1 shows a modified form of Fig. 1.7 (i.e. from the Royal Society report) in which we have included our values for SAI with SO_2, TiO_2 and BC injection.

From the comprehensive analysis of climate changes in Chapter 4 and the direct comparison of SO_2, TiO_2 and BC injection scenarios given above, it is clear that we have done much to answer Goal 1 of this thesis. Goal 2 of this thesis was to determine the quantities of aerosol needed to obtain a certain radiative effect. Our

results from Table 4.3 provide lower limits on the amount of aerosol that would be needed to produce a certain radiative effect due to the lack of a detailed aerosol microphysics scheme in our model [Niemeier and Timmreck, 2015]. Finally, Goal 3 of this thesis was to investigate the extent to which SAI could counteract GHG-induced climate change. Comparing the climate changes in the 2090s in RCP8.5 with geoSulf (e.g. Fig. 4.11) it is clear that for temperature and precipitation, SAI with SO_2 injection would do much to ameliorate seasonal and annual climate change. However, HadGEM2-CCS does not incorporate a stratospheric chemistry module and hence is unable to quantify changes to ozone which could be significant [Tilmes *et al.*, 2009].There is much that can be inferred from the results of this thesis. For instance, in Chapter 5 we found that volcanic aerosol dispersion is highly sensitive to ambient meteorology for low altitude eruptions. This result could be used to design an SAI application in which aerosol is injected on certain days and specific locations depending on the ambient weather conditions, in order to maximise the aerosol's stratospheric lifetime. In Chapter 6 we showed that single-hemisphere stratospheric aerosol enhancements can modulate North Atlantic tropical cyclone frequency. Combined with the results of Chapter 5, it is likely that a major volcanic eruption in which aerosol is emitted into a single hemisphere would significantly perturb tropical storm frequency in the following years. Affected nations might therefore wish to inject aerosol in the opposite hemisphere to the volcanic eruption in order to counteract these storm changes.

7.3. Discussion

Of course, this thesis has only addressed limited aspects of the climatic impacts of SAI. For instance, in Chapter 3 we began to explore surface UV changes for SO_4, BC, and TiO_2 aerosol layer scenarios, but were unable to comprehensively investigate such changes using HadGEM2-CCS (Chapter 4), due to the model's fixed O_3 concentrations. Although previous studies have investigated O_3 (and UV) changes under SAI [Tilmes *et al*., 2008, 2009, 2012; Kravitz *et al*., 2012; Pitari *et al*., 2014; Tang *et* al., 2014; Nowack *et al*., 2016], it would be interesting to directly compare O_3 changes for SAI with different aerosols to SO_4 using a GCM with a detailed chemistry module. Such a study would firstly require the procurement of heterogeneous chemical reaction rates from laboratory-based studies [e.g. Tang *et al*., 2014]. Another uncertain aspect of SAI is how large the aerosol particles would

grow to, which would affect the aerosol residence time and the particle's chemical and radiative properties. HadGEM2-CCS (Chapters 4 and 5) and HadGEM2-ES (Chapter 6) both use fixed aerosol size distributions (Aitken / accumulation) and are therefore unable to grow the SO_4 particles to the coarse modes observed following, for instance, the 1991 Pinatubo eruption [Stenchikov *et al*., 1998]. Therefore, the aerosol injection rates detailed in Chapter 4 might underestimate the injection rates necessary to achieve a certain global radiative effect in practice. The HadGEM2 family of models also exhibit systematic biases in monsoonal precipitation and vegetation [Martin and Levine, 2012], tropical tropopause temperatures [Hardiman *et al*., 2015], and cloud albedo (e.g. over the Southern Ocean [Bodas-Salcedo *et al*., 2014]). These biases will affect the predictive skill of the models, which concomitantly affects the fidelity of the results presented in Chapters 4-6. Additionally, volcanic eruptions are not a perfect analogue for SAI as they are transient events which depend on the ambient weather (Chapter 5) and climate conditions, and because SAI would necessarily alter the baseline stratospheric aerosol layer and concomitantly reduce the efficiency of SAI over time [Niemeier and Timmreck, 2015]. Therefore, although HadGEM2-CCS is able to simulate the Pinatubo eruption with reasonable fidelity (Fig. 4.4), this does not guarantee the same accuracy in the SAI simulations. The next-generation Hadley Centre Earth-System Model (UKESM1) will include the GLOMAP-mode aerosol module (instead of CLASSIC), which utilises two prognostic variables – aerosol number and mass concentration – that combinatively allow for dynamical aerosol growth [Mann *et al*., 2010]. UKESM1 will also include the UKCA stratospheric and tropospheric chemistry module [Morgenstern *et al.*, 2009], which could potentially be used to assess O_3 changes under SAI. In the near future, we plan to utilise UKESM1 to investigate the effectiveness of SAI for different SO_2 injection rates, in order to test whether the radiative response to SAI is nonlinear with injection rate as found by previous studies (Fig. 1.10) [e.g. Heckendorn *et al.*, 2009; Niemeier and Timmreck, 2015].

Another important caveat is that simulations performed for Chapters 4, 5, and 6 were conducted using only one GCM with its own structural uncertainties [Martin *et al*., 2011]. The use of results from multi-model ensembles (MIPs), such as GeoMIP, helps to delineate robust climate responses from model-specific artefacts [Kravitz *et al.*, 2011]. However, the initial scenarios simulated by GeoMIP were highly idealised,

which facilitated in directly comparing the GCM results but did little to answer important policy-relevant questions such as regional climate impacts. GeoMIP conveners may wish to move to a more policy-informed framework in the future, for instance, testing whether SAI could be utilised to maintain global-mean temperature below 1.5 K above pre-industrial levels in the 21st century; which would supplement the Paris agreement [UNFCCC, 2015]. However, it is important to note that global-mean temperature is a very blunt metric that has been used pervasively in the climate change agenda but is completely imperceivable to all individuals. For instance, in Chapter 6 we found that global-mean temperature could be maintained by global, NH-only, or SH-only SAI applications (Fig. 6.3a), but with diametrically different impacts on Sahelian rainfall and North Atlantic TC frequency. SAI research should move away from global-mean metrics (e.g. Fig. 4.6) to answer questions that directly assist policymakers.

SAI is often publicly belittled by detractors as a simple technocratic solution to the climate change problem [e.g. Hamilton, 2014]. Nevertheless, if mitigation efforts continue to stall then SAI could conceivably become the *only* means to rapidly cool the planet and counteract climate change. It is therefore important that SAI-related policy as it develops is well-informed by robust scientific research, which necessitates that SAI research (such as conducted here) continues.

References

Adger, W. N., *et al.* (2003), Adaptation to climate change in the developing world, *Prog. Dev. Stud.*, 3, 3, 179–195. doi:10.1191/1464993403ps060oa.

Adger, W. N., *et al.* (2005), Successful adaptation to climate change across scales, *Glob. Environ. Chang.*, 15, 77–86. doi:http://dx.doi.org/10.1016/j.gloenvcha.2004.12.005.

Albrecht, B. (1989), Aerosols, cloud microphysics, and fractional cloudiness, *Science*, 245, 227–1230. doi:10.1126/science.245.4923.1227.

Allan, R. P. (2011), Combining satellite data and models to estimate cloud radiative effect at the surface and in the atmosphere, *Meteorol. Appl.*, 18, 324–333. doi:0.1002/met.285

Alley, R. B., *et al.* (2003), Abrupt climate change, *Science*, 299, 2005–2010. doi:10.1126/science.1081056.

Altizer, S., *et al.* (2013), Climate Change and Infectious Diseases: From Evidence to a Predictive Framework, *Science*, 341, 514–519. doi:10.1126/science.1239401.

Andreae, M. O., and P. J. Crutzen (1997), Atmospheric aerosols: Biogeochemical sources and role in atmospheric chemistry, *Science*, 276, 1052–1058, doi:10.1126/science.276.5315.1052

Andreae, M. O., and D. Rosenfeld (2008), Aerosol-cloud-precipitation interactions: Part 1. The nature and sources of cloud-active aerosols, *Earth Sci. Rev.*, 89, 13–41. doi:10.1016/j.earscirev.2008.03.001.

Angel, R. (2006), Feasibility of cooling the Earth with a cloud of small spacecraft near the inner Lagrange point (L1), *Proc. Natl. Acad. Sci. U.S.A.*, 103, 17,184–189. doi:10.1073/pnas.0608163103.

Applegate, P. J. and K. Keller (2015), How effective is albedo modification (solar radiation management geoengineering) in preventing sea-level rise from the Greenland Ice Sheet?, *Environ. Res. Lett.*, 10, 84018. doi:10.1088/1748-9326/10/8/084018.

Aquila, V., *et al.* (2012), Dispersion of the volcanic sulfate cloud from a Mount Pinatubo–like eruption, *J. Geophys. Res.*, 117, D06216. doi:10.1029/2011JD016968.

Aquila, V., *et al.* (2013), The response of ozone and nitrogen dioxide to the eruption of Mt. Pinatubo at southern and northern midlatitudes, *J. Atmos. Sci.*, 70(3), 894–900, doi:10.1175/JAS-D-12-0143.1.

Aquila, V., *et al.* (2014), Modifications of the quasi-biennial oscillation by a geoengineering perturbation of the stratospheric aerosol layer, *Geophys. Res. Lett.*, 41, 1738-1744. doi:10.1002/2013GL058818.

Arfeuille, F., *et al.* (2013), Modelling the stratospheric warming following the Mt. Pinatubo eruption: uncertainties in aerosol extinctions, *Atmos. Chem. Phys.*, 13, 22, 11221-11234. doi:10.5194/acp-13-11221-2013

Arrhenius, S. (1896), On the Influence of Carbonic Acid in the Air upon the Temperature of the Ground, *Phil. Mag.*, 5, 41, 237-276. doi:10.1086/121158

Athanasopoulou, E., *et al.* (2008), The role of sea-salt emissions and heterogeneous chemistry in the air quality of polluted coastal areas, *Atmos. Chem. Phys.*, 8, 5755-5769. doi:10.5194/acp-8-5755-2008

Ayash, T., S. Gong, and C. Q. Jia (2008), Direct and indirect shortwave radiative effects of sea salt aerosols, *J. Clim.*, 21, 3207-3220. doi:http://dx.doi.org/10.1175/2007JCLI2063.1

Baede, A. P. M., *et al.* (2001), The climate system: An overview, in Climate Change 2001: The Scientific Basis: Contribution of Working Group I to the Third Assessment Report of the Intergovernmental Panel on Climate Change, edited by J. T. Houghton et al., pp. 85–98, Cambridge Univ. Press, New York.

Bala, G., *et al.* (2008), Impact of geoengineering schemes on the global hydrological cycle, *Proc. Natl. Acad. Sci. U. S. A.*, 105 (22), 7664–7669. doi:10.1073/pnas.0711648105

Baldwin, *et al.* (2001), The quasi-biennial oscillation, *Rev. Geophys.*, 39(2), 179–229. doi:10.1029/1999RG000073.

Baran, A. J., *et al.* (2001), A scattering phase function for ice cloud: Tests of applicability using aircraft and satellite multi-angle multi-wavelength radiance measurements of cirrus, *Q.J.R. Meteorol. Soc.*, 127, 2395–2416. doi:10.1002/qj.49712757711

Barkley, M. P., *et al.* (2008), Global distributions of carbonyl sulfide in the upper troposphere and stratosphere, *Geophys. Res. Lett.*, 35, L14810. doi:10.1029/2008GL034270.

Barrett, S. (2009), Climate treaties and the imperative of enforcement, Chapter 3 in The economics and politics of climate change, [Helm, D. and C. Hepburn (eds)], Oxford University Press, Oxford, 576 pp.

Barry, R., and R. Chorley (2003), Atmosphere, weather and climate, 8th edition, Routledge, London, 421 pp., ISBN 0415271711

Bauer, S. E., *et al.* (2007), Nitrate aerosols today and in 2030: A global simulation including aerosols and tropospheric ozone, *Atmos. Chem. Phys.*, 7, 5043–5059. doi:10.5194/acp-7-5043-2007.

Bellouin, N., *et al.* (2007), Improved representation of aerosols for HadGEM2, Hadley Centre technical note 73, Hadley Centre, Met Office, Exeter, UK, 42pp., available at http://www.metoffice.gov.uk/media/pdf/8/f/HCTN_73.pdf (last accessed 01/16)

Bellouin, N., *et al.* (2011), Aerosol forcing in the Climate Model Intercomparison Project (CMIP5) simulations by HadGEM2-ES and the role of ammonium nitrate, *J. Geophys. Res.*, 116, D20206. doi:10.1029/2011JD016074

Bengtsson, L., *et al.* (2007), Tropical cyclones in a T159 resolution global climate model: comparison with observations and re-analyses, *Tellus A*, 59 (4), 396-416. doi:10.1111/j.1600-0870.2007.00236.x

Berdahl, M., A. *et al.* (2014), Arctic cryosphere response in the Geoengineering Model Intercomparison Project G3 and G4 scenarios, *J. Geophys. Res. Atmos.*, 119, 1308-1321. doi:10.1002/2013JD020627.

Bernauer, T., and L. F. McGrath (2016), Simple reframing unlikely to boost public support for climate policy, *Nat. Clim. Change*, 6, 680–683. doi:10.1038/nclimate2948.

Bluth, G. J. S., *et al.* (1992), Global tracking of the SO_2 clouds from the June, 1991 Mount Pinatubo eruptions, *Geophys. Res. Lett.*, 19, 2, 151-154. doi:10.1029/91GL02792

Bodas-Salcedo, A., *et al.* (2014), Origins of the Solar Radiation Biases over the Southern Ocean in CFMIP2 Models, *J. Clim.*, 27(1), 41–56, doi:10.1175/JCLI-D-13-00169.1.

Bohren, C. F., and D. R. Huffman (1983), Absorption and Scattering of Light by Small Particles, 550 pp., John Wiley, New York

Bollasina, M. A., *et al.* (2011), Anthropogenic aerosols and the weakening of the South Asian summer monsoon, *Science*, 334(6055), 502–505. doi:10.1126/science.1204994

Bond, T. C., *et al.* (2004), A technology-based global inventory of black and organic carbon emissions from combustion, *J. Geophys. Res.*, 109, D14203. doi:10.1029/2003JD003697.

Bond, T. C., and R. W. Bergstrom (2006), Light Absorption by Carbonaceous Particles: An Investigative Review, *Aerosol Sci. and Tech.*, 40:1, 27-67, doi:10.1080/02786820500421521

Boot-Handford, M. E., *et al.* (2014), Carbon capture and storage update, *Energy Environ. Sci.*, 7, 130. doi:10.1039/c3ee42350f

Boucher, O., *et al.* (1998), Intercomparison of models representing direct shortwave radiative forcing by sulfate aerosols, *J. Geophys. Res.*, 103(D14), 16979–16998, doi:10.1029/98JD00997.

Boucher, O., and G. A. Folberth (2010), Atmospheric Methane Removal as a Way to Mitigate Climate Change?, *Atmos. Environ.*, 44, 3343-3345. doi:10.1016/j.atmosenv.2010.04.032

Boucher, O., *et al.* (2013), Clouds and aerosols. In Climate Change 2013: The Physical Science Basis. Contribution of Working Group I to the Fifth Assessment Report of the Intergovernmental Panel on Climate Change. T.F. Stocker, *et al.*, Eds. Cambridge University Press, 571-657. doi:10.1017/CBO9781107415324.016.

Bourassa, A. E., *et al.* (2012), Large Volcanic Aerosol Load in the Stratosphere Linked to Asian Monsoon Transport, *Science*, 337, 6090, 78-81. doi:10.1126/science.1219371

Boville, B. A., *et al.* (1991), Simulation of the Pinatubo aerosol cloud in a general circulation model, *Geophys. Res. Lett.*, 18, 12, 2281-2284. doi:10.1029/91GL02778

Boyd, R., *et al.* (2015), Intended Nationally Determined Contributions: What are the Implications for Greenhouse Gas Emissions in 2030?, Centre for Climate Change Economics and Policy, Grantham Research Institute on Climate Change and the Environment, London.

Brimblecombe, P. (2006), The clean air act after 50 years, *Weather*, 61, 311-314. doi:10.1256/wea.127.06

Bruckner, T., *et al.* (2014), Energy Systems. In: Climate Change 2014: Mitigation of Climate Change. Contribution of Working Group III to the Fifth Assessment Report of the Intergovernmental Panel on Climate Change [Edenhofer, O., *et al.* (eds.)]. Cambridge University Press, Cambridge, United Kingdom and New York, NY, USA.

Bruckner, T. (2016), Decarbonizing the Global Energy System: An Updated Summary of the IPCC Report on Mitigating Climate Change, *Energy Technology*, 4: 19–30. doi:10.1002/ente.201500387

Brühl, C., *et al.* (2012), The role of carbonyl sulphide as a source of stratospheric sulphate aerosol and its impact on climate, *Atmos. Chem. Phys.*, 12(3), 1239–1253. doi:10.5194/acp-12-1239-2012.

Brutel-Vuilmet, C., *et al.* (2013) An analysis of present and future seasonal Northern Hemisphere land snow cover simulated by CMIP5 coupled climate models, *Cryosphere*, 7, 67–80. doi:10.5194/tc-7-67-2013

Budyko, M. I. (1977), Climatic Changes, 261 pp., AGU, Washington D.C

Buesseler, K. O., *et al.* (2008), Ocean iron fertilization: Moving forward in a sea of uncertainty, *Science*, 319, 162. doi:10.1126/science.1154305.

Caesar, J., *et al.* (2013), Response of the HadGEM2 Earth System Model to future greenhouse gas emissions pathways to the year 2300, *J. Clim.*, 26, 3275-3284. doi:10.1175/JCLI-D-12-00577.1.

Caldeira, K., *et al.* (2013). The Science of Geoengineering, *Annu. Rev. Earth Planet. Sci.*, 41(1), 231–256. doi:10.1146/annurev-earth-042711-105548

Calmels, D., *et al.* (2007), Sustained sulfide oxidation by physical erosion processes in the Mackenzie River basin: Climatic perspectives, *Geology*, 35(11), 1003-1006. doi:10.1130/G24132A.1

Camargo, S. J. (2013), Global and regional aspects of tropical cyclone activity in the CMIP5 models. *J. Clim.*, 26, 9880–9902, doi:http://dx.doi.org/10.1175/JCLI-D-12-00549.1

Canadell, J. G., *et al.* (2007), Contributions to accelerating atmospheric CO_2 growth from economic activity, carbon intensity, and efficiency of natural sinks, *Proc. Natl. Acad. Sci. U.S.A.*, 104, 18866–18870, doi:10.1073/pnas.0702737104

Carn, S. A., *et al.* (2016), Multi-decadal satellite measurements of global volcanic degassing, *J. Volcanol. Geotherm. Res.*, 311, 99−134. doi:10.1016/j.jvolgeores.2016.01.002.

Carslaw, K. C., and B. Kärcher (2006), Stratospheric aerosol processes, in Assessment of Stratospheric Aerosol Properties, edited by L. Thomason and T. Peter, WCRP 124, WMO/TD 1295, SPARC Rep. 4, World Meteorolo. Organ., Geneva, Switzerland

Carslaw, K. S., *et al.* (2010), A review of natural aerosol interactions and feedbacks within the Earth system, *Atmos. Chem. Phys.*, 10, 1701–1737. doi:10.5194/acp-10-1701-2010

Casale, G. R., *et al.* (2003), A simple device for the evaluation of the UV radiation index, *Meterol. Appl.*, 10, 115-121. doi:10.1017/S1350482703002032

Casswall, T. H. (2013), Vitamin D deficiency in adolescents living at high latitudes: are we missing something in the recommendations?, *Acta Paediatr*, 102, 569-571. doi:10.1111/apa.12252

Charlson, R. J., *et al.* (1991), Perturbation of the northern hemisphere radiative balance by backscattering from anthropogenic sulfate aerosols, *Tellus B*, 43, 152-163. doi:10.1034/j.1600-0889.1991.t01-1-00013.x

Charlson, R. J., *et al.* (1992), The Sulfur Cycle, Chapter 13 in Global Biogeochemical Cycles, edited by Butcher, S. S., *et al.*, Academic Press Ltd, London, UK, 379 pp.

Chen, Y.-C., *et al.* (2012), Occurrence of lower cloud albedo in ship tracks, *Atmos. Chem. Phys.*, 12, 8223–8235. doi:10.5194/acp-12-8223-2012.

Chiacchio, M., *et al.* (2017), On the links between meteorological variables, aerosols, and tropical cyclone frequency in individual ocean basins, *J. Geophys. Res. Atmos.*, 122, doi:10.1002/2015JD024593.

Chin, M., and D. D. Davis (1993), Global sources and sinks of OCS and CS_2 and their distributions, *Global Biogeochem. Cycles*, 7(2), 321–337. doi:10.1029/93GB00568.

Choi, W., *et al.* (1998), Role of the quasi-biennial oscillation in the transport of aerosols from the tropical stratospheric reservoir to midlatitudes, *J. Geophys. Res.*, 103, 6033-6042. doi:10.1029/97JD03118

Choobari, O. A., P. Zawar-Reza, and A. Sturman (2014), The global distribution of mineral dust and its impacts on the climate system: a review, *Atmos. Res.*, 138, 152-165. http://dx.doi.org/10.1016/j.atmosres.2013.11.007

Chung, S. H., and J. H. Seinfeld (2005), Climate response of direct radiative forcing of anthropogenic black carbon, *J. Geophys. Res.*, 110, D11102. doi:10.1029/2004JD005441.

Church, *et al.* (2013), Sea Level Change. In: Climate Change 2013: The Physical Science Basis. Contribution of Working Group I to the Fifth Assessment Report of the Intergovernmental Panel on Climate Change [Stocker, T.F., *et al.* (eds.)]. Cambridge University Press, Cambridge, United Kingdom and New York, NY, USA.

Chýlek, P., and J. Zhan (1989), Interference structure of the Mie extinction cross section, *J. Opt. Soc. Am. A.*, 6, 12, 1846-1851.

Cionni, I., *et al.* (2011), Ozone database in support of CMIP5 simulations: Results and corresponding radiative forcing, *Atmos. Chem. Phys.*, 11, 11267-11292. doi:10.5194/acp-11-11267-2011.

Clarisse, L., *et al.* (2011), Infrared satellite observations of hydrogen sulfide in the volcanic plume of the August 2008 Kasatochi eruption, *Geophys. Res. Lett.*, 38, L10804. doi:10.1029/2011GL047402.

Collins, W. J., *et al.* (2011), Development and evaluation of an Earth-system model-HadGEM2, *Geosci. Model Dev.*, 4, 1051–1075, doi:10.5194/gmd-4-1051-2011

Collins, M., *et al.* (2013), Long-term Climate Change: Projections, Commitments and Irreversibility. In: Climate Change 2013: The Physical Science Basis. Contribution of Working Group I to the Fifth Assessment Report of the Intergovernmental Panel on Climate Change [Stocker, T.F., *et al.* (eds.)]. Cambridge University Press, Cambridge, United Kingdom and New York, NY, USA.

Corner, A., *et al*. (2013), Messing with nature? Exploring public perceptions of geoengineering in the UK, *Global Environ. Chang.*, 23 (2013) 938–947, https://doi.org/10.1016/j.gloenvcha.2013.06.002

Croft, B., *et al.* (2010), Influences of in-cloud aerosol scavenging parameterizations on aerosol concentrations and wet deposition in ECHAM5-HAM, *Atmos. Chem. Phys.*, 10(4), 1511-1543, doi:10.5194/acp-10-1511-2010.

Crook, J. A., *et al.* (2015), A comparison of temperature and precipitation responses to different Earth radiation management geoengineering schemes, *J. Geophys. Res. Atmos.*, 120, 9352–9373. doi:10.1002/2015JD023269.

Crutzen, P. (2006), Albedo Enhancement by Stratospheric Sulfur Injections: A Contribution to Resolve a Policy Dilemma?, *Clim. Change*, 77, 3, 211-220. doi:10.1007/s10584-006-9101-y

d'Almeida, G. A., *et al.* (1991), Atmospheric aerosols: global climatology and radiative characteristics, A. Deepak Publishing, Hampton, USA

Dankovic, D., *et al.* (2011), Current intelligence bulletin 63: occupational exposure to titanium dioxide., Cincinnati, OH: U.S. Department of Health and Human Services, Public Health Service, Centers for Disease Control and Prevention, National Institute for Occupational Safety and Health, DHHS (NIOSH) Publication No. 2011-160, 2011 Apr; :1-119

Davidson, P., *et al.* (2012), Lifting options for stratospheric aerosol geoengineering: advantages of tethered balloon systems, *Philos. Trans. R. Soc. A*, 370, 4263-4300. doi:10.1098/rsta.2011.0639.

Dee, D. P., *et al.* (2011), The ERA-Interim reanalysis: configuration and performance of the data assimilation system, *Q. J. R. Meteorol. Soc.*, 137, 553–597. doi:10.1002/qj.828

Deepak, A., and H. E. Gerber (Eds.) (1983), Report of the experts meeting on aerosols and their climatic effects (Williamsburg, Virginia, March 1983), Rep. WCP-55, World Clim. Programme, World Meteorol. Organ., Geneva

DeGaetano, A. T. (2009), Time-dependent changes in extreme-precipitation return-period amounts in the continental United States, *J. Appl. Meteor. Climatol.*, 48, 2086–2099. doi:10.1175/2009JAMC2179.1

de Leeuw, G., *et al.* (2011), Production flux of sea spray aerosol, *Rev. Geophys.*, 49, RG2001. doi:10.1029/2010RG000349.

Deshler, T., and R. Anderson-Sprecher (2006), Non-volcanic stratospheric aerosol trends: 1971–2004, in Assessment of Stratospheric Aerosol Properties, edited by L. Thomason and T. Peter, WCRP 124, WMO/TD 1295, SPARC Rep. 4, World Meteorolo. Organ., Geneva, Switzerland

Després, V. R., *et al.* (2012), Primary biological aerosol particles in the atmosphere: a review, *Tellus B*, 64, 15598. doi:10.3402/tellusb.v64i0.15598

Dessler, A. E., *et al.* (2013), Stratospheric water vapor feedback*, Proc. Natl. Acad. Sci. U.S.A.*, 110, 18,087-18,091. doi:10.1073/pnas.1310344110.

Dhomse, S. S., *et al.* (2014), Aerosol microphysics simulations of the Mt. Pinatubo eruption with the UM-UKCA composition-climate model, *Atmos. Chem. Phys.*, 14, 11221-11246, 2014. doi:10.5194/acp-14-11221-2014

Donohoe, A., and D. S. Battisti (2011), Atmospheric and surface contributions to planetary albedo, *J. Clim.*, 24, 4402–4418, doi:10.1175/2011JCLI3946.1.

d'Orazio, J., *et al*. (2013), UV Radiation and the Skin, *Int. J. Mol. Sci.*, 14, 12222-12248. doi:10.3390/ijms140612222

Doughty, C., *et al.* (2011), Can crop albedo be increased through the modification of leaf trichomes, and could this cool regional climate?, *Clim. Change*, 104(2), 379–387. doi:10.1007/s10584-010-9936-0.

Drake, F. (2000), Global Warming: The Science of Climate Change, Arnold, London, 273 pp.

Driscoll, S., *et al.* (2012), Coupled Model Intercomparison Project 5 (CMIP5) simulations of climate following volcanic eruptions*, J. Geophys. Res.*, 117, D17105. doi:10.1029/2012JD017607.

Dunstone, N. J., *et al* (2013), Anthropogenic aerosol forcing of Atlantic tropical storms, *Nature Geosci.*, 6, 534–539, doi:10.1038/ngeo1854

Dykema, J. A., *et al.* (2016), Improved aerosol radiative properties as a foundation for solar geoengineering risk assessment, *Geophys. Res. Lett.*, 43, 7758–7766, doi:10.1002/2016GL069258.

Edwards, J. M., and A. Slingo (1996), Studies with a flexible new radiation code. I: Choosing a configuration for a large-scale model, *Q. J. R. Meteorol. Soc.*, 122, pp. 689-719. doi:10.1002/qj.49712253107

Ehn, M., *et al.* (2014), A large source of low-volatility secondary organic aerosol, *Nature*, 506(7489), 476–479. doi:10.1038/nature13032

Emanuel, K., and M. Mann (2006), Atlantic hurricane trends linked to climate change, *EOS*, 87, 24, 233–244. doi:10.1029/2006EO240001.

English, J. M., *et al.* (2012), Microphysical simulations of sulfur burdens from stratospheric sulfur geoengineering, *Atmos. Chem. Phys.*, 12(10), 4775–4793. doi:10.5194/acp-12-4775-2012.

English, J. M., *et al.* (2013), Microphysical simulations of large volcanic eruptions: Pinatubo and Toba, *J. Geophys. Res. Atmos.*, 118, 1880–1895. doi:10.1002/jgrd.50196.

Ervens, B., *et al.* (2011), Secondary organic aerosol formation in cloud drops and aqueous particles (aqSOA): A review of laboratory, field and model studies, *Atmos. Chem. Phys.*, 11, 11069–11102. doi:10.5194/acp-11-11069-2011

Eyring, V., *et al.* (2010), Multi-model assessment of stratospheric ozone return dates and ozone recovery in CCMVal-2 models, *Atmos. Chem. Phys.*, 10(19), 9451–9472. doi:10.5194/acp-10-9451-2010

Evan, A. T. (2012), Atlantic hurricane activity following two major volcanic eruptions, *J. Geophys. Res.*, 117, D06101, doi:10.1029/2011JD016716.

Fahey, D., *et al.* (2001), The detection of large HNO_3-containing particles in the winter Arctic stratosphere, *Science*, 291, 1026. doi:10.1126/science.1057265

Farman, J. C., *et al.* (1985), Large losses of total ozone in Antarctica reveal seasonal ClOx/NOx interaction, *Nature*, 315, 207–210. doi:10.1038/315207a0

Ferraro, A. J., *et al.* (2011), Stratospheric heating by potential geoengineering aerosols, *Geophys. Res. Lett.*, 38, L24706. doi:10.1029/2011GL049761.

Ferraro, A. J., *et al.* (2014), Weakened tropical circulation and reduced precipitation in response to geoengineering, *Environ. Res. Lett.*, 9, 014001. doi:10.1088/1748-9326/9/1/014001

Fitzgerald, J. W. (1975), Approximation formulas for the equilibrium size of an aerosol particle as a function of its dry size and composition and the ambient relative humidity, *J. Appl. Meteorol.*, 14, 1044–1049., doi:http://dx.doi.org/10.1175/1520-0450(1975)014<1044:AFFTES>2.0.CO;2

Flanner, M. G., *et al.* (2007), Present-day climate forcing and response from black carbon in snow, *J. Geophys. Res.*, 112, D11202. doi:10.1029/2006JD008003.

Ford, J. D., *et al.* (2016), Including indigenous knowledge and experience in IPCC assessment reports, *Nat. Clim. Change*, 6(4), 349-353. doi:10.1038/nclimate2954

Forster, P. M., and K. P. Shine (1997), Radiative forcing and temperature trends from stratospheric ozone changes, *J. Geophys. Res.*, 102(D9), 10841–10855. doi:10.1029/96JD03510.

Forster, P., *et al.* (2007), Changes in Atmospheric Constituents and in Radiative Forcing. In: Climate Change 2007: The Physical Science Basis. Contribution of Working Group I to the Fourth Assessment Report of the

Intergovernmental Panel on Climate Change [Solomon, S., *et al.* (eds.)]. Cambridge University Press, Cambridge, United Kingdom and New York, NY, USA.

Fourier, J. (1824), Remarques générales sur les températures du globe terrestre et des espaces planétaires, *Ann. Chim. Phys.*, (Paris) 2nd ser., 27, 136167.

Franklin, B. (1784), Meteorological imaginations and conjectures, *Manchr. Lit. Philos. Soc. Mem. Proc.*, 2, 122. [Reprinted in Weatherwise 35, 262 (1982).]

Friedlingstein, P., *et al.* (2014a), Uncertainties in CMIP5 climate projections due to carbon cycle feedbacks, *J. Clim.*, 27(2), 511–526. doi:10.1175/JCLI-D-12-00579.1.

Friedlingstein, P., *et al.* (2014b), Persistent growth of CO_2 emissions and implications for reaching climate targets, *Nat. Geosci.*, 7(10), 709–715. doi:10.1038/ngeo2248.

Fromm, M., *et al.* (2014), Correcting the record of volcanic stratospheric aerosol impact: Nabro and Sarychev Peak, *J. Geophys. Res. Atmos*., 119, 10,343–10,364. doi:10.1002/2014JD021507.

Fuzzi, S., *et al.* (2015), Particulate matter, air quality and climate: Lessons learned and future needs, *Atmos. Chem. Phys.*, 15, 8217–8299, doi:10.5194/acp-15-8217-2015

Fyfe, J. C., *et al.* (2013), Biogeochemical carbon coupling influences global precipitation in geoengineering experiments, *Geophys. Res. Lett.*, 40, 651–655. doi:10.1002/grl.50166.

Gantt, B., *et al.* (2011), Wind speed dependent size-resolved parameterization for the organic mass fraction of sea spray aerosol, *Atmos. Chem. Phys.*, 11(16), 8777–8790. doi:10.5194/acp-11-8777-2011.

Gaskill, A. (2004), Summary of meeting with US DOE to discuss geoengineering options to prevent long-term climate change, Environ. Ref. Mater., Inc., Research Triangle Park, N. C.

Gassó, S. (2008), Satellite observations of the impact of weak volcanic activity on marine clouds, *J. Geophys. Res.*, 113, D14S19. doi:10.1029/2007JD009106.

Gettelman, A., *et al.* (2010), Multimodel assessment of the upper troposphere and lower stratosphere: Tropics and global trends, *J. Geophys. Res.*, 115, D00M08. doi:10.1029/2009JD013638.

Gettelman, A., *et al.* (2015), Icelandic volcanic emissions and climate, *Nat. Geosci.*, 8(4), 243–243. doi:10.1038/ngeo2376

Gill, A. E. (1982), Atmosphere-Ocean Dynamics, 662 pp., Academic, San Diego, Calif., USA

Ginoux, P., *et al.* (2012), Global-scale attribution of anthropogenic and natural dust sources and their emission rates based on MODIS Deep Blue aerosol products, *Rev. Geophys.*, 50, RG3005. doi:10.1029/2012RG000388.

Gleason, J. F., *et al.* (1993), Record low global ozone in 1992, *Science*, 260, 523–526. doi:10.1126/science.260.5107.523

Glienke, S., *et al.* (2015), The impact of geoengineering on vegetation in experiment G1 of the GeoMIP, *J. Geophys. Res. Atmos.*, 120, 10,196–10,213. doi:10.1002/2015JD024202.

Goldenberg, S. B., *et al.* (2001), The recent increase in Atlantic hurricane activity: Causes and implications, *Science*, 293 (5529), 474–479, doi:10.1126/science.1060040

Goll, D., *et al.* (2012), Nutrient limitation reduces land carbon uptake in simulations with a model of combined carbon, nitrogen and phosphorus cycling, *Biogeosciences*, 9, 3547–3569. doi:10.5194/bg-9–3547-2012.

Govindasamy, B., and K. Caldeira (2000), Geoengineering Earth's radiation balance to mitigate CO_2-induced climate change, *Geophys. Res. Lett.*, 27(14), 2141–2144. doi:10.1029/1999GL006086.

Govindasamy, B., S *et al.* (2002), Impact of geoengineering schemes on the terrestrial biosphere, *Geophys. Res. Lett.*, 29(22), 3–6. doi:10.1029/2002GL015911

Govindasamy, B., *et al.* (2003), Geoengineering Earth’s radiation balance to mitigate climate change from a quadrupling of CO_2, *Glob. Planet. Change*, 37, 157–168. doi:10.1016/S0921-8181(02)0

Gray, L. J., *et al.* (2009), Stratospheric temperature and radiative forcing response to 11-year solar cycle changes in irradiance and ozone, *J. Atmos. Sci.*, 66, 2402–2417, doi:10.1175/2009JAS2866.1.

Gray, L. J., *et al.* (2013), A lagged response to the 11 year solar cycle in observed winter Atlantic/European weather patterns, *J. Geophys. Res. Atmos.*, 118, 13,405–13,420. doi:10.1002/2013JD020062.

Gu, L., *et al.* (2003), Response of a deciduous forest to the Mount Pinatubo eruption: enhanced photosynthesis, *Science*, 299, 2035–2038. doi:10.1126/science.1078366

Guevara-Murua, A., *et al.* (2015), Consistent decrease in North Atlantic Tropical Cyclone frequency following major volcanic eruptions in the last three centuries, *Geophys. Res. Lett.*, 42, 9425–9432, doi:10.1002/2015GL066154.

Guo, S., *et al.* (2004), Re-evaluation of the SO_2 release of the 15 June 1991 Pinatubo eruption using ultraviolet and infrared satellite sensors, *Geochem. Geophys. Geosyst.*, 5, Q04001. doi:10.1029/2003GC000654

Gupta, J (2010), Global decision making: climate change politics, Chapter 9 in Climate Change: An Integrated Perspective (eds: P. Martens and J. Rotmans), Kluwer Academic Publishers, AA Dordrecht, The Netherlands

Hamilton, C., (2014), Earthmasters: The Dawn of the Age of Climate Engineering, 264 pp., Yale University Press, London, U.K.

Hansen, J., *et al.* (1992), Potential climate impact of Mount Pinatubo eruption, *Geophys. Res. Lett.*, 19, 2, 215-218. doi:10.1029/91GL02788

Hansen, J., *et al.* (1997), Radiative forcing and climate response, *J. Geophys. Res.*, 102(D6), 6831–6864. doi:10.1029/96JD03436.

Hardiman, S. C., *et al.* (2012), The Effect of a Well-Resolved Stratosphere on Surface Climate: Differences between CMIP5 Simulations with High and Low Top Versions of the Met Office Climate Model, *J. Clim.*, 25, 7083–7099, http://dx.doi.org/10.1175/JCLI-D-11-00579.1

Hardiman, S. C., *et al.* (2015), Processes Controlling Tropical Tropopause Temperature and Stratospheric Water Vapor in Climate Models, *J. Clim.*, 28, 6516–6355. doi:10.1175/JCLI-D-15-0075.1

Haywood, J. M., and K. P. Shine (1995), The effect of anthropogenic sulfate and soot aerosol on the clear sky planetary radiation budget, *Geophys. Res. Lett.*, 22, 603–606. doi:10.1029/95GL00075

Haywood, J. M., and O. Boucher (2000), Estimates of the direct and indirect radiative forcing due to tropospheric aerosols: A review, *Rev. Geophys.*, 38(4), 513–543. doi:10.1029/1999RG000078.

Haywood, J. M., *et al.* (2010), Observations of the eruption of the Sarychev volcano and simulations using the HadGEM2 climate model, *J. Geophys. Res.*, 115, D21212. doi:10.1029/2010JD014447.

Haywood, J. M., *et al.* (2011), The roles of aerosol, water vapor and cloud in future global dimming/brightening, *J. Geophys. Res.*, 116, D20203. doi:10.1029/2011JD016000.

Haywood, J. M., *et al.* (2013), Asymmetric forcing from stratospheric aerosol impacts Sahelian rainfall*, Nat. Clim. Change*, 3, 660-665. doi:10.1038/nclimate1857

Haywood, J. M., *et al.* (2014), The impact of volcanic eruptions in the period 2000–2013 on global mean temperature trends evaluated in the HadGEM2-ES climate model. *Atmos. Sci. Lett.*, 15: 92–96. doi:10.1002/asl2.471

Haywood, J. M., *et al.* (2016), The impact of equilibrating hemispheric albedos on tropical performance in the HadGEM2-ES coupled climate model, *Geophys. Res. Lett.*, 43, 395–403. doi:10.1002/2015GL066903.

Heckendorn, P., *et al.* (2009), The impact of geoengineering aerosols on stratospheric temperature and ozone, *Environ. Res. Lett.*, 4, 045108. doi:10.1088/1748-9326/4/4/045108

Helm, D. (2009), Climate change policy: why has so little been achieved?, Chapter 2 in The economics and politics of climate change, [Helm, D. and C. Hepburn (eds)], Oxford University Press, Oxford, 576 pp.

Heng, Z., *et al.* (2014), A study of the distribution of variability of cloud water using ISCCP, SSM/I cloud product, and re-analysis datasets, *J. Clim.*, 27 , 3114–3128. doi:10.1175/JCLI-D-13-00031.1.

Herzog, H. (2009), Carbon dioxide capture and storage, Chapter 13. In: Helm D, Hepburn C (eds) Economics and politics of climate change. Oxford University Press, Oxford, pp 263–283

Hezel, P. J., *et al.* (2014), Modeled Arctic sea ice evolution through 2300 in CMIP5 extended RCPs, *Cryosphere*, 8(4), 1195–1204. doi:10.5194/tc-8-1195-2014.

Hodges, K. (1995), Feature tracking on a unit sphere, *Mon. Wea. Rev.*, 123, 3458–3465, doi:10.1175/1520-0493(1995)123,3458:FTOTUS.2.0.CO;2.

Hodges, K. (1996), Spherical nonparametric estimators applied to the UGAMP model integration for AMIP, *Mon. Wea. Rev.*, 124, 2914–2932, doi:10.1175/1520-0493(1996)124,2914:SNEATT.2.0.CO;2.

Hodges, K. (1999), Adaptive constraints for feature tracking, *Mon. Wea. Rev.*, 127, 1362–1373, doi:10.1175/1520-0493(1999)127,1362:ACFFT.2.0.CO;2.

Hodges, K. I. (2008), Confidence intervals and significance tests for spherical data derived from feature tracking, *Mon. Weather Rev.*, 136, 1758–1777, doi:10.1175/2007MWR2299.1

Hofmann, D. J *et al.* (1992), Observation and possible causes of new ozone depletion in Antarctica in 1991, *Nature*, 359, 283-287. doi:10.1038/359283a0

Holasek, R. E., *et al.* (1996), Satellite observations and interpretation of the 1991 Mount Pinatubo eruption plumes, *J. Geophys. Res.*, 101(B12), 27635–27655. doi:10.1029/96JB01179.

Holton, J. R., P *et al.* (1995), Stratosphere-troposphere exchange, *Rev. Geophys.*, 33(4), 403-439. doi:10.1029/95RG02097.

Hoskins, B. J., and K. I. Hodges (2002), New perspectives on the Northern Hemisphere winter storm tracks, *J. Atmos. Sci.*, 59, 1041–1061

Huffman, J. A., *et al.* (2013), High concentrations of biological aerosol particles and ice nuclei during and after rain, *Atmos. Chem. Phys.*, 13, 6151–6164. doi:10.5194/acp-13-6151-2013

Hugelius, G. (2012), Spatial upscaling using thematic maps: An analysis of uncertainties in permafrost soil carbon estimates, *Global Biogeochem. Cycles*, 26, GB2026, doi:10.1029/2011GB004154.

Huneeus, N., *et al.* (2011), Global dust model intercomparison in AeroCom phase I, *Atmos. Chem. Phys.*, 11, 7781–7816. doi:10.5194/acp-11-7781-2011.

Hwang, Y.-T., *et al.* (2013), Anthropogenic sulfate aerosol and the southward shift of tropical precipitation in the late 20th century, *Geophys. Res. Lett.*, 40, 2845–2850. doi:10.1002/grl.50502.

Illingworth, A. J., *et al.* (2015), The EarthCARE satellite: The next step forward in global measurements of clouds, aerosols, precipitation, and radiation, *Bull. Am. Meteorol. Soc.*, 96 (8). doi:10.1175/BAMS-D-12-00227

International Civil Aviation Organisation (ICAO) (1993), Manual of the ICAO Standard Atmosphere: extended to 80 kilometres (262 200 feet), Doc 7488/3, Third ed.

IPCC (2007), Summary for Policymakers. In: Climate Change 2007: The Physical Science Basis. Contribution of Working Group I to the Fourth Assessment Report of the Intergovernmental Panel on Climate Change [Solomon, S, *et*

al. (eds.)]. Cambridge University Press, Cambridge, United Kingdom and New York, NY, USA

IPCC (2011), IPCC Special Report on Renewable Energy Sources and Climate Change Mitigation (SRREN), [O. Edenhofer, R. Pichs-Madruga, Y. Sokona, K. Seyboth, P. Matschoss, S. Kadner, T. Zwickel, P. Eickemeier, G. Hansen, S. Schlömer, C. von Stechow (eds)], Cambridge University Press, Cambridge, United Kingdom and New York, NY, USA

IPCC (2013), Summary for Policymakers. In: Climate Change 2013: The Physical Science Basis. Contribution of Working Group I to the Fifth Assessment Report of the Intergovernmental Panel on Climate Change [Stocker, T.F., *et al.* (eds.)]. Cambridge University Press, Cambridge, United Kingdom and New York, NY, USA.

IPCC (2014a), Summary for Policymakers. In: Climate Change 2014: Mitigation of Climate Change. Contribution of Working Group III to the Fifth Assessment Report of the Intergovernmental Panel on Climate Change [Edenhofer, O., *et al.* (eds.)]. Cambridge University Press, Cambridge, United Kingdom and New York, NY, USA

IPCC (2014b), Summary for policymakers. In: Climate Change 2014: Impacts, Adaptation, and Vulnerability. Part A: Global and Sectoral Aspects. Contribution of Working Group II to the Fifth Assessment Report of the Intergovernmental Panel on Climate Change [Field, C.B., *et al.* (eds.)]. Cambridge University Press, Cambridge, United Kingdom and New York, NY, USA, pp. 1-32.

Iqbal, M. (1983), An Introduction to Solar Radiation, Academic Press, New York.

Irvine, P. J., *et al.* (2011), Climatic effects of surface albedo geoengineering, *J. Geophys. Res.*, 116, D24112. doi:10.1029/2011JD016281.

Irvine, P. J., *et al.* (2012), Tension between reducing sea-level rise and global warming through solar-radiation management, *Nat. Clim. Change*, 2, 97–100, doi:10.1038/nclimate1351.

Irvine, P. J., *et al.* (2016), An overview of the Earth system science of solar geoengineering, *WIREs Clim Change*, 7, 815–833. doi:10.1002/wcc.423

Izrael, Y. A., *et al.* (2009), Field Studies of a Geo-engineering Method of Maintaining a Modern Climate with Aerosol Particles, *Russ. Meteorol. Hydrol.*, 34, 635. doi:10.3103/S106837390910001X

Jackson, L. S., *et al.* (2015), Assessing the controllability of Arctic sea ice extent by sulfate aerosol geoengineering, *Geophys. Res. Lett.*, 42: 1223–1231. doi:10.1002/2014GL062240.

Jacob, D. J. (1999), Introduction to Atmospheric Chemistry, Princeton Univ. Press, Princeton, N. J

Jacobs, S. S., *et al.* (2011), Stronger ocean circulation and increased melting under Pine Island Glacier ice shelf, *Nat. Geosci.*, 4, 519–523. doi:10.1038/ngeo1188

Jiao, C., *et al.* (2014), An AeroCom assessment of black carbon in Arctic snow and sea ice, *Atmos. Chem. Phys.*, 14, 2399–2417. doi:10.5194/acp-14-2399-2014

Jimenez, J. L., *et al.* (2009), Evolution of organic aerosols in the atmosphere, *Science*, 326, 1525-1529. doi:10.1126/science.1180353.

Jones, C. D., *et al.* (2011), The HadGEM2-ES implementation of CMIP5 centennial simulations, *Geosci. Model Dev.*, 4, 543–570. doi:10.5194/gmd-4-543-2011

Jones, A., and J. M. Haywood (2012), Sea-spray geoengineering in the HadGEM2-ES Earth-system model: Radiative impact and climate response, *Atmos. Chem. Phys.*, 12, 10,887–10,898. doi:10.5194/acp-12-10887-2012.

Jones, A., *et al.* (2013), The impact of abrupt suspension of solar radiation management (termination effect) in experiment G2 of the Geoengineering Model Intercomparison Project (GeoMIP), *J. Geophys. Res. Atmos.*, 118, 9743–9752. doi:10.1002/jgrd.50762.

Jones, A., *et al.* (*submitted*), Drastic mitigation of black carbon and methane offers limited potential for keeping global warming below 1.5C, *submitted to Environ. Res. Lett.*

Jones, A. C., *et al.* (2016a), Climatic impacts of stratospheric geoengineering with sulfate, black carbon and titania injection, *Atmos. Chem. Phys.*, 16, 5, 2843-2862. doi:10.5194/acp-16-2843-2016

Jones, A. C., *et al.* (2016b), Sensitivity of volcanic aerosol dispersion to meteorological conditions: A Pinatubo case study, *J. Geophys. Res. Atmos.*, 121, 6892-6908. doi:10.1002/2016JD025001.

Joseph, J. H., et al. (1976), The delta-Eddington approximation for radiative flux transfer, *J. Atmos. Sci.*, 33, 2452–2459. http://dx.doi.org/10.1175/1520-0469(1976)033<2452:TDEAFR>2.0.CO;2

Kalidindi, S., *et al.* (2015), Modelling of solar radiation management: A comparison of simulations using reduced solar constant and stratospheric sulphate aerosols, *Clim. Dyn.*. doi:10.1007/s00382-014-2240-3.

Kaufmann, R. F., *et al.* (2011), Reconciling anthropogenic climate change with observed temperature 1998–2008, *Proc. Nat. Acad. Sci. U.S.A.,* 108(29), 11, 790–11,793. doi:10.1073/pnas.1102467108.

Kawatani, Y., and K. Hamilton (2013), Weakened stratospheric quasibiennial oscillation driven by increased tropical mean upwelling, *Nature*, 497, 478–481. doi:10.1038/nature12140

Keith, D. W. (2000), Geoengineering the climate: History and prospect, *Annu. Rev. Energy Environ.*, 25, 245–284. doi:10.1146/annurev.energy.25.1.245.

Keith, D. W., *et al.* (2006), Climate Strategy with CO_2 Capture from the Air, *Clim. Change*, 74(1-3), 17–45. doi:10.1007/s10584-005-9026-x

Keith, D. W. (2010), Photophoretic levitation of engineered aerosols for geoengineering, *Proc. Natl. Acad. Sci. U. S. A.*, 107(38), 16428–16431. doi:10.1073/pnas.1009519107

Keith, D. W., *et al.* (2014), Field experiments on solar geoengineering: Report of a workshop exploring a representative research portfolio, *Philos. Trans. R. Soc. A*, 372, 20140175. doi:10.1098/rsta.2014.0175.

Keith, D. W., *et al.* (2016), Stratospheric solar geoengineering without ozone loss, *Proc. Natl. Acad. Sci. U. S. A.*, 113, 52, 14910–14914. doi: 10.1073/pnas.1615572113

Kharin, V. V., *et al.* (2013), Changes in temperature and precipitation extremes in the CMIP5 ensemble, *Clim. Change*, 119:345–357. doi:10.1007/s10584-013-0705-8

Kiehl, J. T., and K. E. Trenberth (1997), Earth's annual global mean energy budget, *Bull. Am. Meteorol. Soc.*, 78, 197-208, http://dx.doi.org/10.1175/1520-0477(1997)078<0197:EAGMEB>2.0.CO;2

Kipling, Z., *et al.* (2016), What controls the vertical distribution of aerosol? Relationships between process sensitivity in HadGEM3–UKCA and inter-model variation from AeroCom Phase II, *Atmos. Chem. Phys.*, 16, 2221–2241, doi:10.5194/acp-16-2221-2016

Kirchner, I., *et al.* (1999), Climate model simulation of winter warming and summer cooling following the 1991 Mount Pinatubo volcanic eruption, *J. Geophys. Res.*, 104(D16), 19039–19055. doi:10.1029/1999JD900213.

Klimont, Z., *et al.* (2013), The last decade of global anthropogenic sulfur dioxide: 2000-2011 emissions, *Environ. Res. Lett.*, 8, 014003. doi:10.1088/1748-9326/8/1/014003.

Kloster, S., *et al.* (2006), DMS cycle in the marine ocean-atmosphere system: A global model study, *Biogeosciences*, 3(1), 29–51. doi:10.5194/bg-3-29-2006

Knippertz, P., and M. C. Todd (2012), Mineral dust aerosols over the Sahara: Meteorological controls on emission and transport and implications for modeling, *Rev. Geophys.*, 50, RG1007. doi:10.1029/2011RG000362.

Koehler, K. A., S *et al.* (2009), Hygroscopicity and cloud droplet activation of mineral dust aerosol, *Geophys. Res. Lett.*, 36, L08805. doi:10.1029/2009GL037348.

Kourtidis, K., *et al.* (2004), Substantial traffic emissions contribution to the global H_2S budget, *Geophys. Res. Lett.*, 31, L18107. doi:10.1029/2004GL020713.

Koven, C. D., *et al*. (2012), Analysis of permafrost thermal dynamics and response to climate change in the CMIP5 Earth System Models, *J. Clim.*, doi:10.1175/JCLI-D-12-00228.1.

Kravitz, B., *et al.* (2011), The Geoengineering Model Intercomparison Project (GeoMIP), *Atmos. Sci. Lett.*, 12: 162–167. doi:10.1002/asl.316

Kravitz, B., *et al.* (2012), Sensitivity of stratospheric geoengineering with black carbon to aerosol size and altitude of injection, *J. Geophys. Res.*, 117, D09203. doi:10.1029/2011JD017341.

Kravitz, B., *et al.* (2013), Climate model response from the geoengineering model intercomparison project (GeoMIP), *J. Geophys. Res. Atmos.*, 118, 8320–8332. doi:10.1002/jgrd.50646.

Kravitz, B., *et al.* (2014a), A multi-model assessment of regional climate disparities caused by solar geoengineering, *Environ. Res. Lett*., 9(7), 074013. doi:10.1088/1748-9326/9/7/074013

Kravitz, B., *et al.* (2014b), Explicit feedback and the management of uncertainty in meeting climate objectives with solar geoengineering, *Environ. Res. Lett*., 9, 044006, http://dx.doi.org/10.1088/1748-9326/9/4/044006.

Kravitz, B., *et al.* (2015), The Geoengineering Model Intercomparison Project Phase 6 (GeoMIP6): simulation design and preliminary results, *Geosci. Model Dev.*, 8, 3379-3392. doi:10.5194/gmd-8-3379-2015

Kremser, S., *et al.* (2016), Stratospheric aerosol—Observations, processes, and impact on climate, *Rev. Geophys.*, 54, 278–335. doi:10.1002/2015RG000511.

Kristjánsson, J. E., *et al.* (2015), The hydrological cycle response to cirrus cloud thinning, *Geophys. Res. Lett.*, 42, 10,807–10,815. doi:10.1002/2015GL066795.

Kurucz, R. L. (1995), 1995 Atomic Line Data [CD-ROM], vol. 23, Smithsonian. Astrophys. Observ., Cambridge, Mass.

Laakso, A., *et al.* (2012), Stratospheric passenger flights are likely an inefficient geoengineering strategy, *Environ. Res. Lett*., 7(3), 034021. doi:10.1088/1748-9326/7/3/034021

Labitzke, K., and M. P. McCormick (1992), Stratospheric temperature increases due to Pinatubo aerosols, *Geophys. Res. Lett.*, 19, 2, 207–210. doi:10.1029/91GL02940

Labitzke, K. (1994), Stratospheric temperature changes after the Pinatubo eruption, *J. Atmos. Terr. Phys.*, 56(9), 1027–1034. doi:10.1016/0021-9169(94)90039-6.

Lacis, A. A., and J. E. Hansen (1974), A parameterization for the absorption of solar radiation in the Earth's atmosphere, *J. Atmos. Sci.*, 31, 118-133, http://dx.doi.org/10.1175/1520-0469(1974)031<0118:APFTAO>2.0.CO;2

Lacis, A., *et al.* (1992), Climate forcing by stratospheric aerosols, *Geophys. Res. Lett.*, 19(15), 1607–1610. doi:10.1029/92GL01620

Lana, A., *et al.* (2011), An updated climatology of surface dimethlysulfide concentrations and emission fluxes in the global ocean, *Global Biogeochem. Cycles*, 25, GB1004. doi:10.1029/2010GB003850.

Landsea, C. W., and J. L. Franklin (2013), Atlantic hurricane database uncertainty and presentation of a new database format, *Mon. Weather Rev.*, 141, 3576–3592.

Latif, M., *et al.* (2007), Tropical sea surface temperature, vertical wind shear, and hurricane development, *Geophys. Res. Lett.*, 34, L01710, doi:10.1029/2006GL027969

Lauvset, S. K., *et al.* (2015), Trends and drivers in global surface ocean pH over the past 3 decades, *Biogeosciences*, 12(5), 1285–1298. doi:10.5194/bg-12-1285-2015.

L'Ecuyer, T. S., *et al.* (2015), The observed state of the energy budget in the early 21st century, *J. Clim.*, 28, 8319–8346. doi:10.1175/JCLI-D-14-00556.1

Lee, C.-L., and P. Brimblecombe (2016). Anthropogenic contributions to global carbonyl sulfide, carbon disulfide and organosulfides fluxes, *Earth-Sci. Rev.*, 160, 1–18, http://dx.doi.org/10.1016/j.earscirev.2016.06.005

Legates, D. R., and G. J. McCabe Jr. (1999), Evaluating the use of "goodness-of-fit" measures in hydrologic and hydroclimatic model validation, *Water Resour. Res.*, 35, 1, 233-241. doi:10.1029/1998WR900018

Legrand, M., and D. Wagenbach (1999), Impact of the Cerro Hudson and Pinatubo volcanic eruptions on the Antarctic air and snow chemistry, *J. Geophys. Res.*, 104(D1), 1581-1596. doi:10.1029/1998JD100032.

Lenton, T. M., and N. E. Vaughan (2009), The radiative forcing potential of different climate geoengineering options, *Atmos. Chem. Phys.*, 9, 5539–5561. doi:10.5194/acp-9-5539-2009

Lesnikowski, A., *et al.* (2015). National-level progress on adaptation, *Nat. Clim. Change*, 6(3), 261–264. doi:10.1038/nclimate2863

Liou, K.-N. (1977), A complementary theory of light scattering by homogeneous spheres, *Appl. Math. Comput.*, 3, 331-358. doi:10.1016/0096-3003(77)90018-2

Liu, D., *et al.* (2013), Ambient black carbon particle hygroscopic properties controlled by mixing state and composition, *Atmos. Chem. Phys.*, 13 (4), 2015–2029. doi:10.5194/acp-13-2015-2013

Lohmann, U., *et al.* (2003), Impact of the Mount Pinatubo eruption on cirrus clouds formed by homogeneous freezing in the ECHAM4 GCM, *J. Geophys. Res.*, 108, 4568, doi:10.1029/2002JD003185, D18.

Lohmann, U., *et al.* (2016), An introduction to clouds: from the microscale to climate, Cambridge University Press, Cambridge, pp. 399, ISBN 9781107018228

Lombardo, *et al.* (2015), Evaluation of Historical and Future Cool Season Precipitation over the Eastern United States and Western Atlantic Storm Track Using CMIP5 Models, *J. Clim.*, 28, 451–467, http://dx.doi.org/10.1175/JCLI-D-14-00343.1

Lorenzoni, I., *et al.* (2007), Barriers perceived to engaging with climate change among the UK public and their policy implications, *Global Environ. Chang.*, 17, 445–459. http://dx.doi.org/10.1016/j.gloenvcha.2007.01.004

Lu, J., *et al.* (2007), Expansion of the Hadley cell under global warming, *Geophys. Res. Lett.*, 34, L06805. doi:10.1029/2006GL028443.

MacCracken, M. C. (2009), On the possible use of geoengineering to moderate specific climate change impacts, *Environ. Res. Lett.*, 4, 045107, doi:10.1088/1748-9326/4/4/045107

MacMartin, D. G., *et al.* (2013), Management of trade-offs in geoengineering through optimal choice of non-uniform radiative forcing, *Nat. Clim. Change*, 3, 365-368. doi:10.1038/nclimate1722

MacMartin, D. G., *et al.* (2014), Dynamics of the coupled human–climate system resulting from closed-loop control of solar geoengineering, *Clim. Dynam.*, 43, 1, 243-258. doi:10.1007/s00382-013-1822-9

Madronich, S., *et al.* (1998), Changes in biologically active ultraviolet radiation reaching the Earth's surface, J*. Photochem. Photobiol. B*, 46, 5-19. doi:10.1039/B700017K

Mahlstein, I., and R. Knutti (2012), September Arctic sea ice predicted to disappear near 2°C global warming above present, *J. Geophys. Res.*, 117, D06104. doi:10.1029/2011JD016709.

Mann, G. W., *et al.* (2010), Description and evaluation of GLOMAP-mode: A modal global aerosol microphysics model for the UKCA composition-climate model, Geosci. Model Dev., 3, 519–551. doi:10.5194/gmd-3-519-2010

Manners, J. (2016), The Radiation Code, Unified Model Documentation Paper 023, UM Version 10.5 / Last Updated 2016-08-31, Met Office, Exeter, United Kingdom

Mao, J., and A. Robock (1998), Surface air temperature simulations by AMIP general circulation models: Volcanic and ENSO signals and systematic errors, *J. Clim.*, 11, 1538-1552. http://dx.doi.org/10.1175/1520-0442(1998)011<1538:SATSBA>2.0.CO;2

Marks, A. A., and M. D. King (2014), The effect of snow/sea ice type on the response of albedo and light penetration depth (e-folding depth) to

increasing black carbon, *Cryosphere*, 8, 1625–1638. doi:10.5194/tc-8-1625-2014

Martin, G. M., *et al.* (2006), The physical properties of the atmosphere in the new Hadley Centre Global Environmental Model, HadGEM1. Part 1: Model description and global climatology, *J. Clim.*, 19, 7, 1274–1301. doi:10.1175/JCLI3636.1

Martin, G. M., *et al.* (2011), The HadGEM2 family of Met Office Unified Model climate configurations, *Geosci. Model Dev.*, 4, 723–757, 2011. doi:10.5194/gmd-4-723-2011

Martin, G. M., and R. C. Levine (2012), The influence of dynamic vegetation on the present-day simulation and future projections of the South Asian summer monsoon in the HadGEM2 family, *Earth Syst. Dynam.*, 3, 245–261, doi:10.5194/esd-3-245-2012

Maycock, A. C., *et al.* (2011), The temperature response to stratospheric water vapour changes, *Q. J. R. Meteorol. Soc.*, 137, 1070–1082. doi:10.1002/qj.822

McClatchey, R. A., *et al.* (1972), Optical Properties of the Atmosphere (Third Edition), AFCRL 72-0497, AD 753075

McClellan, J., *et al.* (2012), Cost analysis of stratospheric albedo modification delivery systems, *Environ. Res. Lett.*, 7, 034019. doi:10.1088/1748-9326/7/3/034019.

McCormick, M. P., and R. E. Veiga (1992), SAGE II measurements of early Pinatubo aerosols, *Geophys. Res. Lett.*, 19, 2, 155-158. doi:10.1029/91GL02790

McCormick, M. P, *et al.* (1995), Atmospheric effects of the Mt Pinatubo eruption, *Nature*, 373, 399-404. doi:10.1038/373399a0

McCoy, D. T., and D. L. Hartmann (2015), Observations of a substantial cloud-aerosol indirect effect during the 2014–2015 Bárðarbunga-Veiðivötn fissure eruption in Iceland, *Geophys. Res. Lett.*, 42, 10,409–10,414. doi:10.1002/2015GL067070.

McCusker, K. E., *et al.* (2015), Inability of stratospheric sulfate aerosol injections to preserve the West Antarctic Ice Sheet, *Geophys. Res. Lett.*, 42. doi:10.1002/2015GL064314.

McKenzie, R. L., *et al.* (2007), Changes in biologically-active ultraviolet radiation reaching the Earth's surface, *Photochem. Photobiol. Sci.*, 6, 218–231. doi:10.1039/b700017k

McKinlay, A. F., and B. L. Diffey (1987), A reference action spectrum for ultraviolet induced erythema in human skin, in Human Exposure to Ultraviolet Radiation: Risks and Regulations, ed. W. F. Passchier and B. F. M. Bosnajakovic, Elsevier, Amsterdam, pp. 83-87

Meehl, G. A., *et al.* (2007), The WCRP CMIP3 multimodel dataset—a new era in climate change research, *Bull. Am. Met. Soc.*, 88:1383–1394, doi:http://dx.doi.org/10.1175/BAMS-88-9-1383

Meehl, G. A., *et al.* (2011), Model-based evidence of deep ocean heat uptake during surface temperature hiatus periods, *Nat. Clim. Change*, 1, 360–364. doi:10.1038/NCLIMATE1229.

Meinshausen, *et al.* (2011), The RCP Greenhouse Gas Concentrations and their Extension from 1765 to 2300, *Clim. Change*, 109, 213. doi:10.1007/s10584-011-0156-z

Mercado, L. M., *et al.* (2009), Impact of changes in diffuse radiation on the global land carbon sink, *Nature*, 458, 1014–1017. doi:10.1038/nature07949.

Mie, G. (1908), Beiträge zur Optik trüber Medien, speziell kolloidaler Metallösungen, *Ann. Phys.*, 330, 377–445. doi:10.1002/andp.19083300302

Mills, M. J., *et al.* (2016), Global volcanic aerosol properties derived from emissions, 1990-2014, using CESM1(WACCM), *J. Geophys. Res. Atmos.*, 121, 2332–2348. doi:10.1002/2015JD024290.

Mimura, N., *et al.* (2014), Adaptation planning and implementation. In: Climate Change 2014: Impacts, Adaptation, and Vulnerability. Part A: Global and Sectoral Aspects. Contribution of Working Group II to the Fifth Assessment Report of the Intergovernmental Panel on Climate Change [Field, C.B., *et al.* (eds.)]. Cambridge University Press, Cambridge, United Kingdom and New York, NY, USA, pp. 869-898.

Mishchenko, M.I., *et al.* (2002), Scattering, Absorption, and Emission of Light by Small Particles, Cambridge University Press, Cambridge, United Kingdom

Mitchell, D. L., and W. Finnegan (2009), Modification of cirrus clouds to reduce global warming, *Environ. Res. Lett.*, 4, 045,102, http://dx.doi.org/10.1088/1748-9326/4/4/045102

Mitchell, D. M, *et al.* (2012), The Effect of Climate Change on the Variability of the Northern Hemisphere Stratospheric Polar Vortex, *J. Atmos. Sci.*, 69, 2609-2618. doi:10.1175/JAS-D-12-021.1

Molina, M. J., and F. S. Rowland (1974), Stratospheric sink for chlorofluoromethanes: Chlorine atom catalyzed destruction of ozone, *Nature*, 249, 820–812. doi:10.1038/249810a0

Möller, D. (1984), Estimates of the global man-made sulfur emission, *Atmos. Environ.*, 18, 19–27. doi:10.1016/0004-6981(84)90225-7

Moore, J. C., *et al.* (2010), Efficacy of geoengineering to limit 21st century sea-level rise, *Proc. Natl. Acad. Sci. U. S. A.*, 107(36), 15699–15703. doi:10.1073/pnas.1008153107

Moore, J. C., *et al.* (2015), Atlantic hurricane surge response to geoengineering, *Proc. Natl. Acad. Sci. U. S. A.*, 112, 13,794–13,799. doi:10.1073/pnas.1510530112.

Morgenstern, O., *et al.* (2009), Evaluation of the new UKCA climate-composition model. Part 1: The stratosphere, *Geosci. Model Dev.*, 1, 43–57. doi:10.5194/gmd-2-43-2009

Moss, R. H., et al. (2010), The next generation of scenarios for climate change research and assessment, *Nature*, 463, 747–756. doi:10.1038/nature08823.

Mu, C., *et al*. (2015), Editorial: Organic carbon pools in permafrost regions on the Qinghai–Xizang (Tibetan) Plateau, *Cryosphere*, 9, 479–486, doi:10.5194/tc-9-479-2015.

Muller, C. J., and P. A. O'Gorman (2011), An energetic perspective on the regional response of precipitation to climate change, *Nat. Clim. Change*, 1, 266–271. doi:10.1038/nclimate1169, 2011.

Muri, H., *et al.* (2014), The climatic effects of modifying cirrus clouds in a climate engineering framework, *J. Geophys. Res. Atmos.*, 119, 4174–4191. doi:10.1002/2013JD021063.

Myhre, G., *et al.* (2004), The radiative effect of the anthropogenic influence on the stratospheric sulfate aerosol layer, *Tellus B*, 56, 294–299. doi:10.1111/j.1600-0889.2004.00106.x

Myhre, G., *et al.* (2013), Anthropogenic and Natural Radiative Forcing. In: Climate Change 2013: The Physical Science Basis. Contribution of Working Group I to the Fifth Assessment Report of the Intergovernmental Panel on Climate

Change [Stocker, T.F., *et al.* (eds.)]. Cambridge University Press, Cambridge, United Kingdom and New York, NY, USA.

Nakicenovic, N., and R. Swart (Eds.) (2000), Special Report on Emissions Scenarios, 612 pp., Cambridge Univ. Press, New York.

National Academy of Sciences (NAS) (1992), Policy Implications of Greenhouse Warming: Mitigation, Adaptation, and the Science Base, Panel on Policy Implications of Greenhouse Warming, Committee on Science, Engineering and Public Policy, National Academy Press, Washington, DC, pp. 433-464

National Research Council (NRC) (2015), Climate intervention: carbon dioxide removal and reliable sequestration, in Report Prepared by the Committee on Geoengineering Climate: Technical Evaluation and Discussion of Impacts, Natl. Acad. Sci., Washington, D. C.

Navarro, J. C., *et al.* (2016), Amplification of Arctic warming by past air pollution reductions in Europe, *Nat. Geosci.*, 9(4), 277–281., doi:10.1038/ngeo2673

Ndour, M., *et al.* (2008), Photoenhanced uptake of NO_2 on mineral dust: Laboratory experiments and model simulations, *Geophys. Res. Lett.*, 35, L05812. doi:10.1029/2007GL032006.

Niang, I., *et al.* (2014), Africa. In: Climate Change 2014: Impacts, Adaptation, and Vulnerability. Part B: Regional Aspects. Contribution of Working Group II to the Fifth Assessment Report of the Intergovernmental Panel on Climate Change [Barros, V.R., *et al.* (eds.)]. Cambridge University Press, Cambridge, United Kingdom and New York, NY, USA, pp. 1199-1265.

Niemeier, U., *et al.* (2009), Initial fate of fine ash and sulfur from large volcanic eruptions, *Atmos. Chem. Phys.*, 9, 9043-9057. doi:10.5194/acp-9-9043-2009

Niemeier, U., *et al.* (2011), The dependency of geoengineered sulfate aerosol on the emission strategy, *Atmos. Sci. Lett.*, 12, 189–194. doi:10.1002/asl.304

Niemeier, U., *et al.* (2013), Solar irradiance reduction via climate engineering: Impact of different techniques on the energy balance and the hydrological cycle, *J. Geophys. Res. Atmos.*, 118, 11,905–11,917. doi:10.1002/2013JD020445.

Niemeier, U., and C. Timmreck (2015), What is the limit of climate engineering by stratospheric injection of SO_2?, *Atmos. Chem. Phys.*, 15(16), 9129–9141. doi:10.5194/acp-15-9129-2015.

Notholt, J. and H. Bingemer (2006), Precursor gas measurements, in Assessment of Stratospheric Aerosol Properties, edited by L. Thomason and T. Peter,

WCRP 124, WMO/TD 1295, SPARC Rep. 4, World Meteorolo. Organ., Geneva, Switzerland

Nowack, P. J., *et al.* (2016), Stratospheric ozone changes under solar geoengineering: implications for UV exposure and air quality, *Atmos. Chem. Phys.*, 16, 4191-4203. doi:10.5194/acp-16-4191-2016

Oman, L., *et al.* (2006a), High-latitude eruptions cast shadow over the African monsoon and the flow of the Nile, *Geophys. Res. Lett.*, 33, L18711. doi:10.1029/2006GL027665.

Oman, L., *et al.* (2006b), Modeling the distribution of the volcanic aerosol cloud from the 1783 Laki Eruption, *J. Geophys. Res.*, 111, D12209. doi:10.1029/2005JD006899.

Pal, J. S., and E. A. B. Eltahir (2015), Future temperature in southwest Asia projected to exceed a threshold for human adaptability. *Nat. Clim. Change*, 6: 197–200. doi:10.1038/NCLIMATE2833.

Paolo, F. S., *et al.* (2015), Volume loss from Antarctic ice shelves is accelerating, *Science*, 348(6232), 327–331. doi:10.1126/science.aaa0940

Park, M., *et al.* (2007), Transport above the Asian summer monsoon anticyclone inferred from Aura Microwave Limb Sounder tracers, *J. Geophys. Res.*, 112, D16309. doi:10.1029/2006JD008294.

Penner, J. E., *et al.* (2015), Can cirrus cloud seeding be used for geoengineering?, *Geophys. Res. Lett.*, 42, 8775–8782. doi:10.1002/2015GL065992.

Peters, G. P., *et al.* (2013), The challenge to keep global warming below 2 °C, *Nat. Clim. Change*, 3, 4-6. doi:10.1038/nclimate1783

Pierce, J. R., *et al.* (2010), Efficient formation of stratospheric aerosol for climate engineering by emission of condensible vapor from aircraft, *Geophys. Res. Lett.*, 37, L18805. doi:10.1029/2010GL043975.

Pitari, G., *et al.* (2014), Stratospheric ozone response to sulfate geoengineering: Results from the Geoengineering Model Intercomparison Project (GeoMIP), *J. Geophys. Res. Atmos.*, 119, 2629–2653. doi:10.1002/2013JD020566.

Pithan, F., and T. Mauritsen (2014): Arctic amplification dominated by temperature feedbacks in contemporary climate models, *Nat. Geosci.*, 7, 181-184. doi:10.1038/ngeo2071

Planck, M. (1900), On the Law of Distribution of Energy in the Normal Spectrum, *Verh. Disch. Phys. Ges.*, Berlin, 2, 237

Pongratz, J., *et al.* (2012), Crop yields in a geoengineered climate, *Nat. Clim. Change*, 2, 101–105. doi:10.1038/nclimate1373.

Pope, F. D, *et al.* (2012), Stratospheric aerosol particles and solar-radiation management, *Nat. Clim. Change*, 2, 713–719. doi:10.1038/nclimate1528

Priestley, *et al.* (2011), Radiometric performance of the CERES Earth radiation budget climate record sensors on the EOS aqua and terra spacecraft through April 2007*, J. Atmos. Oceanic Technol.*, 28, 3–21. doi:10.1175/2010JTECHA1521.1.

Prospero, J. (1999), Long-range transport of mineral dust in the global atmosphere: Impact of African dust on the environment of the southeastern United States, *Proc. Natl. Acad. Sci.* U.S.A., 96(7), 3396–3403. doi: 10.1073/pnas.96.7.3396

Pruppacher, H.R., and J.D. Klett (1980), Microphysics of Clouds and Precipitation, D. Reidel Publishing Company, Dordretch, ISBN: 978-90-277-1106-9, Holland, Reprinted

Pudykiewicz, J. A., and A. P. Dastoor (1995), On Numerical Simulation of the Global Distribution of Sulfate Aerosol Produced by a Large Volcanic Eruption, *J. Clim.*, 8, 464–473. doi:http://dx.doi.org/10.1175/1520-0442(1995)008<0464:ONSOTG>2.0.CO;2

Ran, Y., *et al.* (2012), Distribution of Permafrost in China: An Overview of Existing Permafrost Maps, *Permafrost and Periglac. Process.*, 23, 322–333. doi:10.1002/ppp.1756

Rappaport, E. N. (2000), Loss of life in the United States associated with recent Atlantic tropical cyclones, *Bull. Am. Meteorol. Soc.*, 81, 2065–2073. doi: 10.1175/1520-0477(2000)081<2065:LOLITU>2.3.CO%3B2

Rasch, P. J., *et al.* (2008a), Exploring the geoengineering of climate using stratospheric sulfate aerosols: The role of particle size, *Geophys. Res. Lett.*, 35, L02809. doi:10.1029/2007GL032179

Rasch, P. J., *et al.* (2008b), An overview of geoengineering of climate using stratospheric sulphate aerosols, *Philos. Trans. R. Soc.*, Ser. A., 366, 4007–4037. doi:10.1098/rsta.2008.0131.

Read, W. G., *et al.* (1993), Microwave Limb Sounder measurement of stratospheric SO_2 from the Mt. Pinatubo volcano, *Geophys. Res. Lett.*, 20(12), 1299–1302. doi:10.1029/93GL00831.

Remsberg, E. E., *et al.* (1974), Optical Constants for Sulfuric and Nitric Acids, *J. Chem. Eng. Data*, 19, 3, 263-265. doi:10.1021/je60062a003

Riahi, K., *et al.* (2011), RCP 8.5 - A scenario of comparatively high greenhouse gas emissions, *Clim. Change*, 109, 33–57. doi:10.1007/s10584-011-0149-y.

Ribarsky, M. W. (1985), Titanium dioxide, in Handbook of Optical Constants of Solids, edited by E. Palik, pp. 795–804, Academic Press Inc., San Diego, California

Richardson, K., *et al.* (2011), Climate Change: Global Risks, Challenges and Decisions, Cambridge University Press, Cambridge

Ridgwell, A., *et al.* (2009), Tackling Regional Climate Change By Leaf Albedo Bio-geoengineering, *Curr. Biol*., 19(2), 146–150. doi:10.1016/j.cub.2008.12.025

Ricke, K. L., *et al.* (2010). Regional climate response to solar-radiation management, *Nat. Geosci.*, 3(8), 537–541. doi:10.1038/ngeo915

Roberts, M. J., *et al.* (2015), Tropical cyclones in the UPSCALE ensemble of high-resolution global climate models, *J. Clim.*, 28:574–596., doi: http://dx.doi.org/10.1175/JCLI-D-14-00131.1

Robock, A., and J. Mao (1995), The volcanic signal in surface temperature observations, *J. Clim.*, 8, 1086-1103, http://dx.doi.org/10.1175/1520-0442(1995)008<1086:TVSIST>2.0.CO;2

Robock, A. (2000), Volcanic eruptions and climate, *Rev. Geophys.*, 38, 2, 191-219. doi:10.1029/1998RG000054

Robock, A., *et al.* (2008), Regional climate responses to geoengineering with tropical and Arctic SO2 injections, *J. Geophys. Res.*, 113, D16101. doi:10.1029/2008JD010050

Robock, A. (2008), The 20 reasons why geoengineering may be a bad idea, *Bull. At. Sci.*, 64(2), 14–18, 59. doi:10.2968/064X00000.

Robock, A., *et al.* (2009), Benefits, risks, and costs of stratospheric geoengineering, *Geophys. Res. Lett.*, 36, L19703. doi:10.1029/2009GL039209.

Robock, A. (2014), Stratospheric aerosol geoengineering, *Issues Env. Sci. Tech.* (special issue “Geoengineering of the Climate System”), 38, 162-185. doi:10.1039/9781782621225

Rocquefelte, X., *et al.* (2004), Investigation of the Origin of the Empirical Relationship between Refractive Index and Density on the Basis of First Principles

Calculations for the Refractive Indices of Various TiO_2 Phases, *Inorg. Chem.*, 43, 2246-2251. doi:10.1021/ic035383r

Roe, G. H., and M. B. Baker (2007). Why Is Climate Sensitivity So Unpredictable?, *Science*, 318(5850), 629–632. doi:10.1126/science.1144735

Romanovsky, *et al.* (2010a), Permafrost thermal state in the polar Northern Hemisphere during the international polar year 2007–2009: a synthesis, *Permafr. Periglac. Process.*, 21, 106–116. doi:10.1002/ppp.689

Romanovsky, V. E., *et al.* (2010b), Thermal State of Permafrost in Russia, *Permafr. Periglac. Process.*, 21, 136–155. doi:10.1002/ppp.683

Rosenfeld, D., *et al.* (2014), Global observations of aerosol-cloud-precipitation-climate interactions, *Rev. Geophys.*, 52, 750–808. doi:10.1002/2013RG000441.

Russell, P. B., *et al.* (1996), Global to microscale evolution of the Pinatubo volcanic aerosol derived from diverse measurements and analyses, *J. Geophys. Res.*, 101, D13, 18745-18763. doi: 10.1029/96JD01162

Russell, P. B., *et al.* (1997), Aerosol climate effects: Local radiative forcing and column closure experiments, *J. Geophys. Res.*, 102(D8), 9397–9407, doi:10.1029/97JD00112.

Sabziparvar, A. A., *et al.* (1999), A model-derived global climatology of ultraviolet irradiation at the Earth's surface, *Photochem. Photobiol.*, 69(2), 193–202. doi:10.1111/j.1751-1097.1999.tb03273.x

Salter, S., *et al.* (2008), Sea-going hardware for the cloud albedo method of reversing global warming, *Philos. Trans. R. Soc.*, 366, 3989–4006. doi:10.1098/rsta.2008.0136.

Sardeshmukh, P. D., and B. J. Hoskins (1984), Spectral smoothing on the sphere, *Mon. Wea. Rev.*, 112, 2524–2529.

Sato, M., *et al.* (1993), Stratospheric aerosol optical depth, 1850–1990, *J. Geophys. Res.*, 98, 22987–22994. doi: 10.1029/93JD02553

Saunders, R. W., *et al.* (2012), Interactions of meteoric smoke particles with sulphuric acid in the Earth's stratosphere, *Atmos. Chem. Phys.*, 12, 4387–4398. doi:10.5194/acp-12-4387-2012

Schaefer, K., *et al.* (2014), The impact of the permafrost carbon feedback on global climate, *Environ. Res. Lett.*, 9, 085003, http://dx.doi.org/10.1088/1748-9326/9/8/085003

Schäfer, S., *et al.* (2015), The European Transdisciplinary Assessment of Climate Engineering (EuTRACE): Removing greenhouse gases from the atmosphere and reflecting sunlight away from earth, Funded by the European Union's Seventh Framework Programme under Grant Agreement,306993.

Schär, C., *et al.* (2004), The role of increasing temperature variability in European summer heatwaves, *Nature*, 427, 332–335. doi:10.1038/nature02300

Schirber, S. (2015), Influence of ENSO on the QBO: Results from an ensemble of idealized simulations, *J. Geophys. Res. Atmos.*, 120, 1109–1122, doi:10.1002/2014JD022460.

Schlesinger, W. H., and E. S. Bernhardt (2013), The Global Cycles of Sulfur and Mercury, Chapter 13 in Biogeochemistry: An Analysis of Global Change (3rd ed.), Academic Press, Waltham, Massachusetts, ISBN 978-0-12-385874-0, 672pp.

Schmidt, H., *et al.* (2012), Solar irradiance reduction to counteract radiative forcing from a quadrupling of CO_2: Climate responses simulated by four earth system models, *Earth Syst. Dyn.*, 3, 63–78. doi:10.5194/esd-3-63-2012.

Schmidt, J. A., *et al.* (2013a), OCS photolytic isotope effects from first principles: Sulfur and carbon isotopes, temperature dependence and implications for the stratosphere, *Atmos. Chem. Phys.*, 13(3), 1511–1520. doi:10.5194/acp-13-1511-2013

Schmidt, H., *et al.* (2013b), Response of the middle atmosphere to anthropogenic and natural forcings in the CMIP5 simulations with the Max Planck Institute Earth system model, *J. Adv. Model. Earth Syst.*, 5, 98–116. doi:10.1002/jame.20014.

Schneider, S. H. (1996), Geoengineering: Could - or should - we do it?, *Clim. Change*, 33, 291–302.. doi:10.1007/BF00142577

Schneider von Deimling, *et al.* (2012), Estimating the near-surface permafrost-carbon feedback on global warming, *Biogeosciences*, 9, 649–665, doi:10.5194/bg-9-649-2012.

Schoeberl, M. R., *et al.* (1993a), Tropical ozone loss following the eruption of Mt. Pinatubo, *Geophys. Res. Lett.*, 20, 1, 29-32. doi:10.1029/92GL02637

Schoeberl, M. R., *et al.* (1993b), A simulation of the Cerro Hudson SO_2 cloud, *J. Geophys. Res.*, 98(D2), 2949–2955. doi:10.1029/92JD02517.

Schoeberl, M. R., *et al.* (2008), Comparison of lower stratospheric tropical mean vertical velocities, *J. Geophys. Res.*, 113, D24109. doi:10.1029/2008JD010221.

Schuster, A. (1905), Radiation through a Foggy Atmosphere, *Astrophys. J.*, 21, 1, doi:10.1086/141186

Schwarzschild, K. (1906), Ueber das Gleichgewicht der Sonnenatmosphäre, Nachrichten von der Koniglichen Gesellschaft der Wissenschaften zu Gottingen, Mathematisch-Physikalische Klasse, 1, 41-53

Seinfeld, J. H., and S. N. Pandis (1998). Atmospheric Chemistry and Physics: from Air Pollution to Climate Change. John Wiley, New York. 1326 pp

Seinfeld, J. H., *et al.* (2016), Improving our fundamental understanding of the role of aerosol − cloud interactions in the climate system, *Proc. Natl. Acad. Sci. U. S. A.*, 113(21), 5781–5790, doi:10.1073/pnas.1514043113.

Self, S., *et al.* (2004), Magma volume, volatile emissions, and stratospheric aerosols from the 1815 eruption of Tambora, *Geophys. Res. Lett.*, 31, L20608. doi:10.1029/2004GL020925.

Sheng, J.-X., *et al.* (2015a), Global atmospheric sulfur budget under volcanically quiescent conditions: Aerosol-chemistry-climate model predictions and validation, *J. Geophys. Res. Atmos*., 120, 256–276. doi:10.1002/2014JD021985.

Sheng, J.-X., *et al.* (2015b), A perturbed parameter model ensemble to investigate Mt. Pinatubo's 1991 initial sulfur mass emission, *Atmos. Chem. Phys.*, 15, 11501-11512, 2015. doi:10.5194/acp-15-11501-2015

Shepherd, J. (2009), Geoengineering the climate: Science, governance, and uncertainty, Royal Society Policy document 10/09, ISBN: 978-0-85403-773-5, 82 pp.

Sillmann, J., *et al.* (2013), Climate extremes indices in the CMIP5 multimodel ensemble: Part 2. Future climate projections*, J. Geophys. Res. Atmos.*, 118, 2473–2493. doi:10.1002/jgrd.50188.

Simpson, I. R., *et al.* (2011), Dynamics of the Lower Stratospheric Circulation Response to ENSO, *J. Atmos. Sci.*, 68, 2537–2566, doi:10.1175/JAS-D-11-05.1.

Slater, A. G., and D. M. Lawrence (2013), Diagnosing present and future permafrost from climate models, *J. Clim.*, 26(15), 5608–5623, doi:10.1175/jcli-d-12-00341.1.

Smit, B., & Wandel, J. (2006). Adaptation, adaptive capacity and vulnerability, *Glob. Environ. Change*, 16(3), 282–292. doi:10.1016/j.gloenvcha.2006.03.008

Smith, D. M., *et al.* (2010), Skilful multi-year predictions of Atlantic hurricane frequency, *Nat. Geosci.*, 3, 846–849, doi:10.1038/ngeo1004

Smith, S. J., *et al.* (2011), Anthropogenic sulfur dioxide emissions: 1850-2005, *Atmos. Chem. Phys.*, 11(3) 1101-1116. doi:10.5194/acp-11-1101-2011

Smith, P., *et al.* (2015), Biophysical and economic limits to negative CO2 emissions, *Nat. Clim. Change*, 6(1), 42–50. doi:10.1038/nclimate2870

Soden, B. J., *et al.* (2002), Global cooling after the eruptions of Mount Pinatubo: A test of climate feedback by water vapor, *Science*, 296, 5568, 727-730. doi:10.1126/science.296.5568.727

Solomon, S. (1999), Stratospheric ozone depletion: A review of concepts and history, *Rev. Geophys.*, 37(3), 275–316. doi:10.1029/1999RG900008.

Solomon, S., *et al.* (2010), Contributions of stratospheric water vapor to decadal changes in the rate of global warming, *Science*, 327, 1219–1223. doi:10.1126/science.1182488.

Solomon, S., *et al.* (2011), The persistently variable “background” stratospheric aerosol layer and global climate change, *Science*, 333, 866–870. doi:10.1126/science.1206027.

Spencer, R. W., *et al.* (1998), Tropical oceanic precipitation changes after the 1991 Pinatubo eruption, *J. Atmos. Sci.*, 55, 1707-1713, http://dx.doi.org/10.1175/1520-0469(1998)055<1707:TOPCAT>2.0.CO;2

Spracklen, D. V., *et al.* (2011), Aerosol mass spectrometer constraint on the global secondary organic aerosol budget, *Atmos. Chem. Phys.*, 11, 12,109–12,136. doi:10.5194/acp-11-12109-2011.

Springmann, M., *et al.* (2016), Global and regional health effects of future food production under climate change: a modelling study, *Lancet*, 387, 1937–1946, http://dx.doi.org/10.1016/S0140-6736(15)01156-3

Stenchikov, G. L., *et al.* (1998), Radiative forcing from the 1991 Mount Pinatubo volcanic eruption, *J. Geophys. Res.*, 103(D12), 13837–13857. doi:10.1029/98JD00693.

Stenchikov, G., *et al.* (2002), Arctic Oscillation response to the 1991 Mount Pinatubo eruption: Effects of volcanic aerosols and ozone depletion, *J. Geophys. Res.*, 107(D24), 4803. doi:10.1029/2002JD002090

Stern, A. C. (1982), History of Air Pollution Legislation in the United States, *J. Air. Pollut. Control Assoc.*, 32:1, 44-61. doi:10.1080/00022470.1982.10465369

Stern, D. I. (2006), Reversal of the trend in global anthropogenic sulfur emissions, *Global Environ. Change*, 16, 207–220. doi:10.1016/j.gloenvcha.2006.01.001.

Stocker, T. F., *et al.* (2013), Technical Summary. In: Climate Change 2013: The Physical Science Basis. Contribution of Working Group I to the Fifth Assessment Report of the Intergovernmental Panel on Climate Change [Stocker, T.F., *et al.* (eds.)]. Cambridge University Press, Cambridge, United Kingdom and New York, NY, USA.

Storelvmo, T., *et al.* (2014), Cirrus cloud seeding: A climate engineering mechanism with reduced side effects?, *Phil. Trans. R. Soc. A.*, 372, 20140116. doi:10.1098/rsta.2014.0116

Storelvmo, T., and N. Herger (2014), Cirrus cloud susceptibility to the injection of ice nuclei in the upper troposphere, *J. Geophys. Res. Atmos.*, 119, 2375–2389. doi:10.1002/2013JD020816.

Stowe, L. L., *et al.* (1992), Monitoring the Mt. Pinatubo aerosol layer with NOAA/11 AVHRR data, *Geophys. Res. Lett.*, 19, 2, 159-162. doi:10.1029/91GL02958

Strachan, J., *et al.* (2013), Investigating global tropical cyclone activity with a hierarchy of AGCMs: The role of model resolution, *J. Clim.*, 26, 133–152, doi:10.1175/JCLI-D-12-00012.1.

Sun, Z. (2011), Improving transmission calculations for the Edwards–Slingo radiation scheme using a correlated-k distribution method, *Q. J. R. Meteorol. Soc.*, 137, 2138-2148, doi:10.1002/qj.880

Tang, M. J., *et al.* (2014), Heterogeneous reaction of N_2O_5 with airborne TiO_2 particles and its implication for stratospheric particle injection, *Atmos. Chem. Phys.*, 14, 6035-6048. doi:10.5194/acp-14-6035-2014

Taylor, K. E., *et al.* (2012), An Overview of CMIP5 and the Experiment Design, *Bull. Amer. Meteor. Soc.*, 93, 485–498. doi:http://dx.doi.org/10.1175/BAMS-D-11-00094.1

Tegtmeier, S., *et al.* (2008), Variations of the residual circulation in the Northern Hemispheric winter*, J. Geophys. Res.*, 113, D16109. doi:10.1029/2007JD009518.

Teller, E., *et al.* (1997), Global Warming and Ice Ages: I. Prospects for Physics-Based Modulation of Global Change, Lawrence Livermore National Laboratory Publication, UCRL-JC-128715, 18 pp.

Tilmes, S., *et al.* (2008), The sensitivity of polar ozone depletion to proposed geoengineering schemes, *Science*, 320, 1201–1204. doi:10.1126/science.1153966.

Tilmes, S., *et al.* (2009), Impact of geoengineered aerosols on the troposphere and stratosphere, *J. Geophys. Res.*, 114, D12305. doi:10.1029/2008JD011420.

Tilmes, S., *et al.* (2012), Impact of very short-lived halogens on stratospheric ozone abundance and UV radiation in a geo-engineered atmosphere, *Atmos. Chem. Phys.*, 12, 10945-10955. doi:10.5194/acp-12-10945-2012

Tilmes, S., *et al.* (2013), The hydrological impact of geoengineering in the Geoengineering Model Intercomparison Project (GeoMIP), *J. Geophys. Res. Atmos.*, 118, 11,036-11,058. doi:10.1002/jgrd.50868.

Timmreck, C., *et al.* (1999a), A one and half year interactive MA/ECHAM4 simulation of Mount Pinatubo Aerosol, *J. Geophys. Res.*, 104(D8), 9337–9359. doi:10.1029/1999JD900088.

Timmreck, C., *et al.* (1999b), Simulation of Mt. Pinatubo volcanic aerosol with the Hamburg climate model ECHAM4, *Theor. Appl. Climatol.*, 62(3–4), 85–108. doi:10.1007/s007040050076.

Tjiputra, J. F., *et al.* (2016), Impact of idealized future stratospheric aerosol injection on the large-scale ocean and land carbon cycles, *J. Geophys. Res. Biogeosci.*, 121, 2–27. doi:10.1002/2015JG003045.

Toohey, M., *et al.* (2011), The influence of eruption season on the global aerosol evolution and radiative impact of tropical volcanic eruptions, *Atmos. Chem. Phys.*, 11, 12351-12367. doi:10.5194/acp-11-12351-2011

Trenberth, K. E., and A. Dai (2007), Effects of the Mount Pinatubo volcanic eruption on the hydrological cycle as an analog of geoengineering, *Geophys. Res. Lett.*, 34, L15702. doi:10.1029/2007GL030524

Trenberth, K.E., *et al.* (2007), Observations: Surface and Atmospheric Climate Change. In: Climate Change 2007: The Physical Science Basis. Contribution

of Working Group I to the Fourth Assessment Report of the Intergovernmental Panel on Climate Change [Solomon, S., *et al.* (eds.)]. Cambridge University Press, Cambridge, United Kingdom and New York, NY, USA.

Trenberth, K. E., *et al.* (2009), Earth's global energy budget, *Bull. Am. Meteorol. Soc.*, 90(3), 311–323, doi:10.1175/2008BAMS2634.1

Trenberth, K. E. (2011), Changes in precipitation with climate change, *Clim. Res.*, 47, 123-138. doi:10.3354/cr00953.

Trepte, C. R., and M. H. Hitchman (1992), Tropical stratospheric circulation deduced from satellite aerosol data, *Nature*, 355, 626 - 628. doi:10.1038/355626a0

Trepte, C. R., *et al.* (1993), The poleward dispersal of Mount Pinatubo volcanic aerosol, *J. Geophys. Res.*, 98(D10), 18, 56318, 573. doi:10.1029/93JD01362.

Tropf, W. J, *et al.* (1995), Properties of crystals and glasses, in Handbook of Optics (Volume II): Devices, Measurements and Properties, (M. Bass *et al.* eds), 2nd Ed., McGraw-Hill, New York

Turco, R. P. (1996), Global environmental engineering: prospects and pitfalls, Chapter 7 in Human population and the environmental crisis [Zuckerman, B., and D. Jefferson (eds.)], Jones and Bartlett Publ., Sudbury, Mass., pp. 93-113.

Turco, R. P. (1997), Earth under siege: from air pollution to global change, Oxford University Press, 527 pp

Twomey, S. (1977), The influence of pollution on the shortwave albedo of clouds, *J. Atmos. Sci.*, 34(7), 1149–1152. doi:10.1175/1520-0469(1977)034<1149:tiopot>2.0.co;2.

Tyndall, J. (1861), On the Absorption and Radiation of Heat by Gases and Vapours, and on the Physical Connection of Radiation, Absorption. and Conduction, *Phil. Mag.*, ser. 4, 22. 169-194 and 273-285

United Nations Educational, Scientific and Cultural Organization (UNESCO) (1981), The Practical Salinity Scale 1978 and the International Equation of State of Seawater 1980, Tenth Report of the Joint Panel on Oceanographic Tables and Standards, *UNESCO Tech. Pap. in Mar. Sci.*, 36, 25 pp.

United Nations Framework Convention on Climate Change (UNFCC) (2015), Adoption of the Paris Agreement, FCCC/CP/2015/L.9/Rev1.

van de Hulst, H. (1957), Light Scattering by Small Particles, 370, John Wiley, New York

van Vuuren, D. P., *et al.* (2011), RCP2.6: Exploring the possibility to keep global mean temperature increase below 2°C*, Clim. Chang.*, 109, 95–116. doi:10.1007/s10584-011-0152-3.

Varotsos, C.A., *et al.* (2014), New spectral functions of the near-ground albedo derived from aircraft diffraction spectrometer observations, *Atmos. Chem. Phys.*, 14, 13, 6953-6965. doi:10.5194/acp-14-6953-2014

Vaughan, N. E., and T. M. Lenton (2011), A review of climate geoengineering proposals, *Clim. Change*, 109(3-4), 745–790. doi:10.1007/s10584-011-0027-7

Vergados, P., *et al.* (2015), On the comparisons of tropical relative humidity in the lower and middle troposphere among COSMIC radio occultations and MERRA and ECMWF data sets, *Atmos. Meas. Tech.*, 8, 1789–1797, doi:10.5194/amt-8-1789-2015

Vernier, J.-P., *et al.* (2011), Major influence of tropical volcanic eruptions on the stratospheric aerosol layer during the last decade, *Geophys. Res. Lett.*, 38, L12807. doi:10.1029/2011GL047563.

Vet, R., *et al.* (2014), A global assessment of precipitation chemistry and deposition of sulfur, nitrogen, sea salt, base cations, organic acids, acidity and pH, and phosphorus, *Atmos. Environ.*, 93, 3–100., doi:https://doi.org/10.1016/j.atmosenv.2013.10.060

Villarini, G., and G. A. Vecchi (2012), Twenty-first-century projections of North Atlantic tropical storms from CMIP5 models, *Nat. Clim. Change*, 2, 604–607., doi:10.1038/nclimate1530

von Schuckmann, K., *et al.* (2016), An imperative to monitor Earth's energy imbalance, *Nat. Clim. Change*, 6, 138–144. doi:10.1038/nclimate2876

Vogelmann, A. M., *et al.* (1992), Enhancements in biologically effective ultraviolet radiation following volcanic eruptions, *Nature*, 359, 47–49. doi:10.1038/359047a0

Wang, H., *et al.* (2011), Manipulating marine stratocumulus cloud amount and albedo: A process-modelling study of aerosol-cloud-precipitation interactions in response to injection of cloud condensation nuclei, *Atmos. Chem. Phys.*, 11, 4237–4249. doi:10.5194/acp-11-4237-2011.

Wang, C., *et al.* (2012), Multidecadal covariability of North Atlantic sea surface temperature, African dust, Sahel rainfall, and Atlantic hurricanes, *J. Clim.*, 25, 5404–5415, doi:10.1175/JCLI-D-11-00413.1.

Watanabe, T., and K. Yamazaki (2012), Influence of the Anticyclonic Anomaly in the Subtropical Jet over the Western Tibetan Plateau on the Intraseasonal Variability of the Summer Asian Monsoon in Early Summer, *J. Clim.*, 25, 1291–1303. doi:http://dx.doi.org/10.1175/JCLI-D-11-00036.1

Watson, P. A. G., and L. J. Gray (2014), The stratospheric wintertime response to applied extratropical torques and its relationship with the annular mode, *Clim. Dyn.*, 44, 2513–2537. doi:10.1007/s00382-014-2359-2

Watts, S.F. (2000), The mass budgets of carbonyl sulfide, dimethyl sulfide, carbon disulfide and hydrogen sulphide, *Atmos. Environ.*, 34 (5), 761–779. doi:10.1016/S1352-2310(99)00342-8

Weisenstein, D. K., and S. Bekki (2006), Modelling of Stratospheric Aerosols, in Assessment of Stratospheric Aerosol Properties, edited by L. Thomason and T. Peter, WCRP 124, WMO/TD 1295, SPARC Rep. 4, World Meteorolo. Organ., Geneva, Switzerland

Weisenstein, D. K., *et al.* (2007), Global 2-D intercomparison of sectional and modal aerosol modules, *Atmos. Chem. Phys.*, 7, 2339–2355. doi:10.5194/acp-7-2339-2007

Weisenstein, D. K., *et al.* (2015), Solar geoengineering using solid aerosol in the stratosphere, *Atmos. Chem. Phys.*, 15, 11835-11859. doi:10.5194/acp-15-11835-2015

Wien, W. (1893), Eine neue Beziehung der Strahlung schwarzer Körper zum zweiten Hauptsatz der Wärmetheorie, Sitzungsberichte der Preussischen Akademie der Wissenschaften, 1, 55-62.

Wigley, T. M. L. (2006), A combined mitigation/geoengineering approach to climate stabilization, *Science*, 314, 452–454. doi:10.1126/science.1131728.

Wilcox, L. J., *et al.* (2012), A global blended tropopause based on ERA data. Part I: Climatology, *Q. J. R. Meteorol. Soc.*, 138, 561–575. doi:10.1002/qj.951

Wilcoxon, F. (1945), Individual Comparisons by Ranking Methods, *Biometr. Bull.*, 1, 6, 80-83., doi:10.2307/3001968

Wild, M. (2012), Enlightening global dimming and brightening, *Bull. Am. Meteorol. Soc.*, 93(1), 27–37. doi:10.1175/BAMS-D-11-00074.1

Williams, K., *et al.* (2012), Assessment of GA4/GL4/GO4/GSI4 and progress in addressing key model biases, Hadley Centre Technical Note, Sept. [Available at http://www.metoffice.gov.uk/media/pdf/c/l/AdditionalPaper_GA4_assessment.pdf.]

Williamson, C. E., *et al.* (2014), Solar ultraviolet radiation in a changing climate, *Nat. Clim. Change*, 4, 434–441, doi:10.1038/nclimate2225.

Wiscombe, W. J., and G. W. Grams (1976), The backscattered fraction in two-stream approximations, *J. Atmos Sci.*, 33, 2440–2451. http://dx.doi.org/10.1175/1520-0469(1976)033<2440:TBFITS>2.0.CO;2

Xia, L., *et al.* (2016), Stratospheric sulfate geoengineering could enhance the terrestrial photosynthesis rate, *Atmos. Chem. Phys.*, 16, 1479–1489. doi:10.5194/acp-16-1479-2016.

Xu, L., and J. E. Penner (2012), Global simulations of nitrate and ammonium aerosols and their radiative effects, *Atmos. Chem. Phys.*, 12(20), 9479–9504. doi:10.5194/acp-12-9479-2012

Yanai, M., *et al.* (1992), Seasonal heating of the Tibetan Plateau and its effects on the evolution of the Asian summer monsoon, *J. Meteor. Soc. Japan*, 70, 319–351. wos:A1992HQ62100011

Yang, H., *et al.* (2004), Studying the Mechanisms of Titanium Dioxide as Ultraviolet-Blocking Additive for Films and Fabrics by an Improved Scheme, *J. Appl. Polym. Sci.*, 92, 3201–3210. doi:10.1002/app.20327

Young, R. E., *et al.* (1994), Radiatively forced dispersion of the Mt. Pinatubo volcanic cloud and induced temperature perturbations in the stratosphere during the first few months following the eruption, *Geophys. Res. Lett.*, 21, 5, 369-372

Yu, F., *et al.* (2007), Improved quasi-unary nucleation model for binary H_2SO_4 – H_2O homogeneous nucleation, *J. Chem. Phys.*, 127, 054301, doi:http://dx.doi.org/10.1063/1.2752171

Yu, X., *et al.* (2015), Impacts, effectiveness and regional inequalities of the GeoMIP G1 to G4 solar radiation management scenarios, *Glob. Planet. Change*, 129, 10–22, http://dx.doi.org/10.1016/j.gloplacha.2015.02.010, 2015.

Yuan, T., *et al.* (2011), Microphysical, macrophysical and radiative signatures of volcanic aerosols in trade wind cumulus observed by the A-Train, *Atmos. Chem. Phys.*, 11, 7119-7132. doi:10.5194/acp-11-7119-2011

Zdunkowski, W. G., et al. (1980), An investigation of the structure of typical two-stream-methods for the calculation of solar fluxes and heating rates in clouds, *Contrib. Atmos. Phys.*, 53, 147-166.

Zdunkowski, W. G., and G. J. Korb (1985), Numerische Methoden zur Losung der Strahlungsubertragungsgleichung, *PROMET*, 15, 26-39.

Zdunkowskwi, W., *et al.* (2007), Radiation in the Atmosphere: A Course in Theoretical Meterorology, Cambridge University Press, Cambridge, UK

Zeng, G., and J. A. Pyle (2005), Influence of El Niño Southern Oscillation on stratosphere/troposphere exchange and the global tropospheric ozone budget, *Geophys. Res. Lett.*, 32, L01814, doi:10.1029/2004GL021353.

Zeidler, S., *et al.* (2011), Near-infrared absorption properties of oxygen-rich stardust analogs: The influence of coloring metal ions, *Astron. Astrophys.*, 526, A68.

Zhao, T. X.-P., *et al.* (2013), A global survey of the effect of cloud contamination on the aerosol optical thickness and its long-term trend derived from operational AVHRR satellite observations, *J. Geophys. Res. Atmos.*, 118, 2849–2857. doi:10.1002/jgrd.50278.

Appendices

Appendix 1 (20 pages)

Jones, A. C., J. M. Haywood, and A. Jones (2016a), Climatic impacts of stratospheric geoengineering with sulphate, black carbon and titania injection, *Atmos. Chem. Phys.*, 16, 2843-2862, doi:10.5194/acp-16-2843-2016

Appendix 2 (17 pages)

Jones, A. C., J. M. Haywood, A. Jones, and V. Aquila (2016b), Sensitivity of volcanic aerosol dispersion to meteorological conditions: A Pinatubo case study, *J. Geophys. Res. Atmos.*, 121, 6892–6908, doi:10.1002/2016JD025001.

Atmos. Chem. Phys., 16, 2843–2862, 2016
www.atmos-chem-phys.net/16/2843/2016/
doi:10.5194/acp-16-2843-2016

Atmospheric Chemistry and Physics
Open Access
EGU

Climatic impacts of stratospheric geoengineering with sulfate, black carbon and titania injection

Anthony C. Jones[1], **James M. Haywood**[1,2], **and Andy Jones**[2]

[1]College of Engineering Maths and Physical Sciences, University of Exeter, Exeter, UK
[2]Met Office Hadley Centre, Exeter, UK

Correspondence to: Anthony C. Jones (aj247@exeter.ac.uk)

Received: 12 October 2015 – Published in Atmos. Chem. Phys. Discuss.: 3 November 2015
Revised: 25 February 2016 – Accepted: 26 February 2016 – Published: 4 March 2016

Abstract. In this paper, we examine the potential climatic effects of geoengineering by sulfate, black carbon and titania injection against a baseline RCP8.5 scenario. We use the HadGEM2-CCS model to simulate scenarios in which the top-of-the-atmosphere radiative imbalance due to rising greenhouse gas concentrations is offset by sufficient aerosol injection throughout the 2020–2100 period. We find that the global-mean temperature is effectively maintained at historical levels for the entirety of the period for all three aerosol-injection scenarios, though there is a wide range of side-effects which are discussed in detail. The most prominent conclusion is that although the BC injection rate necessary to produce an equivalent global mean temperature response is much lower, the severity of stratospheric temperature changes ($> +70\,^{\circ}C$) and precipitation impacts effectively exclude BC from being a viable option for geoengineering. Additionally, while it has been suggested that titania would be an effective particle because of its high scattering efficiency, it also efficiently absorbs solar ultraviolet radiation producing a significant stratospheric warming ($> +20\,^{\circ}C$). As injection rates and climatic impacts for titania are close to those for sulfate, there appears to be little benefit in terms of climatic influence of using titania when compared to the injection of sulfur dioxide, which has the added benefit of being well-modeled through extensive research that has been carried out on naturally occurring explosive volcanic eruptions.

1 Introduction

The climatic impacts of continued greenhouse gas (GHG) emissions are likely to be severe which has prompted countenance of new strategies for tackling GHG-induced global warming (e.g Collins et al., 2013). Geoengineering strategies, or large-scale climate interventions that aim to reduce global warming, include strategies to sequester atmospheric carbon dioxide – carbon dioxide removal (CDR) methods, and strategies to reduce solar irradiance at Earth's surface – solar radiation management (SRM) methods (Shepherd et al., 2009). Stratospheric Aerosol Injection (SAI), an SRM scheme which has received significant attention, involves the enhancement of the stratospheric aerosol layer in order to reflect more sunlight back to space. This scheme mimics large volcanic eruptions such as Mt. Pinatubo in 1991, which injected approximately 15–20 Tg of sulfur dioxide (SO_2) into the tropical stratosphere and induced a globally averaged surface cooling of around $-0.3\,^{\circ}C$ for the following 2 years (Stenchikov et al., 2002).

Sulfate (SO_4) aerosols have featured predominantly in SAI research because of the volcanic analogue (e.g., in the Geoengineering Model Intercomparison Project, GeoMIP, Kravitz et al., 2013). General Circulation Model (GCM) simulations suggest that, while sufficient sulfate injection could effectively reduce global-mean temperature, possible side effects include changes to regional precipitation (e.g., Bala et al., 2008; Tilmes et al., 2013), ozone (e.g., Tilmes et al., 2009; Pitari et al., 2014), stratospheric dynamics (Aquila et al., 2014) and sea-ice extent (Berdahl et al., 2014). Precipitation changes could result from changes to the moist static stability of the atmosphere and a concomitant weakening of

the hydrological cycle (Bala et al., 2008); furthermore, the regional precipitation changes under GeoMIP simulations have been shown to be reasonably consistent across a range of climate models (Tilmes et al., 2013). Ozone concentrations could change as a result of enhanced heterogeneous chemistry on the surface of sulfate aerosols or indirectly by changes to the stratospheric dynamics and chemistry (e.g., Tilmes et al., 2009). Stratospheric dynamical changes could occur as the result of tropical heating in the sulfate layer and by changes to wave propagation from the troposphere (e.g., Aquila et al., 2014).

In order to ameliorate the known side-effects of sulfate injection, some authors have proposed alternative aerosols to sulfate (e.g., Teller et al., 1997). Crutzen (2006) suggested the possible injection of black carbon (BC), which would mimic hypothetical nuclear winter scenarios. One advantage of BC over sulfate is that less mass would be needed for an equivalent radiative forcing (Crutzen, 2006). BC particles efficiently absorb solar radiation, unlike sulfate which primarily reflects solar radiation (Ferraro et al., 2011). Alternatively, minerals such as titania (TiO_2), silica (SiO_2) and alumina (Al_2O_3), which have a high refractive index at wavelengths of peak solar radiative flux (~ 550 nm), have also been suggested (Pope et al., 2012). Although the use of alternative aerosols is not a new suggestion (e.g., Teller et al., 1997), comparatively little research has been conducted on their potential utility. Kravitz et al. (2012) simulated a constant BC injection scenario of $1\,\mathrm{Tg\,yr^{-1}}$ in the tropics for small radius (0.03 µm) and large radius (0.15 µm) aerosols. They found that the small particle BC aerosol scenario produced a global surface cooling of $-9.45\,^{\circ}\mathrm{C}$, but also induced stratospheric warming $> +60\,^{\circ}\mathrm{C}$ and global ozone loss of 50 %. The large particle BC aerosol scenario had a negligible climatic impact. Using a fixed dynamical heating (FDH) code, Ferraro et al. (2011) compared the stratospheric heating of sulfate, titania, and BC layers for an equivalent instantaneous radiative forcing. Their results showed a tropical stratospheric warming signal for all the aerosols, though much greater in the case of BC. To date, no work has used a comprehensive fully coupled atmosphere–ocean GCM to directly compare the possible climatic impacts of SAI with alternative aerosols to sulfate, which is the motivation for this research.

In this work, we simulate the stratospheric injection of sulfate, titania and BC against a baseline RCP8.5 concentrations scenario using a fully coupled GCM. Titania is selected to represent an efficient light-scattering aerosol and BC is selected as a light-absorbing aerosol. RCP8.5, which is the high-end carbon-intensive CMIP5 scenario, is selected to give a significant greenhouse effect against which to employ geoengineering, in order to distinguish the climatic impacts specific to each aerosol. Observations have shown that the current global GHG emissions exceed the emissions inherent in RCP8.5 (Peters et al., 2013); therefore our work could be considered as geoengineering against a business-as-usual scenario. Additionally, the next generation of GeoMIP simulations (GeoMIP6) will utilize a carbon-intensive scenario (Kravitz et al., 2015), hence our work will provide a useful supplement to those results. We chose to inject aerosol at a sufficient rate to counterbalance the Top Of the Atmosphere (TOA) global- and annual-mean caused by increasing atmospheric GHGs. Our simulation design is similar to the G3 scenario of the Geoengineering Model Intercomparison Project (GeoMIP), which instead used the RCP4.5 concentrations scenario as its baseline and injected sulfate at a sufficient rate to counterbalance GHG radiative forcing (Kravitz et al., 2011). We analyze the climate changes in the 2090s with respect to a simulated historical period and discuss impacts on a wide range of meteorological parameters.

2 Model

2.1 The HadGEM2-CCS model

For this investigation, we use the HadGEM2-CCS climate model in a fully coupled atmosphere-ocean mode. HadGEM2-CCS is the high-top configuration of the HadGEM2 family of models, and includes a well-resolved stratosphere that is capable of internally generating a realistic quasi-biennial oscillation (QBO) (The HadGEM2 Development Team, 2011). The atmosphere component comprises 60 vertical levels extending to 84 km and a horizontal resolution of $1.25^{\circ} \times 1.875^{\circ}$ latitude by longitude respectively. The 40-level ocean component has a horizontal resolution of 1° by 1° from the poles to 30° N/S, with the latitudinal resolution then increasing smoothly to 0.33° at the equator (The HadGEM2 Development Team, 2011). For this investigation, GHG concentrations, stratospheric ozone, anthropogenic aerosols and aerosol precursor gases are prescribed following the Coupled Model Intercomparison Project phase 5 (CMIP5) (Taylor et al., 2012) protocol, with historical data from 1860 to 2005 and RCP8.5 concentrations from 2005 to 2100. HadGEM2-CCS contains the aerosol module Coupled Large-scale Aerosol Simulator for Studies in Climate (CLASSIC). The module's sulfur cycle is described in detail in Bellouin et al. (2011). Briefly, it includes the oxidation of sulfur dioxide (SO_2) to sulfate aerosol in aqueous and gas phase reactions. Sulfate is represented by Aitken, accumulation and dissolved modes, with hygroscopic growth in the accumulation mode following d'Almeida et al. (1991). Aerosol size modes are represented by lognormal size distributions with a prescribed dry-mode median radius (r_m) and geometric standard deviation (σ).

2.2 Stratospheric aerosol microphysical and optical properties

For this investigation, stratospheric sulfate is modelled using the *volc2* size-distribution from Rasch et al. (2008) for the sulfate accumulation mode, with $r_\mathrm{m} = 0.376$ µm and $\sigma =$

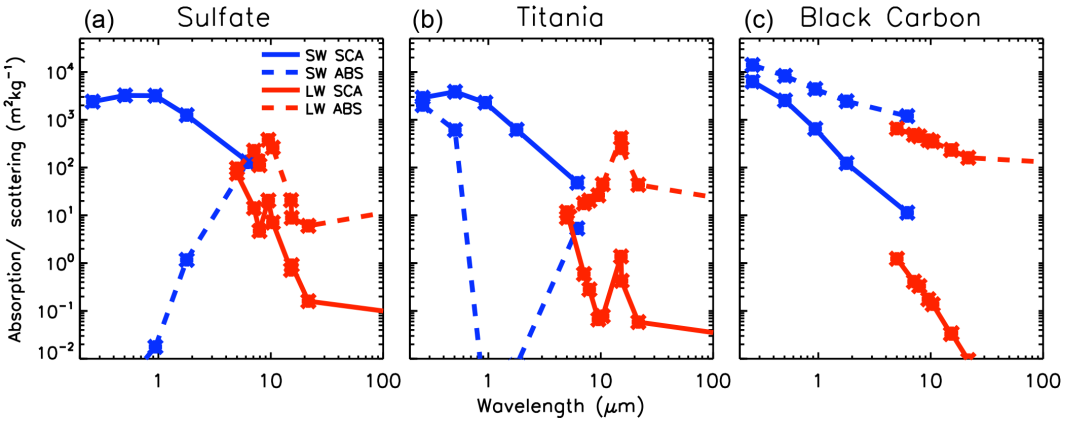

Figure 1. Optical properties as a function of wavelength for **(a)** accumulation-mode sulfate, **(b)** titania, **(c)** black carbon. Points are plotted at the middle of each spectral waveband, as detailed in Bellouin et al. (2007).

1.25; the relatively large r_m is chosen to reflect the high concentrations of SO_2 injected in this experiment.

CLASSIC includes a tropospheric BC scheme with fresh, aged and in-cloud modes (Bellouin et al., 2011). We introduce an additional non-hygroscopic stratospheric BC component and prescribe a lognormal size-distribution with $r_m = 0.0118\,\mu m$ and $\sigma = 2.0$, which is taken from tropospheric BC observations (Deepak and Gerber, 1983). We prescribe a density for BC of $1000\,kg\,m^{-3}$ and take refractive indices from a World Meteorological Organisation report (Deepak and Gerber, 1983).

For stratospheric titania, we assume the non-hygroscopic lognormal size distribution of Pope et al. (2012) with $r_m = 0.045\,\mu m$ and $\sigma = 1.8$. This size-distribution was selected to give the titania aerosol a high scattering efficiency, as shown by Pope et al. (2012). We prescribe a density for titania of $4230\,kg\,m^{-3}$ (Pope et al., 2012), and for the refractive indices we follow Ferraro et al. (2011) and use the average of the extra-ordinary and ordinary values from Ribarsky (1985).

The specific absorption (k_{abs}) and scattering (k_{sca}) coefficients for sulfate (accumulation/dry-mode), titania and BC are plotted in Fig. 1 as a function of wavelength. For sulfate, the specific extinction coefficient (k_{ext}) at 500 nm of $3200\,m^2\,kg^{-1}$ and single scattering albedo (ω_o) of 1 reflects the non-absorbing properties of sulfate. Although titania's 500 nm scattering efficiency ($k_{sca} = 3850\,m^2\,kg^{-1}$) is greater than sulfate's in this instance, titania additionally absorbs SW radiation ($k_{abs} = 2000$ at 250, and $k_{abs} = 600\,m^2\,kg^{-1}$ at 500 nm) which can be explained by the band-theory of solids (Yang et al., 2003). Thus titania is partially absorbing. Our modelled BC efficiently absorbs SW radiation ($k_{abs} = 8300\,m^2\,kg^{-1}$ at 500 nm) but also produces a non-negligible SW scattering effect ($k_{sca} = 2500\,m^2\,kg^{-1}$ at 500 nm) which is comparable in magnitude to the equivalent scattering efficiency of both titania and sulfate. Therefore, to describe titania as an efficient light-scatterer and/or BC as an efficient light-absorber is an over-simplification.

Our choice of particle size and density will impact the aerosol's gravitational sedimentation rate and therefore its atmospheric residence time (the sedimentation rate is also a property of the local atmospheric conditions) (Rasch et al., 2008). To determine the importance of our choice of aerosol properties, we have calculated the respective gravitational sedimentation rates by using the method of Pruppacher and Klett (1979) (which utilizes Stoke's law) and incorporating temperature and pressure values from the International Standard Atmosphere (ICAO, 1993) (Fig. S1 in the Supplement). We find that the average sedimentation rates between 18 and 26 km altitude for our prescribed sulfate, titania, and BC are 23, 9.5 and $0.75\,m\,day^{-1}$, respectively, and the equivalent rates between 26 and 30 km are 52, 22, and $1.8\,m\,day^{-1}$. Therefore, one would expect BC to be advected to much higher altitudes than sulfate in these simulations. For perspective, Schoeberl et al. (2008) deduced from observations that the atmospheric tropical vertical velocity between 18–26 km has an upper limit of $35\,m\,day^{-1}$, and the equivalent velocity between 26 and 30 km is below $61\,m\,day^{-1}$.

3 Method

We first validated the model's stratospheric sulfate scheme by simulating the Mt Pinatubo eruption and then comparing the results with observations. These simulations comprised a 10-member ensemble in which 20 Tg (SO_2) is injected between 16 and 18 km over a single day in June 1991, following the method of Aquila et al. (2012). Figure 2a shows the global- and annual-mean sulfate aerosol optical depth (AOD) anomaly for the HadGEM2-ensemble and for AVHRR and SAGE-II observations. The model clearly captures the peak AOD from the AVHRR data, and the exponential decline thereafter. Figure 2b–d show the zonal-mean AOD anomaly for the same time period. The agreement between the model and observed AOD is reasonable. Some dif-

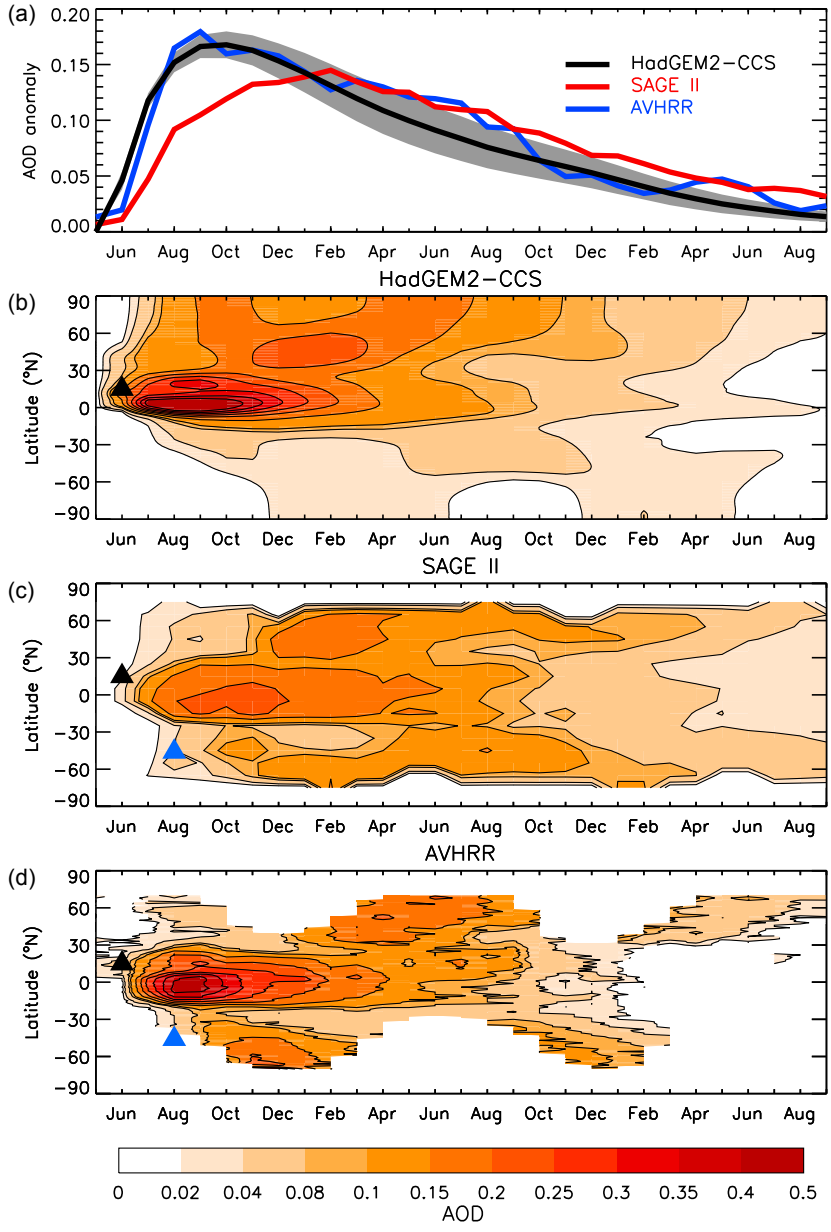

Figure 2. (a) 75° S–75° N-mean 550 nm sulfate AOD anomaly for the Pinatubo simulations and observations, **(b–d)** time series of zonal-mean 550 nm sulfate AOD anomaly.

ferences in the temporal evolution of the AODs in the model and the observations are due to the almost concurrent eruption of Cerro Hudson which injected approximately 3.3 Tg (SO_2) into the Southern Hemisphere (Deshler and Anderson-Sprecher, 2006). This relatively close agreement between observations and HadGEM2 estimates, together with other modeling studies of other volcanic eruptions (Haywood et al., 2010) suggests that the model is a useful tool for stratospheric geoengineering simulations.

The geoengineering investigation was based on a 240-year pre-industrial control simulation (forced by constant 1860s GHGs and aerosol emissions) and historical simulations for the period 1860–2005 following CMIP5 (Taylor et al., 2012) protocol followed by RCP8.5 emission specified from 2005 to 2019. Leading on from these simulations, we performed 3-member ensembles for the period 2020–2100 for RCP8.5 only, RCP8.5 with SO_2 injection (geoSulf), RCP8.5 with TiO_2 injection (geoTiO_2), and RCP8.5 with BC injection (geoBC). Aerosol (or gaseous SO_2 for the geoSulf scenario) was injected at a constant rate between 23 and 28 km altitude in a single vertical column at the equator. The injection altitude and location were chosen to ensure a long stratospheric

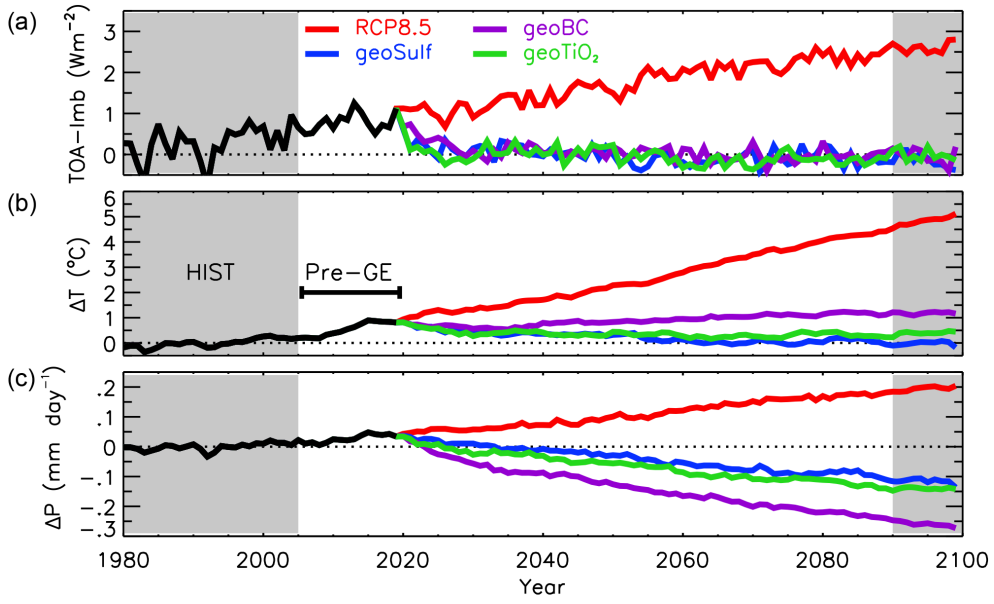

Figure 3. Time series of annual/global-mean **(a)** top-of-the-atmosphere radiative flux anomaly with respect to the pre-industrial control simulation, **(b)** near-surface air temperature anomaly with respect to the HIST period, **(c)** global mean precipitation anomaly with respect to HIST.

lifetime of the aerosol, which is transported poleward by the upper branch of the Brewer-Dobson circulation (Niemeier et al., 2011), and therefore make the geoengineering approach reasonably efficient.

We inject aerosol at such a rate as to maintain the top-of-the-atmosphere (TOA) net radiative flux at piControl levels. Specifically, we define the TOA radiative flux Imbalance (TOA-Imb) as the global- and annual-mean TOA net radiative flux (incoming SW minus outgoing LW + SW) minus the average TOA net radiative flux of the piControl period. The piControl TOA net radiative flux is positive ($+0.27\,\mathrm{W\,m^{-2}}$) as anthropogenic GHGs were emitted prior to 1860 (the piControl reference period). By sufficient aerosol injection, we aim to maintain TOA-Imb = 0. This scenario represents our interpretation of "equal amount of geoengineering" for each aerosol. The advantage of returning net radiation to piControl levels (rather than completely equilibrating TOA fluxes) is that piControl had already been simulated comprehensively for CMIP5 (240 model years), hence permitting robust statistics to be calculated. The TOA radiative imbalance is a metric that satellites are able to measure (e.g., CERES, L'Ecuyer et al., 2015 and EarthCare, Illingworth et al., 2015), albeit with $\pm 3\,\mathrm{W\,m^{-2}}$ accuracy at present (Priestley et al, 2011; von Schuckmann et al., 2016). Therefore our target could be applicable to an actual SAI scenario. In contrast, adjusted Radiative Forcing (RF) (the net radiation perturbation at the tropopause from some external forcing, after stratospheric adjustment), cannot be directly measured by satellites and therefore it would be difficult to obtain a specified radiative forcing in an actual SAI scenario. Of course, other metrics could be chosen (e.g., MacMartin et al., 2013), with each metric having its own signal and noise characteristic.

To determine the injection rates required to maintain TOA-Imb balance, we first conducted 15-year atmosphere-only simulations of 1 Tg aerosol (or SO_2 for sulfate) injection per year to calculate the specific radiative effect for each aerosol. We then used the radiative effect to calculate the injection rate necessary to offset the RCP8.5 anthropogenic radiative forcing (ARF) for the 2020–2100 period (with ARF values from Meinshausen et al., 2011). We used the ARF to estimate the injection rates required to produce TOA-Imb = 0 as this seemed a sensible method for approximating the necessary aerosol injection. As the geoengineering simulations progressed, we altered the injection rate when necessary to ensure that TOA-Imb balance was maintained (Fig. S2). This feedback-orientated method is similar to the methods suggested by MacMartin et al. (2014) and Kravitz et al. (2014). A detailed description of our methods is provided in the Supplement (Sect. S2).

Our analysis focuses initially on the temporal evolution of the TOA-Imb and global mean temperature changes to show that our simulations provide plausible counterbalances to global mean temperature changes under RCP8.5. However, our main focus is on the differences between a recent historical period (1980–2005) (hereafter denoted HIST) and the geoengineering experiments during the period 2090–2100, with an emphasis on different geographical patterns. As we were not explicitly attempting to reach a specific global mean temperature, the choice of reference period was left until af-

ter the geoengineering simulations had been completed. We then selected a recent historical period from which the 2090s global-mean temperature anomaly for geoSulf was negligible (Fig. 3b). The HIST period selected is close to the historical control period used in the IPCC AR5 report (1986–2005) (e.g., Fig. 12.10 from Collins et al., 2013) which facilitates comparison of our RCP8.5 climate changes with the CMIP5 multi-model means.

4 Results

4.1 Effectiveness at maintaining global mean TOA-Imb and near-surface temperature

Figure 3 shows the global- and annual-mean TOA-Imb and near-surface air temperature anomaly for the geoengineering and RCP8.5 simulations, with respect to the HIST period. For all of the geoengineering simulations we were able to maintain TOA-Imb ≈ 0 for the entirety of the 80-year period (Fig. 3a). For geoSulf, geoTiO_2 and geoBC, the TOA-Imb was maintained within ± 0.21, ± 0.18 and $\pm 0.20\,\mathrm{W m^{-2}}$, respectively (1 standard deviation throughout the 2020–2100 period).

The near-surface global temperature response differs between the aerosols with a greater cooling trend for sulfate than for titania or BC (Fig. 3b). To determine the cause of the anomalous warming in geoBC, we assess the net radiative flux at the top of the atmosphere for 2020–2100. Figure S3 in the Supplement shows the global-mean net-downward radiative flux anomaly for the geoengineering experiments, evaluated at the TOA and the tropopause; and the global-mean net-downward heat flux anomaly at the surface. The radiative flux changes at the TOA and tropopause, and the heat flux anomaly at the surface, are comparable for the geoSulf and geoTiO_2 experiments for the duration of 2020–2100. In contrast, geoBC exhibits an increasingly positive net radiative flux anomaly at the tropopause ($+0.2\,\mathrm{W m^{-2}}$ averaged over 2020–2100), despite the negligible TOA radiative flux anomaly. After stratospheric temperature adjustment, radiative perturbations at the TOA and tropopause are equal for a given climate forcing, which implies that the consistently non-adjusted stratosphere (due primarily to increasing aerosol injection rates) is responsible for the differences in TOA and tropopause radiative perturbations in geoBC. Hansen et al. (1997) also found that instantaneous and adjusted radiative forcing differ most when there is a large heating affecting the tropopause. This implies that if we had injected aerosol sufficiently to produce an equal radiative effect at the tropopause, the temperature trends for the geoengineering experiments in Fig. 3 would have been more comparable. If we were to choose stabilization of temperature as our basic metric, then one could approximate the results by simply scaling the results by the ratio of the temperature perturbation relative to 1980–2005 to that for geoSulf. The scaling would be 1 (by design) for geoSulf, 1.1 for geoTiO_2 and 1.28 for geoBC. If the metric chosen were instead to keep the global mean precipitation the same, then the scaling would be 1 (by design) for geoSulf, 0.91 for geoTiO_2 and 0.68 for geoBC. However, we shall see that the changes in many of the variables we consider are dominated by large-scale changes in the spatial patterns of response rather than the 10–30 % changes in magnitude of the response that applying such a scaling would induce. We therefore choose to present un-scaled results here but beware that such a scaling could be applied should we wish to apply a different metric. From Fig. 3b, geoSulf exhibits a near-surface air cooling trend with respect to 2020 despite a net gain of atmospheric energy, which is likely due to an uneven vertical distribution of this energy gain.

Figure 3c shows the global mean precipitation anomaly with respect to the HIST period. The precipitation reduction is greater for BC than for sulfate and titania, despite the positive temperature trend in geoBC (Fig. 3b). The hydrological sensitivity to geoengineering, defined as the global mean precipitation change per unit temperature change, is 2 % for sulfate, 2.5 % for titania, and $4.6\,\%\,^{\circ}\mathrm{C^{-1}}$ for BC. The hydrological sensitivity for RCP8.5 is $1.32\ \%\,^{\circ}\mathrm{C^{-1}}$, which is close to the CMIP5 ensemble-mean (Fig. 12.7 from Collins et al., 2013). For comparison, Bala et al. (2008) found a hydrological sensitivity of 2.4 for solar irradiance reduction and $1.4\,\%\,^{\circ}\mathrm{C^{-1}}$ for CO_2 increase.

4.2 Aerosol distribution

The time-averaged injection rates for the 2090s period are 14 Tg (SO_2), 5.8 and $0.81\,\mathrm{Tg\,yr^{-1}}$ for geoSulf, geoTiO_2 and geoBC, respectively. This SO_2 injection rate is approximately equivalent to 1 Mt Pinatubo eruption per year (Dhomse et al., 2014). These injection rates equate to global aerosol mass-burden anomalies of 49.5, 20.2, and 5.1 Tg for geoSulf, geoTiO_2 and geoBC, respectively. The geoBC mass burden is comparable to the equilibrium burdens of the high-altitude (HA) and small-radius (SmR) experiments from Kravitz et al. (2012), although they injected BC at a constant rate of $1\,\mathrm{Tg\,yr^{-1}}$, around 20 % higher than in our study. Their SmR experiment involved a 10-year injection of BC particles with a uniform radius of 0.0 µm, into a region between 100 and 150 mb altitude and over the latitude range 10° S–10° N, against baseline perpetual year 2000 conditions. Figure 4 shows the 2090s annual, June–July–August (JJA) and December–January–February (DJF) aerosol mass concentration anomalies (annual mean aerosol optical depths are shown in Fig. S4). Peak sulfate concentrations are found at the injection region at the equator (Fig. 4a, d, g) and over the winter pole. Titania and BC reach greater altitudes than sulfate (> 50 km), which is due to their smaller size-distributions and self-lofting from SW absorption (Kravitz et al., 2012). While sulfate aerosol concentrations are highest at the equator, the highest concentrations of BC are found in the

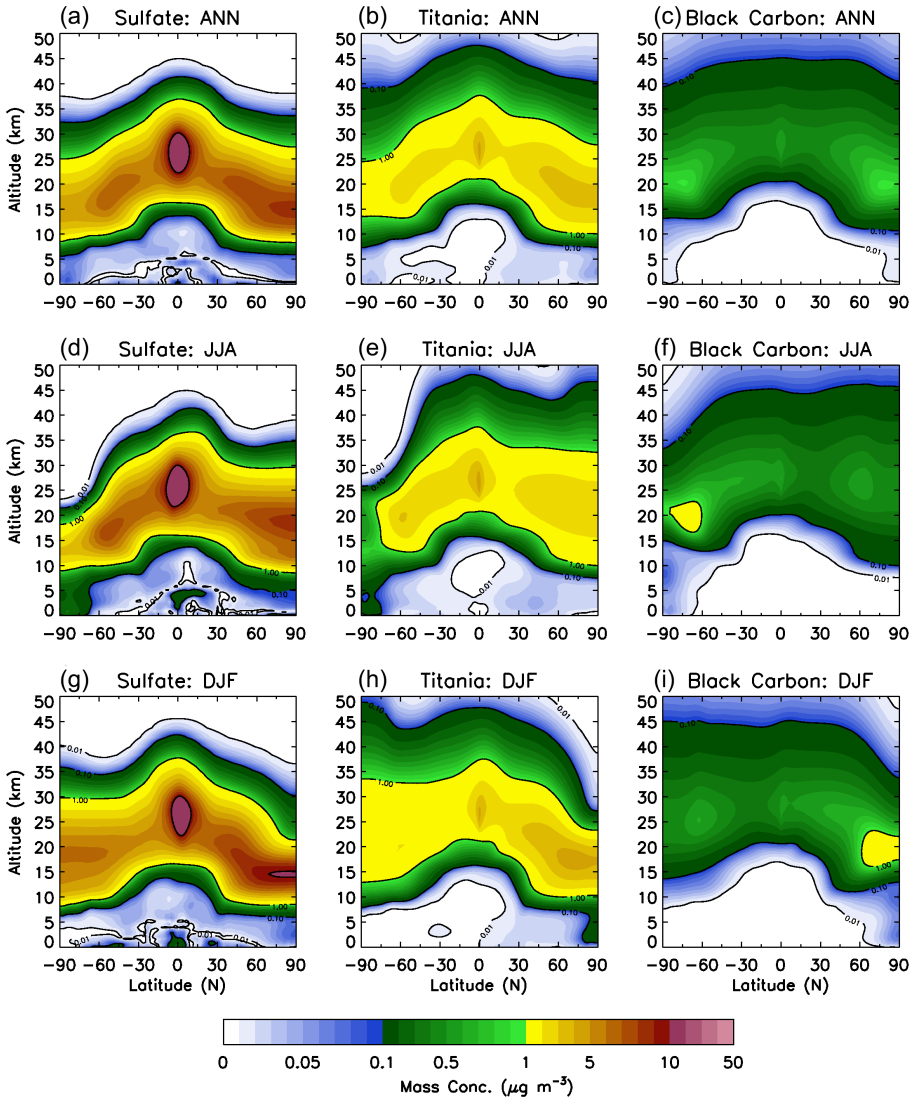

Figure 4. Annual and seasonal zonal-mean mass concentration anomalies for sulfate (geoSulf-left), titania (geoTiO_2-center) and black carbon (geoBC – right).

polar stratosphere. This is because the larger particle size of the sulfate aerosol is subject to a larger sedimentation velocity (Fig. S1) and thus a greater fraction of aerosol is removed close to the source region. The results from titania suggest a spatial distribution intermediate between sulfate and BC owing to the intermediate size distribution.

Figure 5 shows the total annual, JJA and DJF aerosol deposition anomalies averaged over the 2090s (the seasonal cycle of the deposition anomalies are shown in Fig. S5). Sulfate is predominantly deposited in the Northern Hemisphere (NH) extratropics in the boreal spring and summer (Fig. 5d), which is likely attributable to tropopause fold events in the lower branch of the Brewer-Dobson circulation (BDC) (Kravitz et al., 2012). In contrast, Titania and BC are primarily deposited at high latitudes in the polar winter, which is attributable to the diabatic descent of air in the deep branch of the BDC (e.g., Tegtmeier et al., 2008). Kravitz et al. (2012) also found in their SmR experiment that BC deposition was limited to the polar regions, but their maximum deposition was during polar summer rather than polar winter. The global- and annual-mean deposition rates of sulfate and BC from geoengineering are 37 and 1.5 mg m^{-2} yr^{-1}, respectively. These amounts may be compared with 231 and 12.7 mg m^{-2} yr^{-1} from non-geoengineering sources, amounting to increases of 16 and 12 %, respectively. The global- and annual-mean deposition rate for titania is 11 mg m^{-2} yr^{-1}.

4.3 Temperature and precipitation

Figure 6 shows the annual mean near-surface air temperature (Fig. 6a–d) and precipitation anomalies (Fig. 6e–h) with

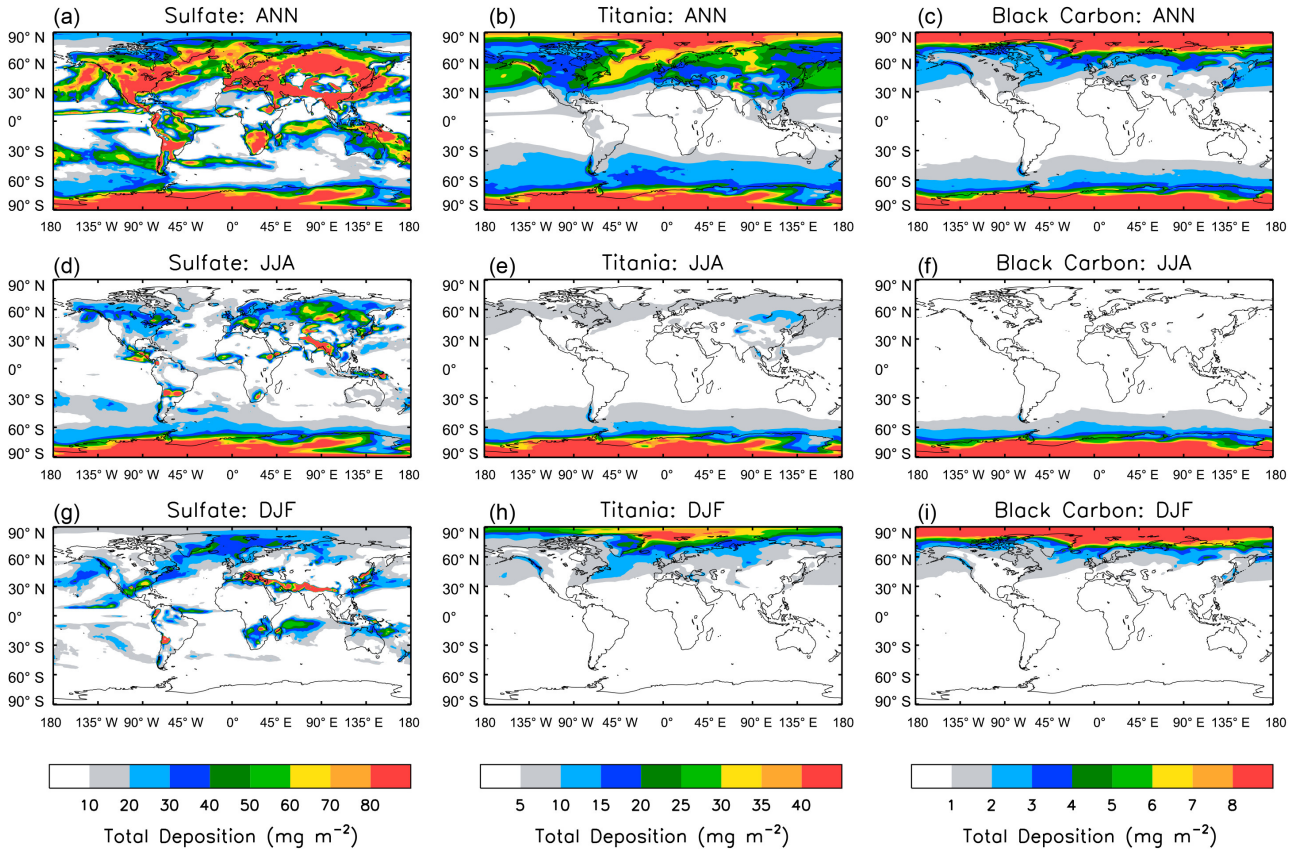

Figure 5. Annual and seasonal total deposition anomalies (in units of mg m^{-2} yr^{-1} and 0.25 × mg m^{-2} yr^{-1}, respectively).

respect to HIST. RCP8.5 (Fig. 6a) shows the typical global warming signal of amplified warming at high latitudes due to temperature feedbacks (Pithan and Mauritsen, 2014) and the surface-albedo feedback (e.g., Kharin et al., 2013). This results in an annual mean warming of +11.3 °C averaged over the Arctic region (> 60° N) and an average NH land warming of +7.3 °C. This figure provides an alarming picture of the change in global mean temperature by the end of this century should global society follow the RCP8.5 (essentially a business as usual) pathway. All three SAI experiments produce a surface-cooling with respect to RCP8.5, with geoSulf exhibiting the greatest global-mean cooling effect of −4.85 °C, considering TOA-Imb is balanced for each geoengineering experiment. The latitudinal distribution of cooling varies markedly between the SAI experiments, with relative tropical cooling for geoSulf and geoTiO_2 (Fig. 6b, d) and polar cooling for geoBC (Fig. 6c). Defining the "SAI cooling effect" as the temperature difference between SAI and RCP8.5, the ratio of cooling effect at high latitudes (> 60°) between geoBC and geoSulf is 1.19 and between geoBC and geoTiO_2 is 1.23. In the tropics and mid-latitudes (< 60°) the equivalent ratios are 0.64 and 0.71, respectively. The high-latitude cooling in the case of geoBC is attributable to the zonal distribution of BC (Fig. 4c, f, i), which is more evenly spread over the stratosphere than for geoSulf and geoTiO_2. The result is a greater surface SW forcing at high-latitudes in the summer hemisphere for geoBC. For instance, in the Arctic (> 60° N) in JJA, the surface SW forcing is −25.65 in geoBC and −3.3 and −6.55 Wm^{-2} in geoSulf and geoTiO_2, respectively. Although the global-mean precipitation rate increases for the RCP8.5 scenario (Fig. 6e), certain regions such as the Amazon basin exhibit a drying trend. This is in line with the CMIP5 multi-model projections documented in the Intergovernmental Panel on Climate Change 5th assessment report (IPCC AR5) (e.g., Fig. 12.10 from Collins et al., 2013). All of the SAI experiments show a global-mean precipitation reduction with respect to both HIST and RCP8.5 (Fig. 6f–h), which is due to the deceleration of the hydrological cycle and is a robust model response to SAI (e.g., Yu et al., 2015; Tilmes et al., 2013; Bala et al., 2008). The magnitude of the precipitation changes are greater for geoBC than for geoSulf or geoTiO_2; for instance, the global mean precipitation anomaly is −0.26 for geoBC compared to −0.12 for geoSulf and −0.14 mm day^{-1} for geoTiO_2. In order to maintain TOA-Imb = 0, BC must produce a greater SW perturbation at the tropopause and at the TOA than sulfate or titania, which is compensated by the increased LW perturbation resulting from stratospheric warm-

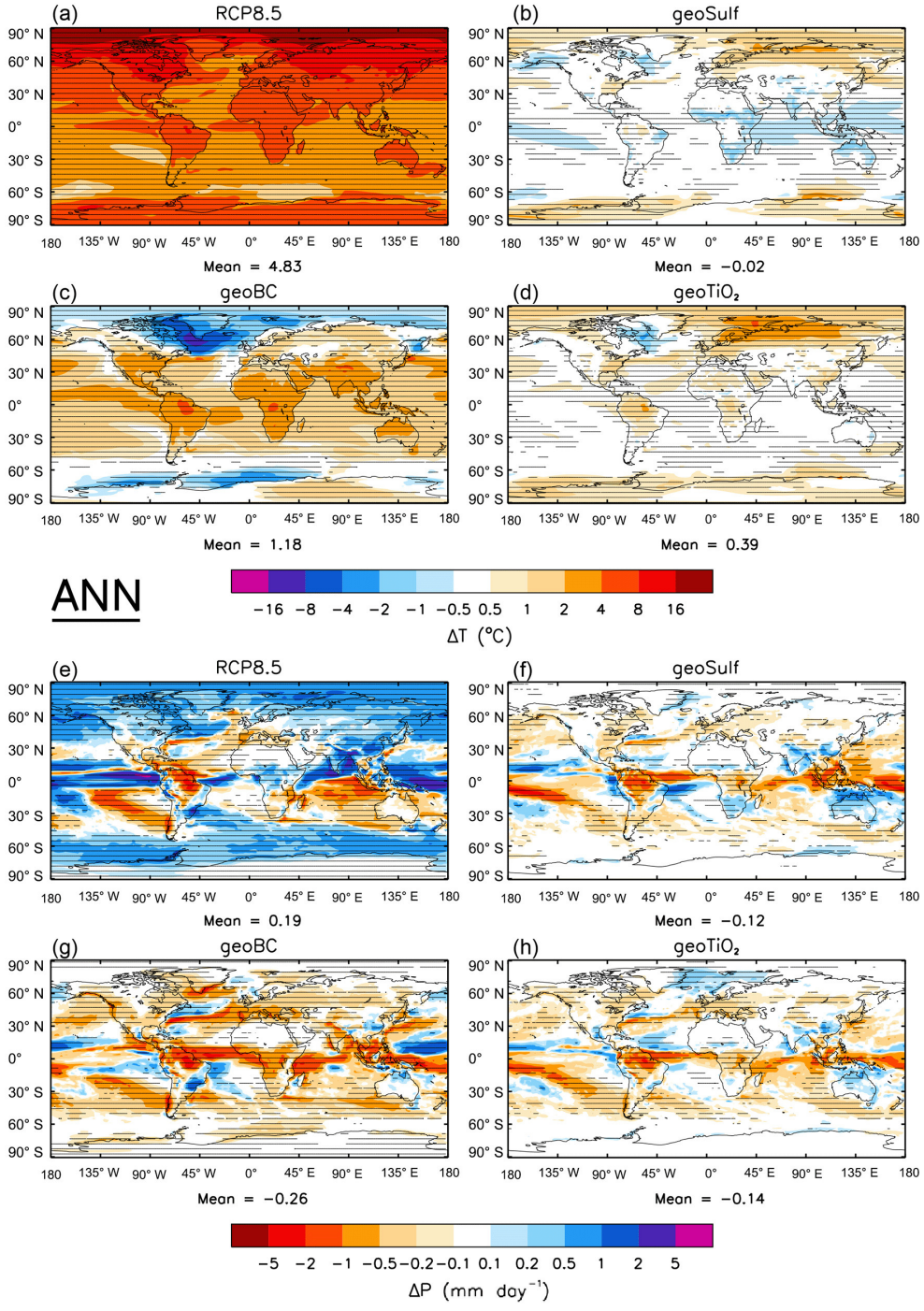

Figure 6. Annual-mean near-surface air temperature (top) and precipitation rate (bottom) anomalies with respect to HIST. Stippling indicates where changes are significant at the 5 % level using a two-tailed Student's *t* test.

ing. The troposphere is relatively transparent to SW radiation but absorbs efficiently in the LW spectrum, therefore the annual-mean surface radiative forcing in the geoBC experiment is greater ($-18.6\,\mathrm{W\,m^{-2}}$) than for geoSulf or geoTiO$_2$ (-7.4 and $-9.6\,\mathrm{W\,m^{-2}}$, respectively – see Fig. S6). Bala et al. (2008) and Muller and O'Gorman. (2011) have shown that the magnitude of the global-mean precipitation response to an imposed forcing is dependent on the energy flux entering and leaving the atmosphere (the radiative forcing of the atmosphere). The radiative forcing of the atmosphere is the difference between net radiative fluxes at the TOA and at the surface. As the net radiative flux anomaly at the TOA

is, by design, equal for the different geoengineering scenarios here and the net radiative flux anomaly at the surface is greater for geoBC (Fig. S6), the precipitation reduction is therefore amplified in the geoBC scenario. It is important to note that if the RCP8.5 warming relative to HIST was completely offset in the geoBC and geoTiO_2 experiments, the hydrological response would be greater than in Fig. 6. Using the hydrological sensitivities calculated in Sect. 4.1, the precipitation changes relative to HIST would be -0.34 for geoBC and $-0.16\,\mathrm{mm\,day^{-1}}$ for geoTiO_2. From Fig. S6, the reduction in surface SW flux in the RCP8.5 scenario is due to increases in water vapor (Haywood et al., 2011). Haywood et al. (2011) report a clear-sky reduction of $-5.7\,\mathrm{W\,m^{-2}}$ while our study is consistent at a value of $-5.4\,\mathrm{W\,m^{-2}}$ (not plotted). However, in all geoengineering cases, this reduction is comprehensively overwhelmed by aerosol direct effects.

Figure 7 shows the JJA temperature (Fig. 7a–d) and precipitation (Fig. 7e–h) anomalies. In the geoSulf and geoTiO_2 scenarios, the temperature is effectively maintained at HIST levels (Fig. 7b, d). However, a slight bias towards high-latitude NH warming in geoSulf and geoTiO_2 results in a northward displacement of the Inter-Tropical Convergence Zone (ITCZ), which is exemplified by the Sahelian precipitation increase in Fig. 7f, h. This phenomenon was noted by Haywood et al. (2013) and has been observed after large hemispherically asymmetric volcanic eruptions (Oman et al., 2006). Although the general pattern of precipitation change is similar for the three SAI scenarios, geoBC again displays a greater drying signal, with 80 % of the total land area experiencing a JJA precipitation reduction in geoBC compared to 70 for geoTiO_2, 57 for geoSulf and 52 % for RCP8.5.

Figure 8 shows the DJF temperature (Fig. 8a–d) and precipitation (Fig. 8e–h) anomalies. The temperature reduction over Greenland in geoBC (Fig. 8c) is due to the significant decrease in downwelling SW radiation at the surface during the Arctic sea-ice formation season (September–October–November), which leads to a positive sea-ice albedo feedback and further localized cooling. This inference is corroborated by Fig. 9, which shows the Arctic DJF sea-ice extent in terms of the average DJF sea-ice boundary (the Antarctic DJF sea-ice extent is shown in Fig. S7). The sea-ice boundary in geoBC (Fig. 9c) extends to well below Greenland, and the total sea-ice extent anomaly is $+1.72$ million $\mathrm{km^2}$ which vastly exceeds the HIST standard deviation of ± 0.52 million $\mathrm{km^2}$. In comparison, the sea-ice extent anomaly of -11 million $\mathrm{km^2}$ for RCP8.5 (Fig. 9a) marks a reduction by 43 % of the total HIST sea-ice extent. Returning to Fig. 8, the poleward shift in the NH extratropical rainbelt over the Atlantic in RCP8.5 (Fig. 8e) is a robust result of GHG-induced global warming and is related to storm track displacement (Lombardo et al., 2015). This same response is evident in the geoengineering simulations (Fig. 8f–h), although to a much lesser extent in geoSulf and geoTiO_2.

4.4 Stratospheric changes

Figure 10 shows the zonal-mean temperature change as a function of latitude and altitude for the JJA and DJF seasons. The stratospheric cooling in conjunction with tropospheric warming in RCP8.5 (Fig. 10a, e) is a robust result of increasing GHG-concentrations (e.g., Schmidt et al., 2013). Aerosols directly affect temperature by absorbing radiation, and indirectly by scattering radiation and by ambient dynamical and chemical changes (Carslaw and Kärcher, 2006). Sulfate predominantly absorbs in the LW and near-infrared spectrum (Fig. 1a). The stratospheric radiative heating in geoSulf is most pronounced in the tropical region, where sulfate absorbs outgoing LW radiation from the warm troposphere below, and then emits comparatively less radiation from the ambient cold stratosphere (Ferraro et al., 2011). In contrast, titania and BC absorb in both the SW and LW spectrum (Fig. 1b, c), and therefore preferentially warm the summer-hemisphere and tropical stratosphere, where solar radiation is most prevalent. geoBC produces the most significant warming effect, with an average stratospheric (15–50 km altitude) temperature increase of $+33\,^{\circ}\mathrm{C}$ and a maximum temperature increase of $+68\,^{\circ}\mathrm{C}$, which occurs in JJA (Fig. 10c, g). The maximum BC-induced heating relative to the baseline RCP8.5 scenario is $+76\,^{\circ}\mathrm{C}$ (Fig. S8), which is comparable to the $\sim 80\,^{\circ}\mathrm{C}$ temperature change Kravitz et al. (2012) found in their SmR scenario. For comparison, the maximum sulfate-induced and titania-induced heating relative to RCP8.5 are far more modest at $+7$ and $+22\,^{\circ}\mathrm{C}$, respectively.

A warming of the lower tropical stratosphere could have multiple climatic repercussions such as a weakening of the tropospheric tropical circulation (Ferraro et al., 2014), strengthening of the polar vortex (Driscoll et al., 2012) and modification of the QBO (Aquila et al., 2014). Additionally, an increase in the Tropical Tropopause Layer (TTL) temperature would increase the specific humidity of air entering the stratosphere (Dessler et al., 2013). Changes to the stratospheric water vapor content could have significant chemical and radiative impacts, contributing to ozone depletion via the HO_x cycle and stratospheric warming via LW-absorption (Kravitz et al., 2012). To assess the effects of geoengineering on stratospheric water vapor, we calculate the time-averaged H_2O mixing ratio averaged between 20° S–20° N and 16–20 km altitude. In the HIST era, the H_2O MMR is 4.2 ppmv, in close agreement with HALOE observations (Gettelman et al., 2010). In the 2090s, the average H_2O MMR is 6.3 for RCP8.5, 4.8 for geoSulf, 7.1 for geoTiO_2, and 32.7 ppmv for geoBC. The stratospheric water vapor feedback is therefore greater for geoBC and geoTiO2 than for geoSulf.

A strengthening of the polar vortex could be instigated by an increased temperature gradient between the tropical and mid-latitude and polar stratospheres, a phenomenon which was observed after the Pinatubo eruption (Stenchikov et al., 2002). We concentrate on the Arctic wintertime (DJF) re-

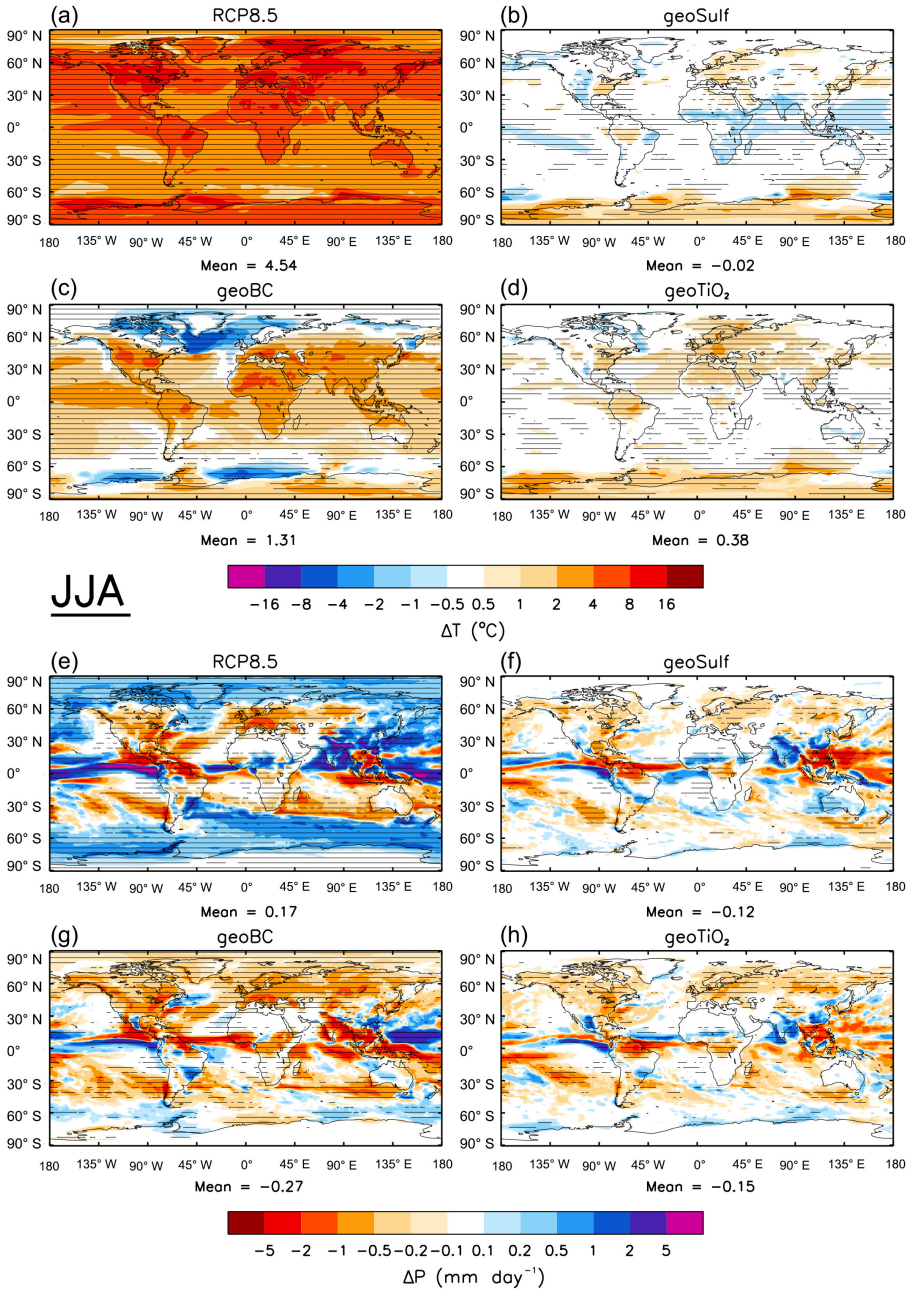

Figure 7. JJA near-surface air temperature (top) and precipitation rate (bottom) anomalies with respect to HIST.

sponse to SAI, and adopt a similar metric to that used by Ferraro et al. (2011) to determine the stratospheric temperature gradient. Explicitly, we determine the difference in temperature between 20° N–20° S (Tropics) and 50–90° N (North Pole) at 17–22 km altitude in the DJF season. Using this metric, the change in temperature gradients for geoBC, geoSulf and geoTiO$_2$ are +10.4, +7, and +10.1 °C, respectively, indicating a steeper temperature gradient between the tropics and poles. Additionally, Fig. 11 shows the 50 hPa DJF geopotential height anomalies over the Arctic for RCP8.5 and the three SAI experiments. The negative geopotential height anomaly centered over the North Pole in all the SAI experiments is indicative of a strengthened polar night jet and a positive Arctic Oscillation phase (Stenchikov et al., 2002). The DJF zonal-mean zonal-wind anomaly (Fig. S9) substantiates our inference of a strengthened polar-night jet under SAI, with increased zonal wind speeds at 65° N 40 km^{-1} altitude of 62, 17, and 37 m s^{-1} for geoBC, geoSulf, and geoTiO$_2$, respectively.

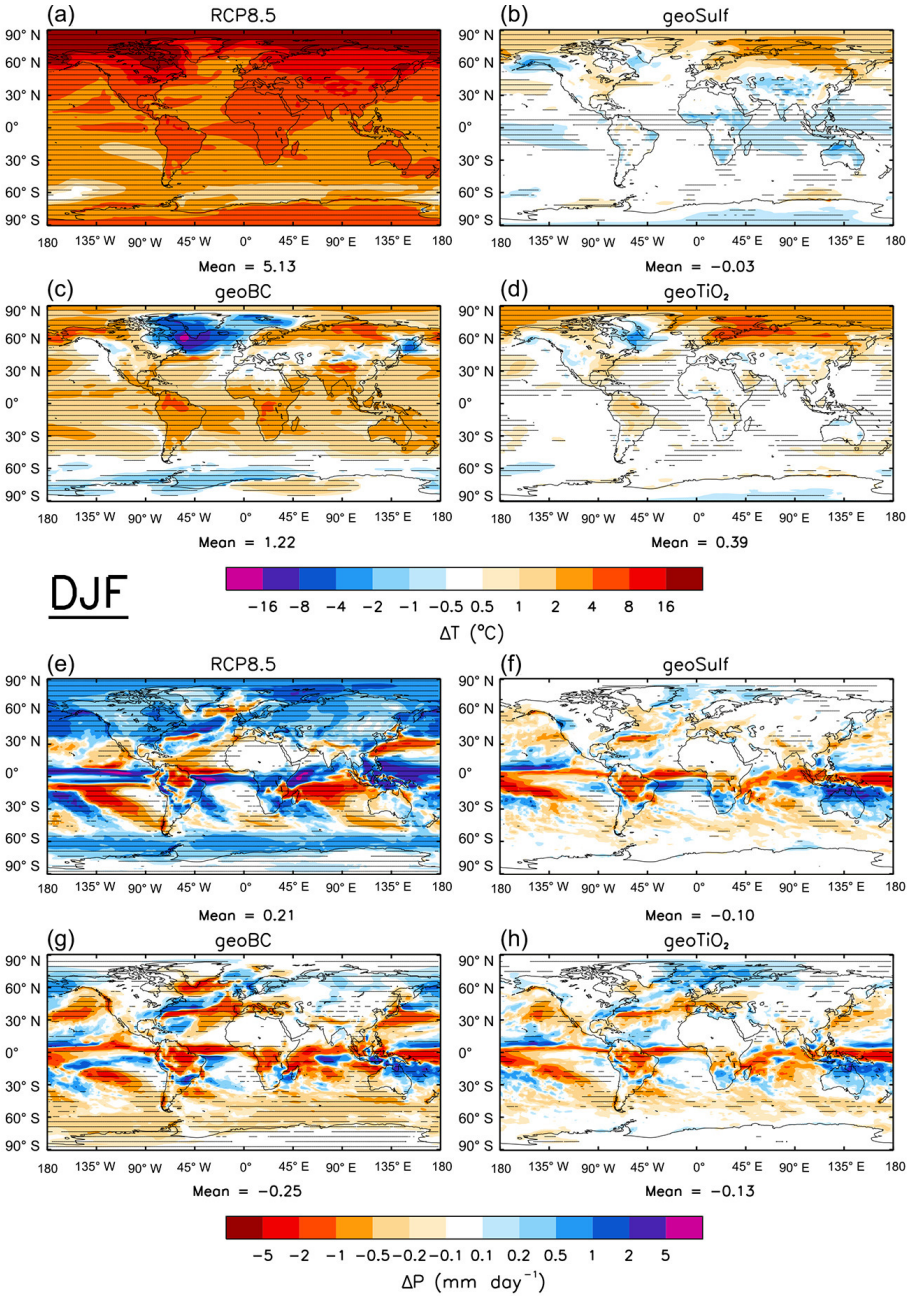

Figure 8. DJF near-surface air temperature (top) and precipitation rate (bottom) anomalies with respect to HIST.

The Quasi-Biennial Oscillation (QBO) is a periodic change in the equatorial zonal wind pattern in the stratosphere, which fluctuates between easterly and westerly shear phases (Baldwin et al., 2001). Aquila et al. (2014) showed that radiative heating in the aerosol layer could prolong the westerly-phase of the QBO (where the phase is defined at 40 hPa) by enhancing the residual-mean upwelling motion and strengthening the westerly winds. HadGEM2-CCS includes a non-orographic gravity wave scheme that permits the model to internally generate a QBO and is therefore capable of assessing QBO changes (The HadGEM2 Development Team, 2011). The average QBO period for the HIST-era ensemble is 27 months (Fig. S10) which agrees closely with observations (e.g., Baldwin et al., 2001). Figure 12 shows the 2090s QBO time series for one ensemble member of the RCP8.5 and SAI experiments (Figs. S11a, b show the QBO time series for the other two ensemble members). The average QBO periods for this timespan, which are determined using all three ensemble members, are 20 months for RCP8.5, 31 months for geoSulf and 36 months for geoTiO_2.

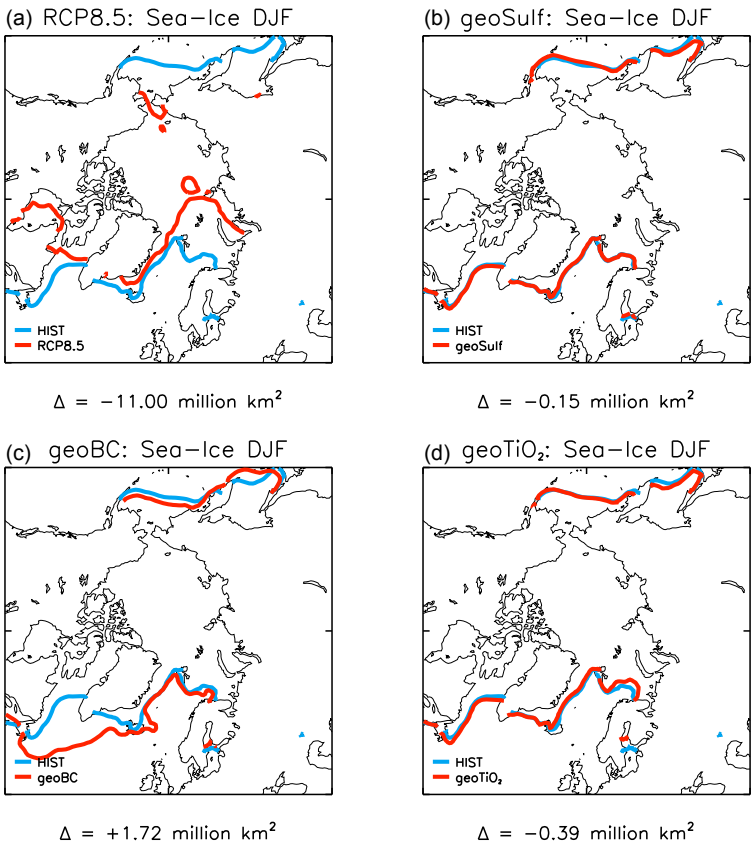

Figure 9. DJF Northern Hemisphere sea-ice edge plotted with the HIST extent.

For geoBC, no QBO-like oscillation can be detected in the 10-year time span, suggesting a persistent westerly-phase such as observed by Aquila et al. (2014) in their 5 Tg $(SO_2)\,yr^{-1}$ injection scenario ($G_5^{22–25\,km}$) scenario. In their HadGEM2-CC simulations, Kawatani and Hamilton (2013) also observed a decline in the QBO period for the RCP8.5 scenario, although they were unable to provide a reason for this. A robust inference from this work is that the magnitude of SAI's impact on stratospheric zonal winds correlates with the magnitude of the stratospheric warming.

5 Discussion

In this work, we have assessed the climatic impacts of sulfate, black carbon and titania-injection against a baseline RCP8.5 scenario, by comparing the 2090s climate with a simulated historical period. We have shown that, although the distribution of climate changes are similar for the three SAI scenarios, the magnitude of the changes differ, for instance BC produces a substantially greater stratospheric warming signal with concomitantly greater changes to stratospheric dynamics. The severity of the stratospheric temperature changes effectively excludes BC from being a viable option for geoengineering. Additionally, we have shown that producing an equivalent top of the atmosphere radiative perturbation with an SW-absorbing aerosol such as BC (or to a lesser extent titania) compared to a SW-scattering aerosol such as sulfate, induces a comparatively greater SW forcing at the surface. Bala et al. (2008) showed that reduced latent heat fluxes compensate for the SW reduction at the surface, instigating a deceleration of the hydrological cycle that is proportional to the magnitude of the SW reduction. This explains the comparatively greater precipitation reduction exhibited by geoBC in Figs. 6–8. Our results complement Niemeier et al. (2013), who showed that an LW-absorbing sulfate layer would produce a greater hydrological perturbation per TOA SW forcing than a simple solar irradiance reduction scenario. The geoBC scenario displays greater cooling at high-latitudes than the geoSulf and geoTiO$_2$ scenarios (Figs. 6–8), which comparatively exhibit a net tropical cooling. This raises the question of whether a combination of aerosols could potentially be injected to produce a latitudinally uniform cooling if necessary. Although SAI with sulfate and titania effectively maintains the regional distribution of temperature at HIST levels, with a slight residual warming at high latitudes, the hydrological cycle decelerates substantially in all SAI scenarios which is exemplified by a global-mean reduction in precipitation. However, annual-minimum sea-ice ex-

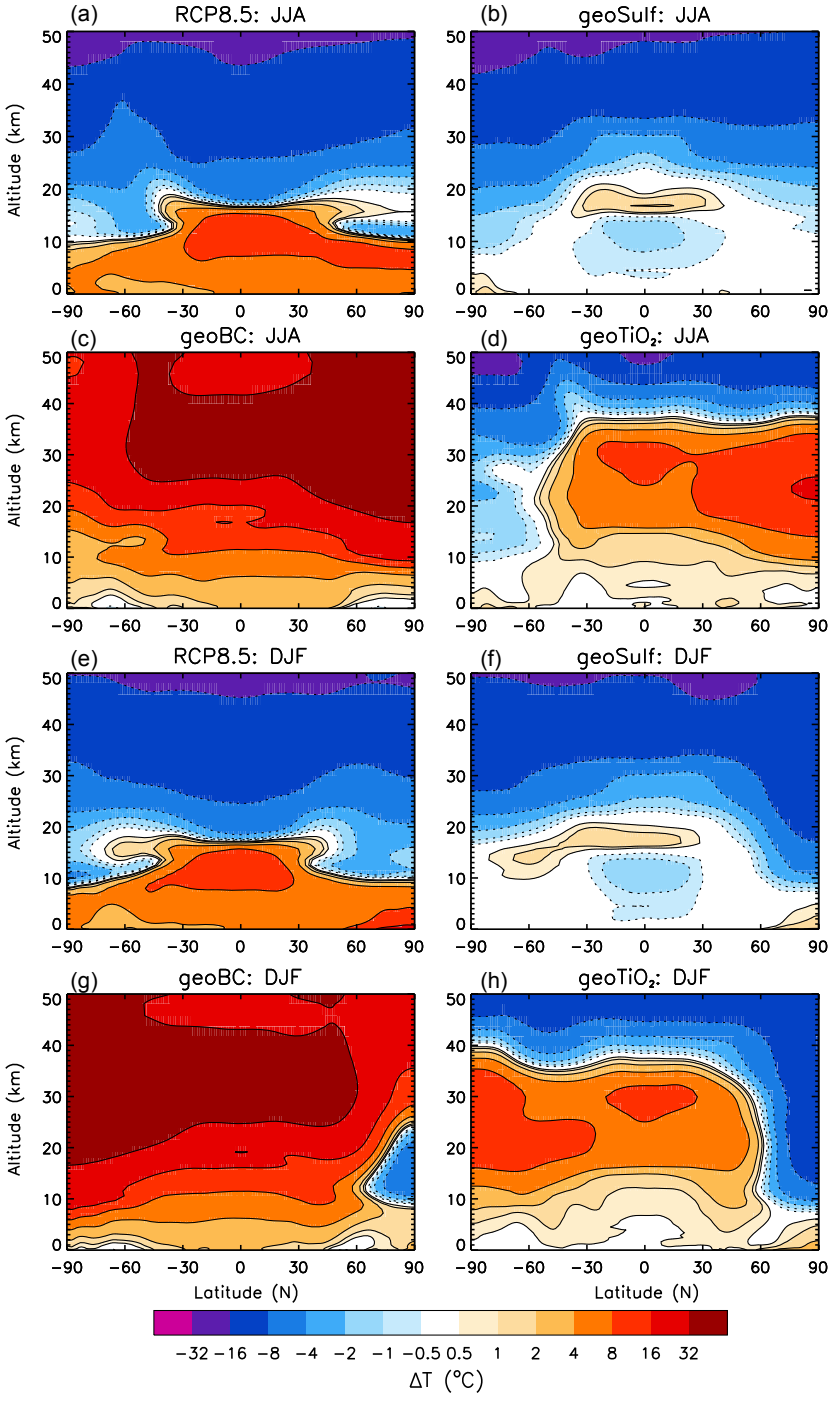

Figure 10. JJA (top) and DJF (bottom) zonal-mean temperature anomaly with altitude, with respect to HIST.

tent in both hemispheres and global-mean thermosteric sea-level (Fig. S12) are almost entirely maintained at HIST levels for all SAI scenarios. The results of our Antarctic sea-ice extent anomalies are comparable to McCusker et al. (2015). In particular, both their Fig. 2 and our Fig. S7 show limited spatial retraction of sea-ice in the sulfate scenario. We have used the same criterion as McCusker for determining which gridcells contain sea-ice (sea-ice fraction of $> 15\,\%$), which aids in the comparison. Additionally, both our results and McCusker's show that SAI can reduce Antarctic temperatures substantially (their Fig. 2, our Fig. 6) compared to the RCP8.5 climate.

We find that sulfate induces less stratospheric warming than titania. In contrast, Ferraro et al. (2011) found that the

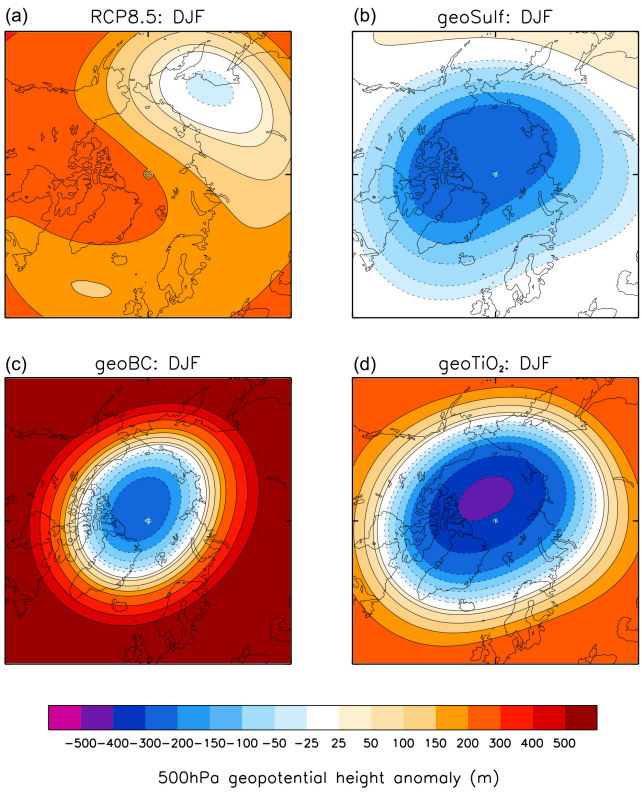

Figure 11. DJF 50 hPa geopotential height anomaly.

peak stratospheric warming for titania was approximately a third of that from sulfate. Although the different climatologies, model configurations, and aerosol spatial distributions will contribute to the difference in stratospheric temperature adjustment between our and Ferraro's work, the primary reason for the disparity is likely to be the aerosol size distributions. Our titania is smaller (median radius = 0.045 compared to 0.1 µm for Ferraro et al., 2011) and therefore scatters and absorbs SW more efficiently, producing a greater localized "solar" warming. Their sulfate distribution contains a larger spread ($\sigma = 2.0$ for Ferraro et al. (2011) compared to $\sigma = 1.25$ here), resulting in more coarse-mode particles and greater LW absorption. This disparity highlights the sensitivity of climatic effects to the specified aerosol size distribution. On a separate note, Ferraro et al. (2011) neglected to alter the titania density component in the calculation of their aerosol mass and specific optical properties (A. Ferraro, personal communication, 2016). The density that they used for titania of 1600 kg m^{-3} is appropriate for sulfate, but should have been altered to ∼4000 kg m^{-3} for titania. Therefore, their titania aerosol burden should be multiplied by 2.5 to give 7.5 Tg, and their optical coefficients divided by 2.5, to obtain appropriate values.

It is important to note that the climate impacts described in Sect. 4 are dependent on the optical properties of the aerosol, which are further dependent on the aerosol particle's size, shape, and composition (e.g., Kravitz et al., 2012). In this investigation, the dry-mode size distribution of the aerosol species is held constant and hygroscopic growth is not represented in the BC and titania schemes, nor are the effects of internal mixing represented. Observations have shown that fresh BC aerosol is predominantly hydrophobic, but the uptake of soluble particulates (e.g., secondary organics) results in increased hygroscopicity (Liu et al., 2013). Mineral dust, which contains 1–10 % titania by mass (Ndour et al., 2008), exhibits low hygroscopicity for radii < 0.1 and similar growth to equivalently sized sulfate aerosol thereafter (Koehler et al., 2009). Although the historical stratospheric water vapor content is low (∼ 4.2 ppmv in the tropical lower stratosphere during the HIST period), aerosol-induced stratospheric warming in the TTL would increase the specific humidity of air entering the stratosphere, therefore impacting hygroscopic growth. The injection of aerosol into pre-existing aerosol layers would lead to larger particles through coagulation and condensation, which would further alter the aerosol's optical and physical properties. The actual size of the aerosol in an SAI scheme would therefore depend on the injection strategy (e.g., location and season) and the size and composition of the injected species (e.g., Carslaw and Kärcher, 2006; Heckendorn et al., 2009). Recent research from Heckendorn et al. (2009), Pierce et al. (2010), English et al. (2012), and Weisenstein et al. (2015) has highlighted the importance of representing aerosol growth in SAI simulations. Incorporating aerosol microphysics would result in a better representation of the aerosol's optical properties; this is particularly important for solid aerosols that form chain-like fractals. However, it is also important that the model's climatology is able to respond to radiative changes induced by the aerosol. A more detailed assessment would couple a 3-D GCM with a detailed aerosol microphysics module, but such experiments over the centennial timescales of this work are currently too computationally expensive. A detailed assessment of the aerosol microphysics for sulfate, BC, and titania injection is therefore not within the scope of this paper, but presents an important subject for future work.

The climatic impacts described in Sect. 4 are specific to geoengineering against a baseline RCP8.5 scenario. If instead we had used a middle-of-the-road GHG-concentrations scenario such as RCP4.5 (Taylor et al., 2012), as used in the first tier of GeoMIP scenarios (Kravitz et al., 2011), then less aerosol-injection would be needed to obtain TOA-Imb = 0 and therefore the aerosol deposition rates and atmospheric mass concentrations would be less than those reported in Sect. 4. One would expect that the magnitude of stratospheric temperature changes (Fig. 8) and therefore zonal-mean zonal wind changes (Fig. 12) would be much less for each of the aerosols, possibly confounding the conclusions given here relating to their comparative efficacy. An estimate for the amount of SAI required for RCP4.5 can be garnered from integrating the temperature anomalies for RCP8.5 and RCP4.5 for the period 2020–2100. The ratio of the integrated tem-

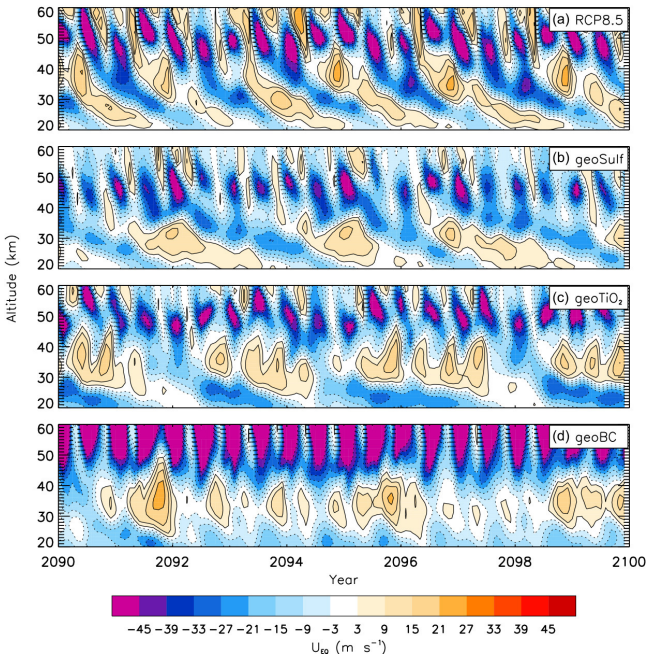

Figure 12. Time series of equatorial (5° S–5° N) zonal-mean zonal wind profile.

perature anomalies for RCP4.5 to RCP8.5 is 0.43, hence we can assume that the injection rates required for RCP4.5 are ∼0.43 of those for RCP8.5, producing a climate perturbation ∼0.43 times as great. A further set of simulations, which instead utilise RCP4.5 as the baseline scenario, would be required to test this hypothesis.

We have used prescribed ozone fields in these simulations because representing stratospheric chemistry is prohibitively computationally expensive for the multiple centennial simulations performed here (The HadGEM2 development team, 2011). Kravitz et al. (2012) showed in their SmR scenario that BC injection could potentially result in global ozone depletion of >50 %, therefore the chemistry changes in SAI could potentially exceed the importance of the physical changes in terms of climatic impacts (e.g., UV radiation at the surface). Tilmes et al. (2012) showed that SW-scattering by geoengineered sulfate could potentially compensate for ozone-loss by back-scattering UV radiation in the tropics, but that this effect was insufficiently compensatory at high latitudes. Their result was scenario-dependent; ozone loss due to heterogeneous chemistry is enhanced for smaller particles and in the presence of higher free-radical concentrations. Therefore, additional research is needed in order to understand the effects on atmospheric chemistry of injecting alternative aerosols. This work has already been started for titania by Tang et al. (2014).

Another important aspect of SAI which is comparatively under-researched is the potential for impacts on human health. Aerosol concentrations in the air near the surface are of interest because of potential human respiratory impacts (Robock, 2008). For instance, the USA's National Institute for Occupational Safety and Health (NIOSH) recommends maximum exposure limits of 0.3 mg m^{-3} for ultrafine titania particles (radius < 0.05 µm) and 2.4 mg m^{-3} for fine particles (radius < 1.5 µm) (Dankovic et al., 2011). After undergoing coagulation and aging in the atmosphere, it is likely that the second exposure limit is more applicable to this work. In our simulations, the maximum 2090s near-surface air concentration of titania (e.g., Fig. 4) for land regions between 60° S and 60° N is 254 ng m^{-3}, which is of the order of 10^2 less than the NIOSH "fine-particle" exposure limit. The equivalent maximum concentration anomalies of BC in geoBC and SO_4 in geoSulf are 10 and 1851 ng m^{-3}, respectively. More work is needed to assess the potential impacts of SAI on air quality and human health.

Another thus far unmentioned aspect of this research is the potential for surface albedo modification by aerosol deposition. In particular, BC deposition on snow reduces the snow albedo through enhanced snow-melt and the coarsening of snow grains, which results in amplified high-latitude warming (Marks and King, 2013). HadGEM2-CCS does not include the BC-on-snow feedback; therefore we estimate it by comparing the deposition rates for 2090s geoBC with the historical period. Jiao et al. (2014) report that the simulated annual mean Arctic (>60° N) BC deposition for the 2006–2009 period ranges from 13 to 35 × 10^7 kg yr^{-1} for the AEROCOM Phase II models. The annual mean Arctic BC deposition for the 2006-2009 period from our HadGEM2-CCS simulations is 23 × 10^7 kg yr^{-1}, which is within the AEROCOM range. The annual mean Arctic BC deposition anomaly for the 2090s period in geoBC is 19.6 × 10^7 kg yr^{-1}. Therefore, the effects of dirty snow in such an SAI scenario would likely be significant, which would have impacts on the distribution of temperature, particularly at high latitudes, potentially confounding some of our conclusions. Although we have emphasized this issue with respect to BC, it is important to note that any particle that absorbs SW radiation will instil this forcing. Therefore, titania, which has a non-unitary single scattering albedo at short wavelengths, will also cause snow-grain coarsening and snow-melt by absorbing solar radiation and warming the top layer of the snow pack.

This research has highlighted potential climate impacts of injecting various stratospheric aerosols in order to ameliorate global warming. However, further research is needed to further assess the climatic impacts of stratospheric aerosol injection such as the impacts on ozone. Whilst research indicates that SAI is capable of averting certain climate changes such as surface-warming, SAI provides no amelioration for other climate impacts, such as ocean acidification. It is therefore important to note that the safest possible solution to avoiding the sort of climate change instantiated by, e.g., Fig. 6a of this report is to effectively mitigate greenhouse-gas emissions.

Data sets

Data used to generate figures, graphs, plots and tables are freely available via contacting the lead author: aj247@exeter.ac.uk.

The Supplement related to this article is available online at doi:10.5194/acp-16-2843-2016-supplement.

Author contributions. Anthony C. Jones designed the experiments, performed the simulations, analyzed the data, and wrote the manuscript with guidance and advice from James M. Haywood and Andy Jones.

Acknowledgements. The authors would like to thank Valentina Aquila for supplying AVHRR and SAGE data, and to Peter Cox, Angus Ferraro, David Keith and Alan Robock for helpful discussions. We also thank two anonymous reviewers and John Dykema for their comments and suggestions. Anthony C. Jones was supported by a Met Office/NERC CASE (ref. 580009183) PhD studentship; James M. Haywood and Andy Jones were supported by the Joint UK DECC/Defra Met Office Hadley Centre Climate Programme (GA01101).

Edited by: B. Kravitz

References

Aquila, V., Oman, L. D., Stolarski, R. S., Colarco, P. R., and Newman, P. A.: Dispersion of the volcanic sulfate cloud from a Mount Pinatubo–like eruption, J. Geophys. Res., 117, D06216, doi:10.1029/2011JD016968, 2012.

Aquila, V., Garfinkel, C. I., Newman, P. A., Oman, L. D., and Waugh, D. W.: Modifications of the quasi-biennial oscillation by a geoengineering perturbation of the stratospheric aerosol layer, Geophys. Res. Lett., 41, 1738–1744, 2014.

Bala, G., Duffy, P. B., and Taylor, K. E.: Impact of geoengineering schemes on the global hydrological cycle, P. Natl. Acad. Sci. USA, 105, 7664–7669, 2008.

Baldwin, M. P., Gray, L. J., Dunkerton, T. J., Hamilton, K., Haynes, P. H., Randel, W. J., Holton, J. R., Alexander, M. J., Hirota, I., Horinouchi, T., Jones, D. B. A., Kinnersley, J. S., Marquardt, C., Sato, K., and Takahashi, M.: The quasi-biennial oscillation, Rev. Geophys., 39, 179–229, 2001.

Bellouin, N., Boucher, O., Haywood, J., Johnson, C., Jones, A., Rae, J., and Woodward, S.: Improved representation of aerosols for HadGEM2, Hadley Centre technical note 73, Hadley Centre, Met Office, Exeter, UK, available at: http://www.metoffice.gov.uk/media/pdf/8/f/HCTN_73.pdf, 42 pp., 2007.

Bellouin, N., Rae, J., Johnson, C., Haywood, J., Jones, A., and Boucher, O.: Aerosol forcing in the Hadley Centre CMIP5 simulations by HadGEM2-ES and the role of ammonium nitrate, J. Geophys. Res., 116, D20206, doi:10.1029/2011JD016074, 2011.

Berdahl, M., Robock, A., Ji, D., Moore, J. C., Jones, A., Kravitz, B., and Watanabe, S.: Arctic cryosphere response in the Geoengineering Model Intercomparison Project G3 and G4 scenarios, J. Geophys. Res.-Atmos., 119, 1308–1321, 2014.

Carslaw, K. C. and Kärcher, B.: Stratospheric aerosol processes, in: Assessment of Stratospheric Aerosol Properties, edited by: Thomason, L. and Peter, T., WCRP 124, WMO/TD 1295, SPARC Rep. 4, World. Meteorol. Organ., Geneva, Switzerland, 2006.

Collins, M., Knutti, R., Arblaster, J., Dufresne, J.-L., Fichefet, T., Friedlingstein, P., Gao, X., Gutowski, W. J., Johns, T., Krinner, G., Shongwe, M., Tebaldi, C., Weaver, A. J., and Wehner, M.: Long-term Climate Change: Projections, Commitments and Irreversibility, in: Climate Change 2013: The Physical Science Basis. Contribution of Working Group I to the Fifth Assessment Report of the Intergovernmental Panel on Climate Change, edited by: Stocker, T. F., Qin, D., Plattner, G.-K., Tignor, M., Allen, S. K., Boschung, J., Nauels, A., Xia, Y., Bex, V., and Midgley, P. M., Cambridge University Press, Cambridge, United Kingdom and New York, NY, USA, 2013.

Crutzen, P.: Albedo Enhancement by Stratospheric Sulfur Injections: A Contribution to Resolve a Policy Dilemma?, Climate Change, 77, 211–220, 2006.

d'Almeida, G. A., Koepke, P., and Shettle, E. P.: Atmospheric aerosols: global climatology and radiative characteristics, A. Deepak Publishing, Hampton, USA, 1991.

Dankovic, D., Kuempel, E., Geraci, C., Gilbert, S., Rice, F., Schulte, P., Smith, R., Sofge, C., Wheeler, M., Lentz, T. J., Zumwalde, R., Maynard, A., Attfield, M., Pinheiro, G., Ruder, A., Hubbs, A., Ahlers, H., Lynch, D., Toraason, M., and Vallyathan, V.: Current intelligence bulletin 63: occupational exposure to titanium dioxide, Cincinnati, OH: US Department of Health and Human Services, Public Health Service, Centers for Disease Control and Prevention, National Institute for Occupational Safety and Health, DHHS (NIOSH) Publication No. 2011-160, 1–119, 2011.

Deepak, A. and Gerber, H. E. (Eds.): Report of the experts meeting on aerosols and their climatic effects (Williamsburg, Virginia, March 1983), Rep. WCP-55, World Clim. Programme, World Meteorol. Organ., Geneva, 1983.

Deshler, T. and Anderson-Sprecher, R.: Non-volcanic stratospheric aerosol trends: 1971–2004, in: Assessment of Stratospheric Aerosol Properties, edited by: Thomason, L. and Peter, T., WCRP 124, WMO/TD 1295, SPARC Rep. 4, World Meteorolo. Organ., Geneva, Switzerland, 2006.

Dessler, A. E., Schoeberl, M. R., Wang, T., Davis, S. M., and Rosenlof, K. H.: Stratospheric water vapor feedback, Proc. Natl. Acad. Sci. USA, 110, 18087–18091, 2013.

Dhomse, S. S., Emmerson, K. M., Mann, G. W., Bellouin, N., Carslaw, K. S., Chipperfield, M. P., Hommel, R., Abraham, N. L., Telford, P., Braesicke, P., Dalvi, M., Johnson, C. E., O'Connor, F., Morgenstern, O., Pyle, J. A., Deshler, T., Zawodny, J. M., and Thomason, L. W.: Aerosol microphysics simulations of the Mt. Pinatubo eruption with the UM-UKCA composition-climate model, Atmos. Chem. Phys., 14, 11221–11246, doi:10.5194/acp-14-11221-2014, 2014.

Driscoll, S., Bozzo, A., Gray, L. J., Robock, A., and Stenchikov, G.: Coupled Model Intercomparison Project 5 (CMIP5) simula-

tions of climate following volcanic eruptions, J. Geophys. Res.-Atmos., 117, D17105, doi:10.1029/2012JD017607, 2012.

English, J. M., Toon, O. B., and Mills, M. J.: Microphysical simulations of sulfur burdens from stratospheric sulfur geoengineering, Atmos. Chem. Phys., 12, 4775–4793, doi:10.5194/acp-12-4775-2012, 2012.

Ferraro, A. J., Highwood, E. J., and Charlton-Perez, A. J.: Stratospheric heating by potential geoengineering aerosols, Geophys. Res. Lett., 38, L24706, doi:10.1029/2011GL049761, 2011.

Ferraro, A. J., Highwood, E. J., and Charlton-Perez, A. J.: Weakened tropical circulation and reduced precipitation in response to geoengineering, Environ. Res. Lett., 9, 014001, doi:10.1088/1748-9326/9/1/014001, 2014.

Gettelman, A., Hegglin, M. I., Son, S.-W., Kim, J., Fujiwara, M., Birner, T.,Kremser, S., Rex, M., Añel, J. A., Akiyoshi, H., Austin, J., Bekki, S., Braesike, P.,Brühl, C., Butchart, N., Chipperfield, M., Dameris, M., Dhomse, S., Garny, H.,Hardiman, S. C., Jöckel, P., Kinnison, D. E., Lamarque, J. F., Mancini, E., Marchand, M., Michou, M., Morgenstern, O., Pawson, S., Pitari, G., Plummer, D.,Pyle, J. A., Rozanov, E., Scinocca, J., Shepherd, T. G., Shibata, K., Smale, D., Teyssèdre, H., and Tian, W.: Multimodel assessment of the upper troposphere and lower stratosphere: Tropics and global trends, J. Geophys. Res., 115, D00M08, doi:10.1029/2009JD013638, 2010.

Hansen, J., Sato, M., and Ruedy, R.: Radiative forcing and climate response, J. Geophys. Res., 102, 6831–6864, 1997.

Haywood, J. M., Jones, A., Clarisse, L., Bourassa, A., Barnes, J., Telford, P., Bellouin N., Boucher, O., Agnew, P., Clerbaux, C., Coheur, P., Degenstein, D., and Braesicke, P.: Observations of the eruption of the Sarychev volcano and simulations using the HadGEM2 climate model, J. Geophys. Res., 115, D21212, doi:10.1029/2010JD014447, 2010.

Haywood, J. M., Bellouin, N., Jones, A., Boucher, O., Wild, M., and Shine, K. P.: The roles of aerosol, water vapor and cloud in future global dimming/brightening, J. Geophys. Res., 116, D20203, doi:10.1029/2011JD016000, 2011.

Haywood, J. M., Jones, A., Bellouin, N., and Stephenson, D.: Asymmetric forcing from stratospheric aerosols impacts Sahelian rainfall, Nature Climate Change, 3, 660–665, 2013.

Heckendorn, P., Weisenstein, D., Fueglistaler, S., Luo, B. P., Rozanov, E., Schraner, M., Thomason, L. W., and Peter, T.: The impact of geoengineering aerosols on stratospheric temperature and ozone, Environ. Res. Lett., 4, 045108, doi:10.1088/1748-9326/4/4/045108, 2009.

Illingworth, A. J., Barker, H. W., Beljaars, A., Ceccaldi, M., Chepfer, H., Clerbaux, N., Cole, J., Delanoë, J., Domenech, C., Donovan, D. P., Fukuda, S., Hirakata, M., Hogan, R. J., Huenerbein, A., Kollias, P., Kubota, T., Nakajima, T., Nakajima, T. Y., Nishizawa, T., Ohno, Y., Okamoto, H., Oki, R., Sato, K., Satoh, M., Shephard, M. W., Velázquez-Blázquez, A., Wandinger, U., Wehr, T., and van Zadelhoff, G.-J.: The EarthCARE Satellite: The Next Step Forward in Global Measurements of Clouds, Aerosols, Precipitation, and Radiation, Bull. Amer. Meteor. Soc., 96, 1311–1332. 2015.

International Civil Aviation Organisation (ICAO): Manual of the ICAO Standard Atmosphere: extended to 80 kilometres (262 200 feet), Doc 7488/3, 3rd Edn., 1993.

Jiao, C., Flanner, M. G., Balkanski, Y., Bauer, S. E., Bellouin, N., Berntsen, T. K., Bian, H., Carslaw, K. S., Chin, M., De Luca, N., Diehl, T., Ghan, S. J., Iversen, T., Kirkevåg, A., Koch, D., Liu, X., Mann, G. W., Penner, J. E., Pitari, G., Schulz, M., Seland, Ø., Skeie, R. B., Steenrod, S. D., Stier, P., Takemura, T., Tsigaridis, K., van Noije, T., Yun, Y., and Zhang, K.: An AeroCom assessment of black carbon in Arctic snow and sea ice, Atmos. Chem. Phys., 14, 2399–2417, doi:10.5194/acp-14-2399-2014, 2014.

Kawatani, Y. and Hamilton, K.: Weakened stratospheric quasibiennial oscillation driven by increased tropical mean upwelling, Nature, 497, 478–481, 2013.

Kharin, V. V., Zwiers, F. W., Zhang, X., and Wehner, M.: Changes in temperature and precipitation extremes in the CMIP5 ensemble, Climate Change, 119, 345–357, 2013.

Koehler, K. A., Kreidenweis, S. M., DeMott, P. J., Petters, M. D., Prenni, A. J., and Carrico, C. M.: Hygroscopicity and cloud droplet activation of mineral dust aerosol, Geophys. Res. Lett., 36, L08805, doi:10.1029/2009GL037348, 2009.

Kravitz, B., Robock, A., Boucher, O., Schmidt, H., Taylor, K. E., Stenchikov, G., and Schulz, M.: The Geoengineering Model Intercomparison Project (GeoMIP), Atmosph. Sci. Lett., 12, 162–167, 2011.

Kravitz, B., Robock, A., Shindell, D. T., and Miller, M. A.: Sensitivity of stratospheric geoengineering with black carbon to aerosol size and altitude of injection, J. Geophys. Res., 117, D09203, doi:10.1029/2011JD017341, 2012.

Kravitz, B., Robock, A., Forster, P. M., Haywood, J. M., Lawrence, M. G., and Schmidt, H.: An overview of the Geoengineering Model Intercomparison Project (GeoMIP), J. Geophys. Res.-Atmos., 118, 13103–13107, 2013.

Kravitz, B., Douglas G MacMartin, D. G., Leedal, D. T., Rasch, P. J., and Jarvis, A. J.: Explicit feedback and the management of uncertainty in meeting climate objectives with solar geoengineering, Environ. Res. Lett., 9, 044006, doi:10.1088/1748-9326/9/4/044006, 2014.

Kravitz, B., Robock, A., Tilmes, S., Boucher, O., English, J. M., Irvine, P. J., Jones, A., Lawrence, M. G., MacCracken, M., Muri, H., Moore, J. C., Niemeier, U., Phipps, S. J., Sillmann, J., Storelvmo, T., Wang, H., and Watanabe, S.: The Geoengineering Model Intercomparison Project Phase 6 (GeoMIP6): simulation design and preliminary results, Geosci. Model Dev., 8, 3379–3392, doi:10.5194/gmd-8-3379-2015, 2015.

L'Ecuyer, T. S., Beaudoing, H. K., Rodell, M., Olson, W., Lin, B., Kato, S., Clayson, C. A., Wood, E., Sheffield, J., Adler, R., Huffman, G., Bosilovich, M., Gu, G., Robertson, F., Houser, P. R., Chambers, D., Famiglietti, J. S., Fetzer, E., Liu, W. T., Gao, X., Schlosser, C. A., Clark, E., Lettenmaier, D. P., and Hilburn, K.: The Observed State of the Energy Budget in the Early Twenty-First Century, J. Climate, 28, 8319–8346., 2015.

Liu, D., Allan, J., Whitehead, J., Young, D., Flynn, M., Coe, H., McFiggans, G., Fleming, Z. L., and Bandy, B.: Ambient black carbon particle hygroscopic properties controlled by mixing state and composition, Atmos. Chem. Phys., 13, 2015–2029, doi:10.5194/acp-13-2015-2013, 2013.

Lombardo, K., Colle, B. A., and Zhang, Z.: Evaluation of Historical and Future Cool Season Precipitation over the Eastern United States and Western Atlantic Storm Track Using CMIP5 Models, J. Climate, 28, 451–467, 2015.

MacMartin, D. G., Keith, D. W., Kravitz, B., and Caldeira, K.: Management of trade-offs in geoengineering through optimal

choice of non-uniform radiative forcing, Nature Climate Change, 3, 365–368, 2013.

MacMartin, D. G., Kravitz, B., Keith, D. W., and Jarvis, A.: Dynamics of the coupled human–climate system resulting from closed-loop control of solar geoengineering, Clim. Dynam., 43, 243–258, 2014.

Marks, A. A. and King, M. D.: The effect of snow/sea ice type on the response of albedo and light penetration depth (e-folding depth) to increasing black carbon, The Cryosphere, 8, 1625–1638, doi:10.5194/tc-8-1625-2014, 2014.

McCusker, K. E., Battisti, D. S., and Bitz, C. M.: Inability of stratospheric sulfate aerosol injections to preserve the West Antarctic Ice Sheet, Geophys. Res. Lett., 42, 4989–4997, doi:10.1002/2015GL064314, 2015.

Meinshausen, M., Smith, S. J., Calvin, K. V., Daniel, J. S., Kainuma, M. L. T., Lamarque, J.-F., Matsumoto, K., Montzka, S. A., Raper, S. C. B., Riahi, K., Thomson, A. M., Velders, G. J. M., and Van Vuuren, D.: The RCP Greenhouse Gas Concentrations and their Extension from 1765 to 2300, Climate Change (Special Issue), doi:10.1007/s10584-011-0156-z, 2011.

Muller, C. J. and O'Gorman, P. A.: An energetic perspective on the regional response of precipitation to climate change, Nature Climate Change, 1, 266–271, 2011.

Ndour, M., D'Anna, B., George, C., Ka, O., Balkanski, Y., Kleffmann, J., Stemmler, K., and Ammann, M.: Photoenhanced uptake of NO_2 on mineral dust: Laboratory experiments and model simulations, Geophys. Res. Lett., 35, L05812, doi:10.1029/2007GL032006, 2008.

Niemeier, U., Schmidt, H., and Timmreck, C.: The dependency of geoengineered sulfate aerosol on the emission strategy, Atmos. Sci. Lett., 12, 189–194, 2011.

Niemeier, U., Schmidt, H., Alterskjær, K., and Kristjánsson, J. E.: Solar irradiance reduction via climate engineering: Impact of different techniques on the energy balance and the hydrological cycle, J. Geophys. Res.-Atmos., 118, 11905–11917, 2013.

Oman, L., Robock, A., Stenchikov, G. L., and Thordarson, T.: High-latitude eruptions cast shadow over the African monsoon and the flow of the Nile, Geophys. Res. Lett., 33, L18711, doi:10.1029/2006GL027665, 2006.

Peters, G. P., Andrew, R. M., Boden, T., Canadell, J. G., Ciais, P., Le Quéré, C., Marland, G., Raupach, M. R., and Wilson, C.: The challenge to keep global warming below 2 °C, Nature Climate Change, 3, 4–6, 2013.

Pierce, J. R., Weisenstein, D. K., Heckendorn, P., Peter, T., and Keith, D. W.: Efficient formation of stratospheric aerosol for climate engineering by emission of condensible vapor from aircraft, Geophys. Res. Lett., 37, L18805, doi:10.1029/2010GL043975, 2010.

Pitari, G., Aquila, V., Kravitz, B., Robock, A., Watanabe, S., Cionni, I., De Luca, N., Di Genova, G., Mancini, E., and Tilmes, S.: Stratospheric ozone response to sulfate geoengineering: Results from the Geoengineering Model Intercomparison Project (GeoMIP), J. Geophys. Res.-Atmos., 119, 2629–2653, 2014.

Pithan, F. and Mauritsen, T.: Arctic amplification dominated by temperature feedbacks in contemporary climate models, Nat. Geosci., 7, 181–184, 2014.

Pope, F. D., Braesicke, P., Grainger, R. G., Kalberer, M., Watson, I. M., Davidson, P. J., and Cox, R. A.: Stratospheric aerosol particles and solar-radiation management, Nature Climate Change, 2, 713–719, 2012.

Priestley, K. J., Smith, G. L., Thomas, S., Cooper, D., Lee III, R. B., Walikainen, D., Hess, P., Szewczyk, Z. P., and Wilson, R.: Radiometric Performance of the CERES Earth Radiation Budget Climate Record Sensors on the EOS Aqua and Terra Spacecraft through April 2007, J. Atmos. Oc. Technol., 28, 3–21, 2011.

Pruppacher, H. R. and Klett, J. D.: Microphysics of Clouds and Precipitation, D. Reidel Publishing Company, Dordretch, ISBN: 978-90-277-1106-9, Holland, 1980.

Rasch, P. J., Tilmes, S., Turco, R. P., Robock, A., Oman, L., Chen, C.-C., Stenchikov, G. L., and Garcia, R. R.: An overview of geoengineering of climate using stratospheric sulphate aerosols, Phil. Trans. R. Soc. A, 366, 4007–4037, 2008.

Ribarsky, M. W.: Titanium dioxide, in: Handbook of Optical Constants of Solids, edited by: E. Palik, Academic, Orlando, Fla, 795–804, 1985.

Robock, A., Oman, L., and Stenchikov, G. L.: Regional climate responses to geoengineering with tropical and Arctic SO_2 injections, J. Geophys. Res., 113, D16101, doi:10.1029/2008JD010050, 2008.

Schmidt, H., Rast, S., Bunzel, F., Esch, M., Giorgetta, M., Kinne, S., Krismer, T., Stenchikov, G., Timmreck, S., Tomassini, L., and Walz, M.: Response of the middle atmosphere to anthropogenic and natural forcings in the CMIP5 simulations with the Max Planck Institute Earth system model, J. Adv. Model. Earth Syst., 5, 98–116, 2013.

Schoeberl, M. R., Douglass, A. R., Stolarski, R. S., Pawson, S., Strahan, S. E., and Read, W.: Comparison of lower stratospheric tropical mean vertical velocities, J. Geophys. Res., 113, D24109, doi:10.1029/2008JD010221, 2008.

Shepherd, J.: Geoengineering the climate: Science, governance, and uncertainty, Royal Society Policy document 10/09, ISBN: 978-0-85403-773-5, 82 pp., 2009.

Stenchikov, G., Robock, A., Ramaswamy, V., Schwarzkopf, M. D., Hamilton, K., and Ramachandran, S.: Arctic Oscillation response to the 1991 Mount Pinatubo eruption: Effects of volcanic aerosols and ozone depletion, J. Geophys. Res., 107, 4803, doi:10.1029/2002JD002090, 2002.

Tang, M. J., Telford, P. J., Pope, F. D., Rkiouak, L., Abraham, N. L., Archibald, A. T., Braesicke, P., Pyle, J. A., McGregor, J., Watson, I. M., Cox, R. A., and Kalberer, M.: Heterogeneous reaction of N_2O_5 with airborne TiO_2 particles and its implication for stratospheric particle injection, Atmos. Chem. Phys., 14, 6035–6048, doi:10.5194/acp-14-6035-2014, 2014.

Taylor, K. E., Stouffer, R. J., and Meehl, G. A.: An Overview of CMIP5 and the Experiment Design, Bull. Amer. Meteor. Soc., 93, 485–498, 2012.

Tegtmeier, S., Kruger, K., Wohltmann, I., Schoellhammer, K., and Rex, M.: Variations of the residual circulation in the Northern Hemispheric winter, J. Geophys. Res., 113, D16109, doi:10.1029/2007JD009518, 2008.

Teller, E., Wood, L., and Hyde, R.: Global Warming and Ice Ages: I. Prospects for Physics-Based Modulation of Global Change, Lawrence Livermore National Laboratory Publication UCRL-JC-128715, 18 pp., 1997.

The HadGEM2 Development Team: Martin, G. M., Bellouin, N., Collins, W. J., Culverwell, I. D., Halloran, P.R., Hardiman, S. C., Hinton, T. J., Jones, C. D., McDonald, R. E., McLaren, A. J.,

O'Connor, F. M., Roberts, M. J., Rodriguez, J. M., Woodward, S., Best, M. J., Brooks, M. E., Brown, A. R., Butchart, N., Dearden, C., Derbyshire, S. H., Dharssi, I., Doutriaux-Boucher, M., Edwards, J. M., Falloon, P. D., Gedney, N., Gray, L. J., Hewitt, H. T., Hobson, M., Huddleston, M. R., Hughes, J., Ineson, S., Ingram, W. J., James, P. M., Johns, T. C., Johnson, C. E., Jones, A., Jones, C. P., Joshi, M. M., Keen, A. B., Liddicoat, S., Lock, A. P., Maidens, A. V., Manners, J. C., Milton, S. F., Rae, J. G. L., Ridley, J. K., Sellar, A., Senior, C. A., Totterdell, I. J., Verhoef, A., Vidale, P. L., and Wiltshire, A.: The HadGEM2 family of Met Office Unified Model climate configurations, Geosci. Model Dev., 4, 723–757, doi:10.5194/gmd-4-723-2011, 2011.

Tilmes, S., Garcia, R. R., Kinnison, D. E., Gettelman, A., and Rasch, P. J.: Impact of geoengineered aerosols on the troposphere and stratosphere, J. Geophys. Res., 114, D12305, doi:10.1029/2008JD011420, 2009.

Tilmes, S., Kinnison, D. E., Garcia, R. R., Salawitch, R., Canty, T., Lee-Taylor, J., Madronich, S., and Chance, K.: Impact of very short-lived halogens on stratospheric ozone abundance and UV radiation in a geo-engineered atmosphere, Atmos. Chem. Phys., 12, 10945–10955, doi:10.5194/acp-12-10945-2012, 2012.

Tilmes, S., Fasullo, J., Lamarque, J.-F., Marsh, D. R., Mills, M., Alterskjær, K., Muri, H., Kristjánsson, J. E., Boucher, O., Schulz, M., Cole, J. N. S., Curry, C. L., Jones, A., Haywood, J., Irvine, P. J., Ji, D., Moore, J. C., Karam, D. B., Kravitz, B., Rasch, P. J., Singh, C., Yoon, J.-H., Niemeier, U., Schmidt, H., Robock, A., Yang, S., and Watanabe, S.: The hydrological impact of geoengineering in the Geoengineering Model Intercomparison Project (GeoMIP), J. Geophys. Res.-Atmos., 118, 11036–11058, 2013.

von Schuckmann, K., Palmer, M. D., Trenberth, K. E., Cazenave, A., Chambers, D., Champollion, N., Hansen, J., Josey, S. A., Loeb, N., Mathieu, P.-P., Meyssignac, B., and Wild, M.: An imperative to monitor Earth's energy imbalance, Nature Climate Change, 6, 138–144, 2016.

Weisenstein, D. K., Keith, D. W., and Dykema, J. A.: Solar geoengineering using solid aerosol in the stratosphere, Atmos. Chem. Phys., 15, 11835–11859, doi:10.5194/acp-15-11835-2015, 2015.

Yang, H., Zhu, S., and Pan, N.: Studying the Mechanisms of Titanium Dioxide as Ultraviolet-Blocking Additive for Films and Fabrics by an Improved Scheme, J. Appl. Polym. Sci., 92, 3201–3210, 2004.

Yu, X., Moore, J. C., Cui, X., Rinke, A., Ji, D., Kravitz, B., and Yoon, J.-H.: Impacts, effectiveness and regional inequalities of the GeoMIP G1 to G4 solar radiation management scenarios, Glob. Planet. Change, 129, 10–22, 2015.

AGU PUBLICATIONS

JGR

Journal of Geophysical Research: Atmospheres

RESEARCH ARTICLE
10.1002/2016JD025001

Key Points:
- Using a global climate model (HadGEM2-CCS), we test the sensitivity of volcanic aerosol dispersion to various SO2 emission scenarios
- Volcanic eruptions initiated on consecutive days could result in vastly different spatial distributions of aerosols
- A 10 day Pinatubo-like eruption is unable to produce the aerosol self-lofting needed to move the aerosol into the southern hemisphere

Supporting Information:
- Supporting Information S1
- Movie S1

Correspondence to:
A. C. Jones,
anthony.jones@metoffice.gov.uk

Citation:
Jones, A. C., J. M. Haywood, A. Jones, and V. Aquila (2016), Sensitivity of volcanic aerosol dispersion to meteorological conditions: A Pinatubo case study, *J. Geophys. Res. Atmos.*, *121*, 6892–6908, doi:10.1002/2016JD025001.

Received 29 FEB 2016
Accepted 2 JUN 2016
Accepted article online 6 JUN 2016
Published online 24 JUN 2016

Sensitivity of volcanic aerosol dispersion to meteorological conditions: A Pinatubo case study

Anthony C. Jones[1,2], James M. Haywood[1,2], Andy Jones[2], and Valentina Aquila[3,4]

[1]College of Engineering, Mathematics, and Physical Sciences, University of Exeter, Exeter, UK, [2]Met Office Hadley Centre, Exeter, UK, [3]Department of Earth and Planetary Sciences, GESTAR/Johns Hopkins University, Baltimore, Maryland, USA, [4]NASA Goddard Space Flight Center, Greenbelt, Maryland, USA

Abstract Using a global climate model (Hadley Centre Global Environment Model version 2-Carbon Cycle Stratosphere) with a well-resolved stratosphere, we test the sensitivity of volcanic aerosol plume dispersion to meteorological conditions by simulating 1 day Mount Pinatubo-like eruptions on 10 consecutive days. The dispersion of the volcanic aerosol is found to be highly sensitive to the ambient meteorology for low-altitude eruptions (16–18 km), with this variability related to anomalous anticyclonic activity along the subtropical jet, which affects the permeability of the tropical pipe and controls the amount of aerosol that is retained by the tropical reservoir. Conversely, a high-altitude eruption scenario (19–29 km) exhibits low meteorological variability. Overcoming day-to-day meteorological variability by spreading the emission over 10 days is shown to produce insufficient radiative heating to loft the aerosol into the stratospheric tropical aerosol reservoir for the low eruption scenario. This results in limited penetration of aerosol into the southern hemisphere (SH) in contrast to the SH transport observed after the Pinatubo eruption. Our results have direct implications for the accurate simulation of past/future volcanic eruptions and volcanically forced climate changes, such as Intertropical Convergence Zone displacement.

1. Introduction

After weeks of precursory activity, Mount Pinatubo in the Philippines (15°N, 121°E) erupted on 15 June 1991 in a volcanic episode that lasted ~9 h starting at 14:00 (local time), although 90% of the total magmatic injecta was emitted in an intense phase that last ~3 h [*Holasek et al*., 1996; *Guo et al*., 2004; *Self et al*., 2004]. The Pinatubo eruption was significant for multiple reasons. It was the first major volcanic eruption to be comprehensively documented by satellite instruments, lidars, and airborne aerosol counters [*McCormick et al*., 1995]; it likely produced the greatest volume of volcanic material injected into the atmosphere of any twentieth century eruption [*Bluth et al*., 1992; *Robock*, 2000]; and it had a broad climatic influence that would prove a vital validation tool for the burgeoning global climate model (GCM) development community. The Pinatubo eruption induced a global mean lower tropospheric cooling of 0.3°C (averaged over the subsequent 4 years) [*Soden et al*., 2002], enhanced ozone reaction catalysis for 1–2 years [*Hofmann et al*., 1992; *McCormick et al*., 1995], disrupted the hydrological cycle [*Spencer et al*., 1998; *Trenberth and Dai*, 2007], induced a tropical stratospheric warming [*Labitzke and McCormick*, 1992], and instigated a wealth of other climatic perturbations [e.g., *McCormick et al*., 1995; *Russell et al*., 1996; *Robock*, 2000].

The primary driver of these climatic impacts was the volcanic aerosol that resided in the stratosphere for multiple years and influenced both the incoming shortwave (SW) radiation and outgoing longwave (LW) radiation [*Stenchikov et al*., 1998]. This aerosol plume was primarily composed of sulfate (SO_4) in the form of liquid sulfuric acid (H_2SO_4) droplets (60–80% by mass) in aqueous solution, formed from the oxidation of gaseous sulfur dioxide (SO_2), which was oxidized to SO_4 with an *e*-folding time of ~35 days [*Bluth et al*., 1992]. Heavier constituents of the initial plume such as ash were removed from the atmosphere within weeks and therefore provided a short-term, localized climatic forcing [*Russell et al*., 1996; *Niemeier et al*., 2009]. Early observations from the Total Ozone Mapping Spectrometer suggested that Pinatubo emitted ~20 teragrams (Tg) of SO_2 [*Bluth et al*., 1992], although a later, revised estimate suggested 14–23 Tg [*Guo et al*., 2004]. Recent Pinatubo simulations with models that incorporate aerosol microphysics suggest that an SO_2 emission of nearer 14 Tg produces better agreement with observations [*Sheng et al*., 2015].

The evolution of the aerosol cloud was observed by the advanced very high resolution radiometer (AVHRR) and Stratospheric Aerosol and Gas Experiment II (SAGE-II) satellite-borne instruments [*Stowe et al*., 1992;

McCormick and Veiga, 1992]. After the eruption, the aerosol plume was rapidly transported westward via zonal stratospheric winds and encircled the Earth within 22 days [*Bluth et al*., 1992]. Additionally, the aerosol cloud was initially advected both northward and southward, crossing the equator within 1 week [*Young et al*., 1994]. Subsequent meridional transport was impeded by the "leaky tropical pipe"—a sharp latitudinal potential vorticity gradient in the subtropical stratosphere—and later by the strong polar night jet in the southern hemisphere (SH) [*Boville et al*., 1991]. For the first couple of months after the eruption, the aerosol cloud was primarily confined to the tropical stratosphere (20°S–30°N), within altitudes of 20–30 km [*McCormick et al*., 1995]. The contemporaneous descending easterly shear phase of the quasi-biennial oscillation (QBO), coupled with a strong lower stratospheric meridional wind gradient in the subtropics, contributed to the initial confinement of the aerosol to the tropics [*Trepte and Hitchman*, 1992; *Trepte et al*., 1993; *Choi et al*., 1998]. By July 1991, aerosol in the lower stratosphere (~16 km/100 hPa altitude) had been transported to high northern hemisphere (NH) latitudes (>50°N), primarily through advection by a tropospheric quasi-stationary anticyclone over Asia [*McCormick et al*., 1995; *Trepte et al*., 1993; *Timmreck et al*., 1999b]. Additionally, aerosol was later transported to the NH at higher altitudes (~25 km/ 30 hPa altitude) in the months following the shift from summer to winter stratospheric dynamics in October 1991 [*Trepte et al*., 1993]. Significant aerosol transport into the SH occurred during September 1991 in the high-altitude regime (~22 km/40 hPa altitude), primarily as the result of transient subtropical anticyclones [*Trepte et al*., 1993]. The global sulfate cloud decayed exponentially with an e-folding time of ~1–2 years [*Kirchner et al*., 1999; *Driscoll et al*., 2012].

Various GCMs have been used to simulate the dispersal of the Pinatubo aerosol cloud. Early experiments treated the aerosol as a passive tracer, which disregards the radiative feedback of the aerosol [*Boville et al*., 1991; *Pudykiewicz and Dastoor*, 1995; *Timmreck et al*., 1999b]. *Young et al*. [1994] combined a 3-D circulation model with an aerosol transport/radiation code to show the importance of including the radiative feedback on the resultant dispersion of the aerosol. *Timmreck et al*. [1999a] showed that the stratospheric dynamical adjustments from aerosol-induced radiative heating could induce a strengthening of the polar vortex, in agreement with observations from 1991/1992 [e.g., *Robock and Mao*, 1995]. However, the simulated tropical aerosol reservoir in *Timmreck et al*. [1999a] was short-lived compared with observations, which the authors attributed to the absence of a QBO in their GCM. The QBO is a periodic oscillation of the equatorial, stratospheric zonal mean, zonal wind direction at ~40 hPa altitude [*Baldwin et al*., 2001]. Pinatubo simulations with GCMs that do not include a QBO have generally exhibited a short-lived tropical aerosol reservoir [*Oman et al*., 2006; *Niemeier et al*., 2009; *Toohey et al*., 2011]. *Niemeier et al*. [2009] coupled an aerosol microphysics module with a GCM to show that radiative heating induced by the short-lived ash ejected by Pinatubo could alter the initial trajectory of the sulfate plume. *Toohey et al*. [2011] showed that the Pinatubo aerosol optical depth (AOD) evolution is sensitive to the season of eruption (particularly in the NH), which they attributed to the state of the Brewer-Dobson circulation (BDC) in the stratosphere. *Aquila et al*. [2012] (hereafter, AQ12) simulated Pinatubo using the Goddard Earth Observing System version 5 GCM, which included a single-moment sulfate-transport scheme and radiatively interactive aerosol, but no QBO representation. They injected 20 Tg [SO_2] at the comparatively low altitudes of 16–18 km over a single day in eight consecutive "15 Junes" and with perpetual year 2000 conditions. The low-altitude specification was selected because sensitivity tests with high-altitude eruptions (16–25, 17–27, 20–27, and 20–30 km) had elevated the aerosol to altitudes that exceeded observations [e.g., *McCormick and Veiga*, 1992]. Their ensemble mean 550 nm AOD evolution (Figure 2 of AQ12) compared well to AVHRR and SAGE II observations. *English et al*. [2013] coupled a 3-D sectional aerosol model to a GCM to study the linearity of atmospheric aerosol burdens to increasing levels of SO_2 emissions, finding a nonlinear relationship due to enhanced aerosol growth and sedimentation. To compensate for the omission of radiatively interactive aerosol and a QBO, *English et al*. [2013] injected over a wide area (2°S–14°N, 95°E–115°E) and vertical span (15–29 km altitude), a technique also utilized by *Timmreck et al*. [1999a], *Weisenstein et al*. [2007], and *Dhomse et al*. [2014]. This "wide-injection" method sidesteps the necessary radiatively induced dynamical changes required to transport the aerosol southward and upward (AQ12). *Dhomse et al*. [2014] used a detailed aerosol microphysics module coupled to a GCM with an internally generated QBO to show that a simulated 10 Tg [SO_2] Pinatubo-like eruption produced aerosol size distributions that matched observations better than the ubiquitously utilized 20 Tg [SO_2] emission rate. *Mills et al*. [2016] also found that a 10 Tg [SO_2] injection produced the best fit to Pinatubo observations, while *Sheng et al*. [2015] found that 14 Tg [SO_2] produced the best fit. However, climate models are imperfect tools for inferring the quantity of SO_2 emitted by a volcanic eruption due to scenario-based uncertainties such as the altitude and composition of the volcanic plume, model-specific

limitations such as coarse spatiotemporal resolutions and parameterized processes, missing processes such as the co-injection of volcanic ash, and internal variability such as meteorological conditions.

A previously unexplored aspect of the Pinatubo eruption is the role of meteorology in the evolution of the aerosol plume, although the ensemble standard deviations in Figures 1 and 3 of AQ12 and Figures 5d–5f of *Toohey et al*. [2011] suggest a high meteorological sensitivity in previous simulations. The spread of the aerosol plume has implications for the climatic impacts of volcanic eruptions. For instance, *Haywood et al*. [2013] showed that enhancement of the stratospheric sulfate burden in a single hemisphere could alter the position of the Intertropical Convergence Zone (ITCZ) and associated monsoon precipitation. The aim of this investigation is to explicitly assess the sensitivity of the Pinatubo aerosol dispersion to the ambient meteorology. Additionally, we compare the aerosol dispersion from a 10 day eruption to the ensemble mean of ten 1 day eruptions, which represent two intuitive methods of overcoming meteorological variability whilst simulating a volcanic eruption. In section 2 we describe the GCM (Hadley Centre Global Environment Model version 2-Carbon Cycle Stratosphere (HadGEM2-CCS)) used for this investigation and the Pinatubo simulation suite. In section 3.1 we compare the global mean sulfate optical depth anomalies for the Pinatubo simulations to observations. In section 3.2 we compare the aerosol dispersion for the ensemble mean of the 1 day eruptions with the 10 day eruption. In section 3.3 we compare the aerosol dispersion for individual 1 day eruption simulations to assess the importance of meteorology. We discuss the significance of our results in the context of potential climatic impacts of future volcanic eruptions and future GCM Pinatubo simulations in section 4.

2. Methods

2.1. Model

We use the HadGEM2-CCS GCM in atmosphere-only mode with prescribed climatological sea surface temperatures and sea ice fields. HadGEM2-CCS is the high-top configuration of the HadGEM2 family of models, with the atmospheric submodel comprising 60 vertical levels extending to approximately 84 km (~0.01 hPa) altitude and with a horizontal resolution of 1.25° latitude by 1.875° by longitude [*Martin et al*., 2011]. We use perpetual Pre-Industrial Control (piControl) baseline conditions derived from Coupled Model Intercomparison Project Phase 5 (CMIP5) specifications [*Jones et al*., 2011; *Taylor et al*., 2012]. This includes prescribed ozone fields following *Cionni et al*. [2011] and fixed atmospheric concentrations of carbon dioxide (CO_2), methane (CH_4), and nitrous oxide (N_2O). Except for the process of methane oxidation, HadGEM2-CCS does not include stratospheric chemistry but does include a well-resolved stratosphere capable of internally generating a realistic QBO [*Hardiman et al*., 2012; *Watson and Gray*, 2014]. The internal QBO is forced by parameterized orographic and nonorographic gravity wave drag schemes [*Martin et al*., 2011]. HadGEM2-CCS has been used for assessing the impacts of climate change on the stratospheric polar vortex strength [*Mitchell et al*., 2012], the climatic impacts of stratospheric geoengineering schemes [*Jackson et al*., 2015; *Jones et al*., 2016], and the influence of solar variability on surface climate [*Gray et al*., 2013]. Additionally, *Haywood et al*. [2010] simulated the 2008 Sarychev volcanic eruption with an atmosphere-only configuration of HadGEM2-CCS (as used here). *Haywood et al*. [2010] found that the simulated SO_2 dispersion closely resembled Infrared Atmospheric Sounding Interferometer observations and the SO_4 showed reasonable agreement with that derived from the Optical Spectrograph and Infrared Imager System limb-sounding instrument.

HadGEM2-CCS includes the Coupled Large-scale Aerosol Simulator for Studies in Climate (CLASSIC) aerosol module, which is described in detail by *Martin et al*. [2006], *Bellouin et al*. [2011], and references therein. The sulfur cycle includes the oxidation of gaseous SO_2 and dimethyl sulfide (DMS) to form sulfate aerosol, which is represented by two optically active modes (Aitken and accumulation) and a dissolved/in-cloud mode. The sulfate scheme represents the processes of nucleation, evaporation, coagulation, diffusion, and hygroscopic growth [*Bellouin et al*., 2011]. Aerosol is removed from the atmosphere via wet and dry deposition (important in the troposphere) and sedimentation (important in the stratosphere) with sedimentation rates calculated by applying Stokes' law [*Jones et al*., 2016]. DMS emissions and atmospheric oxidants (such as the OH^- free radical) are prescribed for the duration of the simulations, according to piControl conditions. CLASSIC's sulfate accumulation mode is modified for this investigation in order to reflect the larger aerosols observed after volcanic eruptions [*Russell et al*., 1996]. The modified accumulation mode is represented by a lognormal distribution with geometric mean radius of $r_m = 0.376\,\mu m$ and standard deviation of $\sigma = 1.25$

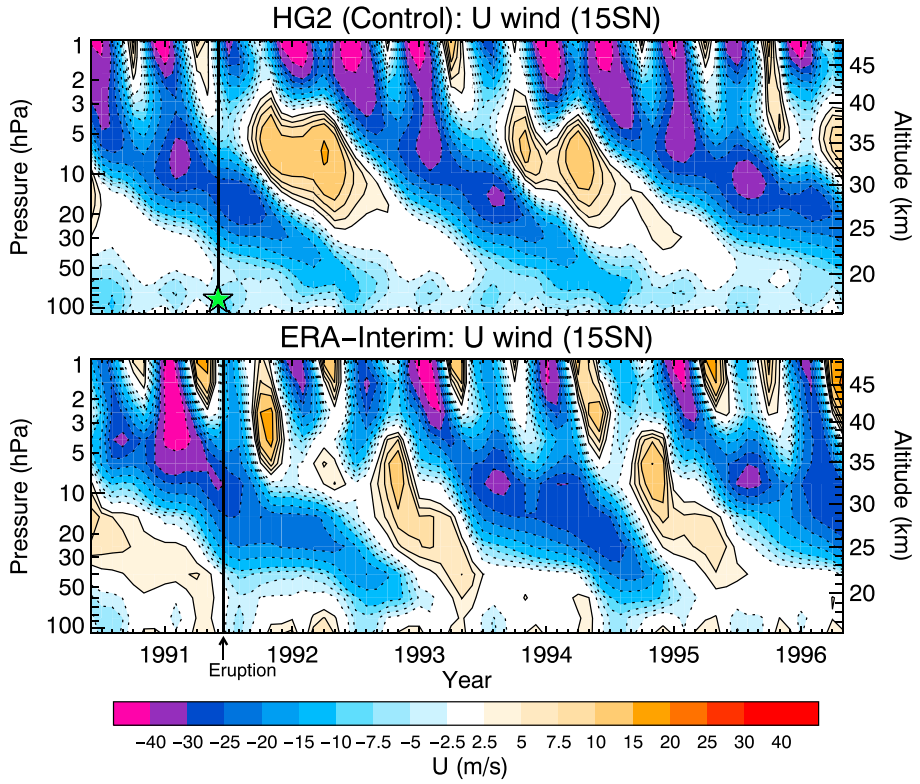

Figure 1. Zonal mean, zonal wind during the Pinatubo-eruption era for (a) the HadGEM2-CCS control simulation and (b) ERA-interim reanalysis data [*Dee et al.*, 2011].

[*Rasch et al.*, 2008], with the corresponding optical properties shown in Figure 1a of *Jones et al.* [2016]. This size distribution is applied throughout the atmosphere, which will have some influence on the tropospheric sulphur cycle and the associated aerosol-radiation and aerosol-cloud interactions. By prescribing a fixed radius, the model is unable to accurately represent the physical and optical properties of the evolving aerosol size distribution within the aerosol plume [*Dhomse et al.*, 2014]. The dry-mode effective radius of this distribution (0.42 μm) is similar to the peak effective radius between 1 to 200 hPa from the Pinatubo simulations of *English et al.* [2013]. The choice of size distribution affects the sedimentation velocity of the aerosol particles. For the size distribution used here, *Jones et al.* [2016] found an average sedimentation rate between 18 and 26 km altitude of 23 m/d and between 26 and 30 km of 52 m/d. The model's radiation scheme [*Edwards and Slingo*, 1996] is coupled to the dynamics, allowing for radiatively induced aerosol self-lofting [*Young et al.*, 1994].

2.2. Pinatubo Simulation Design

A 40 year piControl simulation was initially conducted, from which we selected a model year in which the simulated QBO in June resembled the Pinatubo-concurrent QBO conditions. Specifically, Mount Pinatubo erupted in June 1991, at which time the QBO had entered an easterly phase 2 months previously [*Hansen et al.*, 1992]. *Trepte et al.* [1993] showed that the transport of aerosol after large tropical volcanic eruptions is highly sensitive to the contemporaneous QBO phase. A time series of our simulated QBO compared with the ERA-Interim re-analyses for the Pinatubo period is shown in Figure 1. Our Pinatubo simulations were initiated from June in the selected model year (time/altitude indicated in Figure 1 by a green star). We performed a single control simulation with no additional SO_2 emission, a single simulation with a continuous 10 day eruption (*10D*), in which SO_2 is emitted evenly between 1 and 10 June; 10 simulations with 1 day eruptions (*1D*), in which SO_2 is emitted evenly over a 24 h period on 1, …, 10 June; and 10 simulations with 3 h eruptions (*3H*), in which SO_2 is emitted evenly over a 3 h period from 14:00 to 17:00 on 1, …, 10 June. The *1D* scenario was chosen following the simulation design of AQ12. However, as 90% of the total mass injected by Pinatubo on 15 June occurred during an ~3 h phase from 14:00 to 17:00 [*Holasek et al.*, 1996; *Self et al.*, 2004], we also examine any differences that may occur when representing Pinatubo emissions with a 3 h

Table 1. List of Performed Experiments[a]

Name	Injection Height (km)	Duration of Eruption	Total SO_2 Emitted (Tg)	Ensemble Members	Ensemble Mean Name
Control	N/A	N/A	N/A	1	N/A
10D_HIGH	19–29	10 days	14	1	N/A
1D_HIGH	19–29	1 day	14	10	1D_HIGH_AV
10D_LOW	16–18	10 days	20	1	N/A
1D_LOW	16–18	1 day	20	10	1D_LOW_AV
1D_LOW + CH	16–18 (P)	1 day (P)	20 (P)	2	N/A
	11–16 (CH)	8 h (CH)	3.3 (CH)		
3H_LOW	16–18	3 h	20	10	3H_LOW_AV

[a]For the 1D_LOW + CH simulations, "P" refers to Pinatubo and "CH" refers to Cerro Hudson.

eruption. For each of the Pinatubo simulations, SO_2 is injected into a single horizontal grid cell at (15°N, 120°E). We test two Pinatubo-like eruption scenarios that have been used in the literature. First, we adopt a similar eruption design to AQ12, in which 20 Tg [SO_2] is injected evenly between 16 and 18 km (100–70 hPa) altitude (two vertical model levels), and denote these experiments *LOW*. Second, we adopt a similar eruption design to *Dhomse et al.* [2014] and inject 14 Tg [SO_2] evenly between 19 and 29 km (65–15 hPa) altitude (nine vertical model levels) and denote these experiments *HIGH*. The *HIGH* scenario differs slightly from *Dhomse et al.* [2014], who injected 10 and 20 Tg [SO_2] between 19 and 27 km altitude. *Sheng et al.* [2015] found that 14 Tg [SO_2] injection at high altitudes produces a close match to observations. The experiments are listed in Table 1. The results of the 1 day *LOW* eruption ensemble mean (*1D_LOW_AV*) were also used by *Jones et al.* [2016] for model validation purposes and are plotted in their Figure 2. Although the simulated climatology is "perpetual piControl," we use the equivalent Pinatubo year for plotting/references to facilitate comparison with observations.

3. Results

3.1. Global-Mean Sulfate Optical Depth

The primary climatological field assessed in this research is the 550 nm sulfate aerosol optical depth (AOD), which was diagnosed in the aftermath of the Pinatubo eruption by the AVHRR and SAGE-II satellite-borne instruments, albeit at slightly different wavelengths of 630 nm and 525 nm, respectively [*Stowe et al.*, 1992; *McCormick and Veiga*, 1992]. Figure 2 shows the monthly mean 550 nm AOD anomaly, averaged between 75°S and 75°N, for the HadGEM2-CCS (HG2) *1D* and *10D* simulations and the AVHRR and SAGE-II observations. AVHRR data are only collected over the cloud-free global oceans and are based on the updated data of *Zhao et al.* [2013] (available from https://www.ncdc.noaa.gov/cdr/atmospheric/avhrr-aerosol-optical-thickness). For SAGE II, we use the updated gap-filled aerosol-extinction climatology developed for Chemistry-Climate Model Initiative simulations based on the SAGE_4λ method [*Arfeuille et al.*, 2013]. The SAGE_4λ data set uses observations from the Cryogenic Limb Array Etalon Spectrometer (CLAES) and Halogen Occultation Experiment instruments when SAGE II data are unavailable (*L. Thomason*, personal communication, 2016). To retrieve SAGE_4λ AODs, we integrate aerosol extinctions above the tropopause height, where the tropopause is derived from our HG2 simulations as in *Mills et al.* [2016]. For AVHRR, we subtract the monthly mean AODs from the year 1990 to calculate anomalies, which was the approach used by AQ12 and *Mills et al.* [2016]. For

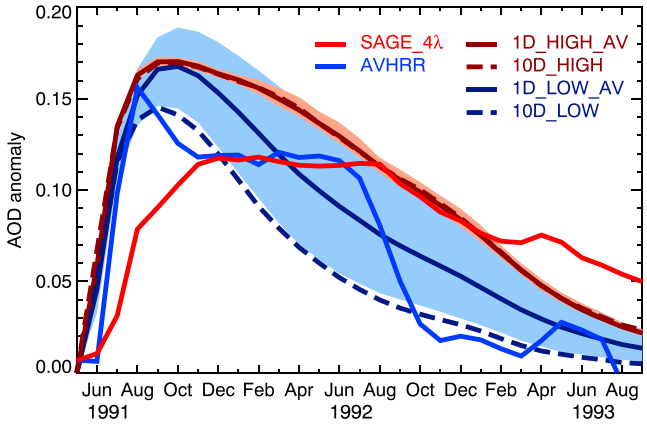

Figure 2. 75°S–75°N mean sulfate 550 nm AOD anomaly for the HadGEM2-CCS simulations and SAGE II (red) and AVHHR (blue) observations. The blue shaded area shows the range of the 1D_LOW ensemble; the orange shaded area shows the range of the 1D_HIGH ensemble.

HG2, we subtract the parallel AOD of the *CONTROL* simulation to calculate anomalies. The blue and orange shaded areas in Figure 2 show the range for the *1D_LOW* and *1D_HIGH* experiments, respectively. From Figure 2, it is clear that both the *1D_LOW_AV* and the *1D_HIGH_AV* AODs are initially in close agreement with the AVHRR values, with a peak in October 1991 of ~0.17 and exponential decline thereafter. As discussed by multiple authors, SAGE II was unable to capture the peak AOD for the first few months after Pinatubo due to saturation at AODs >0.15 [*Russell et al*., 1996]. Despite the integration of CLAES data with SAGE II data to overcome this saturation issue (*L. Thomason*, personal communication, 2016), the updated SAGE_4λ data set is still unable to capture the peak aerosol extinctions in the immediate aftermath of the eruption. However, the greater coverage of the SAGE II observations and the instrument's ability to detect lower AODs than AVHRR (<0.02) [*Stowe et al*., 1992] make it useful for later AOD values. In particular, from January 1992 the aerosol plume had diminished sufficiently for SAGE_4λ and AVHRR AODs to be similar on the global mean scale (Figure 2). A few aspects of the HG2 AODs in Figure 2 are salient: (1) *10D_LOW* is significantly less than *1D_LOW_AV* and peaks in September 1991 at ~0.145 rather than October 1991 with a peak of ~0.17; (2) the *1D_LOW* ensemble spread is broad, for instance, the maximum AOD in April 1992 is ~0.15 compared a minimum of ~0.065; and (3) the *1D_HIGH* ensemble spread is small, suggesting that the aerosol dispersion after a high-altitude SO_2 emission would be less sensitive to the ambient meteorology.

Figure S1 in the supporting information compares the global 550 nm sulfate AOD anomaly for the *3H_LOW* and *1D_LOW* simulations. It is clear that the 3 h and 1 day eruptions produce very similar AODs, both in terms of ensemble mean and the ensemble range. This result could be an artefact of our model; a better representation of the aerosol microphysics within the evolving aerosol plume might yield greater differences between the 3 h and 24 h eruption scenarios than shown here due to differing feedback between the aerosol and the meteorology. However, for the basis of this investigation and due to the similarity between the AOD evolutions, we present results from the aerosol dispersion from the *1D_LOW* simulations instead of the *3H_LOW* simulations for consistency with AQ12.

3.2. 10 day Eruption Against 1 Day Eruption Ensemble Mean

Figure 3 shows the time series of zonal mean AOD anomaly for the *10D* experiments and the ensemble means of the *1D* experiments and for SAGE_4λ and AVHRR observations. For the HG2 experiments, we use the zonal mean AOD over oceans from May 1991 to December 1991 for best comparison with AVHRR. The R^2 values given in Figure 3 for the HG2 AOD fields are calculated with respect to AVHRR from July to December 1991 and SAGE_4λ thereafter (Figure S2 shows the composite AVHRR/ SAGE_4λ field). R^2, the coefficient of determination, describes the proportion of the variance in the observations that can be explained by the model (ranging from 0 to 1, with higher values indicating better agreement) [*Legates and McCabe*, 1999]. While *1D_LOW_AV* captures the transport of aerosol into the SH as observed by SAGE II and AVHRR, the *10D_LOW* volcanic aerosol is entirely confined to the NH. It is clear from the R^2 values that *1D_LOW_AV* describes slightly more of the variability in the observations than *1D_HIGH_AV* (R^2 of 0.31 compared to 0.25) and that *1D_LOW_AV* is a much better fit to the observations than *10D_LOW*. The difference in AOD in the SH between *1D_LOW_AV* and the observations is partially attributable to the Cerro Hudson eruption in August 1991 at (46°S, 73°W), which injected 3.3 Tg [SO_2] into the stratosphere [*Deshler and Anderson-Sprecher*, 2006] and is not represented in these simulations. The Cerro Hudson aerosol was able to penetrate deep into the SH immediately (because of the volcano's location), while the Pinatubo aerosol was contemporaneously confined to the tropical vortex [*McCormick et al*., 1995; *Legrand and Wagenbach*, 1999]. We chose not to represent the Cerro Hudson eruption in these simulations as the primary purpose is to investigate the influence of meteorological variability on the evolution of the plume from Pinatubo from HG2. By omitting representation of Cerro Hudson, a "perfect" Pinatubo simulation would not produce $R^2=1$, because the AVHRR/ SAGE_4λ observations also include the Cerro Hudson aerosol. Therefore, R^2 as used in Figure 3 only provides an approximate measure of "goodness of fit" between the model and observations.

Figure 4 shows the equatorial SO_2 concentration anomaly plotted against altitude in September 1991 for *10D_HIGH*, *1D_HIGH_AV*, *10D_LOW*, and *1D_LOW_AV*. Observations from the Microwave Limb Sounder (MLS) [*Read et al*., 1993] are indicated by the black circles in Figure 4. It is clear that *1D_LOW_AV* best captures the peak of the SO_2 plume as observed by the MLS at ~22 hPa altitude. However, *1D_LOW_AV* overestimates the SO_2 concentrations at ~50 hPa compared to the MLS observations, which could be due to SO_2 removal processes that are not represented in the model such as deposition on ash or ice, or it could be due to the

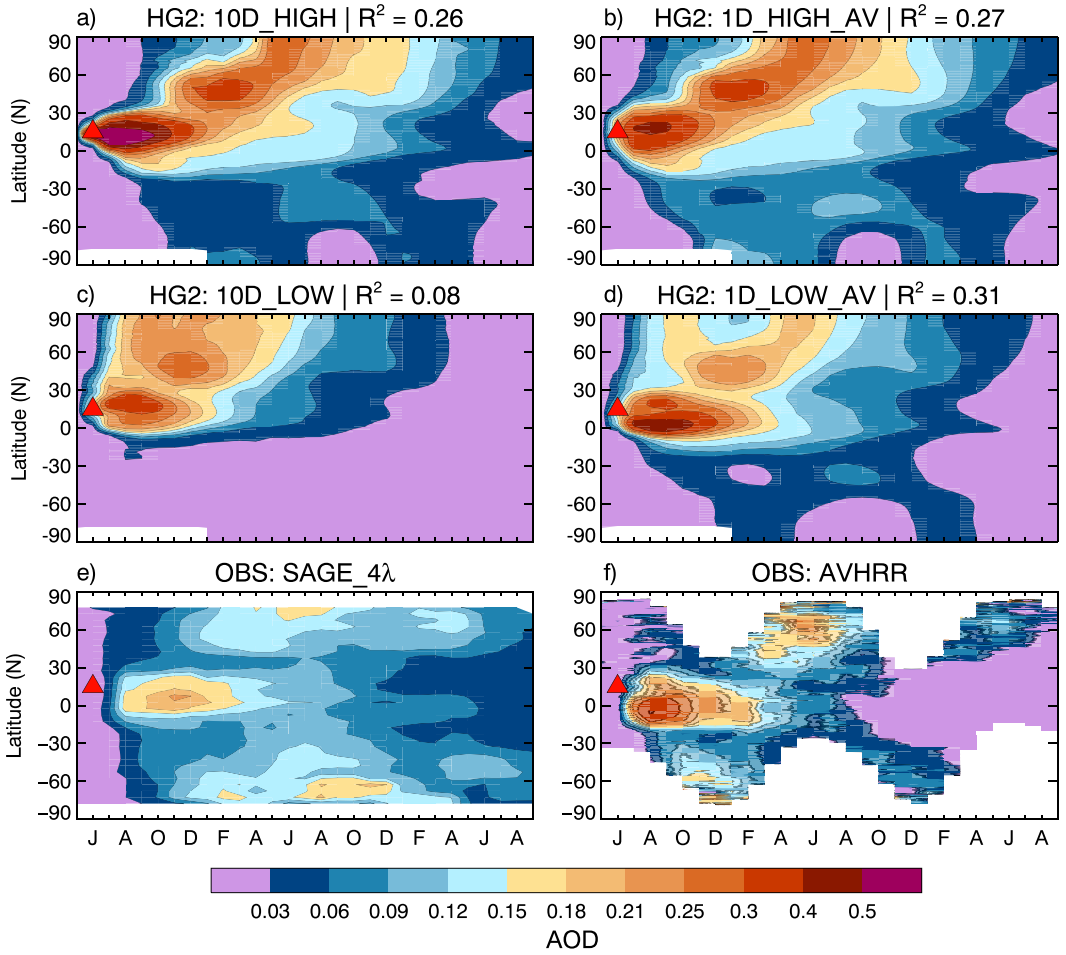

Figure 3. Latitude versus time plot of monthly/zonal mean sulfate 550 nm AOD anomaly for (a) 10D_HIGH, (b) 1D_HIGH_AV, (c) 10D_LOW, (d) 1D_LOW_AV, (e) SAGE II, and (f) AVHRR. The red triangles indicate the Pinatubo eruption.

fixed aerosol radius used here. The 14 Tg [SO_2] *HIGH* simulations fail to capture the peak of the SO_2 plume; however, the *HIGH* simulations do provide a better fit to the MLS observations at ~10 hPa than the *LOW* simulations. This suggests that our simulations of Pinatubo with HG2 are better represented by *LOW* than *HIGH* injection profiles although we recognize that the best representation of injection profile would be somewhat higher than *LOW* but considerably lower than *HIGH*. For the rest of this analysis, we focus on the *LOW* experiments as the *1D_LOW* ensemble mean provides the best fit to the observations such that that while *1D_LOW_AV* has a similar global mean AOD to *1D_HIGH_AV* (Figure 2), it has a better R^2 in the horizontal (Figure 3) and a better vertical SO_2 distribution when compared to observations (Figure 4).

From Figure 4, the *10D_LOW* SO_2 concentrations are much smaller than the Microwave Limb Sounder (MLS) measurements reported by *Read et al.* [1993] and peak at 40 hPa altitude rather than the ~25 hPa altitude from observations. Conversely, the *1D_LOW_AV* and most of the *1D_LOW* ensemble's SO_2 concentrations are similar to observations (e.g., ~14 ppbv at 22 hPa). Figure 5 shows the atmospheric zonal mean SO_4 mass mixing ratio anomalies for *1D_LOW_AV* and *10D_LOW* for July, September, November, and December 1991. From Figure 5, the sulfate reservoir in the tropics in July is at a higher altitude for *1D_LOW_AV* than for *10D_LOW* and closer to the equator; for instance, the peak mass mixing ratio anomaly (indicated by the dashed lines in Figure 5) in July for *1D_LOW_AV* is at 34 hPa, 4°N and for *10D_LOW* is at 41 hPa, 19°N. *Trepte and Hitchman* [1992] showed that aerosol in the lower tropical stratosphere (>40 hPa altitude) is rapidly transported toward high latitudes, while aerosol at higher altitudes (40–10 hPa altitude) is confined to the tropical pipe. By July, 3 Tg [S] of combined SO_2 and SO_4 has been transported to middle/high NH altitudes (>30°N) in *10D*, compared to 1.9 Tg [S] in *1D_LOW_AV* (Figure S3). The sulfate in the tropical reservoir in

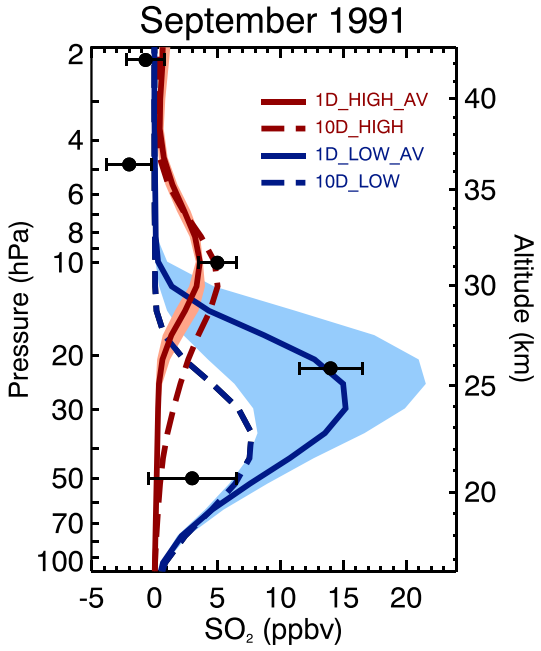

Figure 4. Equatorial (10°S–10°N) mean SO_2 concentration anomaly in September 1991 for 1D_HIGH_AV, 10D_HIGH, 1D_LOW_AV, and 10D_LOW. The black circles indicate Microwave Limb Sounder (MLS) observations as reported in *Read et al.* [1993] with corresponding horizontal lines indicating the standard error of the observations.

1D_LOW_AV is predominantly transported to the SH in the upper branch of the BDC (~30 hPa altitude) in September (Figure 5f), reaching the South Pole by November (Figure 5g), in line with observations [*Trepte et al.*, 1993]. However, the *10D_LOW* aerosol is only transported to the SH in a lower stratospheric pathway at ~100 hPa altitude (Figure 5d).

To explain the difference in meridional transport between *1D_LOW_AV* and *10D_LOW*, it is necessary to compare the radiative heating perturbations. Figure 6 shows (a) the initial clear-sky heating rate anomaly for the duration of the eruption (i.e., 10 days for *10D_LOW* and 1 day for *1D_LOW_AV*) at the eruption location, (b) the equatorial (5°S–5°N) temperature anomaly in July, and (c) the equatorial vertical velocity anomaly in July. The *1D_LOW* simulations clearly exhibit a greater radiative-heating perturbation than for *10D_LOW* (Figure 6a), which is due to the difference in initial mass loading of SO_2. Although the radiative properties of SO_2 are not represented in this model, the SO_4 plume, which immediately begins to form from oxidation of the volcanic SO_2, is also denser for *1D_LOW* than *10D_LOW*, thus inducing a greater radiative heating perturbation, which is counterbalanced by adiabatic cooling from enhanced vertical motion and by temperature tendencies (e.g., equation (3) in *Holton et al.* [1995]). This is exemplified by the greater equatorial heating (Figure 6b) and vertical velocity perturbation (Figure 6c) in *1D_LOW_AV* than *10D_LOW*. The *1D_LOW* aerosol is therefore "self-lofted" to higher altitudes than the *10D_LOW* aerosol and is concomitantly transported in the upper stratospheric pathway in the SH.

The peak aerosol burden anomaly in the *1D_LOW_AV* experiment is 5.8 Tg [S] (Figure S3), which falls within the observed uncertainty range of 3.7 to 6.7 Tg [S] given by *Dhomse et al.* [2014]. By December 1991, 40% of the 10 Tg [S] volcanic sulfur in *1D_LOW_AV* has been removed from the atmosphere. Figure S4 shows the relative contributions to the total sulfur deposition at the surface from the primary removal processes for the first 7 months after the eruption for *10D_LOW* and *1D_LOW_AV*. It is clear that the wet deposition of dissolved sulfate by large-scale precipitation events contributes the largest deposition of sulfur (~60 %), followed by convective scavenging of accumulation-mode sulfate (~25 %). SO_2 deposition by convective scavenging contributes ~4% of the total sulfur deposition, which decreases over time as SO_2 is oxidized to form sulfate.

3.3. "Day 1" Eruption Against "Day 10" Eruption

Figure 7 shows the zonal mean AOD evolution for the individual *1D_LOW* simulations. The first eight ensemble members show reasonable conformity with AVHRR/SAGE_4λ observations, which is quantitatively corroborated by their similar R^2 values (~0.3–0.5). However, the last two simulations (*1D_LOW_9* and *1D_LOW_10*) exhibit minimal transport of aerosol into the SH, in disagreement with the observations (reflected in R^2 values <0.1). The only difference between the simulations is the meteorology encountered by the aerosol plume. Figure S5 shows the zonal mean AOD evolution from AQ12's eight ensemble members (equivalent to our Figure 7). Despite the fact that the meteorology is independent of that in AQ12, we have obtained very similar results—for instance, the difference between their simulations Pin45act4d and Pin45act3d, with the latter showing a persistent NH aerosol plume, is similar to the difference between our *1D_LOW_1* and *1D_LOW_10*.

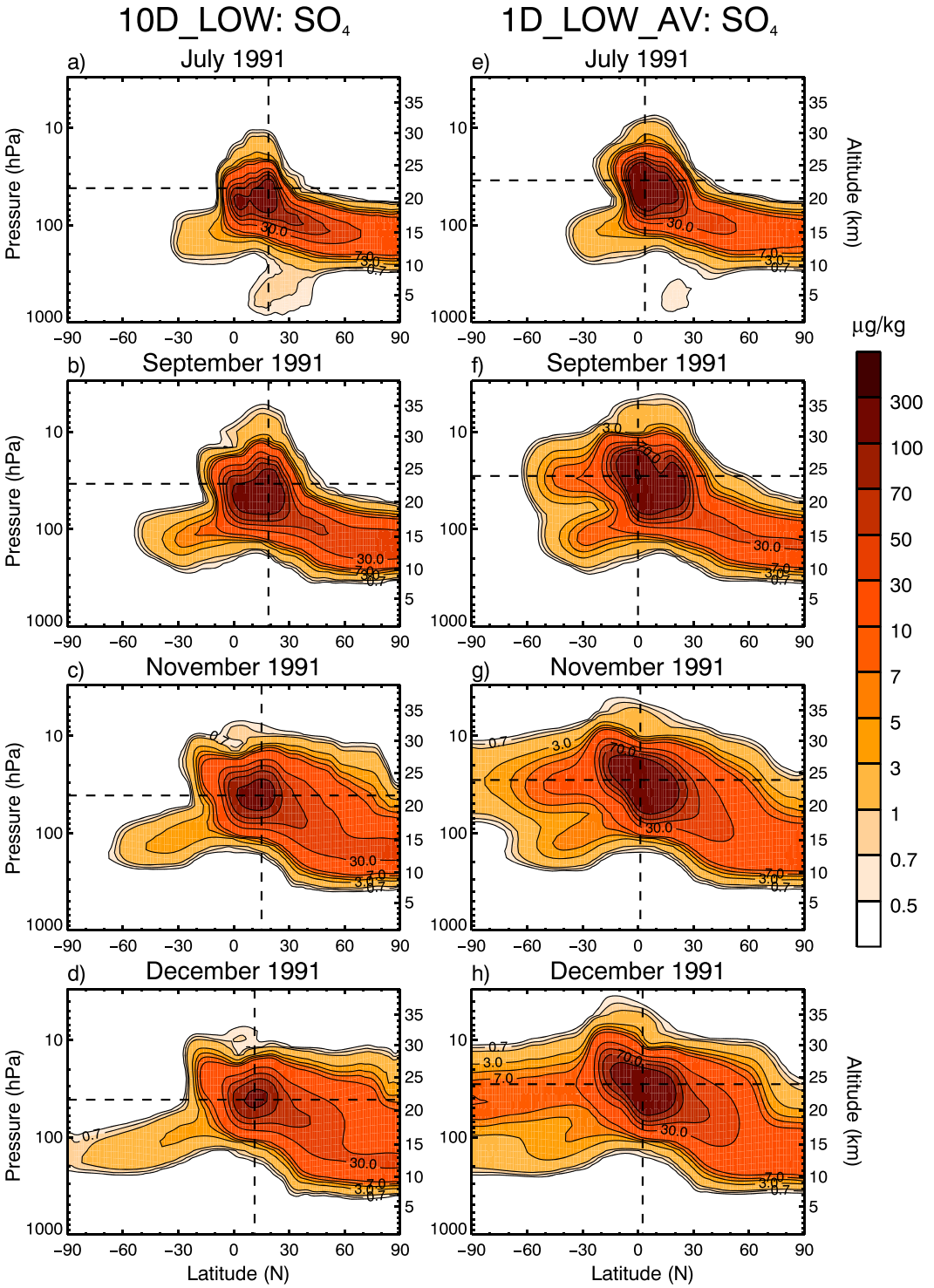

Figure 5. Latitude versus altitude plot of zonal mean sulfate mass concentration anomaly for 10D_LOW and 1D_LOW_AV.

Figure S6 shows the zonal mean AOD evolution for the *3H_LOW* simulations. It is clear that the individual *3H_LOW* simulations are very similar to their counterpart *1D_LOW* simulations; for instance, *1D_LOW_1* and *3H_LOW_1* have R^2 values of 0.50 and 0.48, respectively.

As mentioned in section 3.2, the absence of SH aerosol in the HG2 simulations could partially be attributed to the lack of representation of the Cerro Hudson (CH) eruption, which occurred on 15 August 1991. In order to

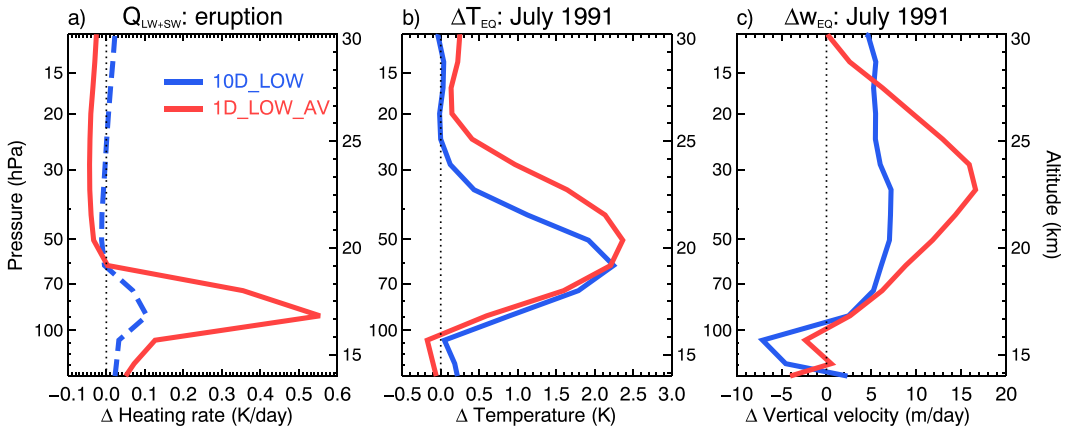

Figure 6. (a) Instantaneous clear-sky heating rate anomaly for the duration of the eruption at 15°N, 120°E, (b) July 1991 zonal mean temperature anomaly averaged between 5°S and 15°N, and (c) July 1991 zonal mean vertical velocity anomaly averaged between 5°S and 15°N.

assess the importance of the CH eruption on SH aerosol in the aftermath of the Pinatubo eruption, we have rerun the 1st and 10th *1D* ensemble members (*1D_LOW_1* and *1D_LOW_10*) with a CH-like eruption included. CH is represented by a 3.3 Tg [SO_2] injection, with SO_2 emitted uniformly between 11 and 16 km altitude from 04:00 to 12:00 on 1 August (2 months after Pinatubo) at 46°S, 73°W [*Schoeberl et al.*, 1993a; *Deshler and Anderson-Sprecher*, 2006]. Figure S7 shows the zonal mean 550 nm AOD evolution for the *1D_LOW_1 + CH* and *1D_LOW_10 + CH* experiments. It is clear that the inclusion of CH in the simulations has not significantly affected the AOD distribution; for instance, the R^2 values for the *1D_LOW_10* and *1D_LOW_10 + CH* experiments are the same (0.09).

Figure 8 shows the total sulfur ($SO_2 + SO_4$) column burden anomaly (g[S]/m^2) for the most disparate *1D_LOW* simulations, *1D_LOW_1* and *1D_LOW_10*, at intervals of 3, 7, 14, and 30 days after the initiation of the eruption (see also Movie S1 in the supporting information). The circled-arrows in Figure 8 show the direction of the

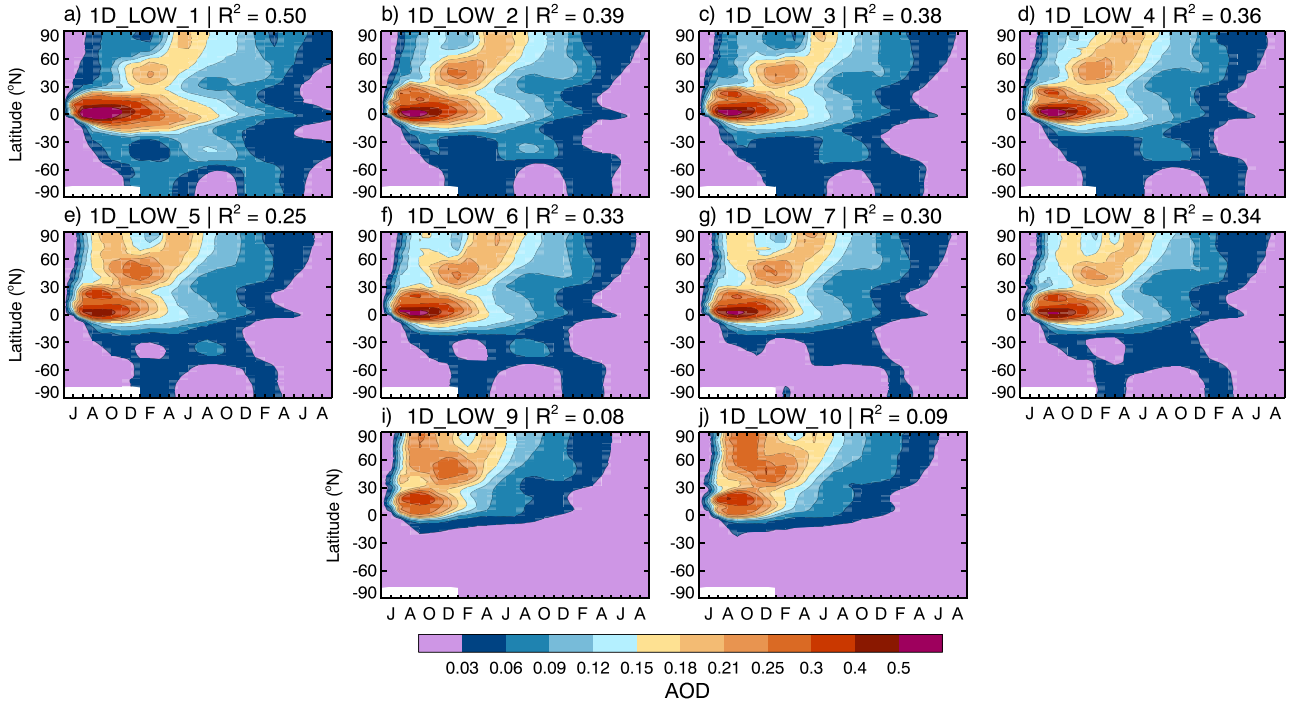

Figure 7. Latitude versus time plot of monthly/zonal mean sulfate 550 nm AOD anomaly for the 1D_LOW ensemble.

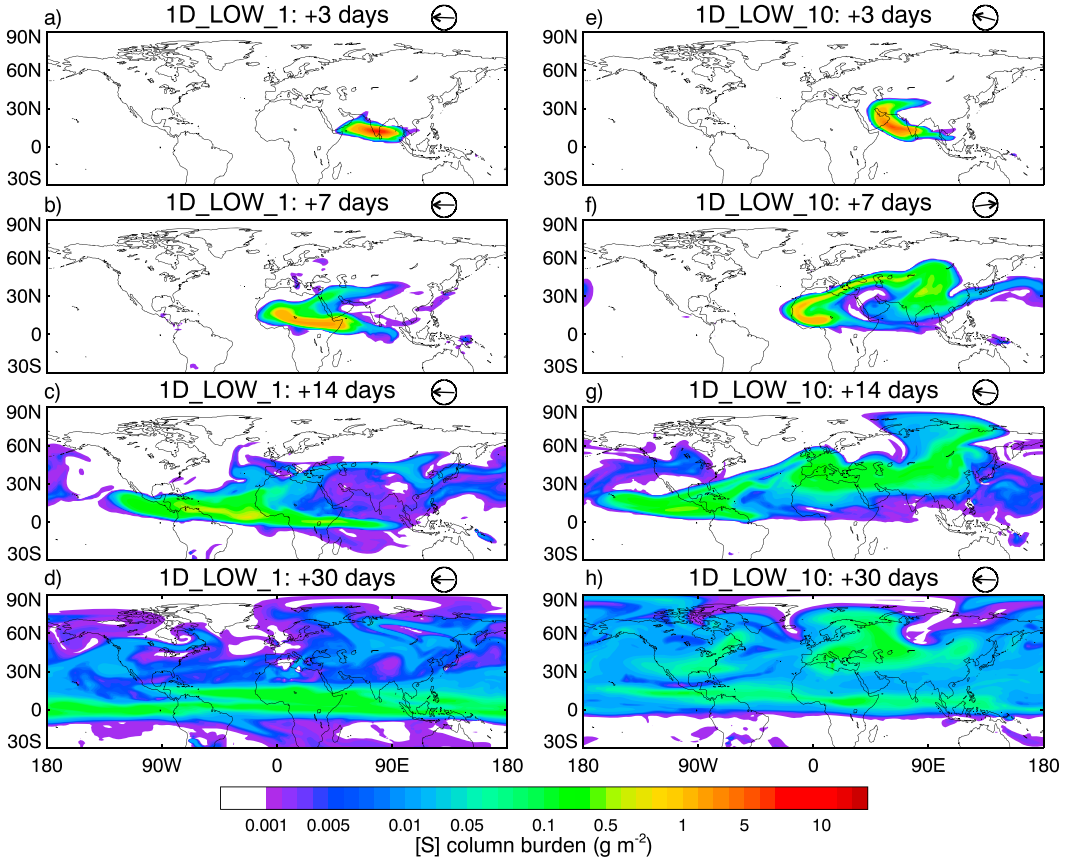

Figure 8. Sulfur ([S]) column burden anomaly for 1D_LOW_1 and 1D_LOW_10 for 3, 7, 14, and 30 days after the eruption. The circled arrows show the direction of the [S]-concentration-anomaly weighted wind vector $[\hat{u}, \hat{v}]$.

[S]-concentration-anomaly weighted wind vector. During the first 3 days following the eruption, the *1D_LOW_10* aerosol exhibits a more northward progression as indicated by the significant aerosol burden at 30°N in Figure 8e. The *1D_LOW_10* aerosol is advected northward by the prevailing southerly wind at ~45°E (Figure 8e), while the *1D_LOW_1* aerosol remains concentrated between 10°N and 20°N. The most dramatic difference in the [S]-weighted wind vector between *1D_LOW_1* and *1D_LOW_10* simulations occurs at day 7. Here *1D_LOW_1* indicates a continued progression westward in the easterly winds, while *1D_LOW_10* shows an almost complete reversal in the direction of advection owing to the influence of the anticyclone over Asia in this simulation. Figure 9 shows the 100 hPa wind vector superimposed on the 100 hPa wind speeds for *1D_LOW_1* and *1D_LOW_10*, evaluated 3 days after the eruption, and for ERA-interim reanalysis on 18 and 20 June 1991 [*Dee et al*., 2011]. It is clear that the northward advection of aerosol in *1D_LOW_10* is driven by the anticyclonic vortex centered over North India (30°N, 75°E) (Figure 9b), which is not present in *1D_LOW_1* at the equivalent time (Figure 9a). Although a similar southerly wind at ~45°E is present on 18 June in the reanalysis data (Figure 9c), it had dissipated by 20 June (Figure 9d). Anticyclogenesis over Asia in June is the result of warming over a region spanning Iraq to Tibet [*Yanai et al*., 1992], with anticyclonic anomalies then propagating eastward along the subtropical jet [*Watanabe and Yamazaki*, 2012] and eventually weakening by August [*Bourassa et al*., 2012]. *Bourassa et al*. [2012] suggested that an anticyclonic vortex over Asia was fundamental in the transport of the volcanic plume immediately after the 2011 Nabro (13°N, 41°E) eruption although these findings have been contested [*Fromm et al*., 2014]. What is clear is that the precise meteorological conditions that prevail during the eruption strongly influence the poleward progression of the aerosol. From Figures 8 and 9 we have shown that the aerosol transport out of the tropics is inextricably linked to the ambient wind direction, with the *1D_LOW_1* aerosol encountering a zonally dominant transport regime (Figure 8a). As a result, by day 30 the *1D_LOW_1* aerosol is primarily confined to the tropics (Figure 8d)

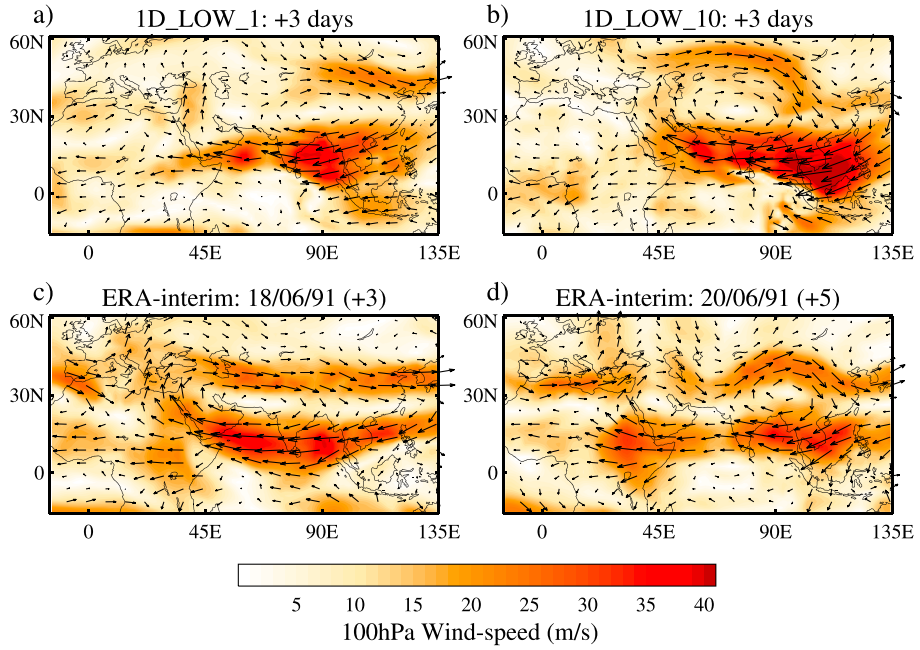

Figure 9. 100 hPa horizontal wind vector plotted on 100 hPa horizontal wind speed for (a) 1D_1 eruption + 3 days, (b) 1D_10 eruption + 3 days, (c) ERA-Interim 18 June 1991, and (d) ERA-Interim 20 June 1991 [*Dee et al.*, 2011].

at altitudes of ~40 hPa, while the *1D_LOW_10* aerosol is primarily confined to the NH (Figure 8h). Consequently, *1D_LOW_1* aerosol is transported into the SH within the upper branch of the BDC (Figure S8). By January 1992, 0.54 Tg [S] of combined SO_2 and SO_4 has been transported to the SH in *1D_LOW_1*, compared to 0.1 Tg [S] in *1D_LOW_10* (Figure S9).

3.4. Potential Climatic Consequences

The spatial distribution of the volcanic aerosol has important implications for the resultant climate impacts. *Haywood et al.* [2013] showed that hemispherically asymmetrical aerosol forcing is causally related to the displacement of the Intertropical Convergence Zone (ITCZ). For instance, the twentieth century NH volcanic eruptions of Novarupta-Katmai (June 1912) and El Chichón (March–April 1982) produced peak sulfate AOD hemispheric-asymmetries ($AOD_{NH\text{-}SH}$) of 0.08 and 0.07, respectively [*Sato et al.*, 1993; *Haywood et al.*, 2013], resulting in significant negative Sahelian precipitation anomalies in the subsequent year. In contrast, Pinatubo produced a peak $AOD_{NH\text{-}SH}$ of 0.04 and no significant shift in the ITCZ [*Haywood et al.*, 2013], although precipitation is generally suppressed subsequent to large volcanic eruptions owing to reductions in surface irradiances leading to reductions in latent heat fluxes and a slowing down of the hydrological cycle [*Trenberth and Dai*, 2007]. In these experiments, *1D_LOW_1* produces a peak $AOD_{NH\text{-}SH}$ of 0.05, which is close to the Pinatubo observations, while *1D_LOW_10* produces a peak $AOD_{NH\text{-}SH}$ of 0.10, which exceeds the observed $AOD_{NH\text{-}SH}$ for Novarupta-Katmai and El Chichón. Figure 10 shows the SW radiative flux anomalies at the tropopause for *1D_LOW_1* and *1D_LOW_10*, averaged over the two complete calendar years (January–December) following the eruption. The SW forcing is more spatially uniform for *1D_LOW_1* than for *1D_LOW_10*, which is a direct result of the location of the aerosol plume. For instance, the SW forcing in *1D_LOW_10* in the SH is negligible ($-0.25\ W/m^2$), while the SW forcing in the NH is significant ($-4.1\ W/m^2$). The standard deviation of the NH (30°N–90°N) mean net SW flux at the tropopause in the control simulation is 0.26; therefore, this SW forcing is significant at the 2σ level.

The aerosol burden in the tropical reservoir has implications for stratospheric dynamics and therefore stratospheric ozone concentrations [*Aquila et al.*, 2014]. Stratospheric sulfate aerosols provide surfaces for heterogeneous reactions between free radicals and ozone, which can result in ozone depletion [*Aquila et al.*, 2013]. Additionally, tropical stratospheric warming due to LW and near-infrared absorption within the aerosol layer would increase the local upwelling velocity and transport ozone-poor air in the lower stratosphere to higher

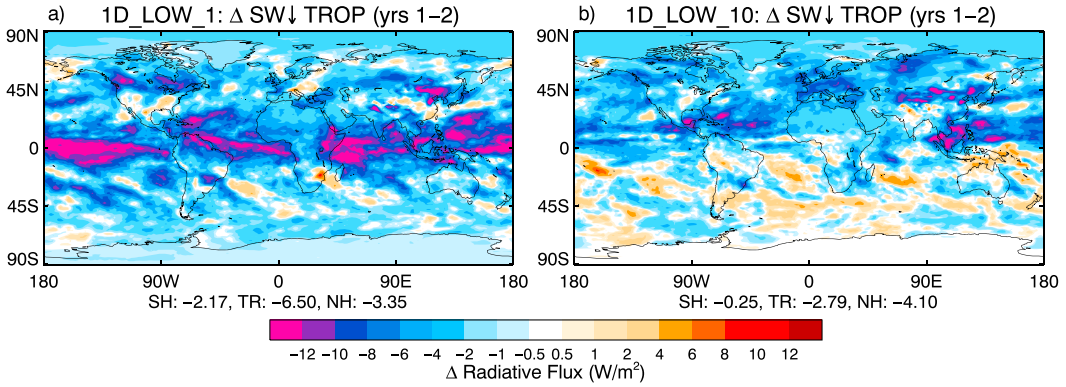

Figure 10. Tropopause short-wave net-downward radiation anomaly for 1D_LOW_1 and 1D_LOW_10 simulations averaged over two subsequent years following the eruption.

altitudes where ozone is more easily destroyed [*Schoeberl et al.*, 1993b]. Figure S10 shows the equatorial zonal mean wind perturbation for *1D_LOW_1*, *1D_LOW_10*, *1D_LOW_AV*, and *10D_LOW*. Tropical stratospheric aerosols promote a prolonged westerly QBO phase [*Aquila et al.*, 2014]. The greater tropical sulfate reservoir in *1D_LOW_1* causes a delay to the downward propagation of the easterly winds, which is exemplified by the positive (westerly) anomaly in *1D_LOW_1* at ~40 hPa following the eruption (Figure S10). *Labitzke* [1994] reports that after Pinatubo observations showed a warming of the lower stratosphere of about 3 K and a delay in the downward propagation of the easterly winds. Figure S11 shows the equatorial zonal mean zonal wind profiles for the Control and *1D_LOW_1* simulations. QBO phase changes are indicated in Figure S11 by the vertical black lines along 40 hPa altitude (where the QBO phase is defined by the zonal wind direction at 40 hPa) [*Baldwin et al.*, 2001]. From Figure S11, the first QBO phase change following Pinatubo is delayed by 1–2 months in the *1D_LOW_1* eruption compared to the control. Additionally, the significant aerosol concentration anomaly at the South Pole in November 1991 for *1D_LOW_1* (Figure 5c) would enhance heterogeneous ozone chemistry within the Antarctic vortex, as observed after the Pinatubo eruption [*McCormick et al.*, 1995].

4. Discussion

We have shown that the dispersion of volcanic aerosol can be highly sensitive to the ambient meteorology, with this sensitivity dependent on the altitude of SO_2 emission. While simulations using the 20 Tg [SO_2] *LOW* injection scenarios show a lot of sensitivity to meteorological conditions, simulations using the 14 Tg [SO_2] *HIGH* scenarios show little sensitivity. While it is difficult to determine whether the 20 Tg [SO_2] *LOW* or the 14 Tg [SO_2] HIGH simulations provide simulations that are more consistent with observations from global mean assessments of the AOD alone, assessment of the spatial distribution in both the horizontal and vertical suggests that, for our modeling study at least, members of the 20 Tg [SO_2] *LOW* ensemble are most consistent with observations. We find that the mean of the ten 1 day eruptions, where 20 Tg [SO_2] is emitted between 16 and 18 km altitude, provides a reasonable consistency with observations, but there is significant variability between the ensemble members. This variability is related to anomalous anticyclonic activity along the subtropical jet, which affects the "leakiness" of the tropical pipe and therefore the amount of aerosol that is retained within the tropical reservoir. We have discussed the implications of our results with respect to resultant climate changes, for instance, the possible effects of hemispherically asymmetric aerosol burdens on Sahelian precipitation, but note that a GCM with an interactive ocean model would be needed to comprehensively evaluate the climatic impacts of the different Pinatubo realizations. We have also compared the aerosol dispersion from a simulated 10 day eruption with the ensemble mean of the ten 1 day eruptions. These simulation designs represent two intuitive methods of overcoming the problem of variable meteorology. We have shown that the 10 day eruption is unable to produce the radiative heating and concomitant aerosol self-lofting required to transport aerosol to the SH; hence, the resultant spatial distribution of sulfate AOD compares inadequately to observations (Figure 3c). In contrast, the 1 day ensemble mean AOD anomaly is much closer to observations (Figure 3d); therefore, performing a 1 day eruption ensemble presents a better

solution to overcoming variable meteorology. However, the intraensemble variability in the *1D_LOW* experiments is significant; for instance, *1D_LOW_9* and *1D_LOW_10* fail to capture the SH transport of aerosol observed after Pinatubo (Figures 7i and 7j). Assuming that the *1D_LOW* results represent the complete set of possible realizations of the Pinatubo eruption, this would mean a 20% chance of obtaining a "failed" simulation for the specific goal of obtaining SH transport.

We have also performed simulations in which 20 Tg [SO_2] is emitted within a 3 h span between 16 and 18 km altitude (*3H_LOW*). The 3 h duration was selected to represent the cataclysmic Pinatubo eruption that occurred on 15 June 1991 [*Holasek et al*., 1996]. We find that our results from a 24 h period are equivalent to those from a 3 h eruption. However, we qualify this result by noting the limitations of the aerosol microphysics scheme employed here, which only consists of two sulfate size modes. Additionally, SO_2 is not the only substance emitted by volcanic eruptions—volcanic ash is co-emitted and would very likely change the heating rates due to the predominance of coarse mode aerosols [e.g., *Niemeier et al*., 2009] that are effective absorbers of infrared radiation. We have also performed simulations in which the Cerro Hudson eruption that occurred on 15 August 1991 is represented by a 3.3 Tg [SO_2] injection between 11 and 15 km altitude at (46°S, 73°W), in an eruption that lasts 8 h. We find little difference in zonal mean AOD between simulations with and without the Cerro Hudson eruption (Figure S7).

Our results are conditional on the selected specifications of the eruption and the specifications of HadGEM2-CCS. For instance, we have shown that the aerosol dispersion after a high-altitude SO_2 emission scenario (19–29 km) is substantially less sensitive to the existing meteorological state, which is due to the limited meteorological variability in the middle stratosphere. It is therefore imperative to precisely identify the initial location of the volcanic plume in order to accurately model the concomitant aerosol transport. An eruption during a different month might also avoid the variability associated with the Asian anticyclone, which is a seasonal (June–August) phenomenon [*Park et al*., 2007], and an eruption during a different QBO phase would alter the permeability of the tropical pipe [*Trepte et al*., 1993]. Additionally, the representation of sulfate aerosol in HadGEM2-CCS is limited to two hygroscopic modes with fixed dry-mode radii [*Bellouin et al*., 2007]. Observations from the post-Pinatubo era showed that the global sulfate size distribution continued to grow for 1.5 years after the eruption to attain effective radii of approximately 0.6–0.8 μm [*Stenchikov et al*., 1998; *Russell et al*., 1996], whereas the accumulation-mode aerosol in these simulations is fixed at a geometric mean radius of a lognormal mode of 0.376 μm. Larger particles experience greater fall velocities [*Rasch et al*., 2008] and absorb more efficiently in the LW and near-infrared spectrum and scatter less efficiently in the SW spectrum. Our model might therefore underestimate the gravitational sedimentation rates and LW heating rates exhibited by the volcanic aerosol. Inevitably, the sea surface temperature and meteorological state in our simulations are unrelated to the observed post-Pinatubo conditions. Our simulations therefore include a subset of possible meteorological conditions that could be encountered by a volcanic-aerosol plume, conditions which would also differ with season and latitude of eruption. For interest, the ongoing model intercomparison project VolMIP (http://volmip.org/experiments.html) also selected to use preindustrial baseline conditions for their eruption simulations. VolMIP's VolLongS60EQ scenario is comparable in design to our simulations (but with a significantly greater SO_2 emission of 100 Tg); therefore a direct evaluation of the aerosol plume evolution in that scenario could prove elucidative. One final caveat is that we prescribed ozone concentrations for the duration of these simulations; therefore, the model excludes simulation of the ozone changes from heterogeneous reactions on the aerosol surfaces (and the resultant feedback) such as observed after Pinatubo [*McCormick et al*., 1995]. We believe that these caveats, however, do not alter the primary result of this research: that volcanic aerosol plume evolution can be highly sensitive to the existing meteorological state.

With the improved representation of stratospheric aerosol in climate models, it is tempting to suggest that the models might disregard the imposition of climatologies of stratospheric aerosol concentrations in favor of simply injecting SO_2 and relying on the aerosol scheme to provide sulfate aerosol concentrations that are self-consistent with the meteorology. However, the extreme variability evidenced by the factor of 2 difference between the AOD in the *1D_LOW_1* and *1D_LOW_10* scenarios (Figure 2) suggests that the meteorological variability may compromise results: studies may "get lucky" and represent a particular volcanic eruption with reasonable fidelity, but they may not. Indeed, the chances of successfully representing all significant volcanic eruptions in the twentieth century (Novarupta-Katmai, Agung (March, May 1963), El Chichón, and Pinatubo) can be estimated from our statistics as around 0.8^4 or ~0.4, indicating that the chances of simulating all

volcanoes with reasonable fidelity is less than 50:50. Our results also suggest that simply averaging by simulating a multiple-day eruption cannot represent the heating rates in the atmosphere and hence correctly model aerosol-dispersion. Our study suggests that centennial scale modeling such as the CMIP6 "deck" may wish to stick to tried and tested climatological stratospheric aerosol concentrations. Our study also suggests that future climate model simulations should account for meteorological variability when simulating volcanic eruptions.

Author Contribution

ACJ designed and performed the simulations and wrote the paper with assistance from all co-authors. Additionally, AJ provided the model configuration and VA provided the SAGE II/AVHRR data and supporting information.

Acknowledgments

A.C.J. was funded by a NERC/CASE PhD studentship (ref. 580 009 138, with CASE partner being the Met Office); J.M.H. and A.J. were supported by the Joint UK DECC/Defra Met Office Hadley Centre Climate Programme (GA01101). The authors would like to thank Larry Thomason for supplying the SAGE II data. Data are freely available by contacting A.C.J. (anthony.jones@metoffice.gov.uk)

References

Aquila, V., L. D. Oman, R. S. Stolarski, P. R. Colarco, and P. A. Newman (2012), Dispersion of the volcanic sulfate cloud from a Mount Pinatubo-like eruption, *J. Geophys. Res.*, *117*, D06216, doi:10.1029/2011JD016968.

Aquila, V., L. D. Oman, R. Stolarski, A. R. Douglass, and P. A. Newman (2013), The response of ozone and nitrogen dioxide to the eruption of Mt. Pinatubo at southern and northern midlatitudes, *J. Atmos. Sci.*, *70* (3), 894–900, doi:10.1175/JAS-D-12-0143.1.

Aquila, V., C. I. Garfinkel, P. A. Newman, L. D. Oman, and D. W. Waugh (2014), Modifications of the quasi-biennial oscillation by a geoengineering perturbation of the stratospheric aerosol layer, *Geophys. Res. Lett.*, *41*, 1738–1744, doi:10.1002/2013GL058818.

Arfeuille, F., B. P. Luo, P. Heckendorn, D. Weisenstein, J. X. Sheng, E. Rozanov, M. Schraner, S. Brönnimann, L. W. Thomason, and T. Peter (2013), Modeling the stratospheric warming following the Mt. Pinatubo eruption: uncertainties in aerosol extinctions, *Atmos. Chem. Phys.*, *13*(22), 11,221–11,234, doi:10.5194/acp-13-11221-2013.

Baldwin, M. P., et al. (2001), The quasi-biennial oscillation, *Rev. Geophys.*, *39*(2), 179–229, doi:10.1029/1999RG000073.

Bellouin, N., O. Boucher, J. Haywood, C. Johnson, A. Jones, J. Rae, and S. Woodward (2007), Improved representation of aerosols for HadGEM2, Tech. Note 73, Hadley Centre, Met Office, Exeter, U. K., 42 pp. [Available at http://www.metoffice.gov.uk/media/pdf/8/f/HCTN_73.pdf (last accessed 01/16).]

Bellouin, N., J. Rae, A. Jones, C. Johnson, J. Haywood, and O. Boucher (2011), Aerosol forcing in the Climate Model Intercomparison Project (CMIP5) simulations by HadGEM2-ES and the role of ammonium nitrate, *J. Geophys. Res.*, *116*, D20206, doi:10.1029/2011JD016074.

Bluth, G. J. S., S. D. Doiron, C. C. Schnetzler, A. J. Krueger, and L. S. Walker (1992), Global tracking of the SO2 clouds from the June, 1991 Mount Pinatubo eruptions, *Geophys. Res. Lett.*, *19*(2), 151–154, doi:10.1029/91GL02792.

Bourassa, A. E., A. Robock, W. J. Randel, T. Deshler, L. A. Rieger, N. D. Lloyd, E. J. Llewellyn, and D. A. Degenstein (2012), Large volcanic aerosol load in the stratosphere linked to Asian monsoon transport, *Science*, *337*(6090), 78–81, doi:10.1126/science.1219371.

Boville, B. A., J. R. Holton, and P. W. Mote (1991), Simulation of the Pinatubo aerosol cloud in general circulation model, *Geophys. Res. Lett.*, *18*(12), 2281–2284, doi:10.1029/91GL02778.

Choi, W., W. B. Grant, J. H. Park, K.-M. Lee, H. Lee, and J. M. Russell III (1998), Role of the quasi-biennial oscillation in the transport of aerosols from the tropical stratospheric reservoir to midlatitudes, *J. Geophys. Res.*, *103*, 6033–6042, doi:10.1029/97JD03118.

Cionni, I., V. Eyring, J. F. Lamarque, W. J. Randel, D. S. Stevenson, F. Wu, G. E. Bodeker, T. G. Shepherd, D. T. Shindell, and D. W. Waugh (2011), Ozone database in support of CMIP5 simulations: Results and corresponding radiative forcing, *Atmos. Chem. Phys.*, *11*, 11,267–11,292, doi:10.5194/acp-11-11267-2011.

Dee, D. P., et al. (2011), The ERA-Interim reanalysis: Configuration and performance of the data assimilation system, *Q. J. R. Meteorol. Soc.*, *137*, 553–597, doi:10.1002/qj.828.

Deshler, T., and R. Anderson-Sprecher (2006), Non-volcanic stratospheric aerosol trends: 1971–2004, in *Assessment of Stratospheric Aerosol Properties*, edited by L. Thomason and T. Peter WCRP 124, WMO/TD 1295, SPARC Rep. 4, chap. 5, pp. 177–218, World Meteorol. Organ., Geneva, Switz.

Dhomse, S. S., et al. (2014), Aerosol microphysics simulations of the Mt. Pinatubo eruption with the UM-UKCA composition-climate model, *Atmos. Chem. Phys.*, *14*, 11,221–11,246, doi:10.5194/acp-14-11221-2014.

Driscoll, S., A. Bozzo, L. J. Gray, A. Robock, and G. Stenchikov (2012), Coupled Model Intercomparison Project 5 (CMIP5) simulations of climate following volcanic eruptions, *J. Geophys. Res.*, *117*, D17105, doi:10.1029/2012JD017607.

Edwards, J. M., and A. Slingo (1996), Studies with a flexible new radiation code. I: Choosing a configuration for a large-scale model, *Q. J. R. Meteorol. Soc.*, *122*, 689–719.

English, J. M., O. B. Toon, and M. J. Mills (2013), Microphysical simulations of large volcanic eruptions: Pinatubo and Toba, *J. Geophys. Res. Atmos.*, *118*, 1880–1895, doi:10.1002/jgrd.50196.

Fromm, M., G. Kablick III, G. Nedoluha, E. Carboni, R. Grainger, J. Campbell, and J. Lewis (2014), Correcting the record of volcanic stratospheric aerosol impact: Nabro and Sarychev Peak, *J. Geophys. Res. Atmos.*, *119*, 10,343–10,364, doi:10.1002/2014JD021507.

Gray, L. J., A. A. Scaife, D. M. Mitchell, S. Osprey, S. Ineson, S. Hardiman, N. Butchart, J. Knight, R. Sutton, and K. Kodera (2013), A lagged response to the 11 year solar cycle in observed winter Atlantic/European weather patterns, *J. Geophys. Res. Atmos.*, *118*, 13,405–13,420, doi:10.1002/2013JD020062.

Guo, S., G. S. Bluth, W. I. Rose, I. M. Watson, and A. J. Prata (2004), Re-evaluation of the SO2 release of the 15 June 1991 Pinatubo eruption using ultraviolet and infrared satellite sensors, *Geochem. Geophys. Geosyst.*, *5*, Q04001, doi:10.1029/2003GC000654.

Hansen, J., A. Lacis, R. Reudy, and M. Sato (1992), Potential climate impact of Mount Pinatubo eruption, *Geophys. Res. Lett.*, *19*(2), 215–218, doi:10.1029/91GL02788.

Hardiman, S. C., N. Butchart, T. J. Hinton, S. M. Osprey, and L. J. Gray (2012), The effect of a well-resolved stratosphere on surface climate: Differences between CMIP5 simulations with high and low top versions of the Met Office climate model, *J. Clim.*, *25*, 7083–7099, doi:10.1175/JCLI-D-11-00579.1.

Haywood, J. M., et al. (2010), Observations of the eruption of the Sarychev volcano and simulations using the HadGEM2 climate model, *J. Geophys. Res.*, *115*, D21212, doi:10.1029/2010JD014447.

Haywood, J. M., A. Jones, N. Bellouin, and D. Stephenson (2013), Asymmetric forcing from stratospheric aerosol impacts Sahelian rainfall, *Nat. Clim. Change*, *3*, 660–665, doi:10.1038/nclimate1857.

Hofmann, D. J., S. J. Oltmans, J. M. Harris, S. Solomon, T. Deshler, and B. J. Johnson (1992), Observation and possible causes of new ozone depletion in Antarctica in 1991, *Nature*, *359*, 283–287, doi:10.1038/359283a0.

Holasek, R. E., S. Self, and A. W. Woods (1996), Satellite observations and interpretation of the 1991 Mount Pinatubo eruption plumes, *J. Geophys. Res.*, *101*(B12), 27,635–27,655, doi:10.1029/96JB01179.

Holton, J. R., P. H. Haynes, M. E. McIntyre, A. R. Douglass, R. B. Rood, and L. Pfister (1995), Stratosphere-troposphere exchange, *Rev. Geophys.*, *33*(4), 403–439, doi:10.1029/95RG02097.

Jackson, L. S., J. A. Crook, A. Jarvis, D. Leedal, A. Ridgwell, N. Vaughan, and P. M. Forster (2015), Assessing the controllability of Arctic sea ice extent by sulfate aerosol geoengineering, *Geophys. Res. Lett.*, *42*, 1223–1231, doi:10.1002/2014GL062240.

Jones, A. C., J. M. Haywood, and A. Jones (2016), Climatic impacts of stratospheric geoengineering with sulfate, black carbon and titania injection, *Atmos. Chem. Phys.*, *16*(5), 2843–2862, doi:10.5194/acp-16-2843-2016.

Jones, C. D., et al. (2011), The HadGEM2-ES implementation of CMIP5 centennial simulations, *Geosci. Model Dev.*, *4*, 543–570, doi:10.5194/gmd-4-543-2011.

Kirchner, I., G. L. Stenchikov, H.-F. Graf, A. Robock, and J. C. Antuña (1999), Climate model simulation of winter warming and summer cooling following the 1991 Mount Pinatubo volcanic eruption, *J. Geophys. Res.*, *104*(D16), 19,039–19,055, doi:10.1029/1999JD900213.

Labitzke, K. (1994), Stratospheric temperature changes after the Pinatubo eruption, *J. Atmos. Terr. Phys.*, *56*(9), 1027–1034, doi:10.1016/0021-9169(94)90039-6.

Labitzke, K., and M. P. McCormick (1992), Stratospheric temperature increases due to Pinatubo aerosols, *Geophys. Res. Lett.*, *19*(2), 207–210, doi:10.1029/91GL02940.

Legates, D. R., and G. J. McCabe Jr. (1999), Evaluating the use of "goodness-of-fit" measures in hydrologic and hydroclimatic model validation, *Water Resour. Res.*, *35*(1), 233–241, doi:10.1029/1998WR900018.

Legrand, M., and D. Wagenbach (1999), Impact of the Cerro Hudson and Pinatubo volcanic eruptions on the Antarctic air and snow chemistry, *J. Geophys. Res.*, *104*(D1), 1581–1596, doi:10.1029/1998JD100032.

Martin, G. M., M. A. Ringer, V. D. Pope, A. Jones, C. Dearden, and T. J. Hinton (2006), The physical properties of the atmosphere in the new Hadley Centre Global Environmental Model, HadGEM1. Part 1: Model description and global climatology, *J. Clim.*, *19*(7), 1274–1301, doi:10.1175/JCLI3636.1.

Martin, G. M., et al. (2011), The HadGEM2 family of Met Office Unified Model climate configurations, *Geosci. Model Dev.*, *4*, 723–757, doi:10.5194/gmd-4-723-2011.

McCormick, M. P., and R. E. Veiga (1992), SAGE II measurements of early Pinatubo aerosols, *Geophys. Res. Lett.*, *19*(2), 155–158, doi:10.1029/91GL02790.

McCormick, M. P., L. W. Thomason, and C. R. Trepte (1995), Atmospheric effects of the Mt Pinatubo eruption, *Nature*, *373*, 399–404, doi:10.1038/373399a0.

Mills, M. J., et al. (2016), Global volcanic aerosol properties derived from emissions, 1990–2014, using CESM1(WACCM), *J. Geophys. Res. Atmos.*, *121*, 2332–2348, doi:10.1002/2015JD024290.

Mitchell, D. M., S. M. Osprey, L. J. Gray, N. Butchart, S. C. Hardiman, A. J. Charlton-Perez, and P. Watson (2012), The effect of climate change on the variability of the Northern Hemisphere stratospheric polar vortex, *J. Atmos. Sci.*, *69*, 2609–2618, doi:10.1175/JAS-D-12-021.1.

Niemeier, U., C. Timmreck, H.-F. Graf, S. Kinne, S. Rast, and S. Self (2009), Initial fate of fine ash and sulfur from large volcanic eruptions, *Atmos. Chem. Phys.*, *9*, 9043–9057, doi:10.5194/acp-9-9043-2009.

Oman, L., A. Robock, G. Stenchikov, T. Thordarson, D. Koch, D. Shindell, and C. Gao (2006), Modeling the distribution of the volcanic aerosol cloud from the 1783 Laki Eruption, *J. Geophys. Res.*, *111*, D12209, doi:10.1029/2005JD006899.

Park, M., W. J. Randel, A. Gettelman, S. T. Massie, and J. H. Jiang (2007), Transport above the Asian summer monsoon anticyclone inferred from Aura Microwave Limb Sounder tracers, *J. Geophys. Res.*, *112*, D16309, doi:10.1029/2006JD008294.

Pudykiewicz, J. A., and A. P. Dastoor (1995), On numerical simulation of the global distribution of sulfate aerosol produced by a large volcanic eruption, *J. Clim.*, *8*, 464–473, doi:10.1175/1520-0442(1995)008<0464:ONSOTG>2.0.CO;2.

Rasch, P. J., P. J. Crutzen, and D. B. Coleman (2008), Exploring the geoengineering of climate using stratospheric sulfate aerosols: The role of particle size, *Geophys. Res. Lett.*, *35*, L02809, doi:10.1029/2007GL032179.

Read, W. G., L. Froidevaux, and J. W. Waters (1993), Microwave Limb Sounder measurement of stratospheric SO2 from the Mt. Pinatubo volcano, *Geophys. Res. Lett.*, *20*(12), 1299–1302, doi:10.1029/93GL00831.

Robock, A. (2000), Volcanic eruptions and climate, *Rev. Geophys.*, *38*(2), 191–219, doi:10.1029/1998RG000054.

Robock, A., and J. Mao (1995), The volcanic signal in surface temperature observations, *J. Clim.*, *8*, 1086–1103.

Russell, P. B., et al. (1996), Global to microscale evolution of the Pinatubo volcanic aerosol derived from diverse measurements and analyses, *J. Geophys. Res.*, *101*(D13), 18,745–18,763, doi:10.1029/96JD01162.

Sato, M., J. E. Hansen, M. P. McCormick, and J. B. Pollack (1993), Stratospheric aerosol optical depth, 1850–1990, *J. Geophys. Res.*, *98*, 22,987–22,994, doi:10.1029/93JD02553.

Schoeberl, M. R., S. D. Doiron, L. R. Lait, P. A. Newman, and A. J. Krueger (1993a), A simulation of the Cerro Hudson SO_2 cloud, *J. Geophys. Res.*, *98*(D2), 2949–2955, doi:10.1029/92JD02517.

Schoeberl, M. R., P. K. Bhartia, and E. Hilsenrath (1993b), Tropical ozone loss following the eruption of Mt. Pinatubo, *Geophys. Res. Lett.*, *20*(1), 29–32, doi:10.1029/92GL02637.

Self, S., R. Gertisser, T. Thordarson, M. R. Rampino, and J. A. Wolff (2004), Magma volume, volatile emissions, and stratospheric aerosols from the 1815 eruption of Tambora, *Geophys. Res. Lett.*, *31*, L20608, doi:10.1029/2004GL020925.

Sheng, J.-X., D. K. Weisenstein, B.-P. Luo, E. Rozanov, F. Arfeuille, and T. Peter (2015), A perturbed parameter model ensemble to investigate Mt. Pinatubo's 1991 initial sulfur mass emission, *Atmos. Chem. Phys.*, *15*, 11,501–11,512, doi:10.5194/acp-15-11501-2015.

Soden, B. J., R. T. Wetherald, G. L. Stenchikov, and A. Robock (2002), Global cooling after the eruptions of Mount Pinatubo: A test of climate feedback by water vapor, *Science*, *296*(5568), 727–730, doi:10.1126/science.296.5568.727.

Spencer, R. W., F. J. LaFontaine, T. DeFelice, and F. J. Wentz (1998), Tropical oceanic precipitation changes after the 1991 Pinatubo eruption, *J. Atmos. Sci.*, *55*, 1707–1713, doi:10.1175/1520-0469(1998)055<1707:TOPCAT>2.0.CO;2.

Stenchikov, G. L., I. Kirchner, A. Robock, H.-F. Graf, J. C. Antuña, R. G. Grainger, A. Lambert, and L. Thomason (1998), Radiative forcing from the 1991 Mount Pinatubo volcanic eruption, *J. Geophys. Res.*, *103*(D12), 13,837–13,857, doi:10.1029/98JD00693.

Stowe, L. L., R. M. Carey, and P. P. Pellegriao (1992), Monitoring the Mt. Pinatubo aerosol layer with NOAA/11 AVHRR data, *Geophys. Res. Lett.*, *19*(2), 159–162, doi:10.1029/91GL02958.

Taylor, K. E., R. J. Stouffer, and G. A. Meehl (2012), An overview of CMIP5 and the experiment design, *Bull. Am. Meteorol. Soc.*, *93*, 485–498, doi:10.1175/BAMS-D-11-00094.1.

Timmreck, C., H. Graf, and I. Kirchner (1999a), A one and half year interactive MA/ECHAM4 simulation of Mount Pinatubo aerosol, *J. Geophys. Res.*, *104*(D8), 9337–9359, doi:10.1029/1999JD900088.

Timmreck, C., H. Graf, and J. Feichter (1999b), Simulation of Mt. Pinatubo volcanic aerosol with the Hamburg climate model ECHAM4, *Theor. Appl. Climatol.*, *62*(3–4), 85–108, doi:10.1007/s007040050076.

Toohey, M., K. Krüger, U. Niemeier, and C. Timmreck (2011), The influence of eruption season on the global aerosol evolution and radiative impact of tropical volcanic eruptions, *Atmos. Chem. Phys.*, *11*, 12,351–12,367, doi:10.5194/acp-11-12351-2011.

Trenberth, K. E., and A. Dai (2007), Effects of the Mount Pinatubo volcanic eruption on the hydrological cycle as an analog of geoengineering, *Geophys. Res. Lett.*, *34*, L15702, doi:10.1029/2007GL030524.

Trepte, C. R., and M. H. Hitchman (1992), Tropical stratospheric circulation deduced from satellite aerosol data, *Nature*, *355*, 626–628, doi:10.1038/355626a0.

Trepte, C. R., R. E. Veiga, and M. P. McCormick (1993), The poleward dispersal of Mount Pinatubo volcanic aerosol, *J. Geophys. Res.*, *98*(D10), 18, 563–18, 573, doi:10.1029/93JD01362.

Watanabe, T., and K. Yamazaki (2012), Influence of the anticyclonic anomaly in the subtropical jet over the Western Tibetan Plateau on the intraseasonal variability of the summer Asian monsoon in early summer, *J. Clim.*, *25*, 1291–1303, doi:10.1175/JCLI-D-11-00036.1.

Watson, P. A. G., and L. J. Gray (2014), The stratospheric wintertime response to applied extratropical torques and its relationship with the annular mode, *Clim. Dyn.*, *44*, 2513–2537, doi:10.1007/s00382-014-2359-2.

Weisenstein, D. K., J. E. Penner, M. Herzog, and X. Liu (2007), Global 2-D intercomparison of sectional and modal aerosol modules, *Atmos. Chem. Phys.*, *7*, 2339–2355, doi:10.5194/acp-7-2339-2007.

Yanai, M., C. Li, and Z. Song (1992), Seasonal heating of the Tibetan Plateau and its effects on the evolution of the Asian summer monsoon, *J. Meteorol. Soc. Jpn.*, *70*, 319–351.

Young, R. E., H. Houben, and O. B. Toon (1994), Radiatively forced dispersion of the Mt. Pinatubo volcanic cloud and induced temperature perturbations in the stratosphere during the first few months following the eruption, *Geophys. Res. Lett.*, *21*(5), 369–372, doi:10.1029/93GL03302.

Zhao, T. X.-P., P. K. Chan, and A. K. Heidinger (2013), A global survey of the effect of cloud contamination on the aerosol optical thickness and its long-term trend derived from operational AVHRR satellite observations, *J. Geophys. Res. Atmos.*, *118*, 2849–2857, doi:10.1002/jgrd.50278.